

PROCEEDINGS OF THE INTERNATIONAL CONFERENCE ON
INSTRUMENTATION FOR COLLIDING BEAM PHYSICS

February 17-23, 1982

Stanford Linear Accelerator Center

Stanford, California

June 1982

Prepared for the Department of Energy

Under Contract Number DE-AC03-76SF00515

Printed in the United States of America. Available from the National
Technical Information Service, U.S. Department of Commerce, 5285 Port
Royal Road, Springfield, VA 22161. Price: Printed Copy A12,
Microfiche A01.

DISCLAIMER

This report was prepared as an account of work sponsored by an agency of the United States Government. Neither the United States Government nor any agency thereof, nor any of their employees, makes any warranty, express or implied, or assumes any legal liability or responsibility for the accuracy, completeness, or usefulness of any information, apparatus, product, or process disclosed, or represents that its use would not infringe privately owned rights. Reference herein to any specific commercial product, process, or service by trade name, trademark, manufacturer, or otherwise does not necessarily constitute or imply its endorsement, recommendation, or favoring by the United States Government or any agency thereof. The views and opinions of authors expressed herein do not necessarily state or reflect those of the United States Government or any agency thereof.

MASTER

EP

DISTRIBUTION OF THIS DOCUMENT IS UNLIMITED

INTERNATIONAL CONFERENCE ON
INSTRUMENTATION FOR COLLIDING BEAM PHYSICS

CHAIRMAN

G. J. FELDMAN

PROCEEDINGS

W. W. ASH

PROGRAM COMMITTEE

D. G. COYNE

H. C. DESTAEBLER

D. G. HITLIN

J. KIRKBY

D. R. NYGREN

INTERNATIONAL ADVISORY COMMITTEE

J. E. AUGUSTIN

F. BONAUDI

S. IWATA

E. LOHRMANN

T. LUDLAM

J. PEOPLES

V. A. SIDOROV

R. H. SIEMANN

K. STRAUCH

W. G. YAN

FOREWORD

The International Conference on Instrumentation for Colliding Beam Physics was held at SLAC from February 17 to 23, 1982. It was the second of a series of conferences, the first of which was held at Novosibirsk in 1977. This second meeting had a larger and more cosmopolitan attendance than the first mainly due to the enormous growth in interest in colliding beam physics in the intervening five years. During this period three new electron colliders, CESR, PEP, and PETRA, were commissioned and hadron collisions were begun in the SPS. Moreover, almost every center of particle physics in the world initiated plans to build at least one new colliding beam device; in alphabetical order, the acronyms include BEPC, CESR II, CHEER, HERA, ISABELLE, LEP, SLC, TEVATRON I, TRISTAN, UNK, and VLEPP. The timing of this conference brought together the first results from new detectors at existing facilities and the development of new ideas for detectors for the future facilities. In all, 140 physicists and engineers from 10 countries in 3 continents attended: 76 from North America, 43 from Europe, and 21 from Asia.

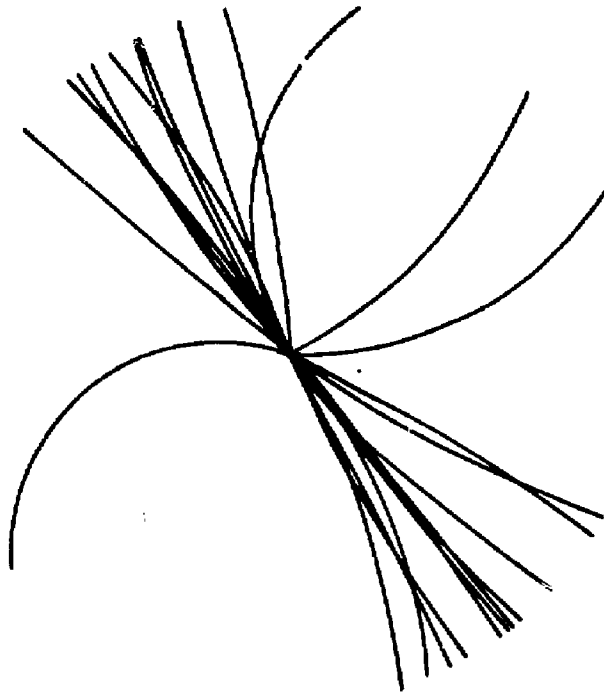
Fifty talks were presented at the Conference, 47 of which are printed here. We regret that we did not receive the written versions of three excellent contributions to the Conference in time to include them in these Proceedings. These were "Recent Developments in Ring Imaging Čerenkov Counters" by T. Ypsilantis, "Readout Methods for Calorimeters" by V. Radeka, and "Application of Geiger Mode for Calorimeters" by W. Carithers.

An innovation at this Conference was the idea of having panel discussions lead by a "provocateur" who was charged with summarizing the issues and focusing the discussion. The provocateurs all took their assignments seriously, provoking the speakers into a critical examination of their ideas. This led to the most informative set of panel discussions that I have ever heard. I extend the Conference's thanks to the provocateurs for their fine efforts: E. Gabathuler on Tracking, D. Ritson on dE/dx , D. Hartill on Čerenkov, Transition Radiation, and Timing, M. Breidenbach on Electronics, and S. Iwata on Calorimeters.

Finally, I wish to extend my personal thanks to all of those who worked on the Conference with diligence and enthusiasm: to the Program Committee and the International Advisory Committee whose wise selection of speakers and topics set the tone of meeting; to Bill Ash, whose untiring efforts in compiling these Proceedings led to their prompt publication; and to Ruth Thor Nelson, Nina Adelman, and Ute Hayes, the Conference secretariat, whose careful and innovative planning never ceased to amaze and delight us.

Gary Feldman
Conference Chairman

May 1982



The conference logo is a Monte Carlo simulation of the decay of a Z^0 boson produced at rest in an e^+e^- annihilation. Twenty-four charged tracks can be seen bending in an axial magnetic field. The event, which shows a two-jet structure from the decay of the Z^0 to a $d\bar{d}$ quark-antiquark pair, is not exceptional in its physics content, but it will challenge the mettle of any detector which attempts to reconstruct it fully. The jet compositions are $(\omega 4\rho^0 \rho^+ \pi^0 \pi^+ \pi^-)$ and $(\bar{K}^{*0} K^{*+} 2\omega \rho^0 \pi^+ 3\pi^-)$.

WELCOMING ADDRESS

Let me welcome you to the International Conference on Instrumentation for Colliding Beam Physics. This is a sequel to the very successful Conference on Experimental Methods for Electron-Positron Storage Rings held at Novosibirsk in September 1977. We wish to continue the tradition that this series of meetings should offer opportunities for the conferees to compare their experiences and expectations in the field. As much as we owe a debt of gratitude to our friends from Novosibirsk for having initiated this series, the roots of our subject of study go even deeper. Let me show you two quotations from old and new Chinese cultures which not only predicted the ever-changing nature of science but also forecast the need for large solid angle detectors which are the principal subject of this Conference.

道可道	非常道
<i>the principle that can be stated</i>	<i>cannot be the absolute principle.</i>
名可名	非常名
<i>the name that can be given</i>	<i>cannot be the permanent name.</i>

A frog in a well says, "The sky is no bigger than the mouth of a well."

That is untrue, for the sky is not just the size of the mouth of the well.

If it said, "A part of the sky is the size of the mouth of a well,"

That would be true, for it tallies with the facts.

It is characteristic that the most successful specialized conferences lose their specialization in time. Let me give you an example: the series of electron-photon conferences was amplified in time to incorporate weak interactions, thus incorporating those two fields which became the primary focus as a result of great recent discoveries. As a result the agenda of that conference became almost indistinguishable from that of the "general" high energy physics conferences. Similarly the topic of the Novosibirsk conference has been broadened as indicated by the change in title to include instrumentation for all colliders. Since the relative importance of colliding beam physics tends to overshadow most, although not all, stationary target physics, there is a threat that the agenda of this Conference will become indistinguishable from a general high energy physics instrumentation conference!

We are pleased to welcome participants from eight countries to this "small" conference of not quite 100 participants. I hope you exchange most useful information and new ideas, and above all, have a good time.

W. K. H. Panofsky
Director, SLAC



TABLE OF CONTENTS

TRACKING

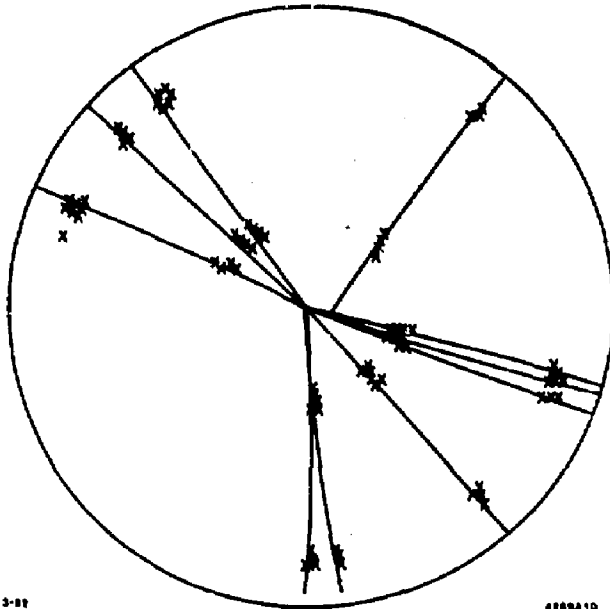
Limits on the Accuracy of Drift Chambers and Calibration Beams	B. Sadoulet	1
Tradeoffs in Drift Chamber Design	A. Seiden	12
The UAl Central Detector	M. Calvetti	16
The MPS II Drift Chamber System	E. Flatner	24
The Mark II Secondary Vertex Detector	J. Jaros	29
The Time Expansion Chamber as a High Precision Drift Chamber	A. H. Walenta	34
The Position Resolution of the Time Projection Chamber at TRIUMF	C. K. Hargrove	41
Tracking with the PEP-4 TPC	A. Barbaro-Galtieri	46
Charge Coupled Devices as High Resolution Position Sensitive Detectors	A. Bross	51
High Resolution Silicon Detectors	B. D. Hyams	56
Proportional Chamber Operation at Low Temperatures	E. P. Solodov	58
ENERGY LOSS -- DE/DX		
Relativistic Particle Identification by dE/dx : the Fruits of Experience with ISIS	W. W. M. Allison	61
Design and Performance of the CLEO dE/dx System	R. D. Ehrlich	71
Particle Identification by dE/dx Measurement in JADE	A. Wagner	76
dE/dx Measurements with ARGUS	H. Hasemann	80
Energy Loss Measurements in the PEP TPC	G. R. Lynch	85
Particle Identification by dE/dx Sampling in Neon	I. Lehrs	90
Particle Identification with a Fine Sampling Ionization Loss Detector	T. Ludlum	96

dE/dx Measurement with Fine Sampling	T. Ohshima	101
Particle Identification and Tracking in Central Detectors	D. Hartill	106
Particle Identification using Ionization Sampling in the Region of Relativistic Rise	Y. Goldschmidt-Clermont	109
CERENKOV, TIMING, AND TRANSITION RADIATION TECHNIQUE		
Preparation of Silica Aerogel and its Application in the TASSO Cerenkov Counters	G. Poelz	113
The HRS Cerenkov Counters	N. Harnew	118
A Transition Radiation Detector for LEP Experiments	W. Struczinski	122
Spark Counter with a Localized Discharge	Yu. N. Pestov	127
Results from the SLAC PSC Development Program	W. Atwood	132
ELECTRONICS		
Microprocessors in Detectors and Analysis	E. J. Siskind	137
FASTBUS at the Front End	R. Downing	142
Status of Event Selection Processors at CERN	C. Verkerk	147
UAL Data Acquisition System	S. Cittolin	151
Trigger Processors for Hadron Colliders	I. Gaines	157
Data Driven Processing	W. Sippach	162
CALORIMETRY		
The UA2 Central Calorimeter	A. Clark	169
The MAC Calorimeters and Applications	W. T. Ford	174
The TASSO Liquid Argon Calorimeters	A. Ladage	180
HARP: High Pressure Argon Readout for Calorimeters	T. Ludlum	185
Saturated Avalanche Calorimeter	M. Atac	189

Plastic Streamer Tube Calorimeters	E. Iarocci	195
Intelligent Towers for Electromagnetic Showers	G. Brandenburg	200
Long Drift Techniques for Calorimeters	L. Price	206
Progress in High Density Projection Chambers	O. Ullaland	212
Properties of Bismuth Germanate and Its Use in Electromagnetic Calorimetry	M. Cavalli-Sforza	216
Photodiode Readout of BGO and NaI(Tl)	H. Vogel	221
POLARIZATION, BACKGROUNDS AND MAGNETS		
Techniques for Longitudinal Polarization in Electron Storage Rings	J. Buon	225
Longitudinally Polarized Colliding Beams	A. N. Skrinsky	230
Background Conditions in the Detector MD-1 with Perpendicular Magnetic Field	A. P. Onuchin	241
Superconducting Magnets for Detectors	R. Kephart	246
LIST OF PARTICIPANTS		257



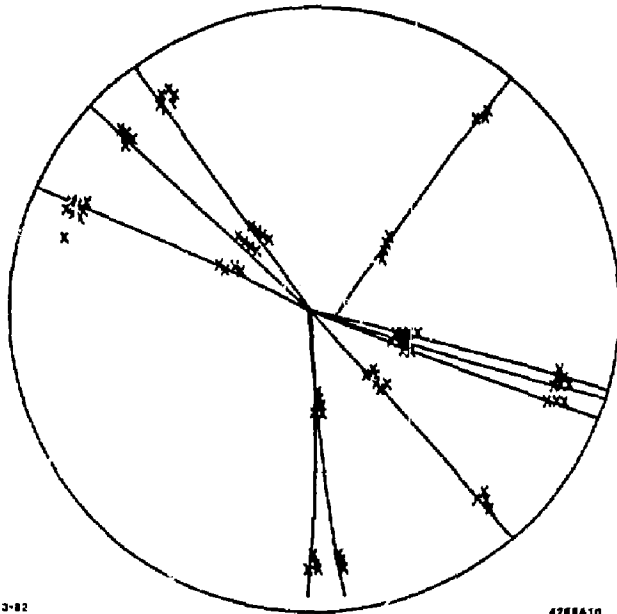
TRACKING TECHNIQUES



3-87

4880A1D

TRACKING TECHNIQUES



3-82

4288A10

LIMITS ON THE ACCURACY OF DRIFT CHAMBERS AND CALIBRATION BEAMS

Bernard Sadoulet
CERN, Geneva, Switzerland

1. Introduction

A glance at the letters of intent for experiments at LEP which have been submitted to CERN on 31 January 1982 show that drift chambers of one type or another are still very popular and are considered as being the main candidate for detecting charged particles even eight years from now.

The understanding of intrinsic limits on the spatial accuracy of drift chambers, and the development of new methods for calibrating them, are therefore still relevant. The present talk attempts to review the state of the art.

In order to see what are the main questions to be asked, I have summarized in Table 1 the main characteristics of the drift-chamber detectors proposed for LEP. These detectors fall into two classes:

- i) Extremely accurate detectors for vertex reconstruction around the interaction region. Precision as

high as 30 μm is looked for and two-particle resolution of 200 μm is claimed. In this field, competition from multi-electron silicon detectors¹, which could reach 10 μm accuracy and 150 μm resolution, is severe.

- ii) Very large detectors of the projection-chamber or imaging-chamber type, where the moderate accuracy of individual measurement ($\sigma_M \approx 200 \mu\text{m}$) is compensated by the relatively large number of points on each track. The accuracy of the momentum measurement is no longer limited by the drift-time precision but by the control of systematics at the level of 30 to 50 μm on the sagitta.

Hence the two questions studied in this talk:

- i) What are the fundamental limits on the accuracy and the two-particle resolution in a gaseous drift chamber (Section 2)? How can performances be improved, by the proper choice of gas and running

Table 1

A glance at LEP letters of intent

Collab.	Detector	Method	Dimensions	Accuracy	Two-particle resolution
Bari, etc. ^{*)}	Minivertex	Silicon			
	Main	TPC 1 atm, 1.5 T	$0.2 < R < 1.8 \text{ m}$ $\lambda = 4.4 \text{ m}$ $d = 2.2 \text{ m}$	$\sigma_M \leq 200 \mu\text{m}$ (21 space pts)	$R\phi = 1.2\text{-}2.4 \text{ cm}$ $z = 1.5 \text{ cm}$
or Axial wires 1 atm, 1.5 T		$0.2 < R < 1.8 \text{ m}$ $\lambda = 4.4 \text{ m}$ $d = 8 \text{ cm}$	$\sigma_M \leq 250 \mu\text{m}$ (192 wires)	$R\phi = 0.75 \text{ cm}$	
OPAL	Main	JADE-like 4 atm, 1 T	$R < 1.6 \text{ m}$	$\sigma_M = 160 \mu\text{m}$ (160 wires)	$R\phi = 0.2 \text{ cm}$
Lund, etc. ^{**)}	Minivertex	Time expansion + side wire pick ups or silicon	$0.065 < R < 0.125$ $\lambda = 0.45 \text{ m}$ $d = 3 \text{ mm}$ $0.15 < R < 0.5$ $d = 6 \text{ mm}$	$\sigma_M = 30 \mu\text{m}$ $\sigma_M = 100 \mu\text{m}$	$R\phi = 0.02 \text{ cm}$
	Main (μ)	Planar imaging chamber	$R < 3.8 \text{ m}$ $\lambda = 6 \text{ m}$	$\sigma_M \sim 250 \mu\text{m}$ $\Rightarrow \sigma_B \leq 30 \mu\text{m}$	
Electra	Minivertex	Axial drift wires	$R < 0.38 \text{ m}$ $\lambda = 2 \text{ m}$	$\sigma_M = 50 \mu\text{m}$ (24 wires)	
	Main	Conventional drift chambers with stereo, 1 T	$R < 1.2 \text{ m}$ $\lambda = 4.5 \text{ m}$ $d = 1 \text{ cm}$	$\sigma_M = 150 \mu\text{m}$ (40 wires)	
DELPHI	Minivertex	Drift chambers with cathode strips	$R < 0.3 \text{ m}$	$\sigma_M = 100 \mu\text{m}$	$R\phi = 1 \text{ mm}$
	Main	TPC 1 atm, 1.2 T	$0.3 < R < 1.26 \text{ m}$	$\sigma_M = 250 \mu\text{m}$	
LOGIC	Main	JADE-like	$0.1 < R < 0.7 \text{ m}$ $\lambda = 2 \text{ m}$	(64 wires)	

*) Bari-CLN-Demokritos Athens-Dortmund-Ecole Polytechnique-Falaiseau-Edinburgh-Glasgow-Heidelberg-Lancaster-MPI Munich-Orsay-Pisa-Rutherford-Saclay-Sheffield-Trieste-Turin-Westfield College London-Wisconsin Collaboration.

**) Lund-Siegen-Max Planck Institute-NIKHEF-ETH-Geneva-Lausanne-LAPP-Frascati-Florence-Madrid-Beijing-Hofei-Hawaii-CalTech-Oklahoma-Ohio State-Carnegie Mellon-Princeton-Yale-Harvard-MIT Collaboration.

conditions, or by better detection methods (Section 3)?

- ii) What, in practice, are the limits encountered in large detectors? Is it possible to limit effects of systematics by proper design of the detector (Section 4)? Can X-ray and UV calibration beams be used (Section 5)? Since most of the other talks presented at this conference will deal with specific practical aspects, I will emphasize mainly the fundamental aspects and the understanding of the basic mechanisms.

* * *

It is clear that, in this review, most of the quoted results and explanations are not mine, and I profited very much from discussions with many colleagues. I would like to thank especially G. Charpak, B.A. Dolgoshein, G. Rubbia, H.A. Walenta and T. Ypsilantis, from whom I have borrowed many ideas put forward in this talk.

2. Fundamental Processes in Drift Chambers

Let us recall the basic processes at work in a drift chamber². Electrons are produced along charged particle trajectories (Fig. 1). They then drift in an electric field towards a detecting cell where they are observed. More and more often the detection is bidimensional, which together with the drift-time measurement allows the reconstruction in space of the extraction point of the original electrons. Let us review each of the successive phases in turn.

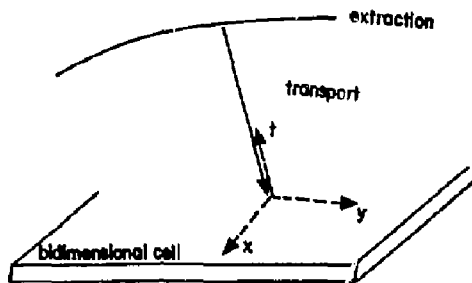


Fig. 1. A drift chamber of the projection or imaging type.

2.1 Extraction and Thermalization of the Electrons

The extraction of primary electrons by a charged particle of velocity βc is now well understood quantitatively³ as the result of an exchange of a virtual photon which ionizes the gas molecule. The differential cross-section can be written as

$$\frac{d\sigma}{dE} = \int \frac{dp}{E/\beta c} f(E,p) \left(\frac{1}{E^2 - p^2 c^2} \right)^2 \sigma_Y(E,p), \quad (1)$$

where E and p are the energy and momentum transferred to the extracted electron; $f(E,p)$ describes the particle-photon vertex; $\sigma_Y(E,p)$ is the off-shell photoionization of the gas molecule which can be approximated³ by the on-shell photoionization cross-section at low

energy (shown in Fig. 2a for argon) and the Rutherford cross-section for large E where electrons are quasi-free. The result for argon is given in Fig. 2b. The various M, L, and K shell peaks appear very clearly.

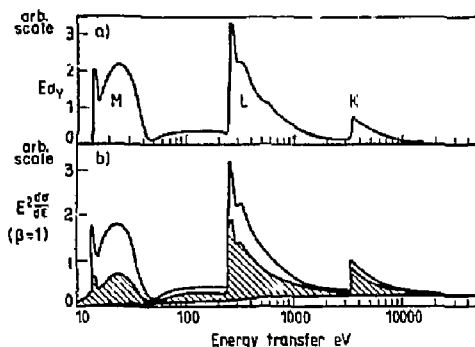


Fig. 2. a) Photoionization cross-section for argon. b) Differential cross-section for the extraction of electrons by a relativistic charge-1 particle (Ref. 3).

The energy is deposited in a discrete way at the macroscopic level. For instance, in argon there are about 30 electrons per cm extracted from the M shell with a typical energy of 30 eV, about 1.5 cm from the L shell with 400 eV, 0.03 cm from the K shell with a typical energy of 4 keV, and 0.03 cm for δ -rays above 4 keV.

Then these electrons slow down by inelastic collisions, through which they extract both photons and electrons until they reach an equilibrium temperature with the electric field and begin to drift. The total number of electrons at the end of the thermalization process is on an average proportional to the deposited energy, with a fairly small fluctuation

$$n_T = \frac{\Delta E}{E_1}. \quad (2)$$

For argon n_T is of the order of 100 electrons/cm.

What matters for drift-chamber application is the distance reached transversally by the slowing down electrons. This practical range of their trajectories, which are convoluted by multiple scattering, is not very well studied either theoretically or experimentally. The best data available to my knowledge are the measurements of absorption lengths of low-energy electrons in gases by Lenard⁴, quoted by Furr et al.⁵. According to this result, in argon at atmospheric pressure one gets a mean absorption length smaller than 0.5 μ m for an M-shell electron, about 1 μ m for an L shell electron of 400 eV, and 15 μ m for a K-shell or δ -ray electron of 4 keV. Extrapolations from results in light materials⁶ give absorption lengths which are 10 to 20 times longer. However, this shows that for the more numerous electrons (M and L shell electrons) the practical range is very small and the half radius of the electron blob is usually of the order of 10 to 20 μ m at most at nominal pressure and temperature.

2.2 The Drift Region

In the drift region, electrons make a random walk between the molecules. Let us first discuss their behaviour in the absence of magnetic field. They are accelerated between successive collisions in which they lose part of their energy and their initial direction. They can be described by the distribution $F(v, \cos \theta)$ of their random velocity v and their angle θ with the electric field. In the absence of magnetic field their drift velocity w_L (much smaller than their random velocity) is then

$$w_L = \int v \cos \theta F(v, \cos \theta) dv d \cos \theta \quad (3)$$

and their mobility is $\mu = w_L/E$.

Their fluctuation around the average position $z = z_0 + w_L t$ (z along the electric field) is controlled by two diffusion coefficients D_T and D_L

$$\frac{d\langle z^2 \rangle}{dt} = 2D_L \quad (4)$$

$$\frac{d\langle \delta x^2 \rangle}{dt} = \frac{d\langle \delta y^2 \rangle}{dt} = 2D_T$$

D_T is given by

$$D_T = \int \frac{\lambda v}{3} F(v, \cos \theta) ,$$

where λ is the mean free path. One can also introduce the characteristic energy

$$\epsilon_K = eD_T/\mu, \quad (5)$$

which is related to the average energy of electrons. It is bounded from below¹ by kT , which therefore means that the transverse diffusion of an electron cloud after a drift distance z

$$\sigma_x = \sigma_y = \sqrt{\frac{2D_T z}{w}} = \sqrt{\frac{2\epsilon_K z}{eE}} \quad (6)$$

is bounded by

$$\sigma_x = \sigma_y = \sqrt{\frac{2kTz}{eE}}. \quad (7)$$

Figure 3 gives experimental measures of D_T and some theoretical estimates². The longitudinal diffusion coefficient is given by a more complicated expression¹. It is different from the transverse coefficient because electrons which have by fluctuation gone faster than the average drift velocity are more energetic since the work of the electric field has been bigger. They are therefore less affected by this field, and their drift velocity is smaller than the average one. Therefore one expects that

$$D_L \leq D_T$$

This statement is true provided the electron momentum transfer cross-section does not decrease too fast and it can be shown on semiquantitative models¹ that the faster the cross-section increases, the smaller is the ratio D_L/D_T .

The gain can be very significant, as shown in Fig. 4 for argon. At low energy $eD_L/\mu = eD_T/\mu = kT$ when the electrons are in thermal equilibrium with the gas. Then the longitudinal diffusion increases faster than the transverse diffusion because the cross-section decreases. At $E/N = 4 \times 10^{-15}$ V/cm² the mean electron

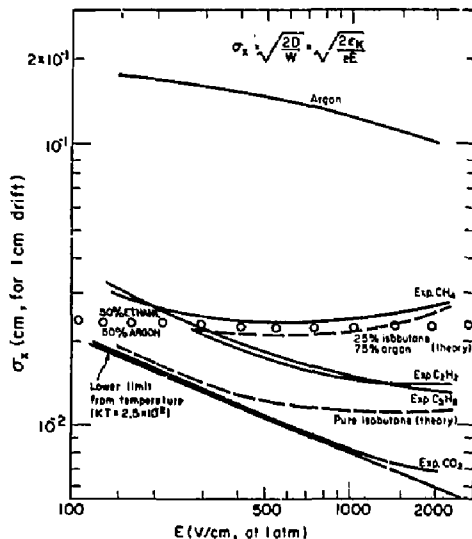


Fig. 3. Transverse diffusion σ_x after 1 cm of drift for various gases.

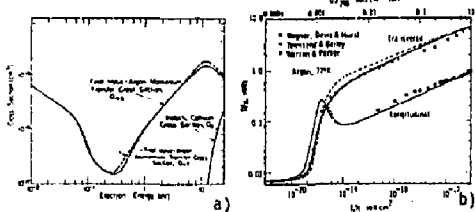


Fig. 4. a) Momentum transfer cross-section for argon (e.g. Ref. 2). b) Transverse and longitudinal diffusion in argon (Ref. 7).

energy reaches 0.2 eV where the cross-section displays a minimum, and when the cross-section begins to increase D_L drops quite significantly to a value seven times smaller than D_T .

This behaviour of the cross-section is also responsible² for the saturation of the drift velocity in most argon hydrocarbon mixtures. Theoretically one expects therefore two situations

- i) In "cool" gases (e.g. CO_2) the electrons have temperatures of the order of kT ; D_L and D_T are comparable and low but, however, the drift velocity is proportional to the field.
- ii) In mixtures with saturated drift velocity, the electrons have higher temperatures but D_L can be significantly smaller than D_T .

In addition to the classical measurements of Wagner, Davis and Huret⁶, new measurements have been made recently by various high-energy physics groups⁵⁻¹².

As an example, Fig. 5 gives the longitudinal diffusion σ_z after 1 cm of drift for various gases.

Values of typically $\sigma_z = 250 \mu\text{m}/\text{cm}^{1/2}$ are obtained for an electric field between 500 V/cm and 1 kV/cm at normal pressure with argon-CO₂, argon-C₂H₆, and argon-C₃H₈. The value for argon-CH₄ is higher around 400 $\mu\text{m}/\text{cm}^{1/2}$. Pure organic vapour or CO₂ have significantly smaller diffusion.

When there is a magnetic field, electrons are not only accelerated by the electric field but are also deflected by the magnetic field. If the magnetic field is perpendicular to the electric field, electrons will drift at an angle α_D often written as

$$\tan \alpha_D = \frac{B}{E} v_D \quad (8)$$

where v_D is the so-called magnetic drift velocity which is somewhat larger than w_L in standard mixtures. The drift velocity w_L along the electric field is affected also, but usually the drift velocity along the electron trajectories is rather constant.

When the magnetic field is parallel to the electric field the transverse diffusion is decreased because the electrons have a tendency to curl in between collisions. However, the reduction factor which is approximately

$$1 + \frac{3}{2} \frac{B^2}{E^2} v_D^2$$

is usually quite close to one.

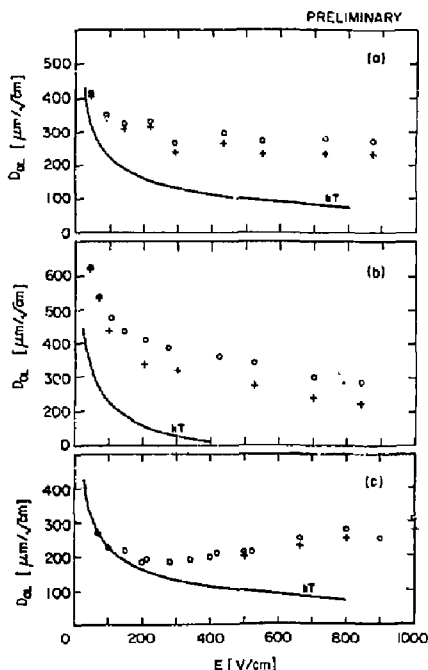


Fig. 5. Longitudinal diffusion σ_z after 1 cm of drift for various gases (Ref. 12): a) Argon C₂H₆ (50-50); b) argon CH₄ (80-20); c) argon CO₂ (80-20). Circles are raw measurements. Crosses are corrections for dispersion due to the differences of electron trajectories.

2.3 The Detecting Cell

After the drift region, the electrons arrive at the detecting cell. The usual method is to have them multiply in the high-field region surrounding a thin "sense" wire. This method has two consequences.

- i) Because the field is cylindrical around the sense wire, some electrons exiting from the drift region far from the sense wire will have to travel longer. Moreover they encounter regions of lower electric field. As a consequence the loci of equal time of arrival on the sense wire are not planes but rather cylinders. Therefore, even for tracks perpendicular to the average drift direction, extracted electrons do not arrive on the wire at the same time. Figure 6 shows as an example the case of the UAL detector in a field of 7 kG.

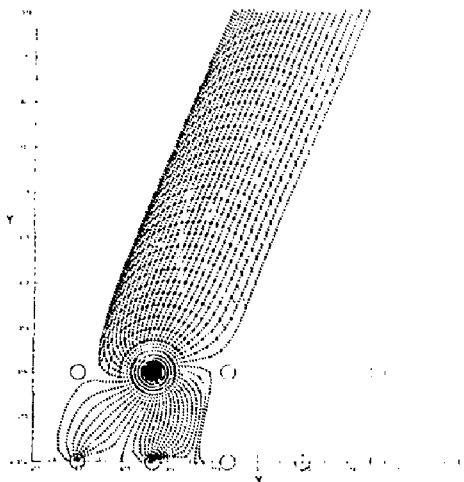


Fig. 6. Electron trajectories and loci of equal drift time from the sense wire in the central detector of UAL (electric field = 1.5 kV/cm, magnetic field = 7 kG).

- ii) The electric pulse which is recorded on the sense wire or on cathode pads is mainly due to the movement of the ions in the $1/r$ electric field around the wire. This gives to the electric current pulse a long tail in $1/r$ which without proper shaping limits two-particle resolution. Note that this tail is absent in the detection by scintillation light¹³.

Parallel-plate chambers¹⁴ where the multiplication occurs in a planar electric field do not have these problems. However, for tracks at an angle with the electric field, it is unavoidable that the electron clusters arrive in the detecting cell at different times.

In order to record the original position of the primary electron in space, two methods are used:

- i) Drift-time measurement with usually a constant threshold discriminator. The measurement is therefore sensitive to the longitudinal diffusion σ_z .

However, the measurement error σ_w is smaller. In a system that is sensitive to the first electron

$$\sigma_w = \frac{1.28 \sigma_k}{\sqrt{2 \log n}} \quad (9)$$

where n is the number of electrons in the cloud. However, if the centre of gravity was detected

$$\sigma_w = \frac{\sigma_z}{\sqrt{n}} \quad (10)$$

In practice, σ_w is smaller than σ_z by a factor of 2 to 3 yielding

$$\sigma_w \approx 80-125 \text{ } \mu\text{m/cm}^{1/2}$$

for usual argon-organic vapour mixtures and fields.

- ii) Centre of gravity with cathode-pad amplitude read-out. The measurement is sensitive to the transverse diffusion σ_x but, in the approximation where electrons are assumed to arrive at the same time, the centre of gravity is measured and

$$\sigma_w = \frac{\sigma_x}{\sqrt{n}}$$

In principle, better accuracies can be achieved with this method (if the preamplifier noise is small enough). However, if the track is at an angle to the sense wire, fluctuations in the primary ionization leads to substantial degradation of accuracy at low pressure¹⁵.

3. Ways to Improve the Accuracy and to Obtain Better Two-Particle Resolutions

The understanding of the various factors controlling accuracy and two-particle resolution is therefore rather good. There is not much which can be gained in the extraction mechanism of electrons. Most of the electrons have ranges smaller than 10 or 20 μm under normal conditions and the few per cent of long-range δ -rays can be rejected either by pulse height or by deviation from the fitted track.

3.1 Decreasing Diffusion

Quite significant gains can be achieved in principle on the transverse or longitudinal diffusion.

- i) A first obvious choice is to reject "hot" gases such as $\text{A}_2\text{-CH}_4$ mixtures where the diffusion is quite large.

It is clear that argon-organic vapour gives higher diffusion and should be abandoned in high-accuracy applications in favour of pure gases such as CO_2 ⁶, C_2H_4 ⁶, and C_6H_6 ².

In CO_2 (Figs. 7a, b) electrons are practically thermal, which means that the drift velocity is proportional to the electric field. It is a bad quencher, but adding a few per cent isobutane considerably improves proportional operation¹⁶.

Ethylene is a good candidate: electrons are not thermal and the drift velocity, although not saturated, does not vary too rapidly (Fig. 7d). It has the nice property of having a longitudinal diffusion which is much lower than the transverse diffusion and which is only slightly higher than that of CO_2 . In practice, a better quencher, such as methylal¹⁰, has to be added to the gas.

With these two gases, one can reach

$$\sigma_z = 80-100 \text{ } \mu\text{m/cm}^{1/2} \quad \text{at } 1 \text{ kV/cm}$$

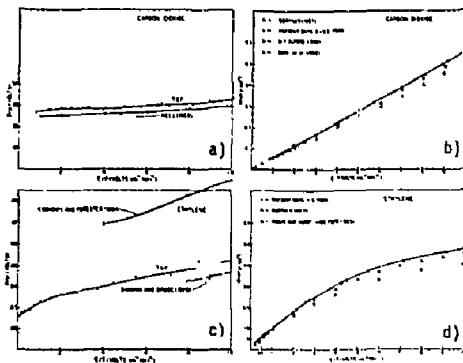


Fig. 7. Drift velocities and diffusion coefficients for CO_2 and C_2H_4 . The horizontal axes are E/P (volts/cm torr). The vertical axes for a) and c) are D/μ (volts); the vertical axes for b) and d) are W (cm/sec).

which is significantly smaller than the usual values obtained in argon-organic vapour mixtures.

- ii) The second parameter that we can use is the pressure P . The ratio eD/μ is a function of E/P only. Therefore increasing P and E proportionally allows one to decrease σ

$$\sigma_x = \sqrt{\frac{eD}{\mu E}} \propto \sqrt{\frac{1}{P}} \quad (E/P = \text{const.}) \quad (11)$$

In practice, for non-thermal gases, eD/μ is a weak function of E/P and nearly the full gain is obtained by increasing P only. In addition, the electron statistics are improved⁷, and through Eq. (9) the measurement accuracy will be improved even further. Dolgoshein and collaborators¹⁶ have attempted to make full use of this property by going to extreme pressures. By going to 300 atm in an argon (99%) + N_2 (1%) mixture they have reached

$$\sigma_z = 10-15 \text{ } \mu\text{m/cm}^{1/2}$$

(measured with scintillation light). Limits are encountered, however, in that direction. Multiple scattering in the wall of the pressure vessel weakens the power of such detectors. Moreover, whether scintillation or electron multiplication is used for detection, only a very small amount of quenching molecules can be added to the noble gas used, and the electron temperature is much higher than in the usual mixture.

It seems more promising to work at lower pressure, where these problems are simplified. This approach was explored rather systematically by Farr et al.⁵ and then used by the JADE Collaboration⁹ (whose experiment runs at 4 atm with an argon- CH_4 - C_6H_6 mixture, which is unfortunately not very good having $\sigma_z = 400 \text{ } \mu\text{m/cm}^{1/2}$ at 1 atm). Dolgoshein and collaborators¹⁷ have pushed this line of research quite far. Using CO_2 at 5 atm (with 0.3 atm of C_6H_6), they obtain a drift measurement accuracy of

$$\sigma_w = 25 \text{ } \mu\text{m}$$

over a drift length of 12 mm and a drift voltage of 3.5 kV. Allowing only clusters produced directly in line with the sense wire to reach it and shaping carefully the pulses, the two-particle resolution at 50% efficiency is 70 μm (the drift velocity w_L is approximately

5×10^5 cm/s). Increasing the pressure does not cause any improvement because of the setting up of parasitic phenomena which are not well understood yet (deviation from E/P behaviour, etc.).

We are not very far from multielectrode silicon detectors with a much simpler technology!

3.2 Can One Detect Original Clusters?

Another place for improvement is the detection method. In principle if the original clusters could be located in space, the measurement accuracy will finally be

$$\sigma_M = \frac{\sigma}{\sqrt{n}}$$

in spite of the difference of trajectories of the electrons. Since the total number of electrons n is fairly large (~ 100 cm under normal conditions), improvement by a factor as large as 3 or 5 can theoretically be made on the standard method. Moreover, since all the information is used magnificent two-particle resolution and dE/dx accuracy can, in principle, be obtained¹⁰.

What does cluster detection require?

- i) A careful shaping of the pulses with proper clipping of the 1/t tail. Full widths at half maximum of 15-20 ns have been achieved¹⁹.
- ii) The drift velocity should be low enough so that this width should be smaller than the natural width of the electron swarm that one wants to separate into clusters. In order to find the centre of gravity of the cloud, a width comparable to that of diffusion is presumably sufficient.

In order to decrease the drift velocity, Walenta¹⁸ proposed to reduce the electric field in the gap (time expansion chambers). Another method is to use a slow gas like CO₂. As we have seen, superb two-particle resolution can be achieved that way¹⁸.

- iii) Various methods have been proposed in order to get rid of the drift-time difference of clusters originating from different places along the track.

The simplest one is to prevent electrons with long drift paths from reaching the sense wire, either mechanically¹⁶ (Fig. 8a) or electrostatically (Fig. 8b). Of course one loses information.

A more ambitious approach has first been proposed, to my knowledge, by Walenta²⁰; he suggests measuring the angle of impact of the electron cluster on the sense wire, therefore allowing the reconstruction of its trajectory and correction for the longer path in the cylindrical region around the wire. This can be done by analysis of the induced pulses on cathode pads around the wire (Fig. 8c) or on two pick-up wires close to the anode (Fig. 8d). Experimentally for X-rays an angular resolution of $\Delta\alpha = 5^\circ$ FWHM has been achieved by measuring the difference between the two induced pulses. For charged particles such a difference would have to be normalized to the sum of the two pulses.

- iv) Although zero crossing methods can be tried²⁰, the discrete nature of the production of electrons will produce direct and induced pulses of a vast variety of shapes which cannot really be treated by hardware. It is probably more promising to use Flash ADCs to register directly the pulse height in bins comparable to the clipped pulse width.

We may therefore conclude that the technique exists to reconstruct cluster origins with accuracy limited by the longitudinal diffusion. It has to be shown in practice that the expected gain in accuracy can be achieved (in spite of local space-charge problems) and that the

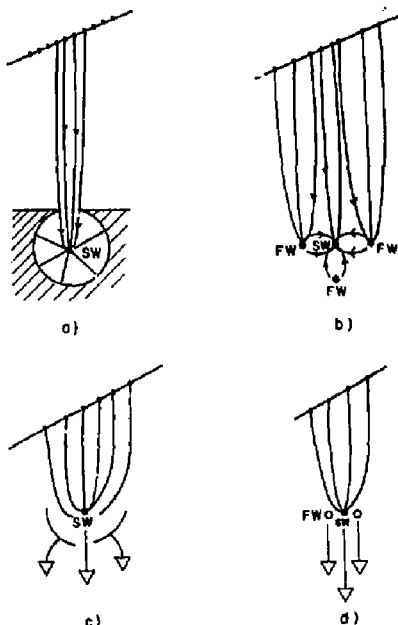


Fig. 8. How to get rid of drift time differences between clusters originating from different places along the track.

additional complexity is worth the effort. Note that this complexity is not much bigger than for cathode pads.

4. Systematic Errors in Drift Chambers

We now turn to more practical problems -- encountered especially in large detectors such as JADE, AFS, or UAL -- which are not limited by the measuring error of each sense wire but by systematics.

4.1 Mechanical Distortion and Stability

It is obvious that the bigger the detector, the more difficult it is to position the wires with sufficient accuracy. Moreover, electrostatic forces and gravity displace the wires by significant amounts in their middle.

In principle, the deviations from a theoretical detector are smooth and can be calibrated away. However, it is difficult to measure these distortions accurately from survey, for instance, and they should be sufficiently stable. Unfortunately, some deformations of large mechanical assemblies are due to temperature gradient, settlement of the supporting structure, etc., and vary with time.

Care has therefore to be exercised in limiting temperature variation of structural elements (good cooling of preamplifiers), in the proper design of the mechanics, and in the method of construction. Dynamic positioning of detector elements has been proposed^{20b}. Ultimately, zero-field tracks and calibration beams have to be used (see next section).

4.2 Knowledge and Stability of Drift Velocity and Drift Angle

For detectors with large drift gap the knowledge of drift velocity v_L and drift angle is critical. In order to get 100 μ m accuracy over 20 cm, v_L has to be known to 5×10^{-4} .

In order not to be too sensitive to temperature variation, distortion in electric field, and variation with gas mixture, the drift velocity should vary as slowly as possible with these parameters. However, the requirements are often contradictory.

In the case of an electric field perpendicular to the magnetic field, a more serious problem is encountered with the drift angle which varies rapidly with the magnetic field and the electric field [Eq. (8)]. One should therefore minimize its influence by reducing it as much as possible (high field, proper choice of gas) and by arranging the detector so that particle trajectories are perpendicular to drifting electron trajectories. In that case drift-angle errors are zero to second order ("cosine" error). The Bari-CERN-Demokritos Athens-Dortmund-Ecole Polytechnique Paris-Edinburgh-Glasgow-Heidelberg-Lancaster-MPI Munich-Orsay-Pisa-Rutherford-Saclay-Sheffield-Trieste-Turin-Westfield College London-Wisconsin Collaboration has proposed an original arrangement of drift cells (Fig. 9) for LEP which has this property for a solenoidal field.

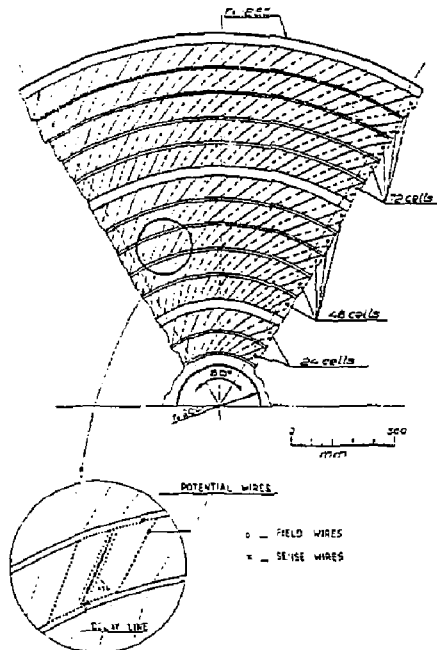


Fig. 9. Proposal for an axial wire drift chamber for LEP by the Bari-CERN-Demokritos Athens-Dortmund-Ecole Polytechnique Palaiseau-Edinburgh-Glasgow-Heidelberg-Lancaster-MPI Munich-Orsay-Pisa-Rutherford-Saclay-Sheffield-Turin-Trieste-Westfield College London-Wisconsin Collaboration (January 1982).

As a general comment, I would like to stress that, instead of trying to measure and monitor all parameters on which the drift velocity and drift angle depend, it is much better to measure them directly in the chamber. This can be done very well in two ways:

- i) The chambers can be designed in such a way as to be "autocalibrating". If tracks can cross different drift gaps, which have a constant and known relationship, the requirement that they line up is a powerful constraint on the drift velocity and drift angle. We have found this to be extremely useful in the UAL detector²¹. Note that this property is absent in normal TPCs or in the JADE-AFS bicycle-wheel structure, but present in designs such as the one of Fig. 9.
- ii) A second method²² is to use several laser beams at fixed and known angles with respect to each other. The drift velocity and drift angle have to be such that the angles are reconstructed correctly. This method is independent of angular correction which makes more direct methods impracticable.

4.3 Distortion of Electric Field

In projection or imaging chambers, where the drift gaps are fairly large, the electric field can be compared to the optics in a visual detector.

Tilting of the field direction or change in its magnitude (which changes drift velocity and, more seriously, drift angle) can be caused either by wrong design (too rough shaping of the field), mechanical displacement of the shaping electrodes, or charging up of insulating material in the chamber.

To these static effects could be added dynamical effects due to a positive ion-current in the gap. If ions are collected by shaping electrodes their voltage should be maintained by a divider with low enough impedance. And by their mere presence in the gap the ions create a global space charge which distorts the electric field²³ and is one of the most fundamental limits to the projection-chamber idea.

One can show²⁴ that for a given particle illumination and amplification the distortion goes as the cube of the drift gap. For detectors in a large background environment, gaps cannot be very large. This was, for instance, a reason to limit the gap in the UAL central detector to 18 cm since, with a uniform background of 10 μ m/cm/h, distortion of 110 μ m in the electric field direction (at an amplification of 10^3) is already caused. The avalanche gain is decreased by about 5%. Non-uniform illumination will produce stronger displacements.

Apart from decreasing the gap length, space charge can be controlled by decreasing the amplification and the proportion of ions which come back to the drift gap. This is difficult because they have a tendency (in the absence of magnetic field) to drift back along the same trajectories as the original electrons. Various pulsed shielding techniques, where pick-up on the sensing elements is minimized by proper balancing, have been proposed in order to turn on the amplification only for interesting events. However, they require a triggering device and may be difficult to implement in large systems.

Another method, since the main effect of space charge is through the drift angle, is to design chambers where errors in drift angle introduce only cosine-like errors.

Once all possible precautions have been taken in the design, one has to learn how to live with space charge. It can be noted that the maximum field distortion occurs in the middle of the drift gap (where it is corrected less by charge images). This induces an apparent curvature of the trajectories in a gap. With what we called an "autocalibrating" chamber, where tracks

usually cross several gaps, the tracks will appear as wiggly lines and fits will partially correct the effect.

One can also imagine using a UV laser beam fired regularly or immediately after a potentially interesting event, which would make a "photograph" of the space-charge situation in the detector.

4.4 Presence of Other Particles

For completeness, we should mention a fourth effect which makes life difficult in practical detectors, namely the presence of other particles close by the particle to be measured, or the fact that the particle is at a large angle to the drift direction.

An obvious first effect is the confusion between two particles, which suppresses a certain number of points along the trajectories and therefore degrades the pattern recognition capability and the accuracy. What we have said on the decrease of diffusion and the improvement of the detecting method for better two-particle resolution is relevant here.

However, more subtle effects occur through cross talk. Some cross talk occurs in the chamber through the movement of ions, which produces positive pulses on neighbouring wires. This can be decreased at the few per cent level by interposing field wires. Their decoupling, however, should be good enough to prevent any significant potential surge which by capacitance will induce a signal on the sense wires. Similarly precautions have to be taken on the packaging and decoupling of the electronics in order to prevent parasitic induction.

Another fundamental effect at work is the possibility of local space charge from previous avalanches disturbing the amplification of the successive electrons. This effect is mainly present for tracks at a large angle to the wire planes.

Here again, in order to extract all the information which is contained in the pulse, continuous pulse-height recording of the sense signal should be an extremely powerful tool.

5. Calibration Beams

In the last section, for many of the practical problems of distortion in large detectors, we have seen the utility of calibration beams. Drift chambers being by their nature analogue devices they need fiducial marks or better infinite momentum tracks to be drawn in them.

We will review briefly the status of the two suggestions made in that field.

5.1 Pulsed X-ray Beams

One possibility is to use pulsed X-rays, as proposed by Hoffmann and Rubbia²⁴. In order to penetrate a large volume of gas, the energy has to be higher than 30 keV. At this energy, electrons are extracted by means of two processes:

- i) the photoelectric effect, which unfortunately gives electrons of too high energy and range,
- ii) the Compton effect, which gives a continuum of energy between 0 and 10 keV (for 50 keV X-rays).

The fact that the energy spectrum is not well adapted to that of primary electrons extracted by charged particles is partially alleviated by two effects:

- i) The high-energy electrons give rather flat distribution in space, while the low-energy electrons have a small range and give a peak in the observed distribution of drift distance. This "Jacobian peak" effect is clearly seen in the results obtained in the UAL Central Detector at zero magnetic field (Fig. 10a).

- ii) The magnetic field can curl up high-energy electrons and clean up the tails (Fig. 10b). A FWHM of 1.5 mm is obtained.

Calibration with X-rays has the nice advantages that diffusion is negligible and that there is no need for any special entrance windows in light detectors. In addition, there is no significant deviation at the chamber interfaces. It can therefore be used to align devices over long distances.

On the other hand, the ionization pattern produced is very different from that of a charged particle. In order not to be saturated by the predominant photoelectric effect, a low enough intensity has to be used (in UAL, 400 X-rays/beam) extracting one useful Compton electron every few cells. This Compton electron gives rise, by thermalization, to a blob of electrons which have properties that are very different from those of the electrons spread along a charged particle track. In particular, they all arrive on the sense wire at the same time, but from pulse to pulse their measured drift time will fluctuate because they are not created along a locus of equal drift time to the wire (see Fig. 6). This can be contrasted with charged particle tracks where the closest primary electron is measured.

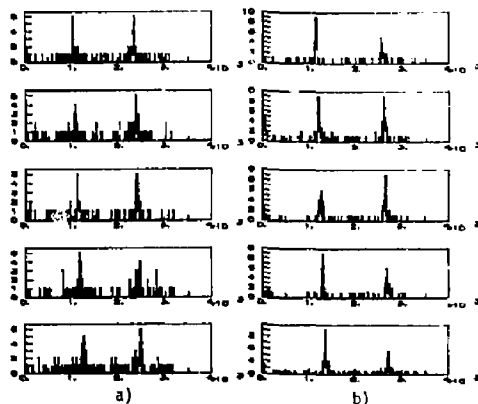


Fig. 10. UAL X-ray beams as seen on one wire of the central detector. Bin width 8 ns. Around 2000 shots a) at zero magnetic field, b) at a field of 2.8 kG.

Therefore the X-ray beam gives intrinsically a wide distribution, which has to be averaged over many pulses. The mean drift distance measured is different from that of a real track in a way which is dependent on the shape of the loci of equal drift time to the wire and on the magnetic field.

Let us add that we have noticed a large background of X-rays scattered in the collimator and in the walls of the detector.

5.2 UV Laser Beam

A much closer simulation of a charged track can, in principle, be made with pulsed UV laser beams.

Direct photoionization of some impurity has not been attempted up to now because with known substances, it was necessary to work in the vacuum UV region. However, the "discovery" of the tetrakis(dimethylamine)ethylene (TMAE) (see, for example Ref. 11) which has an ionization potential of 5.4 eV would allow the use of relatively close UV lamps (not necessarily lasers since the needed intensity is small) at $\lambda \approx 240$ nm. This line of research has not, to my knowledge, been explored yet.

Following the work of Seiler and collaborators²⁶ and independently of Bourotte and Sadoulet²⁷ all groups involved in the field have used double photon absorption which allows one to work in the close UV region (typically 340 nm).

The basic process is shown schematically in Fig. 11a. A first photon excites the molecule usually to a virtual state. This virtual state lives for a time $\tau \sim 10^{-18}$ s. If a second photon arrives during that time, it can ionize the virtual state. The ionization rate is, of course, quadratic with respect to the flux. When the intermediate states exist (Fig. 11b) cross-sections are much larger and one speaks of double-step processes. One can show²⁸ that if the latter process is at work, at low laser energy density, the pulse-height dependence is quadratic with the laser intensity. At an energy density dependent on the first-step excitation cross-section σ_1 and on the ratio between the laser pulse length and the lifetime of the intermediate state, the first transition is saturated and the dependence becomes linear.

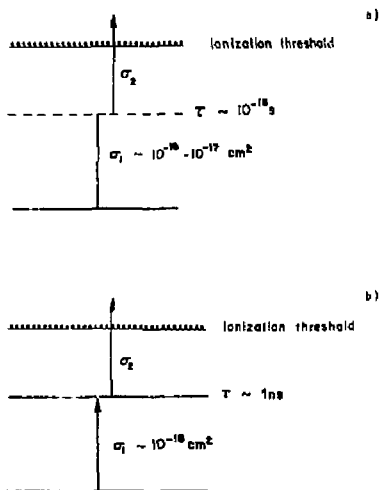


Fig. 11 Double-photon and double-step process.

This is indeed what is observed experimentally. Recently the UAL group have been doing careful measurements^{29,30} (Fig. 12) with a N₂ laser at 337 nm and a pulse length of 300 ps, and have found the expected behaviour with a transition between the quadratic and the linear region at 20 μJ/cm².

This result was obtained without specifically adding any impurity to the Ar-C₂H₂ mixture. If interpreted in terms of the above model, it gives a cross-section $\sigma_1 \approx 2 \times 10^{-16}$ cm² which is quite reasonable.

This measurement significantly clarifies the mystery of pulses, observed by various groups^{27,30} without specifically adding any impurities, which showed linear dependence: the laser energy density was indeed sufficient to be in the saturation region. However, the ionizable impurity is not yet identified. This is not surprising since with reasonable values of σ_2 (10^{-18} cm²) its concentration may be as low as 10^{-12} !

It is clear that, under these conditions, one would like to control the impurity, and for substances with the right excitation levels and the right auto-ionization levels, a very small concentration would be necessary to

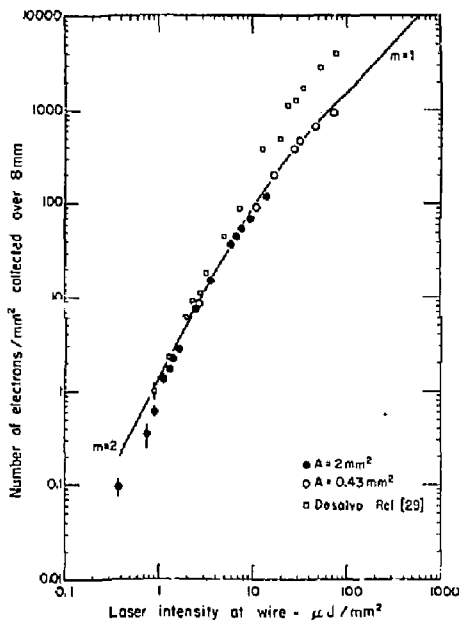


Fig. 12. Number of electrons per unit area and per 8 mm as a function of the laser energy density (Ref. 29). Squares: results of Ref. 29 obtained in a different chamber with a less accurate measurement of the area.

allow ionization by relatively small energy lasers. Up to now, no "magic" substance has yet been identified. Two compounds are known to increase ionization, Diethylaniline²⁷ (ionization potential = 7 eV) at a concentration of approximately 10^{-6} and Nickelocene²⁶ (ionization potential = 6.5 eV). We have recently used that impurity at the level of 1.5×10^{-6} concentration and observed a factor of 7 increase in the yield (Fig. 13). This is not much, but if the absorption spectrum of Nickelocene has a broad maximum^{31a} around 337 nm (3.67 eV) the photoionization spectrum^{31b} has a dip around (7.3 eV) (Fig. 14). We have tried without success other substances such as anthracene, tetracene, pentacene, α naphthylamine and ferrocene at a concentration of the order of 10^{-6} .

In order to use this method practically to calibrate large drift chambers, one faces two problems: in order to produce straight tracks over significant distances the laser beam has to be diffractively limited (at least in one direction); such a beam of 0.6 mm thickness at 337 nm can be used over 2 m). Unfortunately, diffractively limited lasers in this wavelength are very expensive (quadrupled Neodymium Yag lasers) and even N₂ lasers with very poor beam quality are not cheap. Hilke³⁰ made an important step forward by designing with Neracher of Multilasers* a double-cavity N₂ laser which is limited by diffraction in one direction.

Following in the same direction, the UAL Collaboration made a contract with Multilasers for the design of a very small two-cavity N₂ laser ($180 \times 120 \times 32$ mm³), which could be mounted directly on the chambers. The

* Multilasers, BP155, 1218 Grand-Saconnex, Geneva, Switzerland.

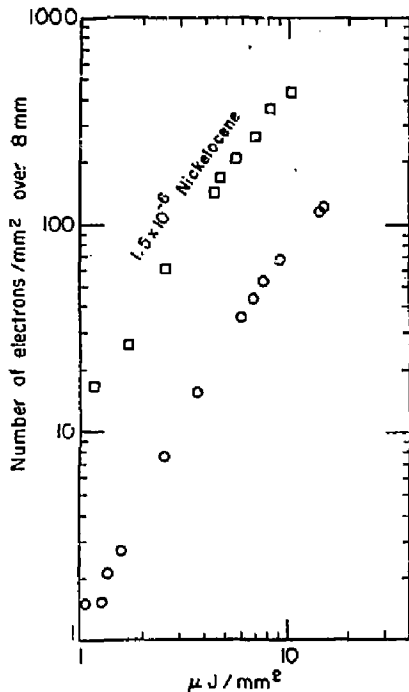


Fig. 13. Increase of signal when introducing Nickelocene at a concentration of 1.5×10^{-8} .

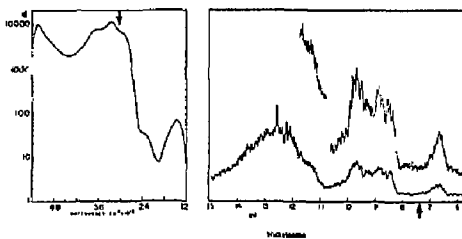


Fig. 14. a) Absorption spectrum of Nickelocene (in solution) around 337 nm. b) Photoionization spectrum of Nickelocene (from Ref. 31).

performance of the prototype is quite satisfactory. The energy in the dense spot is 30 μJ ; its dimension as a function of the distance is given in Fig. 15. It is nearly diffraction limited in the narrow direction and its FWHM of 0.7 mm is maintained over 1 m (within 0.1 mm). This shows that with an afocal system of magnification 1, making the image of the laser at 1 m, a straight beam (within 0.1 mm) can be achieved over 2 m. Moreover, over the same length its effective area will be constant. This is important because, with the laser intensity we have at our disposal and our requirements to make three beams per laser, we are working in the

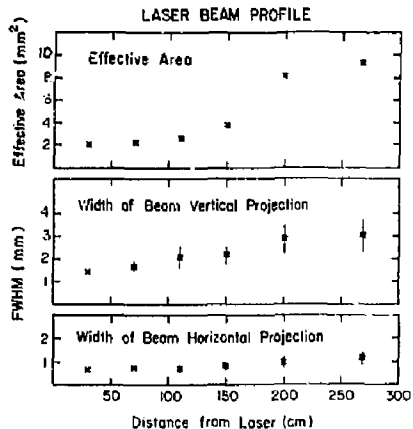


Fig. 15. Optical characteristics of the MOPA 2000 laser (designed by Multilasera) used by the UAL Collaboration.

quadratic region where the number of electrons per cm of track is inversely proportional to the area.

The cost of the laser components is sufficiently small that we can afford to build ourselves 40 lasers providing 120 beams in the UAL central detector.

References

1. B.D. Hyams, High Resolution in Silicon Strip Detector, Talk at this conference.
A. Bross, High Precision CCD detector, Talk at this conference.
2. See, for example,
V. Palladino and B. Sadoulet, Nucl. Instrum. Methods **128**, 323 (1975) and Lawrence Berkeley Laboratory Report LBL-3013 (1974).
F. Sauli, CERN 77-09 (1977).
B. Sadoulet, Phys. Scripta **23**, 433 (1980).
J. Jaros, SLG Workshop Notes CN # 51, SLAC (Dec. 1981).
3. W.W.M. Allison and J.H. Cobb, Ann. Rev. Nucl. Part. Sci. **30**, 253 (1980).
4. P. Lenard, Ann. Phys. (Germany) **12**, 714 (1903).
5. W. Farr et al., Nucl. Instrum. Methods **156**, 175 (1978).
6. E.J. Kobetich and R. Karz, Phys. Rev. **170**, 391 (1968).
7. J.H. Parker, Jr., and J.J. Lowke, Phys. Rev. **181**, 290 and 302 (1978).
8. E.B. Wagner, F.J. Davis and G.S. Hurst J. Chem. Phys. **47**, 3138 (1967).
9. H. Drum et al., Nucl. Instrum. Methods **176**, 333 (1980).
10. A.H. Walenta and C.M. Ma, quoted in Proc. ISABELLE 1981 Summer Workshop, Brookhaven National Laboratory, Upton, NY, BNL 51443 (1981).
11. E. Barrelet et al., A two-dimensional, single photoelectron drift detector for Cherenkov ring imaging, CERN-EP/82-09, 22 January 1982.
12. F. Piuze (CERN), private communication.
13. V.J. Baskakov et al., Nucl. Instrum. Methods **158**, 129 (1979).
A.J. Alikhanian et al., Nucl. Instrum. Methods **158**, 137 (1979).

14. G. Charpak and F. Sauli, Phys. Lett. 78B, 523 (1978).
15. A. Barbaro Galtieri, Tracking in the PEP-4 TPC, Talk at this conference.
G.K. Hargrove, Tests of the TRIUMF TPC, Talk at this conference.
16. B.A. Dolgoshein et al., Serpukhov preprint, 1981, and B.A. Dolgoshein, private communication.
17. B.A. Dolgoshein, private communication.
18. A.H. Walenta, IEEE Trans. Nucl. Sci. NS26, 73 (1979).
19. P. Rehak and A.H. Walenta, IEEE Trans. Nucl. Sci. NS27, 54 (1980).
T. Ludiam et al., Nucl. Instrum. Methods 180, 413 (1981).
20. a) A.H. Walenta, Talk given at the 1981 ISABELLE Summer Workshop at Brookhaven National Laboratory.
b) See also the LEP letter of intent from the Lund-Siegen-Max Planck Institute-NIKHEF-ETH-Geneva-Lausanne-LAPP-Frascati-Florence-Madrid-Beijing-Hofei-Hawaii-CalTech-Oklahoma State-Carnegie Mellon-Princeton-Yale-Harvard-MIT Collaboration.
21. N. Calvetti, Talk at this conference.
22. K. Sumorok, UAI Technical note 81-25, CERN 1981.
23. a) B. Sadoulet, Comments on charged particle detectors for the $\bar{p}p$ large solid angle detector, CERN $\bar{p}p$ Note 16 (May 1977).
b) D. Friedrich et al., Nucl. Instrum. Methods 158, 81 (1979).
c) M. Calvetti and B. Sadoulet, UAI Technical Note 80/06 CERN, 29 January 1980.
24. H. Hoffmann and C. Rubbia, CERN $\bar{p}p$ Note 54, August 1978.
25. M. Rijssenbeck, UAI Collaboration, private communication.
26. H. Anderhub, M.J. Davenport and P.G. Seiler, Nucl. Instrum. Methods 166, 581 (1979) and 176, 323 (1980).
27. J. Bourotte and B. Sadoulet, Nucl. Instrum. Methods 173, 463 (1980).
28. C. Cochet et al., to be published.
29. M. Dessalvo and R. Dessalvo, preprint CERN/SPS 81-23 (1981), submitted to Nucl. Instrum. Methods.
30. H. Hilke, Nucl. Instrum. Methods 174, 145 (1980).
31. a) D.A. Scott and R.S. Becker, J. Chem. Phys. 35, 516 (1961).
b) D.W. Turner et al., Molecular photoelectron spectroscopy (Wiley-Interscience, London, 1970).

TRADEOFFS IN DRIFT CHAMBER DESIGN*

Abraham Seiden
Institute for Particle Physics
University of California
Santa Cruz, California 95064

INTRODUCTION

For the physics of the future, at or above 100 GeV center of mass energy, tracking devices will need: 1) Good segmentation, since particle densities are large. 2) Many samples along each track for pattern recognition, momentum resolution, and possibly dE/dx measurement. As an example, to do a good job separating two high momentum tracks from hadronic decay of the Z^0 , angular segmentation ~ 10 mrad is required; typical nearest neighbor tracks of average momentum are separated by ~ 100 mrad.¹ If we multiply 10 mrad by 1 meter we get a track separation of 1 cm. Although small this is still large enough that the solutions to the tracking problem developed over the past 5 years are applicable. Thus the central detectors presented in the LEP Letters of Intent are typically outgrowths of existing devices.

One solution to the tracking problem is to make a chamber with many small cells; cell full-widths ~ 1 to 2 cm would be needed.² This requires many wires and electronics channels, however each channel is relatively simple in design.

An alternative design, still of the axial type, is to make a chamber with large cells containing several sense wires per cell.³ These chambers have many fewer wires than in the case of small cells, however multi-hit electronics is needed. The electronics must not only allow recording of several hits, but also suppress the long $1/t$ tail of a drift chamber pulse so that later hit information is not degraded by earlier pulses.⁴ This type of chamber has the advantage that most of the very good precision of the drift chamber is available at the pattern recognition stage of track finding since the uniform field over most of the drift path makes a simple linear space-time relation quite accurate. For this reason a local solution of the left-right ambiguity is possible if the wires are slightly (\sim position resolution) staggered, and an accurate local tangent vector to the track can be found by using the times measured by two nearby wires. For tracks coming from the origin this allows a local calculation of the transverse momentum since the radius of curvature is given by:

$$R = \frac{1}{2} \sqrt{\rho^2 + \left(\frac{d\rho}{d\phi}\right)^2},$$

where ρ and ϕ are the cylindrical coordinates of the track.

A third solution is provided by the TPC⁵ and other devices where the sense wires are at the end of the drift volume. These chambers have had, typically, longer drift spaces than the others and have the advantage that no left-right ambiguity exists. I will not discuss these since they are extensively covered in several other contributions.

GENERAL CONSIDERATIONS

Drift chamber performance can be characterized by measurement precision for tracks, ability to separate nearby tracks, ease of pattern recognition, and dE/dx information provided. I will discuss aspects of each of these except for dE/dx which is extensively covered in other conference contributions. The choice of including dE/dx measurement will strongly influence the number of track samples desired, the choice of gas, gas gain, and gas pressure for the chamber.

Momentum Resolution

If we ignore multiple scattering, for large N :

$$\frac{\Delta p_A}{p_A^2} \sim \frac{\sigma}{BR^2\sqrt{N}},$$

where: σ = spatial resolution, B = magnetic field, R = track length, N = number of measurements. As an example: $\sigma = 200 \mu\text{m}$, $B = 5$ kG, $R = 1.5$ m, $N = 30$ gives:

$$\frac{\Delta p_A}{p_A} = .003 \text{ GeV}^{-1},$$

a value which is desirable for physics at the Z^0 .

The small cell option, taking 30 equally spaced layers, cell full-width = 1.5 cm, $R = 1.5$ m, would require 10,000 cells.

Since a large radius R forces the remainder of a detector to be large and expensive, increasing R or decreasing σ would be advantageous since it would allow the same precision for a smaller radius.

Lorentz-Angle. For an axial chamber in a solenoidal field, drift takes place at an angle to the electric field. This angle, $\theta_L \sim \frac{v_{\text{Drift}} B}{E} \sim 15^\circ$ to 20°

for $v_{\text{Drift}} \approx 5$ cm/usec, $B = 4$ kG, $E = 1$ kV/cm. The Lorentz-Angle widens the ionization arrival time spectrum at the sense wire for tracks normally incident on the cell, it makes the cell behavior left-right asymmetric, and also makes it more difficult to associate hits in a multi-wire cell for tracks crossing cell boundaries.

Increasing the Lorentz-Angle substantially beyond 20° would be detrimental to the chamber performance for an axial drift chamber, especially one with large cells. This means that if one wants a B value $\gg 4$ kG, it would be good to reduce v_{Drift} or increase E accordingly. A gas mixture with small v_{Drift} , saturated velocity, and low diffusion for the drifting electrons would be very useful.⁶ An example of the dependence of E on the cell geometry is discussed in a later section.

Diffusion in Gases. For the large drift chambers now functioning, the expected contribution to the resolution from the diffusion of ionization electrons is much smaller than the 200 μm resolution gotten in practice. This implies that improvement in resolution could be gotten if various systematic factors such as wire alignment and sag, as well as an understanding of the time to space relation were better controlled. Figure 1 shows a model calculation of the resolution expected versus impact parameter for several gas choices, based on diffusion and ionization statistics.⁷ We see that if we are satisfied with 200 μm resolution, fairly large cells (~ 5 cm half-width) could be used for a 1 atmosphere 50/50 Ar/Ethane mix before substantial contributions from diffusion occur. The figure also indicates that very good resolution can be obtained in principle for purely organic mixes at a few atmospheres pressure. These gas choices, which might be practical for small vertex detection chambers, typically require rather high voltages (up to a factor of two compared to Argon rich mixes at atmospheric pressure) to get to a reasonable gas gain.

For a configuration where E and B are parallel (TPC configuration) the diffusion can be substantially

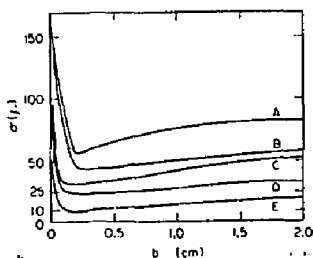


Fig. 1. Model calculations for resolution versus track impact parameter. Curves are: A - 50/50 Argon/Ethane at 1 atm. B - Pure Ethane at 1 atm. C - 50/50 Argon/Ethane at 2 atm. D - Pure Ethane at 2 atm. E - Pure Isobutane at 3 atm.

reduced because of the magnetic field.⁵

Dual-Track Separability for a Parallel Wire Grid

The use of a multi-sense-wire cell allows one to control the ionization sampling and thus the double track separation that is possible in the cell. Figure 2

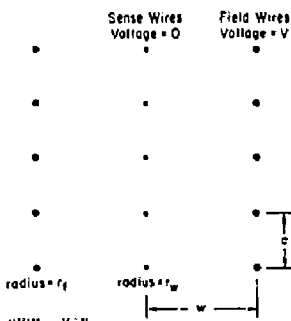


Fig. 2. Multi-sense-wire cell using parallel wire grids.

shows a section of a simple multi-wire cell which is taken as rectangular in shape for simplicity. We look at this simplest parallel wire array since it illustrates the essentials of the problem. The main parameters describing the cell are:

- r_w = radius of a sense wire.
- r_f = radius of a field wire.
- E_w = electric field at the surface of a sense wire.
- E_{cell} = nearly constant drift field over the bulk of the cell.
- a = spacing between wires along the sense wire plane (radial direction).
- w = cell half-width.

The cell height has to be $\geq 1.5w$ to get reasonably

uniform behavior for all the inner sense wires. In the following discussion all field wires and sense wires are assumed to be at a potential V and at ground respectively. To reduce cross-talk, every second wire in the sense plane can be taken to be thicker so it does not amplify and thus is not read-out. In this case the spacing between the sense wires used is actually $= 2a$. We do not discuss here in detail the case of negative voltage on these thicker wires, which can be used to reduce V , and which can be explored as an interesting added degree of freedom.⁶ The case of no negative voltage gives the best dual-track resolution for a given spacing a .

This type of cell is sufficiently simple that its behavior can be thought of as follows: (for simplicity in the discussion we chose the same radius r_w for all sense plane wires)

1. Near each wire we have a roughly radial field varying as $1/r$. This near region extends to a radius $= a/\pi$.
2. The rest of the cell has a nearly constant drift field E_{cell} . Using Gauss' law the field on the sense wires and E_{cell} are related by:

$$E_{cell} = \left[\frac{w r_w}{a} \right] E_w$$

Note: E_w is fixed by the chamber gain for a given r_w . $r_w E_w$ is ~ 250 - 350 volts for typical wires, gains and gases. Thus for $a = 1$ cm we expect $E_{cell} = 1$ kV/cm which is a typical value.

3. The cell dimension w enters only into the determination of the absolute voltage, V , on the field wires. Integrating from a sense to a field wire using a $1/r$ field within a/π of a wire and E_{cell} elsewhere gives a good estimate:

$$V = E_{cell} \left[\left(w - \frac{2a}{\pi} \right) + \frac{a}{\pi} \ln \left(\frac{a}{\pi r_w} \right) + \frac{a}{\pi} \ln \left(\frac{a}{\pi r_f} \right) \right].$$

4. The trajectories of typical drifting ionization electrons are shown in Figure 3 for the case of no

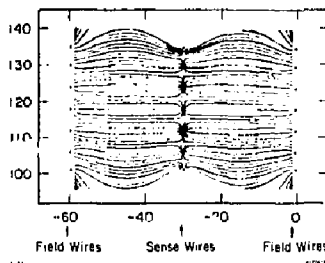


Fig. 3. Representative electron drift trajectories for several normally incident tracks. Cell half-width = 3 cm, wire separation = 6 mm. For simplicity B has been taken = 0.

magnetic field. For the inner wires in the cell the trajectories are parallel straight lines till they reach the near region. Looking at the figure the maximum path difference among the ionization electrons produced by one normally incident

particle is $= a/2$. If we want the arrival of all ionization electrons from two normally incident particles to be separated in time, then the two particles must be incident at impact parameters separated by $> a/2$. Thus $a/2$ is approximately the dual-track separation distance for the cell. Note, the result depends on the extent of the $1/r$ near region, which provides the dual-track limit for other parallel wire arrays.

5. For incidence at an angle θ to the normal, the maximum path difference is $\approx \frac{a}{2}(1+\tan\theta)$. The dual-track resolution is not seriously degraded by non-normal incidence, provided $\tan\theta \leq 1/2$, which occurs at 26° which is a large bend angle. Note, the Lorentz-Angle acts as an additional angle adding or subtracting from θ depending on the track orientation and thus should be minimized.

To check the above characteristics quantitatively, we have looked at the drift cell of Figure 3 for the case $a = 6$ mm and $w = 3$ cm.³ For this case $E_{\text{cell}} = 1.5$ kV/cm. The large value of E_{cell} helps decrease the Lorentz-Angle. Using a Monte Carlo program which generates and follows ionization electrons produced in the cell, Figure 4 shows the distribution of collected

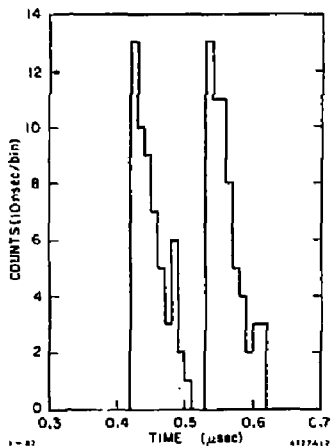


Fig. 4. Ionization electron arrival time spectra produced by two normally incident tracks whose impact parameters are separated by 3 mm in space. Cell is that shown in Fig. 3, but now with $B = 5$ kG.

electrons from two normally incident tracks whose impact parameters differ by 3 mm. The calculation has been done with a 5 kG field and 90/10 Ar/CH₄ gas. The variation of the drift velocity with the local electric field, as well as the local Lorentz-Angle, has been included in the calculation. A dual-track separation of 3 mm should be attainable for such a cell using electronics which suppresses the $1/t$ pulse tail.

We might ask what the limit on dual-track separability is for a parallel array if we use standard leading edge discrimination only. Since wire separations of about 1 to 2 mm are at the limit of what's possible we can expect a limit ~ 1 mm if we stick to standard techniques.

Quality of Information for Pattern Recognition

Drift chamber information is typically used at two stages, the first is for pattern recognition where one would like to get good initial estimates of positions and angles for sorting the left-right ambiguity and linking points or track elements, the second is for high precision fitting of track parameters.

In general, pattern recognition problems will occur for the few tracks which are close together in an event. For a system of single-hit small cells the randomization of the wire pattern from layer to layer tends to provide hits on some layers for each of two tracks which are spatially close together. Thus if the pattern recognition program can find tracks with some missing hits it can handle most of the close tracks.

For a multi-sense-wire cell, with multi-hit electronics, track separations at the few mm level are possible as seen in the previous section. In addition the nearly uniform electric field allows very good precision for certain quantities prior to angular corrections. As an example we can look at the solution of the left-right ambiguity by wire staggering.

If alternate sense wires are staggered by δ we can resolve the left-right ambiguity in an individual cell before pattern recognition. Taking the example of staggered wire triplets, the quantity

$$\Delta = v_{\text{Drift}} \left[\frac{t_1 + t_2}{2} - t_3 \right]$$

where the t_i are the measured times, is centered at $\pm 2\delta$ with the sign giving the side of the cell traversed. Thus if $\delta \gg$ error on Δ we can resolve the left-right ambiguity. Using $\sigma_{\Delta} = \sqrt{\frac{3}{2}} \sigma_{t_i}$, with $\sigma_{t_i} = 200$ μ s, gives $\delta = 280$ μ m if we want $\delta = 5\sigma_{\Delta}$. Figure 5 shows a plot

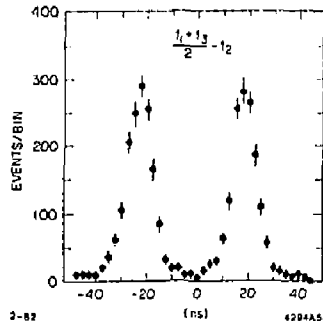


Fig. 5. Correlation of drift times $\frac{t_1 + t_3}{2} - t_2$ into two peaks for a cell with three staggered sense wires. Data is from the MARK III Drift Chamber.

of Δ for data from the MARK III chamber, for which $\delta = 400$ μ m. The constraint on the three times provided by Δ allows the use of the very good resolution of the chamber for the rejection of spurious hits (multi-pulsing, single bremsstrahlung conversions, poorly measured points due to δ -rays, confused points due to crossing tracks in the cell) before pattern recognition begins. This could be particularly useful in an environment containing many soft photons or neutrons which might give a fair number of single hits but very few valid triplets.

To understand why Δ can be measured so accurately we will look at the space-time relation for a parallel

wire array. For concreteness we take the cell used as an example in the previous section. The drift consists of:

1. Uniform drift along the direction given by the Lorentz-angle for ionization produced in the far region where $E = E_{\text{cell}}$.
2. Drift along radius in near region, for radius $\leq a/\pi$. The velocity here can be different than in the uniform region, depending on the gas. We assume below that only one velocity describes the drift in both regions.

The earliest arriving electron trajectories for a track are shown in Figure 6. Measuring distances along the

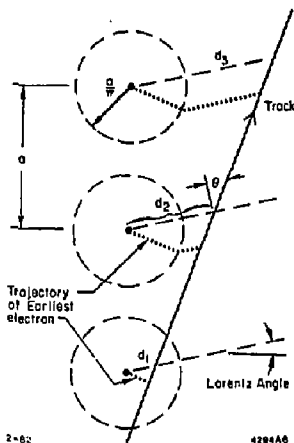


Fig. 6. Relation of drift distance measured and the distance along a line given by the Lorentz-Angle. In the near region:

$$d_1 = v_{\text{Drift}} t_1 / \cos \theta.$$

In the far region:

$$d_2 = v_{\text{Drift}} t_2 + \frac{a}{\pi} \left(\frac{1}{\cos \theta} - 1 \right)$$

$$d_3 = v_{\text{Drift}} t_3 + \frac{a}{\pi} \left(\frac{1}{\cos \theta} - 1 \right)$$

direction for the uniform part of the drift and taking v_{Drift} as the estimate of the distance:

1. Corrections to the estimated distance in the near region go like $1/\cos(\theta)$. For normal incidence this is $1/\cos(\theta_1)$.
2. The correction over most of the cell is proportional to a/π and thus is expected to be small for the case $a = 6$ mm discussed in the previous section.
3. Since the angular correction is a constant for hits not too close to the wire, several quantities for which the correction cancels can be calculated very accurately, for example:
 - a) $\frac{d_1 + d_2}{2} - d_3$, used to solve the left-right ambiguity.
 - b) $d_3 - d_1$, which gives a numerical evaluation of $\frac{d\theta}{d\phi}$, the local tangent to the track. These can be taken at the track finding level to be accurate to a few hundred microns.

REFERENCES

1. Segmentation requirements have been studied both in the SLAC Linear Collider workshop and several LEP workshops. See, for example, K. Winter, "Experimentation at LEP; Hadronic Final States", 1979 LEP Study, p. 93.
2. Examples of chambers with small cells are those used in the MARK II, CLEO, and ARGUS detectors. A discussion of the use of such chambers at higher energies can be found in:

K. Berkelman, Cornell Z^0 Workshop, CLNS 81-490, p. 58.

G. Trilling, SLAC Linear Collider Note #46.
3. Examples of such chamber are those used in the JADE, AFS and MARK III detectors. A description of most of the presently operating chambers can be found in:

Physica Scripta Vol. 23, 1981.
4. R.A. Boie, et al., IEEE Trans on Nucl. Sci., NS-28, 603 (1981).
5. For details on the TPC see PEP Proposal #4, 1976.
6. For a recent look at some gases, as well as references to earlier work, see:

G. Baranko, SLAC Linear Collider Note #45.

J. Jaros, SLAC Linear Collider Note #51.

J. Va'vra and L. Roberts, SLAC Linear Collider Note #31.

F. Gracagnolo, A. Se' m, D.B. Smith, SLAC Linear Collider Note #36.

The UAI CENTRAL DETECTOR

M. Calvetti, P. Cennini, S. Centro, E. Giesi, S. Cittolin, A.M. Cnopa, L. Dumps, D. DiBitonto, S. Geer, B. Haynes, W. Jauk, G. Jorat, V. Karimaki, H. Kowalsky, R. Kinnunen, F. Lacava, G. Maurin, A. Norton, G. Piano Mortari, M. Pimia, A. Placchi, P. Queru, M. Rijssenbeek, C. Rubbia, B. Sadoulet, K.S. Sumorok, C. Tao, V. Vuillemin, J.P. Vialle, H. Verweij and E. Zurfluh

UAI Collaboration

Presented by M. Calvetti

Abstract

The UAI Central Detector is now taking data at the CERN pp Collider^{1,2}. We give a general description of the detector and discuss the aspects that are mainly related to its quality and reliability. Multi-hit electronics is used for the readout of 6000 sense wires uniformly distributed over 25 m³. The analog information, energy, and charge division, is digitized on line every 32 ns. The high density and the precision of the points detected along the tracks is such that the reconstructed events look similar to bubble chamber pictures. Results obtained in the first physics runs are presented.

1. Introduction

The UAI Central Detector is now installed and working at the CERN pp Collider (Fig. 1). An artist's view of the experimental set-up is shown in Fig. 2.

The magnet, a dipole with a nominal field value 0.7 T, has an internal magnetic volume of 80 m³, of which 25 m³ around the beam pipe are occupied by the central detector used for tracking and momentum measurement.

The complexity of the events produced by pp interaction at 540 GeV in the c.m., in terms of rates, multiplicity, and particle density, is such that a careful design of the detector geometry and of the associated electronics was needed. The construction of the detector and the basic features of the associated electronics have been described at the 1980 Vienna Conference on Wire Chambers^{3,4}.

We give here a general description of the detector, concentrating on the points which, on the basis of our experience, are fundamental to contributing to its final quality and reliability: i) geometry, ii) HV system, iii) electronics, iv) calibration.

2. Geometry

The expected topologies of pp interaction at 540 GeV in the c.m., where many particles with high energy are produced in the forward directions, suggested the use of a long detector with a magnetic field orthogonal to the beams.

The detector is composed of six independent half-moonshaped chambers assembled together to form a self-supporting cylinder, 6 m long and 2.2 m in diameter, covering the full solid angle from 5° to 175° with respect to the beam direction.

The cylinder is filled with a mixture of 60% ethane and 40% argon at atmospheric pressure.

The 6000 sense wires and the 17,000 field-shaping wires are parallel to the magnetic field. They are organized in horizontal planes in the four forward modules, and vertical planes in the two central ones (Fig. 3).

One of the most striking features of the system is the cylindrical shell of the chambers supporting the wires. It is a stressed honeycombed structure, 5 cm thick, sandwiched between two Vetronite layers, each 1.5 mm thick. The amount of prestressing, which, after wiring, is entirely counterbalanced by the tension given to the wires, is such that in the median plane the distance between the chamber edges is reduced by about

8 cm. The cylindrical shape, after wiring, depends on the equilibrium between the tension given to the wires and the stresses in the structure.

To measure the mechanical tension of the stretched wires, a simple, precise, and fast method, based on the measurement of the natural oscillation frequency, has been developed⁵.

The sense wires (Ni-Cr, ϕ 35 μ m) and the field-shaping wires (Cu-Be, ϕ 100 μ m for VC-WF wires, 150 μ m for cathode wires) were stretched to 80 g and 200 g, respectively. Figure 4 shows the results obtained for the 1000 sense wires in a module.

The position of the sense wires in a plane is known within 50 μ m, whilst the position of the "average planes" in the 25 m³ of the detector is known to an accuracy of 200 μ m.

The sense wires are surrounded by field-shaping wires, as shown in Fig. 5. The VC voltage balances the electrostatic forces produced by the drift electric field onto the sense wires, whilst WF controls the gas amplification.

Electrons produced by the ionizing particles in the detector drift through large drift spaces (18 cm) to the anode wires, where the individual track coordinates are obtained by the drift time and charge-division method. With a drift field of 1.5 kV/cm, the drift velocity is 5.3 cm/ μ s and the maximum drift time 3.6 μ s, smaller than the time interval between two successive bunch crossings (3.8 μ s). When an interaction takes place, all the ionization (electrons) produced in the previous bunch crossing has already reached the anode wires.

The sagitta in the plane orthogonal to the magnetic field is measured with the drift time, which is far more precise than the charge division (two orders of magnitude). Figure 6 shows some events and the planes structure of the detector. The planes in the central modules are rotated by 90° to have the drift electric field orthogonal to the particle trajectories in the central region.

We can see how the detector "follows" the events, maintaining a constant density of points along the tracks all over the volume. These events were recorded during the November-December 1981 runs; at that time only 40% of the electronics was operational (80% of the sensitive volume). In particular, only one wire out of two was instrumented. With the complete electronics, an average of 100 points per track are recorded, each corresponding to 1 cm of gas sampling.

The high precision of the drift time coordinate, compared to the detector dimension, permits a good pattern recognition in the plane orthogonal to the magnetic field. The charge division coordinate corresponding to a specific hit is then easily reconstructed using the time information associated with the charge collected on both sides of the sense wires (see the section on Electronics).

3. HV system

The drift voltage (VD) applied to the drift volume needs to be degraded all along the edges of the drift space in order to guarantee planar equipotential surfaces. This is achieved with a resistor divider that feeds the tracks of a printed circuit, called "race-track" (RT), with decreasing voltages (Fig. 5). These

resistors are mounted inside the chambers and have a high total resistive value (3.5 G Ω).

It is then clear that any leakage current caused by the supporting structure of the chamber, or current due to the beam and collected by the RT, will drastically affect the potentials determined by the resistive chain, with an intolerable distortion of the electric field. It was therefore decided to connect the RT to 10 low-output impedance power supplies, so that any leakage or beam current would affect the electric field in only a small local region delimited by two power supply inputs. This is the role of the active divider.

The active divider is basically a number of vacuum tubes used as cathode followers connected in series. The maximum output current is roughly equal to the current flowing in the tube (1.5 mA) so that in the event of a short circuit the chain collapses, providing a simple means of current limitation. The voltages are fixed, with a precision of 0.5%, through a resistive divider connected to the grids.

For each drift volume, the currents associated with the intermediate voltages and with the field-shaping voltages VC and VF are measured in the power supplies, whilst the corresponding voltages are measured directly on the chambers. A total number of 308 currents and 308 voltages, corresponding to the 34 independent drift volumes (HV-wise) are continuously monitored by a SUPER CAVIAR computer⁷ which also drives the HV power supply and controls the interlock logic (Fig. 7).

The ripple of the very high VD voltages (cathode) and of the 48 VC-VF voltage are also monitored through parallel wave-form recorders⁸. In case of HV troubles, the transients in all the HV lines are recorded. Careful study of these data turned out to be essential in understanding the behaviour of a detector which is usually inaccessible inside the magnet 200 m away from the control room.

In case of over-current (200 μ A on VD, 50 μ A on VC and VF, integration time about 1 ms) a hardware protection system⁹ (Crowbar, Fig. 7) will disconnect the three (VD, VC, VF) voltages, associated with the same drift volume, in a few milliseconds. Furthermore, in order to avoid direct sparks from the HV race-track onto the wires, two HV transient suppressors (Tranzorb)¹⁰ are mounted on the chamber parallel to the first two intermediate voltages supplied by the active divider.

The VC-VF interlock system is composed of a general-purpose microprocessor controller (CPMC)¹¹ with a MOTOROLA 68B00 microprocessor with 64K EPROM and 2K RAM, which, with two special interface cards, controls the HV outputs and monitors the currents and voltages from the Crowbar boxes. It also controls the thresholds for the alarms and provides software filtering for them. The Crowbar boxes, where the HV relays are located, provide the current measurements through a floating current-to-frequency converter optocoupled to the low-level logic. In case of over-current, the CPMC can decide in a few hundred microseconds, whether to switch the chamber from the HV line to a shunt resistance. It also communicates with the SUPER CAVIAR responsible for the whole central detector activity.

4. Electronics

The block diagram of the electronics for each anode wire is shown in Fig. 8.

The two preamplifier signals at each end of the sense wire feed the charge and time digitizer (CTD)¹². In the CTD (12 channels) there are 12 analog cards containing line receivers, clipping stages (32 ns), integrators, and 12 digital cards where the fast amplitude-to-digital converters (FADC, TRW-IDC1014J) and the memories are located. The analog chain is a.c. coupled. In order to avoid frequency dependence of d.c. offsets, a base line restorer has been introduced before the driver of the FADCs.

The two FADCs of each channel (six-bit accuracy, 32 ns sampling period) are used, respectively, as an analog divider to measure the ratio Q_1/Q_2 (charge division) directly, and with a non-linear response for the measurement of the total energy Q_1 in order to have the dynamic range (more than nine bits) required by Landau fluctuations. Every 32 ns the total charge collected Q_1 and the hit coordinate along the wire Z_1 are recorded.

The digital information is directly stored in successive memory locations in such a way that, at any time, the story of the previous 4 μ s is recorded in the CTD memories (32 ns \times 128).

The Z coordinate is given by the centre of mass¹³ of the Z_i 's weighted by the energy E_i , measured in same time bin

$$Z = \left(\sum Z_i \cdot E_i \right) / \left(\sum E_i \right).$$

In order to have $Z = Z_{\text{true}}$ an infinite integration should be performed. In practice, a good measurement can be obtained with a gate width between 150 and 200 ns, depending on the pulse shape.

In the time channel there is a fine time-stop interpolator, a three-bit TDC of the DTR 247 type, which measures the drift time within a 32 ns window with an accuracy of 4 ns.

Five CTDs are located in each crate together with a readout processor (ROE)¹⁴. The data-acquisition system is described in another contribution to this conference (see S. Cittolin, UAL Collaboration).

The electronics chain has been designed in such a way that it is limited, in the charge division accuracy, by the six bits of the FADC (12). Figure 9 shows the charge division accuracy as a function of the total number of electrons collected on the wire. The stochastic noise of the wire resistance and of the preamplifier correspond to 1.2×10^4 r.m.s. electrons in a gate 150 ns long. In order to be limited in precision by the FADC, a total number of $\sim 4 \times 10^5$ electrons must be collected in 130 ns (five samples), requiring a gas amplification $\sim 10^4$.

The charge collected on one side of the wire depends dramatically on the position of the avalanche along the wire and on the Landau fluctuations. It is therefore essential for the analog part of the readout electronics to be linear over the full dynamic range (five times a minimum ionizing particle). The linearity of the analog chain has been measured by feeding calibrated charges into the preamplifier. Figure 10 shows Z_{measured} versus $Z_{\text{simulated}}$ for a total energy corresponding to a minimum ionizing particle. The deviations from a linear fit to the data are always smaller than 1% all along the wire.

5. Calibration

The central detector electronics is provided with a calibration system (Fig. 11) which is able to feed into any preamplifier a variable charge up to five times a minimum ionizing particle with an accuracy of about 3%. The calibration pulse is obtained by the discharge of a 47 pF capacitor, previously charged to a reference voltage, through a 470 Ω resistance. Each preamplifier has its own RC.

The capacitors to be charged up are previously selected, using a set of serial shift registers HEF4015B. The trigger pulse, arriving at the same time on all the detectors, closes the c-mos switch SD 5100 thus causing the discharge of the capacitors. The shift register chain permits the 12,000 preamplifiers to be pulsed, with any required pattern and simulated charge division coordinate, i.e. two different reference voltages can be applied, one to the left and one to the right side.

A total of 730 pulsers, each driving 16 channels, are mounted directly on the chambers inside the connectors which at the same time support the preamplifiers and feed the VC-VF voltages to the field-shaping wires.

This flexible system, very useful as a debugging tool (in a few minutes we can check the layout and status of the electronics) is fundamental, in particular for the charge division calibration.

The measured charge division coordinate Z_m is related to the true one Z_t by the following expression:

$$Z_m = \frac{g_L Z_t + O_L / Q_{tot}}{(g_L - g_R) Z_t + g_R + O_{tot} / Q_{tot}}$$

where g_L and g_R are the left and right gains, and O_L , O_{tot} are the d.c. offsets eventually present at the inputs of the two FADCs of the charge division and energy, respectively.

In order to control these offsets (1 mV corresponds to about 12 in Z) and avoid energy dependence of the charge division measurement, a set of six DACs, controlled by the ROP, are located on the analog card of each wire.

Using the calibration pulser, it is possible to simulate several positions along the wire for different energy losses. The two DACs controlling the left and right gains and those controlling the O_L and O_{tot} offsets are changed by the ROP and chosen to have $(g_L/g_R) = 1$ and to minimize the offsets. Figure 12 shows the charge division linearity obtained before and after the on-line calibration.

Two other DACs are used for the energy FADC: the first to change the base-line (pedestal of the energy FADC), the second to control the response function of the energy measurement.

A SUPER CAVIAR computer controls the calibration system and the 530 CTDs by means of the 125 ROPs which are connected in series through an advanced data link controller¹⁴. Notice that the ADLC line can also be used during data taking, in spy mode, to read ROP statistics on data acquisition.

All the 6000 channels are calibrated in parallel. Figure 13 shows a computer display obtained using the calibration pulses to simulate a minimum-ionizing particle in the middle of the drift volume. The total energy (full histogram) and the charge division (continuous line) are shown for the 12 wires. Note how the charge division stays more or less constant in the time bins where the charge is collected, and how it deviates from the simulated position outside of the pulses where the noise is dominating.

The charge division linearities of the channels in a crate are shown in Fig. 14 (five CTDs, only one wire out of two was instrumented).

Other displays are used for debugging purposes. For instance, Fig. 15 shows the drift time, the energy base-line, the total energy, and the charge division obtained on 48 wires. It is clear that the broken channels can immediately be found. The relative T_{drift} due to different propagation times along the cables and to the readout electronics are measured with an accuracy of ~ 4 ns. The energy measurements are equalized to the 10% level, well below the Landau fluctuations.

A second off-line calibration is then performed, but this time the corrections to the data are smaller than or comparable to the required accuracies.

6. Internal calibration and results

The electronics calibration cannot take into account the other parameters that contribute to chamber precision, such as absolute T_{drift} 's, drift velocity, drift angle, errors in the wire positions, and the relative positions of the six modules. To correct for these errors, we have to use other methods. There are two possibilities: either to simulate tracks in the detector, using X-rays or laser beams (see B. Sadoulet, this conference); or to use the tracks produced by real events to fit those parameters in order to obtain the best reconstruction.

The X-ray guns and the lasers of the UAI detector are now being installed, and we do not have experimental results apart from tests on prototypes. To analyse the data taken in the last run, we have used the second method.

The chamber geometry, namely the way in which the planes are organized, is such that the "internal" calibration method can be fully exploited. This is due to the fact that the particles usually cross several drift volumes with different drift direction.

The errors in the drift angle, drift velocity, and absolute T_{drift} to generate inclinations and displacements of the various track segments. It is then possible to tune the various parameters and choose the values that correspond to the best reconstruction. Using this method, the drift velocity and the drift angle have been measured independently in the six modules of the detector with a precision of 0.5%, and within this precision they are equal. The measured drift velocity is 53 $\mu\text{m/ns}$, whilst the drift angle is 22.2° ($V = 1.2$ kV/cm, $B = 5.6$ kG).

Figure 16 shows the residuals in the drift time coordinate obtained for different track categories: (a) to (c) show the residuals for tracks crossing one, two, and three drift volumes; the histogram (d) corresponds to tracks crossing different modules. The increase in error from 270 μm to 340 μm shows the presence, at this stage of the analysis, of systematic errors that will, of course, be corrected for.

The over-all precision obtained for all the reconstructed tracks in the 25 m^3 of the detector, in the presence of a 5.6 kG magnetic field, is shown in Fig. 17. A 290 μm accuracy is obtained.

In order to see whether systematic effects due to misalignment of the wire planes or wrong relative position of the six modules could introduce bias on the momentum measurement, we have fitted straight tracks (without magnetic field), using the normal reconstruction program used for events in a magnetic field. Any unknown deformation of the detector geometry is interpreted as curvature of the tracks; hence, in such a case, tracks with low momentum are reconstructed. Figure 18 shows the results. The vertical scale is the number of tracks (arbitrary units) and the horizontal scale is the ratio Q/p , where Q is the charge and p the momentum in GeV/c. The histogram is symmetric; no charge asymmetry in the momentum measurement is found.

We have also studied particle ionization using the dE/dx measurement¹⁵. The data were obtained by exposing one of the central detector modules to a 3 GeV/c muon beam. In Fig. 19 the Landau distribution based on 22,000 samples of energy loss measurements is shown. The absolute energy scale is calibrated using the 5.9 keV peak produced in Ar by an ²⁵²Cf radioactive source. The data are corrected for the inter-channel cross-talk effect: 4% for the adjacent wires and 0.5% for the next two.

Each track was defined by 34 measured points. Figure 20 shows the mean ionization loss of the lowest 70% of the measurements on each track. The Gaussian fit to the distribution gives 1.4 keV for the average energy loss, with 0.16 keV standard deviation. An energy loss resolution of 6% is expected for tracks with 100 detected points. In Fig. 21 we show the prediction for the particle separability in units of standard deviations as a function of the momentum for pions, kaons, and protons. There is no separation between pions and kaons at 1.2 GeV/c nor between kaons and protons at 3 GeV/c. Above these points the separability increases quickly, reaching maximum values at 2-10 GeV/c and flattening out at high momenta.

The charge division accuracy has also been measured in this test in the beam. The results are shown in Fig. 22. A FWHM of 10 cm with 2.2 m long wires is found ($\sigma = 2\%$ of the wire length), compatible with the precision of our calibration system. At this stage of the analysis it is not possible to present definitive results on the charge division accuracy obtained in the reconstructed pp interactions. The data have been taken two

months ago and the complete reconstruction program was attempted recently. We will produce these results in the very near future.

7. Conclusions

In spite of its simplicity, the detector geometry, coupled with the magnetic field, is well adapted to the event structure; drift volumes with opposite electric fields provide a unique tool for internal calibration (drift velocity, drift angle, T_0).

To avoid risks, a highly sophisticated HV system has been provided. Currents and voltages are monitored, and a hardware protection (Crowbar) must run continuously to avoid multiple sparks inside and outside the detector. The capacitor monitors, read by the waveform recorders, turned out to be the most simple and direct way of following the HV activity of the detector.

The flexibility and completeness of the HV system is essential for the remote control of such a complex detector. Because of their complexity, all the UAL central detector components (high voltages, low voltages, calibration electronics, readout electronics, gas system, cooling system of the preamplifiers, temperature measurement all over the detector surface) are controlled by computer. A sophisticated and complete software has been written.

The use of the FADC as a wave-form recorder is a powerful and relatively simple instrument for drift chamber readout, especially for events with a high particle density when the pulse shape has to be used to distinguish the various components in a narrow jet.

We have 300 μm accuracy in the drift time coordinate with magnetic field all over the detector volume. An energy resolution of 6% is expected, using the truncated mean for particles with 100 detected points. The charge division accuracy is measured to be around 3%, compatible with the precision of our calibration system. No internal calibration has yet been attempted on the charge division. The analysis is still in a preliminary stage and there is room for further improvements.

References

1. Staff of the CERN \bar{p} -p project, Phys. Lett. **107B** (1981) 306.
2. G. Arnison et al., Phys. Lett. **107B** (1981) 320.
3. M. Barranco-Luque et al., Nucl. Instrum. Methods **176** (1980) 175.
4. M. Calvetti et al., Nucl. Instrum. Methods **176** (1980) 255.
5. M. Calvetti et al., Nucl. Instrum. Methods **174** (1980) 285.
6. E. Chesi, CERN \bar{p} -p Tech. Note 81/17 (1981).
7. S. Cittolin and B.G. Taylor, Proc. Topical Conf. on the Application of Microprocessors to High-Energy Physics Experiments, CERN 81-07, p. 533.
8. S. Centro, private communication (\bar{p} -p Tech. Note to be published).
9. D. Dibitonto et al., CERN \bar{p} -p Tech. Note 82/07 (1982).
10. C. Rubbia, CERN \bar{p} -p Tech. Note 80/21 (1980).
11. S. Centro and V. Vuillemin, \bar{p} -p Tech. Note 80/81.
12. E. Hallgren and H. Werwei], IEEE Trans. Nucl. Sci. **NS-27** (1980) 333.
13. S. Cittolin and B. Löfstedt, Proc. Topical Conf. on the Application of Microprocessors to High-Energy Physics Experiments, CERN 81-07, p. 91.
14. S. Cittolin, B. Löfstedt and E. Zurfluh, Topical Conf. on the Application of Microprocessors to High-Energy Physics Experiments, CERN 81-07, p. 373.
15. R. Kinnunen, CERN \bar{p} -p Tech. Note 81/30 (1981).

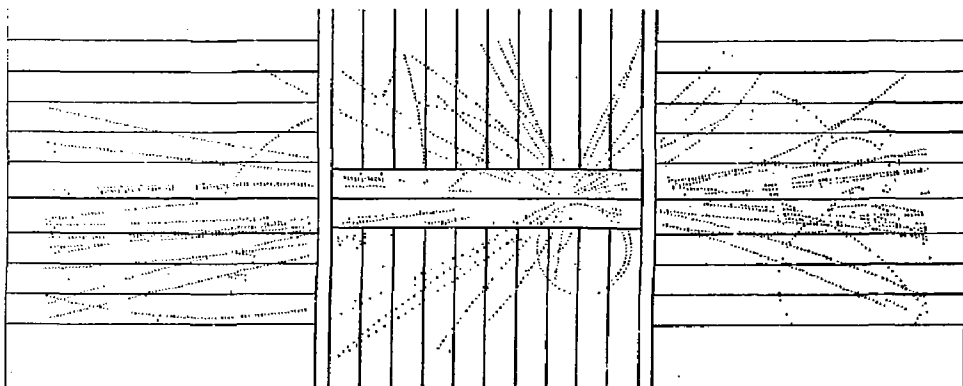


Fig. 1 Proton-antiproton interaction at 540 GeV in the centre of mass'

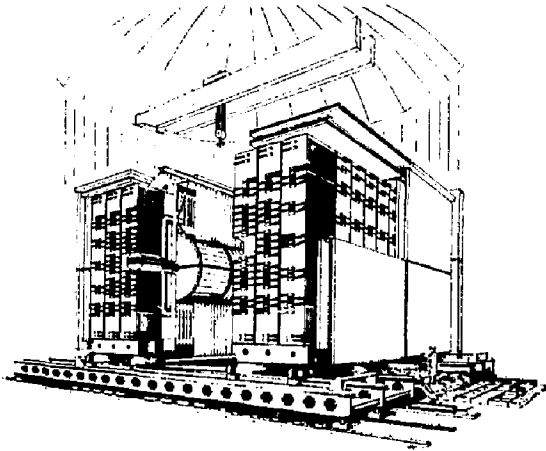


Fig. 2 The UA1 experimental apparatus working at the CERN $p\bar{p}$ Collider

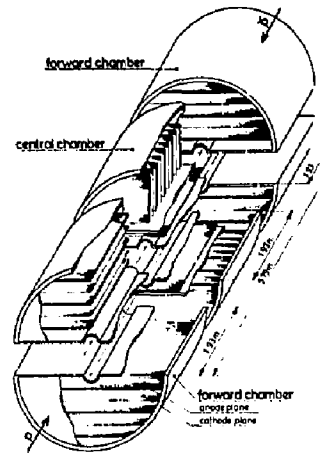


Fig. 3 The UA1 Central Detector. This is composed of six independent modules assembled to form a cylinder around the vacuum pipe.

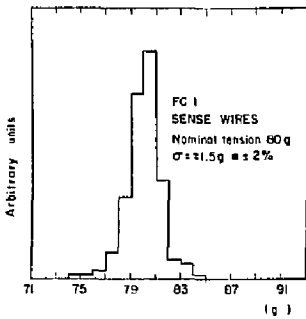


Fig. 4 Typical distribution of the mechanical tension for all sense wires in a module (~ 1000 wires)

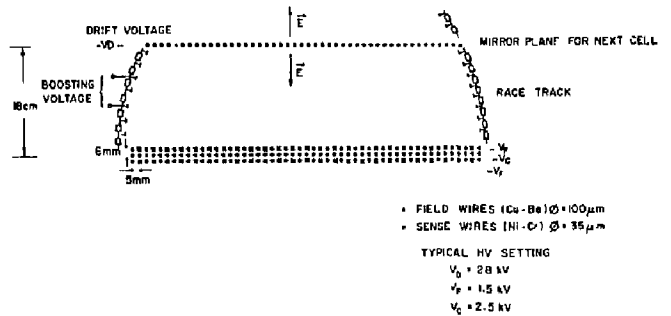
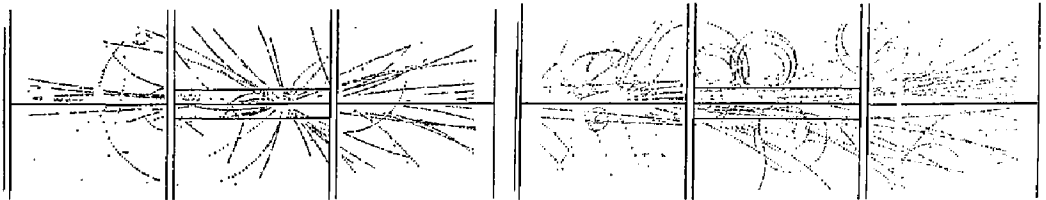


Fig. 5 Drift cell of a forward chamber



a) Proton-antiproton interaction at 540 GeV.

b) Beam-gas interaction.

Fig. 6

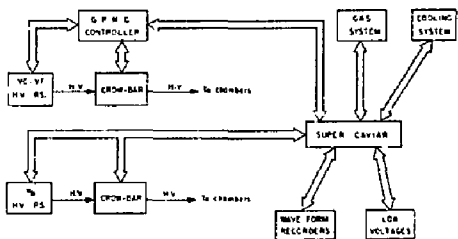


Fig. 7 Block diagram of the interlock system

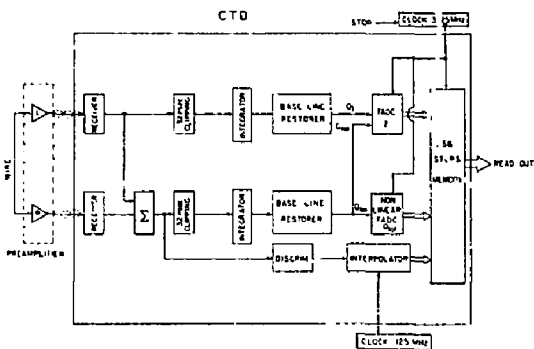


Fig. 8 Block diagram of the electronics associated with each wire

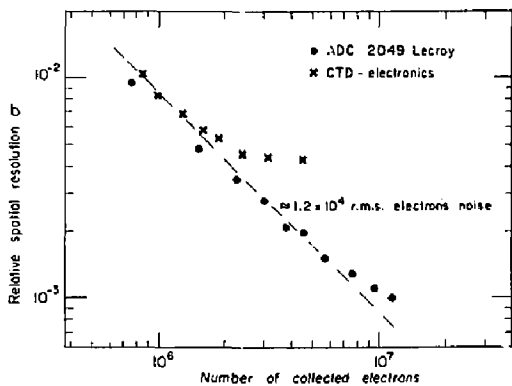


Fig. 9 Charge division accuracy versus number of electrons collected on the wire, in a 150 ns gate.

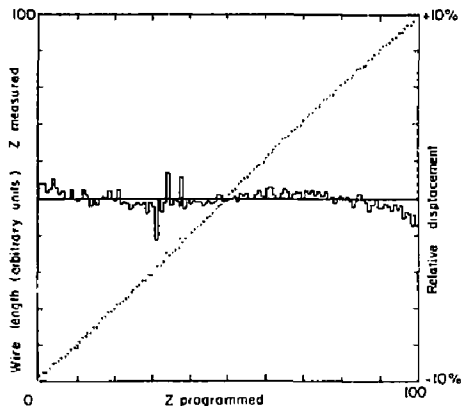


Fig. 10 Linearity of the analog chain

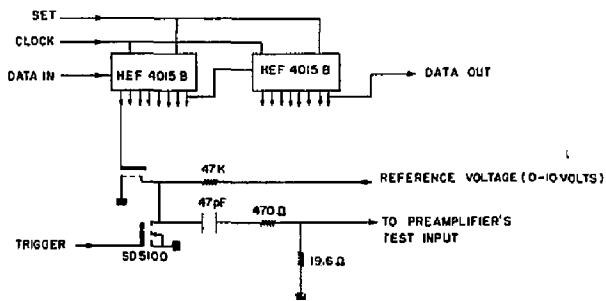


Fig. 11 Calibration pulser associated with each preamplifier

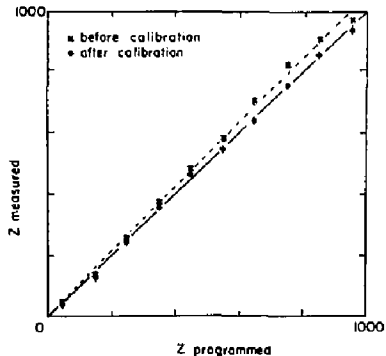


Fig. 12 Charge division linearity before and after the on-line calibration

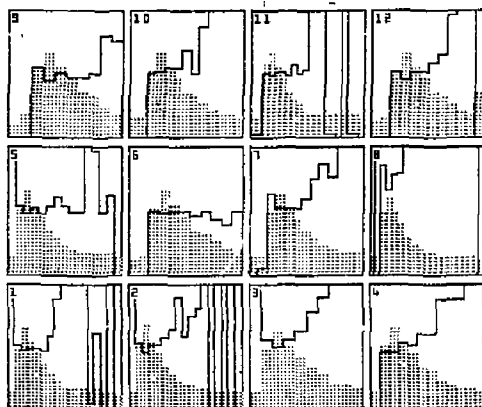


Fig. 13 Calibration pulses simulating a minimum ionizing particle on 12 wires in a CTD module. The total energy (full histogram) and the charge division (continuous line) are measured every 32 ns (32 ns/bin). The vertical scale 0-63 corresponds to the six bits of the FADCs.

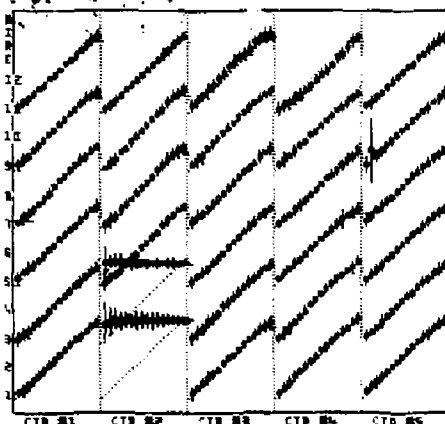


Fig. 14 Charge division linearity of the channels in a crate (five CTDs; only one wire out to two was instrumented).

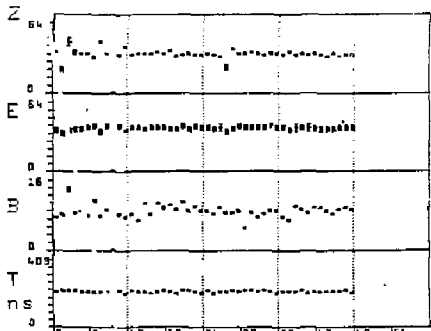


Fig. 15 Drift time, energy base line, total energy, and charge division obtained on 48 wires with the calibration pulser

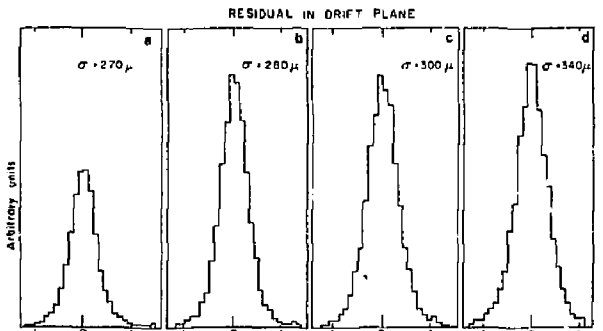


Fig. 16 Drift time residuals for different track categories: a) particles crossing one drift volume; b) particles crossing two drift volumes; c) particles in a complete chamber; d) particles crossing different chambers.

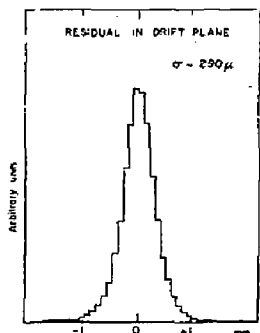


Fig. 17 The over-all precision obtained for all the reconstructed tracks in the 25 m³ of the detector in the presence of a 5.6 kG magnetic field

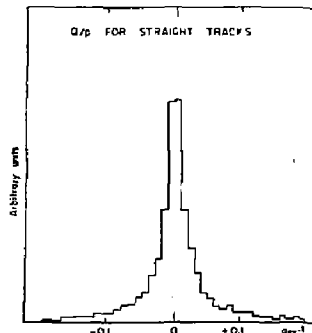


Fig. 18 Measured momentum of straight tracks (data taken without magnetic field). The symmetry of the histogram shows that there is no geometrical distortion in the momentum measurement.

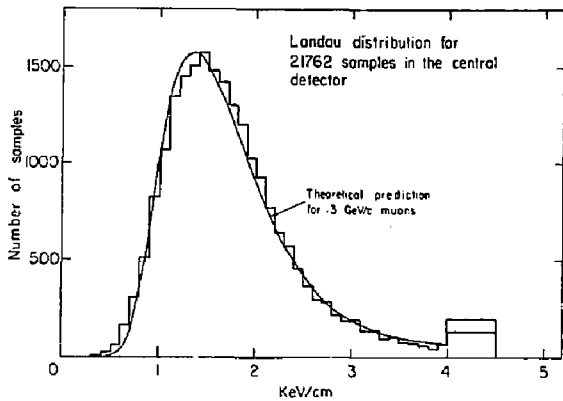


Fig. 19 Landau distribution of the measured energy losses

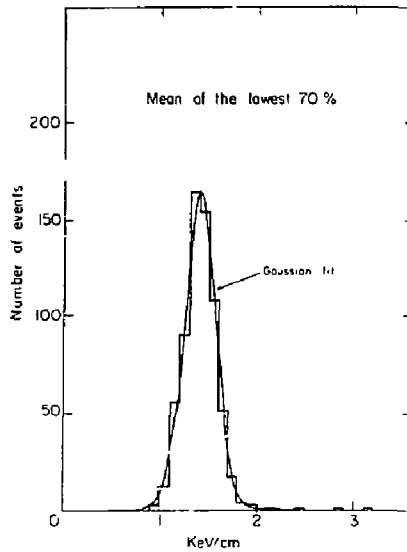


Fig. 20 Truncated mean of the energy losses, i.e., mean, from 34 samples of 1 cm each, of the 70% which are lowest in energy.

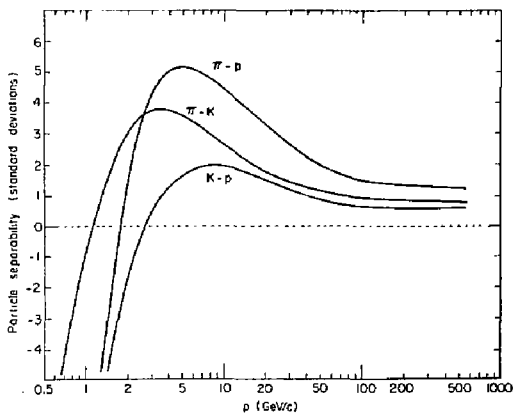


Fig. 21 Expected particle separability in units of standard deviations as a function of the momentum for pions, kaons, and protons.

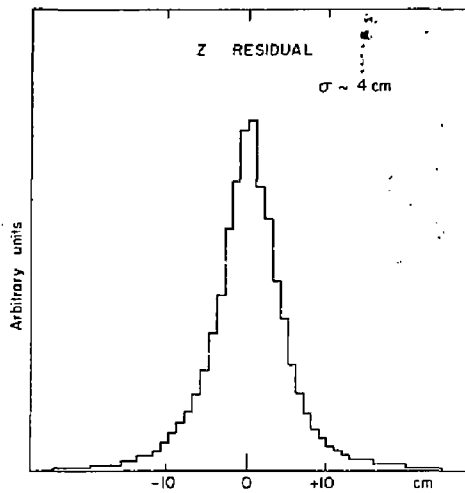


Fig. 22 Charge division accuracy obtained at the very early stage of the analysis. Optimization of the gas amplification and off-line calibration procedure has still to be performed.

Dupe

THE MPS II DRIFT CHAMBER SYSTEM*

Edward D. Platner
Brookhaven National Laboratory
Upton, New York 11973

Summary

The MPS II detectors are narrow drift space chambers designed for high position resolution in a magnetic field and in a very high particle flux environment. Central to this implementation was the development of 3 multi-channel custom IC's and one multi-channel hybrid. The system is deadtimeless and requires no corrections on an anode-to-anode basis. Operational experience and relevance to ISABELLE detectors is discussed.

as a facility instrumented with magnetostrictive spark chambers, PWC's, scintillator and Cerenkov hodoscopes and a variety of user-provided detectors including shower counters and transition radiation devices. However, since its initial operation, the greatest physics interest has fallen into the sub-nanobarn cross section region. Therefore, replacement of the spark chambers with detectors capable of efficient operation in rates ≈ 100 times higher became essential. It was also desirable to improve the position resolution and absolute accuracy of the tracking detectors.

The MPS II Project

The MPS

The BNL MPS (Multiparticle Spectrometer)¹ is a large 10 Kg "C" magnet shown in Fig. 1 with a plane view in Fig. 2. It has been in operation since 1975

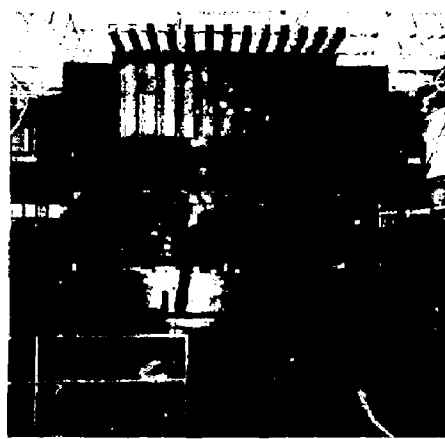


Fig. 1. Brookhaven Multiparticle Spectrometer Magnet

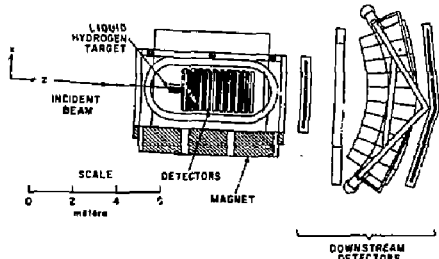


Fig. 2 Plane view of MPS with detectors

Charged Particle Detector Goals

At the outset of this work a substantial amount of computer simulation was used to help optimize detector configurations best suited to the event reconstruction software. In addition, hardware "deficiencies" that impact on computing time were to be minimized. With this background the following set of goals was generated.

- Tracking detector must be capable of very high event rates - electronics to be deadtimeless.
- Good position resolution in a magnetic field with no or very limited position-dependent corrections.
- Minimum need to calibrate - good system stability as a function of channel-to-channel t_0 , time vs. position slope and linearity.
- Compact and reliable - suitable for large detectors with poor accessibility such as inside of a 4 π calorimeter.

Drift Chamber Design

The drift chamber design was determined by the need to operate at very high rates in a magnetic field while minimizing any need for track position or angle-dependent corrections. It was also important from event reconstruction considerations to attempt to resolve the right-left ambiguity and to generate 2-dimensional vectors locally where curvature in the B field is negligible. A geometry that satisfies all these criteria is shown in Fig. 3. These "X" anode, field and cathode wires lie along the B field lines. By arranging 3 such anode planes only 1.2 cm apart, no curvature is seen within the chamber resolution. Also by staggering the anode position in the X₂ plane resolution of the right-left ambiguity will occur in 70-80% of the tracks locally when fits allowing up to 2 σ deviations are done.

The full module consists of the triple X anodes, a pair of Y anodes, one of which is displaced by a drift distance, and a U and a V anode plane which are 30° to the Y (Fig. 4). Therefore locally within a module it is possible to reconstruct 3 dimensional vectors of the particle track. It should be noted that in X the reconstruction finds one or more vectors per hit. If more than one vector is found, in general only one is correct. The correct vector is selected by matching with the vectors in adjacent modules. In Y there are always 4 vectors generated. However there is no curvature in Y so that many of the calculated vectors can immediately be discarded because the track must come from the vicinity of the target.

* Research supported by the U.S. Department of Energy under Contract No. DE-AC02-76CH00016.

CATHODE and FIELD WIRES 0.003" dia. SS
 ANODE WIRES 0.001" dia. Au PLATED W

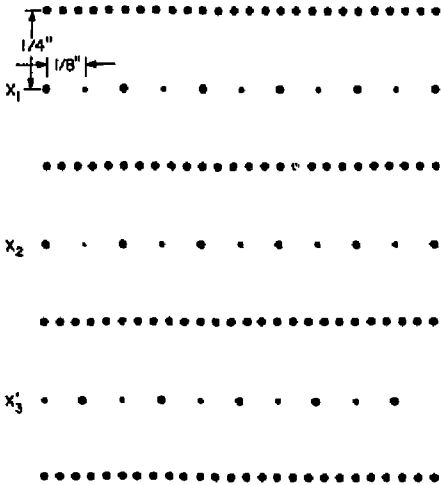


Fig. 3 Three X planes of an MPS II drift chamber module.

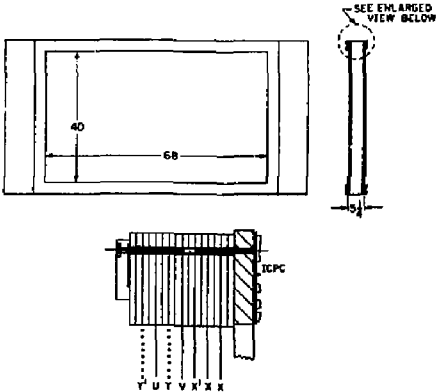


Fig. 4 Full drift chamber module with 7 anode planes.

One of the important features of this drift chamber system is the electronics developments that allow all channel-by-channel circuit elements to be mounted directly on the chamber frame. This circuitry is shown in Fig. 4 and is called the ICPC. Each anode lead is attached to a short flat pigtail cable to the ICPC. On the ICPC are the transresistance amplifiers, pulse shapers, comparators, digital delay and registers required for each anode. Figure 5 is a picture of the complete module with ICPC's, cable harnesses and interface electronics. Figure 6 is a plot of drift time vs. track position in a 10 Kg field. In this gas mixture

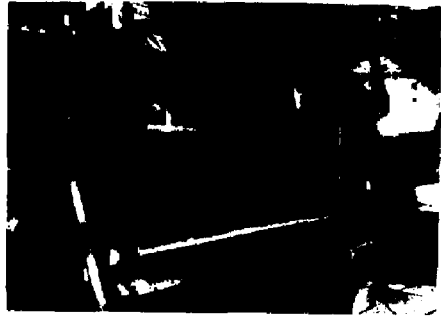


Fig. 5 Picture of completed drift chamber module with ICPC's, cable harnesses and interface circuitry.

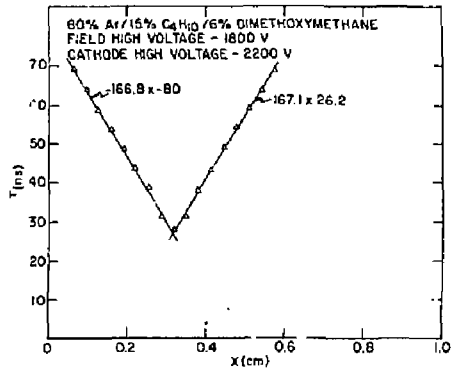


Fig. 6 Drift time vs. track position in a 10 Kg B field.

the drift velocity is fully saturated and the drift time vs. position is linear at the 100 μ level from the anode to near the field wire. Figure 7 is a plot of the HV plateau where the electronics threshold is 4 μ s.

Electronics

The desire to build a system easily expandable to ISABELLE-sized detectors capable of handling ISABELLE event rates, i.e. deadtimeless electronics and requiring an absolute minimum of variable parameters such as time-to-digital conversions that are different for each readout channel led us to develop a number of custom integrated circuits and hybrids. Figure 8 is a block diagram showing 3 custom IC's and a hybrid. Each of these circuits contains 4 channels of electronics. The amplifier specifications are given in Table 1.² It should be noted that the rms noise level is low enough that comparator thresholds as low as 1 μ a are possible. Figure 9 shows 1 channel of the hybrid. This shaping

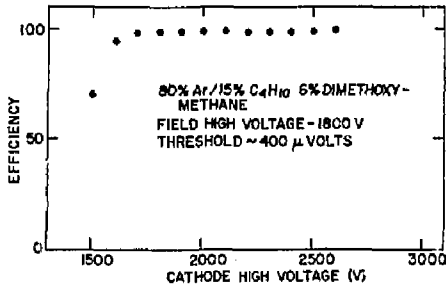


Fig. 7 High voltage plateau for a typical drift chamber.

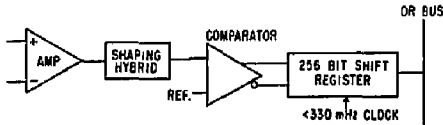


Fig. 8 Electronics block diagram. All of these components are mounted on the ICPC.

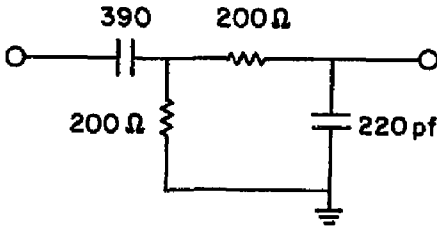


Fig. 9 Pulse shaping hybrid circuitry

network was hybridized to conserve space on the ICPC. A discrete implementation would be much less expensive. Table 2 lists relevant performance of the comparator IC. The device was designed with ≈ 6 mv of hysteresis to improve the circuit stability in large and somewhat noisy situations. The output level swings were determined by the CMOS digital delay-register drive requirements. An alternate version of this comparator having similar specifications but ECL output is available as MVL 406.²

The third IC in this drift chamber electronic system is a state-of-the-art device. It is functionally a 4-channel, 256-bit shift register (SR) that is fabricated with the CMOS silicon-on-sapphire (SOS) process.³ It is capable of acquiring data at > 330 MHz. Figure 10 is a block diagram of the internal structure of one channel. To achieve the required speed, the device is internally an 8 phase register. Thus the maximum speed each phase runs is $330 \text{ MHz} / 8$. To provide practical external clock risetime and amplitude levels, the clocking is done with a 4-phase clock driver. This clock driver then must run at no more than $330 \text{ MHz} / 4$ or 83 MHz , a much simpler task than clocking at up to 330 MHz . A consideration of great importance in a multiphase shift register is the relative delay between the clock

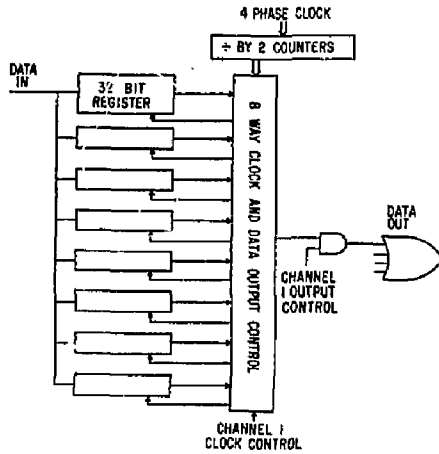


Fig. 10 Single channel of the 8 phase shift register.

pulses and the time data is actually acquired in each of the 8 phases. This has been measured at 250 MHz to be $4 \pm .5 \text{ ns}$ in absolute range on a large number of devices. The standard deviation of this variance, a number of greater importance in drift chamber applications, is $\pm .3 \text{ ns}$.

The 4-channel SR with control (enabling) circuitry is shown in Fig. 11. During data acquisition, 4 "ones"

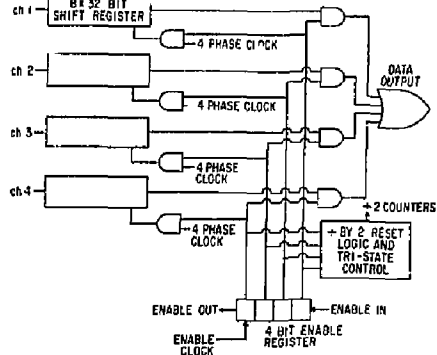


Fig. 11 4 channel shift register with enable circuitry.

are in the enable register. This allows the 4-phase clock to drive all 4 channels of the SR. The data is acquired by running this 4 phase clock at $250/4 = 62.5 \text{ MHz}$. Precisely $1 \mu\text{s}$ after an event of interest has occurred, the 4-phase clock is stopped. Channels with data will then have a string of "ones" somewhere in the last 32 elements in the SR, the position of the furthest 1 being a precise measure of the drift time for that drift chamber cell. Table 3 gives some important specifications for this shift register. Data is extracted by use of the enable circuitry which allows selection for clocking of one channel only and gating of the last register element onto a common "OR" bus. Once a channel

has been selected for readout, the 4-phase clock is turned on at < 20 MHz for 32 primary ticks and the "OR" bus data is digitized by an encoder common to one whole plane of the chamber. In this way the data from a whole X plane (273 anodes) appears on a single coax cable. In addition, 2 cables bring the 4-phase clock to the plane and an additional enable-in coax and enable-clock coax completes the communication with the plane. Thus data and control for 273 (or more for larger chambers) is compacted to 5 coax cables. It should be noted that the enable and clock cables are common for the whole module. Figure 12 is a picture of an ICPC containing the electronics for 64 channels.

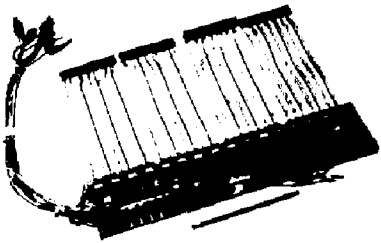


Fig. 12 64 channel ICPC with input pigtail

Test Results

Pulsar

Each ICPC has a capacitively coupled strip across the input lines to the amplifier. To test the overall system timing variations, a pulse is applied to this strip. The rise time and amplitude of this pulse simulate a drift chamber signal of > 40 μ a. With this pulser scheme it is possible to measure the reference time t_0 for each channel. With only moderate care in component selection it is possible to maintain the t_0 variation on a plane to within 4 ns. In addition, one has a quantization error which for the case where the clock is unsynchronized to the pulser or clock stop pulses should on average produce an rms of .34 time bins (4 ns each) if there are no other sources of timing jitter. The actual measured rms value averaged over a typical plane (273 wires) was .44 time bins.

Pulsar data was taken over a period of several weeks and the t_0 's for each channel were compared. No shift of more than .25 time bins was observed. This remarkable stability is of course expected. Having measured it, it is most reassuring and would suggest that operation of much larger drift chamber systems for ISABELLE experiments is viable.

Particle Tracks

As of this writing, 6 full modules have been built, but there has not been a beam of particles available from the AGS. Therefore all track reconstruction has been done from cosmic ray triggers. Most planes will operate with a comparator threshold of 2 μ a as referred to the input. Under these conditions little pickup of the 4-phase clock is observed. When clean single tracks (μ 's) are observed, the pattern recognition already finds unambiguous point-slope in 70% of the events with only 2 modules. This

is without B field. We expect similar results with 3 modules in a B field.

Relevance to ISABELLE Detectors

The NPS II project, in addition to its obvious physics potential, may be regarded as a prototype tested for an ISABELLE detector. The event rate loading objectives are similar. At NPS II the raw beam of 10^7 particles passes through the active area of the drift chambers. If this region can be made to work efficiently, as it is designed to do, then a major step will have been made to handling the 10^7 events/sec rate expected at ISABELLE. This was a major design consideration and should be optimized by an appropriate selection of the filter network parameters because otherwise the system is dc coupled and deadtimeless.

The compact packaging this highly integrated system uses would make detectors of > 10^5 drift wires feasible. With propagation delay selection, t_0 's can be matched to better than 2 ns so that individual channel t_0 corrections need not be made. The time measurements are done strictly digitally by a common clock so that only one drift time-to-digital slope parameter is required for the whole system. Finally this highly integrated electronics should prove very reliable since there is an average of less than 1.5 active components per channel.

TABLE 1

BNL TRA401
AMPLIFIER CHARACTERISTICS²

Characteristics	Minimum	Maximum	Units
Input Type	True Differential		
Input Noise (RMS)		0.25	μ A
Input Resistance		80	ohms
Input Protection		1.13×10^{-4}	J
Transfer Impedance	17		Kohms
Delta Transfer Impedance	-10%	+10%	
Gain Stability		0.25	%/°C
Output Impedance		50	ohms
Rise Time		4.4	nsec
Max. Linear Output	1.2		Volts
Propagation Delay		10	nsec
Delta Propagation Delay		1.5	nsec
Temperature Range	0	50	°C
Supply Currents			
	+5.5 V \pm .1	65	mA
	-2.5 V \pm .1	45	mA

TABLE 2
BNL MVL400
DISCRIMINATOR CHARACTERISTICS²

<u>Characteristic</u>	<u>Minimum</u>	<u>Maximum</u>	<u>Units</u>
Input Resistance	3		Kohms
Input Z Threshold Control	1.5		Kohms
Threshold Control Range (1:1)	0	1.5	Volts
Threshold Hysteresis	6	10	mV
Threshold Match		5	mV
Crosstalk between Inputs of Channels		-40	dB
"0" Logic Level		1.8	Volts
"1" Logic Level	+3.5		Volts
Output Response Time		4.4	nsec
Slewing		3	nsec
Double Pulse Resolution		20	nsec
Input Capacitance		6	pF
Propagation Delay	14.5	17.5	nsec
Operating Temperature	0	50	°C
Supply Currents			
+5 V		200	mA
-5 V		22	mA

TABLE 3
4 CHANNEL 256-BIT SHIFT REGISTER

Clock Frequency (Effective)	DC to > 330 MHz
Phase to Phase Delay Match	< 1 ns
Maximum Readout Frequency (with 16 way or tie)	> 20 MHz
Power Dissipation at 250 MHz	< 210 mw

References

- ¹ Members of the MPS Group are: A. Etkin, K.J. Foley, M.A. Kramer, S.J. Lindenbaum, R.S. Longacre, W.A. Love, T.W. Morris, E.D. Platner, V.A. Polychronakos, A.C. Saulys, Y. Teramoto, C.D. Wheeler.
- ² LeCroy Research, Spring Valley, New York.
- ³ Craig Wolfson, RCA, Solid State Division, Somerville, New Jersey.

THE MARK II SECONDARY VERTEX DETECTOR*

John A. Jaros
Stanford Linear Accelerator Center
Stanford University, Stanford, California 94305

Summary

We have added a high precision drift chamber to the Mark II detector at PEP. The design of the device has been optimized for measuring vertex topologies as accurately as possible. This has involved placing wires within 10 cm of the beam line, using a beryllium beam pipe as the inner gas wall of the chamber, and improving the accuracy of the drift-time measurement. The chamber operates reliably and efficiently and records complex hadronic events accurately. Although the currents drawn by the chamber are moderately high in colliding beam operations, events are "clean," with few spurious tracks or hits. The spatial resolution of the chamber is 80 μ ; this permits tracks to be extrapolated to the interaction point with 100 μ accuracy.

Introduction

During the past year, we have constructed, installed, and begun data taking with a high precision drift chamber which has been added to the Mark II

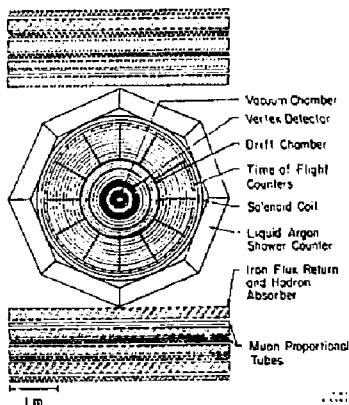


Fig. 1. The Mark II detector at PEP. The muon detection system on the sides is not pictured.

detector at PEP. The chamber, shown in Fig. 1, is located between the vacuum chamber and main Mark II tracking chamber. Its purpose is to provide an accurate picture of the interaction and decay vertices which are produced in high energy e^+e^- interactions. Decays of hadrons containing the c and b quarks and the τ lepton give rise to events with secondary vertices within 1 mm or so of the interaction point. The secondary vertex detector should allow us to measure the location of these secondary vertices accurately enough to determine particle lifetimes. The device may also be useful in tagging events with charm or bottom hadrons.

The design of the chamber was optimized for vertex detection, but it serves in several other capacities as well. It is used at both the primary and secondary levels in the Mark II trigger.² As an adjunct to the main tracking chamber, it improves solid angle coverage and momentum resolution, and of course the reconstruction of K_S^0 and Λ decays. We hope, in the future, to use it for pattern recognition in events with dense hadron jets.

This paper discusses the mechanical design of the chamber and the techniques we used to enhance its performance as a vertex detector. In addition, it summarizes our brief experience operating the chamber at PEP. It concludes with a discussion of the chamber's performance.

Chamber Parameters

Fig. 2 shows a cross section of the vacuum chamber, the vertex detector, and the innermost wires of the main drift chamber. The vertex detector is a cylindrical drift chamber 1.2 meters long and .70 meters in diameter. Wires are strung between the two 5 cm thick end plates in two "bands," one comprising 4 wire layers just outside the beam pipe, the other 3 wire layers near the outer radius. The chamber uses the vacuum chamber as an inner gas seal. The cylindrical outer shell is made of .18 cm thick aluminum and supports the wire tension load on the end plates. There are 825 sense wires in the entire chamber, 270 in the inner band and 555 in the outer band. Table I gives the radius and number of wires in each of the sense-wire layers. All the sense wires are axial and no attempt is made to measure position along the wires. The drift cell radius is 5.30 mm throughout the entire array. The chamber and beam pipe can be operated at pressures up to 2 atmospheres absolute.

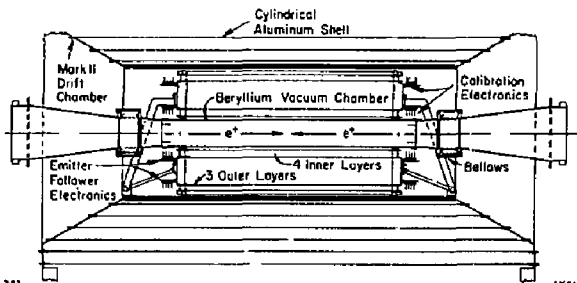


Fig. 2. Cross section of the vertex detector as installed in Mark II.

Table I. Sense Wire Placement in Vertex Detector

	Layer No.	Radius (cm)	No. of Sense Wires
Inner Band	1	10.1223	60
	2	10.9658	65
	3	11.8093	70
	4	12.6528	75
Outer Band	5	30.3668	180
	6	31.2103	185
	7	32.0538	190

Vertex Detector Design

Extrapolated-Track Resolution

The figure of merit of a vertex detector is the accuracy with which a track can be extrapolated to the vicinity of the primary interaction point. In our chamber, there are two important contributions to this "extrapolated-track resolution." The first comes from our finite measurement accuracy, σ_m , and the fact that we must extrapolate the track significantly beyond where it is measured. In the vertex detector, this error can be written

$$\sigma_x = .85 \sigma_m$$

Multiple coulomb scattering in the beam pipe, chamber gas, and wires gives rise to the other part of the error. The resultant angular uncertainty leads to a position uncertainty once a track has been extrapolated. It can be written

$$\sigma_{MCS} = 95 \mu/P \text{ (GeV/c)}$$

for this chamber. These two factors, added in quadrature, give the extrapolated track resolution for the device.

We have followed a straightforward strategy to minimize these tracking errors. We have minimized the distance tracks must be extrapolated by placing the inner wire band as close as possible to the beam pipe. We measure the angle of tracks as accurately as possible by placing the outer band of wires at the largest possible radius. And, of course we have tried to achieve good spatial resolution with the drift-time measurement. Multiple scattering has been kept to a minimum by using a small beam pipe radius, letting the beam pipe double as the inner gas wall for the chamber, and using low Z materials in the construction.

Beryllium Beam Pipe

The beam pipe is a 1.40 m long cylinder, 15.6 cm in diameter, made of 1.42 mm thick rolled beryllium sheet.³ The central beryllium tube has been brazed to an aluminum ring at each end, and this in turn has been electron-beam-welded to an aluminum-stainless steel transition to which the remainder of the beam pipe is welded. The diameter of the tube was chosen to accommodate the swath of synchrotron radiation from the insertion quadrupoles with some clearance. Beryllium was chosen to minimize the thickness of the tube in radiation lengths. A 50 μ thick titanium foil cylinder was inserted inside the beryllium tube and attached with a continuous circumferential weld at each end. Its purpose is to absorb synchrotron radiation which backscatters from heavy masks located 3 meters from the interaction point. We have wrapped the outside of the tube with a 50 μ mylar sheet and 25 μ of aluminum foil; the mylar isolates the beam

pipe from the foil, which serves as a ground shield for the chamber. The chamber's gas volume is sealed off with O-rings between the beam pipe and the end-plates of the chamber.

High Resolution Drift Chamber

To achieve high spatial resolution in the vertex detector, we have located the wires with high accuracy, employed high resolution electronics and calibration techniques, stabilized the gas pressure, and operated the chamber at high gain. As seen in Fig. 3, which

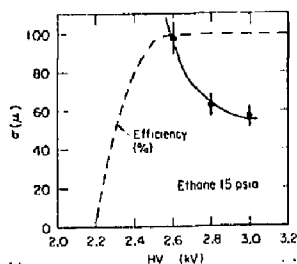


Fig. 3. Spatial resolution as a function of high voltage for pure ethane at 1 atmosphere pressure. The dotted curve shows the efficiency as a function of high voltage. Data are from the vertex detector prototype.

shows spatial resolution in our prototype chamber as a function of chamber voltage, resolution improves significantly when the chamber is operated well above the beginning of the efficiency plateau. The use of organic gases and higher pressure operation should also improve the resolution; once we have assured ourselves that the chamber gas doesn't polymerize in a high background environment, we may try this approach.

Wire Pattern

Fig. 4 shows the wire pattern of the chamber's inner band. The outer band is similar. Two constants characterize the entire array: one is the distance separating a sense wire layer from the adjacent field wire layers (.422 cm); the other is the distance between sense and field wires in a sense-wire layer (.530 cm). With the exception of the outermost and innermost layers, which we call guard layers, all the field wires are run at a common potential; the sense wires are all run at ground potential. Intermediate potentials are chosen for the guard layers to equalize gains on all the sense wires; this also serves to minimize the electrostatic deflections in

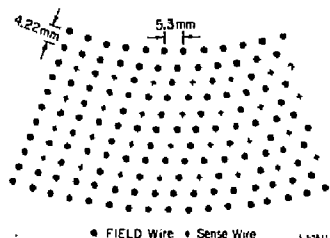


Fig. 4. Arrangement of wires in the vertex detector. The inner band of wires consists of five identical sections; one half section is pictured here.

the array. The presence of a field wire nearly exactly between the two sense wires minimizes cell-to-cell crosstalk. We have used 20 μ diameter gold-coated tungsten wire as sense wires and 150 μ gold-coated field wires. The field wires in the inner band are aluminum, chosen to minimize the multiple coulomb scattering; we use beryllium-copper wire in the outer band. The choice of a fixed sense wire to field wire distance lets us characterize the entire chamber with a single relation between drift time and drift distance. Wires are held in place with the nylon insulating bushing shown in Fig. 5. By selecting the

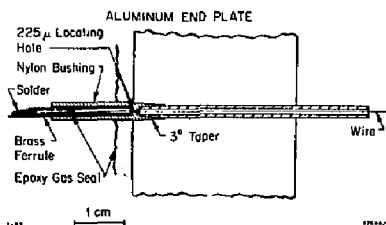


Fig. 5. Nylon insulating and positioning bushing.

bushings individually under a high power microscope and by using high precision machining techniques, we have located the wires to an accuracy of better than 15 μ (rms) throughout the chamber.

Electronics

The electronics associated with the chamber is shown schematically in Fig. 6. Calibration pulses, used to determine a common start time for the entire array, are fanned out to each wire and are simultaneous within 350 ps (rms). The chamber pulse is coupled to 6 m of 50 Ω coax with a fast emitter-follower which serves as an impedance matcher. We use commercial amplifier/discriminators⁴ to drive 17 m of twisted pair; the time between a wire pulse and common stop pulse is measured with a time-to-amplitude converter⁵ which is readout with a dedicated microprocessor⁵ (BADC) which then communicates via Camac with the on-line computer. The TAC/BADC resolution is better than 250 ps throughout the entire system. The TAC has additional outputs used in the primary and secondary triggers. During data taking, the system is calibrated every 8 hours.

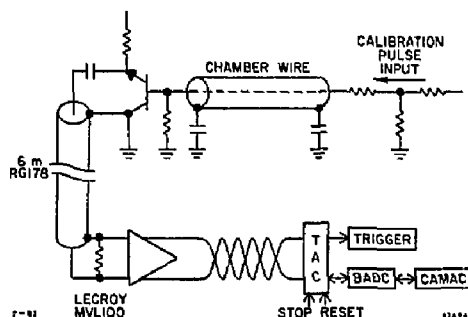


Fig. 6. Calibration and readout electronics.

Operating Experience at PEP

The vertex detector was installed in the Mark II detector at PEP in September of 1981. It was operational for trigger and efficiency studies during the month of November and was used in regular data taking during December when an integrated luminosity of 1500 nb⁻¹ was accumulated at 29 GeV center-of-mass energy.

We are operating the chamber at 15.50 \pm .05 psia with a 50/50 mixture of argon and ethane. The high voltage is set to 2.250 kV and the electronics threshold is 400 μ V at the MVL100 input. With stored currents of 20 ma of both electrons and positrons, there is no beam pickup. Under these same conditions, we have observed a little beam pipe heating; the beam pipe temperature has increased by as much as 3 $^{\circ}$ C when the beams are on. Moderately high currents are drawn by the chamber, especially the inner layers. At the beginning of a fill there is \sim 0.2 μ A/wire in the inner band; only 0.01 μ A/wire is drawn in the outer band. Despite these rather high currents, the information from the chamber is quite "clean"; i.e., we see very few spurious hits or uncorrelated tracks, and there is no noticeable "snow." Fig. 7 shows the pattern of the wires which have been "hit" in a typical hadronic event in the vertex detector. It also demonstrates that cell-to-cell pickup is not a

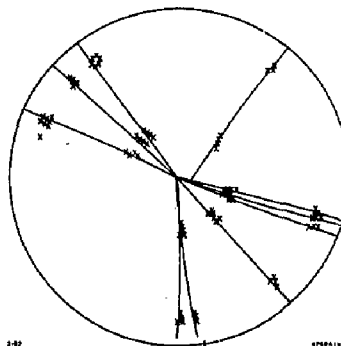


Fig. 7. Hadronic event in the vertex detector.

problem. In general, adjacent cells fire only when a track has passed near enough to a cell boundary that ionization is collected on both wires. Typically, one of the drift-times is very long in these instances.

Chamber Performance at PEP

Efficiency

Fig. 8 shows the chamber efficiency as a function of high voltage for each of the four inner layers.

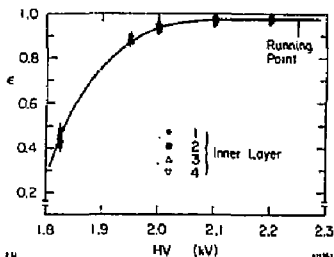


Fig. 8. Efficiency vs. high voltage

Note that, within the statistical errors, all the data seem to lie on one curve. This fact confirms that the wire gains in the four layers have been successfully matched. The chamber is fully efficient above 2050 V; we assume the observed 1 or 2 % inefficiency to be tracking errors, and not a true measure of chamber inefficiency. We run the chamber well above the knee in the efficiency plateau in order to improve the spatial resolution.

Monitoring Drift Velocity

The close packed wire array in the vertex detector is auto-calibrating in the following sense. A typical track passing through the inner layers generates 4 independent drift times. These 4 times can be algebraically related to four other quantities: the slope and intercept of the particle's trajectory, the drift velocity, and the time corresponding to zero drift length. Thus, on a track-by-track basis we can monitor the drift velocity and the stability of the calibration procedure. The linear space-time relation we assume in this procedure is accurate over about 80% of the cell. The technique measures the drift velocity with an error of a few per cent per track; so the drift velocity can be monitored to better than 1/2% in a one or two hour run. We hope to use this technique to study run-to-run drift velocity variations; it will permit corrections to be applied on a short time-scale, if necessary.

Resolution

We are currently studying the time-distance relation and spatial resolution in the vertex detector. Our procedure is to assume a simple form for the relation (we allow linear, quadratic, and cubic terms) and vary the parameters to minimize the χ^2 for an ensemble of tracks. Our studies to date have used the sample of Bhabha scatters collected during the month of December.

Fig. 9 shows the distribution of the sum of the squared residuals per track for tracks which have passed through the four inner layers after the time-distance parameters have been optimized. Two track

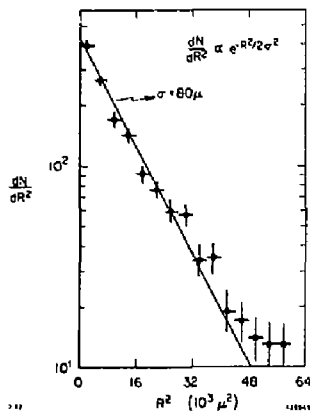


Fig. 9. Distribution of the sum of the squared residuals per track, dN/dR^2 .

parameters, the slope and intercept of the trajectory, are allowed to vary in the fit, so the distribution is proportional to the χ^2 distribution for 2 degrees of freedom. So we can write

$$\frac{dN}{dR^2} = e^{-R^2/2\sigma^2};$$

and the plot lets us determine the resolution graphically. For this subset of the data we have achieved a resolution of 80 μ per layer. We are presently optimizing the time-distance parameters for hadronic events by including angle dependent terms for tracks which pass near the field wires. Assuming a measurement error of 80 μ , the extrapolated track resolution for the Mark secondary vertex detector is

$$\sigma^2 = \sqrt{(70)^2 + \left(\frac{95}{P(\text{GeV}/c)}\right)^2} \quad (\mu)$$

Acknowledgements

We acknowledge the help and advice received from many members of the Mark II collaboration. We especially thank M. Breidenbach, L. Golding, V. Golubev, J. Kadyk, T. Nakashima, R. Leonard, and M. Nelson. Thanks also to K. Dean and the PEP Vacuum Group for building, testing, and installing the vacuum chamber.

*Work supported by the Department of Energy, contract DE-AC03-76SF00515.

References

1. D. Amidei, R. Baggs, D. Briggs, E. Grund, G. Hanson, C. Hoard, J. Jaros, D. Johnson, N. Lockyer, R. Stickley, G. Trilling, Y. Wang.
2. H. Brafsan et al., IEEE Trans. Nucl. Sci., NS-25 692 (1978).
3. The beryllium chamber was fabricated by Electrofusion Corporation, Menlo Park, CA.
4. LeCroy Research Systems Model 7791 16-channel amplifier/discriminator.
5. E. L. Cisneros et al., IEEE Trans. Nucl. Sci., NS-24 413 (1977).
6. M. Breidenbach et al., IEEE Trans. Nucl. Sci., NS-25 706 (1978).

A. H. Walenta
University of Siegen
Siegen, Germany

J. Paradise*
Massachusetts Institute of Technology
Cambridge, Massachusetts, U.S.A.

H. Hofer, G. Viertel and J. Fehlmann
Eidgenössische Tech. Hochschule
Zürich, Switzerland

Abstract

With the principle of the time expansion chamber and the additional measurement of the position of the avalanche along the circumference of the anode wire it is possible to reconstruct the spatial distribution of the primary ionization in space. A position resolution for minimum ionizing tracks of $\sigma \leq 30 \mu\text{m}$ is expected. First tests and concepts for vertex detectors are presented.

Introduction

Particles produced in high energy pp, $p\bar{p}$ and e^+e^- collisions are expected to consist of c, b and t quarks and have a relatively long lifetime, such that they come into the reach of identification by measuring their decay vertex separated from their production vertex. In order to detect these particles with a lifetime of $\tau \leq 10^{-13}$ a position resolution of $\sigma \leq 30 \mu\text{m}$ is needed.

Earlier work¹ has shown that a drift chamber can reach a resolution which comes close to this value. The measurement was performed for several gases and mixtures for increasing pressure P and as a function of the drift length x. It was found that three main contributions to the position resolution σ can be distinguished:

$$\sigma^2 = A^2 + (\Delta x_{\text{ion}})^2 + (\Delta x_{\text{diff}})^2 \quad (1)$$

The last term is due to diffusion

$$(\Delta x_{\text{diff}})^2 = \frac{2BD}{\mu E} x = 2B \frac{D}{\mu} \frac{1}{E/P} \frac{x}{P} \quad (2)$$

with D the diffusion constant, μ the electron mobility, E the electrical field and B a correction factor which takes into account that a number of electrons participate in generating the stop signal. This contribution Δx_{diff} can be easily separated, because it becomes the main contribution for large x.

Δx_{ion} is a contribution due to the fluctuation of the primary ionization. Since a minimum ionizing particle leaves on its path through a gas only a few statistically distributed clusters of ionization ($\bar{n} \approx 10 \dots 40 \text{ cm}^{-1}$) at atmospheric pressure, the track looks microscopically fuzzy as can be seen from enlarged cloud or bubble chamber pictures. A drift chamber measures the position of the cluster with the shortest drift time to the anode (leading edge discrimination of the anode pulse) and therefore is sensitive to the random position of the cluster along the particle track.

Δx_{ion} depends on the mean distance between clusters $\lambda_{c1} = 1/\bar{n}$ with \bar{n} the mean number/cm track length and therefore decreases proportionally with pressure.

The maximum of this contribution is at $x = 0$ with $\Delta x_{\text{ion}} = 1/2 \lambda_{c1}$ and decreases rapidly with increasing x, a purely geometrical effect.

The constant contribution A was found to be independent of pressure, but different for different gases and mixtures. The lowest value $A = 20 \mu\text{m}$ was found for a mixture of $\text{C}_2\text{H}_4 - \text{C}_3\text{H}_8$ (3:1). This effect could be due to the range of the primary electrons, fluctuations of the avalanche or resolution of the electronics.

The analysis of these data shows that it will be very difficult to improve the overall resolution further but indicates the basic problems. Therefore, a new type of chamber, the time expansion chamber,² has been investigated with respect to its application as a high precision vertex chamber which, in principle, corrects the limitations of the standard drift chamber described above, giving high position resolution already at atmospheric pressure and good double-track resolution at the same time. This type of chamber also opens the possibility for a position measurement of the second coordinate with the same high precision as in drift direction.

Principle of the Vertex Chamber

The best position resolution for the track of a minimum ionizing particle can be achieved if the position of each primary ionization cluster can be measured separately, and a straight (or slightly curved line in a magnetic field) is fitted through these points. Then the contribution Δx_{ion} as introduced above can be eliminated.

Furthermore, if the position of each cluster is measured separately, the measurement of the center-of-gravity of its spatial distribution after diffusion gives a precision of $\sigma_{c1} = \sigma_0/\sqrt{m}$, where σ_0 is the diffusion of a single electron and m is the number of electrons/cluster. If a total of n clusters is measured, the total contribution of the diffusion will be

$$\sigma = \sigma_0/\sqrt{m \cdot n} = \sigma_0/\sqrt{N} \quad (3)$$

with $N = m \cdot n$ the number of electrons released in the track section under consideration. This represents a considerable reduction of the contribution of diffusion as compared to the method of leading edge discrimination. Also, the contribution A may be reduced if it is caused by the range of the primary electrons (for higher energy, called δ -rays) by rejecting the position measurement of "big" clusters, or if it is caused by fluctuations of the avalanche or the electronic timing by increasing the relative speed of the avalanche.

These improvements are in principle possible with a special readout of the time expansion chamber. There are two main features which distinguish this chamber from a standard drift chamber (Fig. 1)

(a) The drift region is separated from the gas amplification region by a fine grid. The electric field strength and gas mixture are adjusted to result in a small drift velocity ($v_{Dr} = 5 \mu\text{m/ns}$) as compared

* Now at ETH, Zürich, Switzerland.

to the usual value ($v_{Dr} = 50 \mu\text{m/ns}$). The full drift velocity is maintained in the gas amplification region and therefore the anode signal can follow the fluctuations of the primary ionization and even resolve individual clusters.

(b) Two pick-up wires are placed close to the anode wire. The difference signal is given by $\Delta PW = \sin\alpha$ with α the angle of the fieldline carrying the cluster to the anode as shown in Fig. 1. Since α determines the fieldline it also determines the coordinate y along the track.

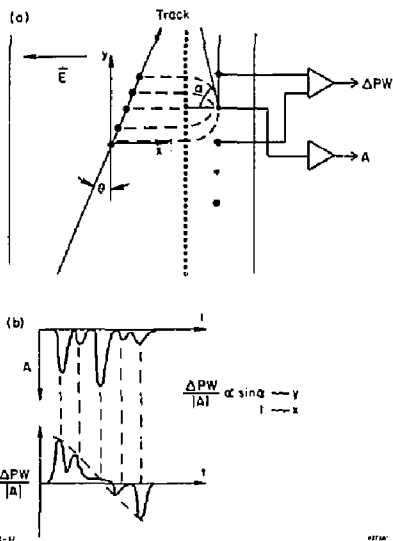


Fig. 1. Principle of time expansion chamber. (a) Layout with pick-up wires. (b) Signals.

Therefore, a track inclined with respect to the grid by an angle θ (Fig. 1) will allow the measurement of the individual clusters in two coordinates, x by the center-of-gravity of the drift time and y by determining α . For smaller θ the clusters will eventually merge and it will be difficult to eliminate large clusters and determine y . Still, the measurement of the center of gravity will result in an improved position resolution particularly since the y coordinate has less weight for smaller θ . Nevertheless, one may design the chamber layout such that a minimum angle θ is guaranteed (see Fig. 13).

A vertex detector is most effective close to the vertex and therefore a very good double-track resolution is of importance. The feature (a) of the time expansion chamber will automatically give a high double track resolution Δx only limited by the overlap of the projected track segments (Fig. 2) $\Delta x = d \cdot \tan\theta$ with d the segment in y direction accepted by an individual anode. At this point a compromise has to be found between position resolution ($\sim 1/\sqrt{d}$ because of the number of electrons N measured), a minimum θ for separating clusters, drift velocity and double track resolution.

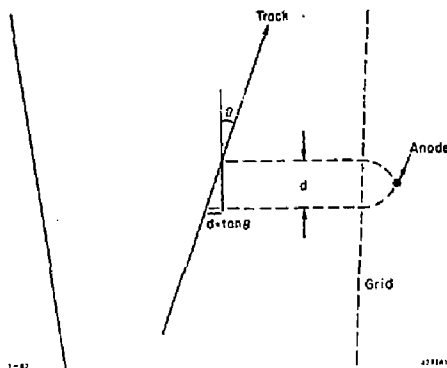


Fig. 2. Limit of double-track resolution due to the width of the projected ionization.

Measurements

Measurements have first concentrated on investigating the novel features of the time expansion chamber which lead to the reconstruction of the primary ionization.

The time expansion effect has been primarily introduced to accommodate the speed and response of the gas amplification to the time sequence of the arriving ionization. Therefore, it is convenient to discuss the time expansion chamber as a system (Fig. 3) consisting of a "delay line" (the drift space) connected to an "amplifier" (the "avalanche amplifier" plus electronic preamplifier). The "delay line" transforms the projection of a charge distribution $\rho(x)$ into a time

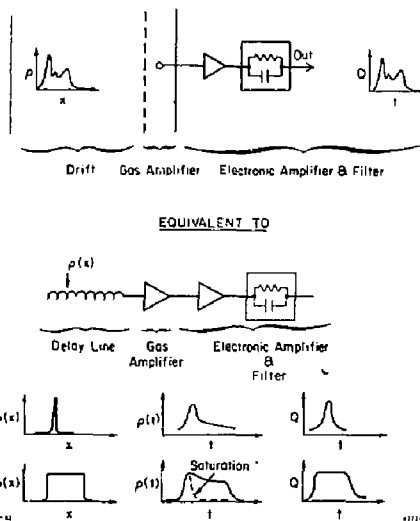


Fig. 3. The time expansion chamber and its electronic analogue; $\rho(x)$ spatial distribution of charge, $Q(t)$ signal.

sequence $\rho[x(t)]$ with $x(t) = v_{Dr} \cdot t$ and the amplifier transforms it into an electric signal $Q(t) = S \rho[x(t)]$ with S the amplification factor.

The "avalanche" amplifier and the electronic pre-amplifier are considered as one unit while the latter is assumed to cancel linear deformations of the "avalanche" amplifier by appropriate shaping (see, for example, Ref. 4).

Bandwidth of the Amplifier

Figure 4 shows the signal of one cluster produced by an ^{55}Fe X-ray in gain region behind the grid which can be considered as the response of the system to a δ -function $\rho(x-x_0) = \rho_0 \delta(x-x_0)$. A width of $\Delta t = 10$ ns (fwhm) and almost complete cancellation of the tail has been achieved with the circuit shown. Sharper clipping reduced the amplitude without shortening the signal indicating the high frequency limit given by the "avalanche" amplifier.

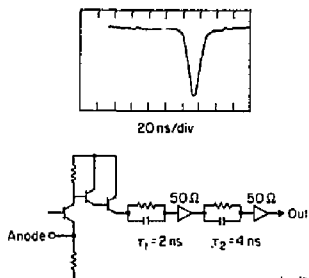


Fig. 4. Response to pointlike charge distribution (^{55}Fe). Grid to anode = 1.6 mm, ϕ anode = 20 μm .

Noise of the Amplifier

The noise of the "electronic" amplifier was a typical noise spectrum with an equivalent noise charge $\sqrt{\text{ENC}} = 5 \cdot 10^3$ electrons (rms), a relatively high value. With a careful design of amplifier and chamber, better values can be achieved.⁵ The noise of the "avalanche" amplifier would manifest itself in an amplitude variation which usually is identified as the energy resolution of the counter in the pulse mode. Also spurious signals would contribute to noise which could be expected as "after" pulses at high gain. By counting individual pulses in a pulse train for minimum ionizing particles as shown in Fig. 5, a plateau was reached for increasing gas gain, indicating that only ionization clusters contribute to signals. The mean number of measured clusters per track (the plateau-value) as a function of gas pressure shows that up to 1 atm no dead-time effects can be observed, which is interpreted as absence of nonlinear distortions (Fig. 6).

Drift Characteristics

The drift velocity has to be adjusted to $v_{Dr} = 5$ $\mu\text{m}/\text{ns}$, such that with the given bandwidth of the amplifier the spacial structure of roughly 50 μm of $\rho(x)$ can be recorded. This low drift velocity is obtained by operating with a drift field far below saturation, the mode which usually is used in drift chambers. The field is considered to be "low" if it has not yet heated up the electrons considerably and they are still close to thermal equilibrium. Then in good approximation one obtains⁶ for the drift velocity

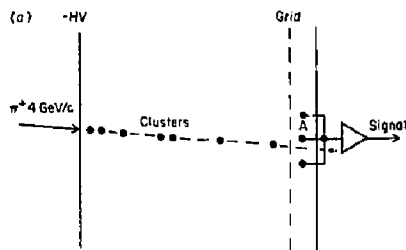


Fig. 5. Layout and signals for cluster measurement. Drift gap 10 mm, maximum drift time 1 μs .

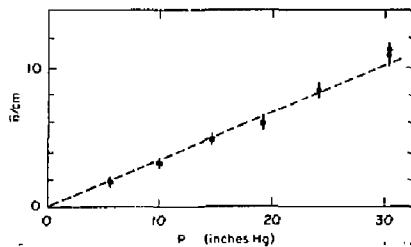


Fig. 6. Number of clusters/cm in 92% Ne + 8% methylal as a function of pressure.

$$v_{Dr} = \frac{2}{3} \frac{e}{m} \frac{E}{N} \frac{1}{\sigma v} \quad (4)$$

with N the gas density (molecules/volume), σ the momentum transfer cross section and v the mean electron velocity. It can be seen that the drift velocity increases under these conditions linearly with E/N , a result which is also important for calibration and stability (see below). Figure 7 shows the measured drift velocity for increasing concentration of methylal in argon which shifts this linear behavior to higher E/N .

Methylal has a large cross section for inelastic electron scattering and therefore tends to keep the electron energy in equilibrium with the gas. The diffusion coefficient is given by

$$D = \frac{1}{3} \frac{\bar{v}}{N \sigma} \quad (5)$$

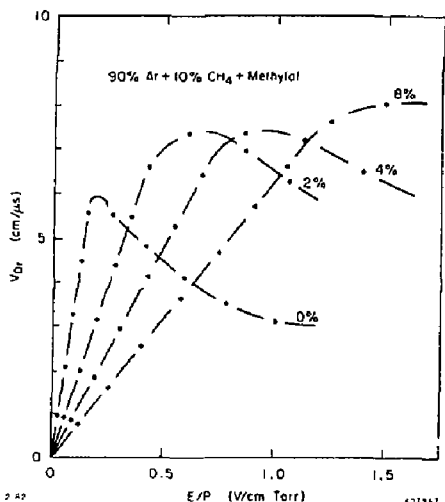


Fig. 7. Drift velocity of center of gravity (ionization from pointlike X-rays). The admixture of methylal is shown on the curves.

and together with the Einstein relation $\sigma = \sqrt{2Dt} = \sqrt{2D/v_{Dr}} \cdot x$ one obtains

$$\frac{\sigma^2}{x} = 2 \frac{\epsilon}{eE} \quad (6)$$

where ϵ is the mean electron energy. For ϵ in equilibrium with the gas σ^2/x decreases ideally as $1/E$, as shown in Fig. 8 (solid line). Measurements were performed with the time expansion chamber where the anode pulse width Δt was recorded from photographs and the diffusion determined by $\sigma = 0.43 v_{Dr} \cdot \Delta t$. The standard drift gas (Ar + isobutane) shows very clearly a deviation from the ideal behavior (as expected⁷) while C_2H_4 + methylal gives lower values and follows to high E/N the diffusion data measured by different means.⁸ This shows again that the anode signal follows the structure of $\rho(x)$ with a precision sufficient for the determination of the center-of-gravity of the signal.

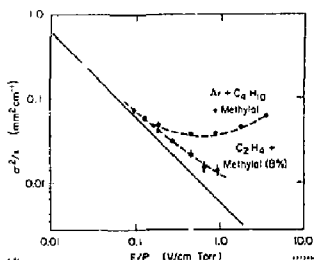


Fig. 8. Diffusion σ^2 for a drift length x as a function of E/P for $P = 1$ atm. Ar, C_2H_4 , methylal from Ref. 7. Points with error bars measured in time expansion chamber; dashed line measured by Ref. 8 for C_2H_4 .

Angular Measurement

The above mentioned feature (b), i.e., the angular measurement, has been tested with a cylindrical chamber without grid but with two pick-up wires close to the anode. X-rays (8 keV) have been used to simulate single ionization clusters under a given angle α . The difference signal has been clipped to a width of $\Delta t = 20$ ns (FWHM) and its amplitude spectrum recorded for different α (Fig. 9). The width of this distribution corresponds to an angular resolution of $\Delta\alpha(\text{rms}) = 2.3^\circ$, partially due to the width of the collimation, limited mechanical accuracy or fluctuations in the avalanche. The resolution expected from the noise of the preamplifier⁹ is negligible, namely $\Delta\alpha(\text{rms}) = 0.8^\circ$.

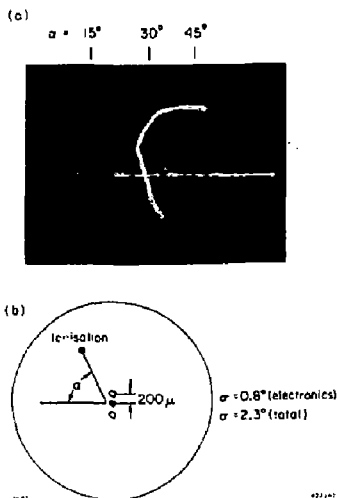


Fig. 9. (a) Pulse height distribution of difference signal ΔPW from pick-up wires for several values of α . (b) Electrode arrangement.

Double Track Resolution

An example of the double track resolution obtainable is shown in Fig. 10. The signals from three wires are displayed on the scope simultaneously by mixing them linearly after delaying two of them. γ -rays (bremsstrahlung from ^{106}Ru) occasionally produce pairs which are recognized by giving signals in two scintillators behind the chamber and two separate signals for the last wire. The central wire shows double signals too and a minimum distinguishable separation of $\Delta x = 200 \mu\text{m}$ was found. This is in agreement with the expected diffusion, $\sigma_{\text{diff}} = 70 \mu\text{m}$ for a drift length of $x = 5$ mm.

Readout

After amplification the anode signal (A) and the difference signal from the pick-up wires (ΔPW) are digitized with flash ADC's in 10 ns time samples and stored in 6 bit RAM's (1k memory) (Fig. 11). A prototype 512 bits deep has been tested successfully.¹⁰ With drift velocity $v_{Dr} = 5 \mu\text{m/ns}$ the sampling speed of $\Delta t = 10$ ns corresponds to $\sigma = 15 \mu\text{m}$, even if no center-of-gravity calculation is performed.

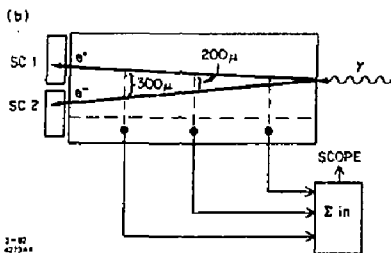
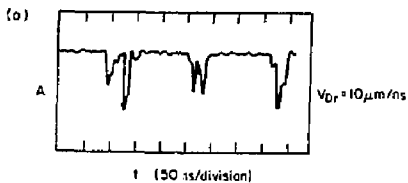


Fig. 10. (a) Signals from three anode wires displayed on scope. (b) Layout for measurement (SC: scintillators).

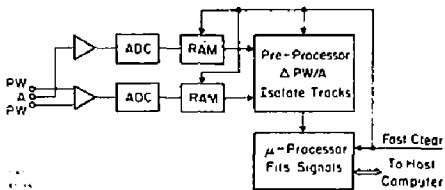


Fig. 11. Readout (schematically).

A preprocessor isolates and defines single track segments and calculates $\Delta PW/A$. In principle, this information can be forwarded to the on-line computer but it may be convenient to process the data in dedicated μ -processors (one per wire) to increase computing power and reduce the amount of data written on tape.

Discussion

The reconstruction of the projection of the charge distribution $\rho(x)$ by measuring the pulse train $Q(\tau)$ is based on the assumption that the grid acts as a virtual amplification plane. This is achieved by a large time expansion factor where the drift velocity v_{Dr1} in the amplification zone is large compared to the value in the drift region v_{Dr2} , such that the longer drift path on field lines reaching the anode at large x becomes negligible. A time expansion factor of 10 ($v_{Dr1} = 5 \mu\text{m/ns}$, $v_{Dr2} = 50 \mu\text{m/ns}$) seems to be sufficient, but larger factors can be considered.

The fact that the chamber does not operate at saturated drift velocity turns out to be an advantage for the stability. The drift time for ionization in a point $P(x, y, z)$ is given by

$$t_{Dr} = \int_x^{x_0} \frac{ds}{v(x, y, z)}$$

with x_0 the position of the grid. Because of the choice of the gas we have

$$v_{Dr} = v_0 E/N \quad (7)$$

with v_0 depending on the gas mixture and E/N the reduced field strength. Furthermore, as long as the geometry of the chamber is unchanged $E(x, y, z) = U_0 F(x, y, z)$ with U_0 the applied high voltage and $F(x, y, z)$ a function depending only on geometry. Therefore, one obtains

$$t_{Dr} = \frac{N}{v_0 U_0} \int_x^{x_0} \frac{ds}{F(x, y, z)} \quad (8)$$

Every measured drift time can be corrected with the same factor and only one point has to be monitored once the integral is known for each point from test beam measurements.

Another aspect of this detector is worth being mentioned. Once the cluster sequence has been measured from the anode signal, the measurement of the center-of-gravity on the pick-up wires would be sufficient to determine the exact location of the track, assuming its angle θ is known from the rough position measurement of other wires. This option would considerably reduce the electronics needed for readout.

The same principle offers the possibility of measuring the second coordinate (along the wire) with very high precision. From signal (Q) to noise (ΔQ) considerations, it can be shown that with proper design of amplifiers and detectors the readout of the center-of-gravity of induced signals on cathode strips (width d) can give a resolution¹¹

$$\sigma = \frac{\Delta Q}{Q} d \sqrt{2 \sum_1^{k/2} \frac{1}{n^2}}$$

with $k \cdot d$ the width of the induced signal (about twice fwhm). A resolution of $\sigma \approx 15 \mu\text{m}$ should be possible for $d = 2 \text{ mm}$, $Q = 5 \cdot 10^6$ and the chamber geometry of the time expansion chamber.

However, measurements and analysis of the data^{12, 13} show that limits of position resolution for minimum ionizing particles are determined by the fact that the center-of-gravity of the projected charge is measured and the latter is subject to large fluctuations. Only for $\phi = 0$ (Fig. 12) does this effect disappear.

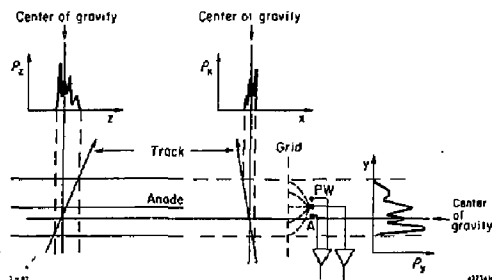


Fig. 12. Principle of three-dimensional center-of-gravity measurement. Coordinates as in Fig. 1. z along the anode wire.

Figure 12 also shows how the chamber described above can correct for these effects. A track crossing a gap

d and producing a charge distribution $\rho(s)$ (with s along the track) is shown in three projections. Depend on the angles ϕ and θ these projections are linear images of each other. It follows then that the lines of back projections of the center-of-gravity of each view meet in a point which is exactly on the track.

This figure also illustrates the need for time expansion and shows two aspects. First, the time expansion must be large enough to allow the anode signal to follow the ionization structure in order to be able to determine its center-of-gravity. Second, it is the only measurement which can give the detailed structure. The measurement of the induced signals on the cathode strips or the pick-up wires gives a certain mean value which, for fine cathode strips, is the center-of-gravity but for the pick-up wires is given by

$$\overline{\Delta PW} \sim \int c_y g(y) dy$$

where $g(y)$ includes the function mapping the field lines onto the circumference of the anode wire (angle α) and the function $\Delta PW = \sin \alpha$ producing the induced signals. For a not too large and careful design of the field lines $g(y)$ approximately equals y and no further treatment is needed.* If these approximations are too coarse, the precise knowledge of ρ_x in drift direction can be used to obtain corrections. In this case the chamber geometry has to be arranged such that all tracks have $\theta \neq 0^\circ$.

Chamber Layout

A possible layout for a vertex detector around a beam pipe for intersecting storage rings is shown in Fig. 13. Here the individual cells have been tilted by 11.3° to guarantee inclined tracks for the high precision readout, particularly for the second



Fig. 13. Layout as vertex detector. Inner radius 6 cm, outer radius 17 cm; maximum drift path 2.6 cm.

* For a TPC detector, this would be a possibility to increase the precision of position measurement without time expansion.

coordinate. It may prove, however, that the gain in resolution is not large and then it will be more convenient to have the cells point to the center. This also would improve the double track resolution as discussed above.

In order to improve the pattern recognition, the high precision wires (with the readout of pick-up wires) have been interspaced with a pair of "pattern recognition" wires (Fig. 14) where $d' = 1$ mm is relatively small giving high double track resolution. They also resolve the right/left ambiguity. The position resolution of these wires will be roughly $100 \mu\text{m}$ in drift direction and 2 mm (rms) along the wires using charge division.

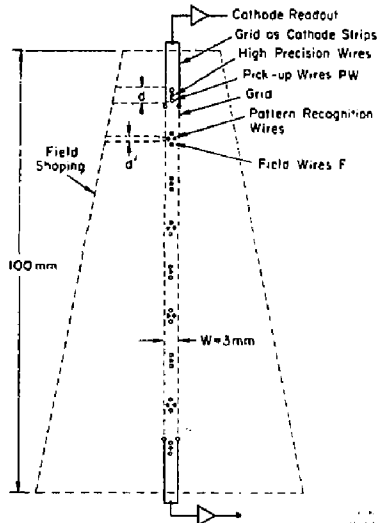


Fig. 14. One cell of vertex detector (schematically). Position of PW and F not to scale. F arranged to give $d' = 1$ mm. Double wire spacing 1 mm. Gap width $w \approx 3$ mm, depending on d . Cathode strips at ends of separate frames serving as grid.

The innermost and outermost high precision wires are equipped with cathode strip readout for the high precision measurement along the wire. Since the chamber is relatively short ($l = 50$ cm) a delay line split in five parts can be used in connection with the inner high precision wires (not shown) that can be designed for a precision of $50 \mu\text{m}$ (rms).

If this detector is mainly used for vertex reconstruction, a TPC-like geometry may be favorable. With a maximum drift length of 25 cm, a time expansion factor between 5 and 10 can be used and the three-dimensional reconstruction described above could give space points with typically $40 \mu\text{m}$ (rms). In addition, pressure would improve this value proportional to $1/P$.

Conclusion

The time expansion chamber equipped with additional readout of induced signals allows, in principle, the reconstruction of the spacial distribution of the ionization of minimum ionizing tracks. The precision of the reconstruction seems so far to be limited only

by diffusion which can be further reduced by increasing the ionization density. Occasionally the range of the primary electrons may limit the resolution but little information is available up to now. The time expansion chamber may provide the missing data.

References

1. W. Farr, J. Heintze, K. H. Hellenbrand and A. H. Walenta, Nucl. Instrum. Methods, 154 (1978) 175.
2. A. H. Walenta, IEEE Trans. Nucl. Sci. NS-26 No. 1 (Feb. 1979) 73.
3. J. Fischer, H. Okun and A. H. Walenta, IEEE Trans. Nucl. Sci. NS-25 (1978) 794.
4. R. A. Boie, A. T. Hrisoho and R. Rehak, IEEE Trans. Nucl. Sci. NS-28 No. 1 (1981) 603.
5. W. D. Farr and G. C. Smith, to be published.
6. See, for example, H.S.W. Massey and E.H.S. Burhop, "Electronic and Ionic Impact Phenomena," Oxford 1969.
7. V. Palladino and B. Sadoulet, LBL Report LBL-3013 (1974).
8. L. W. Cochran and D. W. Forester, Phys. Rev. 126 (1962) 1765.
9. The amplifier is a more recent design following the description given in "State of the Art of Low Noise Amplifiers for Semi-Conductor Radiation Detectors," V. Radeka, Proceedings of Int. Symposium on Nuclear Electronics, Versailles, 1968, Vol. I, page 46/1.
10. W. D. Farr, private communication.
11. See, for example, ISABELLE Proceeding of the 1978 Summer Workshop, BNL 50885, pp. 136-158.
12. C. H. Hargrove, private communication, and these proceedings.
13. A. E. Bondar, A. F. Gnuchin, V. S. Pavlin and V. I. Telnov, "Special Resolution of the Induced Proportional Chambers," Preprint 82-017, Novosibirsk 1982.

THE POSITION RESOLUTION OF THE TIME PROJECTION CHAMBER AT TRIUMF

Cape

C.K. Hargrove, H. Mes
National Research Council of Canada, Ottawa, Ont., Canada K1A 0R6

A. Bennett, B.A. Bryman*, M. Hasinoff†, J.A. Macdonald, J.M. Poutissou†, T. Numao*, J. Spuller
TRIUMF, Vancouver, B.C., Canada V6T 2A3

G. Azueloe, R. Poutissou
Université de Montréal, Montréal, P.Q., Canada H3C 3J7

M. Blecher, K. Gotow
Virginia Polytechnic Institute and State University, Blacksburg, VA, USA 24061

A.L. Carter
Carleton University, Ottawa, Ont., Canada K1S 5B6

Summary

We have investigated the spatial resolution of the TRIUMF time projection chamber (TPC). The dominant effects on the resolution are diffusion, track-anode crossing angle, $E \times B$ forces in the region of the anode wire and clustering of the primary ionization. A formulation of these effects has been used to determine the mean collision time, the diffusion constant, the Lorentz angle in the anode wire region and the spatial resolution as a function of the crossing angle for a gas mixture of Ar (80%), CH₄ (20%) at atmospheric pressure. The minimum resolution, $\sigma \sim 200 \mu\text{m}$, occurs when the track crossing angle equals the Lorentz angle. As the angle moves away from this value the resolution deteriorates rapidly due to the discrete nature of the ionization process.

Introduction

An apparatus based on the principle of the time projection chamber (TPC)¹ has been developed to search for the lepton number violating nuclear muon capture reactions:

$$\mu^- Z \rightarrow e^- Z$$

$$\mu^- Z \rightarrow e^+ (Z-2)$$

The TPC is a large volume drift chamber with uniform parallel electric and magnetic fields. Several effects which influence the spatial resolution of the TPC have been studied. An important aspect of TPC operation is the reduction of transverse diffusion of the ionization electrons in the presence of parallel electric (E) and magnetic (B) fields ($E \times B = 0$) in the drift region. In the neighbourhood of the endcap proportional wires there are necessarily regions where $E \times B \neq 0$ which significantly affect the shape of the drifting ionization cloud in a manner which depends on the angle at which the track crossed the wire. In addition, density fluctuations and clustering of the primary ionization deposited by a charged particle traversing the chamber gas are important considerations.

The TRIUMF TPC

The TRIUMF TPC^{2,3} is shown in Fig. 1. Ionization tracks of charged particles which have traversed the chamber drift under the force of the electric field $E = 250 \text{ v/cm}$ onto proportional wire modules in the endcaps. The gas used is a mixture of Ar (80%) and CH₄ (20%) at atmospheric pressure and the magnetic field has a maximum operating value of $B = 9.5 \text{ kG}$. The drift velocity was measured to be $U = 7 \text{ cm/}\mu\text{sec}$. The endcap modules have 12 slots separated by 2.56 cm as shown in Fig. 2. A point charge on the anode would induce a charge distribution on the segmented cathode spreading over 2-3 pads each of width $S = 0.6 \text{ mm}$. By measuring the width of the cathode

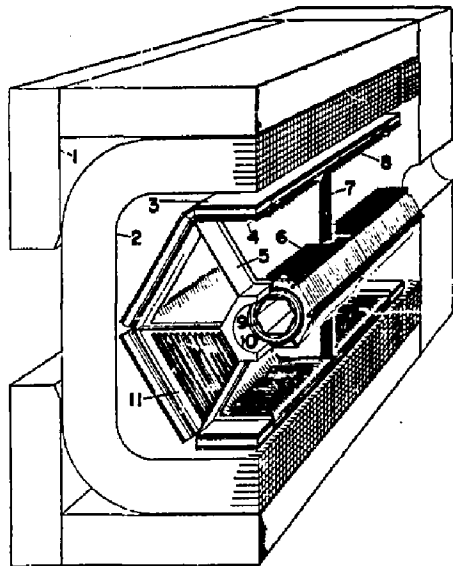


Fig. 1. A perspective view of the TPC. The numbered elements are: 1) the magnet iron, 2) the coil which has an inside field volume of $1.5\text{m} \times 1.2\text{m} \times 0.9\text{m}$, 3) outer trigger scintillators, 4) outer trigger proportional counters, 5) endcap support frame, 6) central electric field cage wires, 7) central high voltage plane, 8) outer electric field cage wires, 9) inner trigger cylindrical proportional wire chamber, 10) inner trigger cylindrical proportional wire chamber, 11) endcap proportional wire modules for track detection.

charge distribution the true anode charge distribution can be determined.

The cathode signal feeds a LRS TRA 510 amplifier and its output is digitized by the LRS 2280 12 bit ADC system. The amplifier pulse width at the base is $1.2 \mu\text{sec}$. The noise of the system is $\sim 2 \text{ fC}$ and the wire gain is $\sim 5 \times 10^6$. The sum of induced signals on the pads for minimum ionizing tracks is $\sim 0.2 \text{ pC}$.

Data Analysis

The Pad Distributions

The distributions of charge on the cathode pads were fitted with a function $f(x)$ chosen to minimize biases in the estimates of the centroids. Such biases were found to be as large as $200 \mu\text{m}$ for a simple Gaussian function. The function used was

* and University of Victoria
† and University of British Columbia

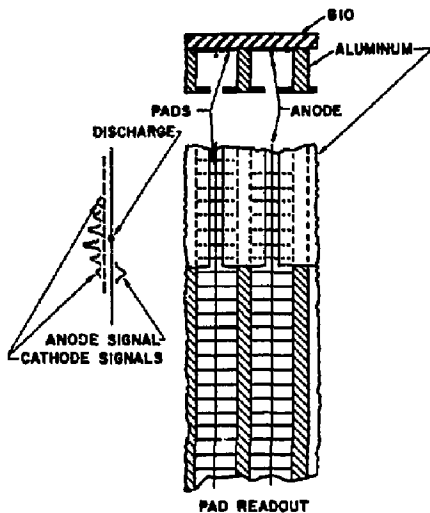


Fig. 2. Anode wire slots. The slots are machined out of a 19 mm thick plate. They are 19 mm wide and 17 mm deep. The remaining 2 mm has a 6.3 mm slot cut in it to allow the ionization access to the anode wires. The plate has a 6.3 mm G10 back plate which supports the anode wires in the slot and has the 6 mm wide cathode pads etched on it. The anode is 4 mm above the pads. The electrical connection to the pads is made by pins which go through the G10.

$$f(x) = \exp[-\sqrt{w^2 + m^2}(x - x_0)^2], \quad (1)$$

where: p is the amplitude parameter, w is the width parameter, x_0 is the centre of the distribution and m is a constant. The full width at half maximum (FWHM) of this distribution is given by:

$$W = \frac{2S}{m} \sqrt{\ln 2 (\ln 2 + 2w)}, \quad (2)$$

Three important effects contribute to the observed width W^* of the charge distribution induced on the cathode plane:

1. W_1 the intrinsic width of the measuring system
2. W_2 the width due to diffusion, and
3. W_3 the width due to the track-anode crossing angle and Lorentz forces.

The FWHM for a point source distribution is a constant $W_1 = Cl$.

Diffusion

Diffusion plays an important role in spreading the charge distribution along the anode wire. The FWHM of diffusion normal to the drift direction in one dimension is:

$$W_2^0 = 2.35 \sqrt{\frac{2Dz}{U}} \quad (3)$$

where D is the diffusion constant, z the drift length and U the drift velocity. The diffusion constant is

*Since the distributions approximate a normal distribution it is assumed that if the width is due to a number of independent contributions then the individual widths can be added in quadrature. The FWHM is taken to be 2.35 times the rms (root mean square) deviation.

reduced in the presence of a magnetic field B according to the relation:

$$D(B) = D(0)/(1 + \omega^2 \tau^2). \quad (4)$$

ω is the electron cyclotron frequency and τ is the mean electron collision time. This diffusion width normal to the track direction is projected onto the anode wire leading to:

$$W_2 = \frac{2.35}{\cos \theta} \sqrt{\frac{2D(C)z}{U(1 + \omega^2 \tau^2)}}. \quad (5)$$

The Angle Effect

In the absence of a magnetic field when the tracks are at an angle θ to the normal to the anode wire slot (Fig. 3a), the charge distribution at the anode wire is a square function with width H given by:

$$H = L \tan \theta. \quad (6)$$

Here L is the width of the slot. The observed cathode charge distribution is broader than that induced by a point source. The contribution to the FWHM of a square uniform distribution is:

$$W_3^0 = \frac{2.35H}{2\sqrt{3}}. \quad (7)$$

E×B Effects in the Anode Slot

Effects of non-parallel electric (\vec{E}) and magnetic (\vec{B}) fields are large in the position sensing region of the chamber. To a first approximation the average position of a track is unaffected since the forces are symmetric about the track centre. However, these forces can significantly change the anode charge distribution. In a coordinate system in which x is along the wire, y is normal to the wire and z is parallel to the magnetic field, the electrons drift with velocity v_y toward the anode. A $\vec{V} \times \vec{B}$ force results which causes the electrons to drift at an angle α (the Lorentz angle) to the y direction where

$$\tan \alpha = \omega \tau. \quad (8)$$

Electrons drifting toward the anode wire will reach the wire with a displacement proportional to $\tan \alpha$.

Figure 3b illustrates the electron drift in the slot in the x - y plane as determined by Eq. (8). The

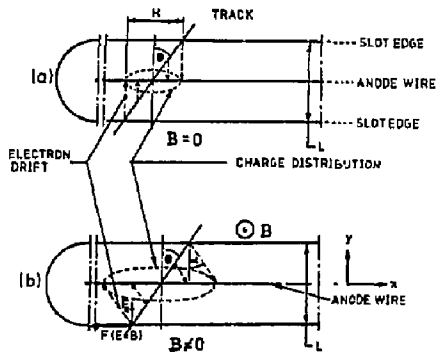


Fig. 3. Electron drift in the anode region. a) In the case of no magnetic field, the electrons drift in the y -direction and the charge is distributed along the anode in the dashed region. b) The magnetic field is out of the plane of the figure and the electrons drift under the Lorentz force at the angle α . The charge is spread along the anode in the dashed region. If $\theta = 0$ the charge spread neglecting diffusion is zero.

actual electron path is not a straight line in the x-y plane since τ varies considerably during the drift, particularly in the region close to the wire. However, the data is adequately reproduced by assuming τ is constant and using an average value of $\tan \alpha$.

Including the additional term which accounts for the $\vec{E} \times \vec{B}$ angle α , the width of the distribution as a function of track angle is given by

$$W_3 = \frac{2.35(\tan \theta - \tan \alpha)}{2\sqrt{3}} \quad (9)$$

Variation of Total Width

The calculated cathode charge distribution has a FWHM which is the quadratic sum of the above components W_1 , W_2 and W_3 :

$$\begin{aligned} \phi^2 &= W_1^2 + W_2^2 + W_3^2 \\ &= C_1^2 + \frac{C_2^2 z}{\cos^2 \theta} + C_3^2 (\tan \theta - \tan \alpha)^2 \end{aligned} \quad (10)$$

C_1 , the minimum width, includes the intrinsic width of the cathode charge distribution plus diffusion effects in the slot, electronic noise and other unknown components.

$$C_2 = 2.35 \sqrt{\frac{2D(0)}{U(1+w^2\tau^2)}} \quad (11)$$

represents the effects due to diffusion in the drift region of the chamber and

$$C_3 = \frac{2.35 L'}{2\sqrt{3}} \quad (12)$$

takes into account the crossing angle and $\vec{E} \times \vec{B}$ effects in the slot. Here L' is the effective slot width. From Eq. (10) it can be seen that the width is symmetric about $\theta=0$ only when $\tan \alpha$ is zero, i.e. $B=0$. In the case of $B \neq 0$, the minimum width occurs at an angle θ_{\min} which depends on both B and the drift distance z . By differentiation of Eq. (10) with respect to θ it is found that

$$\frac{1}{\tan \theta_{\min}} = \frac{1}{\tan \alpha} + \frac{C_2^2 z}{C_3^2 \tan \alpha} \quad (13)$$

The minimum width occurs at an angle θ_{\min} which decreases as z increases.

Spatial Resolution

The spatial resolution depends on the precision with which the centroid of the charge distribution on the anode can be determined. For a point charge the resolution will depend on a number of poorly determined factors such as electronic noise, diffusion in the slot, fitting uncertainties and other factors. The parametrization of the resolution includes all these effects in a single parameter C_0 .

As the track moves away from $z=0$ the effects of diffusion become important. When the crossing angle changes from the Lorentz angle the centroid of the charge distribution is affected by the charge distribution along the track. At atmospheric pressure the rms deviation of the centroid of the distribution is dominated by the clustering of the charge along the track. The FWHM of the resolution is⁷

$$\rho^2 = C_0^2 + \frac{C_2^2 z}{N_1 \cos \theta} + \frac{C_3^2 (\tan \theta - \tan \alpha)^2 R \cos \theta}{N_1} \quad (14)$$

where R is the ratio of the second to first moment of the charge distribution deposited along the track. N_1 is the number of electrons projected onto the normal to the slot direction. The second term is the contribution of diffusion to resolution and third term takes into account the crossing angle and clustering. R has been evaluated from the calculated charge distributions of Lapique and Puiz⁸ to be $R=7.5$. The last term in

Eq. (14) dominates the resolution at angles significantly different from α due to the large value of R .

Results

Width as a Function of Angle

Data from cosmic ray events that went through a single sector of the TPC were fitted to Eqs. (10) and (13) and the resultant parameters were extracted. The diffusion constant, w and τ have been derived and the resolution compared with that predicted by Eq. (14). Magnetic fields of 0, 2.3, 4.1, 5.7 and 8.5 kG were used. The data have been divided into bins of constant drift length z , averaged over the angle of the track to the z -axis, and the width of the cathode charge distribution plotted against the angle at which the track crossed the wire, θ . A typical set of measurements is shown in Fig. 4. It displays the main features of the width variation described in the previous section. The most important feature is the asymmetric position of the minimum relative to $\theta=0$ caused by the $\vec{E} \times \vec{B}$ effect in the slot. The minimum occurs close to the angle α at $z=3.5$ cm and it moves towards $\theta=0$ as z is increased, as predicted by Eq. (10).

Equation (10) also predicts that a plot of the width squared vs z at $\theta=0$ will be a straight line. Figure 5 shows such plots for various magnetic fields, and from them the values of C_2 for varying B were obtained. C_2 is related to the diffusion constant D , and the mean time between collisions in the gas, τ , according to Eq. (11). Table I lists the observed values of C_2 , D , τ and w and the predicted value of $w\tau$, using the equation (in Gaussian units) taken from ref. 1:

$$w\tau = B*U/(E*c) \quad (15)$$

where c is the velocity of light. Figure 6 is a plot of $w\tau$ versus B and shows that the relation is linear, as expected since τ is independent of B .

According to Eq. (13) $1/\tan \theta_{\min}$ is proportional to z , and has an intercept which is related to the angle α which describes the $\vec{E} \times \vec{B}$ effects near the anode wire. The angle θ_{\min} was determined by fitting the data to Eq. (13) with z and B fixed. Figure 7 shows a plot of

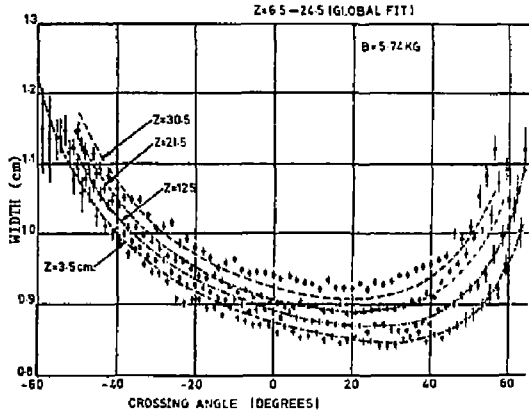


Fig. 4. The measured width of the pad distributions as a function of crossing angle for the case of $B=5.74$ kG. The four curves are for the drift distances shown and are averaged over a 3.0 cm interval. The curves are the result of fitting Eq. (10) to the data over drift distances from 6.5 to 27.5 cm. The χ^2 per degree of freedom of this fit was 1.3

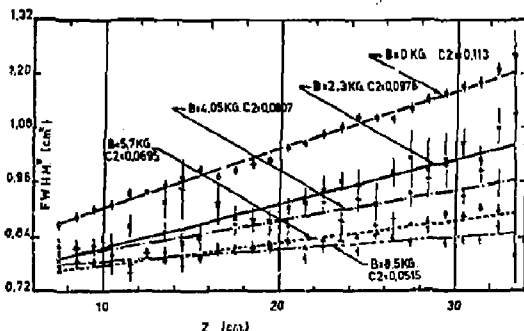


Fig. 5. The plots of $FWHM^2$ vs drift distance for the 5 magnetic fields studied. The slope is proportional to the diffusion constant and decreases with increasing magnetic field. The constant C_2 is proportional to the diffusion constant.

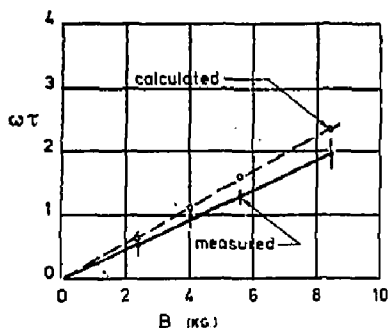


Fig. 6. Measured and calculated value of $\omega\tau$ vs magnetic field.

Table I.

B(Tesla)	C_2 (mm)	$\omega\tau$	$\omega\tau$ (Calc.)	\dot{r} (acc $\times 10^{-11}$)	D(mm 2 /sec)
0.00	0.356 \pm 0.005	0	0	-	(8.0 \pm 0.8) 10^5
0.23	0.309 \pm 0.025	0.61 \pm 0.2	0.64	1.4 \pm 0.5	(6.1 \pm 1.4) 10^5
0.41	0.255 \pm 0.022	1.0 \pm 0.2	1.13	1.4 \pm 0.3	(4.1 \pm 1.0) 10^5
0.57	0.220 \pm 0.006	1.3 \pm 0.1	1.61	1.3 \pm 0.1	(3.1 \pm 0.4) 10^5
0.85	0.163 \pm 0.016	1.9 \pm 0.3	2.38	1.3 \pm 0.2	(1.7 \pm 0.5) 10^5

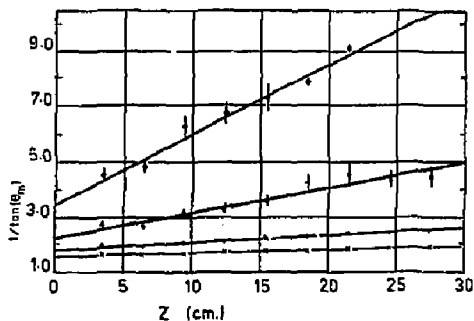


Fig. 7. Plots of $1/\tan \theta_{\min}$ vs z . The solid lines are least squares fits of $1/\tan \theta_{\min}$ vs z . The intercepts are equal to $1/\tan \alpha$.

$1/\tan \theta_{\min}$ versus z , from which the angle α was determined. Figure 8 shows the measured and calculated values of α .

Resolution

Using the parameters determined above, the position resolution along the anode wire has been calculated using Eq. (14) for $B=8.5$ KG. The data has been plotted in Fig. 9 for short drift distances $z \sim 3$ cm. The lower solid line represents the calculated resolution. C_0 has been set equal to 180 μ m, the value at the minimum. The upper curve is the calculated resolution for $z=34$ cm, the maximum drift distance.

The resolution deteriorates away from the minimum and is asymmetric. At $B=8.5$ KG, the diffusion has only

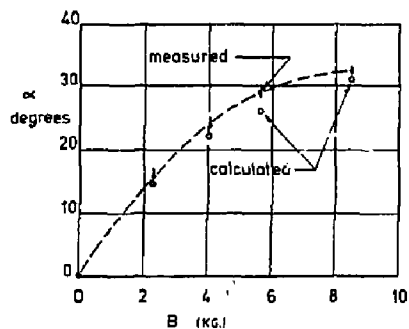


Fig. 8. The measured and calculated values of the Lorentz angle α in the anode slot as a function of magnetic field.

a small effect on the resolution even for the longer drift distances as can be seen by the small increase in the widths represented by the upper curve in Fig. 9. The variation of resolution is strongly dependent on the value of R in the last term in Eq. (14) which results from the clustering of the primary ionization. The resolution may be improved by reducing R , reducing C_3 or increasing N_4 . C_3 is proportional to the width of the track which is accepted and one may reduce this at the cost of reducing N_4 . Increasing the pressure would reduce R and also increase N_4 .

The asymmetry of the position resolution about $\theta=0$ has consequences for the momentum resolution of charged particles traversing the chamber. Since the present system is designed to observe a limited $\sim 70^\circ$ arc of the trajectory for particles which fire both the inner and

Conclusions

The position resolution of the TRIUMF TPC has been measured for Ar-CH₄ (80-20) at atmospheric pressure at electric field $E=250$ v/cm and with magnetic field $B=8.5$ kG. A formulation has been worked out which describes the behavior of the resolution quantitatively. The factors contributing to the resolution involve diffusion, track-anode crossing angle, Lorentz forces and charge clustering of the initial ionization.

The resolution is determined by the precision with which the centroid of the charge distribution on the anode may be determined. The induced charge distribution on the cathode pads has been measured as a function of magnetic field. The diffusion constant, ωt in the drift region, and the Lorentz angle in the anode region have been determined and are in reasonable agreement with expectations.

It has been found that the minimum resolution at the Lorentz angle is $\sigma \sim 180$ μ m. This rapidly deteriorates as the angle moves away from the Lorentz angle due to the large rms deviations of the centroid of the track charge distribution caused by the discrete nature of the primary ionization.

References

1. D. Nygren et al., SLAC PEP-4 proposal.
2. C.K. Hargrove et al., *Physica Scripta* **23**, 668 (1981).
3. H. Mes et al., to be published.
4. F. Lapique and F. Puij, *Nucl. Instrum. and Methods* **175**, 297 (1980).

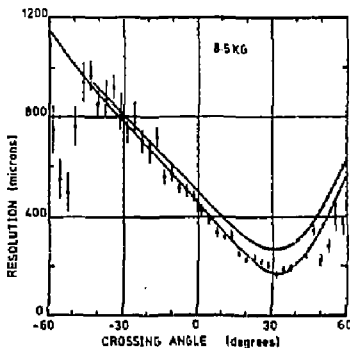


Fig. 9. The resolution as a function of crossing angle θ . The data are for 3.5 cm drift distance and $B=8.5$ kG. The curves are produced from Eq. (14). The lower (upper) curve uses $z=3.5$ cm (34 cm).

outer trigger scintillators, negative and positive particles tend to cross the anode wires at $\theta > 0^\circ$ and $\theta < 0^\circ$, respectively. For $p=100$ MeV/c and $B=8.5$ kG the average crossing angle is $\theta \approx 30^\circ$ for negatively charged particles and is $\theta \approx -30^\circ$ for positively charged ones. This results in considerably better position resolution and consequently is expected to result in better momentum resolution for negatively charged particles. Based on the results of this analysis the momentum resolution (FWHM) of the TPC expected for 100 MeV/c electrons is $\Delta P/P \sim 4\%$ and for 100 MeV/c positrons $\Delta P/P \sim 6\%$.

3.0 Position Resolution

Only pad information is used for tracking, at this time. Important factors that determine the position resolution are: electronic noise, diffusion in the 1 m drift space, and ionization fluctuations. The geometry of the sectors and the electronics design were optimized to provide, for a given cost, a position resolution adequate to achieve a momentum resolution of $dp/p^2 = 0.4\%$ for a magnetic field of 15 KG. We will discuss below our understanding of the system at this time. More work is needed to achieve the desired resolution.

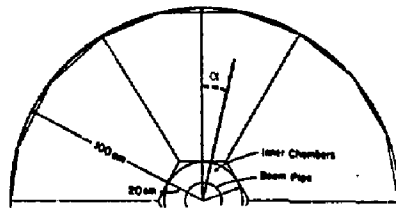


Fig. 2. Sector geometry. The angle α , local to each sector, is defined as the angle with the normal to the sector inner edge.

3.1 Pad Response

For the geometry of the TPC sectors the induced cathode signal on a pad receives contributions from the avalanches on the wire just above it and 2 more adjacent wires at each side. The couplings of the wires to the pads have been measured in a test set up with very similar geometry. The pad response has been found to have a shape very close to gaussian.⁶ The σ_0 of the gaussian distribution for the present geometry is expected to be 3.5 mm, which means that a point on a track produces a signal in 3 pads or less. In order to achieve 150 μ resolution, the pulse height in the 3 pads will have to be measured with high precision, i.e., very low noise level and good electronic calibration is desirable. A discussion of the calibration of the system is included in ref. 4.

For the sample of events analysed, 12% of the points on tracks had signals on 3 pads, 79% had 2 pads, the remainder had 1 pad. For the 3-pad points we calculate the peak and the σ of the gaussian. For the 2-pad points we calculate the position of the peak using the σ information determined from the 3-pad data. The peak position provides the coordinate along the pad row. The y coordinate is determined by the center of the pad row. For tracks that traverse the pad row at an angle, correction to the y coordinate is obtained by using the pulse heights of the 5 wires contributing to the pad signals. This geometry, 5 wires contribute to one pad signal, has the advantage that the Landau ionization fluctuations are reduced in the pad signal.

We have parametrized the rms deviation of the gaussian pad response as follows:

$$\sigma^2 = \sigma_0^2 + \sigma_D^2 L / L_{\max} + \sigma_a^2 \tan^2 \alpha \quad (1)$$

where σ_0 depends only on the geometry of the sector, σ_D is the contribution due to diffusion and depends on the pressure of the TPC, L is the drift distance ($L_{\max} = 1$ m), and σ_a includes the spreading of the gaussian response for tracks traversing the pads at an angle, α , defined in Fig. 2. The α dependence is due to broadening of the distributions when adding displaced gaussians for the 5 different wires and from Landau fluctuations within the collection region of each wire.

The α dependence is shown in Fig. 3 for the 8.6 atm data. We have not studied this effect in detail yet, the value obtained for the data in Fig. 3 is $\sigma_a = 3.74$ mm. The diffusion term is calculated from the dependence of σ on the drift length. This is shown in Fig. 4 for a run at 8.6 atm. Each data point corresponds to an average over

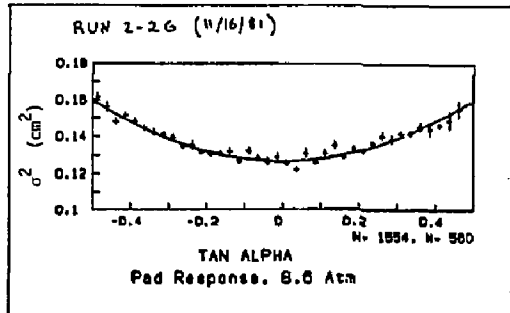


Fig. 3. Pad response dependence on α , for 8.6 atm data. The curve is a parabolic fit.

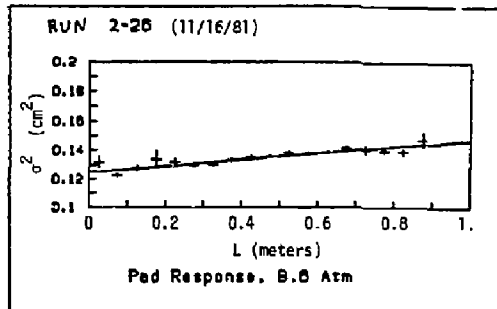


Fig. 4. Pad response dependence on L , drift distance, for 8.6 atm data. Average value over many tracks with the same L . A straight line fit is also shown.

many tracks at an average distance L from the sector. We have done some studies on the diffusion term and will discuss this in the next section.

When the data are corrected for the α and L dependence of formula (1), we get a distribution for σ_0 that looks gaussian as shown in Fig. 5. Table I shows the values of σ_0 obtained for different pressure and magnetic field conditions. As expected the measured σ_0 is independent upon these variables, indicating that all the data are internally consistent.

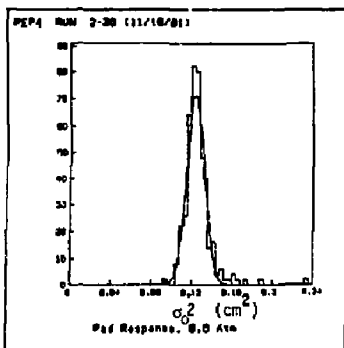


Fig. 5. Distribution of σ_0^2 , the standard deviation of the gaussian pad response, after the L and α dependence have been corrected according to Eq. (1).

3.2 Diffusion

The diffusion dependence on the magnetic field, B, and on the pressure is shown in Table I. These values are averages over many runs, and the errors are statistical only. In absence of magnetic field the diffusion term increases with decreasing pressure with the \sqrt{P} law, as expected. This can be seen in the values of σ_D for B = 0 shown in the last column, $\sigma_D \times \sqrt{P}$, which are scaled to 1 atm.

Table I. Pressure and B dependence of σ_0 and σ_D .

P	B	σ_0	σ_D	$\sigma_D \times \sqrt{P}$
(atm)	(KG)	(mm)	(mm)	(mm)
8.6	0.	3.59 ± 0.04	1.44 ± 0.10	4.23 ± 0.41
4.0	0.	3.62 ± 0.03	2.05 ± 0.08	4.11 ± 0.15
1.5	0.	3.54 ± 0.05	3.30 ± 0.08	4.04 ± 0.10
8.6	3.9	3.59 ± 0.08	1.43 ± 0.05	4.20 ± 0.18
4.0	3.9	3.63 ± 0.02	1.71 ± 0.04	3.43 ± 0.05
1.5	3.9	3.51 ± 0.03	1.96 ± 0.06	2.40 ± 0.07

The comparison of the σ_D values for data with and without magnetic field is also of interest. We expect

$$\sigma_D(B) = \sigma_D(0) / \sqrt{1 + (\omega\tau)^2}$$

where $\omega = eB/cm$ and $\tau = 1.09mv_e/eE$ are the cyclotron frequency of the electron and the mean collision time respectively, and v_d is the drift velocity. By taking the ratio of $\sigma_D(B)$ and $\sigma_D(0)$ we obtain measured values of $\omega\tau$, shown in Table II, and can compare them with the calculated values. Assuming $\omega\tau = 1.09 v_d B/Ec$ and using the drift velocity measured in this experiment we calculate the values shown in Table II. The agreement between $(\omega\tau)_m$ and $(\omega\tau)_c$ is quite good, again showing self consistency in the data that we are analyzing.

Table II. Drift velocity and $(\omega\tau)_m$ measured in this experiment. Values of $(\omega\tau)_c$ are shown for comparison.

P	E	$(\omega\tau)_m$	$(\omega\tau)_c$	v_d
(atm)	(KV/cm)			(cm/ μ sec)
8.5	75.0	0.10 ± 0.50	0.27	4.67 ± 0.08
4.0	35.0	0.66 ± 0.14	0.56	4.51 ± 0.09
1.5	13.2	1.36 ± 0.11	1.33	4.06 ± 0.08

The value of σ_D in Table I is the expected value for one electron. At different pressures we can estimate the effective number of electrons in the avalanche and calculate the contribution of diffusion to the resolution, as σ_D/\sqrt{N} . We obtain the values of 135 μ , 218 μ , and 404 μ for 8.6, 4.0, and 1.5 atm respectively, for 1 meter drift.

3.3 XY and Z Resolution

The spatial resolution is obtained by calculating the deviation of the pad points from the fitted track. The dependence of r_{msxy} on the drift distance L is shown in Fig. 6 for the 1.5 atm data.

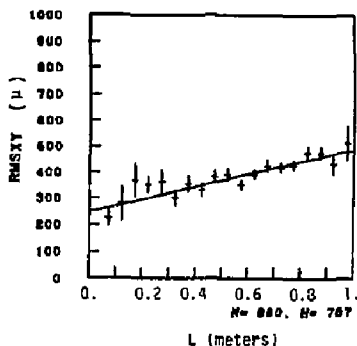


Fig. 6. Dependence of r_{msxy} on the drift distance for 1.5 atm data.

Here the effect of the diffusion is more pronounced than at higher pressure. The contribution of the diffusion can be calculated by taking the value of r_{msxy} at L = 1.0 m and subtracting in quadrature from it the value at L = 0. We find:

$$(r_{msxy})_D = 420 \pm 23 \mu$$

which is in good agreement with the value of 404 μ calculated in the previous section from the pad response.

The dependence of r_{msxy} on α for one of the runs at 8.6 atm is shown in Fig. 7. Although the statistics is not large, it is evident that there is an α dependence for $|\alpha| > 15^\circ$. It is independent of angle for $|\alpha| < 10^\circ$ and we can use this region to calculate the actual σ_{xy} . The distribution of r_{msxy} for these events is shown in Fig. 8 for the 8.6 atm data. To calculate the resolution we take

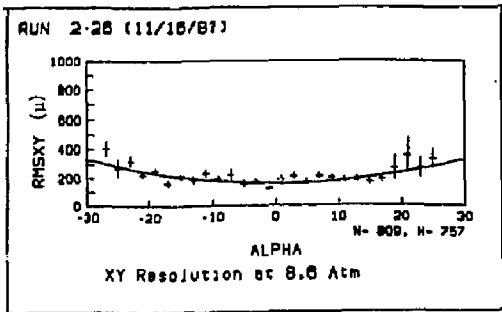


Fig. 7. Dependence of rmsxy on the angle α for 8.6 atm data.

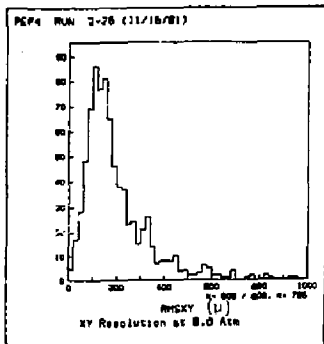


Fig. 8. Distribution of rmsxy for tracks with $|\alpha| < 10^\circ$. From it we obtain $\sigma_{xy} = 260 \mu$.

the mean of this distribution and add it in quadrature to its standard deviation. Note that the distribution of Fig. 8 is not gaussian and that the peak value falls well below the quoted resolution. At the different pressures we obtain the values shown in Table III.

We use a similar method to measure the z resolution. We see little dependence of $rmsz$ on L , the drift distance, therefore we average over all tracks. The distribution of $rmsz$ has a similar behavior as Fig. 8, and the average is calculated in the same way as for σ_{xy} . The results are shown in Table III.

Table III. Resolution in xy and z at different pressures.

P(atm)	$\sigma_{xy}(\mu)$	$\sigma_z(\mu)$
8.6	260	654
4.0	299	810
1.5	439	857

The xy resolution of 8.6 atm is worse than the 150μ we expected to achieve. There are many factors that can deteriorate the resolution.

(a) Electronic noise. The noise level at this time is about 2.4 counts, i.e., 1% of the signal for a minimum ionizing track. This is expected to contribute 64μ to the resolution.

(b) The electronic calibration is not optimized. We are working on improving the stability of the system.

(c) We expect distortions due to $E \times B$ effects, that is effects due to radial components of B . We have not included these corrections in the analysis yet. Corrections are expected to be as large as 120μ .

(d) Electrostatic distortions. The electric field is not uniform across the drift volume. We have observed some distortions in regions very close to the inner and outer radius of the TPC. Corrections for these distortions are not included.

The z resolution is also worse than expected, but again electronic noise and unreliable calibration affect this resolution.

We expect to improve the resolution when these effects are better understood and corrected.

4.0 Momentum Resolution

This can be calculated by comparing the curvature of the cosmic rays in the two track sections in opposite sectors. The distribution of the difference of curvatures for one of the data runs at 8.6 atm is shown in Fig. 9. The rms

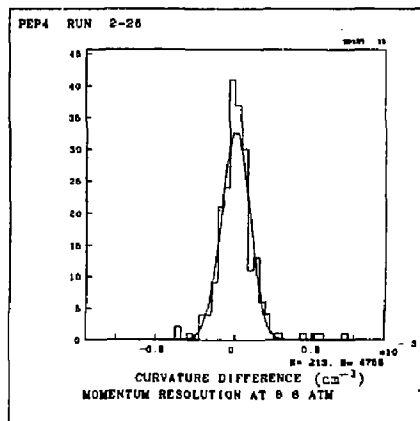


Fig. 9. Distribution of curvature difference for the same cosmic ray in two track portions. The standard deviation of this distribution yields $dp/p^2 = 0.081(\text{GeV}/c)^{-1}$.

deviation of this distribution, after normalization, gives $dp/p^2 = 0.081(\text{GeV}/c)^{-1}$. The resolution we expect to achieve for a 4 KG field is $dp/p^2 = 0.016(\text{GeV}/c)^{-1}$.

At this time the measured resolution is a factor 5.1 worse than expected. Part of this discrepancy is due to the electrostatic distortions we mentioned earlier. For this reason, a shorter track length is used in the fit; two inner and two outer pad rows are not included. We are presently studying the time stability of the distortions and how to correct for them.

The dp/p^2 resolution depends on the point resolution, σ_{xy} , the length of the track measured, L , the magnetic field, and the number of measured points, N , approximately according to the relation:

$$dp/p^2 \propto \sigma_{xy}/(BL^2\sqrt{N})$$

For a 4 KG field, this dependence would predict a deterioration of the resolution by a factor 4.5; we observe a factor 5.1. This indicates that the momentum resolution we measure is not inconsistent with the results discussed so far. By correcting for the known effects we expect to improve the resolution considerably.

5.0 Performance of the TPC in e^+e^- Beams

The TPC has been operating for a week at PEP in 14 GeV beams. An event with 16 prongs reconstructed on line is shown in Fig. 10 and 11.

Figure 10 shows the projection of the event on the endcaps. Only pad clusters were used for track reconstruction. Each track found is identified by a number or a letter. The algorithm used was developed on Monte Carlo data; improvements are needed. Most clusters not associated with tracks are due to electronics noise.

EXP= 4, RUN= 2B, EVENT= 539

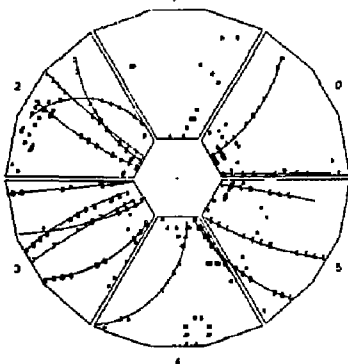


Fig. 10. End view of an hadronic event observed in 14 GeV e^+e^- beams. The event was reconstructed on line using only pad data.

Figure 11 shows the wire information for the tracks, found using pad data, in one of the sectors; specifically tracks one through 4. The peculiar band with no data is due to a group of 16 electronics channels missing at the time the event was detected. Bad z calibration can be seen here by noticing that groups of 16 channels are out of line. There are some unassociated clusters. One

set is clearly a spiraling electron. Another set, in the upper corner, is due to the tail of a saturated pulse, not properly shaped. This problem is now understood and being fixed.

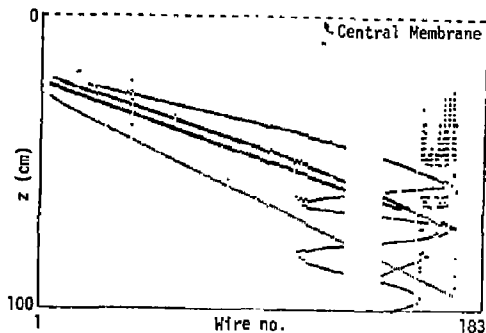


Fig. 11. Wire information in one of the sectors for 4 tracks of the event of Fig. 10.

So far, we have not detected any large effects due to positive ion feedback. More detailed analysis is needed. The luminosity during data taking was 5×10^{30} $\text{cm}^{-2}/\text{sec}$ or less.

References

1. Proposal for a PEP Facility based on the Time Projection Chamber, Johns Hopkins University, Lawrence Berkeley Laboratory, University of California at Los Angeles, University of California at Riverside, Yale University; PEP Experiment No. 4, SLAC report PUB-5012 (1976).
2. D. R. Nygren, The Time Projection Chamber, SLAC and LBL Reports PEP-144 (1974), and PEP-198 (1975). D. Fancher et al., Nucl. Inst. and Meth. **161**, 383 (1979).
3. R. C. Jared, D. A. Landis, and F. S. Goulding, IEEE Trans. on Nucl. Science, Vol. NS-29 (1982) and LBL Report LBL-13183 (1981).
4. G. R. Lynch and N. J. Hadley, Energy Loss Measurements in the PEP TPC. These Proceedings.
5. L. Galtieri, N. Hadley, and G. Lynch, "Preliminary Results of the November TPC Test," LBL Report LBL-TPC-82-01 (1982).
6. A. C. Schaffer and D. L. Fancher, LBL Report TPC-LBL-77-44 (1977).

INVESTIGATION OF THE USE OF CHARGE
COUPLED DEVICES AS HIGH RESOLUTION
POSITION SENSITIVE DETECTORS OF IONIZING RADIATION

A. Bross

Lawrence Berkeley Laboratory
University of California
Berkeley, CA 94720

Introduction

The use of charge-coupled devices (CCD's) as analog shift registers, optical imagers, and high density memories has been successfully demonstrated during the past ten years. CCD's are capable of very low noise operation (a S/N ratio of 1:1 with 10 electrons per pixel has been demonstrated) and, as imagers, afford high resolution and precise image geometry and stability. The signal charge can be electrically injected into the device via an input structure, can be generated internally by photoelectric processes or, as we shall show, can result from the creation of electron-hole pairs by energetic charged particles.

Basically a CCD is a metal-oxide-semiconductor (MOS) structure forming an array of capacitors. The MOS capacitors are capable of collecting and storing in discrete packets (buckets) charge that has been "injected" into the device by one or more of the mechanisms described above. If the capacitors are packed closely together, charge stored in a particular capacitor (pixel) can be transferred to an adjacent pixel by applying clocking voltages to transfer electrodes. In this fashion charge collected at any one pixel may be moved to an output structure on the CCD device, and an analog signal proportional to the charge stored at that site may be obtained. For a complete discussion of the CCD concept and device implementation we refer the reader to the literature.^{2,3}

There are two basic approaches we can take in order to utilize CCD's as particle detectors. The first is to use monolithic CCD area arrays. Commercially available optical CCD imagers are the most common example of this technology. They have been fabricated in formats as large as 800 x 800 elements with cell sizes as small as 15 microns. The sensitive thickness of devices of this type is limited to the depth of the depletion region (5-10 μm) and thus limits the signal that one can obtain to approximately 500-1000 electrons per track. In order to increase the amount of this signal charge, a CCD with a much thicker depletion depth would be required. However, the problems involved in fabricating a monolithic CCD with a thick depletion region (upwards of 100 μm) are quite substantial, and the current level of CCD technological expertise appears to be inadequate to develop such a device.

The second approach circumvents this problem by introducing the use of hybrid CCD detectors. In this scheme the detector (usually a silicon device) and the CCD multiplexer are separate devices. Charge collected in the detector is injected into the CCD via microscopic metallic interconnects (one per CCD pixel). The advantage of this technique is that both the detector and the CCD can be optimized for the desired performance characteristics. In this way the silicon detector can be made relatively thick and still give excellent charge collection efficiency throughout its volume.

Monolithic CCD Area Array Detectors

It has already been reported⁴⁻⁵ that cooled optical CCD's are sensitive to the passage of charged particles. In fact in long exposures for some optical astronomy observations cosmic rays present a significant background problem. If we assume that a minimum ionizing particle penetrates a CCD, the amount of charge deposited within the depletion region (typically 10

microns) is:

$$\begin{aligned} & [2.33\text{g/cm}^3 \times 1.66 \text{ MeV/g/cm}^2 \\ & \times 10^{-3} \text{ cm} \times (3.81 \text{ eV/e}^-)^{-1}] \\ & = 1070 \text{ electrons}^6 \end{aligned}$$

A S/N ratio of 20:1 is therefore obtainable for minimum ionizing events using many commercial CCD's provided that they are cooled.

Fairchild 202

Operational Characteristics. We have recently completed studies involving the Fairchild 202 CCD, a 100 x 100-element interline transfer area imager. (See Figure 1.) The device utilizes two-phase buried

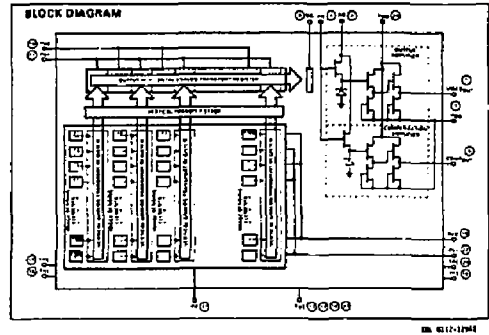


Fig. 1. Functional Block Diagram for Fairchild 202. (c) 1976, Fairchild Semiconductor Components Group, Fairchild Camera and Instrument Corporation.

channel technology in a 30 μm x 40 μm cell format. The readout is parallel/serial to an on-chip amplifier.

The readout rate used for our measurements was 100 kHz. Video processing consisted of a differential amplifier stage with a gain of 50 followed by a double correlated sample and hold (Figure 2). An optical

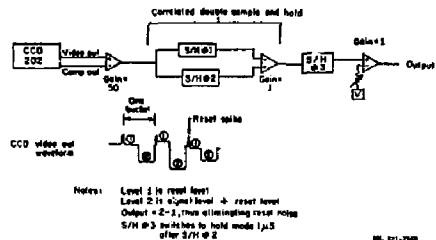


Fig. 2. CCD output circuit and waveform. The correlated double sample/hold processing function is also shown.

setup projected a standard TV bar pattern resolution chart (Figure 3) onto the CCD and was used for clock driver optimization.

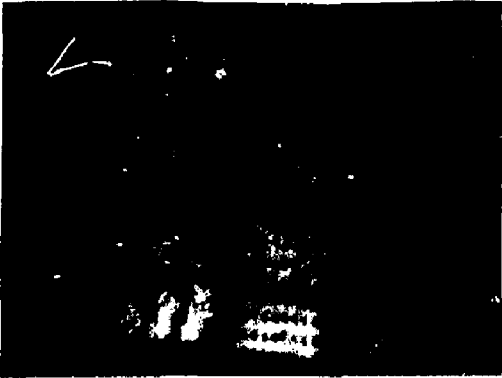


Fig. 3. Optical setup video display. The line-to-line spacing for the smallest set of horizontal lines is approximately 4 pixels.

Sr⁹⁰ Exposure. The CCD was mounted in a cryostat (Figure 4) and operated at temperatures between 145°

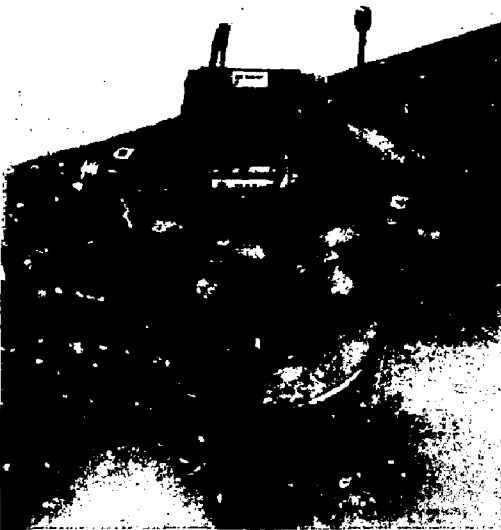


Fig. 4. CCD Cryostat.

and 210°K. The 202 was then exposed to a Sr⁹⁰ source and read out continuously at the 100 kHz pixel rate. Figure 5 shows the CCD output displayed on a video monitor showing single hits due to beta's from the Sr source. Each dot in Figure 5 represents a single pixel

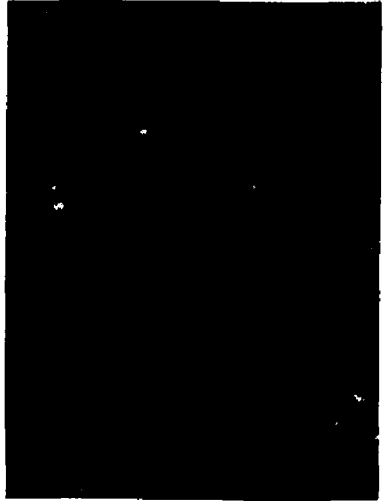


Fig. 5. Single hit Video Display Events from Sr beta's.

with a spatial resolution of 30 $\mu\text{m} \times 40 \mu\text{m}$. The CCD output was also sent to a multichannel analyzer in order to obtain the pulse height spectrum from the exposure. The 202 has a depletion depth of 7 $\mu\text{m} \pm 1 \mu\text{m}$; therefore, for a minimum ionizing particle we would expect approximately 700 electrons. From Figure 6 the

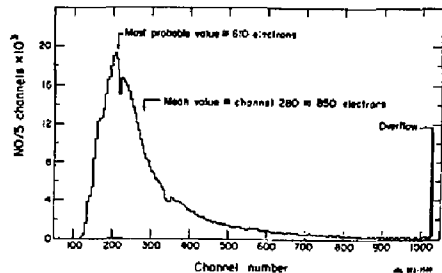


Fig. 6. Pulse height spectrum for Sr⁹⁰ beta's. Effective detector thickness = CCD depletion depth = 7 microns.

most probable value for energy loss is approximately 610 electrons. The mean value is channel 280 corresponding to 1050 electrons. The spectrum exhibits a typical Landau tail and has a most probable value agreeing quite well with what we would expect for a 6 μm -8 μm depletion depth. The measured rms noise from the 202/processor system was between 200 and 250 electrons. A threshold cut at channel 120 was used to obtain Figure 6. The detection efficiency for the 202 system averaged over a number of runs was measured to be 50-60%. This measurement was accomplished by

masking off a thick scintillator to give a 3 mm x 4 mm window corresponding to the active (sensitive) area of the 202. We then placed the scintillator in the same geometric relationship to the source as was done with the 202 and measured the count rate (window open) - count rate (window closed). This number was defined as the 100% efficient count rate to which the CCD rate was compared. The CCD efficiency number was limited by the relatively high noise value we obtained for this chip which was due in part to our clock driver electronics and in part to a relatively high noise value for the particular 202 chip we were using. An optical system using a 202 CCD has reported⁷ a noise figure of 30 electrons, and we believe this number is more indicative of the noise characteristics that are obtainable with the 202.

Virtual Phase CCD

We are also beginning work using a Texas Instruments 200 x 200 element area array based on the virtual phase-buried channel technology. Virtual phase devices function in a manner similar to a two-phase operation where one of the phases is kept at a constant D.C. potential and the other phase clocked above and below this level. Thus in this way only a single clock is needed to drive the CCD. See Figure 7 (Ref. 8). In

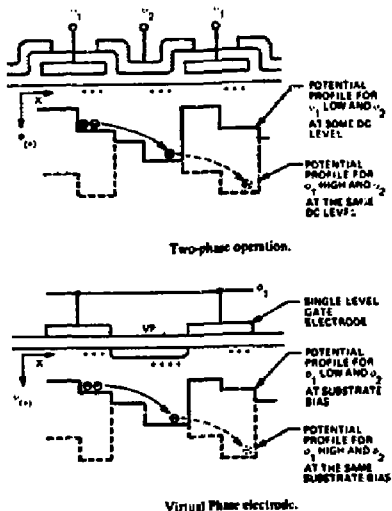


Fig. 7. Two-phase CCD operation vs. Virtual-phase operation.

the virtual phase device the "D.C. clock" electrode is not placed over the oxide layer but is built into the surface of the silicon by an ion implant. This biases this "D.C. phase" of the device at the substrate potential. The directionality of the transfer is defined by the doping profile used to define the clocked and virtual sections in the silicon. The advantages of the "virtual phase" technology are: 1. Simplified fabrication procedures giving the possibility for much higher yields and the ability to build very large devices, 2. High reliability, 3. Low dark current, and 4. High resistance to radiation damage. Virtual phase devices have exhibited dark current values an order of magnitude better than other buried channel CCD's. It is the fabrication procedure used for VP CCD's that yields oxide layers that have much better radiation hardness

than those obtained in multiple phase technologies. Virtual phase CCD's given an exposure of 10^5 RAD have shown no measurable increase in dark current (versus a 20-fold increase for a 3-phase device at an exposure level of 10^4 RAD).⁹ A group at the Jet Propulsion Laboratory working with a Texas Instruments 800 x 800 VP CCD imager has measured the dark current for the device to be 0.4 nA/cm² (25 C) with a noise floor of 18 e⁻/pixel. This device was exposed to a Sr⁹⁰ beta source and gave a most probable energy loss corresponding to approximately 700 electrons.

Our current plans at LBL involving the TI VP CCD's include device studies and characterization of dark current, min noise floor, maximum operable clock frequency and studies of possible readout problems encountered when operating the devices in high magnetic fields. Beam studies involving a three-plane CCD spectrometer are also envisioned for the near future. These studies are needed to accurately measure CCD tracking resolution and efficiency. In addition, we can study the one dimensional mode of CCD operation in this environment. Normal CCD readout requires that one row at a time be loaded into the output register and then read out, thus retaining X-Y information (Figure 8). Alternatively, the information from all the rows

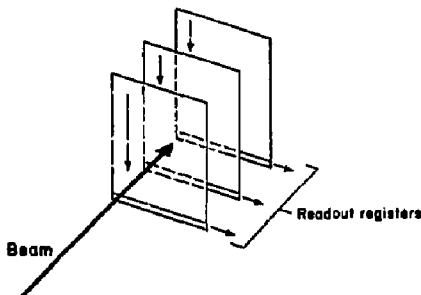
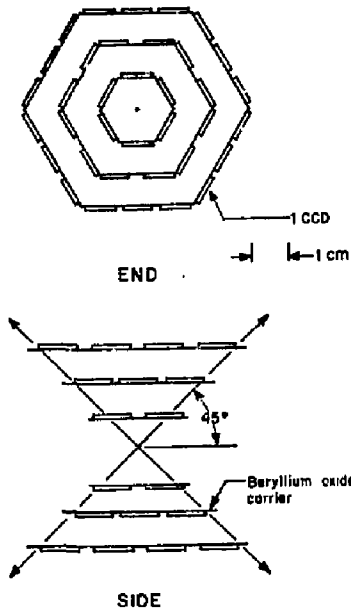


Fig. 8. CCD Planar spectrometer, operable in either one- or two-dimensional modes.

in the CCD can be summed in the output register, and then this register need only be read out once instead of many times per CCD read. Only one-dimensional information is retained, but the readout time is substantially reduced. This scheme increases the usefulness of monolithic CCD systems for fixed target accelerator experiments, since readout time for this mode of operation can be as short as 50 nS. CCD's operated in this manner are functionally equivalent to a microstrip detector with a built-in readout structure.

One Application - A CCD Vertex Detector for the Stanford Linear Collider.

Assuming the viability of the VP CCD for HEP experiments, we can visualize a vertex detector for the SLC based on 120 CCD's. The SLC is an ideal accelerator for this system, since the proposed beam pipe for the machine is only 1 cm in diameter, and the repetition rate of 180 pulses per second allows for a relatively long readout time. The basic detector in this system would be a commercial optical CCD. The most probable format would be 500 x 400 elements with a cell size of 15-30 μ m. Using a 20 μ m cell size, the system in Figure 9 uses 120 CCD's with overlapping concentric planes in order to get efficient solid angle coverage. This detector would cover 45° with respect to the beam. Solid angle coverage could be increased, of course, by adding additional CCD's. (60° coverage would require



TOTAL NO. OF CCD'S = $2 \times 6 + 3 \times 12 + 4 \times 18 = 120$

Fig. 9. End and side views of CCD vertex detector system for the SLC.

approximately 220 CCD's.) The total number of elements is 2.4×10^7 , but there are only 120 output channels. Readout time for the system would be on the order of 10-15 ms. Also, due to the x-y nature of the CCD's, the cracking is unambiguous, each plane giving both x and y coordinates. Beryllium oxide that was copper clad and then etched could be used as the chip carrier, thus providing input and output lines and a cooling substrate. Rough estimates on the cost of such a system are

CCD's	$120 \times \$500 = \$60k$
Electronics	$120 \times \$800 = \$96k$
	(Including FLASH AJC's)
Carrier/Fixturing	$\$150k?$

Our general conclusion concerning monolithic CCD's is that emerging commercial CCD technology is producing devices that will be able to detect minimum ionizing particles with nearly 100% efficiency (within the chip's active area) with pixel sizes as small as $15 \mu\text{m} \times 15 \mu\text{m}$ and formats as large as 800×800 elements. In addition, the radiation hardness of some of these devices appears to make them useful as detectors for High Energy Physics Experiments. These devices present great promise as high resolution vertex detectors in experiments where the cross sectional area of the CCD system does not have to be excessively large.

Hybrid CCD's

As we mentioned above, in this approach the detector and the CCD multiplexer are separate devices. This allows for great flexibility in designing the detector, since we are not restricted by the CCD parameters.

Our current hybrid work involves studies of the Rockwell International 30311 CCD multiplexer using a general purpose CCD driving system and low-noise correlated double sample and hold processor. The CCD is a 32×32 element area array with $88 \mu\text{m} \times 88 \mu\text{m}$ cell size using a 4-phase surface channel structure. A diagram of the injection scheme is shown in Figure 10. Charge

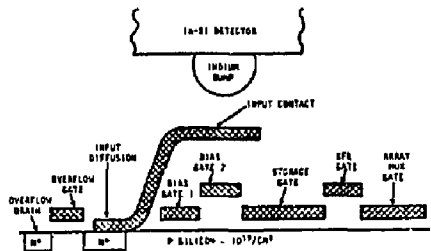


Fig. 10. Cell structure and injection scheme for Rockwell 30311.

collected from the detector is injected into the CCD via the input diffusion and stored under the storage gate. Readout is accomplished by transferring the charge under the storage gate to the CCD shift registers (array mux gate) to be read out in typical parallel/serial fashion. Data rates for this device are a maximum of approximately 1 MHz. The connection between the detector and the CCD is accomplished via microscopic indium bumps. The bump pattern applied to the detector corresponds to the CCD input node geometry. The CCD and the detector are then aligned in a microscope and cold-weld bonded together. With the use of a number of CCD multiplexers to read out a single detector, a bulk CCD can be fabricated. A detector designed in this fashion and used as an active target in a fixed target experiment is depicted in Figure 11.

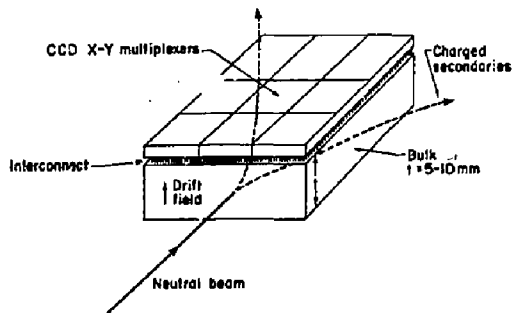


Fig. 11. Bulk CCD Detector.

Due to the flexibility of the hybrid design, this target system can be configured to suit the requirements of a particular experiment (segmented target etc.). In addition, readout rates of 10 MHz are possible with some hybrid devices, so a detector using fast CCD's with a 32×32 -element format would have a system readout time of approximately 100 μs . This active target would thus be fast enough to provide secondary level trigger decisions in addition to particle tracking data.

Micro Needle Detector

Another possible (but somewhat speculative) application of hybrid CCD arrays would be their use as the readout structure for what we have called the micro needle detector. The operation of the needle detector has been demonstrated,¹¹ but their widespread application has been limited due to their relatively poor resolution and by the lack of a simplified readout scheme to be used in conjunction with the needles. What we envision is an integrated approach to the "needle" design. With the use of standard MOS integrated circuit fabrication techniques the structure in Figure 12 could be

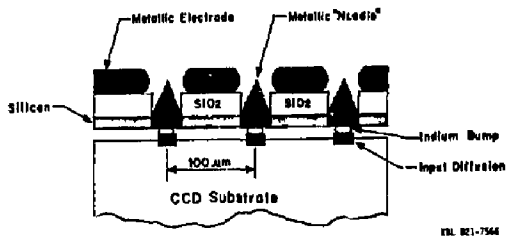


Fig. 12. Micro needle structure "bumped" to CCD multiplexer

produced. The "needle" detector could be fabricated on a silicon substrate with aluminum needles grown into etched holes. Silicon dioxide would be used as an insulator and the metallic focussing electrode is aluminum. This structure is very simple by IC standards, and a 50-100 μm needle spacing makes the dimensions large compared to those typical in IC fabrication practices. The coupling to the CCD (shown below the needle detector in Figure 12) would be accomplished using the indium bump technique, as we have discussed above. Figure 13 shows an electrostatic field calculation

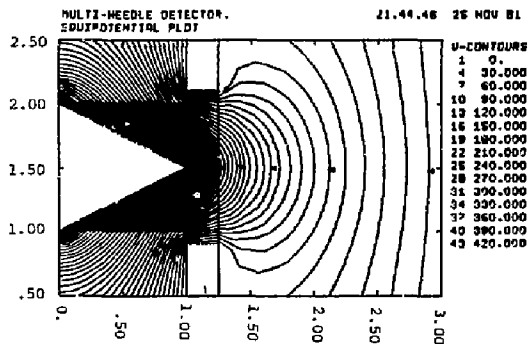


Fig. 13. Electrostatic equipotential plot for a single cell of the micro needle detector.

using the needle structure shown in Figure 11. With the proper voltage applied to the metallic electrode, the correct field shaping can be achieved for getting good field mapping of the active volume onto the needle and sufficient field strength near the needle in order to start an avalanche. There are obvious advantages to such a gas/silicon hybrid. Since the "active" volume is gaseous it can be made very large compared to what could be done with a solid state device. Of course, what is obtained is a two-dimensional projection of the

event onto the needle plane with the charge collected by the needle injected into the CCD. The needle plane would be limited in size by the CCD structure. The signal strength (upwards of 10^6 electrons) would make CCD signal processing extremely simple, and the problem of reading many needle channels is, of course, solved by the CCD.

The main questions concern electrostatic stability and CCD survivability. The electrostatic stability of the needle structure would depend heavily on the fabrication steps involved in the production of the needle devices. The simplicity of the design, however, would help to minimize variations in the final product. CCD survivability in this environment is an open question and can only be determined accurately once a suitable needle structure has been developed.

Conclusion

We believe that 100% detection efficiency for minimum ionizing particles is possible with a number of commercially available optical CCD's (within their active area). The VP CCD technology seems to be able to produce devices that have the resolution, low noise and radiation hardness qualities that will be needed to be useful as high resolution detectors for HEP.

Hybrid CCD detectors, using a much more sophisticated technology, present the possibility of producing CCD detectors with a much thicker active volume with a very small dead region. These detectors could be used as "active" targets at fixed-target accelerators. "Thick" CCD detectors, if used to track particles normal to their surface, as we have done with optical CCD's, could be operated without cooling and would have very little dead area, since bonding pad structures are on the backside of the detector.

Charge Coupled Devices present great promise as high resolution vertex detectors in experiments where the cross sectional area of the CCD system is not excessively large.

References

1. Wen, D. D., "Low Light Level Performance of CCD Image Sensors," Proc. 175 Int. Conf. Solid-State Circuits, Vol. SC-9, pp. 410-414, 1974.
2. Sequin, C. H. and Tomsett, M. F., Charge-Transfer Devices, Academic Press Inc., 1975.
3. Barbe, P. F., "Imaging Devices Using the Charge-Coupled Concept," Proc. of IEEE, Vol. 63, No. 1, January, 1975.
4. Marcus, S., Nelson, R., and Lynds, R., "Preliminary Evaluation of a Fairchild CCD 221 and a New Camera System," SPIE, - Proc., Vol. 172, 1979
5. Meyer, S. S., "Astronomical Spectrometer Using a Charge Coupled Device Detector," Rev. Sci. Instrum., 51 (5), May 1980, p. 638.
6. Bertolini, G., and Coche, A., Semiconductor Detectors, John Wiley and Sons, Inc., 1968.
7. Op. cit., Meyer, p. 638.
8. Janesick, J. R., Rynceck, J., and Blouke, M. M., "A Virtual Phase Imager for Galileo," SPIE Proc. Vol. 290, p. 165.
9. Op. cit., Janesick, p. 168.
10. Janesick, J. R., Private communication.
11. Crunberg, C., and LaDevehat, J., "The Needle Chamber: A New Highly Versatile Detector," Nucl. Inst. and Methods, 118, 1974, p. 457-463.

HIGH RESOLUTION SILICON COUNTERS

B. Hyams and U. Koetz
 CERN, Geneva, Switzerland
 E. Belau, R. Klanner, G. Lutz, E. Neugebauer and A. Wylie
 Max Planck Institute, Munich, Germany
 J. Kemmer
 Technische Universität, Munich Germany

Summary

A brief description of our development of silicon strip counters is given, with some recent measurements of their performance. A few comments are made on the outlook for the use of these devices with colliders.

Introduction

First here is a brief review of the relevant characteristics of silicon as a detector. Wafers of monocrystalline silicon with resistivity ρ Ω cm and thickness t cm are doped suitably to form a diode structure which is depleted of majority carriers at a voltage V volts (for n-type silicon)

$$V \approx 4 \times 10^8 \frac{t^2}{\rho}$$

(70 volts depletes 300 μ m of 5000 Ω cm material). The wafer is used as an ionization chamber which should have a leakage current ~ 1 μ A/cm² and gives 1 electron hole pair per 3.6 ev. energy loss, leading to a signal of some 2.5×10^4 electrons per 300 μ m track length for a minimum ionization particle. The detector noise can be negligible, but the preamplifier noise is not, and depends on the bandwidth and detector capacity.

For pulse-shaping time constants of ~ 200 nsec we obtain an rms amplifier noise of ~ 500 electrons with a slope of 15 electrons/pf. This determines the thickness of silicon required. Typically strips on a 300 μ m wafer have a peak signal/rms noise = 30/1. In fact 280 μ m to 350 μ m thickness are industrial standards and easy to handle. Typical numbers quoted will be for 300 μ m material.

Physical Limitations to Measurement Accuracy

There is a spread of charge around a minimum ionization particle's trajectory due to electron (and hole) diffusion of some 5 μ m radial width, and a much smaller spread due to space charge repulsion. These introduce a negligible error in the position of the centre of gravity of the charge (CGC). For tracks perpendicular to the counter surface high energy knock-on electrons give a lateral displacement of the CGC of ~ 5 μ m rms but if the signal amplitude is measured, and large signals are rejected (or suitably weighted) track coordinates may be measured with an rms error of ~ 2 μ m. For inclined tracks the small "Landau" fluctuations give rise to an additional error in coordinate measurement \sim approximately equal to $1/30 \times$ counter thickness for 45° inclination.

Design Considerations and Results

Some possible strip configurations are shown in Fig.1.

One coordinate can be read out on each strip (a), using charge division read out is only necessary every n th strip (b), counters have been constructed reading out x and y coordinates on one wafer (c).

We, a CERN, Munich collaboration, have chosen to start with a charge division system because we want to measure to $\sigma < 10$ μ m for a charm vertex search at the

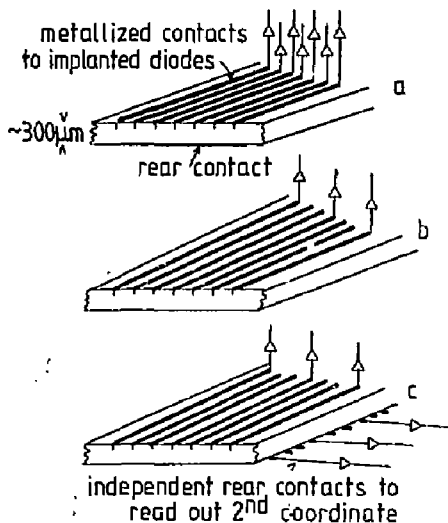


Fig. 1.

CERN SPS. Industrial bonding wire is at least 20 μ m thick (and squashes on bonding) so although a 20 μ m pitch pattern gives ~ 7 μ m resolution there is no convenient way to connect to each of a large array of such lines. The structure we have chosen is shown in Fig.2. The active area is 24×36 mm². On this there are 1200 strip diodes of which 240 are bonded to a fanout card. The whole device has a leakage current of around 1 μ amp (~ 1 namp per diode) at its working voltage.

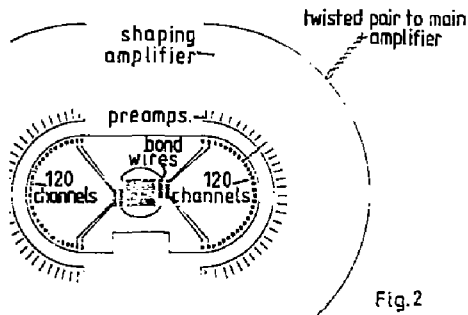


Fig.2

Possibilities for Colliders

Although charge division will probably give ~ 10 μm resolution across 120 μm spacing we need to read out every 60 μm in the forward direction where close track resolution is required. We have found also that although 20 μm pitch lithography is relatively easy a closer pitch is technically difficult for wafers of our size.

We have chosen charge-sensitive preamplifiers with shaping time constants of 180 nsec as a compromise between counting high fluxes and getting adequate signal/noise to use charge division. The noise per channel in the set-up is ~ 600 electrons. We plan to use some 1200 channels. The arrangement used is shown in Fig.3.

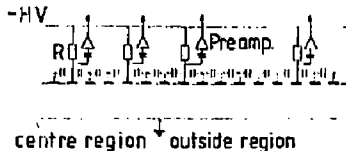


Fig. 3.

There is a capacitive divider network given by the interstrip capacities. The floating strips have to be charged up to the full bias voltage by a resistive layer. The resistive layer is only required to maintain the D.C. potential and does not enter into the charge division process. Fig.4 shows the resolution obtained in a 200 GeV beam for measurements across strips read out every 60 μm and every 120 μm .

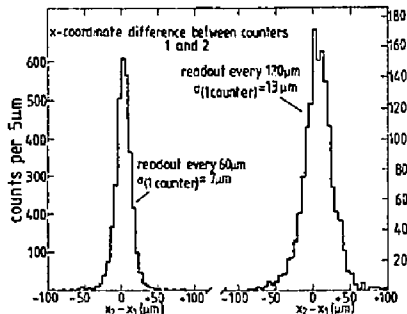


Fig. 4.

The devices we have made are satisfactory for high energy external beam experiments where the particles are concentrated in a forward cone leaving "sideways" free for the fanout and electronics. However, a cylindrical array with 10 amplifiers every millimeter is a clumsy object. In fact a twisted pair cable fills ~ 30 times more cross-section than the channel it reads out. Counters about 15 cm long could be read out with a signal/noise ratio of $\sim 30/1$ but the problem of fitting amplifiers around a 10 or 20 cm diameter cylinder is difficult, and the cost deterring.

For any bunched beam collider it is clear that sequential readout is required. With on chip (or near chip) electronics reading, say, 10 strips in sequence the problems of space, cost, and cooling would be resolved. At MPI and CERN we are designing such systems.

Finally it is worth remembering that high resolution counters are only useful for high energy particles. 100 μm of silicon scatters as much as 10 cm of argon (at NTP).

With a detector a distance r_1 from a vertex for 100 μm of silicon, the scattering at r_1 introduces a lateral vertex error of 5 μm for 1 GeV particles with $r_1 = 1$ cm, and for 10 GeV particles with $r_1 = 10$ cm.

PROPORTIONAL CHAMBER OPERATION AT LOW TEMPERATURES

L.M.Barkov, G.A.Blinov, B.I.Hazin, V.M.Morev,
N.M.Ryskulov, E.P.Solodov, V.N.Zaitsev

Institute of Nuclear Physics,
Novosibirsk 630090, USSR

1. Introduction

In order to study the e^+e^- annihilation at the storage ring facility VEPP-2M [1], a cryogenic magnetic detector (CMD) [2] has been made. A schematic view of the detector is shown in Fig.1. The six-gaps optical spark chamber (6) is mounted inside a superconducting solenoid (7). The solenoid and the spark chamber axes are parallel to the direction of particle motion in the storage ring. The distinctive feature of the detector is its operation at low temperature to get a higher density of a gas mixture in the spark chamber. The chamber operation at a temperature of 180 K and pressure of 2 atm allows a spatial resolution of about 50 μm . For triggering of the spark chamber two cylindrical multiwire

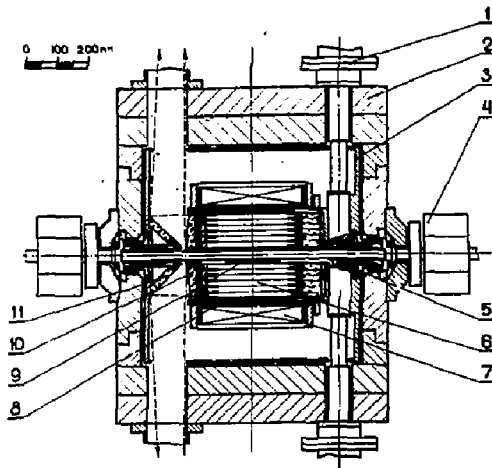


Fig.1. The schematic cross section of the detector: 1 - high voltage feeding, 2 - yoke, 3 - nitrogen shell, 4 - magnetic lens of the storage ring, 5 - compensating solenoid, 6 - spark chamber, 7 - main solenoid, 8 - outer MWPC, 9 - inner MWPC, 10 - optic lens, 11 - mirror.

proportional chambers (8,9) (MWPCs) operating with the same gas mixture are used. The absence of additional walls between the spark chamber and MWPCs decreases a multiple scattering of charged particles in the detector.

The momentum resolution $\sigma_p/p = 0.05 \cdot p$ (GeV/c) has been obtained at 32 kG magnetic field in the centre of the detector. The solid angle covered by the CMD is $0.6 \times 4\pi$. Two compensating superconducting solenoids (5) are employed to cancel the influence of the main solenoid field on the circulating beams. Only charged particles are detected by the CMD.

2. Experiments with MWPCs at low temperatures

The operation of MWPC at low temperatures was studied to find a suitable gas mixture at the lowest temperature. Some results of these experiments were given in Refs.3,4. The gases CH_4 and CO_2 were used as quenching admixtures to noble gases for normal operation of MWPC at low temperature. The CH_4 admixture allows to operate at a temperature of 78 K (liquid nitrogen temperature) and for CO_2 this temperature is about 160 K. At these temperatures the vapour pressures of CH_4 and CO_2 are 0.015 atm and 0.03 atm, respectively. In our detector the volume percentage of these gases cannot be more than 3-5% because of the deterioration of the efficiency and the spatial resolution of the spark chamber.

In those experiments the MWPC with 3 mm gap between 28 μm gold plated tungsten wire and cathode electrodes was used. This gap was chosen to minimize a volume of the MWPC triggering system in the magnetic field of the detector. The wire spacing was 2 mm, the wire length was 15 cm. The $\text{Ne} + 0.7\%\text{CH}_4 + 2.5\%\text{Ar}$ gas mixture at 78 K and a pressure of 2 atm was used as MWPC filling. The operating high voltage (HV) under this condition was 1500 V. The MWPC counting rate was 10^3 Hz per wire caused by the radioactive source.

The following phenomena were observed under these conditions:

a) The MWPC with cathode electrodes made of metals with oxide films on their surfaces did not work. The copper, aluminium, titanium, stannum, stainless steel were tested. A few tens of seconds after switching on a HV current of 100 μ A appeared through the chamber, the voltage drop on the limiting resistor increased that caused decreasing of the HV on the chamber and the MWPC lost its sensitivity.

To reduce the electric field in the vicinity of the cathodes, the wire spacing was changed from 2 mm to 4 mm, that led to decreasing the electric field from ~ 3000 V/cm to ~ 1500 V/cm. This gave the opportunity for MWPC with aluminium cathodes to operate during about 30 hours. Then the sensitivity was lost due to HV decreasing.

This kind of behaviour of MWPC could be explained by an increase in the resistivity of the oxide film on the cathode surfaces at low temperature. The ions built up the surface charge on this film, put out the electrons from the cathodes and the current appeared. The building time of the ion surface charge required for the appearance of a current through the chamber strongly depends on the electric field in the vicinity of the cathodes.

b) The MWPC with the gold plated cathode and a 2 mm wire spacing operated about 8 hours. Then the current appeared and the sensitivity was lost due to HV decreasing. The temperature increase by 10-15 degrees led to disappearing the current through the cham-

ber for a few hours. These steps continued up to the temperature at which CH_4 could be replaced by CO_2 . The non-regular dark film was found on the surface of the cathodes which could be partly washed out by alcohol.

At room temperature the MWPC operation with this mixture is stable for a long time. This behaviour could be explained by the CH_4 radicals polymerisation which increased at low temperatures. The similar effects of current appearance in the MWPC at room temperature was described in Refs. 5,6,7,8,9.

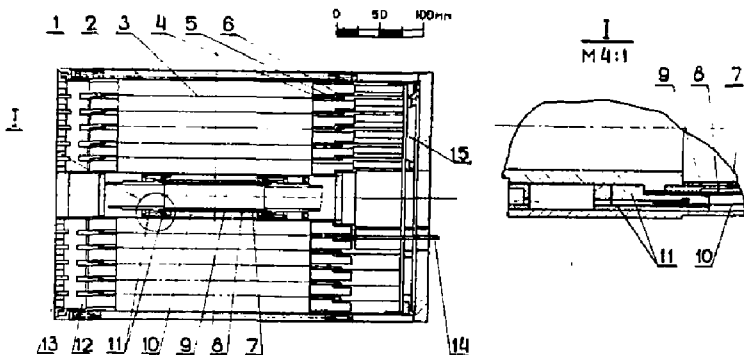
The noble gases with admixture of CO_2 are suitable for MWPC operation at temperatures higher than 160 K.

3. The MWPC construction and gas mixture used in the CMD

The construction of the MWPCs and the spark chamber used in the CMD is shown in Fig.2. The inner and outer MWPCs have been wound with the 28 μ m gold plated tungsten wires (10) with 4 mm wire spacing, 3 + 3 mm gaps width for outer and 3 + 4 mm gaps for inner ones because of the small radius of the inner MWPC. The inner MWPC has been mounted on the vacuum pipe of the storage ring. The wires are soldered to the copper strips put on the plexiglass isolating rings (11). The sizes of the plexiglass rings and aluminium cathodes (8) which had different heat expansion coefficients were selected to have the constant wires tension with cooling.

The stainless steel pipe (7) with a 0.05 mm wall thickness was used as a storage ring vacuum pipe near the beam interaction point.

Fig.2. The elements of the spark chamber and MWPCs: 1,4,5 - isolating rings, 2 - outer electrode of the spark chamber, 3 - foil electrode, 6 - aluminium ring, 7 - vacuum pipe, 8 - MWPC electrode, 9 - berillium pipe, 10 - sense wire, 11 - isolating ring, 12 - front wall, 13 - prisms, 14 - HV electrode, 15 - back wall.



A berillium pipe (9) with a wall of 1 mm thick put inside the vacuum pipe to prevent it from the outer pressure destruction. The cathodes of the inner MWPC have been made of 0.15 mm gold plated aluminium. The total thickness of the vacuum pipe and the electrodes of the MWPC is equal to 0.3 g/cm^2 or 0.009 radiation length.

The mixture of Ne + 8%Ar + 2.5%CO₂ was found to be suitable at low temperature for the spark chamber and MWPCs. The chambers operate at a temperature of 180 K and a pressure of 2 atm. The gas flow rate is about 5 cm³ per minute. Under this condition the operating HV of the MWPCs is about 1500 V and MWPCs have the plateau width of about 100 V with nearly 100% efficiency. The MWPCs time resolution is $2\tau = 100 \text{ ns}$.

4. The operation of the MWPCs as a CMD triggering system

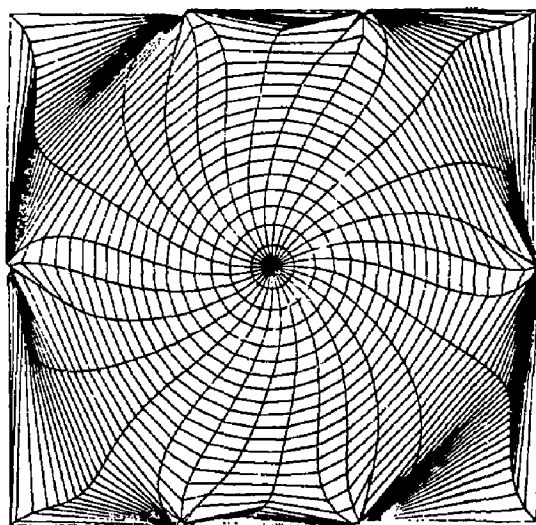
The wires in each MWPC were ordered in 16 groups. The high voltage was applied to the sense wires. The signals from every group were taken through a dividing capacitors and proceeded via 50 Ω cables to the amplifiers, which were placed outside of the detector at a 5 m distance. The input threshold was adjustable and was normally set at 3 μA . The selection of the desirable coincidence was carried out by the block of the trigger logic, which could be changed. The triggering rate of the detector was less than 1 Hz at maximum

luminosity of the storage ring. The inner MWPC operated at about 10^4 Hz per wire and the outer one operated at $\sim 10^2 \text{ Hz}$ per wire. Every $2+3 \cdot 10^4$ discharges in the spark chamber caused the 20 V increase in the operating HV on the MWPCs due to the gas mixture changing. The gas mixture used to be replaced after about 10^5 triggers of the spark chamber. The MWPCs operate with CMD about four years. There were no broken wires and no changes in MWPCs' parameters were noticed.

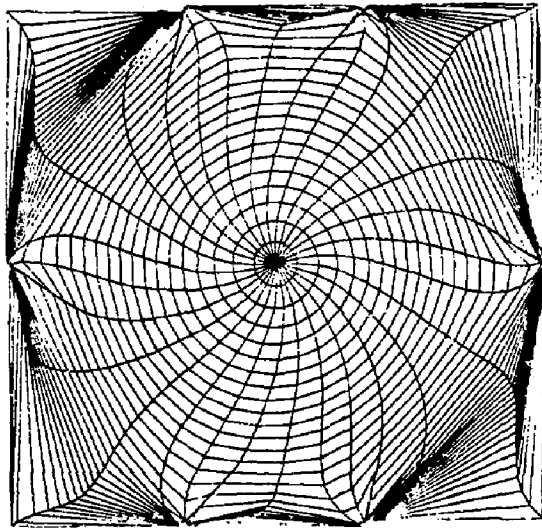
References

1. I.B.Vasserman et al. Proceedings of the Fifth National Meeting on Charged Particle Accelerators. Moscow, 1976.
2. L.M.Barkov et al. NFI Preprint 76-121, Novosibirsk, USSR, 1976.
3. E.P.Solodov, B.I.Hazin. II International Meeting on Proportional and Drift Chambers, JINR, D13-9164, Dubna, 1975.
4. L.M.Barkov et al. III International Meeting on Proportional and Drift Chambers, JINR, D13-11807, Dubna, 1978, 225.
5. L.Malter. Phys.Rev. 50 (1936) 48.
6. S.A.Korff and K.P.Present. Phys.Rev. 10 (1944) 274.
7. S.S.Friedland. Phys.Rev. 74 (1948) 898.
8. E.C.Farmer and S.C.Brown. Phys.Rev. 74 (1948) 902.
9. G.Charpak et al. Nucl.Instr.Meth. 99 (1972) 278.

ENERGY LOSS--DE/DX



ENERGY LOSS--DE/DX



RELATIVISTIC PARTICLE IDENTIFICATION BY dE/dx :

THE FRUITS OF EXPERIENCE WITH ISIS

W.W.M. Allison
Department of Nuclear Physics,
Oxford University, Oxford, UK.

Summary

The experience of ten years of studying dE/dx is summarised. First, a helpful, if qualitative, picture of the electromagnetic field of a relativistic particle passing through a medium is discussed. Second, the salient steps in a rigorous calculation of dE/dx are outlined. Results of calculations for a variety of gases and configurations are given and the weakness of the calculation is pointed out. In the third section the practical experience gained from the ISIS project is discussed. The systematic effects that have been overcome are listed and the status and successes achieved with ISIS1 and ISIS2 to date are described.

A Qualitative Picture of the Field of a Particle in a Medium

A charged particle passing through a medium carries with it a pulse of electromagnetic field. To simplify the picture we may ignore the vector nature of the field and pretend that we are working in two dimensions only - x in the direction of the particle velocity v and y transverse. The pulse is made up of a full spectrum of frequency components. Let us consider the component of frequency ω and suppose that the phase velocity of e.m. waves of frequency ω in the dispersive medium is $u(\omega)$. This component will have a wave-vector k which must satisfy:

$$\frac{\omega}{|k|} = u.$$

Furthermore, since the phase of the component is static as seen by an observer co-moving with the charged particle, the x -component of k must satisfy:

$$\frac{\omega}{k_x} = v. \quad (\text{or } \omega = k_x v)$$

The transverse component of k is therefore given by

$$k_y = \frac{\omega}{v} \left(\frac{v^2}{u^2} - 1 \right)^{1/2}$$

There are two cases of interest.

If $v > u$, k_y is real and the component of frequency ω represents a real travelling wave at an angle $\cos^{-1}(u/v)$. This is the case of Cerenkov Radiation.

If $v < u$, k_y is purely imaginary and the component propagates as an evanescent wave in the transverse direction:

$$\exp i \frac{\omega}{v} (x - vt) \exp - \frac{y}{y_0}$$

where the range y_0 is given by

$$y_0 = \frac{v}{\omega \sqrt{1 - \frac{v^2}{u^2}}}$$

Re-expressed in terms of $\beta' = \frac{v}{u}$, $\lambda' = \frac{v}{\omega}$ and $\lambda = \frac{u}{\omega}$, the free wavelength over 2π , the range becomes

$$y_0 = \lambda' \beta'^{-1}$$

The transverse range of the e.m. field expands with a factor β'^{-1} as the Cerenkov threshold is approached. It is this expansion, normally referred to as the relativistic expansion but in reality only depending on the wave nature of the field, which is responsible for the 'relativistic rise' of the ionisation cross section for a particle moving in a medium.

Relativistic kinematics only enters through the limit $v < c$. There are then two cases of interest. First, below the principal absorption lines and in the optical region where the refractive index is greater than unity, $u < c$ and the field expands as v is increased and the Cerenkov threshold may be reached. Second, in the u.v. and X-ray regions where the refractive index is less than unity, $u > c$ and, although the field starts to expand as v is increased, the Cerenkov threshold is beyond the limit $v = c$. The expansion therefore saturates with a maximum range

$$y_0 = \lambda' \frac{c}{u} \left(1 - \frac{c^2}{u^2} \right)^{-1/2}$$

Expressed in terms of the refractive index $n = \frac{c}{u}$ and the familiar $\beta = \frac{v}{c}$ and $\gamma = (1 - \beta^2)^{-1/2}$

$$y_0 = \lambda' \left[\frac{1}{\gamma^2} + (1 - n^2) \beta^2 \right]^{-1/2}$$

which is effectively reached already when $\beta = n$. This is the Fermi plateau region. The saturation is sometimes called the density effect because its onset depends on the density through n .

As an illustration, consider $\omega = 80$ eV. At this u.v. energy, the refractive index of argon at normal pressure is about 0.99999 and the range of free photons is a few hundred microns. Fig. 1 shows the transverse range of the field as a function of the velocity of the charged particle. Fig. 2 shows the same on a vastly expanded non-linear velocity scale including the kinematic limit $v = c$.

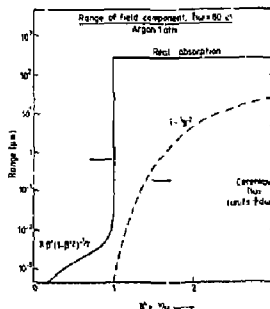


Fig. 1 Transverse range of a field component as a function of velocity.

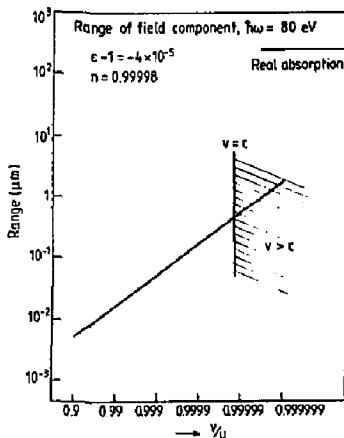


Fig. 2 As Fig. 1 but with kinematic limit. Note non-linear scale.

Of course such a crude picture, though qualitatively correct, is no basis for calculation. For this we must turn to the Photoabsorption Ionisation Model.¹

The Photoabsorption Ionisation Model for Calculation of dE/dx

This has been described in detail elsewhere.¹ Here we point out the five main steps involved.

Step 1

Step 1 is a student problem in Classical Electrodynamics. We solve Maxwell's Equations in a medium ($\mathbf{D} = \epsilon \mathbf{E}$, $\nu = 1$) due to a charge density $\rho = \epsilon \delta^3(\mathbf{r} - \beta \mathbf{c}t)$ and current density $\mathbf{j} = \beta c \rho$, which together describe the charge moving with velocity βc . In the Coulomb Gauge one obtains

$$\phi(\mathbf{k}, \omega) = 2c \delta(\omega - \mathbf{k} \cdot \beta \mathbf{c}) / k^2 \epsilon$$

$$\mathbf{A}(\mathbf{k}, \omega) = 2c \frac{(\omega \mathbf{k} / k^2 c - \beta)}{(-k^2 + \epsilon \frac{\omega^2}{c^2})} \delta(\omega - \mathbf{k} \cdot \beta \mathbf{c})$$

and

$$\mathbf{E}(\mathbf{r}, t) = \frac{1}{(2\pi)^3} \iint [i \frac{\omega}{c} \mathbf{A}(\mathbf{k}, \omega) - i \mathbf{k} \phi(\mathbf{k}, \omega)] \times \exp i(\mathbf{k} \cdot \mathbf{r} - \omega t) d^3 k d\omega$$

Step 2

The energy loss is due to this electric field doing work on the particle itself.

$$\frac{dE}{dx} = \frac{e \mathbf{E}(\beta \mathbf{c}t, t) \cdot \beta}{\delta}$$

Step 3

Step 3 is to point out that this energy loss, which is expressed as an integral over Fourier components, is not a smooth rate of energy loss but needs to be re-interpreted, as in semiclassical radiation theory, as a probability of energy transfers $h\omega$.

Thus

$$\frac{dE}{dx} = - \int_0^m \int_0^{\infty} N E \frac{d^2 \sigma}{dE dp} \pi^2 d\omega dk$$

where N is the electron density, $E = h\omega$, $p = h k$ and $\frac{d^2 \sigma}{dE dp}$ is the double differential cross section per electron. Doing the implied algebra we get

$$\frac{d^2 \sigma}{dE dp} = \frac{2c^2}{N \beta^2 \pi^2} \left[p(\beta^2 - \frac{E^2}{p^2 c^2}) \mathcal{I}_m \left(\frac{1}{\epsilon E^2 - p^2 c^2} \right) - \frac{1}{p c^2} \mathcal{I}_m \left(\frac{1}{\epsilon} \right) \right]$$

Step 4

The only unknown in this expression is ϵ . All we need therefore is $\epsilon(k, \omega)$, which is essentially the inelastic structure function of the medium. This involves a model¹ derived from:

- detailed photoabsorption spectra and their sum rules²
- Kramers Kronig relation for the real part of ϵ
- dipole approximation for the small k off-mass-shell region of ϵ
- constituent (i.e. electron) scattering and sum rules for the large k off-mass-shell region of ϵ .

Step 5

Involves integrating the cross section over momentum transfer analytically and then folding the cross section numerically to derive the dE/dx spectrum in a finite thickness of gas.

A FORTRAN program is available to calculate spectra etc. for gas mixtures, pressures, sample thicknesses and velocities of interest.

Results of Calculations

We have calculated the 'relativistic' rise for a number of gases at atmospheric pressure together with the corresponding resolution. One must be specific about what is being calculated in considering these results. Table I shows data relevant to dE/dx spectra in 1.5 cm samples. Rises, defined as the ratio for electrons to protons at 4 GeV/c, are quoted for the peak, the half-height point on the low side and half-height point on the high side of the dE/dx spectrum. The resolution is the FWHM figure per (metre)⁻¹ derivable from a maximum likelihood fit (for protons at 4 GeV/c). The figures show that, whereas noble gases have the larger rises, they also have the poorer resolutions. In large measure these two effects offset one another. In the last six columns of Table I we show figures indicating the separation of masses divided by the FWHM resolution at 4 GeV/c and 20 GeV/c. The values are remarkably independent of the choice of gas. It is important to note however that for the noble gases with their larger rise and poorer resolution, systematic effects in practical devices will be less important than would be the case for molecular gases.

In Fig. 3 we show the effect of changing the density. The calculation is for pure argon. As the density increases, the rise decreases due to the 'density effect' but the resolution improves. However, the effective mass separation does not improve much beyond 2-3 bar. The choice of gas density depends to a certain extent on whether separation is required at higher momenta.

TABLE I

Calculated Performance of Different Gases

Gas	Peak	Rel. Rise %		Resolution % FWHM	Mass Separation (FWHM) units per metro ^{1/2}			At 20 GeV/c: c/ π π /K K/p		
		Lo Point	Hi Point		At 4 GeV/c: e/ π	π /K	K/P	c/ π	π /K	K/p
He	58	86	45	15	1.5	.9	.3	.3	.9	.5
Ne	57	72	57	13	1.8	1.1	.4	.6	1.1	.6
Ar	57	66	49	12	1.6	1.1	.4	.6	.9	.6
Kr	63	65	61	11	2.2	1.3	.5	.9	1.1	.7
Xe	67	76	64	13	2.2	1.2	.4	1.0	1.0	.6
N ₂	56	59	48	11	1.8	1.5	.4	.7	1.0	.7
O ₂	54	54	47	11	2.0	1.5	.5	.7	1.1	.8
CO	55	56	48	11	2.0	1.3	.5	.7	1.1	.8
NO	54	56	47	10	2.0	1.5	.5	.7	1.1	.8
CO ₂	48	52	41	8	2.0	1.6	.5	.6	1.1	.9
N ₂ O	48	52	41	8	2.0	1.6	.5	.7	1.1	.8
CH ₄	43	45	39	9	1.6	1.5	.5	.5	1.0	.8
C ₂ H ₄	42	46	38	8	1.7	1.5	.5	.6	1.0	.8
C ₂ H ₆	36	41	34	8	1.6	1.6	.5	-	-	-
C ₄ H ₁₀	23	24	21	6	1.8	1.3	.3	.6	1.0	.8
Ar/20% CO ₂	55	62	48	12	1.9	1.2	.4	-	-	-

a) % Rise of peak

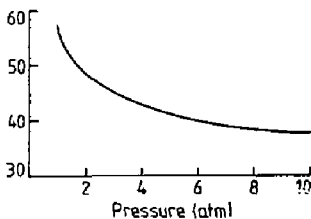
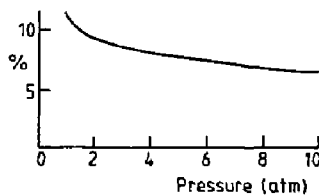
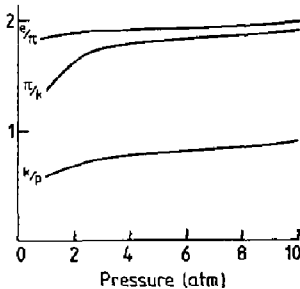
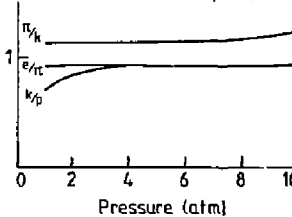
b) Resolution (FWHM) per (metre)^{1/2} for electronsc) Separation at 5 GeV/c
Resolution (FWHM) per (metre)^{1/2}d) Separation at 15 GeV/c
Resolution (FWHM) per (metre)^{1/2}

Fig. 3 Calculated variation of relativistic rise, resolution and mass separation for 1.5 cm samples of argon as a function of pressure (at normal temperature).

Fig. 4 shows the results of calculations on sample size. As the sample size is increased the relativistic rise decreases and the resolution per metre gets worse. Both effects tell us to sample as finely as possible. However, below 1 cm atm thickness in argon (or equivalent for other gases) the dE/dx distribution is no longer a smooth shape. It develops structures whose relative importance changes with velocity.³ Fitting these, to realise the ideal resolution may not be practicable. The effect of diffusion in generating cross talk between fine samples is equally important in limiting how finely one should measure dE/dx in practice.⁴

Critical Discussion

There have been calculations of dE/dx before. All have been found wanting at some stage. The present PAI Model would appear to be at least as good as presently available data. Nevertheless we summarise here its weaker points.

First, the available photoabsorption spectra are not beyond criticism.² However, when they are massaged to satisfy the sum rules representing the electron density and the static dielectric constant (by adding

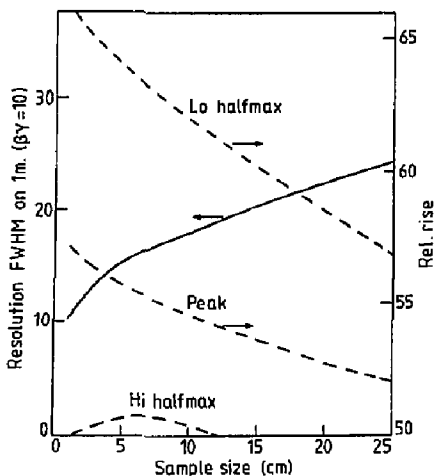


Fig. 4 Resolution and relativistic rise as a function of sample size for argon at normal density.

oscillator strength near threshold) they cannot be too far wrong.

Second, the model for the $\epsilon(k,\omega)$ is very crude. However, in very thin samples the important collisions are largely governed by the dipole approximation anyway. Results are therefore rather insensitive to the model.

Third, the assumed linear relation between energy deposited and number of ionisation electrons is physically implausible. The model assumes that the relation holds at least statistically with the same proportionality for every type of collision. Would the momentum of the secondary electron be a better guide to the probability of further ionisation? I believe that this weakness will give rise to discrepancies between theory and experiment sooner or later.

The Fruits of Experience with ISIS

The ISIS project for the Identification of Secondaries by Ionisation Sampling started ten years ago. Those most closely involved in it have been C.B. Brooks (project engineer), J.H. Cobb (pioneering graduate student) and P.D. Shield (electronics engineer). After the initial idea in April 1972^{5,6} we built a first 1m drift prototype, ISIS0. This was run in a test beam in November 1975 and showed clear evidence both for the space charge problem and the separation of pions and protons after an 85 cm drift.⁷ After further tests and proposals the 2m drift prototype, ISIS1, was constructed in 1978. Following successful operation in a test beam at NIMROD⁸ it was used in anger as part of the European Hybrid Spectrometer at CERN in 1980 for the NA16 small bubble chamber charm experiment.⁹ Since then it has been replaced by ISIS2 which ran in a preliminary experiment in July 1981 and is now running again in NA27, the second charm experiment (March 1982).

I will sketch the basic idea of ISIS first and then enumerate the principal problems, illustrating the points with data from our experience. Finally, I will show you where we have got to.

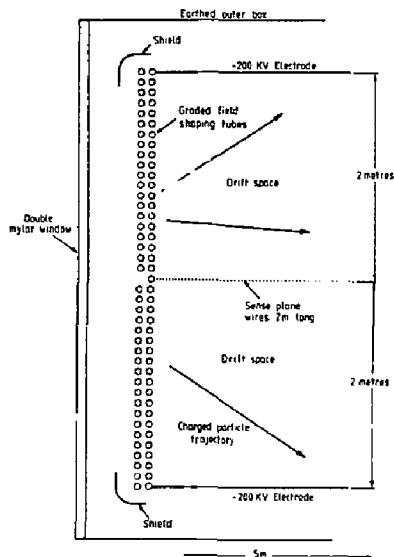


Fig. 5 Schematic diagram of ISIS.

The Idea

ISIS is a pictorial drift chamber similar to the more recent TPC but working at ambient pressure in a Cartesian geometry at a fixed target accelerator. Its prime role is particle identification; tracking is a free but impressive by-product. Fig. 5 shows a diagram of the chamber in the beam plane. Track signals are drifted to a single central wire plane perpendicular to the diagram. Multihit electronics can record between 30 and 50 hits per event on each wire. The electronics have been described elsewhere.¹⁰ They record the drift time and pulse height for each hit. The third coordinate is not measured and the up-down ambiguity is not resolved by the chamber alone. Table 2 gives the "vital" statistics of ISIS1 and ISIS2. The only important difference is the length, i.e. the number of samples per track.

	ISIS1	ISIS2
Acceptance	4 x 2m ²	4 x 2m ²
Drift distance	2 x 2m	2 x 2m
Voltage (present < 120)	100-200KV	100-200KV
Samples	60-80	320
Volume	50m ³	120m ³
Ionisation resolution, FWHM	14%	7%

Table 2

Hazard 1 Base Line Restoration

Generally dE/dx pulse heights are measured from a.c. coupled signals. It follows that the mean signal is zero. In particular, if the signal occupancy is $f\%$ within one a.c. coupling time constant, the baseline will shift by $f\%$ of the pulse height. See Fig. 6. This is an unacceptably large effect in general. It cannot be computed from the amplitude of earlier pulses with good confidence in software because of the uncertainties surrounding the frequent saturating signals. The problem

cannot be solved with linear filters. There are two solutions. Either you digitise the background level between pulses and correct in the software or you feedback the background signal level in the electronics itself. We have chosen the latter method.¹⁰ Once this problem is solved one can achieve excellent rejection of low frequency hum or at least its linear consequences.

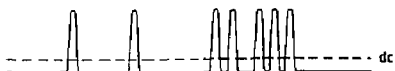


Fig. 6 a.c. coupled signals

Hazard 2 Pulse Shape

The impulse response of the gas amplifier has a $1/t$ tail.¹¹ Inverting this to provide optimal clipping without undershoot is a linear problem. In ISIS we do it with 3 passive filter time constants - 2 is probably enough.

Hazard 3 Shape-Independent Integration of Track Signals

Even after filtering, track signals are not sharp due to the combined effects of diffusion, track angle, drift path variation as well as the finite band-width of the electronics. Because these effects vary from track to track, to measure the signal charge it is necessary to do a proper gated integration. The track signal must be integrated from some time before the discriminator fired until 99% of the shaped pulse has arrived. This may be done in software if the whole signal has been digitised or in hardware with 'on' and 'off' thresholds. In ISIS we do the latter. The strict definition of complete integration ($\pm 1\%$) carries with it a conservative 2-track resolution. Fig. 7 shows the 2-track resolution in ISIS. The line superimposed on the histogram is the expectation of Poisson statistics. All track hits above 12 μ ms are resolved. The figures below each bin show the mean pulse height for the first and second hits of such pairs. We note that resolved hits above 12 μ ms are unaffected by the presence of the other at the level of 1-2%.

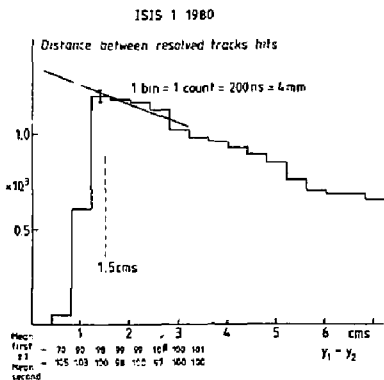


Fig. 7 Distribution showing loss of track hits at close separation.

Hazard 4 Bulk Space Charge

As a result of cosmic, background and earlier events the drift volume of a large device always contains positive ions released during the gas amplification process. It is usually possible to estimate roughly the space charge density knowing the gas amplification, the mean ionisation rate and the positive ion drift velocity (≈ 1 cm/s/volt/cm). Bulk space charge will be a problem for both spatial and dE/dx distortion if

$$\frac{\int \rho(z) dz}{\sigma} > f$$

where the integral is the line integral of the space charge density through the drift volume and σ is the drift electrode charge density per unit area. f must be of order 10^{-3} . We have seen spectacular effects from such space charge^{7,8}.

In ISIS we have cured it by gating the gas amplification off except during the bubble chamber sensitive time.⁸ We currently run in a beam of 3×10^4 s⁻¹, gas gain 10^4 , EHT 100 KV, 30 Hz x 2 ns sensitive time.

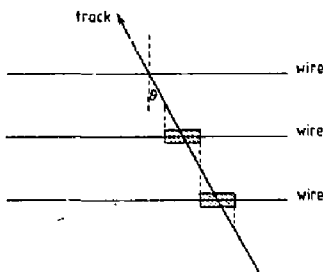


Fig. 8 Avalanche region for track at angle θ .

Hazard 5 Local Space Charge

Consider the track shown in Fig. 8 which crosses a number of anodes at an angle θ to the normal. The avalanche for this track (ignoring diffusion) takes place over a length of wire $s\theta$. The size of the avalanche is of order

$$G(\text{gain}) \times P(\text{bar}) \times 10(\text{electrons/mm}) \times s(\text{cm}) \times 1.6 \times 10^{-19}$$

giving a linear density

$$GP \theta^{-1} \times 1.6 \times 10^{-18} \text{ Coulombs/mm}$$

If this charge density is significant compared with the charge density on the wire causing the avalanche, the gain will be non linear. The latter is typically 12 pC/mm for 25 μ m wire. To avoid this problem at the 1' level we need $GP \theta^{-1} < 2 \times 10^5$. In ISIS we have $GP = 10^4$ so that saturation effects should be confined to tracks at less than 50 mrad. This may be responsible for a 25% loss of measured pulse height in the beam region ($\theta=0$) in ISIS1. Certainly this figure agrees within a factor 2 with the empirical bench test observations of local space charge by Frehse et al.¹² No such effect has been observed in ISIS2 where the chamber is rotated so that no track has an angle less than 50 mrad.

This problem is serious if GP must be kept high to get good charge division as in JADE and UAL. The problem in TPC should be no worse than in ISIS. In practice diffusion will help a bit. The problem may be compounded if the local rate is so high that a second track arrives before the positive ions from the earlier one have moved away.

Hazard 6 Calibration

In every event in ISIS there is both an electronic track fed to all preamps and a false trigger track that samples 'zero pulse height' background. These are monitored carefully. All signals are corrected for gain and pedestal variations although the variation is now small enough that this is unnecessary.

Hazard 7 Cross Talk

Capacitive nearest neighbour cross talk is not serious, as shown by Monte Carlo simulation. Diffusion between neighbouring gas samples is potentially more serious. Because the dE/dx distribution is highly skewed, cross talk can, not only change the shape of the spectrum but actually shift the peak. This has not been observed yet. It is a small effect.

Long range coupling between many channels whether capacitive in the chamber or a technical problem in the electronics can be disastrous for the resolution.¹³ Coherent pick up has the same effect.

Hazard 8 Gas Purity

For long drift paths and accurate pulse heights the gas must be pure. This requires leak tight systems, purification and instrumentation to measure the oxygen concentration. In our experience at purities of 1 part per million and less the latter causes the most trouble. In ISIS2 we are able to measure the attenuation directly by fitting the measured pulse heights on steep tracks. We assume that

$$\ln p_i = 2n \omega_i - \alpha t_i$$

where p_i is the measured signal, ω_i is a sample from a dE/dx distribution uncorrelated with t_i where t_i is the drift time. Moments accumulated for a track give a value of α . A thousand or so tracks give a distribution of attenuation factors α which enable the loss factor to be determined with an error of order 1%. Our best performance so far is about 14% loss on 2 metres. We expect a significant improvement on this soon.

Ionisation Fitting

As described elsewhere we employ a single parameter maximum likelihood fit.³ Fig. 9 shows how this works for a particular track. The histogram of pulse heights is fitted with a sliding scale parameter to a tabulated dE/dx function. In this case the track was known to be an electron from the spectrometer reconstruction where it associated with a γ conversion in the Bubble Chamber. Even with the modest statistics of ISIS1 the data clearly confirm the electron identification. Also shown in Fig. 9 are the data for an ISIS track which was associated to two tracks in the spectrometer. The likelihood fit correctly found the ISIS track to be 3 x minimum ionising although most of the pulse heights saturated the ADC. Such a case cannot be treated by a truncated mean method.

Fig. 10 shows new data from ISIS2 on the dE/dx distribution. The curve is the best calculation (without correction for cross talk) for the Argon/20% CO_2 mixture used. The data are actually fractionally sharper than the model. (The energy axis of the data has been scaled to give a best fit.)

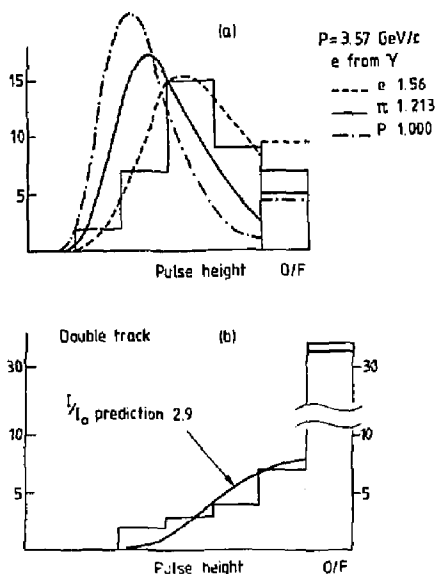


Fig. 9 (a) Pulse height histogram for a known electron with predictions for e , π , p . (b) Histogram for a known double track with prediction.

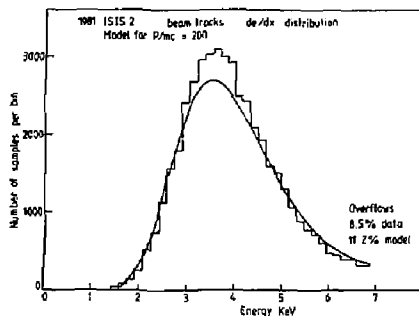
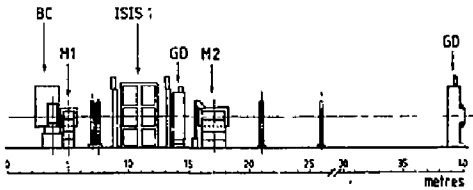


Fig. 10 Experimental and theoretical dE/dx distributions.

Particle Identification with ISIS1 in the NA16 Experiment

Fig. 11 shows the layout of the European Hybrid Spectrometer at CERN with ISIS1 downstream of the LEBAC bubble chamber as run in 1980.^{9,14} Fits of ISIS1 tracks to the spectrometer gave residuals of 4 mm and 5 mrad RMS. Samples of electrons from γ conversions in the bubble chamber and pions from K^0 decays in the bubble chamber were used to test the performance of ISIS1. Fig. 12 shows the ratio of observed to expected ionisation for these tracks. The width of 18.6% FWHM is significantly worse than found previously⁹ and predicted (14%). The systematic discrepancy is due to various problems that have been cured in ISIS2 (see below). Nevertheless Fig. 13 shows clear separation of electrons and pions in the two cases.

Fig. 14 shows a real case of physics interest. The bubble chamber picture (reproduced here with some difficulty) contains a $D^0\bar{D}^0$ pair. The \bar{D}^0 decays to $K^+\pi^-\pi^+\pi^-$.



EHS version J for NA16 June 1980

Fig. 11

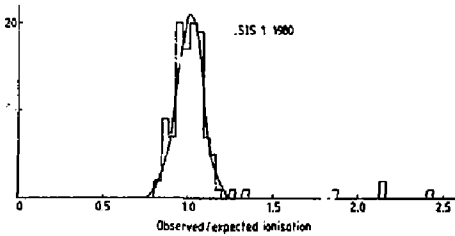


Fig. 12 Resolution of ISIS1. Curve is 18.6% FWHM.



Fig. 14 A bubble chamber photograph from NA16 showing a $D^0\bar{D}^0$ event. The first decay is 4.2mm from the vertex.

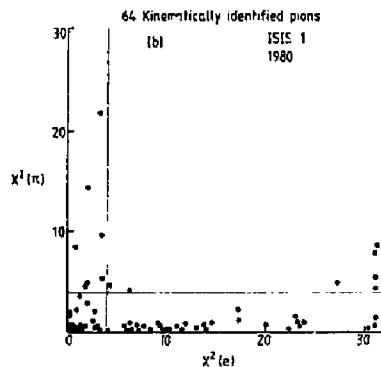
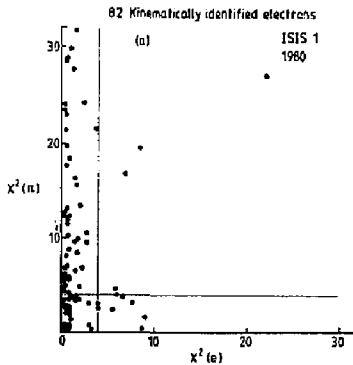


Fig. 13 The chisquare for one degree of freedom for electron and pion mass assignments for tracks of known identity. The lines in the plots represent the two standard deviation limits.

The ionisation for the K^+ track has a χ^2 of 10.1 (1d.f) when interpreted at π^+ . The proper time is 4.5×10^{-13} s. The D^0 decays as a 2 prong vee which does not point to production. The positive track has a momentum of 18 GeV/c and is associated with a shower of this energy in the EHS lead-glass γ -detector. For this track the ISIS ionisation χ^2 are 3.4 and 0.07 for the π^+ and e^+ interpretation respectively. Although this analysis is preliminary, it is interesting as a first clear use of

relativistic dE/dx for physics and as a clear case of the infrequent semileptonic decay of a D^0 .

Particle Identification with ISIS2

ISIS1 was built as a prototype. For full $e/\pi/K/p$ separation the extra resolution and better systematics of ISIS2 are needed. Fig. 15 shows views of the mammoth $100m^2$ device during construction. Fig. 16 shows the



Fig. 15a Construction of electronics in Oxford for ISIS2.



Fig. 15b View of ISIS2 during construction. The double wall of field-shaping tubes and the epoxy-impregnated wooden frames can be seen.



Fig. 15c Corner shield of ISIS2 to prevent breakdown



Fig. 15d View of chamber complete except for the lower tubes. The wire plane at 2m is just above technician's head.

layout of EHS more or less in its present form. In July 1981 a conventional diffraction experiment was run and ISIS2 used for the first time. Fig. 17 shows a fairly high multiplicity event in which many secondaries and decay products are seen passing through the chamber. The tracks have sagittae of $400 \pm 1000 \mu\text{m}$ over their 5m length. Typically there are 250 good resolved spatial points per track with 230 good pulse heights. The pulse generator artificial track is seen at the top of the picture. Its mean pulse height has a variation 1.0% FWHM from event to event and a jitter after reconstruction of 1.2 mms and 0.2 mrad. It is reconstructed and

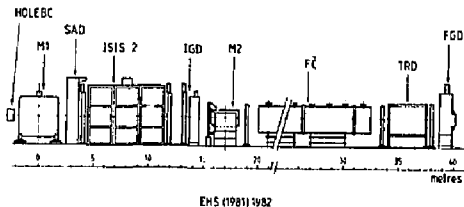


Fig. 16

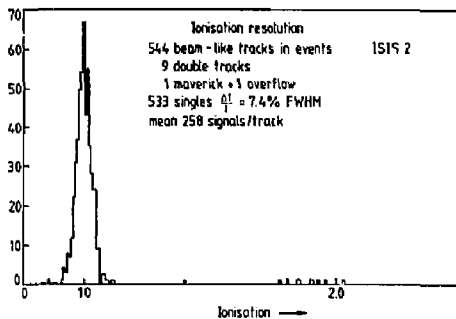


Fig. 18 The measured ionisation of beam tracks in ISIS2. The horizontal scale is chosen for convenience. The 'maverick' track is at 1.4. The 'overflow' is the only track not plotted.

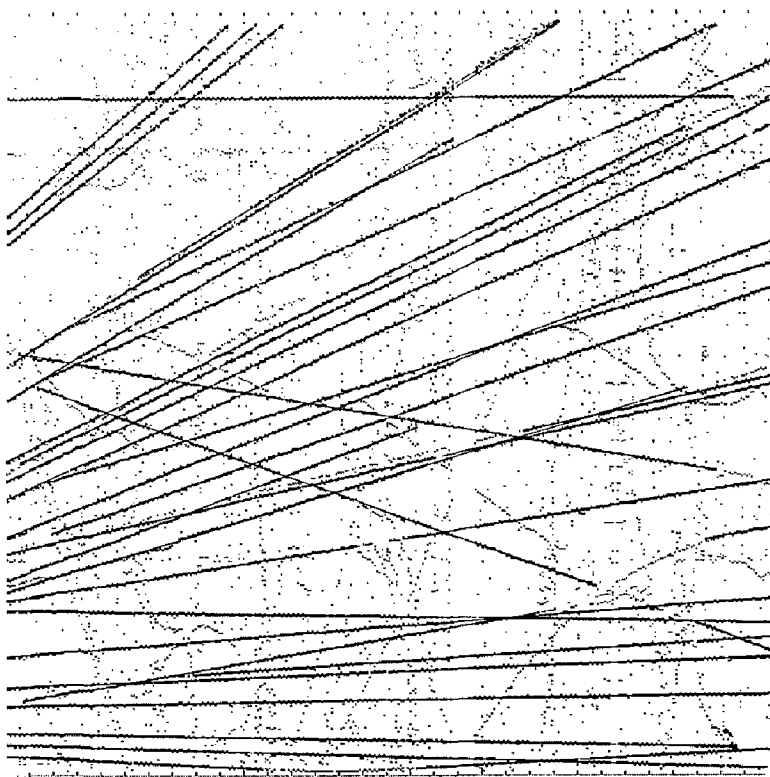


Fig. 17 Spatial data for a single event in ISIS2. Each point is a track hit and is associated with a measured pulse height (not shown). The horizontal axis (512cm) is the wire number. The vertical axis (2x200cm) is the drift direction. Tracks, low energy electrons and noise hits may be seen. Track vectors reconstructed in ISIS space are superposed on the raw data.

recognised by the software in 99.85 (± 15)% of events.

Fig. 18 shows the ionisation of out-of-time beam tracks found within these events. These show a resolution of 7.4% FWHM. There is no evidence of the significant gain variations found in the beam region in ISIS1. This is attributed to better control of space charge effects. We expect that this resolution will be confirmed for other tracks although this analysis is not yet complete.

Conclusion

In Fig. 19 we show contours of resolution as a function of device length and number of samples. The resolution values are theoretical and assume a full analysis by maximum likelihood ratio. These curves, which change a little with β_y , are in fair agreement with more empirical estimates for sample thickness greater than 1 cm atm. Below this the difference between the use of a truncated mean method and a likelihood ratio analysis is significant. For this reason other workers predict a worse resolution than shown here.¹⁵

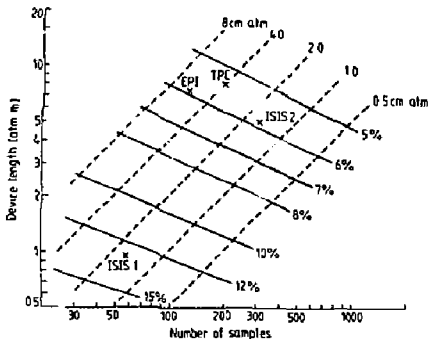


Fig. 19 The ionisation resolution (%FWHM) of a multi-sampling detector filled with pure argon calculated with the PAI model for $\beta_y = 100$. The dashed lines are loci of constant sample thickness.

The cross labelled 'ISIS2' shows the ideal resolution for a track with 320 points. With 230 points as realised in the analysis of ISIS2 data after excluding double track regions, bad channels and lost pulse heights, the theoretical resolution is 6.8%. (Walenta predicts 7% on 300 samples or 8% on 230).¹⁵ This is to be compared with our observed resolution of 7.4%.

We consider that these figures support the view that there is no real uncertainty about calculations of ionisation resolution or indeed the consequent mass resolution. The important questions concern systematics. In ISIS2 we believe we are close to realising the full potential of the dE/dx technique.

References

1. W.W.M. Allison and J.H. Cobb, Ann. Rev. Nucl. Part. Sci. 30 (1980) 253.
2. J. Berkowitz, Photoabsorption Photoionisation and Photoelectron Spectroscopy, Academic Press, New York (1979).
3. W.W.M. Allison, Physica Scripta, 23 (1981) 348.
4. F. Lapique and F. Piuz, Nucl. Inst. Meth. 175 (1980) 297.
5. W.W.M. Allison, Proc. Mtg. on MWPC Rutherford RHEL/M/821 (1972) 81.
6. J. Mulvey, Int. Conf. on Inst. for High Energy Physics, Frascati (1973) 259.
7. W.W.M. Allison, et al, Nucl. Inst. Meth. 119 (1974) 499.
8. W.W.M. Allison et al, Nucl. Inst. Meth. 163 (1975) 331.
9. "The European Hybrid Spectrometer", submitted to Nucl. Inst. Meth. (1982).
10. C.B. Brooks et al, Nucl. Inst. Meth. 156 (1978) 297.
11. G. Charpak, Ann. Rev. Nucl. Sci. 20 (1970) 195.
12. H. Frehe et al, Nucl. Inst. Meth. 156 (1978) 87.
13. W.W.M. Allison et al, Nucl. Inst. Meth. 135 (1976) 325.
14. S. Reucroft, Proc. Int. Conf. on High Energy Physics, Lisbon (1981).
15. A.H. Walenta, Physica Scripta 23 (1981) 384.

6×10^4 lb.) We can afford to make the end pressure plates very massive because they are located at the edges of the CLEO octants. They are made of 7.5 cm thick trapezoidally shaped steel plates. The two end plates are held together along their parallel sides by two aluminum sheets. The sheet nearest the beam line is .94 cm thick and the other sheet is .63 cm thick. The steel end plates themselves do not come into direct contact with the dE/dx modules. Between the outermost dE/dx module and the pressure plate is inserted a flat aluminum sheet. Contact between the sheet and the end plate is made through a large number of swivel head tensioning bolts. The tensioning bolts are used to squeeze the 124 accordion like modules down to the overall nominal dimension of $3.14 \pm .13$ cm. Lucite spacer blocks are inserted between the modules; the tensioning bolts are adjusted until the modules are flush against the spacer blocks. On average, the dE/dx system presents only ~ 3 radiation lengths of material to a particle coming from the interaction region.

Electrical Considerations

We require that our performance not be compromised by either systematic or unacceptably large statistical variations in the gas-amplification of the wires. Most important has been careful control of wire diameter and maintenance of uniform spacing (wrinkle-free) between cathode planes. We tested several wires in each module to ensure gain uniformity to $\pm 4\%$. The 60 KeV line from Am^{241} was used to fluoresce the copper clad foils. The primary radiation easily penetrates the aluminum frames. The same technique was used to determine empirically the electrostatic cross-talk between sense wires, by observing the oppositely signed pulses on wires neighboring a struck wire. This cross talk is removed in our hardware by a resistive network which couples the output of all amplifiers in such a way as to cancel the electrostatic chamber effect, as well as circuit board cross talk.

Amplifier Performance

Each of the sense wires is ganged to nine neighbors with a simple single filament daisy-chain. The resultant independent groups total 1400 channels per octant. These are connected by ~ 20 ft. of coaxial cable to the charge sensitive amplifier inputs; each circuit board handles 60 channels.

The amplifiers have a charge gain of about 5 ADC channels/fC. Our typical signal at a gas gain of $\sim 5 \times 10^3$ is 40 fC. The rms white noise is about 1 fC, a negligible amount. With careful shielding and filtering, incidental sources of coherent noise give less than 1 channel, or less than 1% of a single minimum ionizing signal. Gains are calibrated by impressing a small voltage pulse on the cathode planes.

Gas Mixture

The gas used is a 9% CH_4 , 91% Argon mixture. Its composition is carefully controlled to $\leq 0.5\%$ in the relative CH_4 concentration. This keeps gain shifts down below 1 percent. We also control the density of the gas mixture by requiring the octant absolute pressure to be strictly proportional to the measured absolute temperature.

^{55}Fe Monitoring

Finally, within each octant we have placed four small ^{55}Fe sources, whose spectrum as seen by representative wires is continuously monitored.

CLEO Performance

Fig. 6 shows the appearance of events in a dE/dx octant. The "clean" hit patterns are typical of non-interactive hadrons and muons. The "overlapping" patterns are indicative of interactions, overlapping tracks, or showering electrons.

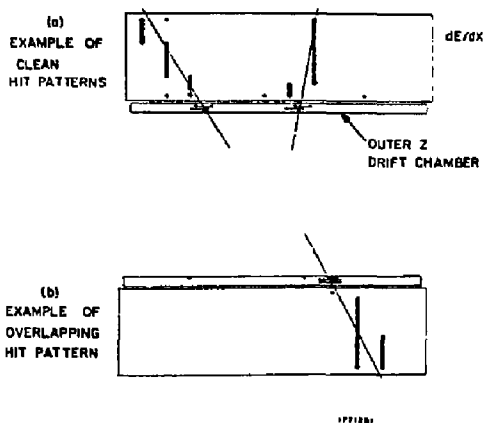


Fig. 6. Examples of (a) clean hit patterns and (b) overlapping hit patterns.

Clean tracks are internally divided into 3 segments. They are retained for hadron identification only if the pulse height distributions of the segments are consistent. The estimate of dE/dx used is the mean of the smallest 50% of the pulse heights (TM50). In Fig. 7, we show the TM50 vs. raw drift chamber momentum for ~ 9000 clean tracks collected in the summer of 1981. These events, collected during the T(3S) running are required to

- 1) have more than 90 hits
- 2) to be in the fiducial volume for uniform gain
- 3) to scatter by no more than 5° from the projected drift-chamber extrapolation.

They are corrected for path length in a trivial way. Clean pion, kaon, and proton bands are evident. We stress that no hypothesis dependent manipulation has been performed, even though the particles pass through the solenoid coil (~ 30 g/cm 2) at a variety of angles. Figure 8 shows the TM50 plots for particles identified by the CLEO time-of-flight system (TOF). The (imperfect) agreement between the devices is quite good, though it is apparent that perhaps 20% of the TOF kaons are in fact dE/dx pions. Such contrasts between redundant detectors are invaluable for understanding true rejection ratios.

Resolution in Practice

Perhaps, the cleanest test of the in situ capability of the dE/dx system is provided by QED muons. Except for occasional final state radiation, these low multiplicity non-interacting particles ought to give optimum resolution.

Figure 9 shows the histogram of the muon tracks plotted versus the measured TM50 pulse height. In fact, the peak is located within 1% of the expected position, but the width is broader than expected from test beam performance. Both for this sample, and for pions in the neighborhood on minimum ionization, it appears that some systematic broadening of about 3% (in quadrature) is

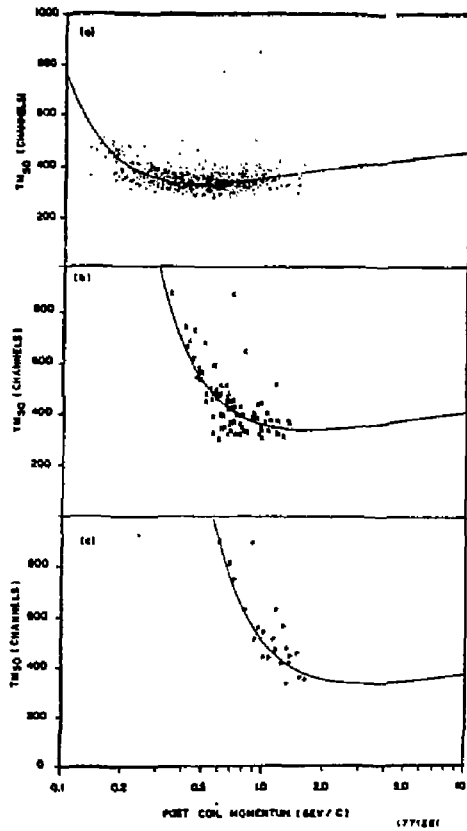


Fig. 8. "Most probable" energy loss (TM_{50}) versus momentum of tracks as measured in the CLEO drift chamber.

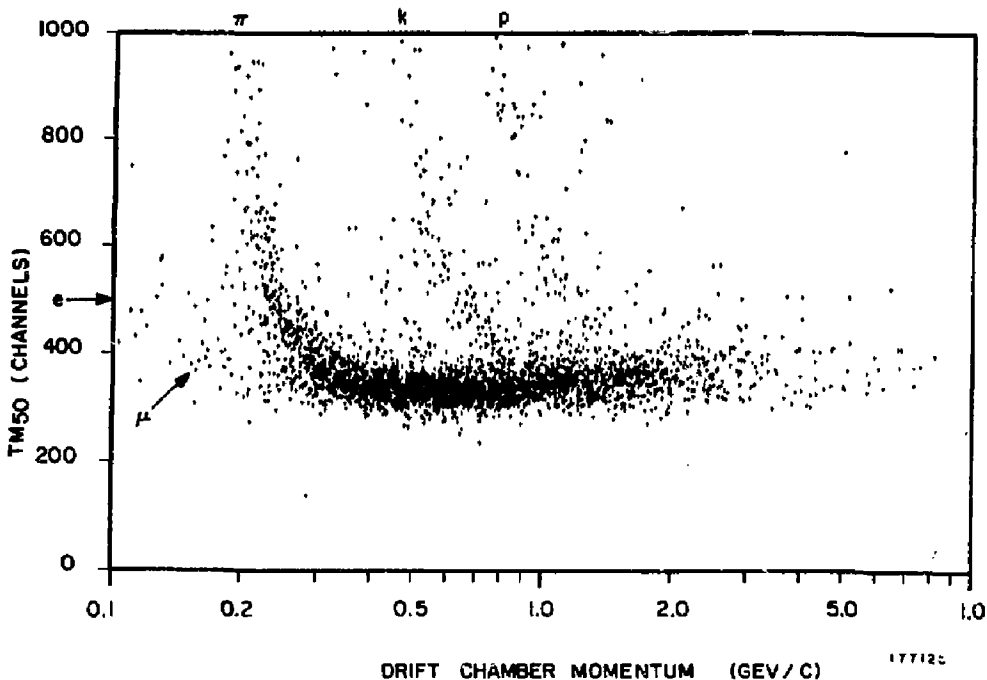


Fig. 7. TM_{50} versus momentum in the dE/dx device for particles identified by the CLEO time-of-flight system as (a) pions, (b) kaons, (c) protons. The curves are the theoretical energy losses expected.

operative. Currently we favor uncompensated variations in gas density as an explanation, but no certain cause has been identified. The resolution is nevertheless adequate to do useful high momentum π/K separation. Heretofore, running at a field of 0.4 Tesla we have been reluctant to trust momentum measurements; with our current 1 Tesla field, and improved tracking and luminosity, we expect to study the relativistic rise region.

Acknowledgements

I would like to give credit to my colleagues in the dE/dx effort at CLEO; particularly to Saj Alam, Sheldon Stone, Dick Talman, Rainer Wilcke, and Tom Gentile. Thanks for support and encouragement are due to Al Silverman and B. D. McDaniel.

Reference

1. See E. Nordberg and A. Silverman, "The CLEO Detector" CBX 79-6, Cornell Laboratory of Nuclear Studies, Cornell University, Ithaca, NY 14853, and S. Stone, *Physica Scripta* **23**, 4:2 (1980) 605.

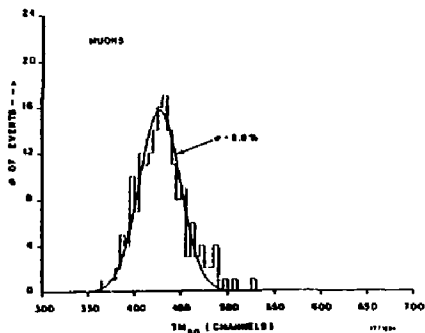


Fig. 9. "Most probable" energy loss for 5.15 GeV/c muons. The curve is a Gaussian of 5.5% r.m.s. fit to the data.

A. Wagner*
 Physikalisches Institut der Universität
 Heidelberg, Germany

Summary

The jet-chamber, used as the central track detector in the JADE experiment at PETRA, is briefly described. The present status of the dE/dx resolution, results from the measurements and the applications of particle identification in the event analysis are discussed.

The Jet-Chamber System

For the central tracking chamber of the JADE detector [1] at the e^+e^- storage ring PETRA a new type of drift chamber, the so-called jet chamber, has been developed [2-4]. This chamber is capable of recording events of high local track density (jets) with good space and double track resolution and with the possibility of particle identification within a solid angle close to 4π sterad. The concept of this chamber was developed in 1976 and data taking at PETRA has started in 1979. Details about the jet chamber and its performance have been published previously [5,6]. Before discussing particle identification the principle of the jet chamber is shortly described.

The sensitive volume of the jet chamber is a cylinder surrounding the beam pipe. The outer diameter is 1.6 m, the inner diameter 0.4 m, the length 2.4 m. The chamber is subdivided into 24 modules, two of which are shown schematically in fig. 1. Each module contains 4 cells with 16 anode wires each. A uniform drift field with equipotential planes parallel to the median plane is provided by field electrodes. The drift trajectories are up to 8 cm long. The gas gain ($\sim 4 \cdot 10^4$) is adjusted through the high voltage applied to the potential wires, located between the anode wires. In the range of polar angles $34^\circ < \theta < 146^\circ$ (measured with respect to the direction of the incident positrons), 48 points are measured along each track. The track length in radial direction is 57 cm. At least 8 points on a track are obtained over a solid angle of 97% of 4π . At each point three coordinates, r , ϕ and z are given by the wire position, drift time and charge division measurement. The charge division method requires the measurement of the integrated charge from each hit at both ends of the anode wire. The ratio of these amplitudes determines z and the sum of both amplitudes measures the energy loss dE/dx of the particle in the chamber gas. This measurement of the total charge, determined up to 48 times along each track, is used for particle identification by multiply sampling.

The electronics [7] connected to each of the 1536 wires of the detector consists of preamplifiers on both ends of the wire, a discriminator-integrator and fast analog and time memories with a capacity of 8 hits per wire. The discriminator provides the signal for the drift time measurement and the gating signal for the charge integrators.

Different tracks within one cell do not interfere with each other provided they are separated by drift times greater than the sum of integration and dead

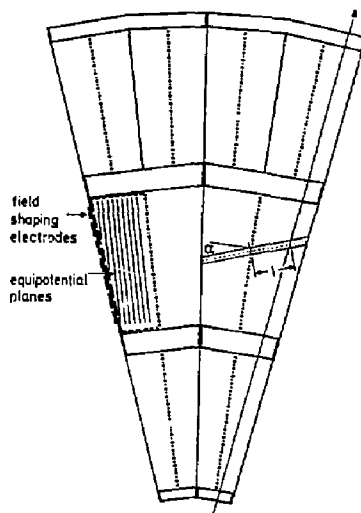


Fig. 1. Cross section through two segments of the jet chamber. l is the length of the drift path, θ the Lorentz angle. The position of the anode wires (small points) and of the potential wires (large points) are indicated.

time (20 ns). The double track resolution can be varied by adjustment of the integration time, which is currently set to 120 ns, leading to a double track resolution of 7 mm.

A pulser system allows to inject pulses of known charge at both ends of each anode wire. This system is used to calibrate the gain factors of the electronic system. The chamber is operated with an argon-methane-isobutane mixture (0.887 : 0.085 : 0.028) at a pressure of 4 atm. This pressure is chosen for mainly two reasons: to improve the space resolution by reducing the longitudinal diffusion and to enhance the effective sample thickness in order to obtain a better dE/dx resolution. The gas temperature is kept constant to 0.5 degrees.

A solenoid provides a magnetic field of 4.8 kG parallel to the axis of the chamber. The magnetic field is orthogonal to the electric drift field and causes a rotation of the drift trajectories by a Lorentz angle of 20 degrees.

The average values of the space resolution achieved in the central detector of JADE are:

$$\sigma(R, \phi) = 160 \mu\text{m}, \quad \sigma(z) = 13 \text{ mm}.$$

The average transverse momentum resolution is

$$\Delta P_T / P_T = 2.2\% \cdot P_T [\text{GeV}/c].$$

*Work supported by the Bundesministerium für
 Forschung und Technologie

*Heisenberg Foundation Fellow

Fig. 2 shows an example of a jet event as seen in the central detector and the surrounding lead glass detector.

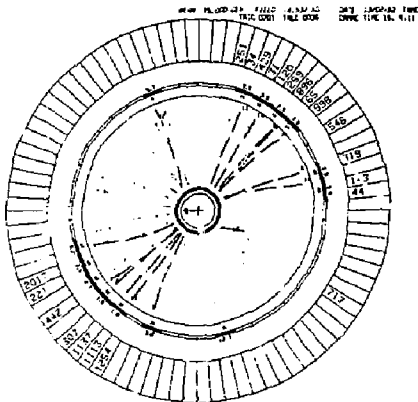


Fig. 2. Display of a typical jet event as seen looking along the e^+e^- beams.

dE/dx Evaluation

The energy loss in the chamber is calculated from the sum of the integrated charges measured at both ends of the wire. Up to 48 ionisation samples are measured per track, however for jet like events the mean number of useful samples is reduced (only 50% of all tracks have more than 30 useful samples). This reduced sample size is due to tracks which leave the chamber through the endplates and due to overlapping tracks, where hits in the region of overlap have to be rejected.

The mean energy loss for a given track is calculated by taking the average of the 60% lowest pulse heights thereby eliminating the influence of large Landau fluctuations (method of truncated means). Before taking an average, each individual integrated charge has to be corrected for several effects:

- 1) The ionisation is proportional to the sample thickness, which is 1 cm normal to the drift direction. The measured charge is corrected according to the track direction.
- 2) The gas and electronics calibration differ from wire to wire. These individual gain constants are determined by using the electronic pulser system and a large number of tracks during actual data taking. The long term stability of this calibration was found to be better than 2%.
- 3) A correction for cross talk between neighbouring wires is made, which improves the resolution by 10%.
- 4) The chamber volume is disconnected from the external gas supply during data taking periods. A pressure drop of 1% per month is observed, which causes an increase in gas amplification $\Delta A/A = -7.2 \Delta P/P$. This change in amplification is corrected.
- 5) It was found that the pulse height drops with increasing drift time like $\exp(-\alpha \cdot t_{\text{Drift}})$ due to electron attachment in gas impurities, where the coefficient α depends on the time after a new gas

filling. The correction reaches values of up to 30% for $t_{\text{Drift}} = 1.5 \mu\text{s}$.

- 6) Since the chamber is operated at a gas gain of $4 \cdot 10^4$ the effective gas amplification depends strongly on the angle θ of the track with respect to the wire and on the drift time. This saturation effect is biggest for tracks orthogonal to the wire and for short drifttimes, when all electrons arrive nearly at the same time at the same point on the wire. The amount of saturation as function of θ and t_D was determined empirically from clean tracks during data taking.
- 7) A correction which depends on the angle between track and drift direction is presently under investigation.

The entire calibration relies on tracks collected during data taking. No radioactive sources or other external calibration tools are available at present.

dE/dx Resolution

The dE/dx resolution is limited by three factors:

- 1) Statistical fluctuations in the energy loss,
- 2) statistical fluctuations in the gas amplification,
- 3) systematic errors. The choice of gas and pressure determines the contributions from 1) and 2). The dE/dx resolution expected in the jet chamber is $\sigma/E = 4.5\%$ or (10-11)% FWHM, with a relativistic rise of 1.45 [8,9]. The observed relativistic rise is 1.48, the resolution for electrons from Bhabha scattering is $\sigma/E = 5.7\%$ or (13-14)% FWHM [fig.3].

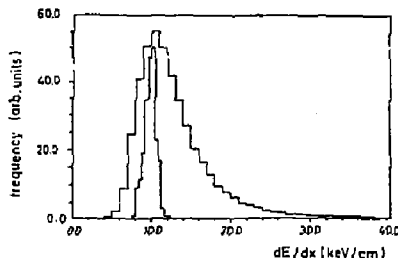


Fig. 3. Landau distribution and truncated mean for electrons from Bhabha scattering.

The resolution obtained in high multiplicity events is worse however, $\sigma/E = 9.4\%$ or 22% FWHM. This deterioration is partly due to shorter effective track length and partly due to the fact that the majority of tracks in jets is of low momentum with large track inclination with respect to the wire plane. As mentioned above the inclination correction is not yet properly taken into account.

Even in the case of high momentum electrons the expected resolution was not reached. This discrepancy is due to remaining systematic errors mainly caused by saturation corrections. If one calculates for individual Bhabha events $R = (\Delta E(e^-) - \Delta E(e^+))/\sqrt{2}$, one obtains a resolution which is $\sim 20\%$ better than the value quoted above and close to expectation. This can be understood since by calculating R in this way a number of systematic errors cancel.

Test Measurements

When the JADE experiment started no experimental information was available about dE/dx resolution in gases at elevated pressure. For this reason and in order to study sources of systematic errors, a series of test measurements was performed. The test chamber is shown in fig. 4a.

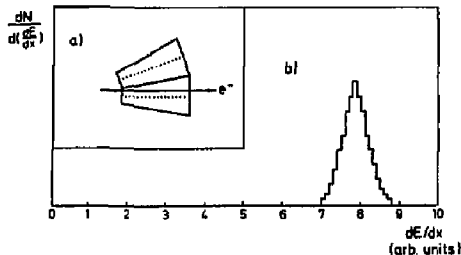


Fig. 4a. Cross section through test chamber
4b. Distribution of the mean energy loss (truncated mean) as obtained by adding three tracks.

It consists of two jet chamber cells, cut out of two completed segments and read out with the same electronics as used in the JADE experiment. Gas and voltage settings were also the same. The test chamber was scanned with an electron pencil beam. Three tracks were added in order to create tracks with 48 samples. In the test setup it was possible to map the dE/dx correction factors for each wire as function of the track angle θ and drift time with an accuracy of $< 1\%$. Using these correction factors a resolution of $\sigma/E = 4.6\%$ or 10.8% FWHM was obtained for a large variety of track directions and drift distances (fig. 4b), in excellent agreement with the expected resolution.

The test measurements therefore have shown two things:

- 1) The theoretically predicted improvement of dE/dx with pressure is correct.
- 2) An accurate determination of the correction factors can largely reduce the contribution of systematic errors to the resolution.

Encouraged by this result we presently use the high statistics data from fall 1981 to redo the entire calibration of the JADE jet chamber.

Application of Particle Identification

Although the dE/dx resolution of the JADE jet chamber has presently not reached the theoretically possible performance, the identification of all particles in an event is a very useful feature of the experiment. Fig. 5 shows the dE/dx information for all tracks of the event shown in fig. 2. One high momentum track (13) is strongly ionizing. A detailed analysis shows that this kind of track can be explained as complete overlap of two tracks with small azimuthal separation [10]. Particle identification by dE/dx has been used to separate π , K and P in the non relativistic region (where in jet events the TOF information is deteriorated by frequent double occupancy of the counters), for quark search [10] (fig. 6), for the identification of baryons [11], and for the determi-

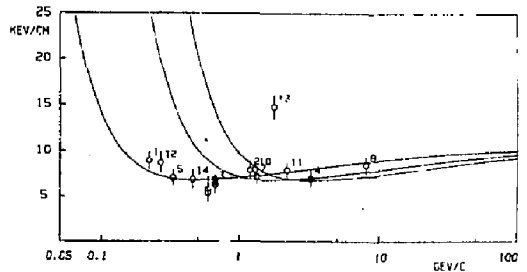


Fig. 5. dE/dx information of the event shown in fig. 2. For each track the truncated mean energy loss is plotted versus the momentum. The curves show the expectation for e , π , K and P.

nation of the $\pi/(K+P)$ ratio [12] in the region of the relativistic rise. Here the particle identification was done on a statistical basis rather than on an event to event identification, due to the limited resolution ($\sim 2\sigma$ separation). The dE/dx information was used to separate low momentum pions from electrons in the analysis of the reaction $e^+e^- \rightarrow e^+e^-\pi^0$ [13]. Further applications are in progress.

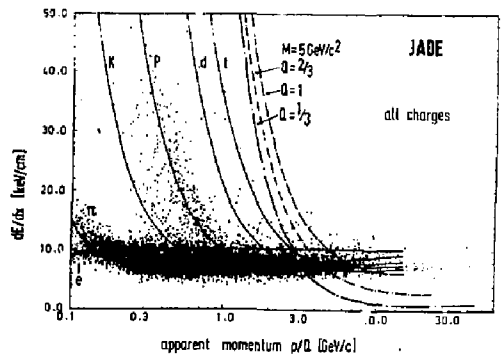


Fig. 6. Mean energy loss as function of the apparent momentum P/Q , where Q is the particle charge.

Integration Time and Gas Gain

In order to combine a good tracking quality of the jet chamber with a good dE/dx resolution, certain compromises had to be made in JADE:

- 1) Integration time: In order to avoid large fluctuations in charge collection one would like to work with a long integration time (> 200 ns). Good double track resolution on the other hand requires short integration time (< 100 ns). The 120 ns chosen in the present electronics is a compromise between both extremes. Recently the development of a new electronics

system has been started [14] in which this problem will be eliminated.

2) Gas gain: The accuracy of the z measurement using charge division is determined by the signal to noise ratio. Good z accuracy therefore requires high gas gain ($\sim 10^5$). In order to avoid large systematic corrections due to saturation effects in the gas amplification one would however like to operate the chamber at low gas gain ($< 10^4$). Two possible solutions exist to avoid this problem: One is to run the chamber at low gas gain, and to measure two accurate z points in separate chambers at the inner and outer radius of the main chamber. The second solution might be the use of thicker anode wires where the saturation effect seems to be smaller [15].

Conclusion

The combination of tracking information and particle identification has been very useful in the analysis of the events produced in e^+e^- annihilations even though the resolution presently achieved is a factor 1.2 - 1.8 (depending on the multiplicity) worse than expectation. Measurements with a test chamber in an electron beam have shown that in a situation, where an accurate calibration is possible, the expected resolution can be achieved. The observed difference between the measured and expected resolution is therefore attributed to the fact that the present calibration accuracy, due to low event rates, is insufficient to reach the intrinsic resolution. We try at present to make use of our recent high statistics data in order to further improve the resolution.

Acknowledgement

I would like to thank all members of the JADE Collaboration, who have helped to achieve the present performance of the central detector. The results presented here are the fruits of their combined efforts.

References

- [1] W. Bartel et al., JADE Collaboration, Physics Lett. **88B**, (1979) 171
- [2] J. Heintze, Nucl. Instr. and Meth. **156**, (1978) 227
- [3] W. Farr et al., Nucl. Instr. and Meth. **156**, (1978) 283
- [4] H. Drumm et al., IEEE Trans. Nucl. Sci. **26.1**, (1979) 81
- [5] H. Drumm et al., Nucl. Instr. and Meth. **176**, (1980) 333
- [6] J. Heintze, Proceedings of the International Symposium on Nuclear Radiation Detectors, March 1981, Tokyo, Japan
- [7] W. Farr and J. Heintze, Nucl. Instr. and Meth. **156**, (1978) 301
- [8] A.H. Walenta et al., Nucl. Instr. and Meth. **161**, (1979) 45
A.H. Walenta, Physica Scripta **23**, (1981) 354
- [9] W.W.M. Allison, Physica Scripta **23**, (1981) 348
- [10] W. Bartel et al., JADE Collaboration, Z. Physik C, Particles and Fields **6**, (1980) 295
- [11] W. Bartel et al., JADE Collaboration, Phys. Lett. **104B**, (1981) 325
- [12] D. Pandoulas, Proc. XXth Int. Conf. on High Energy Physics, Madison, Wisc.
- [13] W. Bartel et al., DESY 82-007
- [14] OPAL Collaboration, Letter of Intent for LEP, 1982
- [15] K.H. Hellenbrand, Diploma thesis, Heidelberg 1980, unpublished
J. Va'vra et al., SLAC-PUB-2882, Feb. 1982

DE/dx MEASUREMENTS WITH ARGUS

H. Nasemann
DESY, Hamburg, FRG.

Summary

The use of pure heavy hydrocarbons like propane or isobutane has some advantages for drift chambers that measure the specific ionisation for particle identification. With a prototype of the ARGUS drift chamber various gases were tested with a 3 GeV/c electron beam. We found a dE/dx resolution for propane of $Fwhm = 10.4\%$ and for isobutane $Fwhm = 9.9\%$, by a factor of ≈ 1.6 better than that for argon-methane (92:8) mixture with $Fwhm = 16.4\%$.

This improvement corresponds to an increase in effective gas length by a factor of 4 compared to pure argon. In isobutane and propane we found a broadening of the $55Fe$ -pulseheight spectrum with increasing gas amplification, showing in isobutane a clear two peak structure for gas amplifications above $\approx 3 \cdot 10^4$. However, neither gas showed a broadening of the truncated Landau distribution for electrons.

Introduction

For the DORIS storage ring at DESY a new universal magnetic detector named ARGUS¹ is now under construction and will be installed in the beam in the middle of this year. The central detector of ARGUS is a drift chamber 2 meters long and 1.7 m in diameter, which will serve for coordinate measurement of charged tracks and particle identification by dE/dx measurement. So far mainly argon gas mixtures have been used for detectors which are designed to measure the specific ionisation loss.

We report here on measurements with isobutane and propane which show that these gases are advantageous for some applications.

Compared with these heavy hydrocarbons, argon has a larger relativistic rise of ionisation loss, which simplifies the control of systematic measurement errors. It can be used also under pressure to increase the effective gas length, but the short radiation length then tends to spoil the momentum resolution of the chamber. It also has a broad Landau distribution and hence poor dE/dx resolution. Isobutane and propane have a long radiation length, an extremely narrow Landau distribution, and low diffusion. They seem to be ideal for use in a detector like ARGUS, designed to achieve very good mass and dE/dx resolution for the low momentum particles most abundant at DORIS energies.

We will give some estimates of dE/dx resolution which can be obtained with the ARGUS chamber. Amplification saturation effects and polymerisation in isobutane and propane will be discussed.

The ARGUS Drift Chamber

This chamber has 5940 identical drift cells of nearly square cross section in 36 concentric layers, filling the whole chamber volume without dead space. The structure of the chamber is shown in Fig. 1.

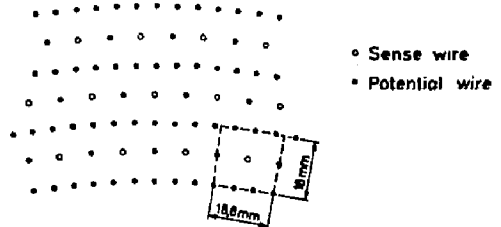


Fig. 1 : Cross section of the drift chamber showing a typical cell

The use of identical drift cells minimizes corrections, simplifies pattern recognition, and gives good granularity. There is thus no need to use electronics with multi hit features, where the extremely short gate length required for double track resolution can cause deterioration of dE/dx resolution for neighbouring tracks.

The isochrones calculated for a magnetic field of 0.8 Tesla parallel to the sense wires, are shown in Fig. 2. They are nearly perfect circles in 80% of the cell, so that in this region no angular corrections will be necessary.

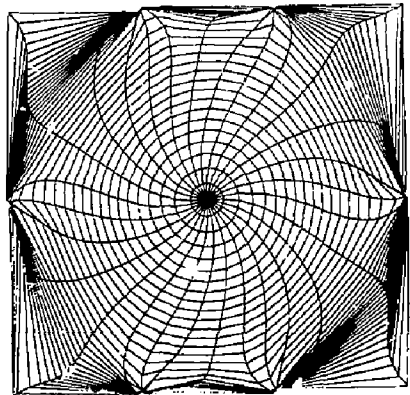


Fig. 2 : Calculated isochrones and field lines in the ARGUS drift cell.

The ARGUS chamber determines z-coordinates by a small angle stereo wire arrangement, the sequence of stereo orientation within the 36 layers being 0,+,-,0,-,0 ...

In a cylindrical geometry, the stereo wires form hyperboloids. The maximal sagittal displacement of all sense wires in the chamber has a constant value of 1mm. This is achieved by varying the stereo angle from 40 mrad in the innermost layer, to 80 mrad in the outermost; and by further giving the shielding wires between all layers a stereo angle which gives such a shielding wire half the sagittal displacement of the neighbouring stereo sense wire. In this wire arrangement the maximum amplification variations along the sense wires do not exceed 10% and can be corrected for. The chamber has 5940 30µ tungsten sense wires and 24588 potential wires of 75µ Cu-Be.

Fig. 3 shows a picture of the ARGUS chamber during construction. The light reflections indicate adjacent layers of wires with different stereo angles. At the time of writing all wires are strung and the chamber is nearly completed.

With an expected accuracy of 150 µm for coordinate measurement and a magnetic field of 0.8 T a momentum resolution of $\Delta p/p = 1\%$ at 1 GeV/c is expected from Monte Carlo simulation.

Fig. 4 shows a reconstructed Monte Carlo event in the r-φ plane of the ARGUS chamber.

Each sense wire has a preamplifier mounted directly on the chamber and a main amplifier-discriminator after 30 meter of 50 Ohm coaxial cable. The main amplifier-discriminator gives a stop signal for the LeCroy TDC-system 4290 and a delayed analog signal for the LeCroy ADC-system 2280. The minimum signal for a TDC

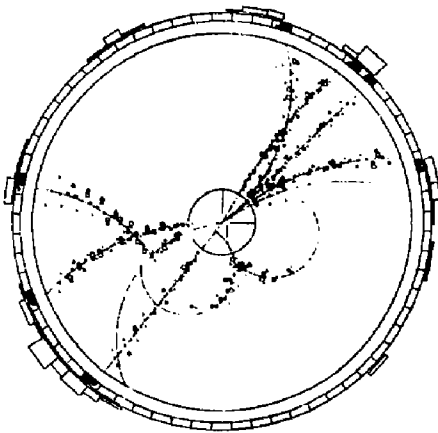


Fig. 4 : Reconstructed Monte Carlo event in the r-φ plane of the chamber. The circles indicate the measured drift time.

Fig. 3 : ARGUS - chamber during construction



start is 25 μV on 50 Ohms at the input of the preamplifier. This allows for gas amplifications below 10^4 with 99% cell efficiency. The electronics have a dynamic range of 50 dB which is sufficient to measure the variation of dE/dx with angle and momentum of different particles, including the large fluctuations of the Landau distribution.

Test measurements were made with three different chambers : a small tube with the ARGUS cell geometry, a full length prototype chamber with 16 sense wires with the ARGUS wire arrangement, and a chamber with 36 adjacent ARGUS drift cells.

Test Measurements

Using a ^{55}Fe X-ray source, pulse height spectra were taken in pure propane and isobutane and in the argon-methane (92:8) mixture. For low gas amplifications of $5 \cdot 10^3$ we found a line width of $\text{Fwhm} = 17\%$ in both argon-methane and propane, and an increased width of 24% in pure isobutane. For higher gas amplifications of $5 \cdot 10^4$ we found a broadening of the line width in propane and a distinct two peak structure of the line in isobutane. Such a complicated mechanism leading to a double peak structure of the amplitude distribution has also been observed in argon-isobutane-freon mixtures and has been attributed to the appearance of secondary photon avalanches².

For different sense wires (20 μ , 30 μ , and 37 μ) we found the same behaviour.

For 3 GeV/c electrons we did not see any increase in the width of the Landau distribution. We found $\text{Fwhm} = 45\%$ for propane and isobutane and $\text{Fwhm} \sim 70\%$ for argon-methane mixture for gas amplifications from $3 \cdot 10^3$ to 10^5 .

Fig. 5 shows the collected charge vs. sense wire voltage for a ^{55}Fe source and 3 GeV/c electrons with different angles to the sense wire. Data for electrons are normalized to 18 mm tracklength. Two points at the same voltage for ^{55}Fe indicate the double peak structure of the spectrum.

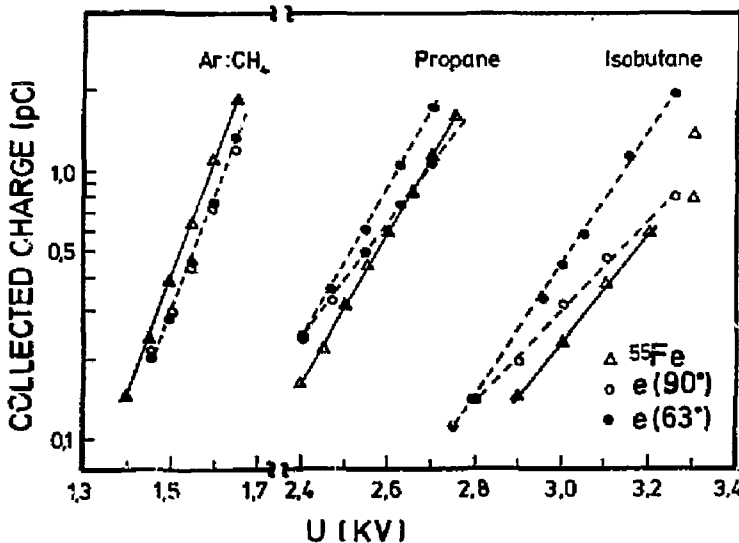


Fig. 5 : Collected charge vs. sense wire voltage for a ^{55}Fe X-ray source and electrons inclined and perpendicular to the sense wire. Data for electrons are normalized to 18 mm gas length. Straight lines are to guide the eye.

Space charge saturation leads to a deviation from exponential behaviour and to different slopes for electrons perpendicular and inclined to the sense wire. This effect seems to be small in argon due to its larger diffusion. In isobutane even ^{55}Fe shows space charge saturation.

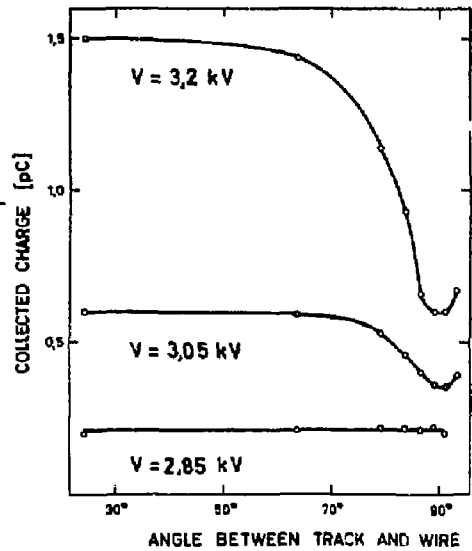


Fig. 6 : Dependence between entrance angle and collected charge for 3 GeV/c electrons for different voltages at the sense wire in isobutane. The track length is normalized to 18 mm gas length.

Fig. 6 shows the dependence between entrance angle and normalized collected charge for different gas amplifications in isobutane.

For dE/dx measurement these saturation effects have to be corrected for with an accuracy better than the dE/dx resolution, i.e. on a 1-2% level. This seems to be only possible for gas amplifications below 10^4 .

The dE/dx resolution for the 36 layers of the ARGUS chamber was estimated by applying the well known truncation method³, using the corresponding number of signals from a single cell. These results were compared with those obtained from the 36 cell test chamber. We found good agreement showing that correlations between adjacent cells and systematic errors are small. The relative standard deviation of the truncated average distribution was taken as the dE/dx resolution. The distribution of the truncated average (mean of the smallest 60% of each 36 cell sample) shows an approximate Gaussian form. The truncated mean approximately coincides with the maximum of the Landau distribution.

For 3 GeV/c electrons we found a ratio between the truncated means of argon-methane (92:8) mixture, propane and isobutane of 1 : 1.8 : 2.1. For this measurement the gas amplification was normalized with a 55Fe-source.

The resolution dependence on the fraction of the signals used for averaging (truncation factor) is shown in Fig. 7. This indicates that, for isobutane and the ARGUS geometry, a truncation factor of about .6 - .7 is optimum.

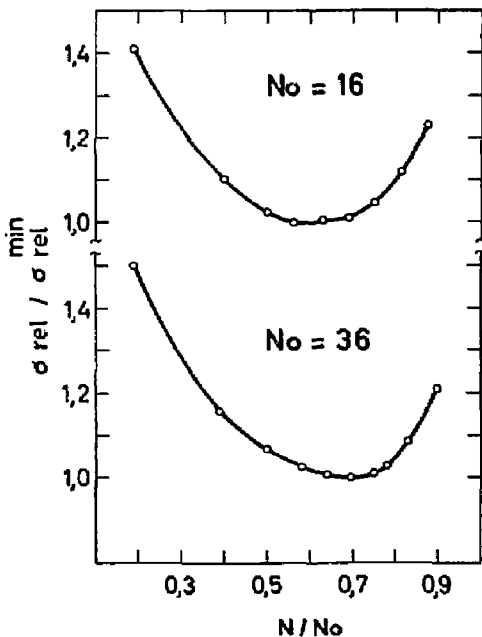


Fig. 7 : The dependence of dE/dx resolution in isobutane on the fraction of signals used for truncation.

Fig. 8 shows the dE/dx resolution obtained with different gas mixtures and different numbers of 18 mm long drift cells. Indicated is a measurement in argon- CO_2 (80:20) mixture from Ref. 4 which shows good agreement with our measurement.

To give some predictions we compared our results in terms of the scaling variable z/I which describes the variation of ionisation loss for different gases. We used the formula given by Allison et al.⁵ which is an approximation based on Monte Carlo calculations.

$$\sigma_{rel} = 34.5 n^{-.46} (z/I)^{-.32}$$

where n = number of layers,

I = mean ionisation potential,

$z = 0.135 (Z/A) pt$ (MeV for pt in g/cm^2).

The solid lines in Fig. 8 were calculated using this formula. They include fluctuations in energy loss, but not measurement errors.

From this our measurement error can be estimated to be ~ 13% for the single cell measurement in propane and slightly higher in isobutane (possibly correlated with the increased width of the 55Fe line in isobutane).

We can conclude that we have obtained 50% better dE/dx resolution in heavy hydrocarbons than in argon under the same conditions.

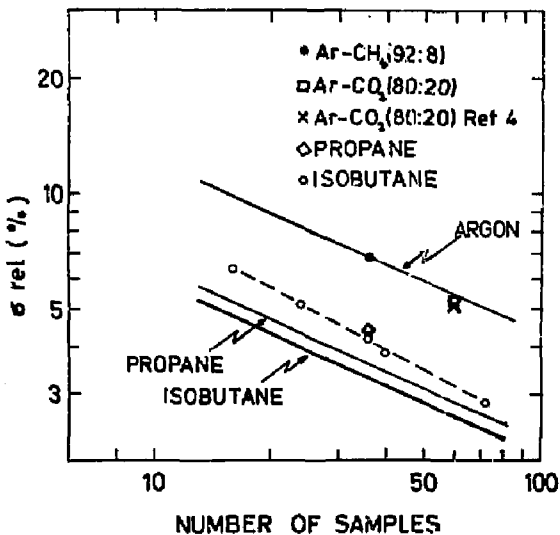


Fig. 8 : Relative dE/dx resolution in different gases vs. the number of 18 mm long drift cells used for ionisation loss measurement. The solid lines were calculated according to Ref. 5.

The expected dE/dx resolution for several detectors which use argon is shown in Fig. 9 taken from Ref. 6. We have added a point to this figure to indicate the expected resolution for ARGUS. It shows that the sample size in ARGUS is near the optimum and dE/dx resolution would not be increased appreciably by increasing the number of layers at fixed gas length.

It also shows that we win a factor of four in gas length compared to the use of pure argon.

The use of heavy hydrocarbons will provide better separation of non-relativistic particles. However, the relativistic rise of ionisation loss in propane is less pronounced than in argon⁷. In the momentum range above 3 GeV/c only a slightly better particle separation can be expected for heavy hydrocarbons and this only if systematic errors can be kept small.

Polymerisation in heavy hydrocarbons can ruin a drift chamber due to a polymer sheath on the sense wires⁸. To estimate the polymerisation for the ARGUS chamber we irradiated a sense wire with a ¹⁰⁶Ru source over a length of a few millimeters.

In an isobutane methylal (95:5) mixture we found no effect after a dose of $3 \cdot 10^9$ particles/mm corresponding to a collected charge of $2 \cdot 10^3$ pC/mm. In pure propane without methylal admixture we found first polymerisation effects for a dose of a factor of 10 smaller than in the isobutane methylal mixture. This was clearly indicated by a broadening of the 55Fe line and a considerable decrease of gas amplification in the irradiated part of the wire.

These effects disappeared after "training" the chamber for some time with pure argon and opposite high voltage polarity. Even assuming a background rate of 10^4 particles/wire·sec during ARGUS operation, it would take over ten years of operation until the background dose would exceed the dose used for the polymerisation test in isobutane methylal mixture. For propane we need further tests to understand the influence of methylal admixture on polymerisation.

Conclusions

The dE/dx resolution which can be obtained over a fixed track length is about the same for propane or isobutane at atmospheric pressure and argon at a pressure of 4 atm.

The advantage of propane is an 8 times larger radiation length compared to argon, which leads to an improved momentum resolution for tracks with momenta below 1 GeV/c. Also disturbing walls of a pressure vessel are omitted. However, due to space charge saturation and polymerisation the acceptable particle rates and gas amplification are limited. For a drift chamber detector at the e^+e^- storage ring DORIS, propane seems to be the best counting gas.

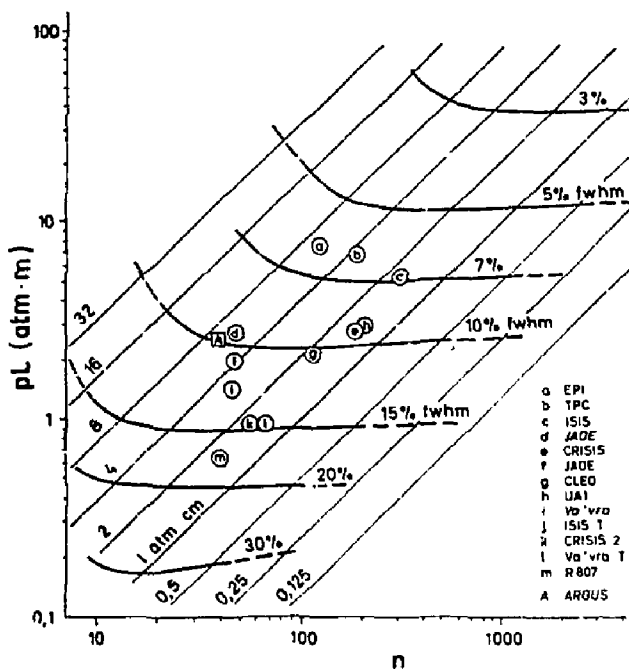


Fig. 9: Expected dE/dx resolution in argon for different detectors taken from Ref. 5. The expected resolution for ARGUS is indicated by inserting a point A.

References

- 1) H. Hasemann et al., DESY Internal Report F15/Pro 148 (1978)
- 2) J.L. Lacy and R.S. Lindsey, Nucl. Instr. and Meth. 119 (1974) 483-498
J. Fischer, H. Okuno and A.H. Walenta, Nucl. Instr. and Meth. 151 (1978) 451-460.
- 3) W.A. Okan, Nucl. Instr. and Meth. 97 (1971) 151-154
- 4) W.W.M. Allison et al., Nucl. Instr. and Meth. 161 (1979) 331-341
- 5) W.W.M. Allison and J.H. Cobb, Relativistic Charged Particle Identification by Energy-loss, Oxford University 13/80
- 6) A.H. Walenta, Proceedings from Int. Conf. on Experimentation at LEP, Uppsala 1980, Physica Scripta vol 23, (1981) 354-370
- 7) A.H. Walenta, J. Fischer, H. Okuno and C.L. Wang, Nucl. Instr. and Meth. 161 (1979) 45-58
- 8) G. Charpak et al., Nucl. Instr. and Meth. 99 (1972) 279

ENERGY LOSS MEASUREMENTS IN THE PEP TPC*

G. R. Lynch and N. J. Hadley
Lawrence Berkeley Laboratory
University of California, Berkeley, California 94720

Summary

The Time Projection Chamber (TPC) in the PEP-4 experiment has been tested with cosmic ray muons in the past few months. These tests have shown that the TPC is capable of measuring the ionization of single tracks with an accuracy of three percent, and that the results of the small dipole TPC¹ have successfully been scaled to the full device.

Description of the TPC

The PEP TPC¹ is a cylinder two meters long with a radius of one meter filled with argon mixed with 20% methane. The TPC can operate at pressures from one to 10 atmospheres. When a particle traverses the TPC, the electrons liberated by ionization drift parallel to the cylinder axis (z-axis) at about 5 cm per microsecond. The detector plane at each end is divided into six sectors, each of which has 183 detection wires, as shown in Fig. 1. The pulse heights from these wires are used to measure the track ionization. In each sector on the end plane there are 15 rows of pads. The pad spacing is 7.5 mm. The data from these pads provide three dimensional measurements of the track position. For both the pads and the wires a z-position is calculated from the drift time. For the pads an azimuthal position is calculated from the pad pulse heights.

Calibration

There are three distinct types of calibrations that are needed for ionization measurements in the TPC, the wire gain maps, the electronics calibration, and the end plane source calibration.

Before the sectors were installed, extensive measurements were made using Iron 55 sources to obtain maps of the variations in wire gain along the wires. As long as the sectors are not changed mechanically, these maps are expected to be permanent properties of the sectors. This assumption of gain map invariance was demonstrated to be a good one for the two sectors that were used in the cosmic ray tests in July and August. Figure 2 shows the gain map made for 4 typical wires in one of these sectors before and after that run. For most sectors the gain variations have an RMS of 3 to 4 percent and are not a serious problem. In fact, for the two sectors used in the August cosmic ray tests the same ionization measurement resolution of 1.3% was obtained whether or not we made these gain map corrections.

Electronics calibrations of all of the approximately 7000 TPC electronics channels in one of the two end caps have been done and used in the analysis. We are still learning how to control the time stability of the calibration and reduce the electronic noise. We expect to improve our resolution by these efforts. However, the ionization measurements are much less sensitive to these things than are the position measurements. Our ionization measurements will gain little from these improvements.

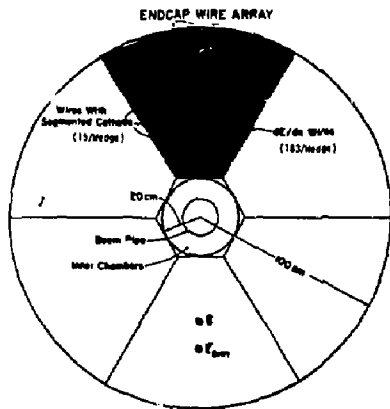
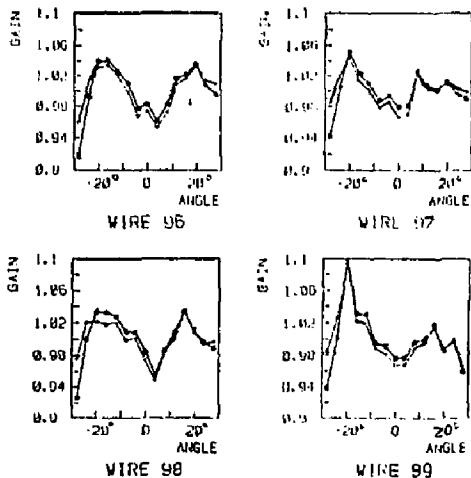


Fig. 1. A schematic drawing of one of the detection end planes of the TPC. All six sectors have the same construction, with 183 wires and 15 pad rows.



RUN 40 5/31

Fig. 2. This figure shows two gain calibrations for 4 wires in a sector that was calibrated in May, taken to IR-2 and used in cosmic ray tests and then recalibrated in October. The gain variations of a few percent reproduced very well except very near to the edge of the sector.

* This work was supported by the Director, Office of Energy Research, Office of High Energy and Nuclear Physics, Division of High Energy Physics of the U.S. Department of Energy under contract No. W-7495-ENG-48

Each TPC sector is equipped with three rows of Iron 55 sources with a remotely controllable shutter that are used to make end plane source calibrations for each wire. These calibrations will be used for three purposes. They can eliminate the sector to sector and wire to wire gain variations, which are on the order of 15%. They can be used to correct the wire gain map for gain variations due to temperature variations. In the construction of the TPC sectors much care was taken to eliminate these temperature variations and we have no proof from our cosmic ray data that such corrections are needed. The third use of these calibrations is to obtain an absolute energy calibration. This end-plane source calibration system has been operated successfully. As yet these calibrations have not been incorporated into the analysis.

Track Finding in the TPC

The raw data from the TPC arrive in the form of pulse heights in CGD buckets that are 100 nanoseconds, or about 5 mm, apart. A typical track produces a cluster of about five such raw data words on each wire. The first task of the analysis is to find these clusters and determine their peak heights and z -positions. For the pads there is an additional clustering of adjacent pads.

In our present analysis system the pad data only are used to find tracks. After the tracks are found, the wire clusters are associated with the tracks and a selection is made of the wire clusters that are to be used in the ionization measurements. Figure 3 shows an example of a set of wire clusters that have been associated with a track.

To be used in the dE/dx analysis, a wire cluster has to be within one centimeter in z from the track trajectory that was determined from the pad data. A track crosses from 155 to 183 wires if it goes the length of a sector. In our cosmic ray tests in November most sectors have about 10 missing wires, primarily due to calibration problems. Wire clusters are rejected from the sample if there is another cluster or another fitted track within three cm in z on the same wire. This allows us to reduce the interference from other tracks, especially delta-rays. Wire clusters are also rejected from the sample if the clusters on the track on either of the adjacent wires were so large that the electronics were saturated. About 2% of the wire clusters from cosmic ray muons were rejected in this way.

Event Selection for dE/dx Analysis

To study the ionization measurements we selected events that have one and only one track in each of two opposite sectors and we required that they be approximately colinear. This selects a fairly pure sample of cosmic ray muons. In addition, we required that both tracks have at least 120 wires remaining in the sample after all rejections. Figure 4 shows the distribution of the number of wires used in the dE/dx analysis for the track in these events that had the fewest wires used.

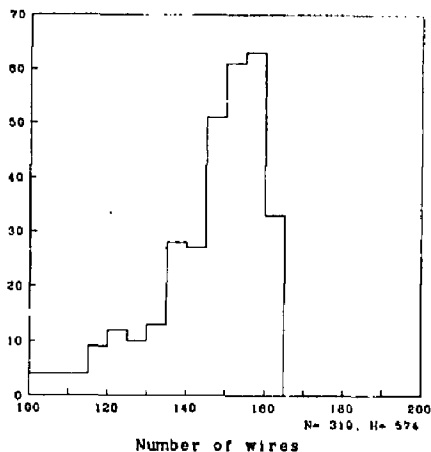


Fig. 4. The dE/dx resolution studies used events with a cosmic ray track found in two sectors. This figure is a distribution of the number of wires used in the dE/dx analysis for the sector that had the fewest number of wires used.

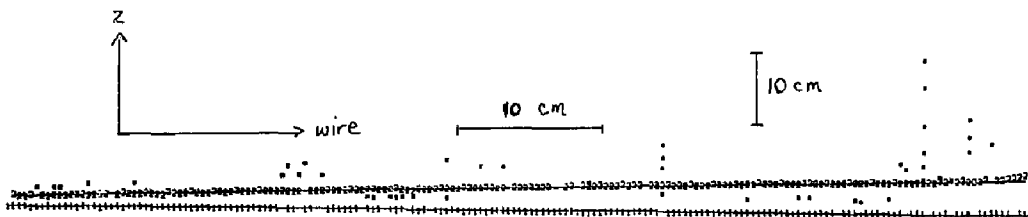


Fig. 3. The wire data for a cosmic ray event in the TPC are plotted in z versus wire number coordinates. The straight lines are the orbits obtained from the fits to the pad data. The numbers are wire clusters that were put onto a track. The asterisks are clusters that were not put on a track. The two tracks seen here are actually one track that is seen in two sectors.

Figure 5 shows for one cosmic ray run at 8.6 atmospheres a dE/dx distribution for all clusters in all tracks in one sector in this sample. The typical threshold for a channel is at about 0.3×10^3 . One can see from this plot that we have no large low pulse height contamination and that the threshold does not bias the distribution.

Each track has a dE/dx distribution similar to that of Fig. 5. We choose to use as a measure of the energy loss the mean of the lowest 65% of the pulse heights per unit length. The choice of 65% for the truncated mean was intended as the optimum for 8.5 atmospheres. A larger value for this percentage is probably better at lower pressures. But, the resolution is not very sensitive to this choice.

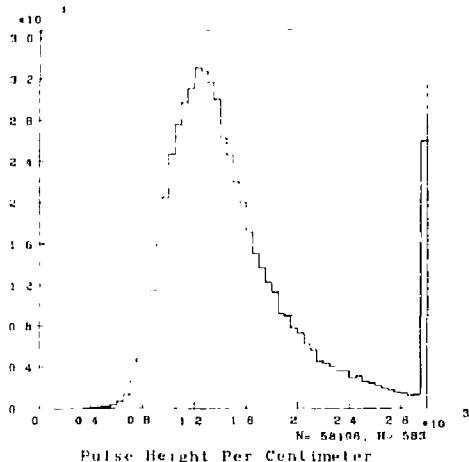


Fig. 5. A distribution of the pulse height (in arbitrary units) per unit length of all cosmic ray muons that were used. The right most bin contains all of the tracks that overflowed the histogram.

The Ionization Measurement Resolution

To measure the resolution for energy loss we compare the two measurements of ionization for a track in the two sectors. Figure 6a shows for one 8.6 atmosphere run a scatter plot of this fractional difference on the x-axis and the tangent of the angle that the track makes with the vertical plane on the y-axis. Figure 6b has the projection onto the x-axis. The σ of the Gaussian that fits this distribution, divided by $\sqrt{2}$ is $3.0 \pm 0.2\%$, which is our resolution. We have done this measurement on many runs and Fig. 6b is typical in that the distribution fits a Gaussian rather well, with very few events out in the tail. Therefore, in contrast to the spatial resolution, which has a non-Gaussian tail, the ionization resolution is fairly straight-forward to measure and interpret.

The fact that we can get this good Gaussian fit in Fig. 6b and that the scatter plot in Fig. 6a has no slope to it shows that we are able to correct well for electron capture. In fact, for the run used for Fig. 6 the electron capture rate was 0.60 per meter, and a track at the center of the TPC has a pulse height of 55%

of the pulse height of a track with the same velocity at the end of the TPC. Although we can operate with such high electron capture, we intend to fix the problem and return to the conditions of our August cosmic ray tests when the capture was consistently less than 10%.

We have measured the dE/dx resolution for many runs in our November cosmic ray tests. The dE/dx resolutions measured at the same pressure and magnetic field agree with one another. The results that we obtained at three different pressures, averaged over all runs at 4 kG magnetic field, were:

Pressure (Atm)	dE/dx resolution (%)
8.64	(2.80 ± 0.06)
4.02	(3.56 ± 0.09)
1.90	(4.65 ± 0.14)

These errors are statistical only. We estimate that there are systematic errors of about 0.2% also.

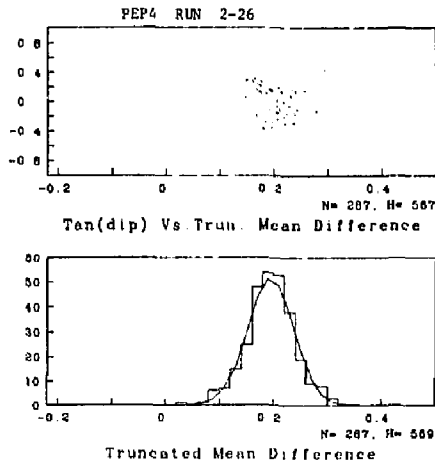


Fig. 6. a) A scatter plot for one 8.6 atmosphere run of the tangent of the angle that the cosmic ray track makes with a vertical plane against the fractional difference in the 65% truncated means measured for the track measured in two sectors, and b) a projection of this truncated mean difference. The width of the Gaussian fit corresponds to a dE/dx resolution of 3.0%.

Comparison with Expectations

The 2.8% resolution that we found at 8.6 atmospheres is better than the 3% that we set for our goal at 10 atmospheres. How much better could we do? We know that we can increase the number of wires that we use and that we can reduce the wire gain fluctuations. With these improvements we should be able to reduce the 2.8% to 2.6%. The Monte Carlo simulations that we made before we built the TPC indicated that 2.5% was the best that we could do. If we use the dE/dx distribution that we observe (one like the one in Fig. 5, but with minimum ionizing tracks only) as the input to a Monte Carlo, we estimate that 2.4% is the best that we can do at 8.6 atmospheres. Therefore, the 2.8% resolution that we see at 8.6 atmospheres seems to be

within 20% of the best that we can expect to do.

Relativistic Rise Measurements

We have measured the relativistic rise in the energy loss distribution for our cosmic ray muons. Such a measurement is shown in Fig. 7. Plotted also on this figure, with arbitrary normalization, is a calculation of the most probable value³ of the ionization. The disagreement between the measurement and the calculation at high momentum is due to a presently poor momentum resolution and a rapidly falling momentum distribution. At present, our momentum resolution is about 50% at 6 GeV.

We characterize the relativistic rise by the ratio of the $k\pi$ separation at 3.5 GeV to minimum ionizing, which we measure with our muons as

$$k\pi \text{ separation} = \frac{dE/dx (2.65 \text{ GeV}) - dE/dx (0.75 \text{ GeV})}{(dE/dx)_{\min}}$$

Our measurements of these values are:

Pressure	$k\pi$ separation at 3.5 GeV
1.50	0.176 ± 0.009
4.02	0.151 ± 0.005
8.64	0.121 ± 0.005

These values of $k\pi$ separation agree with the calculations that we made, as seen in Fig. 8, though they are somewhat smaller than those predicted by others.⁴

When we combine our measured resolutions with the calculated $k\pi$ separation, we can calculate the number of standard deviations of $k\pi$ separation that we can expect. These are

Pressure	Expected Standard Deviations of $k\pi$ Separation
1.50	3.41 ± 0.16
4.02	3.76 ± 0.13
8.64	3.92 ± 0.15

Thus our findings are that there is little pressure dependence for the $k\pi$ separation in the TPC. The separation at 8.6 atmospheres is only $15 \pm 6\%$ better than at 1.5 atmospheres.

Actual Resolution

The resolutions that we have quoted so far involve comparing a track with itself. A more severe test of the resolution is to compare many different tracks at the same momentum. The resolutions that we get by this method are worse than the previously quoted resolutions by about 35% at all three pressures. This is true even for minimum ionizing particles for which the momentum resolution does not seriously degrade out dE/dx resolution. We have not yet understood this.

Particle Identification in Multi-Track Events

The TPC has just moved into the beam at PEP and we have, as yet no experience with its ability to do particle identification in multi-track events. Our simulations indicate that for Q-Qbar events at 15+15 GeV we can get reliable dE/dx measurements for tracks that are at least 3 cm away from other tracks in z . The effect of this is to get good ionization measurements for about 90% of the tracks and get poor accuracy on the rest.

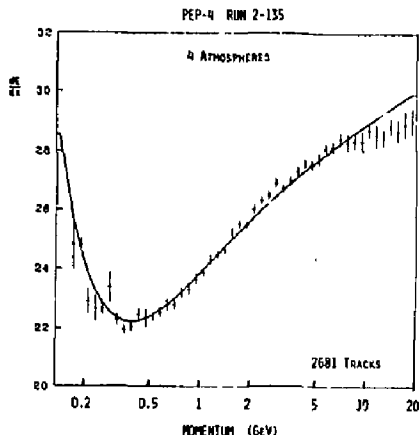


Fig. 7. TPC measurements of the ionization of cosmic ray muons at 4 atmospheres. The data points are averages of 65% truncated means. The dashed curve is a calculation (arbitrarily normalized) of the most probable energy loss.

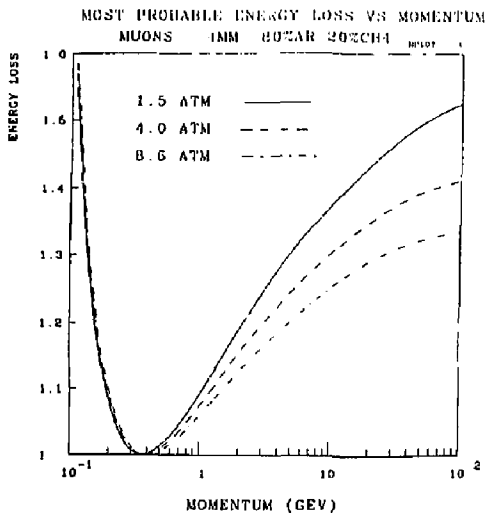


Fig. 8. A calculation of the most probable value for the energy loss in the TPC for three different pressures.

References

1. D. Fancher, et al., Nucl. Inst. and Meth. 161, 383 (1979); "Proposal for a PEP facility based on the time projection chamber (TPC);" Johns Hopkins University, Lawrence Berkeley Laboratory, University of California at Los Angeles, University of California at Riverside, Yale University, PEP Experiment No. 4, PUP-5012 (1976); D. R. Nygren, PEP-198 (1975).
2. L. Galtieri, N. Hadley, and G. Lynch, "Preliminary Results of the November TPC Tests," TPC-LBL-82-01, Lawrence Berkeley Laboratory report.
3. G. Lynch, "Measurement of Energy Loss in the TPC," Lawrence Berkeley Laboratory report, TPC-LBL-81-06.
4. A. H. Walenta, "Performance and Development of dE/dx Counters," Physica Scripta, 23, 354 (1981).

PARTICLE IDENTIFICATION BY dE/dx SAMPLING IN NEON

I. Lehraus, R. Matthewson and W. Tejessy
CERN, Geneva, Switzerland

Summary

Systematic studies of identification efficiency for e/p were performed in a variety of noble gas mixtures and in pure hydrocarbons at pressures up to 5 atm using a 15 GeV/c tagged beam. Neon mixtures were found to give the best results (6.7 σ m/p separation at 1 atm). Replacing the conventionally used argon by neon would permit a reduction of detector depth by almost a factor of two. The measurements were carried out in a detector with 64 pairs of 2×2 cm² proportional counters and a 50 cm drift space.

Performance of the neon mixture was verified in a longitudinal drift chamber consisting of 16 stages of 4.7 cm drift each using Flash ADC with 25 ns sampling intervals. The results are similar to those obtained by charge integration over large samples in a detector of the same total length.

Introduction

Efficient particle identification by ionization sampling in the relativistic rise region requires resolution in the 8-9% FWHM range. This is difficult to achieve in a compact colliding beam detector, in which a typical track length will be of the order of 1.5 m. Increasing the operating pressure improves the resolution, but this effect is practically cancelled by a reduction of the relativistic rise slope at high pressures. Therefore, an extensive study of a wide variety of gas mixtures is clearly required to determine the best performance.

Furthermore, optimization of the design parameters of a colliding beam detector demands precision which can only be realized in a full-size detector segment. Indeed, a combination of several secondary effects, which were not even noticed in the first generation of colliding beam devices designed for operation below the minimum of ionization (typical resolution about 15% FWHM), may now appear at a high order level.

The present experiment was dedicated to a detailed study of limits of resolution and linearity of response in various gas mixtures at pressures from 0.5 to 5 atm with up to 50 cm of drift. In addition, a multistage longitudinal drift chamber with fine sampling was used and its performance compared to results obtained by classical charge integration over large samples.

Measurements with 64 samples of 4 cm

The experimental set-up has been described in detail in ref. 1. The detector illustrated in fig. 1 consists of 64 pairs of 2×2 cm² proportional cells, separated by a double grid from a 50 cm drift space. The cell structure is given in fig. 2. The HV, signal and field wire spacing is 1 cm and the distance between the two separation grids is 0.5 cm. For the signal wires 25 μ diameter stainless steel was chosen. The

gas amplification factor was kept in the 10¹ range to assure linear amplitude response. The grid transparency was optimized as shown in the example on fig. 2 by using the beam aligned on the boundary and adjusting the grid potentials. Transparency was always above 0.94. The charges collected by the individual cell pairs were integrated, amplified and processed by a set of 64 ADC's with 8-bit resolution. The measurements were performed at 15 GeV/c in a tagged beam of protons, pions and positrons. The beam spot size was 4 cm FWHM and the momentum bite $\pm 0.25\%$. A general description of the measurement procedure and an elaboration of the results for all studied gases is given in ref. 2. Here we put the emphasis on neon mixtures and those aspects of their ionization behaviour that make the use of neon attractive.

The width of the single 4 cm sample dE/dx distribution at 1 atm is plotted in fig. 3, taken from our previous paper², for noble gases and pure hydrocarbons. Surprisingly, the results for neon, argon, krypton and xenon show practically the same resolution. Pure hydrocarbons have narrower distributions which, in contrast to the noble gases, improve with increasing molecular weight.

For Ne + 10% C₂H₆, fig. 4 shows an example of truncated mean (lowest 40%) distributions from 64 samples of 4 cm at 1 atm, corrected for individual cell response.

In fig. 5 the final resolution as a function of pressure for 64 x 4 cm samples is shown. At 1 atm the resolutions for Ne, Kr and Xe are all very close to 9.5% FWHM. Using neon instead of argon means a reduction of the detector depth by a factor of 1.7. Neon could thus replace much more expensive krypton and xenon. The hydrocarbons give much better resolution but, unfortunately, their relativistic rise is very low and so the advantage is lost. This is apparent in fig. 6 where the e/p peak ratio at 15 GeV/c is plotted as a function of pressure. As expected, xenon has the highest relativistic rise, followed by krypton. The difference between neon and argon is only about 10%. All hydrocarbons show considerably lower values of relativistic rise.

By expressing the distance between various particle peaks in units of the standard deviation of the final resolution, we obtain the resolving power D/σ . This is plotted in fig. 7 as a function of pressure. At 1 atm neon, krypton and xenon have practically the same merits for m/p separation at about 6.5 σ whereas argon is at the 5.3 σ level. Only ethylene and propane give results comparable to argon. Note that neon at 0.5 atm, which corresponds to about 1.3 m detector depth equivalent, gives (in our particular case) the same result as argon at 2 atm. The e/m separation is at 2.5 σ for neon compared to 3.0 σ for argon. Pure hydrocarbons are grouped at the 1.5 σ level.

Signal attenuation by electron attachment in different gases was measured over 41 cm of drift distance and is shown in fig. 8. Clearly, all noble gases and methane could be used at moderate pressures without problems. Ethylene and ethane are acceptable at atmospheric pressure and propane may still be useful in very small samples.

Drift velocity in neon mixtures

Drift velocity measurements were made in a small test chamber. As shown in fig. 9, saturated drift velocities in the 3-4 cm/us range can be reached in several neon mixtures already at low E/p values. Low percentages of either propane or isobutane seem to be the most satisfactory. The neon/argon mixtures have the advantage that their density is practically equal to air, which is important in some applications.

Longitudinal drift and fine sampling

This method was originally proposed at BNL³. A multistage longitudinal drift chamber was constructed and tested using the same neon mixtures, so that a direct comparison could be made between charge integration over large samples and fine sampling with many small intervals.

The geometry of the detector is presented schematically in fig. 10 where two stages from the total of 16 are shown. In all stages the ionization deposited in the drift space (the 4.7 cm between the 2, μ thick aluminium-foil HV electrode and the grid) was drifted along the particle trajectory into proportional cells of 0.8 x 0.8 cm² section. The 15 cm long HV and field wires are 50 μ in diameter, the signal wires are of 10 μ diameter silver plated tungsten. Another foil electrode separates the adjacent stages. Uniform drift field is maintained by a cage structure formed by tubular brass electrodes. The total detector length is 88 cm without the gas tight box. The beam direction was perpendicular to the wires. The triggering scintillation counters were 0.6 cm wide, aligned on the central cells and 3 cm long, covering the middle part of the wires. A veto scintillation counter guarding the full detection area was used to remove background and multiple hits.

A modified circuit of the original fast amplifier developed at BNL (described in ref. 4) was connected as close as possible to the signal wire of each cell. When excited by an input delta function, the shaped output pulse had a rise time of 18 ns, fall time of 26 ns and a FWHM of 32 ns. Single-electron cell response produced a positive 7 mV output signal when the chamber was operated at a gas amplification of 10⁴ and the noise was 1300 electrons referred to the amplifier input.

The output signals were transmitted via coaxial cables to a 16 channel 6-bit FADC system which was operated continuously with a sample interval of 25 ns. Data were stored in fast 256-bit RAM buffers upon receipt of the event logic decision. Between consecutive particles, these data were transferred to an intermediate buffer until the end of the beam spill, and then read into the on-line computer between ejections.

The 15 GeV/c beam particle flux was kept low to avoid space charge from positive ions and to limit the data transfer load (up to 4000 bytes of information per particle). A dead-time defining veto was provided to prevent pile-up problems.

A typical example of one particle registered in a single stage, using a waveform recorder, is shown in fig. 11. The sampling interval was 10 ns and the drift

velocity in Ne + 5% C₂H₆ was 2.2 cm/us. The spike at the beginning corresponds to the addition of ionization from both sides of the signal wire of the track segment crossing the proportional cell.

Summing up corresponding samples from all 16 stages and for many particles creates the familiar shape shown in fig. 12. The sampling interval was 25 ns and the drift velocity in the Ne + 10% C₂H₆ mixture was about 3.6 cm/us so that the distance between samples was close to 0.95 mm.

The arrows on fig. 12 indicate the 35 chosen samples on the plateau used for the further data analysis. Single sample distributions for 15 GeV/c protons and positrons are plotted in fig. 13 within the 6-bit FADCs' dynamic range.

The final distributions of mean of 40% smallest values from 560 samples (16 stages of 35) for tagged protons, pions and positrons are plotted in fig. 14. The differences between individual stage responses and the 2-3% droop from sample 16 to 50 were not here corrected. The first effect has only a limited influence on the final distribution - the ionization fluctuations being predominant. The droop is difficult to correct for every individual track due to a dependence on the ionization values registered in the preceding samples.

The results obtained in Ne + 10% C₂H₆ at 1 atm for 560 samples of 0.95 mm interval are summarized as follows:

Resolving power D/ σ	Mean of smallest				
	10%	20%	40%	70%	100%
e/p	3.82	4.60	4.61	4.52	3.42
e/ π	1.01	1.18	1.29	1.18	1.18
π /p	2.81	3.42	3.33	3.34	2.24

Conclusions

A new gas mixture containing neon and a low percentage of hydrocarbons (C₂H₆, C₃H₈ or iC₄H₁₀) is proposed for dE/dx sampling applications in the relativistic rise region. Particle identification efficiency in neon was found to be equal to results obtained in xenon and krypton. Note that atmospheric krypton is contaminated by the β -emitting ⁸¹Kr isotope which prevents its use in big volume detectors. Use of neon instead of argon opens the possibility to reach 6 σ separation for π /p up to about 20 GeV/c in a detector depth below 1.5 m and at atmospheric pressure. At the same time, the radiation length in neon is about 3 times longer than in argon.

Comparing results obtained in identical conditions using charge integration in 84 x 4 cm samples and longitudinal drift with fast sampling in 560 x 0.95 mm intervals, we found similar e/ π /p ionization ratios in both cases. On the other hand, the resolving power D/ σ was reduced by a factor of two in the longitudinal drift approach. This is in fair agreement with a square root of the total length ratio for the two detectors. It should be remembered that, from the total length of 88 cm for the longitudinal drift chamber, only 60% (i.e. 16 stages x 35 x 0.95 mm) were exploitable for ionization sampling. Some improvement

of the performance of this method is certainly possible, but there seems to be very little difference in the depth required for either of these detectors. For the longitudinal drift resolution no gain is to be expected by increasing the pressure, since for a given maximum sampling rate the amount of ionization deposit between samples is increased in proportion. In the case of inclined and curved tracks the implications of varying interval length during the fine sampling are hard to assess, especially when the average distance between the ionization clusters is of the same order as the diffusion in the gas and the sample interval itself. Furthermore, for the data acquisition and later data analysis it should not be overlooked, that in the longitudinal drift method the amount of data to be processed will vastly increase in comparison to charge integration over large samples.

Acknowledgments

The pressure vessel for the first detector was designed and constructed by G. Linsler and G. Schmidlin. We acknowledge the contribution of J.D. Gapt in the

design and assembly of both detectors and are obliged to Dr. P. Rehak (BNL) for participation in the design of the fast amplifiers for the longitudinal drift detector. We are indebted to E. Chiaveri for tuning and operation of the S3 beam and to the members of the Beam and Detectors Group of the EP Division for their participation in the construction work and during the tests. Continuous support and encouragements from Drs P. Lazeyras and A. Hanten were greatly appreciated.

References

1. I. Lehrsus et al., CERN/EP 81-4 (1981) (to be published in Nucl. Instr. & Meth. in Phys. Res.).
2. I. Lehrsus et al., CERN/EP 82-1 (1982) (to be published in Nucl. Instr. & Meth. in Phys. Res.).
3. T. Ludlam et al., IEEE Trans. Nucl. Sci. NS-28 (1981), No. 1, 439.
4. R.A. Boie et al., IEEE Trans. Nucl. Sci. NS-28 (1981), No. 1, 603.

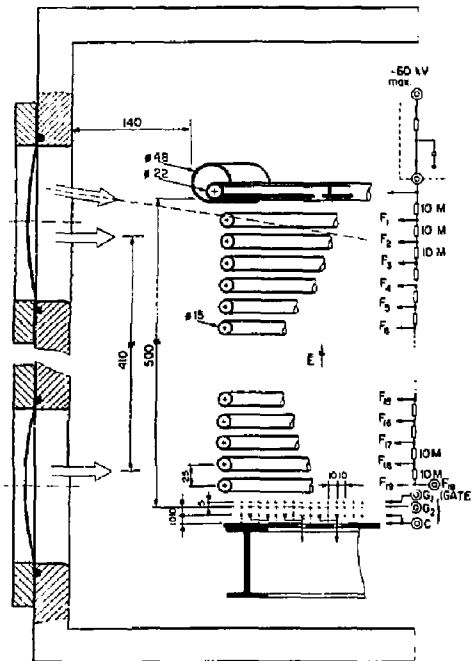


Fig. 1 - Electrode structure of detector used in studies of resolution in various gases and at various pressures. 64×4 cm samples, 50 cm drift space.

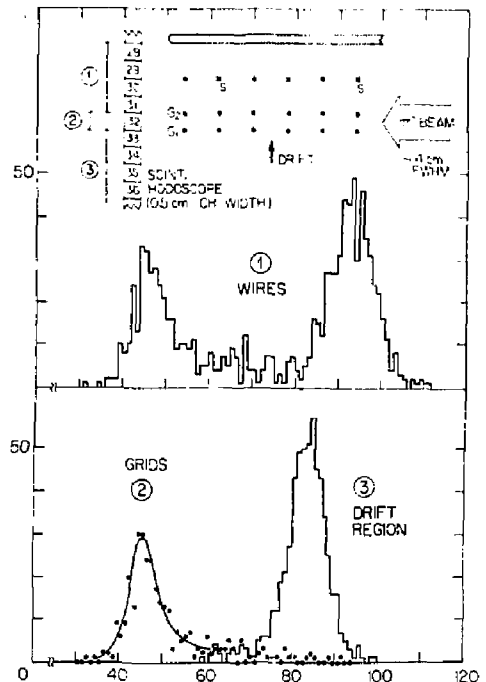


Fig. 2 - Details of the 2×2 cm² proportional cell geometry including the separation grids. Example of optimization of grid transparency by adjusting the grid potentials so as to merge the peaks of the truncated mean distributions measured inside the cells (1) and in the drift space (3). Beam aligned on the boundary; the secondary peak (2) comes from the region between the grids.

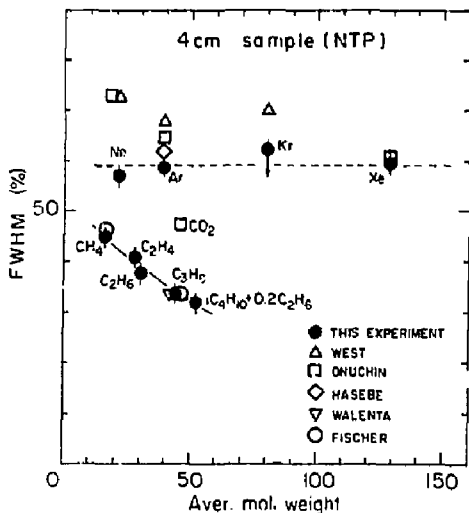


Fig. 3 - Width of the single 4 cm sample distribution for 15 GeV/c pions at 1 atm as a function of average molecular weight of the gas.

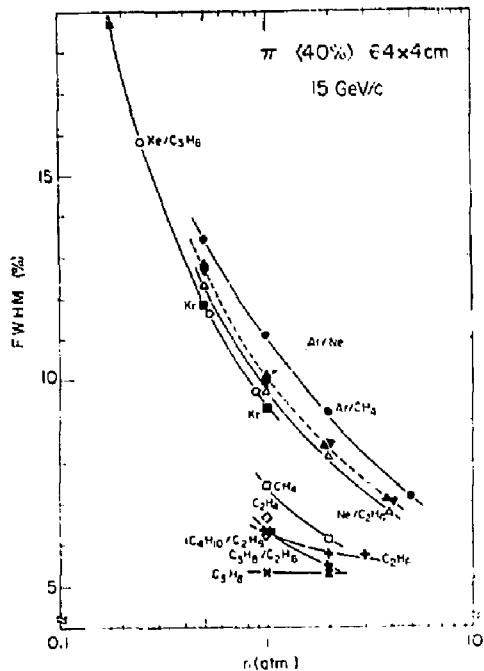


Fig. 5 - Final resolution of mean of smallest 40% of 64 samples of 4 cm for pions at 15 GeV/c as a function of pressure.

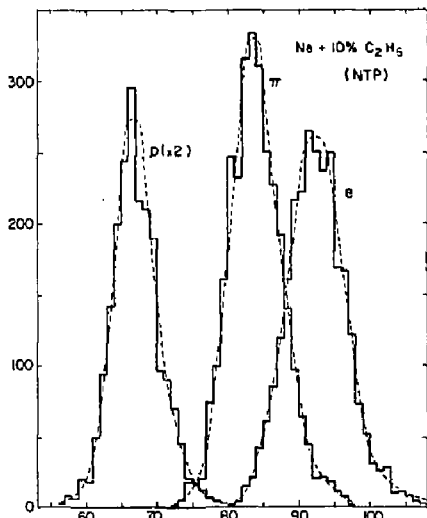


Fig. 4 - Distribution of mean of 40% smallest values of 64 x 4 cm samples in Ne + 10% C₂H₆ at 1 atm, 15 GeV/c tagged protons, pions and positrons.

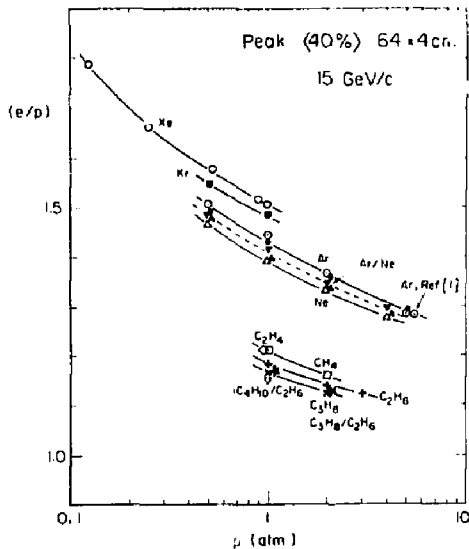


Fig. 6 - Relativistic rise at 15 GeV/c for e/p truncated mean distributions of 64 x 4 cm samples as a function of pressure.

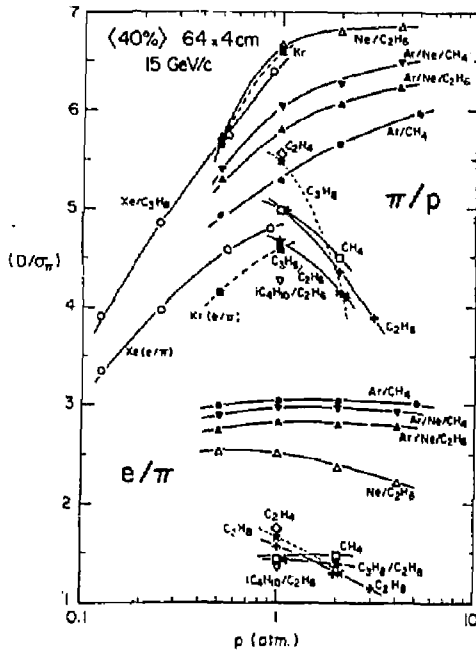


Fig. 7 - Resolving power D/σ for π/p and e/π for various gases as a function of pressure.

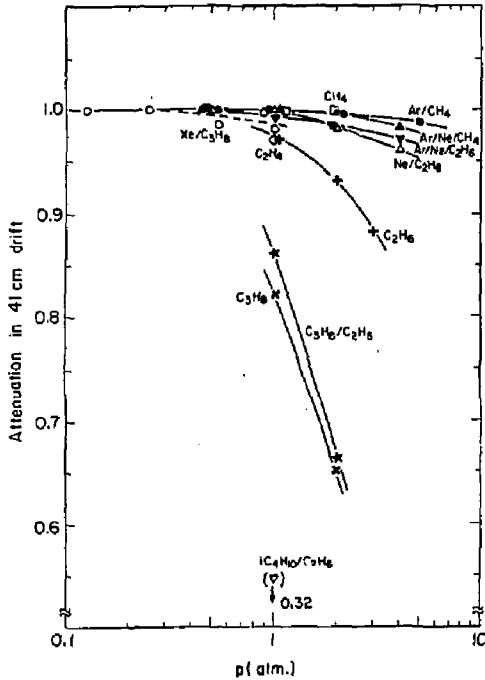


Fig. 8 - Pressure dependence of attenuation over 41 cm in the drift region.

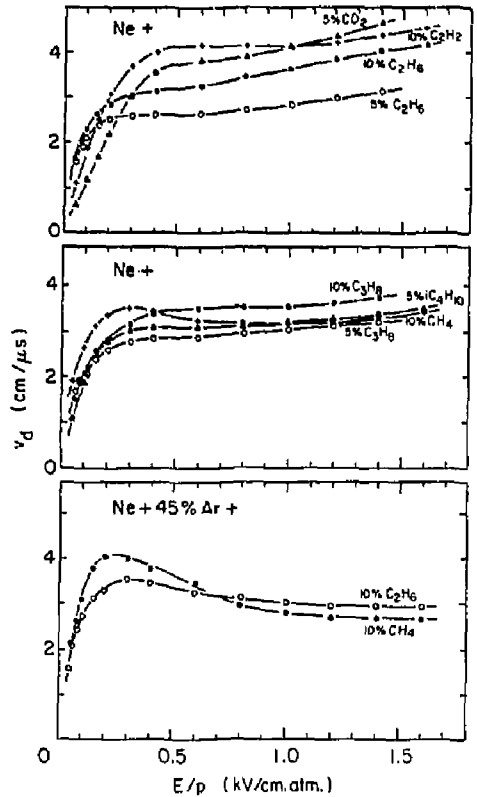


Fig. 9 - Drift velocity for neon and neon/argon with various quenchers.

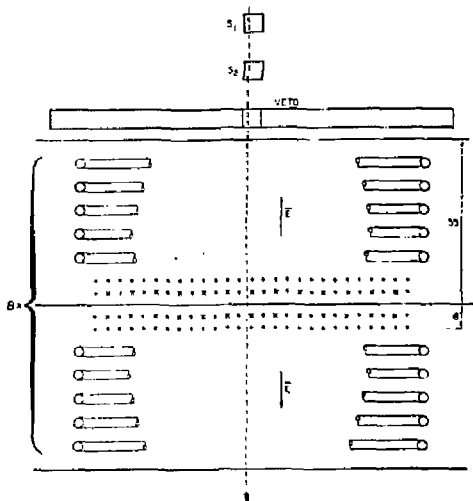


Fig. 10 - Simplified diagram of 2 stages out of the 16 stage longitudinal drift chamber. The alignment of the triggering scintillators on the central cells is schematically shown; the true position of the chamber is between S_1 and S_2 .

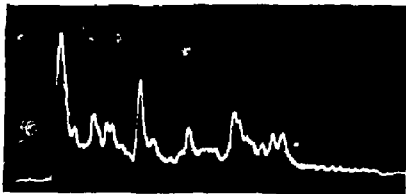


Fig. 11 - Example of a single event in one stage (4.7 cm of drift). Ne + 5% C_2H_4 , $v_d = 2.2$ cm/ μ s, 10 ns sampling interval.

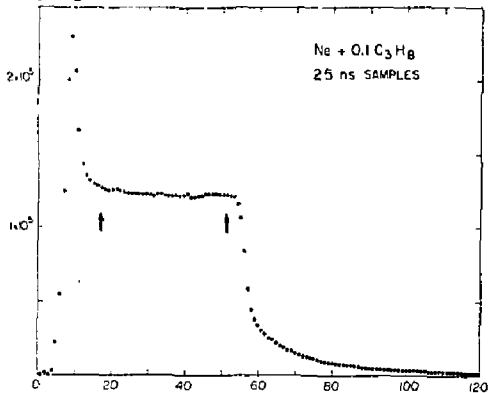


Fig. 12 - Accumulated ionization values for many particles (combined corresponding samples from all 16 stages). Ne + 10% C_2H_4 , sampling interval 25 ns. Arrows indicate range of samples used for the data analysis.

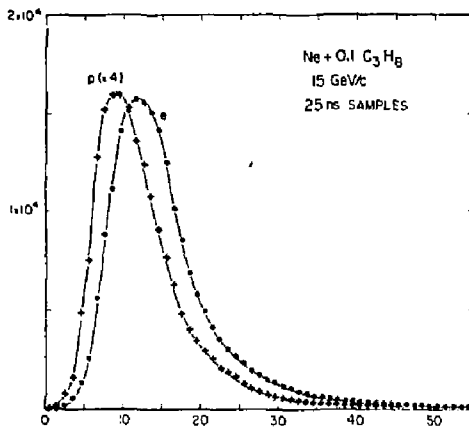


Fig. 13 - Single 25 ns sample distributions using the 35 samples marked in fig. 12 in each of the 16 stages for 15 GeV/c protons and positrons in Ne + 10% C_2H_4 .

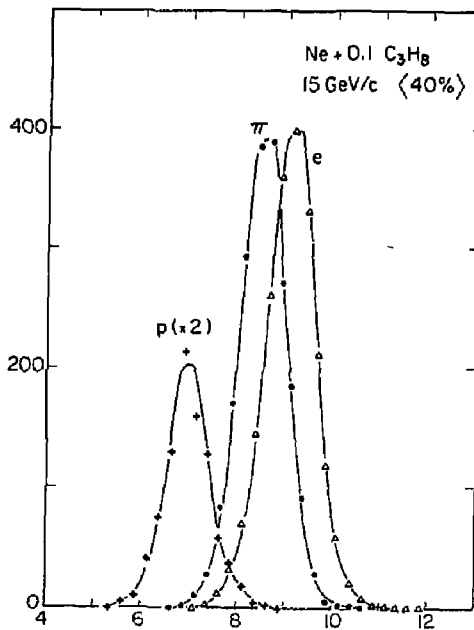


Fig. 14 - Final distribution of mean of 40% smallest values for 15 GeV/c tagged protons, pions and positrons. 560 samples of 25 ns, Ne + 10% C_2H_4 .

PARTICLE IDENTIFICATION WITH A FINE SAMPLING

IONIZATION LOSS DETECTOR*

T. Ludlam, E.D. Platner, V.A. Polychronakos
Brookhaven National Laboratory
Upton, New York 11973

S.J. Lindenbaum
BNL and City College of CUNY
New York, NY 10031

E. Rosso, P. Quercu
CERN
Geneva 23, Switzerland

N.A. Kramer, Y. Teramoto
City College of CUNY
New York, NY 10031

T. Akesson, G. Jarlskog, L. Rounnbarn
University of Lund
Lund, Sweden

Introduction

In a recent series of tests¹ it has been shown that the sensitivity for charged particle identification via the relativistic rise in ionization loss can be enhanced by using longitudinal drift and fast electronics to effect very small sampling intervals. With the chamber geometry illustrated in Fig. 1a (i.e., operation in the "time expansion" mode) electrons from individual ionizing collisions drift sequentially onto the anode wire with a time structure determined by the drift velocity in the gas. After fast pulse shaping the resultant waveform is digitized with a flash-encoding ADC at a frequency of 100MHz. For the tests described in Ref. 1 the smallest sampling interval was 1/4 nsec, and the sensitivity of mass (velocity) discrimination was studied for 1 meter of track length with sampling intervals ranging from 1/4 mm/sample to 16 mm/sample, the upper end of this range being typical of conventional ionization sampling devices.

The results of these initial tests are summarized in Fig. 2 as a function of the sample size. The result achieved with 1 meter of conventional sampling (ISIS-1, Ref. 2) is shown for comparison. For large sample sizes the results are comparable to those of traditional techniques, and a significant improvement is achieved when the sampling frequency is increased by roughly an order of magnitude. These results were gotten with a small test chamber in which meter-long tracks were simulated by piecing together many traversals of a single drift gap. We report here on the status of further studies to see whether this improvement in sensitivity can be duplicated with a chamber of practical dimensions and many readout channels.

Test Configuration

For the present tests we use a multiplane chamber incorporating the geometry illustrated in Fig. 1b. Here the sense planes (anode plus field wires) are located symmetrically between planes of cathode wires with electrons drifting from either side. Each sense plane is instrumented with 10 active anode wires. The wire length is 20 cm and the anode wire diameter is 20 μ m. The chamber has 10 such planes (100 active wires) for a total depth along the beam of 40 cm. The test detector, which was constructed by the CERN EF Division, is shown in Fig. 4.

All tests have been carried out with a gas mixture of 80% argon/20% CO₂. The potentials on the cathode and field wires are adjusted to give a drift electric field of ~ 300 V/cm and an avalanche gain (for full

*Work supported by the U.S. Dept. of Energy.

charge collection) of $\sim 10^4$. The drift field was chosen to give an electron drift velocity of 1 cm/ μ sec, $\sim 1/5$ the saturated velocity in this gas mixture. The volume of uniform field (adequate for longitudinal drift measurements of dE/dx) extends to within ± 1 mm of the sense plane and ± 1 mm of the cathode planes. Hence, in principle, 80% of the track length through a chamber of this geometry is usable for ionization loss measurements.

The readout electronics chain is illustrated in Fig. 4. A low-noise, common-base preamplifier is attached directly to the end of each anode wire, followed by a shaping and filter amplifier which consists of a semi-Gaussian integrator with a pole-zero tail cancellation.³ The pulse width (FWHM) of the response to a single cluster of electrons (x-ray source) was set to be 20 nsec. For these tests the outputs of all preamplifiers in a given plane were summed as input to a single shaping amplifier. The shaped signal was digitized with a 6-bit (64 level) flash encoder operating at 100MHz. The digital output from each channel was buffered in a 6 x 256 bit shift register operating at the same clock speed,⁴ allowing the storage of ~ 2.5 μ sec of drift information in each channel. For the chamber configuration of Fig. 1a, and the chosen drift velocity, the total drift time is 1.8 μ sec and each 10 μ sec digitizing interval corresponds to .27 cm of track length.

The results reported here were obtained in a 3.5 GeV/c positive beam at the CERN Proton Synchrotron. Protons, pions and electrons were tagged with a pair of threshold Cerenkov counters and a lead glass shower counter. The beam was normally incident on the sense wire planes as indicated in Fig. 1.

Test Results

Figure 5 shows the ADC response for a single track crossing a drift cell. The first signal arrival at the anode wire occurs in bin 19, prior to which one sees a DC off-set level of ~ 13 counts which was provided in order to study the baseline behavior as the signal develops. Typical structure is observed, corresponding to the sequential arrival of clusters of drifting electrons. Individual clusters (i.e. the results of single ionizing collisions) are not resolved, but are blurred by the effects of electron diffusion, finite pulse shaping width, and the fact that the observed signal in a given time interval is a superposition of ionization loss from either side of the sense plane. At the beginning of the pulse train the signal is characteristically large, corresponding to the portion of track

(≈ 23 mm) which lies in the high-field region near the sense wire plane. There the drift velocity is essentially saturated, and the collected charge per unit time is greater than that from the uniform drift region by a factor of about 5. For the illustrated track this initial pulse exceeds the dynamic range of the ADC.

Our procedure for evaluating the effectiveness of very fine sampling intervals for particle discrimination is to divide each track into sampling intervals of 2, 4, 16 or 64 of the rudimentary time bins. The charge is integrated in each interval, after subtracting the baseline, and the resultant samples used to evaluate a parametric estimator (e.g. the truncated mean) of the ionization loss for the track. By spreading the ionization charge over many measurements, each involving a small signal, the longitudinal drift technique is extremely sensitive to the stability of the baseline, and changes in the zero level during the charge collection time must be corrected for. Ideally, the signal processing electronics should obviate the need for such corrections. The tail-cancelling networks, for instance, are designed to remove one source of baseline shift. For the circuitry which we used in these tests another source, with similar effect, comes into play for collection times which are long compared to the single-electron shaping time: the cumulative effect of AC coupling in the system gave a time constant of ≈ 10 nsec, which is appreciable compared to the total drift time of ≈ 2 μ sec. Hence the level of the baseline falls off during the course of the pulse train at a rate which is proportional to the signal charge. To the extent that the ADC data include a complete time history of the signal on the wire, this effect can be corrected for, on a track-by-track basis as illustrated in Fig. 5. Figure 6 shows the signal, for incident protons, averaged over many track segments. The shaded area indicates the contribution accounted for by the baseline correction, which is substantial. We stress that this off-line correction, which is necessary for the analysis of the present data, should not be necessary in principle and indeed is not consistent with the requirements of a practical detector. We are presently designing circuits which will incorporate dynamic baseline restoration in an effectively DC coupled amplifier chain.

In Fig. 7 we show pulse height distributions obtained from the data for electron and proton tracks, for both "large" and "small" sampling intervals. The 17 mm samples (Fig. 7a) were obtained by summing the digitized information over groups of 64 successive 10 nsec time bins. The 1/2 mm samples are similarly obtained, by summing in groups of 2. (Two successive digitizations span a time interval equal to the 20 nsec width of the shaping circuit's response to an impulse of charge.) The horizontal scales are in ADC counts, with 2 ADC counts corresponding roughly to the signal charge induced by a single drifting electron. The distributions in Fig. 7a are consistent with results obtained from conventional measurements of ionization loss in similar thicknesses of gas, except that the delta ray tail at large pulse heights is somewhat suppressed in our data by the limited dynamic range of the flash encoders. The small samples (Fig. 7b) exhibit a more pronounced dependence of the shape of the energy loss distribution on particle velocity: both the protons (minimum ionizing) and the electrons (on the Fermi plateau) have some contribution at zero pulse height, the electrons having a substantially broader spectrum. The relativistic rise, as measured, e.g. by the ratio of most probable energy loss for electrons and protons, is larger for the smaller sample size.

To compare the sensitivity for particle identification with previous results, we calculate the truncated mean pulse height for 1-meter track lengths. At the time of this test only 6 of the 10 planes in our chamber were fully instrumented with readout electronics, corresponding to ≈ 20 cm of usable track length for

each incident particle. The useful track length was further restricted, by about a factor of two, by the requirement that the initial pulse from charge near the anode wire not exceed the range of the ADC. This was necessary for the baseline reconstruction discussed above. Hence, although one of the aims of this test was to investigate the performance of a device incorporating many of the characteristics of a full-scale detector, it was still necessary to assemble 1-meter track lengths from data accumulated over several successive particle traversals.

Having assembled an ensemble of 1-meter track lengths, each track was subdivided into various sampling intervals ranging from small (≈ 2000 samples/meter) to large (≈ 60 samples/meter) and the truncated mean, retaining the 40% smallest pulse heights, was calculated for each case. The results as a function of sample size, are shown in Fig. 8. The resolving power for distinguishing electrons and protons clearly improves as the sampling frequency is increased. The separation ($S_{sep} = 3.6$) obtained with 17 mm sample size is comparable to that achieved with conventional dE/dx measurements over 1 meter of track length, as indicated by the point labeled ISIS-I on Fig. 2. The same set of tracks shows significantly better separation as the fine-sampling information is exploited. With the smallest sample size (1850 samples/meter of track) the figure of merit S_{sep} is improved by a factor of ≈ 2 over the conventional sampling geometry. The origin of this improved sensitivity is made visually clear in Fig. 8 (and is explored in detail in Ref. 1): the relativistic rise is enhanced at small sample sizes, with no degradation in rms width of the truncated mean distributions.

The values of S_{sep} obtained in this test fall systematically below those of our previous measurements, which are summarized in Fig. 2. We may list several reasons contributing to the difference:

1. The present measurements involve a large chamber, with many readout channels. The previous tests employed a single readout channel.
2. Ionization charges drifting from either side of the symmetrically placed anode plane are simultaneously recorded in the present tests. This saves space, but must cost something in resolution.
3. Residual errors remain, for the present data, after the baseline correction discussed above. The previous tests involved much shorter drift times (≈ 400 ns), and no such corrections were required.

The first, and probably also the second, of these points are endemic to a large chamber of practical geometry utilizing this technique. We believe that errors associated with baseline stability can, with modified readout electronics, be reduced to the level at which no off-line correction is required.

Conclusions

In our earlier work¹ and in new results by other groups presented at this conference^{5,6} one has seen the potential for significantly improving the resolving power of relativistic rise measurements by exploiting longitudinal drift and fast digitizing electronics to achieve very fine sampling of the ionization loss. This opens the possibility of compact and uncomplicated structures for particle detectors covering large solid angles in colliding beam experiments. In the work presented here we have investigated the fine sampling technique in a chamber of many readout channels, incorporating electrode structures readily amenable to the construction of a large detector which optimizes the ratio of fiducial track length to total detector length. We conclude that, in terms of the separation parameter defined in Fig. 2, a discrimination power corresponding to $S_{sep}(3.5 \text{ GeV}/c) \approx 7$ is a realistic expectation for a

full scale detector of 1 meter fiducial length. This can be achieved with a detector whose total length is $\lesssim 1.5$ m. A conventional device, with 1-2 cm samples, would require $\gtrsim 3$ m fiducial length to achieve the same sensitivity. (For the latter estimate we use the calculation of Allison & Cobb,² which has accurately predicted the performance of several large devices.)

We list here some of the issues which need further investigation before a full scale device can be feasibly undertaken:

- Stable control of the zero-signal level in the amplifier chain, as discussed above.
- Study of the response as a function of incident track angle; e.g. the sensitivity to local gain variations due to space charge effects.
- A systematic study of the momentum (velocity) dependence of the resolution.

In the meantime, a conceptual design for implementing such a detector in the environment of a high energy colliding beam experiment is given in Ref. 7.

Acknowledgments

We thank the staff of the CERN PS for assistance and technical support during the test beam runs, and we wish to acknowledge the excellent work of the technical staff of the CERN EF division in the design and construction of the test detector. We are indebted to R. Boic and V. Radeka of the BNL Instrumentation Division for assistance with the signal processing electronics. We thank Dr. A. Dwurazny for assisting with the data taking phase of this work.

This research supported in part by the U.S. Department of Energy under contracts DE-AC02-76CH00016 and DE-AC02-79ER10550.

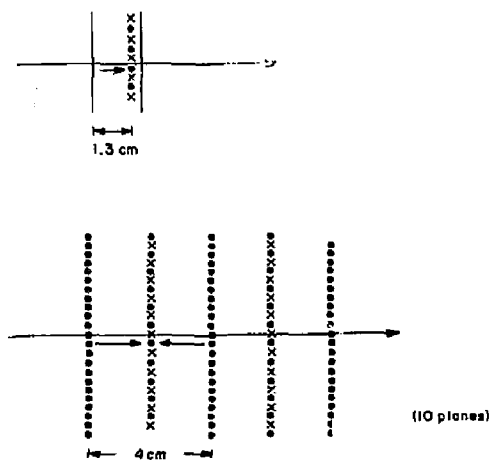


Fig. 1 (a) Electrode geometry for the test chamber of Ref. 1. The long arrow represents a particle trajectory; the short arrow gives the direction of electron drift. The cathode planes are metal foils separated by 1.6 cm; (b) The geometry used for the tests reported here. The cathodes are wire planes. The full chamber consists of 10 active planes, of which 2 are shown here.

References

1. T. Ludlam *et al.*, IEEE Trans. Nucl. Sci., **NS-28**, 439 (1981).
2. W.W.M. Allison and J.H. Cobb, Ann. Rev. Nucl. Part. Sci., **30**, 253 (1980).
3. R. Boic *et al.*, IEEE Trans. Nucl. Sci., **NS-28**, 603 (1981).
4. E. Platner, these proceedings.
5. F. Naito *et al.*, Univ. of Tokyo preprint INS-J-163 (1982) (Presented by T. Goshima at this Conf.)
6. R. Arai *et al.*, National Laboratory for High Energy Physics, Tsukuba preprint (1982) (Presented by Y. Wataoe at this Conf.)
7. T. Ludlam and E. Platner, Proc. 1981 ISABELLE Summer Workshop, BNL 51443, p. 1330 (1981).

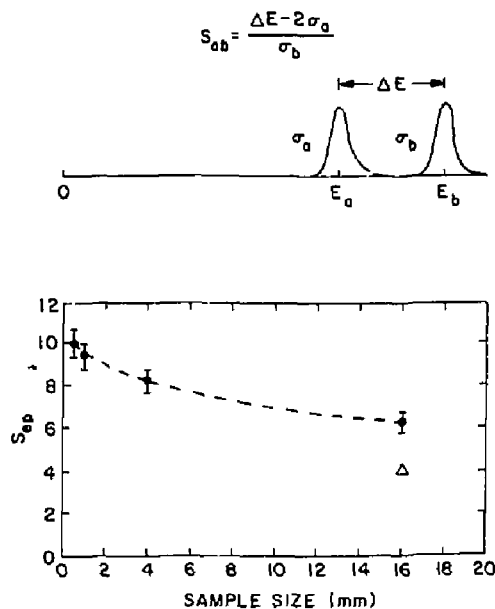


Fig. 2. The separation parameter S_{ab} is defined in the upper drawing, in terms of the difference ΔE between the centroids of the truncated mean distributions for particle types a and b, and the rms widths of the distributions. The lower plot summarizes the results from Ref. 1 for electrons and protons at 3.5 GeV/c, with 1 meter track lengths, as a function of the sample size. The open triangle gives the result from the ISIS-1 detector (Ref. 2).

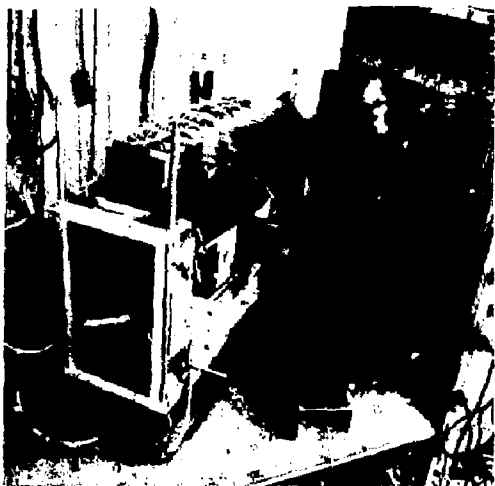


Fig. 3. The chamber just prior to insertion in the test beam. Direction of incidence is from the lower left. The wires are vertical, and the preamplifiers, seen at the top of the chamber, are attached directly to the ends of the anodes (there are 10 preamplifiers on each of 10 sense wire planes).

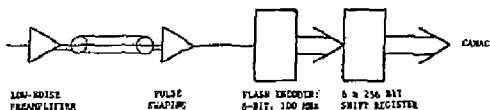


Fig. 4. The readout electronics chain.

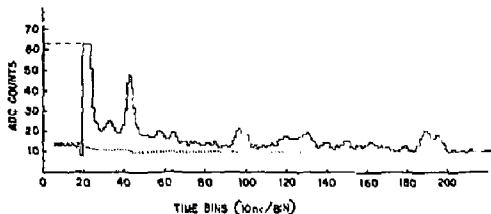


Fig. 5. The ADC response from a typical track through one cell (4 cm) of the chamber. Full range of the ADC is 64 counts on the vertical scale. The dotted curve under the signal gives the computed baseline for this event (see text).

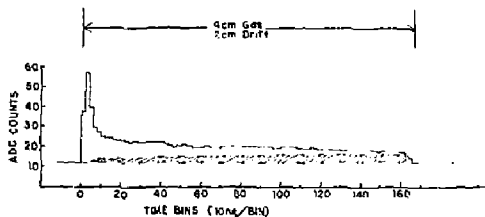


Fig. 6. The ADC response averaged over many (proton) tracks, after baseline correction. The shaded area falls below the baseline in the uncorrected data.

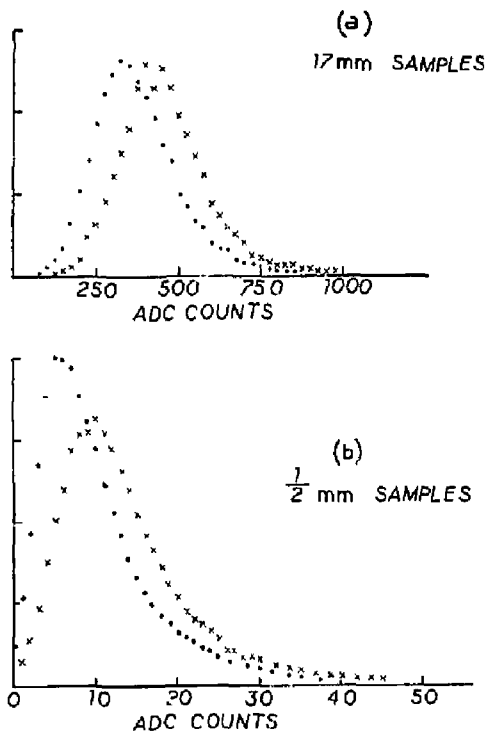


Fig. 7. Pulse height spectra for protons (dots) and electrons (x's). (a) 17 mm samples (64 time bins per sample); (b) 1/2 mm samples (2 time bins per sample). Electrons and protons are normalized to the same area in each plot.

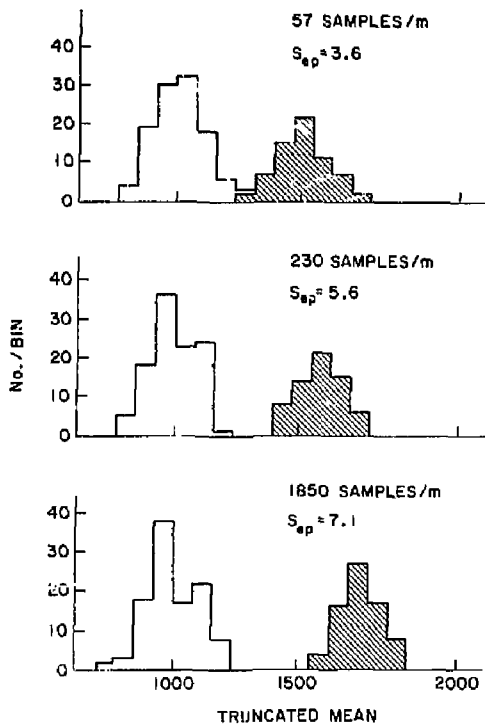


Fig. 8. The truncated means for 110 proton tracks (open histogram) and 72 electron tracks (shaded). Each track is 1 meter long. The results are shown for 3 different sample sizes.

DE/DX MEASUREMENT WITH FINE SAMPLING

T. Ohshima, A. Imanishi, T. Ishii
H. Okuno, K. Shiino
Institute for Nuclear Study
University of Tokyo, Tanashi, Tokyo 188, Japan
and
F. Naito
Faculty of Technology
Tokyo University of Agriculture and Technology,
Koganei, Tokyo 154, Japan

Introduction

Improvement of particle separation by means of fine dE/dX sampling brings forth an idea of central tracking detector with particle identification capability in the colliding beam experiment. Ludman et al. (hereafter referred as BNL measurement) at the first time reported their test results on the dE/dX measurement with the sub-mm sampling intervals, which indicated that the particle separation could be improved appreciably compared to that obtained with the ordinary sampling intervals (1-2 cm). As a result, total gas thickness could be much reduced and particle separation in the relativistic rise region could be realized even with a 1 m long chamber at an atmospheric pressure. However, for a practical application of this method, following basic features have to be further investigated.

The length of drift space:

With the longer drift space, the total number of sense wires can be reduced, but particle separation would become worse because of the diffusion and attachment of drifting electrons.

The width of unit cell:

The linear relation between the distance of the ionization point and the drift time to the sense wire is distorted because of the cylindrical electric field around the sense wire, and this distortion may deteriorate resolution of dE/dX measurement for inclined tracks against the drift field.

The effect of magnetic field:

The above effect would be much enhanced in the magnetic field because of the distorted trajectory of drifting electrons.

Readout electronics:

Sophisticated readout electronics for signal shaping and fast-sampling of pulse amplitudes are required. For the large-scale application, more than 10^6 wires may be used and the construction cost is dominated by the cost of fast Flash ADC and fast shift registers. Therefore, simpler and cheaper electronics have to be considered from the viewpoint of economical compromise.

Gain variation, cross talks, etc:

These effects would deteriorate particle separation in a large-scale multi-layer detector.

With above in mind, we have investigated the fine dE/dX sampling method with a longitudinal drift chamber (LTD) having a longer drift space and with simpler readout circuits than BNL's. Here, results obtained without magnetic field are presented.

Description of the Apparatus

Beams

A series of measurements were done using electron and pion beams of 500 MeV/c, which were obtained from the bremsstrahlung beam at the 1.3 GeV electron synchrotron of Institute for Nuclear Study. At this momentum, dE/dX for pion is at its minimum and that

for electron is in the Fermi plateau region. So, our results can be compared directly with the BNL's.

Chamber

The LTD, as shown in Fig.1, has a drift region of 51 mm long and twelve cells of 10 mm \times 10 mm for gas amplification. Applied electric field on the drift region was about 0.8 KV/cm and electron drift velocity was about 35 mm/ μ s in the gas mixture of 90% Ar + 10% CH₄. Applied high voltage on sense wires was 1.55 KV which resulted in gas amplification gain of about 2×10^4 .

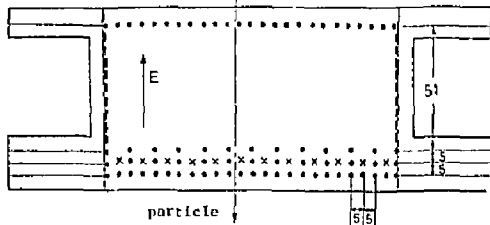


Fig.1. Scheme of our longitudinal drift chamber (LTD).

Electronics

Sampling time interval of 40 ns was chosen because of easiness to obtain commercially available Flash ADC (TRW TDC-1014J), and this choice helped to simplify the readout circuit. As for pulse shaping, only a long signal tail with time constant of about 200 ns had to be filtered out in our case. On the otherhand, BNL's 10 ns sampling required to suppress two signal components with time constant of larger than 10 ns. Then,

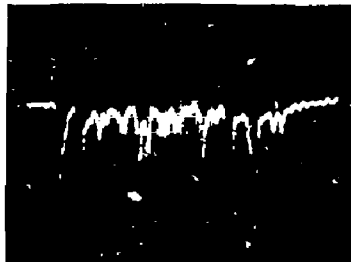


Fig.2. Input signal to ADC for the pion of 500 MeV/c. Vertical scale is 200 mV/div. and horizontal scale is 200 ns/div.

we used a fast and low noise pre-amplifier developed by Boie et al.² by modifying it to match with 40 ns sampling interval.³ Only one pole-zero shortening filter with time constant of 60-70 ns was used instead of two pole-zero's and a semi-Gaussian integrator in BNL's. A semi-Gaussian integrator with time constant of 15 ns was introduced on a particular channel to study its effect. Observed equivalent noise charge of the pre-amplifier was about 4000 electrons. A limiter was also introduced to prevent overload of succeeding amplifier for large pulses. Amplitudes of the signal from the amplifier were sampled by 6-bit FADC with the dynamic range of -1.1 V and digitized data were stored on three dual shift registers (TRW TDC-1005J). The offset level of +100 mV was applied on FADC in order to study the detailed behaviour of small amplitude noises. Fig.2 shows an input signal to FADC for the pion passing through the LTD.

Gain Monitoring

We used ⁵⁵Fe X-rays irradiating a particular sense wire to monitor the long term gain drift of the system. The pulse height spectrum for X-rays were measured between the beam spill cycles with LeCroy QVT module. We observed gain variation of 1-2% for whole test period and it was corrected at the off-line analysis.

Analysis and Results

Accumulated signal shape

Fig.3 shows an accumulated signal shape for pion events. The smaller pulse height at the leading edge

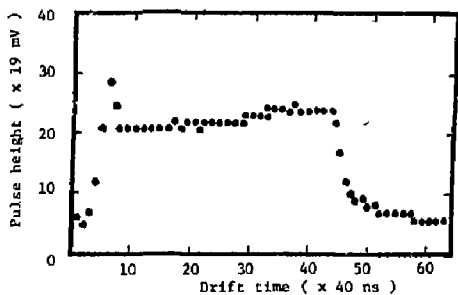


Fig.3 Accumulated signal shape for pions. One horizontal bin represents the sampling time interval of 40 ns and one vertical bin represents FADC resolution of 19 mV that corresponds to dE/dX of about 15 eV. The offset of +100 mV can be seen.

compared with BNL's can be attributed to the effects of pulse height limitation by FADC dynamic range, different gas mixture and unadjusted timing of the leading edge. The long plateau region of about 1.4 μ s corresponds to the drift region of 51 cm in the LTD. Slow rise of the average pulse height in the plateau is seen and this will be discussed later.

In the following, we analyzed the samples in the whole plateau region between the bin number 11 and 40 in Fig.3. This sampling range corresponds to the drift time of about 1.2 μ s and to the gas thickness of 42 cm, which occupies 70% of the total thickness of our chamber and this percentage is quite large compared to 31% of BNL's.

Pulse height distributions

Pulse height distributions for pions and electrons with 40 ns sampling are shown in Fig.4 together with Landau distribution functions whose parameters were chosen to fit the data at smaller energy loss side. Single sample resolution W/E_0 , where W is the FWHM of the pulse height distribution and E_0 is the most probable energy loss, is plotted in Fig.5. Our data for gas thickness of 1.4 cm is on the linearly extrapolated line from the wide samplings in the figure.⁶ The measured ratio of the most probable energy losses for electrons and pions of 500 MeV/c is 1.7 ± 0.1 , which is lower than the predicted value of 2.0⁵.

σ/E and R

A one-meter long track was simulated by using 720 samples of 40 ns intervals from the successive events.

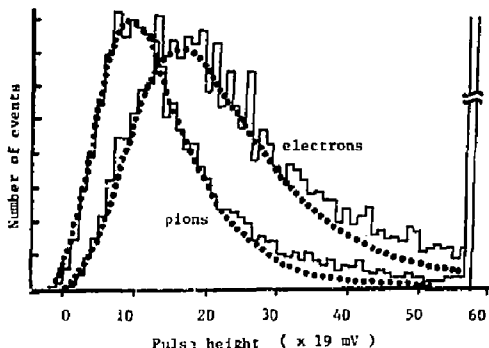


Fig.4. Pulse height distributions for pions and electrons of 500 MeV/c. Dotted curves are Landau distribution functions. +100 mV offset is subtracted.

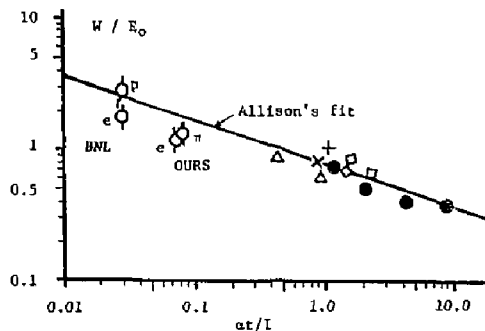


Fig.5. Single sample resolution W/E_0 . \diamond are data points of our and BNL measurements. Other data and Allison's curve are referred from ref.4.

Fig.6 shows the r.m.s. resolution σ/E of the truncated mean energy loss for a one-meter-long track as a function of the sample retention. The resolution for pions is worse than that for electrons and which might be due to the relatively large electronics noise contribution for pions. Relativistic rise $R (=E_0/E_{\pi})$ is shown in Fig.7.

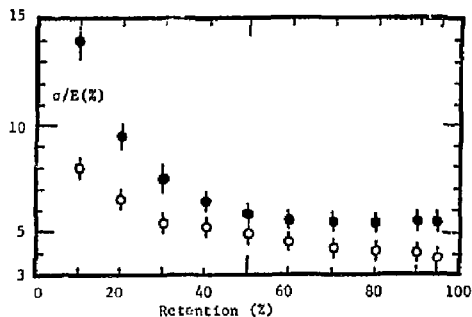


Fig. 6. σ/E of the truncated mean energy loss for a one-meter-long track as a function of the sample retention.
◆ is for pions and ○ is for electrons.

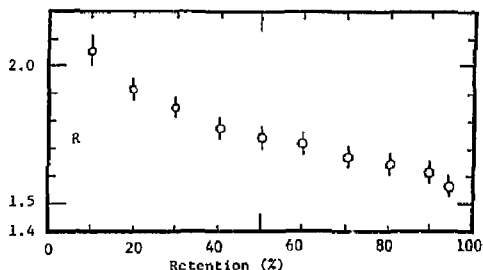


Fig. 7. Relativistic rise of the energy loss v.s. retention for 1.4 mm sampling intervals

Particle selectivity S

A figure of merit S as a measure of particle separation is defined as

$$S = \frac{|E_e - E_\pi| - (\sigma_e + \sigma_\pi)}{\langle \sigma \rangle}$$

where $\langle \sigma \rangle = (\sigma_e + \sigma_\pi)/2$, E_x and σ_x are the mean of the truncated energy loss for a one-meter-long track of particle X and its standard deviation, respectively. Fig. 8 shows distributions of truncated mean pulse heights for pions and electrons with the retention rate of 60%. Fig. 9 is a relation between S and retention rate, where the plateau of $S = 8$ can be seen at retention rate from 40% to 90%.

S in the narrow plateau region

The plateau region of the accumulated signal shape was divided into three regions to examine the dependence of S on the drift length. Same S values of about 10 was obtained over three regions. This increment of S value can be understood from the fact that the uniformity of the average pulse height is better in the narrow region. Slow rise of the plateau as seen

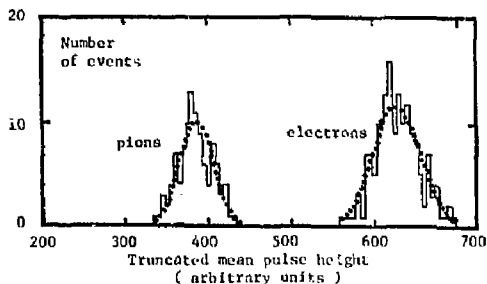


Fig. 8. Distributions of truncated mean pulse heights for one-meter-long tracks with retention of 60%, of pions and electrons at 500 MeV/c. Dotted curves are fitted Gaussian distributions.

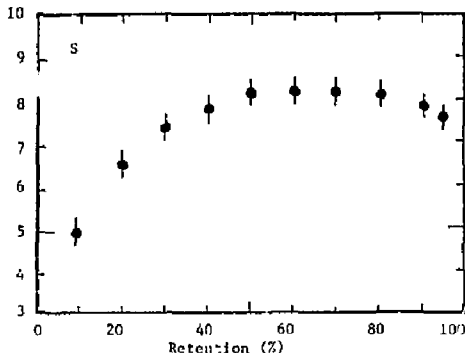


Fig. 9. Relation between S and retention rate for one-meter-long tracks, where samples from the whole plateau region were used.

in Fig. 3 contributes to make the resolution worse when the data in the wider region are used. The origin of slow rise could be attributed to the superposition of remaining signal tails, because an accumulated signal shape for ^{59}Fe X-rays has shown that the tail of 1-2% of its peak amplitude remains at the time 1 μs after the peak.

No appreciable difference between the cases with and without a semi-Gaussian integrator was observed on every items described above.

S v.s. sample size

The relation between S and the sample size was studied by assembling wider sample sizes with neighbouring 40 ns samples. Data obtained through a channel with a semi-Gaussian integrator were used, because overflowed event rates from the FADC dynamic range are very small at this channel whose gain was 1/4 of other's. Fig. 10 shows S v.s. sample size for samples in the central plateau region from the bin number 21 to 30 in Fig. 3. Result of BNL measurement with different gas mixture are also plotted and good agreement between ours and BNL's can be seen. With 1.4 mm sampling gas thickness (= 40 ns sampling

time interval), improvement of particle separation by a factor of 1.7 has been achieved compared with 21 mm sampling.

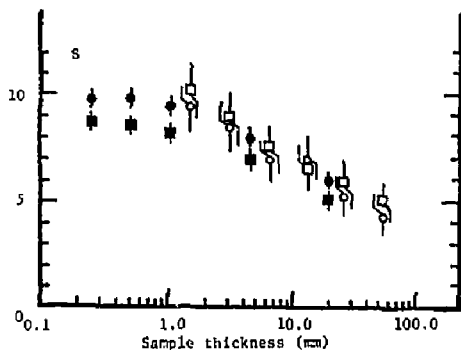


Fig. 10. Relation between S and sample size for one-meter-long tracks, where samples from the central plateau region were used.

◊ and ◊ indicate our measurement with retention rate of 40% and 60%, respectively. ♦ and ♦ indicate BNL measurement with 40% and 60% retention, respectively.

FADC resolution

Effect of FADC resolution on S value was examined by tailoring the data with 3, 4 and 5 bit resolutions at the stage of off-line analysis, where the dynamic range of FADC was kept constant (-1.1 V). Almost the same S values were obtained at 4, 5 and 6 bit resolutions, while about 15% deterioration was observed in the case of 3 bit. However, when the dynamic range is reduced to -300 mV, which corresponds to 60% retention for electrons, the S value with 6 bit resolution is reproduced even with 3 bit FADC.

Discussions

Attainable maximum S

We studied attainable maximum S value with 40 ns sampling using samples in the central plateau region. For this purpose, we simulated a one-meter-long track by randomly picking up 40 ns samples from all data, and calculated the truncated means. S value was much

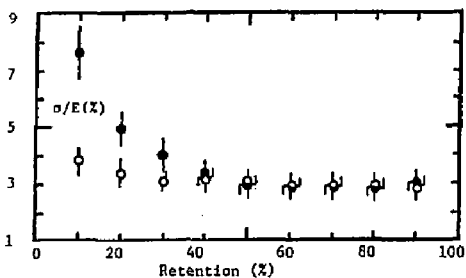


Fig. 11. σ/E v.s. retention rate, calculated from randomly picked up samples. ♦ is for pions and ◊ is for electrons.

improved to about 14.5. Resultant σ/E , R and S are plotted in Fig. 11, 12 and 13, respectively. This means that the short range correlation between samples has to be reduced to obtain higher S value. The short range correlation may come from the extended ionizations, diffusion of drifting electrons and the slow response of electronics circuits. But it is not clear yet at our present understanding.

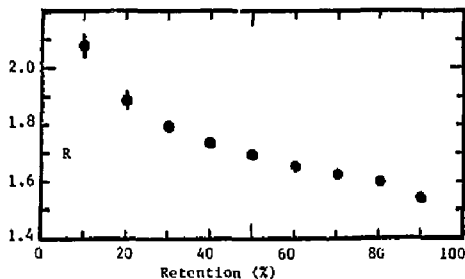


Fig. 12. R v.s. retention rate, calculated from randomly picked up samples.

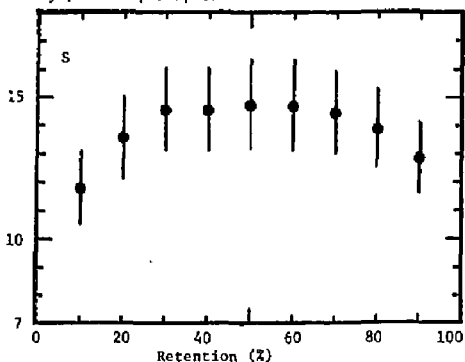


Fig. 13. S v.s. retention rate, calculated from randomly picked up samples.

Signal rail suppression

As described above, S value deteriorates about 20%, when samples are taken from the whole plateau region, due to contribution of remaining tails. Then, one more pole-zero filter with time constant of about a few μ s might be required for further rail suppression.

δ ray clipping

We examined a δ ray clipping method, reported by Bateman⁶, at the stage of off-line analysis. Pulse heights larger than a certain level were replaced by a limited value, and means were calculated including the overflowed samples. Resultant σ/E , R and S for 40 ns samples from the whole plateau region are shown in Fig. 14, 15 and 16, respectively. S value obtained with δ ray clipping is the same with the one with the truncation method. Plateau region of S value appears in the clipping level region between 200 eV and 900 eV of energy losses in gas thickness of 1.4 mm.

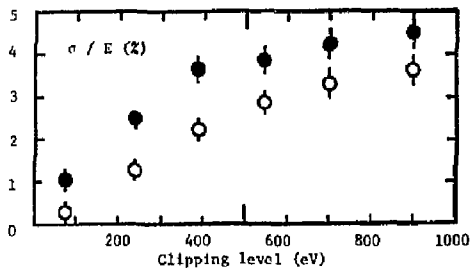


Fig. 14. σ/E v.s. clipping level. The latter is presented by the value of energy loss. Retention rate of 50% is corresponding to the clipping levels of about 300 eV for pions and about 400 eV for electrons. ● is for pions and ○ is for electrons.

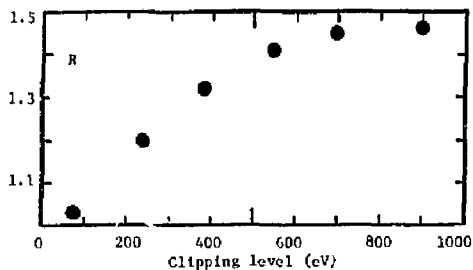


Fig. 15. R v.s. clipping level.

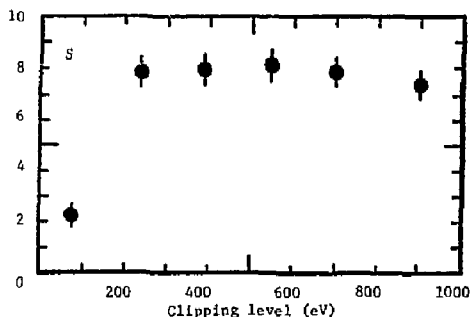


Fig. 16. S v.s. clipping level.

Although δ ray clipping technique does not improve S value, it suggests a simple scheme for readout electronics. Essential points of the electronics for the fine dE/dX sampling are on the fast and low noise amplification, and on the sufficient signal tail suppression both in the truncation and δ ray clipping method. In the latter case, clipping and integration can be done with, for instance, a limiter and an

ordinary RC integrator circuits, respectively. Then, FADC and shift registers which dominate the cost of electronics is not necessarily required.

Summary

With a simpler readout electronics and a longitudinal drift chamber with a longer drift space, improvement of particle separation with the fine dE/dX sampling was obtained. Signal tail suppression is found to be essential to achieve good S values with the longer drift space.

Also it is suggested that the maximum S value of 14.5 would be obtained if the short range correlation between samples are successfully removed.

δ ray clipping technique will make simplification of the readout electronics possible without deteriorating the S value.

Note: A group of KEK⁷ also investigated the fine dE/dX sampling with the longitudinal drift chamber similar to ours. They tested the performance with the pion and proton beams of 2 and 3 GeV/c. Their results without the magnetic field are in good agreement with ours and BNL's. In the magnetic field up to 5 KG, no appreciable degradation of the particle separation has been observed, which encourages application of this method to the central tracking detector at the colliding beam experiment.

Acknowledgements

We would like to thank Profs. S. Ozaki, F. Takasaki, Y. Watase and Y. Fukushima at KEK for their kind support throughout this work, and thank the members of the High Energy Physics Division and Computer Center at INS for their various help during the experiment.

References

1. T. Ludlam, E.D. Platner, V.A. Polychronakos, S.J. Lindnerbaum, M.A. Kvamer and Y. Teramoto, IEEE Trans. Nucl. NS-28, 439 (1981).
2. R.A. Boie, A.T. Hrisoho and P. Rohak, IEEE Trans. Nucl. NS-28, 603 (1981).
3. "Readout Electronics for Fine dE/dX Sampling with a Longitudinal Drift Chamber". INS-TH, to be published.
4. A.H. Walenta, Physica Scripta 23, 353 (1981).
5. A.H. Walenta, J. Fischer, H. Okuno and C.L. Wang, Nucl. Instr. & Meth. 161, 45 (1979).
6. J.E. Bateman, Nucl. Instr. & Meth. 164, 279 (1979).
7. Y. Watase, private communication.

PARTICLE IDENTIFICATION AND TRACKING IN CENTRAL DETECTORS

Donald L. Hartill*
 Laboratory of Nuclear Studies
 Cornell University, Ithaca, NY 14853

Combining particle identification by dE/dx and tracking in central detectors for the coming generation of colliders, e^+e^- in the 100 GeV region and pp , pp in the 200 to 1000 GeV region, places constraints on these detectors which may force compromises on their performance as either identifiers or tracking devices or both. The average charged multiplicity for e^+e^- interactions at 100 GeV is $\langle n_{ch} \rangle = 25$ with $\langle n_{ch} \rangle = 25$, which imply a very fine granularity for both tracking and identification. A typical Monte Carlo generated Z^0 decay is shown in Figure 1 and Figure 2 is a histogram of the opening angle distribution between pairs of charged particles for a large sample of Monte Carlo generated Z^0 decays. The peak of this distribution is at $\theta_{opening} = 60$ mrad or 6 cm at 1 meter imposing a granularity requirement of ≈ 1 cm for reasonable efficiency in both identification and tracking.

Ideally the chosen central detector would be a zero mass device with spatial resolution of better than 100 microns in all coordinates and a dE/dx resolution of better than 1% to assure complete identification of particles of all momenta with a granularity of a few millimeters. Coupled to this ideal detector would be a data acquisition and software reconstruction system which would require less than a few seconds of VAX CPU run time to completely reconstruct the event. Of existing detectors the projected performance of the TPC central detector of PEP-4 comes closest to this ideal detector. The initial cosmic ray test results from the TPC and the first colliding beam runs presented at this conference are very encouraging and hopefully their remaining problems will be quickly overcome.

What are the alternatives to the TPC, which has been a very long and expensive development program? The other central detectors which provide both particle identification and tracking are the JADE drift chamber at PETRA, the UAI drift chamber at the pp collider at CERN, the AFS drift chamber at the ISR at CERN, the new ARGUS drift chamber at DORIS and, in the near future, the CLEO drift chamber at CESR. In all of these detectors the dE/dx resolution ($\sigma_{dE/dx} \leq 12\%$) is only sufficient to provide hadron identification in the non-relativistic ($1/\beta^2$) part of the dE/dx curve and partial electron identification for some momenta. The particle trajectories in these detectors are measured by drifting perpendicular to the sense wires and by either current division or small angle stereo in the coordinate along the sense wires.

Before comparing the performance of existing detectors it is useful to recall that the momentum resolution for a typical central detector illustrated schematically in Figure 3 operating in a uniform solenoidal magnetic field of magnitude B is given by

$$\left(\frac{dp_T}{p_T}\right)_{\text{measurement}} = \frac{p_T}{.03} \frac{\sigma_{r,\phi}}{L_B} \frac{75C}{(N+5)} \quad (1)$$

where p_T = momentum transverse to \vec{B} . The units are GeV/c, kilogauss, and meters with $\sigma_{r,\phi}$ = spatial resolution of the detector in the plane perpendicular to \vec{B} and N = the number of equally spaced measuring points over the path length L of the particle through

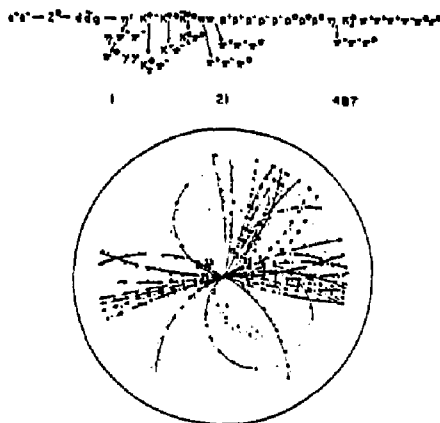


Fig. 1. Monte Carlo generated Z^0 decay.

MIN. ANGLE $\langle \theta \rangle$ BETWEEN CHARGED TRACKS

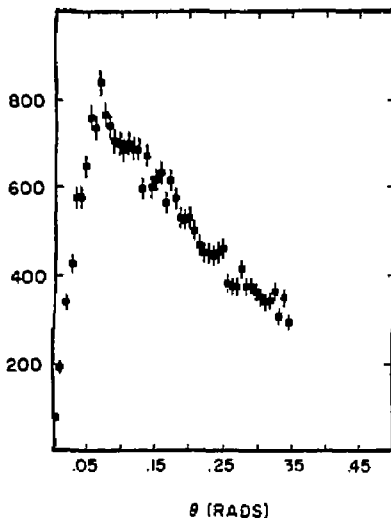


Fig. 2. Minimum opening angle θ between charged particle track pairs for Monte Carlo generated Z^0 decays.

the detector. In addition there is a contribution due the multiple scattering in the material of the detector

*Work supported by the National Science Foundation.

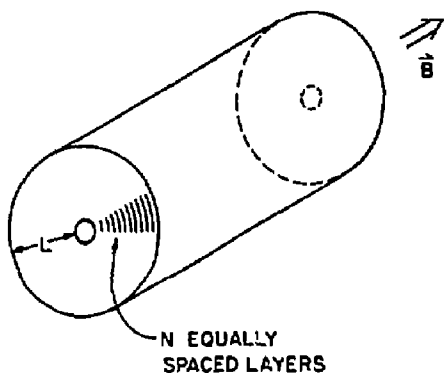


Fig. 3. General Central Drift Chamber with N equally spaced concentric cylinders spanning a radial distance L.

which is given by

$$\left(\frac{dp_T}{p_T}\right)_{\text{multiple scattering}} = 0.5 \frac{1}{LB} (1.43 \frac{L}{x_0})^{1/2} \quad (2)$$

where x_0 = average radiation length of the detector in meters. There is a crossover momentum where these two contributions are equal which is given by

$$p_{\text{crossover}} = 0.15 \frac{L}{a_{r,\phi}} \left(\frac{L}{x_0} \frac{1.43}{750} (N+5)\right)^{1/2} \quad (3)$$

with multiple scattering dominating for momenta below this value and the spatial resolution dominating above.

For typical central detectors at atmospheric pressure and operating in a 5 to 10 kilogauss field this crossover momentum is about 1 to 2 GeV/c. The z-resolution (along \vec{B}) of the detector comes into the total momentum measurement via the polar angle measurement with

$$p_{\text{total}} = \frac{p_T}{\sin\theta} \quad (4)$$

To achieve good dE/dx resolution in Argon + Ethane with no saturation of the relativistic rise, tests¹ have shown that the total charge collected on a sense wire should be less than 0.1 picocoulombs. A factor of two increase in the charge collected will decrease the relativistic rise by $\approx 20\%$. In addition, for a fixed length of gas these tests show that the dE/dx resolution improves as $N^{1/2}$ for sample lengths > 1 cm-atmosphere; for pressures less than ≈ 4 Atmospheres the resolution improves as (pressure)^{-1/2}. Above 4 Atmospheres there seems to be very little improvement in the resolution. The small collected charge requirement is in direct conflict with determining the z coordinate by charge division since the error in that determination is given by

$$\frac{\Delta z}{z} = 2.54 \left(\frac{kT C_0}{Q_{\text{total}}}\right)^{1/2} \quad (5)$$

where C_0 = sense wire capacitance and Q_{total} in the total charge collected. For simple single level discriminators providing the start pulse for the time-to-digital converters to determine the drift time, the time slewing due to noise and pulse rise time also argues for high gas gain operation which is again in conflict with good dE/dx resolution.

The JADE central detector², which has been in operation for over two years at PETRA, represents the kind of performance that a combined particle identification tracking detector gives. Figure 4 shows the end view of one of the sectors illustrating the sense wires and drift field shaping electrodes in the chamber which operates with Argon 90% + 10% Methane at 4 Atmospheres. All sense wires are parallel to the 4.5 kgauss magnetic field with the z-coordinate measured

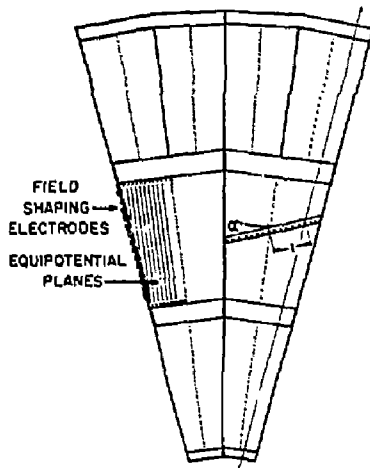


Fig. 4. End view of sector of JADE Drift Chamber with inner sense wires at $r = 21$ cm and outer sense wires at $r = 79$ cm.

by current division. The r,ϕ coordinate is determined by drifting, with an average achieved resolution of $\sigma_{r,\phi} \approx 150$ microns. For a gas gain of 5×10^4 the z-resolution is $z = 13$ mm ($\frac{\Delta z}{z} = 0.5\%$) and the relativistic rise as measured with Bhabha electrons compared to minimum ionizing particles is 1.4 ± 0.05 which seems very good for this large total collected charge on the sense wires. The dE/dx resolution for hadronic events is $\sigma_{dE/dx} = 9.10\%$ and on Bhabhas is $\sigma_{dE/dx} = 6\%$. Figure 5 is a scatter plot of measured dE/dx vs momentum for events from JADE which shows a clear proton band and pion band in the $1/p^2$ part of the spectrum. Figure 6 shows similar results from the AFS Detector³ at the ISR. The new ARGUS central detector⁴ presently under construction at DESY for use in the revised DORIS storage ring will have similar dE/dx resolution. It operates at atmospheric pressure and uses small angle stereo for the z coordinate measurement and is described elsewhere in these proceedings.

There are several operating central drift chambers (Mark II, CLEO, TASSO, and CELLO) with similar cell electrode configurations, with Figure 7 showing the CLEO cell structure. An interesting question is whether or not these detectors can be operated so that they provide a measurement of dE/dx which would be useful for identification of low energy K's and protons and perhaps electrons. By looking at the field lines for the cell configuration shown in Figure 7 and using a 1.5 μsec integration time the effective collection length for the primary ionization is about 2 cm. Using a prototype CLEO chamber with 9 layers (identical to a pie shaped section of the

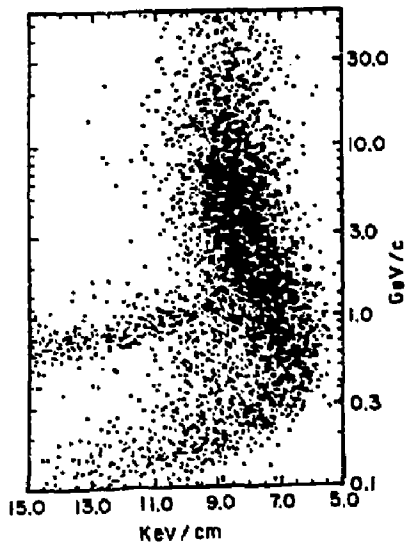


Fig. 5. Scatterplot of dE/dx measurements of hadrons with JADE.

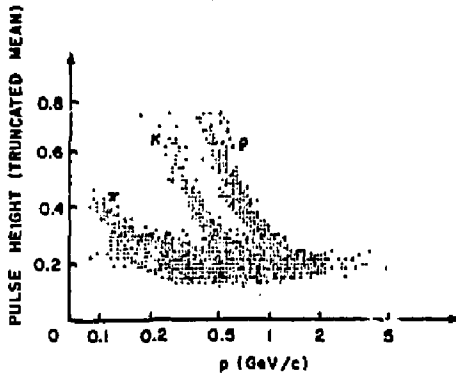


Fig. 6. Scatter plot of dE/dx measurements with AFS.

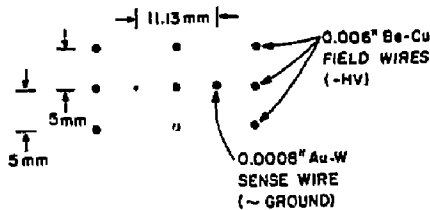


Fig. 7. Electrode configuration of CLEO Drift Chamber cell.

CLEO drift chamber) and full length wires, the typical pulse height distribution for normally incident minimum ionizing particles for a single layer is shown in Figure 8. The gas gain was 10^4 and the gas mixture used was 50% Argon + 50% Ethane. The cell to cell gain uniformity was better than 10% and the variation along the wires was also better than 10%. The fwhm of

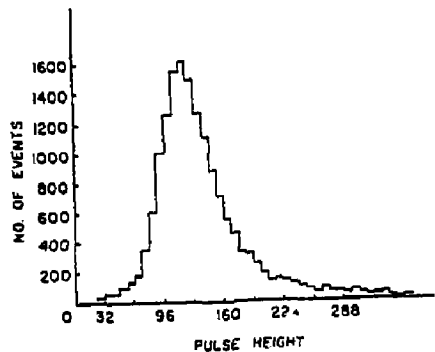


Fig. 8. Pulse height distribution of dE/dx for minimum ionizing particles passing through a single layer of CLEO Drift Chamber.

this pulse height distribution divided by the most probable pulse height is 65%. Using the smallest 5 of the 9 pulse heights the distribution narrows by $\sqrt{5}$ as expected. Extrapolating this performance to the CLEO chamber we expect $\sigma_{dE/dx} < 12\%$ which will be adequate to identify low energy K^0 's and protons. The new electronics to accommodate the simultaneous timing and pulse height measurement will be installed during the fall of 1982.

In summary it is possible to combine both tracking and dE/dx in central detectors. Using current division to measure the z coordinate is in conflict with the limits on total charge collected to avoid saturation of the relativistic rise for electrons. The dE/dx resolution that can be achieved for an 80 cm path length with an ARGUS type chamber with as many wires installed as possible is probably limited to 8%. This combined with a spatial resolution of $\sigma_{r,\phi} = 150$ microns and $\sigma_z = 1.5$ mm (small angle stereo) provides an excellent central detector. For particle identification in the relativistic rise region $\sigma_{dE/dx} \leq 4\%$ which can only be obtained with a TPC like device. The high pressure TPC has yet to demonstrate an r,ϕ spatial resolution better than $\sigma_{r,\phi} = 300 \mu$ which is about a factor of 2 worse than the JADE or CLEO type chamber, and which may be a problem.

References

1. R. D. Ehrlich, et al. Particle Identification by Ionization Measurements: Description of the CLEO dE/dx System. CLNS-B2/521 (1982). To be published in Nuclear Instruments and Methods. Also see R. D. Ehrlich these Proceedings.
2. A. Wagner, Particle Identification by dE/dx Measurements in JADE. These Proceedings.
3. W. Willis et al., Experience with the Axial Field Spectrometer Drift Chamber at the ISR, Proceedings of the 1981 Isabelle Summer Workshop Vol. 4.
4. H. Hasemann, dE/dx Measurements with the ARGUS Drift Chamber. These Proceedings.

PARTICLE IDENTIFICATION USING IONIZATION SAMPLING IN THE REGION OF THE RELATIVISTIC RISE

V. Baruzzi,^a B. Carosio,^b F. Crijns,^c L. Gerdyukov,^{*d} Y. Goldschmidt-Clermont,^e A. Grant,^e
 D. Johnson,^f P. Ktuner,^g I. Lehrs,^c R. Matthewson,^e C. Milstene,^h V. Nikolaenko,^{*d}
 Y. Petrovikh,^{*d} R. T. Ross,^e P. Sixel,ⁱ M. Spyropoulou-Stassinaki,^j A. Stergiou,^c
 W. Tejessy,^c G. Vassiliadis,^j P. Wright,^c J. Zoll^e

Presented by Y. Goldschmidt-Clermont, CERN

ABSTRACT

Fast secondary particles arising from interactions of K^+ at 70 GeV/c in the BEBC hydrogen bubble chamber, are identified by use of the relativistic rise of ionization in Argon. The ionization is measured in a large multicell proportional counter system, the External Particle Identifier (EPI). Results with identified tracks show the expected separation. The resolution in experimental conditions is studied and compared to that obtained during calibration runs. Individual particles, e.g., secondary kaons are identified at a confidence level of 86%.

Particle identification by ionization sampling in the relativistic rise region is illustrated by preliminary results obtained with the EPI (External Particle Identifier) used in conjunction with the BEBC hydrogen bubble chamber in a study of K^+p interactions at 70 GeV/c. The incident particles from an RF separated beam were tagged before entering the chamber by two multiple finger hodoscopes and two threshold Cerenkov counters. Details about the beam, the bubble chamber and the data reduction methods were published.¹

A previous publication² describes the EPI design and construction methods. It contains results obtained in a calibration run. The EPI consists, essentially, of 4096 proportional counters (cells) of $6 \times 6 \text{ cm}^2$ cross section and 1 m height, stacked in an array of 32 chambers wide and 128 layers deep. The gas used is 95% Ar + 5% CH_4 . Each cell is connected to the data acquisition system, a NOR-10 computer, via its individual amplifier and 8-bit ADC. The individual cells and corresponding electronic channels were calibrated during a separate test run using a high energy pion beam. A feedback loop using a β -source irradiating one channel, acted upon the high voltage supply to balance changes due to atmospheric pressure variations. A residual slow time dependent decrease of gas amplification was corrected for in the offline analysis.

The layout of the bubble chamber, the shielding and the EPI is shown on Fig. 1, which also illustrates the pattern of hits in the EPI. The opening in the shielding wall allowed for identification of forward particles only. The low-momentum limit at about

10 GeV/c was imposed by available space and track curvature in the 35 kG BEBC magnetic field.

Positive tracks reconstructed in the bubble chamber were followed through the stray magnetic field of the BEBC magnet to the EPI. Wire chambers were used at approximately mid-distance and attached to the front and back planes of the EPI (not shown on Fig. 1) to assist the tracking. The hit cells of the EPI were associated into strings and these into tracks (over several strings) by a pattern-recognition program, and matched to the bubble chamber tracks. A local cleaning algorithm was developed to localize the cells hit by crossing tracks or other local background (slow electrons, δ -rays, etc.). Overall, the ratio of the number of tracks N_g found with > 50 clean cells ("good" EPI tracks) to the total number N_B of tracks followed from BEBC, through the relatively narrow exit window and into the EPI front plane N_B was $N_g/N_B \approx 0.3$ for $0.15 < X_F < 1$ where X_F is the Feynman scaling variable. The ratio N_g/N_B is practically independent of P_T . As illustrated by Fig. 1, the background was due to crossing tracks arising from secondary interactions in the BEBC exit windows and shielding, and in the EPI frame. Events with excessive background were rejected, they were largely responsible for the losses and for the relatively low value of N_g .

The ionization along the reconstructed tracks was computed from the measurements in each clean cell (corrected by the corresponding calibration values) using the truncated (smaller 40%) mean, with the requirement of ≥ 50 clean cells.

Scatter plots of the ionization versus momentum for subsamples of known tracks are shown on Fig. 2 and Fig. 3. The well identified tracks of Fig. 2 are positive tracks arising from the decay of V^0 events identified in the bubble chamber ($K^0 \rightarrow \pi^+\pi^-$, $\Lambda \rightarrow p\pi^-$, $\delta \rightarrow e^+e^-$).

The tracks of Fig. 3 are mostly kaons arising from the decay $K^{*0} \rightarrow K^+\pi^-$ where the K^* (890) are selected by cuts (viz. $X_F(K^+\pi^-) > 0.8$ and $0.84 < m(K^+\pi^-) < 0.94$), the remaining pion contamination is estimated at $\sim 15\%$.

* Participating under the terms of the 1967 Agreement between CERN and the USSR State Committee for the Utilization of Atomic Energy.

a Now at Olivetti S.A., Ivrea, Italy.

b Università di Genova, Genova, Italy.

c University of Nijmegen, Nijmegen, Netherlands.

d Institute for High Energy Physics, Serpukhov, Protvino, USSR.

e CERN, Geneva, Switzerland.

f Inter-University Institute for High Energy Physics, Brussel, Belgium.

g University of Innsbruck, Innsbruck, Austria.

h Now at Tel-Aviv University, Tel-Aviv, Israel.

i Physikalisches Institut, Aachen, Federal Republic of Germany.

j Now at University of Athens, Athens, Greece.

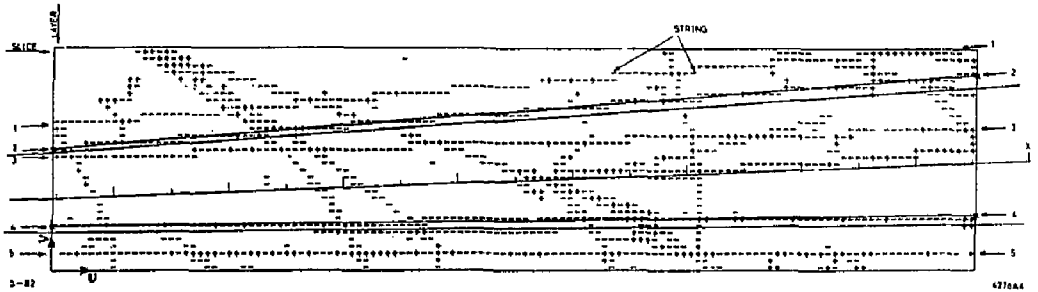
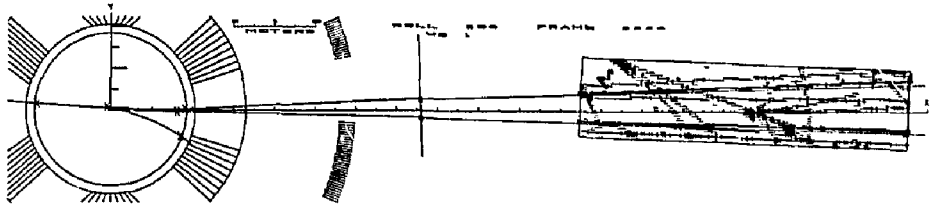


Fig. 1. Top: Layout of the bubble chamber, exit window in the shielding, intermediate MwPC and EPI. A reconstructed event shows tracks followed into the EPI.

Bottom: Pattern of cells hit in the EPI. In addition to the tracks from the reconstructed event, background tracks and secondary interactions are seen.

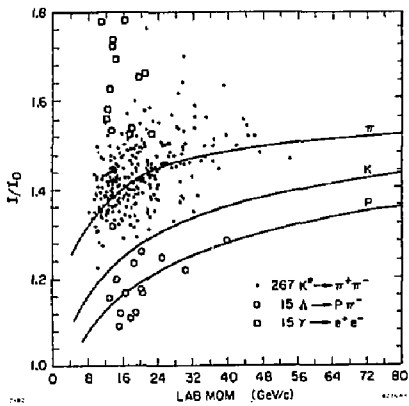


Fig. 2. Ionization vs. momentum for tracks identified by ν^0 decays reconstructed in the bubble chamber. The curves are taken from the calibration run.²

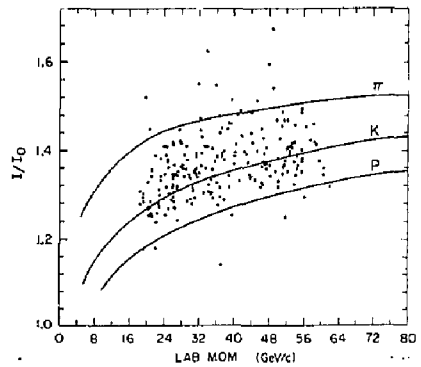


Fig. 3. Ionization vs. momentum for tracks arising from K^+ decay ($\sim 85\%$ kaons). The curves are taken from the calibration run.²

The accumulation of points around the expected line for kaons is clearly seen.

A sample of tracks with more than 95 cells, taken amongst all secondaries from interactions in BEBC, is shown on Fig. 4. The accumulation of points corresponding to pions (top) and to kaons (bottom) are visible, as well as the kaons arising from the elastic and diffraction peaks at high momentum. In this plot, the beam-tagging information has been used to remove events arising from a small contamination of the incident beam in protons and deuterons.

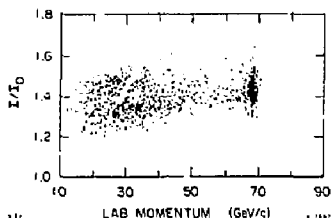


Fig. 4. Ionization vs. momentum for 3071 secondaries of K^+p interactions at 70 GeV/c, for tracks with more than 95 cells. The small beam contamination in protons and deuterons is removed using information from the tagging system.

The distribution of ionization for a sample of tracks where the beam contamination was not removed, and laying in a chosen momentum interval is shown by Fig. 5. It was fitted by three gaussian distributions G_i of the form

$$N(I/I_0) = \sum N_i G_i(\langle I/I_0 \rangle_i, \sigma_i)$$

where $i = p, K, \pi$ and the N_i measures the number of tracks attributed to the $p, K,$ and π populations ($\sum N_i = N$, the number of measured tracks.)

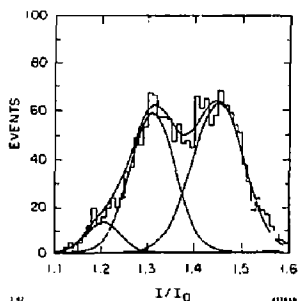


Fig. 5. Distribution of ionization for tracks in the momentum range $22 < p_{LAB} < 28$ GeV/c.

The curves are fitted gaussian distributions corresponding to $p, K,$ and π .

The fitted peak values $\langle I/I_0 \rangle_i$ are plotted against momentum on Fig. 6, showing a good agreement with the curves obtained from the previous calibration run.²

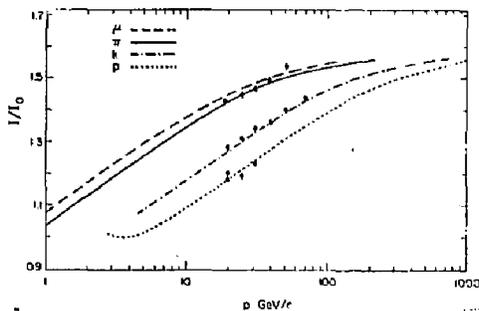


Fig. 6. Average values of ionization as obtained by the gaussian fits vs. momentum. The curves correspond to the calibration values.²

The expected width of the gaussian distributions, which gives a measure of the resolution, varies from track to track according to the number n of available clean cells, which depends in turn on the angle of incidence, on the removal of cells during the cleaning process (because of the background due to crossing tracks, δ -rays, etc.). The dependence of the resolution on n , which is roughly of the form $n^{-1/2}$, was determined experimentally on a sample of calibration tracks. In order to estimate the intrinsic width, i.e., the value σ_{118} ($n=128$) for an ideal track crossing the whole length of the EPI and with ionization measurements in all 128 cells, the following procedure was followed. For several subsamples of tracks, the expected resolution σ_{res} was computed by a convolution of the values for each track i expected from the calibration and the value of n_i . The expected values σ_{res} were compared to the observed values σ_G resulting from the gaussian fit. If the expected σ_{res} were equal to the observed σ_G , they would fall on the diagonal of a scatter plot. The observed values show a slightly degraded overall resolution. This degradation is probably related to such experimental circumstances as residual background, e.g., a not fully efficient filtering of crossing tracks. For tracks with ≥ 50 cells in the momentum region $22 < p_{LAB} < 60$ GeV/c, the gaussian fits give $\sigma \approx 3.8\%$.

The ratios K_i/N with $i = p, K, \pi$ and $N = \sum N_i$ as defined by the gaussian fits are shown on Fig. 7 as functions of momentum. In this plot, the proton population was not corrected for protons arising as secondaries from interacting beam protons, as may be done by using the tagging information.

Preliminary results based on these measurements were presented at the Notre Dame Conference.³

For each measured track, three χ^2 values can be computed as

$$\chi^2_i = \left(\frac{(I/I_0)_{meas} - \langle I/I_0 \rangle_i}{\sigma(n)} \right)^2$$

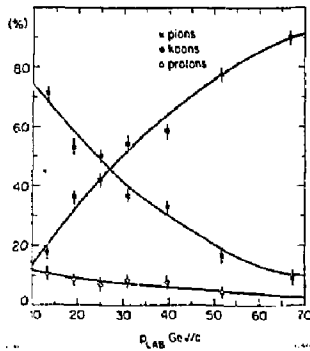


Fig. 7. The populations of p, K, and π amongst secondaries of K^+p interactions at 70 GeV/c as a function of momentum, determined by the gaussian fits. The curves are empirical polynomial fits.

where $i = \pi, K, p$ (one degree of freedom). The probability that the track be i is then estimated as

$$P_i = \frac{N_i}{N} P(\chi^2_i)$$

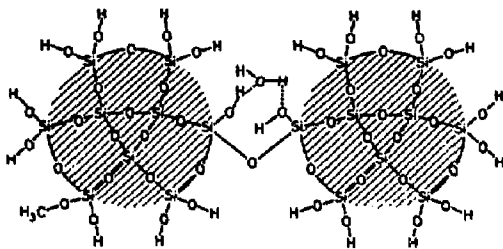
where N_i are defined as above. The choice of the highest probability P_i isolates tracks identified as p, K, π . It is estimated, for instance, that the sample of identified kaons contains a contamination of $\leq 14\%$ of pions. Thus, the individual kaon tracks are identified at a confidence level of 86%.

Similar results are available for an exposure to a RF separated K^- beam at 110 GeV/c.⁴ A detailed account of the methods of analysis and of the results is in preparation.

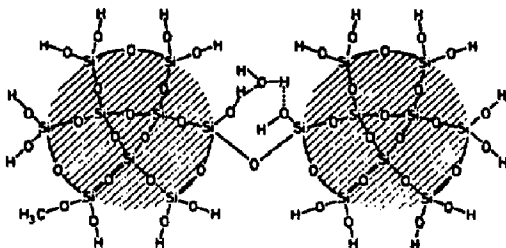
References

1. M. Borch et al., *Zeit. Phys. C2* (1979) 285.
2. I. Lehraus, R. Matthewson, W. Tejessy, and M. Aderholz, *Nucl. Instr. & Meth.* 153 (1978) 347, and N. Aderholz, P. Lazeyras, I. Lehraus, R. Matthewson and W. Tejessy, *Nucl. Instr. & Meth.* 123 (1975) 237.
3. M. Spyropoulou-Stassinaki, Paper presented at the 12th International Symposium on Multiparticle Dynamics, Notre Dame 1981. CERN-EP/81-122, October 1981.
4. P.R.S. Wright. *Thesis, Imperial College of Science and Technology, London, 1981.*

CERENKOV, TIMING,
AND
TRANSITION RADIATION TECHNIQUES



CERENKOV, TIMING,
AND
TRANSITION RADIATION TECHNIQUES



PREPARATION OF SILICA AEROGEL AND ITS APPLICATION IN THE TASSO CERENKOV COUNTERS

G. Poelz

II. Institut für Experimentalphysik der Universität Hamburg*
2000 Hamburg 52 - Notkestrasse 85 - Germany

Summary

The Cerenkov counters in TASSO consist of 3 elements, one filled with aerogel and two with Freon 114 and CO₂. The 1700 liters of aerogel cover an area of 11.8m² with a thickness of 13.5 to 18 cm. Most cells are filled with an index of refraction between 1.023 and 1.026. In a running period of 2 months after installation $\langle N_e \rangle = 3.9 \pm 0.2$ photoelectrons were observed. The mean value over 17 months is $\langle N_e \rangle = 3.0 \pm 0.2$. The aerogel was manufactured at DESY with a rate of up to 90 l/week. The dimensions of the samples are 17 x 17 x 2.3 cm³. The refractive index of 986 pieces with n around 1.025 is distributed with $\sigma_n = 0.0013$. The transmission length for light with $\lambda = 438$ nm is $\Lambda = 2.64$ cm with $\sigma_\Lambda = 0.22$ cm. For 100 samples with $n = 1.017$, $\Lambda = 3.8$ with $\sigma_\Lambda = 0.6$ was found. In recent investigations the transmission length for aerogel with $n = 1.025$ could be improved to $\Lambda = 5.1$ cm.

The charged hadrons in the TASSO detector^{1,2} at PETRA are identified by time-of-flight counters and a Cerenkov system combined with the momentum information of the central detector. This Cerenkov system consists of 3 threshold counters filled with 1700 liters of aerogel, with Freon 114 and CO₂. All the aerogel was manufactured at DESY. This paper describes the method used for the production of aerogel³, its performance and the properties of the Cerenkov detectors.

In aerogel small colloidal particles of silica with 4 nm in diameter are linked to branched strings. They form a porous structure with voids of about 20 to 200 nm in diameter. The index of refraction results from an average within a wavelength of light. It depends on the density ρ (g/cm³) of the aerogel by (Fig. 1)

$$n - 1 = (0.210 \pm 0.002) \cdot \rho$$

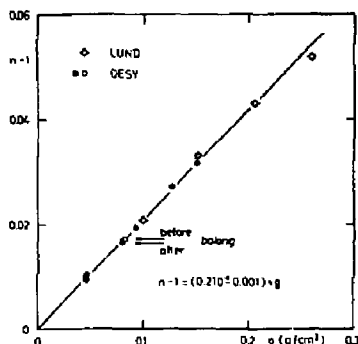
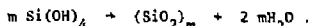
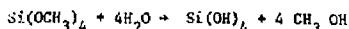


Fig. 1. Refractivity of silica aerogel produced at DESY and LUND³ as function of its density.

Preparation of aerogel

Aerogel for Cerenkov radiators is usually prepared³ out of tetramethoxysilan. It decomposes by hydrolyzation and then condensates to silica colloids



When grown to the right size ($m \sim 700$), the particle come into contact and are bound together (Fig. 2) forming a gel. It takes the same volume as the initial liquid mixture. If more or less methanol is added at the beginning, gels with different densities can be prepared and different indices of refraction are obtained.

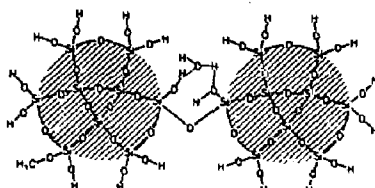


Fig. 2. Sketch of 2 colloidal particles bound by a siloxan link (Si-O-Si) and by a water bond.

The speed of gelation is in good approximation proportional to the concentration v_c (by volumes) of the added catalyst (NH₃OH)

$$1 / t_g = a \cdot v_c$$

with the gelling time t_g . The coefficient a in turn depends linearly on the concentration v_s of the silan. From Fig. 3 one finds that below $v_s = 0.1$ no gelation takes place and refractive indices below $n = 1.01$ cannot directly be obtained with this mixing procedure.

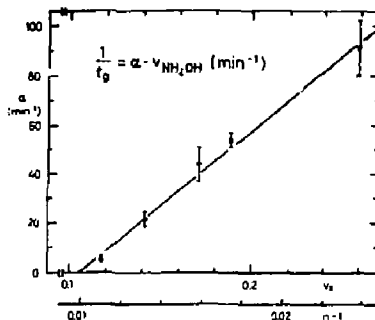


Fig. 3. Coefficient a of gelling speed $1/t_g$ as a function of the concentration v_s (by volumes) of the silan. The catalyst is a solution containing 25% ammonia. The concentration of this solution in the mixture is given by $v_{\text{NH}_3\text{OH}}$.

* Supported by the Deutsches Bundesministerium für Forschung und Technologie.

After gelation the pores of the gel are still completely filled with alcohol and water. To extract these liquids without harm to the delicate structure of the gel they have to be transferred into the gaseous phase (Fig. 4). The alcohol is heated in a pressure vessel slowly beyond the critical temperature (Fig. 5) and then the vapour is released at constant temperature. Now the gel can be cooled down and air penetrates the voids.

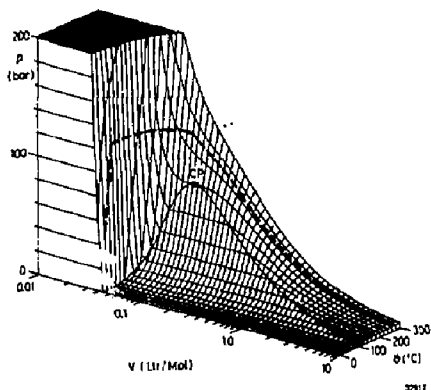


Fig. 4. Pressure-volume-temperature diagram for methanol calculated from the Redlich-Kwong equation modified to $p = RT/(V-b) - a/(\sqrt{T} V(V+c \cdot b))$. With $c = 15.97$ the parameters a and b are almost linear functions of the absolute temperature T . R is the gas constant. The extraction cycle in the autoclave follows the broken line.

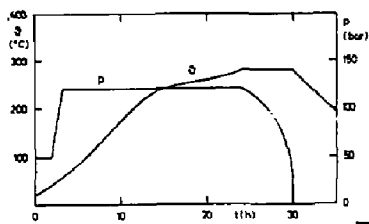


Fig. 5. Temperature and pressure inside the pressure vessel as a function of time. The rise in temperature and the decrease of the pressure take care of the changing density and viscosity of methanol.

Some residual methanol and water can be removed by baking the aerogel at 400°C in normal atmosphere for 3 hours. The optical properties of the gel is changed simultaneously. We find for samples with refractive indices around $n = 1.025$

$$n_i - n_f = 0.0065 - 0.15 (n_f - 1) = 0.003 \text{ for } n_f = 1.025$$

$$\mu_i - \mu_f = 0.27 - 0.45 \mu_f (\text{cm}^{-1}) = 0.1 \text{ cm}^{-1} \text{ for } \mu_f = 0.38 \text{ cm}^{-1}$$

The transmission coefficient μ was measured at a wavelength $\lambda = 436 \text{ nm}$ and i and f indicate the initial and final values.

Also the OCH_3 groups on the surface of the colloids are burned and OH groups remain. The initially hydrophobic aerogel is changed to a hydrophilic one.

The whole production cycle needs about 2 weeks for samples with $n = 1.025$. The freshly prepared gel should age at room temperature (22 - 24°C) for about 10 days to strengthen the bonds between the colloidal particles. The bottle-neck in the production rate is the treatment in the pressure vessel. It takes 2 days.

At DESY we have 2 pressure vessels with a volume of 50 l each (90 cm x 26 cm ϕ). This allows a production rate of 100 to 140 samples per week with pieces of $17 \times 17 \times 2.3 \text{ cm}^3$ corresponding to 65 to 90 l/week.

The index of refraction and the transmission coefficient of each sample is measured. For 986 samples produced under similar conditions with n around 1.025 n is distributed with $\sigma_n = 0.0013$. The transmission length $\Lambda = 1/\mu$ was found to $\langle \Lambda \rangle = 2.64 \text{ cm}$ with $\sigma_\Lambda = 0.22 \text{ cm}$. The examination of 100 pieces with $n = 1.017$ yielded $\langle \Lambda \rangle = 3.8 \text{ cm}$ with $\sigma_\Lambda = 0.6 \text{ cm}$.

The refractivity measured at different points of the $17 \times 17 \text{ cm}^2$ surface of an aerogel sample is plotted in Fig. 6. The scatter of the values of about $\pm 5\%$ is mainly due to systematic uncertainties of the measurement because of the uneven surface of the sample.

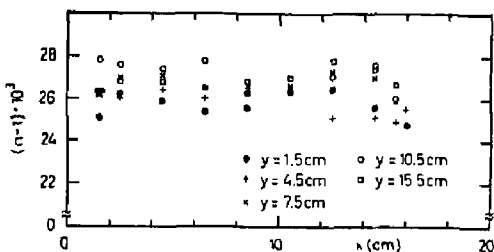


Fig. 6. Distribution of the refractivity in an aerogel sample across its surface of $17 \times 17 \text{ cm}^2$.

The scattering of light shows the expected λ^4 behaviour of Rayleigh scattering (Fig. 7). The absorption was measured by the decay time of the photon intensity within a diffuse reflecting box in the presence of aerogel. In the visible spectrum the absorption is smaller than the scattering. The corresponding lengths differ by at least one order of magnitude.

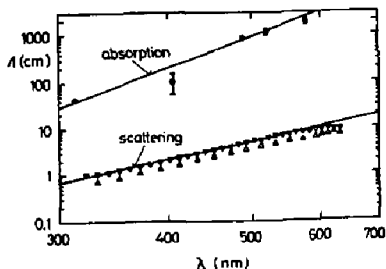


Fig. 7. Scattering length for unbaked (Δ) and baked (\square) aerogel and absorption length (\star) measured as a function of the wave length of light. The slope of the fitted lines is given by λ^6 and λ^4 respectively.

In recent experiments the transmission coefficient could be improved by a factor of 2 (Fig. 8). With a short gelling time t_g and chemicals cooled to 10°C a coefficient of $\mu = 0,2 \text{ cm}^{-1}$ was obtained.

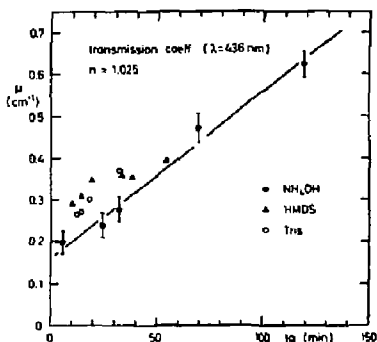


Fig. 8. Transmission coefficient μ as function of gelling time t_g at room temperature. As catalysts were used ammonia, hexamethyldisilazane and Tris(hydroxymethyl)-aminomethane. The left most point was obtained with a temperature of the liquids of 10°C ($t_g = 12 \text{ min}$). Its position in the plot is scaled to room temperature.

All our samples were prepared in glass moulds and remained there also in the evaporation cycle. The moulds had to have rounded edges. With this shape the gel will not break when it detaches from the walls. We now succeeded to produce also aerogel with sharp edges without cracks. The gel is cast in a mould with removable walls (Fig. 9) and then transferred to a wider dish.

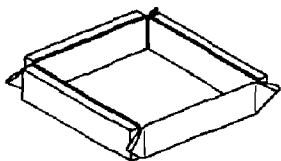


Fig. 9. Mould with removable walls to obtain aerogel slabs with sharp edges. A thin plastic foil separates the gel from the walls.

Aerogel-Cerenkov counters

The mean number of photoelectrons $\langle N_e \rangle$ detected by a phototube like RCA 8854 or XP 2041 in a Cerenkov counter can be estimated by

$$\langle N_e \rangle = n_0 \cdot \sin^2 \theta_c \cdot d_{\text{eff}} \cdot \eta_c$$

with $n_0 = 100 \text{ cm}^{-1}$, the Cerenkov angle θ_c , the effective thickness of aerogel $d_{\text{eff}} = \lambda(1 - \exp(-d/\lambda))$, the real thickness d , and the light collection efficiency η_c (for λ see below).

For the collection of the Cerenkov light two different systems are usually recommended:

With mirrors one may obtain a high collection efficiency, a particle with wrong direction is not detected and the signal is prompt. But to put the mirrors in the right position space is needed and the high collection efficiencies can only be reached with mirrors of complicated shapes. The collection efficiency tends to be inhomogeneous over the area of the aerogel.

λ is determined by the transmission length of the aerogel $\lambda \sim \lambda_{\text{trans}} \sim 2.5 \div 5 \text{ cm}$ and η_c is limited by the reflectivity of the mirrors $\eta_c \leq 0.9$.

With diffuse reflecting walls one collects the direct and scattered light. The counter is easy to design and the collection efficiency is homogeneous. But to obtain a reasonable collection a high reflectivity is needed ($r \geq 0.95$). Photons with many reflections arrive within longer time intervals at the photomultiplier. The counter is sensitive to all particle directions.

The effective thickness of aerogel is here determined mainly by the absorption length λ_a of the gel. $\lambda \sim \lambda_a \sim 11 \text{ cm}$ and

$$\eta_c = t \cdot F / (1 - r(1 - F))$$

with the combined transmission of the light funnel and the photocathode $t = 0.4$ and F the fractional area of the photocathode $F = \text{area (PM)}/\text{area (total)}$.

In small counters a high yield is easily obtained. The counter in Fig. 10 with dimensions of $24 \times 20 \times (21.5 \sim 38) \text{ cm}^3$ was lined with millipore. With 18 cm of aerogel 12 photoelectrons were produced by relativistic electrons. The aerogel slabs had an index of refraction of 1.023 and were not baked.

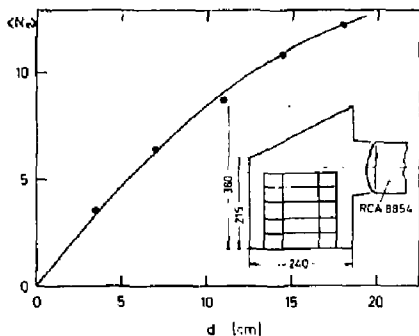


Fig. 10. Photoelectron yield of a small counter with diffuse reflecting walls and with different aerogel layers of thickness d . The counter was tested in a beam of relativistic electrons.

One cell of the aerogel Cerenkov detector used in TASSO is sketched in Fig. 11. The area of aerogel is about $35 \times 100 \text{ cm}^2$. The long distance between the radiator and the photomultipliers was determined by the adjacent detector components. Monte Carlo computations for the different collection systems showed that the diffuse reflection scheme should be favoured. The total cell is lined with one layer of millipore. The aerogel slabs were cut with a diamond saw to the right shape and stacked into a drawer which is then inserted into the counter cell. The aerogel pieces

are held in place by cotton threads.

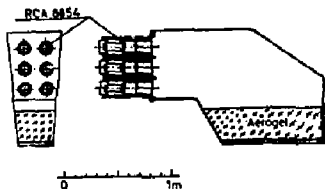


Fig. 11. Sketch of a detector cell used in TASSO.

A prototype was tested in pion beams at DESY and CERN. Fig. 12 shows the threshold curve for 18.5 cm of aerogel with $n = 1.024$. The signal below threshold is almost due to δ electrons. For the light produced in the millipore we found $2.4 \cdot 10^{-2}$ photoelectrons.

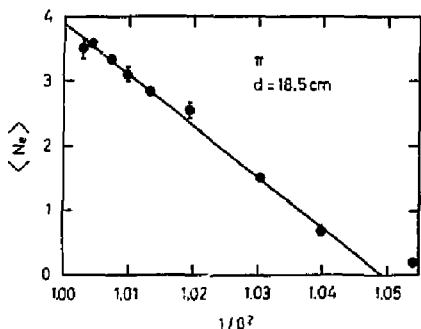


Fig. 12. Threshold curve for a TASSO cell like Fig. 1) tested in a pion beam.

The light yield was investigated in a beam of pions with a momentum of 3.4 GeV/c (Fig. 13). The data for different radiator thickness are fitted with an effective absorption length of $\lambda_a = 9 \pm 1 \text{ cm}$.

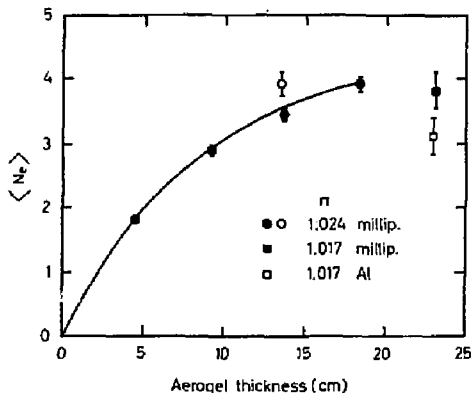


Fig. 13. Mean number of photoelectrons vs thickness of aerogel with $n=1.024$ (●) measured with a TASSO cell. A pion beam of 3.4 GeV/c was used. The open point (○) gives the mean value from 16 cells with cosmic muons beyond 4 GeV/c. The squares are results with

$n = 1.017$ and cosmic muons ($p > 1.4 \text{ GeV/c}$). The light was collected by millipore (■) and aluminized mylar (□).

In a measurement with aerogel of $n = 1.017$ in a layer of 23 cm thickness and cosmic muons ($p > 1.4 \text{ GeV/c}$) we obtained a comparable yield of $\langle N_e \rangle = 3.9 \pm 0.3$ (Fig. 13). The lower number of Cerenkov photons is compensated by the higher transparency of the gel. With aluminized mylar at the walls and an appropriately bent foil opposite to the aerogel the yield decreased to 3.1 ± 0.1 photoelectrons.

The assembly of the 32 cells in the Cerenkov detector of TASSO is shown in Fig. 14. The Cerenkov counters are arranged in 2 horizontal arms and subtend a solid angle of 19% of 4π (see Table 1).

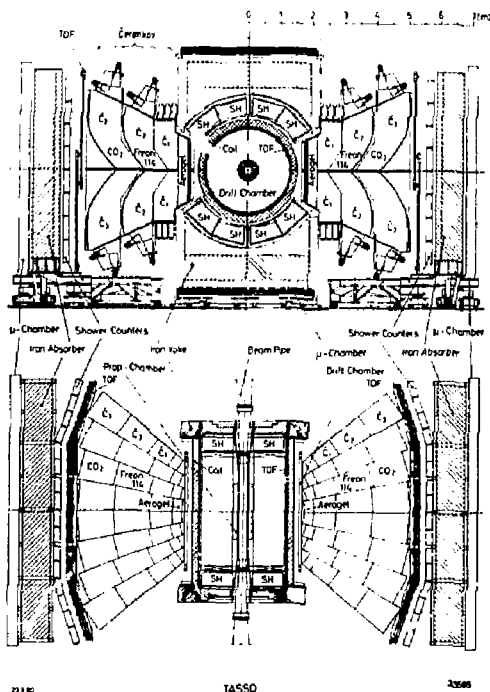


Fig. 14. End and top view of the TASSO detector.

The 16 cells below the mid plane can be tested by cosmic muons in parallel to the data taking runs. In the first 2 months after installation a yield of $\langle N_e \rangle = 3.9 \pm 0.2$ for particles with $p \geq 4 \text{ GeV/c}$ was observed.

Table 1 - The aerogel Cerenkov counters in TASSO

Solid angle	$19\% \pm 4\%$
$\theta = 90^\circ \pm 40^\circ$	
$\phi = 26^\circ \pm 26^\circ$	
Substructure	32 cells
Area of aerogel	11.8 m^2
Volume of aerogel	1700 l
Aerogel thickness	$d = 13.5 \text{ cm}$ in 28 cells $d = 18.0 \text{ cm}$ in 4 cells
Index of refraction	$n = 1.023 \pm 1.026$ in 24 cells $n = 1.020 \pm 1.023$ in 8 cells.

The threshold curve for cosmic muons averaged over the whole run period (February 1979 to July 1981) is plotted in Fig. 15. The number of photoelectrons here reaches $\langle N_{pe} \rangle = 3.0 \pm 0.2$. Fig. 16 shows the result of the evaluation of hadronic data. The fraction of charged particles seen by the aerogel counters relative to all candidates is plotted versus the particle momentum. The arrows indicate the threshold for π^- , K-mesons and protons. The solid line is computed assuming constant particle ratios. The effect of pions and kaons are clearly seen.

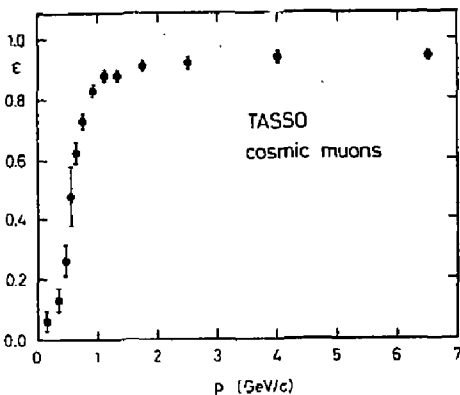


Fig. 15. Threshold curve for cosmic muons of all TASSO cells below the horizontal mid plane. The data are collected during 1.5 years parallel to the runs.

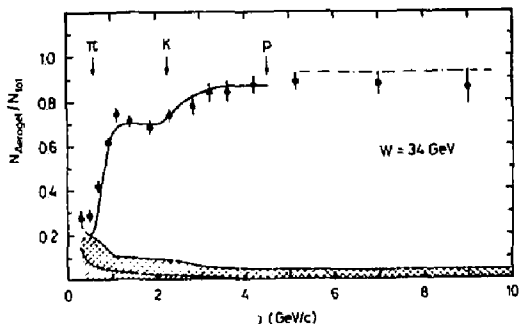


Fig. 16. Fraction of charged hadronic particles detected by the TASSO aerogel counters relative to all candidates. The arrows indicate the respective threshold. Dashed line: maximum limit caused by a software cut. A fast dropping electron background and a flat background from neighbouring showers is also shown.

References

- 1) TASSO Collaboration, R.Brandelik et al. "Properties of Hadron Final States in e^+e^- Annihilation at 13 GeV and 17 GeV Center of Mass Energies" Phys. Lett. 83B, 261 (1979)
- 2) H.Boerner, H.M.Fischer, H.Hartmann, B.Löhr, M.Wollstadt, D.G.Cassel, U.Kötz, H.Kowski, B.H.Wiik, R.Fohrmann, and P.Schmüser. "The Large Cylindrical Drift Chamber of TASSO" Nucl.Instr. and Meth. 176, 151 (1980)
- 3) H.Burkhardt, P.Koehler, R.Riethmüller, B.H.Wiik, R.Fohrmann, J.Franke, H.L.Krasemann, R.Maschuw, G.Poelz, J.Reichardt, J.Ringel, O.Römer, R.Rüsch, P.Schmüser, R.van Staa, J.Freeman, P.Lecomte, T.Meyer, Sau Lan Wu and G.Zobernig. "The TASSO Gas and Aerogel Cerenkov Counters" Nucl. Instr. and Meth. 184, 319 (1981)
- 4) G.Poelz and R.Riethmüller. "Preparation of Silica Aerogel for Cerenkov Counters" DESY preprint 81-055, to be published in Nucl. Instr. and Meth.
- 5) S.Henning and L.Svensson, "Production of Silica Aerogel". Physica Scripta 23, 697 (1981)
- 6) M.Cantin, M.Casse, L.Koch, R.Jouan, P.Mestreau, D.Roussel, F.Bonnin, J.Moucel and S.J.Teichner "Silica Aerogels used as Cerenkov Radiators" Nucl. Instr. and Meth. 118, 177 (1974)
- 7) Landolt - Börnstein New Series, ed. K.-H.Hellwege, IV, 3, p. 18 (Springer-Verlag Berlin, Heidelberg, New York 1975)
- 8) TASSO Collaboration, to be published.

THE HRS CERENKOV COUNTERS*

J. Chapman, N. Harnaw, S. Koeliman and D. I. Meyer
The University of Michigan
Department of Physics
Ann Arbor, MI 48109

Summary

We have successfully tested an ultraviolet photoionization Cerenkov Counter in a 10 GeV/c pion beam preparatory to building a large system to be installed in the HRS spectrometer. The counter has been tested to 11 atmospheres of pressure for use as a π/K separator.

Introduction

The separation of charged kaons from the more copiously produced pions adds significantly to the analyzing power of e^+e^- detectors. Time-of-flight techniques provide this separation up to about 1 GeV/c. However, at PEP and PETRA energies a large proportion of particles have momenta above this range. A useful device to tag kaons above 1 GeV/c would be a threshold Cerenkov counter. Due to the tight bunching of particles in jets, the counter must have high segmentation. Unfortunately the need to keep phototubes of a conventional counter outside a magnetic field makes a light guide system difficult if not impossible to design. For this reason Cerenkov counters which use proportional chambers to detect the ultraviolet part of the spectrum (1150 - 1350 Å) have been developed.¹⁻³ The proportional chambers are doped with a small amount of benzene. Benzene is chosen because it has a high photoionization probability in this wavelength range.

This paper describes tests of a prototype cell of the ultraviolet threshold Cerenkov counter system which is to be installed in the High Resolution Spectrometer (HRS), a PEP detector. The counter will consist of 13 individual torii placed around the beam as shown in Fig. 1. The design allows for high segmentation (64 cells per torus) while the amount of material contributing to multiple Coulomb scattering is minimized. Each torus is constructed of 8 flanged units which bolt together to form a polygon of 16 segments. A group of 4 proportional chambers share a common planar - elliptical mirror. The Cerenkov radiator will be an argon/nitrogen mixture at 16 atmospheres pressure. This gives a τ threshold at 1.1 GeV/c and will allow π/K separation from 1.1 to 3.9 GeV/c. In addition, time-of-flight counters give a one standard deviation separation of π 's and K 's up to 1.3 GeV/c.

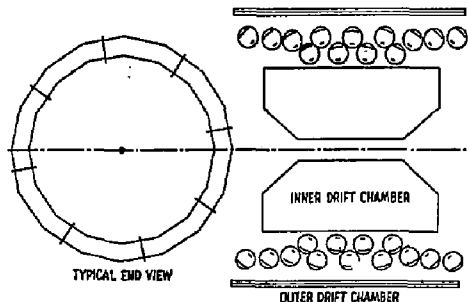


Fig. 1. End and side view of the planned Cerenkov counter system for the HRS.

* Supported by the U. S. Department of Energy.

Principle of Operation

The principle of the photoionization Cerenkov counter is much the same as that of a conventional gas threshold Cerenkov counter. The particle traverses and radiates photons in a gas, the number of photons per unit length of the radiator is given by

$$\frac{dN}{dz} = 370 \int_e \sin^2 \theta \, dE$$

where z is the particle path length in cm, θ is the Cerenkov angle, E is the photon energy in electron volts and e is the photon detection efficiency. e is dependent on the U-V transmission of the proportional chamber window (typically 45% for magnesium fluoride) and the mirror reflectance (typically 75%), both of which vary with photon energy.² The wavelength window is defined by the photoionization efficiency of benzene which is zero above 1350 Å and approximately 50% down to 1160 Å. CO₂, which is used as a quenching gas in proportional chambers, is absorbing below 1160 Å. Also a radiator gas must be chosen which is transparent or absorbs U-V photons only weakly.

The choice of Cerenkov radiator was a 85% argon, 15% nitrogen mixture. Argon is known to be transparent in the wavelength range of interest.² The nitrogen was added to quench scintillation light. Argon and nitrogen have similar refractive indices at these wavelengths; however nitrogen is known to absorb ultraviolet photons weakly.⁴ Although the absorption length of nitrogen is large (187 cm) absorption becomes significant in a pressurized system. Xenon and krypton are known to transmit UV³ and have higher refractive indices than argon, however the photon yields would be inadequate for the proposed HRS detectors.

Neglecting the effects of dispersion, the number of photons per unit length can be simplified to

$$\frac{dN}{dz} = N_0 \sin^2 \theta$$

where N_0 is a constant dependent on the parameters described above. An estimation of these parameters yields an expected value of 70 for N_0 .²

Experimental Setup

A prototype of the cell geometry to be used in the HRS was built. This geometry is shown in Fig. 2. The test section consisted of a 25.4 cm diameter aluminum tube of 0.32 cm thickness (1/8th of a complete torus). Contained inside the tube was a 22.9 cm wide cylindrical mirror with an elliptical cross section. The proportional chamber was placed 15 cm from the mirror at its first focus. The second focus would correspond to the e^+e^- intersection point, 200 cm away.

The structure of the proportional chamber is shown in Fig. 3. The design has gone through a variety of stages.³ The chamber was 15.2 cm long and contained six cells, each 0.5 cm wide. The dead region between cells was 0.5 mm. A 2 mm thick MgF₂ window was sealed to the proportional chamber with an O-ring. Each cell contained a sense wire (38 microns diameter gold-plated tungsten) which was positioned 2.4 mm from the window. The six cell structure was chosen for two reasons. The proportional chamber runs at atmospheric pressure and therefore must support the MgF₂ window. Also the chamber presents a dead region since if a particle goes through the proportional chamber it will fly regardless of

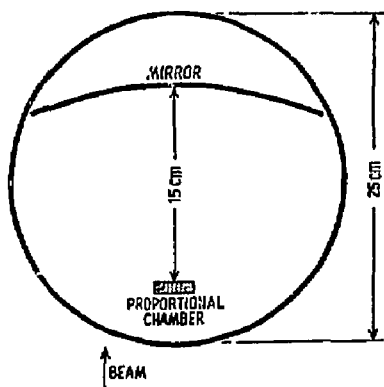


Fig. 2. Cross-sectional view of the Cerenkov counter test vessel.

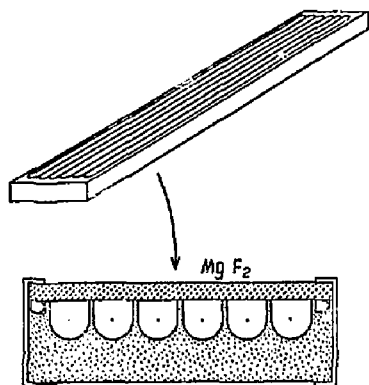


Fig. 3. Structure of the proportional chamber.

whether the particle was above threshold or not. If the chamber has discrete cells, 5/6 of the chamber is still active for Cerenkov light when a call is struck. However, to reduce electronic read-out costs, pairs of cells are grouped together.

The preamplifier is a crucial element in the system. It must have low noise to detect single photoelectron avalanches efficiently. Each proportional chamber cell pair fed a separately housed low noise FET charge to voltage preamplifier with an 800 ns output time constant. Since linearity is not required the preamp can be of very simple design. The preamplifier output was firstly RC coupled to a discriminator of adjustable threshold via an external amplifier and secondly to an ADC channel with composite sensitivity 96 counts/femto-Coulomb. In this case the readout electronics operated at a signal to noise of 4/1 for signals above 0.3 femto-Coulomb.

The mirror reflectivity has been measured to be 75% at 1216 Å. The mirror was made of glass, 2 mm thick. It was slumped on a graphite form which had the desired elliptical curvature. The glass was then vacuum aluminized with a MgF_2 overcoating to prevent oxidation.⁵

The mirrors were chosen to give one dimensional focusing in the elliptical plane. This means there is no focusing in the direction of the magnetic field bend. Because the counters form a complete azimuthal ring (see Fig. 1) this does not lead to an efficiency loss.

Preliminary Tests

The addition of benzene as a photoionizing chemical tends to destabilize the proportional chamber. When a proportional avalanche occurs many argon atoms are excited. The argon emission spectrum is centered around 1000 Å. These photons can photoionize the benzene causing further avalanches. A suitable quenching agent must absorb these photons while transmitting UV light in the 1150 to 1350 Å region. CO_2 has a short absorption length below 1160 Å and a "window" at the desired wavelengths.⁵ We experimented with a number of gas mixtures — argon with 1% C_6H_6 and 1%, 10%, 20%, and 30% CO_2 . We found that more CO_2 is needed than for a standard proportional chamber, a useful mixture being 1% benzene, 20% CO_2 and 79% argon. It was found that 30% CO_2 raised the operating voltage by 100 volts but did not affect the chamber stability or improve the single photon detection efficiency. The 1 mole percent benzene was chosen so that there are several mean absorption lengths for the UV photons in the chamber.

An interesting feature of the proportional chamber was its ability to detect visible photons as evidenced by its sensitivity to an overhead room light. We attributed this to the photoelectric effect off the aluminum oxide layer on the chamber walls. Silvering the proportional chamber surface eliminated the effect.

One worry was that the proportional avalanches would affect window transmission. The transmission of the MgF_2 window was measured to be 50% using a Lyman-alpha (1216 Å) hydrogen discharge lamp. The chamber was run for 10¹⁰ counts just below breakdown and the MgF_2 transmission was remeasured. No noticeable difference was observed indicating that breakdown products formed by counter avalanches do not degrade the window transmission.

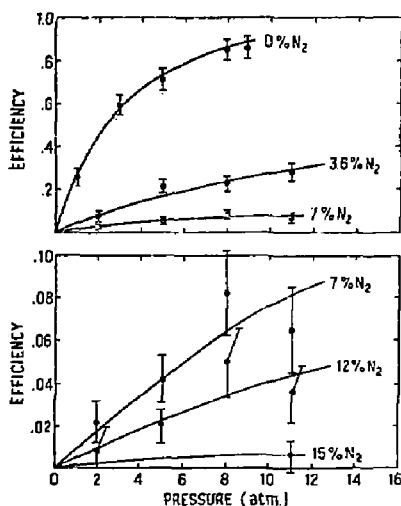


Fig. 4. Efficiency for detecting scintillation light as a function of pressure and nitrogen percentage.

Scintillation light can be produced by a particle below its Cerenkov threshold thus destroying the usefulness of the counter for particle identification. Tests were made³ to determine the scintillation properties of argon-nitrogen mixtures as a function of nitrogen percentage and pressure. The results are shown in Fig. 4 where the efficiency for detecting scintillation light as a function of argon gas pressure is plotted for various fractions of nitrogen. It can be seen that an 85% argon, 15% nitrogen mixture keeps the scintillation light level below 1%. We consider this fraction to be the optimum mixture, the addition of more nitrogen will cause the unnecessary absorption of Cerenkov photons.

Results

The Cerenkov counter was initially tested with the discriminator electronics in a 10 GeV/c negative pion beam at SLAC. The threshold behavior of the counter is shown in Fig. 5. Here the efficiency is shown as a function of Cerenkov gas pressure for a 90% argon — 10% nitrogen and a 100% nitrogen radiator. The efficiency rises to 98.4% for the 90% argon — 10% nitrogen mixture. The small inefficiency is consistent with the antiproton contamination in the beam. Unfortunately there was no low energy beam available at SLAC with which to measure the momentum dependence. The effect of nitrogen absorption is clear. If the nitrogen curve is corrected for absorption in order to agree with the argon curve, the resulting value obtained for the absorption length is within 10% of the published value.⁴ The argon/nitrogen gas used both had purities of 99.999% which was sufficient to make absorption by gas impurities unimportant. The solid curve in Fig. 5 is a fit to the data and shows the efficiency expected for $N_0 = 43.5$ based on Poisson statistics.

The counter was further tested in a 10 GeV/c e^+ beam using the previously described low-noise preamplifier and ADC. The performance of the test vessel was evaluated by calculating N_0 (from the Cerenkov efficiency) for a series of ADC pulse height cuts at a constant pressure of 3 atmospheres absolute. The results are shown in Fig. 6. Here N_0 is plotted as a function of ADC channel cut. The ADC pulse height spectrum is shown in Fig. 7. ADC channel 70 is 4 standard deviations from the mean of the widened pedestal and represents an observed N_0 of 65 (see Fig. 6). Using this value of N_0 we can deduce the efficiency of a 16 atmosphere system proposed for the HRS. Taking into account bending in the magnetic field, finite beam crossing

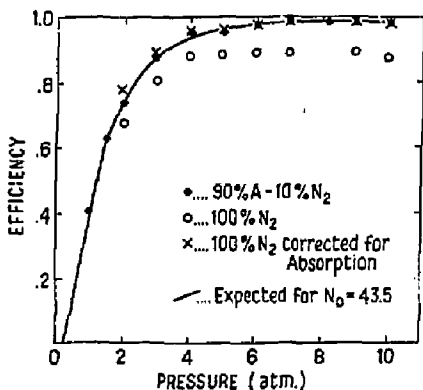


Fig. 5. Efficiency of the counter as a function of pressure for various gas mixtures.

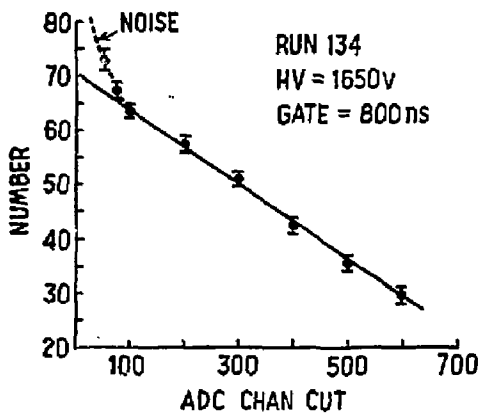


Fig. 6. The measured value of N_0 as a function of ADC channel cut.

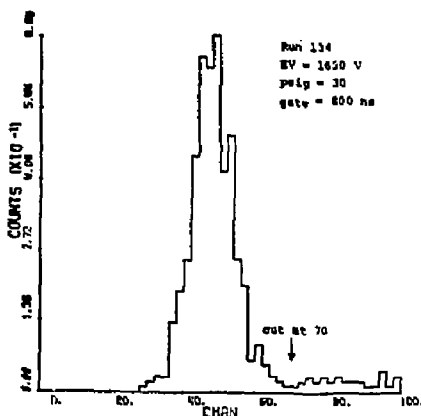


Fig. 7. The ADC pulse height spectrum showing the pedestal representing preamplifier noise.

size, etc. and incorporating the geometry of Fig. 1, the efficiency as a function of momentum was evaluated using Monte Carlo techniques. The results of this study are shown in Fig. 8.

The first torus was installed in the HRS detector during the summer of 1981 and collected data during the fall. Construction of the remaining tori and electronics is to proceed through the spring of 1982 with plans to install the complete system during the summer.

We would like to extend our gratitude to R. Thun for general advice and assistance; also to B. Cork for his assistance with the mirrors. We would also like to thank the SLAC Linac Operators for their help with the beam.

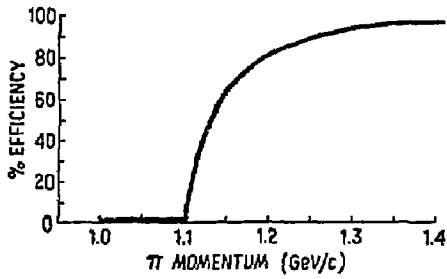


Fig. 8. Expected efficiency of a system of counters as a function of π momentum.

References

1. J. Seguinot and T. Ypsilanti, *NIM* 142, 377 (1977).
2. J. Chapman, D. Meyer and R. Thun, *NIM* 158, 387 (1979).
3. N. Harnew and D. Meyer, *NIM* 186, 513 (1981).
4. Y. Tomkiewicz and E. Garwin, *NIM* 114, 413 (1974).
5. E. C. Y. Inn *et al.*, *J. Chem. Phys.* 21, 1648 (1953).
6. G. Hass and R. Tousey, *J. Opt. Soc.* 49, 593 (1959).

A TRANSITION RADIATION DETECTOR FOR LEP EXPERIMENTS*

B. Bauche, V. Commichau, M. Deutschmann, K. Hangarter,
P. Havelka, D. Linnhöfer, W. Struczinski and M. Tonutti

III. Physikalisches Institut Technische Hochschule Aachen, Aachen Germany

Summary

We are planning to build a transition radiation detector TRD for the identification of prompt electrons in one of the proposed LEP detectors. Tests to be described in this paper show that rather little space is required for such a TRD to achieve a n/e rejection of at least 20 : 1 at 95% acceptance for electrons with momenta in excess of ~ 2 GeV/c. Combining the TRD with an additional electromagnetic shower calorimeter in the LEP detector, a total hadron rejection of the order of 10^3 : 1 or better can be obtained.

Introduction

Transition radiation TR is emitted when a fast charged particle crosses the boundary between two materials of different dielectric constants, e.g. a dense material and a gas. Highly relativistic particles produce these TR quanta in the x-ray-region (typically 5 - 15 keV) in a narrow forward cone. Unfortunately the average energy loss per interface is very low: $E = \frac{2}{3} \tau \omega_p \gamma$, where ω_p is the plasma frequency of the dense material and $\gamma = E/mc$. To overcome the small factor $\alpha/3$ one needs several hundred interfaces of alternating slabs of material (typically ~ 10 μ m thick) and gas (e.g. air or helium ~ 200 μ m thick) to produce sizeable TR signals in a subsequent xenon wire chamber. Optimum materials for such radiators have to combine high electron density (large ω_p), on one hand, with low atomic number Z, on the other, to reduce self absorption of TR quanta in the radiator. Some choices of materials more or less fulfilling both conditions are listed in Table 1.

Table I

Material	$\tau \omega_p$	Comments (availability)
Li	14	best radiators
LiH	19	but safety
Be	27	problems
B	31	not available
B ₄ C	32	in thin form
C	28	fibres, foam etc.
mylar (C ₅ H ₄ O ₂)	24	inexpensive but
polyethylene (CH ₂)	19	less efficient

The TRD model set up

Lithium as one of the best radiator materials has been used with good success by the Willis group¹ in a practical TRD at the CERN ISR. Lithium, Beryllium and their compounds are, however, highly toxic, particularly in finely distributed form. Therefore, their application in large quantities, of the order of tons, in an underground hall at LEP appears to be prohibitive. A reasonable and not too expensive compromise in efficiency is carbon, being available in form of fibres of 6 - 12 μ m diameter at densities between 1.6 and 1.85 g/cm³. The radiators of the model TRD to be described below have been produced from irregularly stacked short cut fibres pressed to overall densities between 0,06 and 0,15 g/cm³ to keep average fibre to fibre distances in the 100 - 200 μ m range (formation zone in air). A problem arises from the fact that the fibres tend to stick together to form clusters of aligned filaments, thereby reducing the required air gaps. The problem is worse for high density fibres which, due to their brittleness, can only be delivered with a thin (rather adhesive) coating.

Fig. 1 shows an experimental set-up recently tested at DESY in an electron beam at momenta between 1 and 6 GeV/c. The TRD is composed of 5 carbon radiators, each followed by a 1 cm thick multiwire proportional chamber filled with 95% xenon plus 5% CH₄, or with 90% xenon plus 10% C₂H₄ during different parts of the

* Work supported by the Bundesminister für Forschung und Technologie, Federal Republic of Germany

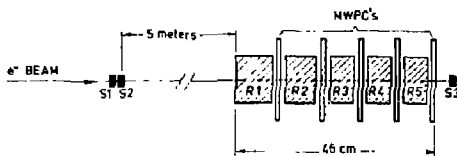


Fig. 1. Schematic view of the test set-up showing 5 carbon radiators R1-R5, each followed by a xenon chamber in a beam defined by counters S1-S3.

run. The chambers are identical to those described in reference ². The radiators were not of equal length but staggered with 10, 6 and 3 x 5 cms for the 5 units, respectively, giving the detector a total length of 46 cm (including gaps at the chambers). Staggering reduces the detector length and makes average signals in all chambers equal, since the TR produced in one of the radiators is not fully absorbed by the subsequent chamber but partly added to that of the following unit.

The finger counters S₁, S₂ and S₃ defined a beam size of 1 cm² in the chambers. In the so defined beam region four wires in each chamber (5 mm wire spacing) were connected in parallel to a fast charge sensitive preamplifier with two outputs feeding two separate channels, one for integral pulse height measurements and the other - with sharp differentiation - for cluster counting. Both informations were transferred via CAMAC into a PDP11. The gas gain was monitored by means of Fe⁵⁵ sources attached to each chamber. The electronic stability was regularly checked with artificial pulses induced on the sense wire.

Results

Fig. 2 shows measurements of the mean (integral) pulse height per chamber as function of the electron momentum. All errors (not indicated) are of the order to 0.2 - 0.4 keV and result from uncertainties in the pulse height calibration. The points on the central curve (c) were obtained with all radiators taken out of the beam; i.e. they represent the mean ionization loss -dE/dx and are well compatible with a Fermi Plateau as shown by the horizontal line. Different symbols of points represent different types of radiators and/or of quenching gasses (CH₄ or C₂H₄).

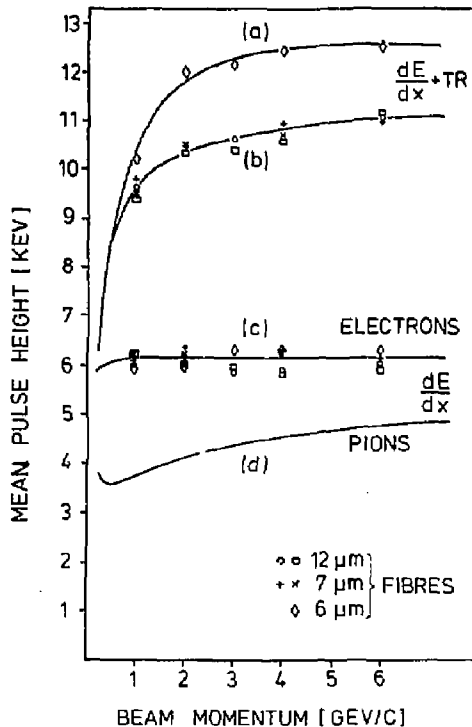


Fig. 2. Mean pulse height as function of the beam momentum. Points on the curves (a) and (b) are measured with radiators in the beam, those on curve (c) without radiators. Curve (d) is taken from reference ⁴.

Corresponding points on the two upper curves (a) and (b) were measured during neighbouring running hours with radiators in place. Points marked "*" were taken with the full set of 5 radiators, whereas for all other measurements only one radiator of 10 cm length in each case and one chamber were used. The upper two curves are eyeball fits through the points with partial adjustment to former measurements taken below 1 GeV/c.² The points on curve (a) are obtained with our best radiator made of 6 μm high density (1.85 g/cm³) fibres which, to avoid clustering, have been treated specially³ by washing in acetone and by blowing up in an air stream (a method probably not applicable in case of large quantities). All other radiators show a very similar performance, in

spite of so different fibre diameters as 7 and 12 μm . The 12 μm fibres were, however, of low density, i.e. 1.6 g/cm^3 as compared to 1.7 g/cm^3 in case of the 7 μm type. Other low density materials like carbon foam and hollow spheres have also been tested and gave poor results.³

The shape of the lower curve (d) in fig. 2 marked "pions" is taken from measurements of Walenta et al.⁴ of the ionization loss in xenon at atmospheric pressure. It has been normalized to the Fermi plateau of our electron data (curve c) and will be used in the following part to calculate the m/c discrimination. (A pion beam was not available during our tests.)

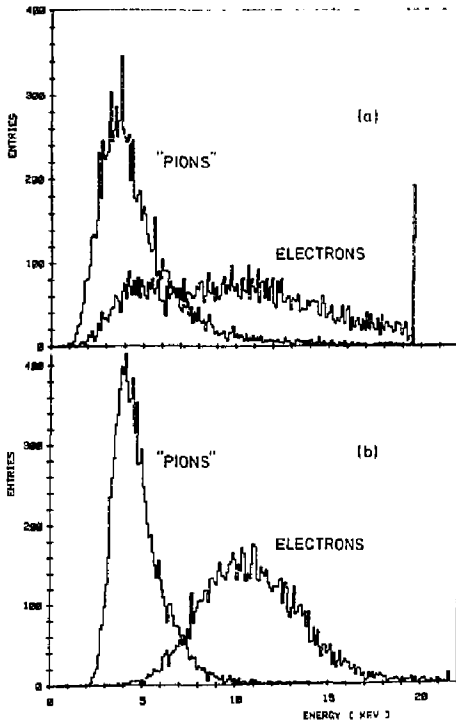


Fig. 3. Pulse height distributions: (a) single hits, (b) the arithmetic mean over 5 chambers. Corresponding histograms contain equal numbers of entries.

Fig. 3 shows in its upper part (a) pulse height distributions from measurements with and without radiators at 6 GeV/c electron momentum. The Landau distribution marked "pions" originates from our electron data without radiators scaled down in the abscissa by a factor of 0.71 as obtained from the normalization in fig. 2. The effect of transition radiation by electrons is clearly seen, although the two distributions still strongly overlap. The overlap is reduced to about 5% in the lower subfigure (b) where the arithmetic mean over the five chambers is plotted.

Applying simple pulse height cuts in distributions of the type shown in fig. 3b we obtain in fig. 4 the pion contamination as function of the electron acceptance. The vertical position of both curves is subject to systematic errors resulting from the above mentioned uncertainties of the pulse height calibration. The figure shows that e.g. at 95% electron acceptance and for momenta above 2 GeV/c the contamination by pions is of the order of 5%.

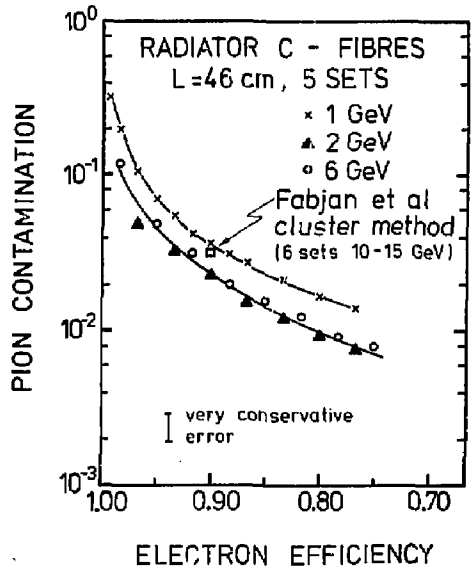


Fig. 4. The pion contamination as function of the electron acceptance.

Fig. 4 also shows a single point from a publication of Fabjan et al.⁵ which compares well with our data. It is obtained with a similar set-up but with

the cluster method and is valid for 6 sampling units at somewhat higher momenta of 10 - 15 GeV/c.

We should mention that our results on electron versus pion discrimination by means of the cluster method are roughly comparable to those found with the (integral) pulse height method but show a tendency to be somewhat inferior. We therefore do not present them here.

It is interesting to see which e/π discrimination would result with our best radiator made of high density fibres. Having only one radiator available we simulated a set of 3, 4 and 5 sampling units by taking consecutive independent events. The result is shown in fig. 5. Comparing with fig. 4 one sees that an improvement by a factor of ~ 5 could be achieved.

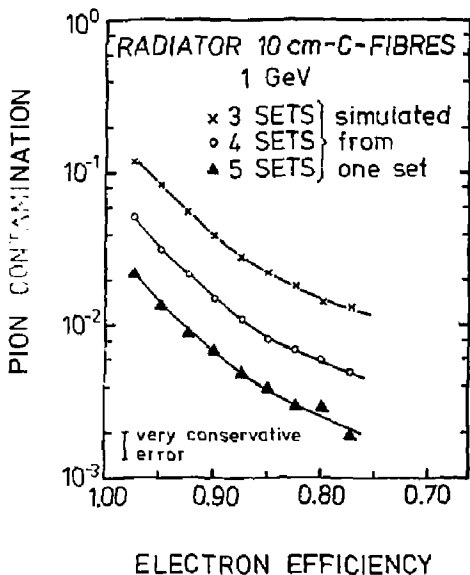


Fig. 5. Same as fig. 4 but from measurements with one radiator (6 μ m fibres) only, simulating 3 - 5 sampling units

The TRD for LEP Experiments

Fig. 6 is a schematic view of the ELECTRA detector recently proposed⁶ for experiments at the large electron-positron storage ring LEP. One of the salient features of this detector will be good lepton identification and high precision in charged particle

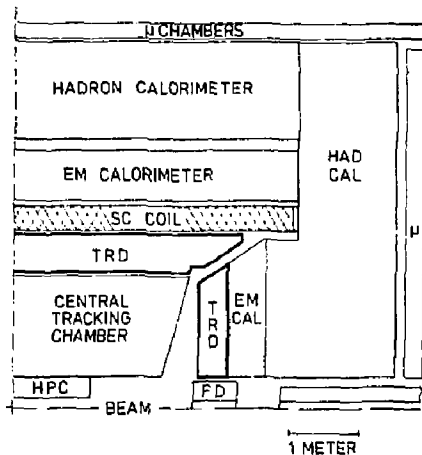


Fig. 6. Schematic view of one quarter of the proposed ELECTRA detector for LEP.

tracking and photon measurement. The figure shows that inside a superconducting coil (1 Tesla) of 4.6 meter inner diameter two types of transition radiation detectors, a barrel TRD and two endcap TRD's will be arranged to cover $\sim 85\%$ of the full solid angle. According to actual plans, the barrel TRD will be arranged in form of 16 segments and each endcap TRD will consist of 4 quadrants. Both types of TRD will be composed of 5 sampling units and will be ~ 46 cm thick, i.e. most probably they will be structured according to our test set-up shown in fig. 1.

The intention is to identify prompt electrons by two fully independent methods, the TRD's and the electromagnetic shower calorimeters, whose positions are shown in fig. 6. As the two devices are expected to provide electron versus hadron discriminations at the few percent level, the total hadron rejection will be of the order of $10^3 : 1$ or better.

References

1. J. Cobb et al., Nucl. Instr. and Meth. 140 (1977) 413.
2. V. Commichau et al., Nucl. Instr. and Meth. 176 (1980) 325.

3. A. Stulgies, Diplomarbeit, III. Physikalisches Institut Technische Hochschule Aachen, June 1981 (unpublished).

4. A.H. Walenta et al., Nucl. Instr. and Meth. 161 (1979) 45.

5. C.W. Fabjan et al., Nucl. Instr. and Meth. 185 (1981) 119.

6. The ELECTRA Collaboration (Aachen, Belgium, Cambridge, CERN, Clermont-Ferrand, Frascati, Hamburg, Imperial College, LAPP, Liverpool, Marseille, Naples, Oxford, Queen Mary College, Rome, Rutherford, Siegen, Technion, Tel Aviv, Vienna, Weizmann). Letter of Intent to study e^+e^- Annihilations at LEP. January, 31, 1982.

SPARK COUNTER WITH A LOCALIZED DISCHARGE

G.V.Fedotovitch, Yu.N.Pestov and
K.N.Putlin

Institute of Nuclear Physics,
630090, Novosibirsk 90, USSR

Summary

The principle of operation of spark counter with a localized discharge are described from the view point of the improvement of its time characteristics. The application results of these counters in the experiment at the colliding beam facility VEPP-2M and status of the spark counter program in Novosibirsk are discussed.

Introduction

We see two main application of spark counters with a localized discharge [1] in detectors for experiments at colliding beam facilities: 1) precise time measurements for the particle identification by TOF and 2) an application in the electromagnetic shower and hadron calorimeters for the energy, coordinate and time measurements. The advantages of these spark counters compared to others gaseous detectors and scintillation counters are the high time resolution (~ 10 times better than that for scintillation counters) and the same accuracy in position measurements as that in the case of drift chambers. The pulse amplitudes of few volts and a rise time ~ 0.1 ns simplifies the electronics.

The operation principle of these counters will be described from the view point of improvement of its time characteristics. The results of the application of the counters in the colliding beam experiments at the VEPP-2M facility and the spark counter program status in Novosibirsk are discussed.

1. Spark Counter with a Localized Discharge

The spark counter with a localized discharge consists of two plane-parallel electrodes separated from each other by a gas gap. These electrodes are supplied with a constant voltage above the threshold value at which the particles begin to induce discharges between the electrodes. The sparks discharge a limited area of electrodes. The radius of this region is of the order of the spark gap size. Under these conditions the sensitivity to the particles situated on the remaining counter area is preserved. Discharge location is achieved by using semiconductive glass with high resistivity ($10^9 + 10^{10} \Omega \cdot \text{cm}$) for one of the counter electrodes and choosing a special gas mixture which absorbs photons prior to their travelling to the regions of the high electric field [2].

A principal lay-out of the counter is shown in Fig. 1. The anode is made of the semiconductive glass and the cathode is an ordinary glass onto which a layer of copper is vacuum-deposited. A typical gas mixture

consists of a noble gas with an addition of

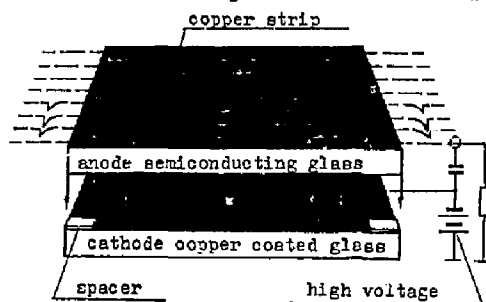


Fig. 1 The principal lay-out of the localized discharge spark counter.

organic gases whose total absorption spectra cover a wide range of photon wavelengths below 225 nm: 2.5% 1,3 butadiene; 1.9% ethylene; 10% isobutane; and 85.6% argon under a total pressure of 12 atmospheres (Fig. 2).

The signals propagate in both directions of the counter along the strip transmission lines formed by the cathode and conductive strips 10 mm wide. These copper strips are deposited onto the high-resistivity electrode's surface opposite to the spark gap (Fig. 1). The pulse amplitude is several volts at a load of 50Ω . The arrival times of the signals from the opposite ends of the counter τ_1 and τ_2 provide information on the time of particle passage ($(\tau_1 + \tau_2)/2$) and

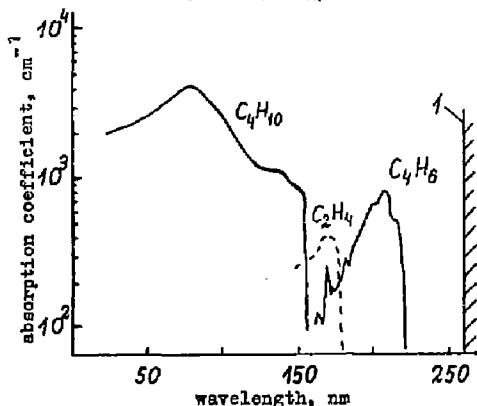


Fig. 2 Photon absorption coefficient for gas mixture used in spark counter: 1 - red boundary of the photoeffect for copper.

the coordinate along the strip lines $((x_1 - x_2)/2)$. The transverse coordinate may be determined by using the standard procedures for finding the centre of gravity of the signals induced on strips.

Counters have been constructed with areas up to 30 cm x 30 cm and with the 1.0, 0.2 was achieved at a gap of 0.1 mm and was $\sigma_x = 24$ ps. The accuracy of the coordinate along the counter's strips is measured to be equal to ≈ 0.2 mm.

2. Some possible ways of improvement of the counter time characteristics

According to streamer's theory, electron in the strong electric field quickly avalanches, and this process can be described by

$$N = e^{\lambda X} \quad (1)$$

where X is the distance from the start point of an avalanche, and λ - the first Townsend coefficient [3]

$$\lambda = A \cdot P \cdot \exp(-B/P/E) \quad (2)$$

where A and B are the constants depending on gas mixture; P, E are the applied gas pressure and electric field.

When the number of electrons $N_{cr} \sim 10^8$ ($\lambda X \sim 20$), an avalanche turns into streamer, which quickly bridges the counter gap [3]. Hence the time delay from single electron is defined by formula

$$t_D^{(1)} = \frac{2Q}{2V} \quad (3)$$

where V is the electron drift velocity.

The delay time fluctuation is defined by the fluctuations both of gaseous amplification and transition moment from avalanche to streamer. Both of them are proportional to the delay time and therefore, the total time resolution is equal to

$$\sigma_x^{(1)} = a t_D = a \cdot \frac{2Q}{2V} = \frac{\beta}{2V} \quad (4)$$

where a and β are proportional coefficients.

In the gas of counter relativistic particle creates on average, N_0 (1/cm) of primary electrons. If the average distance between them is more than the characteristic length $1/d$ where the avalanche growth by "e", then it is possible to consider the development of avalanches independently.

The situation in the counters is close to this case as

$$1/N_0 \sim 25 \mu\text{m} \gg 1/d \sim 2 \div 4 \mu\text{m}.$$

The delay time fluctuations are determined by the transition moment from the first (in time) avalanche to the streamer. In this case, the distribution of discharge delay time can be written by the formula

$$F(t) = \sum_{N=1}^{\infty} \frac{N^N e^{-N}}{N!(1 - e^{-N})} \phi(t) \left[\int_0^t \phi(t') dt' \right]^{N-1} = \\ = \frac{N}{(e^N - 1)} \phi(t) \cdot \exp\left[N \cdot \int_0^t \phi(t') dt'\right] \quad (5)$$

where $\phi(t)$ is the delay time distribution for a single electron; N - the number of electrons, with the average number of primary electrons \bar{N} , which may cause the discharge in

the gap. The calculations performed for the distribution (5) with the normal curve [4] for $\phi(t)$ and the same with

$$\phi(t) = \frac{1}{2} \exp(-t/1) \quad (6)$$

vary slower compared with \sqrt{N} dependence of the delay time fluctuation on \bar{N} (Fig. 3).

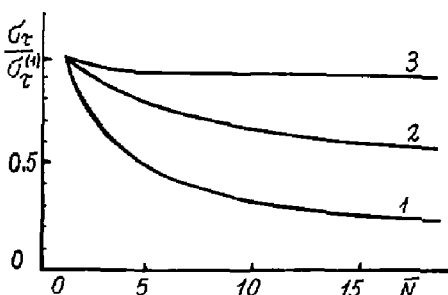


Fig. 3 The time resolution dependence on the number of primary ion pairs:

(1) $\sigma_x/\sigma_x^{(1)} = 1/\sqrt{N}$; (2) the calculation of Eq. (5) with $f(t) = \exp(-t^2/2)/\sqrt{2\pi}$; and (3) the same with $f(t) = \exp(-|t|)/2$.

The comparison of time resolution for various number of initial ion pairs in the gap was made experimentally. With the pressure of a gas mixture increased by a factor of 1.5, the time resolution did not change with the accuracy of 10% at the same overvoltage. With the spark gap increased by factor of 1.85, the time resolution measured with the same accuracy changed in proportion with the time delay (4). The results of these experiments show slower compared with \sqrt{N} dependence of the delay time fluctuation on \bar{N} .

The time resolution and delay time dependences on voltage applied to electrodes are given in Fig. 4. One can see, that the ratio of delay time to the time resolution is approximately constant and both are changing very rapidly with the voltage increase. However, when the high voltage is about two times higher than its threshold value the main discharge from particle is accompanied by afterpulses, and their number increases rapidly with the high voltage.

The model explaining all our experimental results consists in the assumption that the avalanches series develop in the region around the main discharge, where the electric field is small, which results in the discharge in the region where the voltage is above its threshold value (Fig. 5). According to this model the initial electrons, appear from the cathode under influence of low energy photons (220-250 nm) where the gas mixture has no absorption (Fig. 2). These photons couldn't ionize the gas molecules, since their energy is less than ionization potential. Experimental facts explaining by this model, consist in the following.

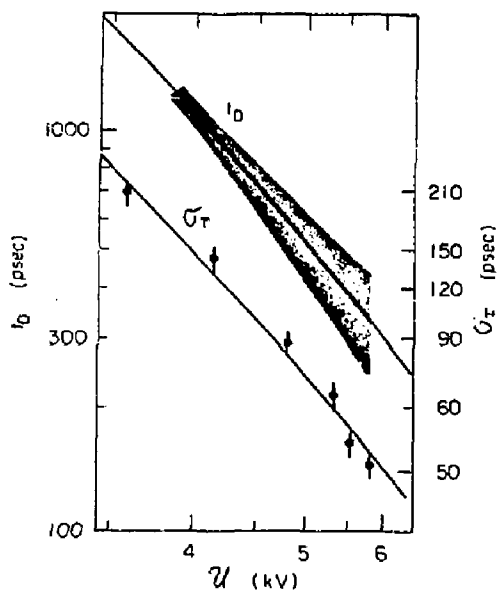


Fig. 4 The delay time t_D and time resolution σ_T versus the voltage U for the spark counter with the 0,2 mm gap.

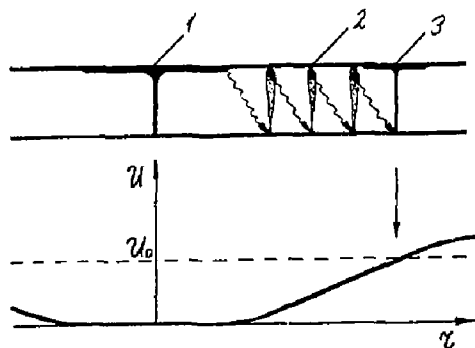


Fig. 5 The model of the afterpulse: 1 - the main discharge, 2 - avalanches serie, 3 - the afterpulse. The curve shows the high voltage distribution on the distance of the main discharge. U_0 - the threshold voltage.

1. The number of afterpulses does not increase with increasing the absorption component pressure ($\lambda < 220$ nm).
2. The average delay time between the main pulse and the afterpulse $\Delta t \sim 100$ ns (Fig. 6) one can explain with the time necessary for the electron avalanches serie creator in a low electric field.

3. The afterpulse amplitude is less than the main pulse amplitude, since it takes place in the electric field about threshold value.

4. The dependence of afterpulses frequency on the properties of polymer film on the electrode surface was observed.

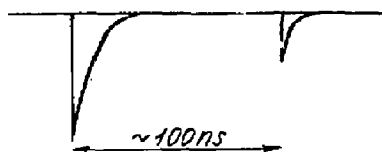


Fig. 6 A main pulse with afterpulse.

The gas mixture, used in the counter, has no absorption for the photons with the wavelengths ranging from 220nm to the photo-effect red boundary for an copper cathode. For the first turn-on of counter after its assembly, the "burning-in" period is required to obtain the localized discharge. This is accomplished using an intense radioactive source, and at the same time, high voltage is slowly increased. During this initial period of use, the electrode surfaces are coated with a film of polymerized gas, changing the work function of electrodes and localizing discharge. The properties of this film depend on the gas mixture. As was shown, the adding of a small quantity of diethyl ether results in the film formation, which reduces the number of afterpulses and enables to reach the higher overvoltage and hence to improve the time resolution. The time distribution of events with cosmic particles obtained for two counters with 0,1 mm spark gaps and each 1×11 cm² in size, is shown in Fig. 7. The

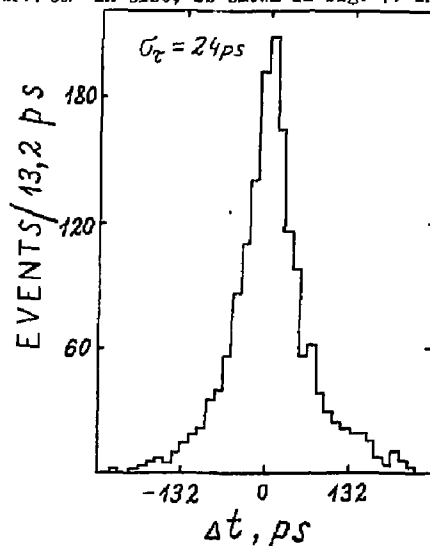


Fig. 7 Distribution of the time difference of two spark counters.

gas mixture contained 2.5% i-3 butadiene, 1.9% ethylene, 3.3% diethyl ether, 6.6% isobutane, 85.7% neon under the total pressure of 12 atm. The counter time resolution of $\sigma_T = 24$ ps was obtained at an operating voltage 4.5 kV, (the threshold for ionizing radiation to produce discharges was $U_0 = 1.97$ kV). Obviously, the creation of film with higher work function results in further improvement of time resolution.

The full solution of the problem will be using the gaseous admixture absorbing the photons in 220 λ <math>< 250</math> nm range. Our search in this direction does not give us a positive result yet. When this problem will be solved, one can expect the improvement of counter time resolution to $\sigma_T \sim 8$ ps due to increasing the electric field at a factor of two above the previous value. It is supposed that electric field strength of $E \approx 1$ MeV/cm is still too low to produce autoelectron emission from cathode.

3. The Measurement of the Pion Form Factor

The Localized-discharge spark counters were used for the first time in the experiments on measuring the pion form factor near $e^+e^- \rightarrow \pi^+\pi^-$ reaction threshold at the VEPP-2M facility (Novosibirsk) [5]. A time-of-flight spectrometer in Fig. 8 has been designed on the basis of these counters with 0.1 mm spark gap. Two spark counters of 11 cm x 11 cm and 30 cm x 30 cm in size were located at a distance of 12 cm and 62 cm in a vertical plane on both sides of the beam interaction region. They were used for measuring the time of flight and coordinates of the collinear pairs of the produced particles.

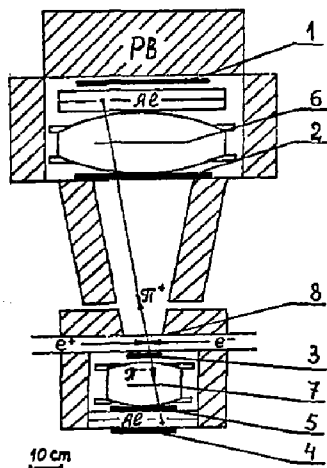


Fig. 8 General view of time of flight spectrometer: 5 - scintillation counters; 6, 7 - upper and lower spark counters, 8 - wall of vacuum chamber of VEPP-2M storage device.

Scintillation counters were utilized as range counters since the pions stopped in an aluminium absorber not reaching scintillation counters 1 and 4. The event distribution over time delay between the passage of the collision pairs through the spark counters at an energy of 2×219 MeV for the particles which are not registered in scintillation counters 1 and 4 is shown in Fig. 9. The delay time between two peaks, $\Delta T \sim 500$ psec, corresponds to the time of flight difference for electrons and pions over the 50 cm differential flight path of the spectrometer.

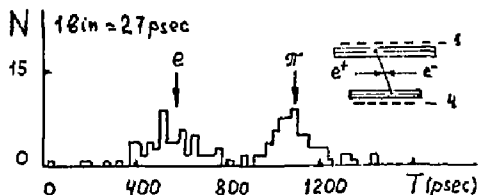


Fig. 9 The event distribution over time delay between operation of two spark counters with no signal from scintillation counters 1 and 4.

For this experiment the gas mixture mentioned earlier was used. The operating voltage was such that the resolution $\sigma_T \approx 50$ ps for each counter. The specific feature of a spectrometer was the absence of conventional tracking chambers, their role was played by spark counters. In this experiment the pion form factor near the $e^+e^- \rightarrow \pi^+\pi^-$ reaction threshold was measured, an electromagnetic pion mean square radius, $\langle r_\pi^2 \rangle = 0.37 \pm 0.05$ f^2 was found, which is in agreement with the result $\langle r_\pi^2 \rangle = 0.31 \pm 0.04$ f^2 of the FNAL-Dubna πe^- scattering experiment [6]. The data collection for this experiment lasted for about 60 days.

4. Status of the spark counter program in Novosibirsk

The typical sizes of detectors for large physical devices are of 2+3 meter. Our estimations and experiments have shown that the manufacturing of spark localized-discharge counters of such sizes seemed to be quite realistic. The main difficulties confronted are due to the preparation of the large, fine, nondefective electrode surfaces before assembly of counters. To find the principal solution of this problem, we are currently constructing a counter of 90 cm long. This counter will be composed of three sections connected in series, each 30 cm in size.

The other important problem is to find new gas mixtures with better time characteristics and less prone to polymerization induced by the discharges.

The comparison of various noble gases influence on the counter characteristics was made. Neon compared to Ar and Xe decreases the threshold value and has good time resolution. The low operating voltage should improve the gas mixture stability. The search of the new absorption admixture, according

to the above mentioned principles, is in progress now.

To our opinion, the advantage of these detectors are the high time and coordinate resolutions in combination with an ease of signal processing, using time-amplitude converters. Moreover, since each particle discharges a small region of the counter, the signal amplitude of several particles is proportional to the number of particles. This may enable one to design electromagnetic shower and hadron calorimeters on the basis of localized discharge spark counters.

References

1. V.V.Parchomchuk, Yu.N.Pestov, N.V.Petrovykh, Nucl. Instr. and Meth., 93, 269 (1971).
V.D.Laptev, Yu.N.Pestov, N.V.Petrovykh, Pribory i Tekh. Eksperim., 6, 36 (1975).
A.D.Afanas'ev, V.D.Laptev, Yu.N.Pestov, B.P.Sannikov, Pribory i Tekh Eksperim., 6, 39 (1975).
V.D.Laptev, Yu.N.Pestov, Pribory i Tekh. Eksperim., 6, 41 (1975).
Yu.N.Pestov, G.V.Fedotovich, Preprint IYAF 77-78, Novosibirsk, (1977).
V.D.Laptev, Yu.N.Pestov et al. Izv. Akad. Nauk SSSR, 42, 1488 (1978).
2. Yu.N.Pestov, N.V.Petrovykh, The certificate of author, USSR, N 349651 (1971).
3. Raether H. "Electron Avalanches and Breakdown in Gases". Butterworth's, London (1964).
4. Kalashnikova V.I., Kosodaev M.S. Elementary Particles Detectors". Nauka, Moscow (1966).
5. I.B.Vasserman, P.M.Ivanov, Yu.N.Pestov et al., Yadernaya Fizika, 33, 709 (1981).
6. E.B.Dally, D.J.Drickey et al., Phys. Rev. Lett., 39, 1176 (1977).

RESULTS FROM THE SLAC PSC DEVELOPMENT PROGRAM

W. B. Atwood
Stanford Linear Accelerator Center
Stanford University, Stanford, California 94305

Plannr Spark Counters (PSC's) have unique detection properties for charged particles. These counters have achieved the best time resolutions of any particle detector.¹ This in combination with their other properties makes PSC's attractive for use in high energy particle physics. At SLAC a program to develop this technology has been in progress since 1978.⁴ Last year we tested a pair of PSC's at the PEP storage ring and I will report on the results here.³

Provided that one can extend the PSC technology to large devices, PSC systems could have time resolutions of 50 psec or better. In Fig. 1 I have plotted the momentum for 50 and 100 psec time-of-flight particle separation over a 1.7 m flight path for various pairs of particle. It is seen from this figure that such a system would make good inroads on the difficult 1-2 GeV momentum region. PSC systems will have a granularity dictated by the cost of electronic channels: at least an order of magnitude over conventional scintillation counter systems is not unreasonable, e.g., a cylindrical array of 1,000 PSC strip lines compared to one hundred or so scintillation counters. This feature will reduce ambiguities arising from more than one particle striking a single detector element.

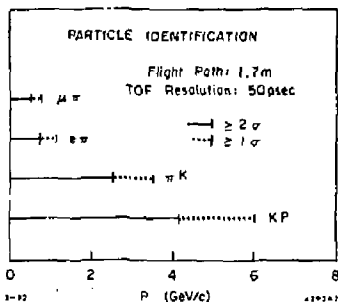


Fig. 1. Time-of-flight separation for various pairs of particle types.

As I will show later in this report, PSC's measure space-time points. The accuracy of the coordinate along the PSC strip-line can be as good as 200 μ m,² while the resolution of the coordinate transverse to the PSC strip will be set by its width. If the strips are made narrow enough to have appreciable pulse height sharing, excellent transverse coordinate information may be obtained. In addition, the pulse height from the PSC strips provide a good indicator of the number of particles striking that strip.

PSC Counter Details

Some details of the PSC design used at SLAC are shown in Fig. 2. Most of our counters have an area of 9 cm \times 9 cm with a gap dimension of 185 μ m. Two to three microns of copper deposited over \sim 100 \AA of chromium on a substrate of ordinary window glass is used for the cathode. Four indium plated brass washers determine the gap dimension. The variations in the gap are required to be less than 3 microns. Semi-

conducting glass with a volume resistance of about $10^{10} \Omega$ cm is used for the anode. Copper strip lines were vacuum deposited on the side opposite the gap to conduct the high frequency signals to coaxial output cables. Coupling to the cathode is accomplished using a parallel plate capacitor with mylar dielectric. The capacitance of the coupler is about 180 pF.

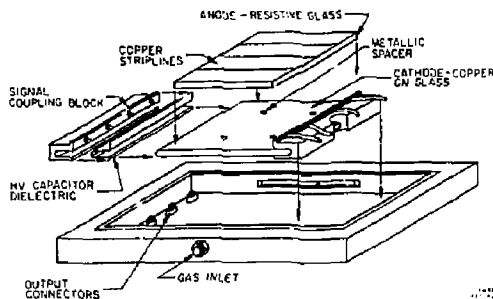


Fig. 2. Exploded view of SLAC PSC construction.

We have run our PSC's at gas pressures in the range of 6-12 atmospheres. The components of the gas we use are 70% argon or neon, 16% isobutane, 3.3% ethylene, 3.3% 1-3 butadiene and 7.4% hydrogen. We have also added up to 1-1/2% ether for some runs.³ The gas is recirculated through the spark gap with a linear velocity of about 10 cm/sec. The only purifiers in the gas system are a .03 μ m dust filters located just in front of the counters' gas inlets.

Using this gas mixture with argon for the noble gas, we observe a threshold for sparks at about 3,500 volts across the spark gap. By 4,000 volts the counter has plateaued with a singles counting rate of about .02 Hz/cm² (constant with the cosmic ray background). At 7,000 volts the counting rate has risen to about .025 Hz/cm² and then quickly increases with further high voltage increases. We operate our counters just before this rapid rise in the singles rates. We attribute the excess counting rate to after pulsing in our counters with second sparks following the initial discharge by up to 300 nsec. Experience has shown that extended operation in this region eventually leads to a "run-away" situation from which the counter does not recover.

The output pulse from our PSC's has a rise time of about 200 psec, is 1-2 volts in amplitude, and has a width of 5-10 nsec. Our measurements of the frequency response of the strip lines; the PSC's have shown them to be similar to RG17 coaxial cable and we attribute the 200 psec rise time in our counters to the limitations of the strip lines. We have measured the rise-time through 80 cm of PSC strip line using a 25 psec rise time input pulse. A 600 psec rise time output pulse was observed.

In Figs. 3-5 I show typical results from our $9\text{ cm} \times 9\text{ cm}$ PSC's obtained using cosmic rays. The time-of-flight shown in Fig. 3 is the time difference between the PSC's. The time for each PSC is the average of the times measured from the two ends of the PSC strip-line with the largest pulse height for that event. The coordinate resolution shown in Fig. 4 is the location of the hit in the PSC inferred from the difference in times from the two ends of the hit strip minus the predicted hit location determined by a drift chamber equipped cosmic ray telescope. Our coordinate resolution is consistent with the least count accuracy of the TDC units used for measuring the times from the PSC strip lines.

Figure 5 shows a PSC pulse height distributions from the cosmic ray running. The PSC was operated at the end of the high voltage plateau curve for this data. The FWHM is approximately equal to 100% of the mean. At lower voltages this distribution becomes narrower.

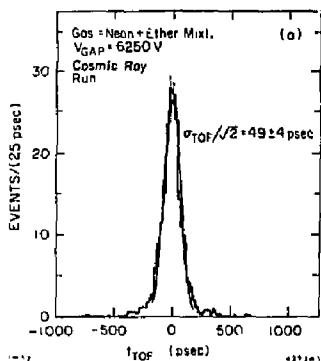


Fig. 3. Time-of-flight distribution from PSC's using cosmic rays.

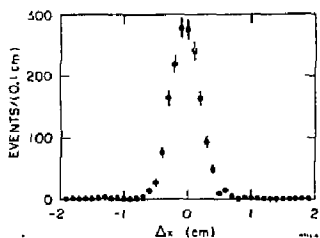


Fig. 4. Spatial coordinate resolution of PSC's along the strip lines from cosmic ray data.

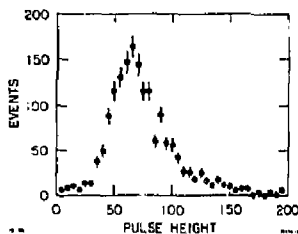


Fig. 5. PSC pulse height distribution from cosmic ray data.

PSC Tests at PEP

In June of 1981 a pair of $9\text{ cm} \times 9\text{ cm}$ PSC's were installed and operated in IR6 at the PEP Storage Ring.³ Figure 6 shows details of this installation. The PSC's were mounted on the face of the DELCO luminosity monitors and covered about 30% of one sectant on each side. The luminosity monitor itself had aperture defining, face counters (F1 and F2) backed by wave-bar read-out, sampling shower counters (L1 and L2). The trigger for data taking was F1.L1.F2.L2 and had a large component of small angle Bhabha scattering. The trigger rate was about 1 Hz. Of these triggers about 1/10 had PSC hits. The pulse heights from L1 and L2 are shown in Fig. 7 and the events with large, correlated pulse heights in the two shower counters are from Bhabha scattering.

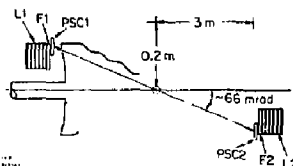


Fig. 6. Schematic of PSC installation in IR6 at PEP.

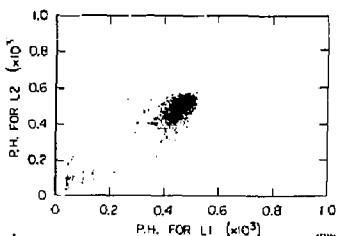


Fig. 7. Scatter plot of luminosity shower counter pulse heights, L1 and L2.

The counting rates into our PSC's in these locations varied between 1 and 5 kHz/81 cm². This rate was a factor of 10 higher than the rates which the counters had been previously subjected to using a Co⁶⁰ source. The RC recovery time for a PSC is approximately equal to the product of the dielectric constant and the volume resistivity (ρ) of the semiconducting glass. For our counters $\rho = 3$ and $6 \times 10^{10} \Omega \text{ cm}$ which results in time constants of ~ 25 and ~ 50 msec. At a 2 kHz rate into our PSC's the mean time between sparks in the same local area ($\sim 25 \text{ cm}^2$) is about 150 msec. Thus we expect to see some rate effects arising from partially recovered regions of the spark gap. These effects may be lowered by about an order of magnitude by using more conductive glass (the lower limit is $\rho \sim 10^9 \Omega \text{ cm}$).^{1,5} The rate effect should worsen the time resolution and lower the pulse height. We observed both.

Figure 8 shows the pulse height distributions from the two PSC's for Bhabha events in which both PSC's recorded a hit (pulse height ≥ 20 channels above pedestal). In both counters we observe a long tail extending to large pulse heights. We interpret these events as ones in which more than one particle struck the PSC. In Fig. 9 scatter plots for L1 vs L2 are shown for the cases (a) when both PSC's are hit and (b) when both PSC's are hit by one particle. The events which are eliminated are likely to be "spray" events caused by electrons (positions) showering off the edges of small angle lead masks in front of the luminosity counters.

The single counter time resolutions are shown in Fig. 10 for Bhabha events. The start for the TDC was the discriminated, beam button, pick-up signal and the TDC stops were the discriminated pulses from the PSC strip lines. The time that the PSC was hit is gotten by averaging the times from the two ends of the hit strip. We see in the comparison of PSC1 and PSC2 that the counter with the higher resistive semiconducting glass has a worse resolution as expected from the high counting rate conditions.

We also observed "albedo events" in our PSC's. These are events in which the pulse heights from L1 and L2 are consistent with the Bhabha signal but only one of the PSC's registered a hit. This may arise from shower particles (mostly gamma rays) coming back out of the shower counter and converting to the PSC. The time distribution for these events is shown in Fig. 10 by the shade area. It is seen to be on the average later and broader than the distribution for the events in which both PSC's were hit, consistent with the longer and varied flight paths albedo events would have to follow to register in the PSC's.

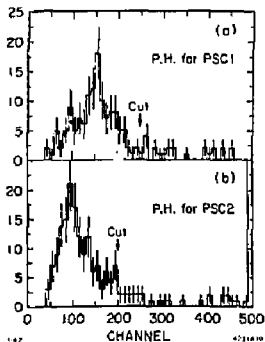


Fig. 8. Pulse height distributions from PSC1 and PSC2 from small angle Bhabha scattering.

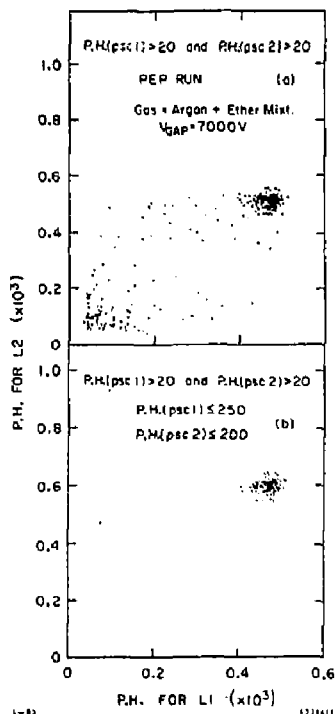


Fig. 9. Correlated shower counter distributions L1 and L2 before (a) and after (b) requiring PSC's to be hit by one particle.

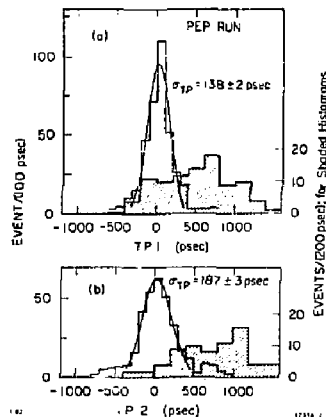


Fig. 10. Single PSC time distributions using the beam crossing signal for the TDC start. Data cut on Bhabha events from L1 and L2 pulse heights.

In Fig. 11 the time difference (t_{TOF}) of the single counter times is plotted. Any jitter in the TDC start signal will be correlated for t_{TOF} and drop out. Using the single counter times (TP1 and TP2) together with t_{TOF} we can estimate the contributions to the measured time resolutions from various sources:

$$\sigma^2(TP1,2) = \sigma^2(PSC1,2) + \sigma^2(X) + \sigma^2(BUNCH)$$

$$\sigma^2(t_{TOF}) = \sigma^2(PSC1) + \sigma^2(PSC2) + 2\sigma^2(BUNCH)$$

The σ 's labeled PSC1 and PSC2 are the counter resolutions, $\sigma(X)$ is the contribution arising from jitter in the start pulse for the TDC's and $\sigma(BUNCH)$ is the contribution from the finite bunch length of the stored beams ($\sigma(BUNCH) = 2$ cm). As such

$$\left. \begin{array}{l} \sigma(TP1) = 138 \text{ psec} \\ \sigma(TP2) = 187 \text{ psec} \\ \sigma(t_{TOF}) = 192 \text{ psec} \\ \sigma(BUNCH) = 68 \text{ psec} \end{array} \right\} = \left\{ \begin{array}{l} \sigma(PSC1) = 76 \text{ psec} \\ \sigma(PSC2) = 148 \text{ psec} \\ \sigma(X) = 93 \text{ psec} \end{array} \right.$$

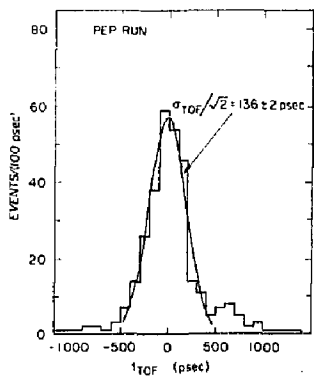


Fig. 11. Time difference of PSC1 and PSC2 measured on Bhabha events.

Due to the highly collinear nature of Bhabha scattering the locations of the hits in our PSC's should be anticorrelated. The PSC strip lines were oriented to be vertical and perpendicular to the beam direction. We call this the Y coordinate. In Fig. 12(a) the Y coordinate is plotted for each PSC derived from the time difference of the two measured times on the hit strip. (The signal velocity on the PSC strip lines is about 15 cm/nsec.) Figure 12(b) shows the sum of $Y(PSC1)$ and $Y(PSC2)$. The width of this distribution has contributions from the least count accuracy of the TDC's ($\sigma(TDC)$), radiative correction to Bhabha scattering ($\sigma(RAD)$), and variations in the vertical position of the beam ($\sigma(BEAM) < 1$ mm). We calculated $\sigma(RAD)$ using a Monte Carlo program and estimate it to be ~ 2 mm. Using these we estimate $\sigma(TDC) \sim 18$ psec (2.6 mm) which is not inconsistent with the TDC accuracy due to its 50 psec bins ($50 \text{ psec}/\sqrt{2} = 35 \text{ psec}$).

A major concern was the lifetime of PSC's under storage ring conditions. Both PSC1 and PSC2 were powered up for about 150 hours with circulating beams present. At the start of the PEP running PSC1 was about 1 year old and PSC2 was 2 months old. We observed

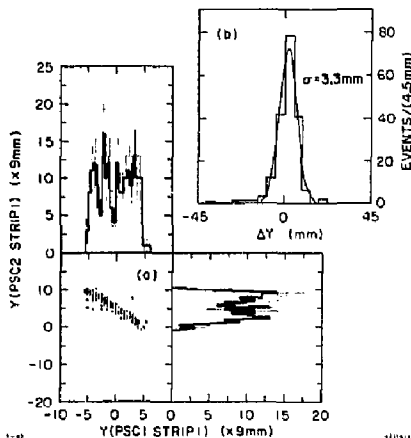


Fig. 12. (a) PSC1 and PSC2 Y coordinate correlation for Bhabha events, and (b) sum of $Y(PSC1) + Y(PSC2)$ for Bhabha events.

no deterioration in these PSC's operating characteristics during or after the PEP running. In fact the time resolution measured on cosmic rays shown in Fig. 3 was taken with these PSC's after PEP had shut down for the summer.

Our conclusions from this test are:

- (1) There were no surprises. PSC's perform as other HEP particle detectors even under high rate conditions near the beam.
- (2) High rates degraded pulse height and time resolution by a factor of 2-4. The rate dependence was due to the unnecessarily high resistance of the semiconducting glass anodes. The rate dependence can be improved by a factor of 10 by using more conductive glass.
- (3) The correlated information of two times and one pulse height from each strip gives a space-time point of good accuracy and the strip multiplicity for each event. This provides a powerful tool for understanding various event types.
- (4) PSC's can withstand harsh experimental environments.

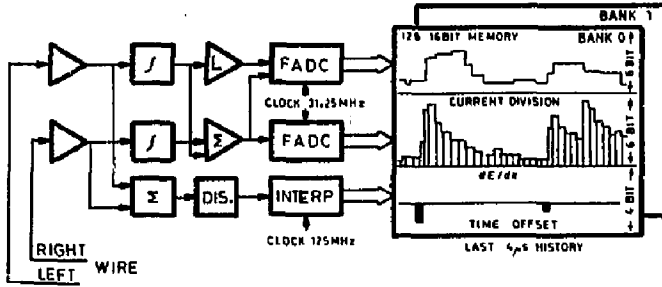
The SLAC PSC development project is presently building two 10 cm x 120 cm counter. We are also making a 20 layer, atmospheric pressure, electromagnetic shower counter using PSC's as the sampling detectors. And finally, we are investigating the use of various semiconducting plastics from which to make the electrodes.

References

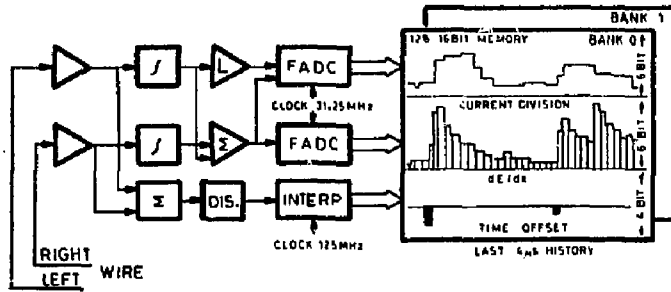
1. G. V. Fedotov *et al.*, Spark Counters with a Localized Discharge, these proceedings.
2. W. B. Atwood, SLAC Summer School (1980), SLAC Report No. 239, p. 287.
3. W. B. Atwood *et al.*, SLAC-PUB-2848 (to be published).
4. Yu. Pestov, Proceedings of INS International Symposium on Nuclear Radiation Detectors, 1981.
5. V. D. Laptev *et al.*, UDC 539.1.074.27, 1698 (1975); V. D. Laptev *et al.*, UDC 539.1.074.27, 1703 (1975); A. D. Afanas *et al.*, UDC 539.1.074.27, 1701 (1975); Yu. N. Pestov *et al.*, SLAC translation 184 (1978).



ELECTRONICS



ELECTRONICS



MICROPROCESSORS IN DETECTORS AND ANALYSIS*

Eric J. Siskind
 ISABELLE Data Acquisition Group
 Brookhaven National Laboratory
 Upton, New York 11973

Copy

Introduction

The increasing need in high energy physics experiments for computation power for both online and offline applications, coupled with the current "microprocessor revolution," has led us to examine the use of microprocessors in various aspects of HEP computing. The following article is a brief (and admittedly somewhat biased) review of current hardware products, the costs of developing and producing hardware systems, and the costs of providing appropriate software support tools which allow one to make effective use of physicists' time, and the applicability of certain systems to the various needs of HEP computing.

What is a Microprocessor?

The term "microprocessor" is currently used to describe two distinct entities which, although somewhat related, have sufficiently different characteristics, costs, and optimum uses as to merit individual consideration. The following discussion should help elucidate the difference between a microprocessor and a microprocessor!

The first use of the term describes the processing element of a microcomputer system, as distinguished from minicomputers, midcomputers, etc. The hardware is invariably implemented in LSI or VLSI chips, with a complete processor occupying one or a few chips or substrates. Such a processor executes machine instructions which can be generated via assembly of a program written in a language which is identical for all examples of this processor (and often for an entire family of processors, e.g. LSI-11's use of the same assembly language as all PDP-11 processors), or which can be generated via compilation of programs written in FORTRAN, PASCAL, C, or other higher level languages. The execution of a single machine instruction typically requires more than one basic clock cycle of the processor. The machine instruction sets typically contain integer arithmetic, including multiplication and division, as well as logical operations (e.g. bit manipulation), and occasionally implement floating point operations with additional or even integral hardware. The execution of complicated instructions, implying multiple clock cycles per instruction, requires the use of instruction decoding and execution sequencing hardware within the microprocessor. Table I lists several important characteristics of some of the microprocessors of this type which are currently available.

The other use of the term "microprocessor" describes an engine which executes microcode,¹ as distinguished from the usual macrocode instructions. Microcode is in some sense "closer to the hardware," can have instruction formats and widths which differ from application to application using the same hard-

ware, can describe multiple operations (in different execution units) in a single instruction, and typically specifies instructions which execute in one machine clock cycle (although the instruction may contain a field which indicates that it is to be executed multiple times in a row), with each instruction capable of less powerful manipulations than that of macrocode. As an example, it is rare machine of this type which can execute an integer multiply operation without instruction repetition, although exceptions to this rule exist (e.g. FNAL M7²). The hardware for such machines varies quite considerably, with the data paths often built out of MSI chips with SSI control gates in order to obtain a configuration optimized for certain types of calculations. When built in this fashion, a microprocessor may contain hundreds or even thousands of integrated circuit packages. However, LSI chips containing a "slice" several bits wide of either standardized data paths or sequencing logic are commercially available, and are typically expandable to configure machines of arbitrary word width. Such machines are referred to as "bit-slice microprocessors," and a sampling of characteristics of such devices is included in Table II. It should be noted that even with the use of such chips, the instruction format is still dictated by the hardware designer.

Table I. Characteristics of General Purpose Micro-Processors. Source - EDM. 11/11/81

Chip	Word (Bits)	Add. Word (Bits)	Flms (D/A)	Clock Rate (MHz)	Cost (100 lot)
8080	8	16	8/16	1-3	3.70
8085	8	16	8/16	1-5	4.40
5800	8	16	8/16	1-2	4.95-6.20
280	8	16	8/16	2-6	8.00-15.00
8C86	16	16	16	5-10	58.50-127.40
8088	16	16	8	5	14.10
68000	32	23	16/23	6-12.5	86.00-149.00
28000	16/32	24	16	8	35.90
432	32	24	16	8	1470.00

Table II. Characteristics of Bit-Slice Micro-Processors. Source - EDM. 11/11/81

Chip	Width (Bits)	Family	Registers	Clock Rate (MHz)	Price (100 lot)
2901	4	STTL	16	16.67	9.95
2903	4	STTL	16	10	21.00
29203	4	STTL	16	10	?
29116	16	STTL	32	10	?
10800	4	ECL 10K	0	20	48.75
10902	8	ECL 10K	0	50	100.00
10022G	8	ECL 100K	1	50	?

With the notable exception of the SLAC 168/E,³ code for such machines is generated via meta-assembly of symbolic source code in a form which is unique to the particular processor, and is quite difficult to generate. Therefore, such machines rarely employ programs containing more than a few thousand

*Work performed under the auspices of the U.S. Department of Energy.

Hardware Costs

instructions. A typical estimate is that microcode is an order of magnitude more difficult to generate than typical machine assembly language macrocode. This results from the need to specify multiple operations in each instruction, timing problems associated with different propagation delays (i.e., varying number of transfers) associated with moving data into distinct registers, the need to consider the frequently pipelined nature of microcode execution, and the typical lack of sophisticated debugging tools. The 168/E differs from the norm in that its microcode is generated by the translation of the object modules (or load modules) produced by the compilation of FORTRAN programs on the host machine, and so frequently large volumes of microcode are produced, often requiring overlaying in the relatively large program memory.

Although such machines were first developed as a means of implementing the central processors of newer computers with more complicated instruction sets and formats without proportional increase in the amount of hardware in such a processor, they also find applications wherever special processing requirements exist. Table III includes characteristics of the central processors of various computer systems. Note that faster microprocessor clock speed does not necessarily imply faster macroinstruction execution, but that memory access times and the presence of special hardware or additional connectivity in the microprocessor data paths may have far more profound effects (e.g. the VAX-11/780 is around 5 times more powerful than a PDP-11/34, yet the latter machine has the faster microprocessor clock speed). Also, note that the fastest processing units prefer the route of more hardware rather than microcoding instructions (e.g. CDC 7600, Cray I and II). Table IV indicates the variety of microprocessors found in a typical VAX-11/780 system, while Table V gives a sampling of microprocessors which have been developed for use in high energy physics.

Table III. Micromachines in Commercial CPUs

Machine	Cycle Time (Nanoseconds)	μ C Width (Bits)	μ C Length (Kwords)
LSI-11/2	400	22	1
PDP-11/04	260	40	3.25
PDP-11/34	180	48	0.5
PDP-11/45	150	64	0.25
PDP-11/60	170	48	2.5
VAX-11/750	320	80	20
VAX-11/780	200	96	4+:(RAM)
IBM-3081	26	?	?
CDC-7600	25	Not Microcoded	
CRAY I	12.5	Not Microcoded	
CRAY II	4.0	Not Microcoded	

Table IV. Microcoded Processors in a VAX-11/780 System

Model	Description	ALU	μ C Width (Bits)	μ C Length (Kwords)
KA-780	Central Processor	74S181	96	4+1(RAM)
FP-780	Floating Point Unit	74S381	48	0.5
DW-780	Unibus Adapter	None	44	0.5
DR-780	I/O Channel	2901	40	1
RX-02	Floppy Disk	2901	16	1
DMC-11	Serial I/O Unit	74S181	16	1

Table V. Microcoded Processors Developed for HEP

Model	Description	ALU	μ C Width (Bits)	μ C Length (Kwords)
H7 ²	Trigger Processor	10181	64	4
BADC ⁴	Digitizer Processor	2901	48	0.5
TDS ⁵	Digitizer Controller	10181	32	1
168/E ³	Mainframe Emulator	2901	24	32
VCC ⁶	CAMAC Channel	2903	64	4
UPI ⁷	Fastbus Channel	2901	80	2

We now turn to the costs of developing and producing microprocessor systems. There is an implicit assumption in the following discussion that the microprocessor has very little in the way of private peripherals outside of the hardware directly under its control, but instead talks to humans or media via a connection to a host computer. I note in passing that if this is not so, but instead the micro is equipped with a complete set of support peripherals, including terminal, printer, floppy disks, etc., then the cost of such a development system is currently in the range of \$25K.

In developing a hardware configuration for a typical microcomputer such as an 8086 or 68000, a standard estimate might be of order a man-year of engineering plus prototyping costs, or a figure of order \$100K. Considerable design savings may be effected by careful use of existing hobbyist development cards or crate/bus systems such as S-100 or Multibus (or ultimately Fastbus!). On the other hand, the engineering of a bit-slice system involves somewhat higher development costs. A crude estimate for the SLAC BADC system⁶ was 3 man-years of engineering plus \$100K of prototype hardware construction, for a total of \$250K.

The final product board of either type of microprocessor system, containing both processor and memory, has an estimated cost in the neighborhood of \$1K. The estimated processing power of a current 16 bit micro is of order a few times 10⁵ instructions per second, for a cost effectiveness of order a few hundred instructions per second per dollar, while the power and cost effectiveness of bit-slice systems for those applications which can be programmed effectively on them is about an order of magnitude higher than those for the single chip processor. For comparison, note that the cost effectiveness of the best of the current midis or mainframes is only around 10 instructions per second per dollar (e.g. VAX's run around \$100K for a cpu executing around one million instructions per second (MIPS) while the TBM 3081 runs a couple of megabucks for around 15 MIPS of processing power).

This set of numbers leads to two distinct conclusions. The first is that microprocessors are sufficiently more cost effective than current mainframes to merit serious study of their use in conventional compute bound HEP applications such as offline production and Monte Carlos. In addition, their cost effectiveness will shortly bring the use of high level trigger processors constructed from arrays of microprocessors programmed in FORTRAN or some equivalent language and providing instruction processing powers of order 10⁵ instructions per event on data streams of order 10³ events per second into an affordable regime. The second conclusion is that once you have engineered the hardware for a system, you should stick with the hardware until there is a clear need to engineer a new system. As an example, given an engineered 80E in a Fastbus crate with a cost effectiveness of 200 instructions per second per dollar, one should not be tempted to develop a more cost effective piece of bit-slice hardware until that enhanced cost effectiveness will offset the \$250K development, i.e. until the processing requirement exceeds 50 MIPS (50 VAX or 5 CDC 7600 equivalents!) even assuming that the new hardware has infinite cost effectiveness. In real life, there obviously may be some other overriding consideration which necessitates such a hardware development project, but it should not be cost. Similarly, one should typically

not bow to the desires of your hardware engineer to play with the latest new chip which is twice as fast as the old one (and is NOT a plug-in replacement) unless he is willing to pay the development costs out of his pocket. This conclusion will gain even more strength when one adds the costs of software support to the hardware development.

Software Costs

A number of system architectures have been proposed for multi-microprocessor systems for various applications in high energy physics.^{9, 10} These architectures all have the common feature that they contain a number of computers connected by some form of bus to a common host node which is responsible for code development and some of the I/O handling. Each computer can talk to its own local memory and possibly to local peripherals without tying up the multiprocessor bus, and in some cases can talk to other peripherals for I/O purposes via the bus but without the aid of the host. This architecture is also that of the CM*,¹¹ a multiprocessor built from 50 LSI-11's at Carnegie-Mellon University to study such configurations and their operating systems. The unique feature which HEP adds to the CM* is the knowledge that either an application is assigned for all time to a particular processor because of a need to access peripherals that are only connected to that processor (e.g. distributed controls systems), or else that the computing load is naturally divided into "events" which can be distributed among the processors with a time scale which is known to the application programmer, and thus the distribution of work is never handled by the multiprocessor operating system.

Having listed the similarities among such systems, note that such systems differ in whether the slave processors execute the same instruction set as the host and in whether a particular application must be forced into a particular slave or is free to be located in any slave or set of slaves. The software developments necessary to support two particular systems will now be described.

The first system is one in which the slave processor is of a different type than the host, and the application is constrained to live in a particular slave. This is the classic case of microprocessor support using development tools on a remote system. The system in question is the controls upgrade for the SLC linac,⁸ which uses Sytek system 40 as the multiprocessor bus. However, an essentially identical specification has been promulgated for a BNL-LBL-SLAC collaboration¹² which is attempting to introduce Fastbus as the multiprocessor bus to existing PEP experiments, starting with the Mark II. The software specification is as follows: (1) a FORTRAN cross-compiler implementing FORTRAN 77 extended to be essentially compatible with VAX FORTRAN will be provided; (2) a suitable cross-linker and downline loader will be provided; (3) the run-time support system at the slave node will support FORTRAN FORMAT statements (i.e. the programmer need know nothing about the internal machine representation of floating point numbers), timer services (What time is it? Execute a specified routine at a specified time. Execute a specified routing at a specified time from now), and connect to interrupt services (execute a specified routine whenever a specified interrupt driven event occurs); (4) an interactive symbolic cross-debugger will be provided. The last item, which is definitely the most important, will allow a programmer sitting at a terminal on the host machine to place breakpoints in any program executing in any slave proces-

sor, and to investigate variables in the slave program by their symbolic names. It is estimated that the development of such a software support system will cost between \$250K and \$500K.

The second system is one in which the slave processor is assumed to have an instruction set identical to that of the host, and in which the entire set of slave processors is used to boost the processing capacity of the host system. An application can be moved from the host system into the slaves, requesting, at the time of the move, the use of any number of identical slaves available in the slave pool maintained by the host system. The use of an identical instruction set allows the debugging of any new application by developing code with the aid of the host symbolic debugger, followed by transfer to the slave processors with no code changes. A cross-debugger is not provided. The software specification allows any process running on the host machine to perform the following actions: (1) allocate a cluster of slave processors; (2) specify a program to run in any of its slave clusters; (3) get the status of a cluster; (4) wait for the status of a cluster to change (e.g. wait for slave program execution to terminate); (5) connect any logical unit (e.g. FORTRAN device 6) of any cluster of slaves to any file or device on the host, to any logical unit of the host process which owns the cluster, or to any logical unit of another cluster owned by the same host process. This system is being built at BNL to allow a VAX host system to access LSI VAX processors through a Fastbus multiprocessor link. A slight modification of this system may be used in the Fermilab Colliding Detector Facility to allow management of LSI VAX processors via Fastbus for use as a programmable trigger filter. The estimated software development cost is of order \$250K.

This seems to lend us to another pair of conclusions. The first is that given a sufficient initial software effort, it seems possible to develop support tools which can manage microprocessors connected to a host system to perform essentially arbitrary tasks, as long as there is sufficient capacity on the multiprocessor bus and in the host system. In particular, it is not unreasonable to expect that after initial development costs of \$100K for hardware and \$250K for software, a \$1M investment in microprocessors can add of order 100 MIPS of manageable processing capacity (e.g. 10 CBE 7600 equivalents) to any current online VAX system in an experimental pit. In an age of \$50M experiments, this is not a large price to pay for such an outstanding amount of computing. The second conclusion concerns development of software support tools such as those mentioned in the first example above. In general, the \$250K minimum software cost necessary to support a new microprocessor far outweighs the hardware development effort (estimated at \$100K above), and thus again it pays even more to restrain your engineer from his desire to play with the latest chip. In the extreme, the software development cost and software production cost so far exceed the hardware cost that the method of choosing hardware is to find that hardware for which the software development costs will be minimized. Typically, a reasonable additional constraint is that the software support system be designed so as to be immediately compatible with any new hardware releases the manufacturer has in mind for the next 5-10 years.

Of course, these observations are not really new. In fact, in perusing the proceedings of the 1979 Data Acquisition Conference I noted several papers in which the management of arrays or networks

of cheap computers was presented as the outstanding problem of HEP computing for the next decade.^{13, 14} One speaker also indicated that all of his comments had already been made at a conference ten years earlier. The only new development is that a few attempts to build complete integrated hardware/software systems are finally in progress. However, I personally find it exceedingly distressing that, given the exceedingly large development costs for a complete system including the necessary support tools, so many distinct and noncommunicating microprocessor development projects exist in the various laboratories and universities. In my view, the high energy physics community can afford (especially in the light of the current budget problems) to support one 16 bit microprocessor system, and (at the appropriate later date) one 32 bit microprocessor system. Given the extreme difference in costs between an engineer's perception that development requires a hundred dollars or so for the cpu and a few hundred dollars at most for memory, and the total project costs including all overheads and software support of many hundreds of thousands of dollars, anyone who believes that they should start yet another microprocessor development project should be firmly directed towards employment in the private sector.

HEP Computing

Table VI presents a list of some of the computing tasks associated with high energy physics experiments. Of particular importance is the column which indicates whether a task is proportional to the number of physicists on the experiment or the volume of data taken (event size multiplied by trigger rate), or to neither of these. In the last case, the magnitude of the problem is typically still proportional to the overall scale of the experiment. A summary of microprocessor applicability to the tasks follows.

Table VI. Experimental HEP Computing Tasks

Task	Scale	Comp. Rqmt. for Hadron Collider
Control	Neither	10^4-10^5 inst./sec./application
Zero Supp. ^{4, 5}	Data	10^5 channels/event 10^3 events/s
Calibration ⁴	Data	10^4 channels/event 10^3 events/s
Trigger ^{2, 15, 16}	Data	10^4 analog channels/event 10^5 events/s
Event Filter	Data	10^5 inst./event 10^3 events/sec.
Online Mon.	Data	10^7 inst./event 10^2 events/sec.
Production ³	Data	10^7 inst./event 10^8 events/year
Simulation	Data	Identical to Production
Code Dev.	People	10^5 instructions/second/physicist
Physics	People	10^5 instructions/second/physicist

Controls

Control of high voltage, gas systems, cryogenics, etc. was one of the first areas of experimental HEP in which single chip microprocessors were applied. These systems are typically quite limited in computational power requirements, but require special applications coding for each new usage. This is clearly an area in which the availability of a complete development package for a slave of identity distinct from that of the host, complete with interactive symbolic cross-debugging aids, would be most helpful.

Zero Suppression

Intelligent digitizers have now been around for several years, with the SLAC BADC⁴ as the logical culmination of attempts by commercial manufacturers to make "smart" ADC units. Recent developments such as the FNAL TDS/RABBIT⁵ system have concentrated on

improving conversion speed, channel density, and dynamic range, as well as adding redundant paths for fault tolerance in applications with limited hardware accessibility. Given the need to custom design a digitizer controller, as well as frequent constraints on overall speed to minimize deadtime, this has been an area where microcoded hardware rather than general purpose microprocessors have traditionally been applied.

Calibration and Transformation

This function has frequently (e.g. BADC) been, but is not necessarily constrained to be, combined with the zero suppression function. The application typically requires a very small algorithm, and would seem to be a natural for bit-slice implementations. In general, it seems that if the functionality can be added to an existing zero suppressing digitizer, it should be, but if the task requires development of an additional microcoded calibration processor, one should do a careful analysis to see if the use of an existing packaged general purpose microprocessor coded in assembly language would be more cost effective.

Event Filtering

In this category, I include processing which makes a trigger cut based on consideration of an entire event's data buffer, rather than the restricted subset used by most trigger processors (which may even make their decisions before digitization of the majority of the data has commenced). To my knowledge, this type of processing has yet to be attempted in any large, high data rate experiment, probably because the processing power requirements are so immense, although the FNAL Colliding Detector Facility¹⁷ is showing a strong interest in including such an option. The basic requirement here is the need to execute a large algorithm which is probably coded in FORTRAN so that personnel on shift can both understand the trigger and rapidly modify it for changing running conditions and physics needs. This would seem to require an array of 32 bit general purpose microprocessors, although a bit-slice solution along the lines of the 168/E (i.e. equipped with FORTRAN programming tools) is also a possibility.

Online Monitoring

This again requires the use of a FORTRAN coded system handling large algorithms for a sampling analysis of complete events. Recent modular software techniques which divide this analysis into a number of cooperating independent tasks, some being parts of a "standard" analysis, and some being interactive based searches for special characteristics of a restricted class of events, rather than the traditional single large "background" analysis, might slightly favor a uniform architecture cpu booster implemented in 32 bit general purpose microprocessors, which have extensive easily programmed I/O capabilities, over a microcoded emulator approach, but the latter alternative has the virtues both of being a proven performer and of having a better cost effectiveness of the final hardware.

Offline Data Reduction and Simulation

The offline production problem for the SLAC LASS experiment was the original motivation for the 168/E development project. Again, the requirements are FORTRAN and large program memories, and can be met

both by 32 bit general purpose LSI microprocessors or by translated microcode bit-slice systems. Careful analysis of costs is necessary to determine whether or not the better cost effectiveness of the microcoded system is outweighed by the relative ease of programming and upward compatibility with new faster hardware releases of the general purpose microprocessor systems.

A few moments' reflection will hopefully convince you that the vast majority of the tasks which are proportional to the volume of data taken can be tackled with microprocessor based solutions, leaving only the highly interactive problems of code generation and physics results preparation for the types of processors currently in use in the field. Given that the volume of data taken in HEP experiments has been growing considerably faster than the number of physicists, microprocessors can make meeting our future computing needs considerably less painful.

Actually, bit-slice microprocessors have already found considerable use in the areas of zero suppression and data calibration, as well as in some aspects of trigger processing and data reduction. The next major advance will hopefully be the harnessing of current and future generations of complete one chip or few chip processors to the tasks of high level trigger processing, online analysis, and offline data reduction and Monte Carlo generation.

References

1. M.V. Wilkes, Manchester University Computer Inaugural Conference, July, 1951, 16 (1953); M.V. Wilkes, J.B. Stringer, Proc. Cambridge Phil. Soc., pt. 2, 49, 30 (1953).
2. T.F. Droege *et al.*, IEEE Trans. Nucl. Sci., NS-25, 698 (1978).
3. Paul F. Kunr *et al.*, IEEE Trans. Nucl. Sci., NS-27, 582 (1980).
4. H. Breidenbach *et al.*, IEEE Trans. Nucl. Sci., NS-25 706 (1978).
5. T. Droege, paper presented at this conference; T.F. Droege *et al.*, Fermilab Redundant Analog Bus Based Information Transfer system document PIN 52.
6. D.J. Nelson *et al.*, IEEE Trans. Nucl. Sci., NS-28, 336 (1981).
7. H. Larwill *et al.*, IEEE Trans. Nucl. Sci., NS-28, 385 (1981).
8. M. Breidenbach, private communication.
9. R. Manner, B. de Luigi, IEEE Trans. Nucl. Sci., NS-28, 390 (1981).
10. U.O. Hertzberger, Amsterdam Report NIKHEF-H/81-3 (1981).
11. R.J. Swan *et al.*, AFIPS Conf. Proc. 46, 637 (1977); *ibid*, AFIPS Conf. Proc. 46, 645 (1977).
12. F. Siskind, S. Loken, H. Breidenbach.
13. Marvin Johnson, IEEE Trans. Nucl. Sci., NS-26, 4433 (1979).
14. John L. Brown, IEEE Trans. Nucl. Sci., NS-26, 4438 (1979).
15. C. Halatsis *et al.*, CERN Report DD/79/7 (1979).
16. T. Lingjaerde, CERN Report DD/75/17.
17. A.E. Brenner *et al.*, Fermilab Colliding Detector Facility note CDF-108; *ibid*, paper presented at the 1981 IEEE Nuclear Science Symposium.

FASTBUS AT THE FRONT END

R. W. Downing
Loomis Laboratory
University of Illinois, Urbana, IL 61801

SUMMARY

A major consideration in the initial design of FASTBUS was its applicability to front end hardware. A number of features have been incorporated to allow the front end designer a large degree of freedom but still maintain compatibility with the standard.

GENERAL

It is this author's view that we are in an era of great change in electronic equipment for high energy physics. Microprocessors and their cousins, the smart controllers, being incorporated in many designs. We are also now seeing devices such as FPLA's, PAL's, etc. becoming larger, faster, and more useful in replacing large amounts of "discrete" logic. On our doorstep are gate-arrays of all types. Smaller (100-1000 gates) in ECL provide the high speed we need; larger (1000-10,000+ gates) in slower logic families can be designed for certain specialized computations for physics.

All these new devices tend to be design intensive. Mistakes cannot be repaired by cutting plating and patching wires where necessary. The engineer must do more careful design checking before committing a design to hardware. At the same time, we are living with budgets which are not expanding. One solution not available is to hire more people to work on these new designs.

Where does FASTBUS fit in? Many papers over the past several years have discussed FASTBUS in terms of the handling and processing of data. To accommodate the microprocessor revolution this bus standard was definitely needed. CAMAC simply could not provide the necessary bandwidth or multiple control capabilities. Standard assignment of bits in control and status registers have been made for software compatibility. A FASTBUS diagnostic language (FDL) is in the final stage of testing and will be released shortly. FASTBUS also provides a well defined mechanical package. The printed board specification is standard commercial tolerances. The board itself rides in the card guide. Front panels are not necessary and can be eliminated if one feels the cost savings merit it. The voltages specified are standard. The power supplies

are not part of the card cage specification so the user may tailor them to the specific system. FASTBUS fits all around the users design providing standard building block and frees the designer to concentrate on unique parts of the system.

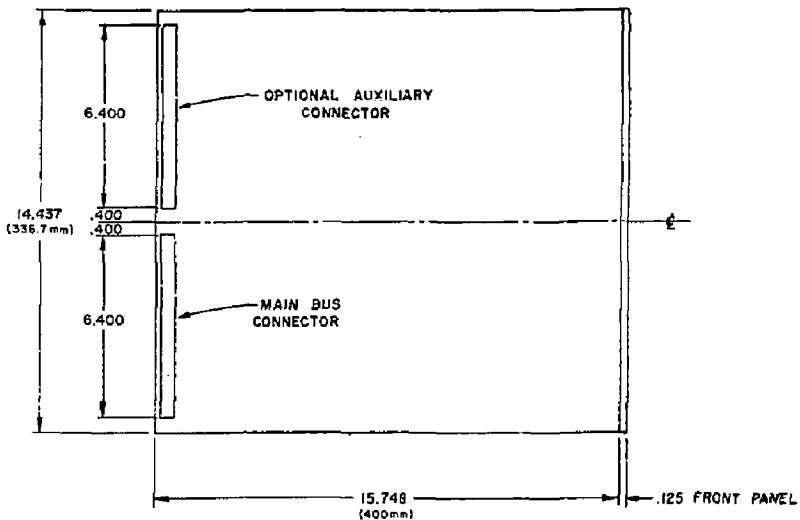
HARDWARE

The preliminary specifications were published for the purpose of evaluating the standard and, where necessary, fix problems with it before the final document was published. The review at the end of the FASTBUS prototyping period showed that not enough room had been allotted in the auxiliary area for making connections. The card size was increased by one 'U' (1.75 in.) and the connectors on the card repositioned. The board outline remains, as before, compatible with the Eurocard system. By maintaining this level of compatibility some economic gains are available to the user from the standardization of chassis parts.

The hardware used in a FASTBUS system can be as simple or as complex as necessary. The things that are specified in detail are the card size, the main bus connector, and the position of that connector on the printed circuit board. The specification for the chassis is that it accommodate the card and provide the connection to the main bus. The method of construction of the chassis and backplane is left to the user. Obviously, standard chassis will be sold by companies and, although they will contain features one does not need for some jobs, the user must decide if he can justify the design and prototyping cost of constructing his own version.

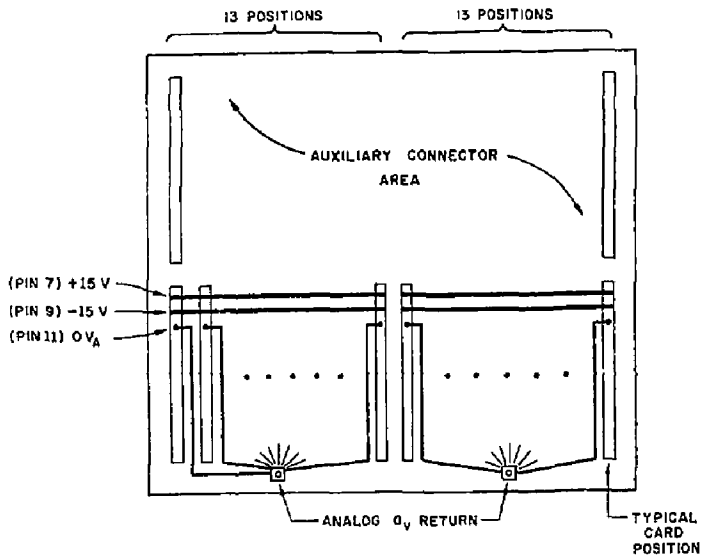
Both the main bus connector and the recommended connector in the auxiliary area are two piece post and box type on .100 in. grid. The main connector is two rows on this .100 in. grid providing 130 pins. If the user wishes, the recommended auxiliary connector can be identical with the main connector. These connector patterns are symmetrical about the horizontal centerline of the card. Figure 1 shows the essential dimensions.

Work supported by Department of Energy,
contract DE-AC02-76ERO-1195



FASTBUS CARD OUTLINE

FIGURE 1.



**FASTBUS BACKPLANE
ANALOG POWER DISTRIBUTION**

FIGURE 2.

The pins in the auxiliary area also project in the rear of the backplane. Since they are on .100 in grid many types of insulation displacement connectors may be directly attached. By using the auxiliary area as a feedthru panel, the usual mess (mess) of cabling that is hanging in the front of racks may be moved to the rear. Removing these cables from the front allows easy servicing of modules without disturbing the cabling to the detector or elsewhere.

If the user needs some special connectors, the recommended chassis design provides for methods of attaching transition printed circuit boards to these rear projecting pins. The main advantage here with the FASTBUS standard is the flexibility the designer has in solving cabling problems and still work with a standard design.

The MARK III experiment implemented the trigger using three prototype FASTBUS chassis. All signals that come into the trigger from the detector attach in the rear. There are a total of 1280 channels (2560 connections) made with flat ribbon cable using 34 position insulation displacement connectors. Most of these cables loop through the trigger giving a factor of two more connections. The experience with this technique has been very good. No connections have failed to date. About 75 prototype FASTBUS sized cards make up this system. Cards are easily serviced. The chance of making a cabling error when reconnecting has been effectively eliminated.

FASTBUS allows the user to purchase only the power required for each installation by decoupling the card cage and power system in the specification. A 'standard' package has been described for general use. This power supply will probably have its main use in single chassis installations or for lab test facilities. The power supply described in Appendix J can deliver 1500 watts on both the +5 and the -5 volt rails. Typically, one has a maximum of 1500 watts total in a FASTBUS chassis. Therefore one half the power is not being used at any one time. At \$1.50 a watt installed this is about \$2000 per power supply that would be wasted at each chassis in a large system. Large semipermanent FASTBUS installations can achieve significant cost savings by purchasing only the power actually required.

The backplane design for standard FASTBUS crates has tried to optimize the distribution of analog voltages. Figure 2 shows schematically the +15 volt, -15 volt, and the 0 volt return (quite ground) as implemented in the 58 SLAC prototype backplanes. The + and - 15 volt distribution is split into two parts, each supplying power to 13 card positions. The zero volt return for each of the 13 positions is brought to a single point on the backplane. This allows the analog designer to use a single point (radial) grounding technique to eliminate ground loops.

What about costs of multilayer backplanes? The current design is a nine layer board. The two outer layers contain the

main bus. The inner layers, except for one which has the 'T' pin, carry just power. Three of the inner layers should be a minimum of four ounce copper, the rest are two ounce copper. A backplane such as this costs about \$300 before the connectors are inserted. The advantage this construction method has is that after the connectors are pressed in place both the signal and power wiring are complete. Backplanes with only 2 layers can be purchased for about \$100 but one still has to buy busbars and attach them. It is very difficult to deliver 300 amperes to a card cage and control the voltage drops correctly. Large copper sheets are very effective in delivering currents of this magnitude with drops of 10 millivolts or less over the entire backplane. The connector cost must be added to this, however, that cost is essentially independent of the method of mounting and attaching to the pins. On the average this cost will be six to eight cents per pin. The mated cost per line will be from fifteen to twenty cents per line. This is about what one pays for edgecard connections, remember the gold fingers are not free.

The last hardware problem most often encountered and least often considered at the initial design phase of a system is cooling. FASTBUS considered the cooling problem early in the writing of the standard. The guidelines for chassis construction, air flow, and heat removal in general are detailed in the document and its appendices. These should be of great help to the designer. In addition, many internal FASTBUS reports are available on this subject. The designer should seriously look at this portion of FASTBUS early in the design phase. It is difficult, if not impossible to retrofit cooling into a 1500 watt chassis.

BUS COMPATIBILITY

The fundamental operations on the bus are asynchronous in nature. A bus master issues timing request signals which are expected to be answered by timing response lines. The standard protocol also has a synchronous data transfer operation specified, however this probably does not gain one by operating speed when the communication is confined to a single backplane.

To be compatible with standard FASTBUS devices only a minimum number of lines need to be obeyed. Ten lines are used to handle the multimaster arbitration. The bus has two lines (RB and BH) which are used to reset all devices on the bus. Two timing lines (AS and AK) define the master to slave lock. The ten arbitration lines along with these four lines must be used in a standard fashion.

The designer, if there are definite needs, can remain physically and electrically compatible by simply obtaining control of the bus in the standard fashion, obeying the protocol on the four lines mentioned above, and then running any protocol he desires on the remaining 46 bus lines.

If the user wishes to communicate from one chassis to another through standard Segment Interconnects two more timing lines

must be obeyed; DS and DK. Additionally, the direction of information flow must be consistent with the direction standard protocol would cause the Segment Interconnect to point its transceivers. The user could then invent a private protocol on the remaining 44 lines.

Within the standard backplane are additional lines for use by front end equipment. Two sets of daisy chain lines along with an associated return line may be used to sequentially scan modules. The disadvantage of this type of readout is the inability to skip bad units or remove a card and continue operating without patching the daisy chain across to the next unit. These systems are also difficult to trouble shoot due to the inability to sit on a suspected faulty unit and continuously access it.

Another point needs to be made about daisy chain systems. A study group, early in the design of FASTBUS, tried to see if significant readout speed was gained by using daisy chain instead of a handshake protocol such as FASTBUS. Their conclusion was that the daisy chain had no advantage over a handshake protocol. Some of the reasons in the past concerning economics of hardware I believe are no longer viable when one considers the total cost including testing and maintenance. A standard readout system comes out ahead.

In addition to the daisy chain lines a 'N' line type pin is available at each position in the chassis. These pins are the 'T' pins, so called because they connect in a 'T' fashion at each card slot to the corresponding data bus line. For example, the 'T' pin at position 5 is connected to Address/Data <05>, etc. These lines may be used in conjunction with a control line to either point at one position or obtain one bit of data from a position. Since these pins are hooked to the 32 bit data bus, the operation may be carried out in parallel to all positions in the chassis simultaneously.

Fast readout schemes can be conceived using the 'T' pins. For example, the controller does a pattern read to the entire chassis. Each device containing data asserts its 'T' pin. This operation gives the controller cards which contain data. Next it points at the cards which previously indicated data present by a 'T' pin type addressing, or maybe converts the pattern data to a five bit geographical address and obtains the data in a more conventional FASTBUS manner.

MONITORING AND TESTING

Probably the most serious electronic problem facing large experiments, other than design time, is the testing and monitoring of the equipment. Access to large amounts of electronics is severely limited at colliding beam machines. When access is gained, it may be only for short periods. This means that problems must be diagnosed as much as possible remotely so efficient use is made of what access time is allotted.

FASTBUS has provisions in the standard to allow just this type of remote diagnostic capability. Designers are encouraged to implement control and status registers. Since these are standardized for the more common functions it is easy for other people familiar with FASTBUS to check the system. Computer readable ID numbers in modules insure that parts of the system are correctly in place. A quick computer scan of the system can save many hours of lost running due to misplugged modules.

The asynchronous nature of the FASTBUS control along with the Wait (WT) line lets monitoring modules stop operation, single step the bus, and possibly control the bus if necessary. This single stepping feature along with a 'back door' serial diagnostic system will let the FASTBUS user obtain a maximum amount of information even if the computer does not have access to a crate via the main bus. SLAC has a SNOOP module under construction to serve just this function. The bus protocol is under software control when it acts as a master. This allows the SNOOP to simulate some private protocols and serve as a diagnostic tool for more than just standard FASTBUS protocol devices.

The serial system in FASTBUS is similar to ETHERNET, although at the moment it operates at about 100kHz instead of the 10mbps proposed for ETHERNET. When the LSI integrated circuits become available the serial diagnostic system will be upgraded. It is possible that ETHERNET devices may be coupled to FASTBUS and give the user another method of attaching computers and peripheral equipment.

One issue raised when discussing the additional diagnostic registers is the added cost of the IC's. That is true; IC's and their cost of installation are not free. However, when accelerator time is costing many thousands of dollars an hour, the savings from a few IC's soon turn into large additional costs. With current budgets severely restricted, the accelerator operating time will become more valuable and force experimenters to use it more efficiently.

Next lets look at FASTBUS and testing. Often the last thing considered when building special systems is the design of test fixtures. Here again adherence to a standard can be of help. If one assumes a standard crate and power supply are available in the lab, a portion of the test fixture is automatically present. If one also has a general purpose register driven FASTBUS interface then the entire test fixture may be present with a little programming. Staying with a standard will also provide one automatically with extenders, test boxes with switches, or a host of other devices. How much effort has been wasted because a special piece of electronics didn't have all the tools to test it available? Following the standard also has the advantage of giving one the same tools away from home.

The problem is compounded when a good design at one place is used by someone at a

second place. The new user is now faced with no chassis, no test gear, no extenders, etc. The cycle repeats --- the first place cannot loan the equipment since they need it for their own operation and don't have a spare.

CONCLUSION

The FASTBUS standard has attempted to solve not only sophisticated communication and data processing problems but also provide a vehicle for building to a standard systems that were in the past only doable with special designs. This is not to imply that all electronics for High Energy Physics will be FASTBUS. A large amount of older equipment in CAMAC and other packages is still useable. Certain restrictions at the very front end electronics which directly mount on the detector require special layouts. There may also be some very fast triggers which also require special connections --- these may be, however, candidates for a FASTBUS hardware only package. It does seem to this author that, once the signal processing passes the directly attached printed circuit boards that very serious considerations must be given

before designing hardware which does not conform to all, or at a minimum, at least a portion of a standard.

FURTHER INFORMATION

Anyone interested in FASTBUS should obtain a copy of the latest document from:

Louis Costrell
National Bureau of Standards
Center for Radiation Research
Washington, DC 20234

Many additional internal FASTBUS committee reports and reprints of articles are also available. Approximately 140 such documents are cataloged. To obtain a list write:

Ray Larsen
SLAC
P.O. Box 4349, Bin 26
Stanford, CA 94305

STATUS OF EVENT SELECTION PROCESSORS AT CERN

C. Verkerk
European Organisation for Nuclear Research
Geneva-Switzerland

Summary

A brief review is given of the uses in event selection of different processors, following the same classification scheme as has been used earlier. The developments which took place at CERN during the last year are described. The progress made with three processor systems, namely MICE, 168/E and FAMP will be emphasized.

Introduction

A year ago, a wealth of information was presented at the Topical Conference on the Use of Microprocessors in High-Energy Physics Experiments¹). The coverage of this field was so complete, that it will be difficult for some time to come to discover an aspect of the use of (micro) processors in particle physics which was not mentioned. If we try to measure progress against what had been achieved already a year ago, we must admit that apparently - as far as CERN is concerned - no spectacular new things have seen the light. In the absence of real innovations however, more solid experience has been gained with a number of processors for event selection. A large part of the progress has been made in the new Underground experiments and the experience of one of them is the subject of a separate presentation at this conference²). The present paper will briefly review what has happened in the field, outside the UAI experiment. Three processing systems will receive most of our attention MICE, 168/E and FAMP. A year ago these had just begun to find their way into experiments.

This brief review will be structured according to a classification scheme³) adopted earlier and based on the principal use of the processor: pre-processing, event-selection, monitoring and control, tests. Inside each class a subdivision is made according to the implementation, which - in some complex way - is related to speed.

Pre-processing and data-acquisition

In the course of the year, it was decided to provide a limited support for CAB⁴), the Camac Booster developed at Ecole Polytechnique, Paris. This is an And 2900 based microprogrammable processor, packaged as an auxiliary crate controller. In an earlier version it was very successfully used in the real-time analysis of a small angle scattering experiment at the PS⁵). Due to its short micro-word (24 bits), microprograms for this processor have a familiar flavour of normal assembly language programs. Cross-software for CAB is available on CDC Cyber machines. The software which has been developed at CERN aims at easy integration of CAB in the standard data-acquisition systems.

A typical example of the use of CAB is given by experiment NA3. Three Camac branches are controlled by one CAB each. Approximately 60 events per burst are created; the CABs perform the read-out and the compaction of ADC data. Individual pedestals are subtracted and whenever a signal above threshold is detected, the adjacent cells are inspected and registered even if their signals are below threshold. The CABs are also used for calibration. One of the processors reads out 1500 words per event, the others approximately 300 each. The treatment takes 3 ms maximum. The events are dumped

into an external memory from where they are read back and recorded during the time between bursts.

Event-Selection

Hardwired Processors

It had already been remarked that a large difference exists between Europe and the US in the application of hardwired processors. In Europe hardwired processors have been developed for a few experiments in an ad-hoc manner. No serious attempt was made to define a set of modules from which the physicist could build himself complex event-selection processors.

MBNIM⁶) satisfies a number of the requirements and is well suited for fast decision making with some pre-processing, but it lacks so far the more complex modules needed to perform algorithmic processes for track finding or vertex reconstruction. A memory for look-up purposes and an arithmetic unit are part of the module set, but do-loop indexers and other control-of-flow modules do not exist yet. We are still far away from having an ECL-Camac or a Nevis modular system at CERN and there seems to be no great urge either to import those systems.

Microprogrammable Processors

8 ESOPs continue to be used in 4 different experiments, at CERN⁷). An additional processor is used in an experiment at Saclay. The preparation of the programs for these uses has shown up a few shortcomings of ESOP which make writing code rather difficult and introduce unnecessary overheads in execution. An improved design, called XOP⁸), is being worked on at present. Helped by the experience, better ways of shuffling data - or better avoiding to move them around - have been investigated. The new design has register files and allows for nesting of loops and subroutines. The microcode memory will be distributed over the modules. The important advantage is that modularity can be easier achieved, but loading of programs becomes more complicated. For this and other reasons an M68000 control processor is foreseen. The programs will need to be written entirely in microcode, as was the case for ESOP. In spite of the high speed of XOP, this may limit its future use. The building of a prototype should start this year.

Emulators: MICE

Before we give some examples of the present use of MICE⁹), we recall its more important characteristics.

MICE was designed for real-time use, for those cases where both speed and easy programming are important. The machine emulates the PDP11 instruction set and due to its implementation in ECL logic reaches three times the speed of the fastest processors in the PDP11 family: the 11/45 and 11/70. MICE is a true emulator: PDP11 machine code is executed by a micro-programmed interpreter. Programs can therefore be written in any language for which a compiler producing PDP11 code exists. Programs written in assembler, PL11 and Fortran run in fact on MICE without difficulty and always much faster than on a PDP11, except when many

byte-oriented instructions are used.

To preserve this high speed operation, the capabilities of MICE have been deliberately restricted in some other respects. The maximum memory size of MICE is therefore limited to 28 Kwords. As programs for event selection must be fast, thus short and simple, this is not felt to be a serious restriction. Fixed point multiplication is done by hardware in 3 cycles (315 ns), but division is implemented in microcode. A floating-point processor was not foreseen originally, again because we felt it was not really needed in event-selection applications. Other applications may however profit from a user microprogrammable floating-point unit so that, for instance, a FFT algorithm could be run at maximum speed. Such a unit is being designed. MICE has a simplified Unibus, so that simple peripherals can be attached without difficulty. A Camac interface is provided for program loading into MICE, for reading of results and for debugging.

MICE has a 1 K writeable control store, 5/8 of which is used for the emulation of the PDP11. A unique feature of the machine is its user micro-programmability. User-written microprograms can be invoked from within PDP11 code, in a way similar to a subroutine call. Depending on the program, an extra factor of 2-5 in speed can be gained by microcoding. On MICE the microcoding can be done for selected parts of the program only. Frequently 90 % or more of a program's execution time is spent in 10 % or less of the code. Such a small piece of code can then be replaced by microcode and the overall speed increased by a factor 2 or more, with a minimal effort.

It is not surprising that these characteristics of MICE were attractive to a number of experiments. At present MICE has been in use in three experiments and three others have definitely decided to use it.

The following three examples of the use of MICE highlight one user-aspect each.

MICE in Computer-Aided Tomography. In this application¹⁾ MICE collects the data for every positron annihilation and reconstructs the line of flight of the two photons. The intersection points of this line with twelve planes is calculated and 2-dimensional histograms built up in a number of Camac modules. These histograms will undergo a further treatment off-line (e.g. FFT Δ 1 its inverse) to produce the final tomographs.

The program running in MICE was written in PL11 and was able to handle 2500 events/second. The inner loop of the program was then recoded into 20 micro-instructions. This gave an improvement of a factor 2 in overall speed. The rate of events that can now be handled in real-time (5000 s^{-1}) should be compared with the rate (6000 s^{-1}) at which histogramming can be done off-line on an IBM 370/168. The rate obtained matches the limit of both the Camac hardware and the processing in MICE.

The microcode was designed, written and debugged in a couple of days by an expert of MICE. It is highly optimized in the sense that the possibilities of pipelining and parallelism of MICE are fully exploited. This example shows that with a modest effort considerable improvements in speed can be obtained, even if a slow I/O system imposes constraints.

MICE in a track selection application. The WAI neutrino experiment provides another example of the use of MICE. Here it is used to select cosmic ray muons which are closer than 250 mrad to the horizontal direction. These muons, collected in the time between

neutrino bursts are used for calibration. MICE reads the data needed via a ROMULUS branch, makes the necessary checks on wordcounts, etc. and suppresses the zero data words, converts the wire number into a space coordinate and stores these numbers in an array. All this is done on the fly, by a program written in PDP11 assembly language. As ROMULUS delivers one word every 1.5 μs and MICE takes only 630 ns to reject a zero data word, there is plenty of time left for treating the non-zero data ($\approx 5 \%$). When the read-out is finished - after 1.6 ms - the analysis program written in Fortran finds the horizontal track, or rejects the event. The overall event rate is limited by the time - 50 ms - to read an accepted event into the MORD 10 computer. The processing time in MICE is negligible: it does not exceed 400-500 μs on average. 40 % of all events are rejected almost immediately by applying simple criteria. 7.5 % of the total number of events are accepted after a modest amount of work. One third of the events are sufficiently complicated that more work has to be done to detect 2.5 % of acceptable tracks amongst them.

A peculiar effect caused by the FIFO-buffers resulted in a decrease (from ≈ 100 to 64) of the total number of events read during a 6 second period, but in the critical regions of the detector ten times more tracks are now found than before.

The example shows that MICE can be usefully employed with a modest programming effort, ≈ 350 lines of assembly code and ≈ 250 lines of Fortran.

MICE in a SC experiment. MICE was used during one week of data taking in an experiment with a ^{12}C beam. MICE simply replaced a PDP11/04, did the Camac read-out via its Unibus extension and sorted the events into five classes. Full buffers were transferred to a PDP11/34. An existing stand-alone program was used. It needed adaptation to replace the DMA transfers from Camac by programmed transfers. The total effort spent was 2 programmer days. The data taking rate was improved by a factor 4.

Emulators : 168/E

At present the only on-line application at CERN of the 168/E is in the central detector of UA1. In December a single processor was used to test the algorithms. The results will be given by S. Cittolin²⁾. As far as the hardware is concerned the present plans are to have 2 processors installed end April. The CPUs are built at CERN, the memory boards with increased capacity for data will come from Saclay. The event size is such that a data memory of 128 Kwords is needed. A smart Camac module with a programmable sequencer will read out the 5 Remus branches in parallel at 0.5 $\mu\text{s}/\text{word}$, using the S1 pulse only. The data is sorted into the appropriate blocks and sent to one of the 168/Es for track processing. This arrangement will also require new interfaces to the 168/Es to adapt to an improved version of the data bus.

This application of 168/Ea exploits an old idea in event multiprocessing: a complete event is treated by one processor and the next event is sent to another processor. The present plans are for two 168/Es but presumably later extensions are foreseen. It will be interesting to see how such a multiprocessing scheme behaves under real-time conditions.

Off-line applications of 168/E. Although not really the subject of this talk, it is interesting to describe briefly the present status of off-line processing with 168/Es. At end 1981 2.2×10^7 events had been processed, which corresponds to 2000 hours of 370/168 CPU-

times. The machines are now grouped in an off-line pool, which will eventually consist of 7 processors : 2 systems with 3 machines and one system with 1 machine. A system includes a PDP11 and the MOSTER memories for overlaying. The two large systems are intended for production, the smaller for tests and software development. Four user groups use the facility at present : EMC, SFM, R807 and Asterix. Full track reconstruction for SFM may need upgrading of some of the machines to 64K, to make space for the magnetic field map.

3081/E. In May 1981 plans were presented for an improved version of the 168/E¹², now baptized 3081/E. In principle an agreement was reached with SLAC to collaborate in this development. The project should get off the ground after this spring.

Multi-processor Systems

Systems built from a number of identical and cheap processors should in principle be capable of very high throughput, if the intercommunication and I/O problems can be satisfactorily solved. Many high-energy physics experiments do use some sort of a distributed processor system, but most of them have grown in an ad-hoc manner by adding something to an already existing configuration. Rather few attempts have been made to design a modular multiprocessor system which, with a modest effort, can be adapted to a variety of real-world situations.

Computer scientists recognize that multiprocessing still presents many problems for which no general solution has yet been found. It is then probably wise to adhere to a guiding principle : Simplicity. When we manage to keep things simple, particle physics may profit from the improved price/performance ratios of the modern 16-bit microprocessors. Systems which do not make conscious use of the fact that data is structured in events - or worse, which are upset by it - will have little chance of success in experiments. Simplicity also means that a multiprocessor system be configured once and for all together with the data-acquisition system and that no attempts be made to implement concepts such as dynamic reconfiguration or dynamic task allocation. They only add complications and overheads in our environment. These remarks do not contradict the fact that multiprocessor configurations have emerged rather naturally and without too much difficulty in those cases where the tasks were restricted to data-acquisition and pre-processing. Examples abound in these applications.

The scene changes however when we consider event-selection. Obviously the final decision can only be taken by one processor alone. For colliding beam experiments, if the total task is too large to be performed on a single processor in the time available between successive triggers, only two possibilities are left for implementation : a "hierarchical" system or a "collegial" system. The latter is based on a mutual agreement "I'll see this event through from beginning to end; you others take care of the events that occur while I am busy". We saw an example in UAL.

The FAMP¹³ system, developed in Amsterdam, and using Motorola M68000s, is a hierarchical system. Slave processors perform subtasks and report their results to a supervisor via messages deposited in dual-port memories. The supervisor can at any moment take a decision and stop further processing by the slaves with an interrupt.

In experiment NALL a FAMP system of 1 supervisor and 2 slaves is about ready to operate. For UAL the

implementation of a second level decision process for the muon chambers is well advanced. The final system will consist of 6 slave processors and one supervisor. Data from drift tubes will be used, truncated to a limited precision. Each slave processor will search for muon tracks in a part of the detector and for one projection only. The supervisor will take a decision on the basis of the results for two projections. The programs running in the slave processors are written in assembly language and occupy at present 2 K. They make extensive use of large look-up tables for the definition of cones in which to look for tracks and for the transformation of drift times into bit patterns which can be ANDed to detect a straight track. For the next run, the decision time is expected to be a few milliseconds. This time should be considerably reduced when more a-priori information will become available from the first level trigger.

Conclusion

In this review, the examples of the use of event selection processors at CERN came mainly from fixed target experiments. What then is the relevance for colliding beam experiments ?

In the absence of a burst structure, events cannot be buffered for long periods and the rates that can be handled are directly proportional to the speed of the processing system (including data acquisition). Processing speed is thus a very important factor. Very few physicists seem however to be ready to sacrifice everything else for the sake of speed. So easy programming, easy interfacing and easy adaptation to changing experimental conditions are equally important. The first point, easy programming, will prevail when the events become very complex at higher energies. The availability of good information from the first level trigger will then be a necessity. Much time can be saved if a program knows where to search for tracks.

When we require good programming capability and speed together, the choice of processors narrows down considerably. In my opinion, of the systems mentioned in this review only three then remain : MICE, 168/E and FAMP. The first two seem rather expensive for use in large quantities but they are very well suited when they can handle the job alone. For multiprocessor configurations it is obviously much more attractive to use the relatively cheap microprocessors. But the number of processors that can be made to work together constructively is limited, either by overheads or by the impossibility to divide the job into independent tasks.

For a simple experiment my preference still goes to a single processor system for event selection, but then, are there still simple experiments ?

Acknowledgements

I would like to thank my colleagues at CERN who so willingly gave me the information I needed to update my knowledge. In particular I would like to thank the following persons : C. Bizeau, J. Bourotte, S. Cittolin, L.O. Hertzberger, D. Halthuizen, D. Jacobs, M.F. Letheren, D. Townsend, H. Verweij and H. Wahl. All errors and omissions are the author's responsibility.

References

1. Proceedings of the Topical Conference on the Application of Microprocessors to High-Energy Physics Experiments, Geneva, May 1981, CERN 81-07. (hereafter to be referred to as TCAMIEP, CERN 81-07)

2. S. Cittolin, these proceedings.
3. C. Verkerk in TCAMHEP, CERN 81-07, p. 395.
4. E. Barrelet, R. Marbot, P. Matricon : "Camec Booster", (CAB system), in H. Söyer (ed.), Proc. Real Time Data Handling and Process Control, Berlin, October 79.
5. E. Barrelet et al., Phys. Letters 94 B (1980) 541.
6. F. Bourgeois, Modular trigger logic techniques at the CERN Omega Spectrometer, IEEE Trans. Nucl. Sci NS-27, 594 (1980).
7. C. Lötjens, in TCAMHEP, CERN 81-07, p. 236.
8. T. Lingjaerde, in TCAMHEP, CERN 81-07, p. 454.
9. J. Anthonioz-Blanc et al. in TCAMHEP, CERN 81-07, p. 266.
10. A. Jeavons et al., in TCAMHEP, CERN 81-07, p. 276.
11. D. Lord et al., in TCAMHEP, CERN 81-07, p. 341.
12. L.O. Hertzberger et al., in TCAMHEP, CERN 81-07, p. 70, also p. 83.

UAL DATA-ACQUISITION SYSTEM

UAL Collaboration
CERN, Geneva, Switzerland
(Presented by S. Cittolin)

Abstract

The data-acquisition system of the UAL experiment running at the CERN pp collider is described. The front-end electronics generates 1.6 Mbytes of raw data for each event. Parallel data-stream processors reduce the typical event data to 60,000 bytes in a time of less than 10 ms. Data are read out by Remus CAMAC branches, formatted data streams being read in parallel by buffer units with multi-event storage capability. For test and monitoring, the data flow can be accessed by local processors associated with each detector subsystem. Alternatively, the over-all system can be partitioned off in a set of independent subsystems running their own data acquisition with or without a synchronous trigger. On-line functions are assured by a number of multi-task and dedicated-task 16-bit and 32-bit computers. A variety of microprocessor-based systems with autonomous capabilities control the experimental apparatus.

Introduction

The UAL experiment is a general-purpose detector system assigned to provide a full solid-angle coverage of the LSS5 intersection region at the CERN pp collider. The apparatus is composed of a variety of complementary detectors surrounding the collision region to provide particle tracking, electromagnetic and hadron calorimetry, muon identification, and magnetic analysis. The over-all detector structure has been described elsewhere¹, and the image chamber central detector is the subject of a separate contribution to this conference.

The data-acquisition system presented in this report is a Remus CAMAC readout system with distributed intelligence and function separation facilities. Its development started at CERN in 1979, and data taking commenced in July 1981 during the collider machine development period. This report describes the general components of the system and the way in which its major functions are at present implemented.

1. Trigger Rate

When six proton-antiproton bunches are circulating in the collider, a beam crossing occurs every 3.8 μ s. At the ultimate luminosity of 10^{31} cm⁻² s⁻¹ the expected collision rate is about 50 kHz.

The total number of channels in the detector (ADC, TDC, wires) is about 20,000, and the digital information, accumulated by the front-end electronics after a trigger, consists of 1.6 Mbytes. The majority of these data come from the central detector, where wire pulses are sampled every 32 ns over a time of 4 μ s. The typical event data are reduced to 60,000 bytes by a set of parallel processors at a rate of 100 Hz. The maximum data-taking rate is limited to 10 Hz by the tape writing speed.

The data-acquisition system is structured in three distinct stages: data reduction and formatting, data collection and filtering, and computer data-taking. Each stage of the data acquisition runs with its own dead-time, so corresponding levels of trigger decision are combined in order to reduce the rate between stages.

To reduce the trigger rate from 50 kHz to 100 Hz, two levels of trigger decision take place before the data reduction phase is initialized. The first-level decision is made between beam crossings; events are selected on the basis of energy deposition in the calorimeter and a muon particle identification. The second-level trigger is only activated if a muon candidate is identified in

the first level. By means of microprocessors, the muon drift chamber information is analysed to determine, with more accuracy, if the muon candidate comes from the interaction region.

A third-level trigger makes decisions based on the analysis of the event data; it uses processors programmable in high-level language (168E) and it is part of the data-collection stage of the system. Levels two and three are at present still in a state of development and they will not be described here.

2. Data Reduction and Formatting

The data reduction phase takes place at the occurrence of a first-level trigger (and second level if enabled). It consists of the suppression of null information channels and data re-formatting with or without arithmetic computations.

The information coming from the calorimeters, the muon chamber (without second-level trigger), and the very forward chamber (VFC) is either already packed by the digitizer electronics or directly treated by hard-wired devices with a fixed and simple algorithm such as the LRS 2280 ADC processor. The amount of data generated by this part of the apparatus is of the order of 20,000 bytes and the reduction time is more or less constant at 3 ms.

The handling of the information coming from the central detector is more complex.

The basic principle of each sense-wire readout electronics² is represented in Fig. 1.

By means of two six-bit fast analog-to-digital converters (FADC's), the digitizing electronics samples the two wire-edge pulses every 32 ns, measuring a non-linear function of the energy loss dE/dx and, directly, the track position along the wire by charge division method. The drift time within the window of 32 ns is measured by a three-bit time-to-digital (TDC) interpolator with an accuracy of 4 ns, and an additional bit, the time tag, flags the sample at which a start of pulse (hit) has been detected.

The digital outputs of the two FADCs, the TDC, and the time tag are then stored in a circular buffer memory, 128 words deep, of 16 bits, providing a continuous record of the last 4 μ s wire information (the maximum drift time in the chamber is about 3.6 μ s).

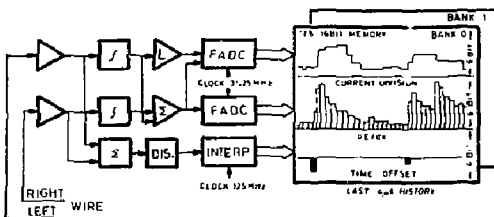


Fig. 1. Central detector wire readout block diagram.

To allow all the electronic channels to operate with identical performances and to obtain the maximum of accuracy in charge division measurement, two gains and four off-sets in each signal processing channel are adjustable over a small range by means of six-bit digital-to-analog converters (DACs).

A four-unit CAMAC module, the charge and time digitizer (CTD), supplies the digitizing and control electronics for 12 wire channels.

The elementary system for the central detector data reduction is a CAMAC crate containing one time-stop interpolator, five charge and time digitizers, and one readout processor (ROP)³. Each crate can handle up to 60 wires, and the complete set-up consists of 110 crates.

Given the functions of the digitizing electronics, at the occurrence of a trigger 15,360 bytes are accumulated in the CTD memories of each crate and 1.6 Mbytes in all the system. This primary information must be reduced as quickly as possible in the form of single-hit coordinates, such as the drift time, the wire number, the track position along the wire, the energy loss, and the pulse duration. This is one of the tasks of the ROP unit.

2.1 The central detector readout processor

The ROP is a dual processor system that combines the fast handling of the CTD data with more sophisticated functions for monitoring and calibration of the central detector electronics.

The ROP is a four-unit CAMAC module containing a data formatter processor and a control processor (Fig. 2).

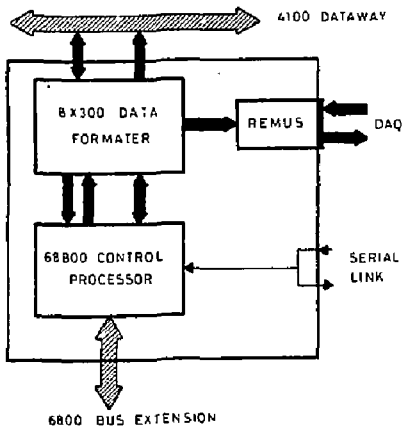


Fig. 2 ROP block diagram

The data formatter (DF) is based on the 8-bit Signetics 8X300 microprocessor (250 ns cycle) with instruction word extended to 24 bits to define bus-source and bus-destination addresses and a few direct actions. Its hardware comprises 256 24-bit control store memory locations, two 16-bit summing registers, a 4K 12-bit look-up table, a 1K 16-bit Remus port output FIFO, and a variety of registers for control, status, and data communication. The control processor (CP) is based on the 68B00 microprocessor with 8K RAM, 24K EPROM, 4 DMA channels, an advanced data-link controller (ADLC) port⁴, and parallel input/output to communicate with the DF and the module front-panel.

The two processors play complementary roles in the ROP crate system. The DF acts as the input/output processor for data acquisition, while the CP supervises the crate operations testing all the internal module functions, bootstrapping and controlling the DF programs, and monitoring the performance of the electronics. The CP has also its own data-handling tasks in order to evaluate the characteristic parameters of each electronics channel and adjust the associated gains and off-sets via on-line calibration procedures.

2.2 Central detector data re-formatting

During data acquisition each ROP crate accepts Trigger, Clear, and Read signals from the experimental logic. At the occurrence of a first-level trigger, the CTD digitizers are stopped by the beam-crossing signal delayed by 4 μ s; then, if the event is accepted by the second level of decision, a Read signal starts the CTD scanning and the data formatting process. All these operations are executed in parallel on all the ROP crates under the control of the DF processors.

The more important data-reduction algorithms at present implemented in the DF software are the 'unpacked data format' and the 'packed data format'.

CTD unpacked format

The DF initializes the CTD 0-skipping procedure. A fast search for a non-zero time tag is done by the CTD at a rate of 4 μ s per wire. For each pulse found, a two-byte hit header word is created, packing the drift time and wire address followed by a variable length data block containing the CTD module number and the current division and dE/dx samples associated with the pulse, the end-of-pulse being detected by a comparison of the dE/dx sample with a given threshold.

All processed data are output into the Remus 1K data FIFO and are optionally sent, together with wire statistics information and error flags, to the CP for monitoring and local data sampling.

The number of bytes generated by each hit depends on the pulse length and the chosen end-of-pulse threshold. The average hit length is of the order of 20 bytes. Typical events produce up to 100 hits per crate, corresponding to about 2000 bytes. The dead-time of this kind of data reduction is 200 μ s per hit.

CTD packed format

This format is currently used during data taking. The hit search and header word construction proceed in the same way as for the unpacked format, but the pulse information is reduced by the calculation of the total charges deposited at the two edges of the wire and the pulse duration. By means of the DF look-up table, preloaded with suitable conversion parameters, the dE/dx sample, corrected for its base line shift, is transformed by a quantity proportional to the wire total charge contribution of the sample. In the same manner the current division measurement, weighted with the corresponding dE/dx sample, gives the evaluation of the charge deposited at one edge of the wire, as given by the following formulae:

$$Q(\text{total}) = \sum \{B(1-A)(F_i - BL) / [(63-BL)(63-AF_i)]\}$$

$$Q(\text{left}) = \sum \{Z_i B(1-A)(F_i - BL) / [(63-BL)(63-AF_i)]\}$$

(sum over the pulse samples).

where Z_i and F_i are the current division and dE/dx samples, A and B are fixed parameters defining the non-linear response of the dE/dx FADC channel, and BL is the adjustable base line of the dE/dx channel. The charge integrals

are accumulated over the pulse samples until an end-of-pulse is found or when a given number of samples have been added (usually eight, corresponding to 256 ns).

The total hit information produced with this format consists of a minimum of six bytes containing the drift time, the wire and CTD module number, the Q(total) and Q(left) charges, and the pulse length expressed in number of samples. For long pulses the charge evaluations are repeated every eight samples, and an additional four bytes are output. The time needed to process a single hit is of the order of 30 to 100 μ s, depending on the length of the signal. For events with up to 100 hits per crate the reduction dead-time varies from 3 to 10 ms.

3. Data Readout

The complete UAL readout system consists of about 200 crates housed in a mobile electronics control room near the experimental apparatus. All front-end data digitizer electronics are allocated in CAMAC crates; however, only the calorimeters and trigger information readout (ADC, TDC, scalers) use standard CAMAC, whilst the central detector CTD crates run the ESONE COMPEX protocol.

The data collection is performed using the CERN Romulus/Remus method of reading CAMAC⁵. This system is based on two types of CAMAC modules: the branch driver (CERN type 243) and the crate controller (CERN type 244 and the ROP processor). These units connect crates together in branches (vertical bus) organized in a tree-like network, always terminating with a single branch driver sitting in a standard CAMAC crate. The V-bus essentially carries the data stream from the front-end to the branch driver. Crates are read autonomously; markers and word counts are generated to format the data, in this way minimizing the software and hardware overheads during a computer DMA transfer.

To increase the flexibility of the system and improve the performance of the readout, the V-bus data handling was extended with the addition of two auxiliary Remus modules: the Remus Router Unit (RRU) and the Remus Data Buffer (RDB).

3.1 Data Flow and System Partitioning

By means of a RRU the data flow can be switched between two separate V-bus highways, so that the complete system can be partitioned off in a set of independent data-acquisition subsystems which are synchronously or asynchronously triggered.

Alternatively, one V-bus can spy the data whilst they are being read out by the second one performing as master. Local processors can thus access the data in parasitic mode for monitoring purposes, without affecting data acquisition.

This data-routing strategy is applied at two levels. Near the front-end electronics, CAVIAR microcomputers⁶ are used as local processors for each individual branch of the detector. During the assembly and development of the apparatus, the CAVIARs are used to perform test and debugging functions, whilst during data acquisition they run monitoring and display programs without altering the front-end data in any way.

The data-routing technique is applied at a second level to the collection of the complete event data in the main control room. This allows the various computer systems to sample data from a full event record simultaneously.

3.2 Parallel Readout

The V-bus is read in an autonomous mode, by means of a buffer unit, and event data are temporarily stored in a dual port memory operating as a FIFO, 4K or 16K deep. The buffer stores all the V-bus data and control

bits at the speed of 1 μ s per word, so many event data blocks can be pipelined without losing their original data structure, whilst the data readout continues at the output port driven by the subsequent elements of the V-bus tree. The input triggers are counted in each memory, and the results from all memories are compared during output to verify that all data blocks are synchronized on the same event. Through input control signals, the buffer can operate in single event, multievent, or transparent mode, and further triggers are inhibited by a Busy output signal during the upstream data reading.

The block diagram of the UAL V-bus structure is represented in Fig. 3. All the digitizer crates ... grouped in 30 sub-branches, each driven by a buffer unit. The partition of the crates and the size of the memories were chosen in such a way as to have a total storage capacity of up to four events with an average distribution of data per branch of 2000 bytes for typical events of 60,000 bytes.

At this level the data acquisition runs in parallel, taking a total time of the order of 1 ms. The data reduction time being 3 to 10 ms according to the trigger, the full experiment electronics dead-time is 4 to 10 ms, allowing maximum peak rates of 200 and 100 events per second.

The computer readout procedure and the event data structure are not affected by the parallel readout. The latter can be switched off by setting all buffer units in transparent mode. The data taking can continue as before but with the experiment dead-time limited by the full event computer reading.

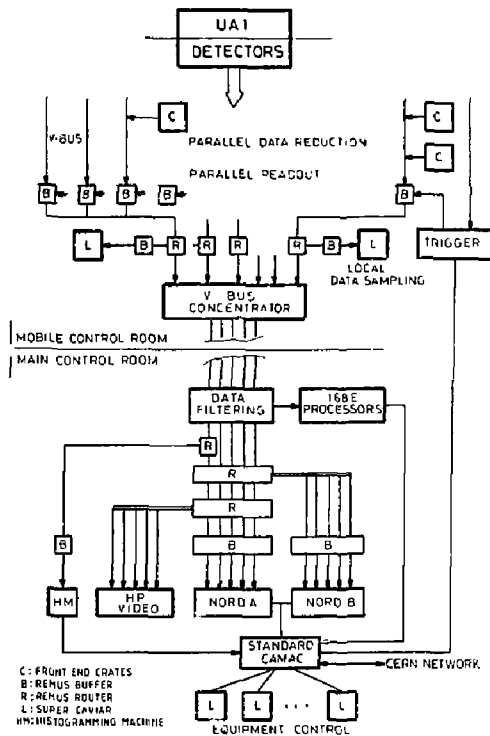


Fig. 3 UAL data-acquisition block diagram.

3.3 Data Collection

After the first stage of parallel readout, data are collected and merged into five branches and transmitted to the Main Control Room, one hundred metres away. The long-distance transmission causes a slowing down of the data rate to 0.75 Mbyte/s per single branch (3.7 Mbyte/s when the five branches are read in parallel). Before terminating in the data-acquisition computer, the main data stream goes through different levels of routers, each one driven by a large memory buffer of 64 kbytes operating this time in single event mode and allowing a maximum trigger rate of 50 events per second. This last stage of parallel readout allows the same event information to be read by different computers (one acting as master and the others as spy); or, by appropriate dynamical change of the router position, selected event data can be dispatched to different data-acquisition systems in order to increase the over-all experiment maximum data rate to more than 10 events per second and eventually to associate the acquisition of different trigger types with separate computers. It is planned to install the third-level trigger at the top of this structure. This trigger is based on 168E processors that have parallel access to the five main branches via a CAMAC-168E bus interface being developed at CERN.

4. On-line Computers

4.1 The Machines

The UAL general computing support is based on the Norsk Data ND 100/500 16-bit and 32-bit machines. In addition, three iP21MXE minicomputers are assigned to dedicated functions, such as video-tape mass storage, mass histogramming, and luminosity chamber data acquisition. A set of CAVIAR and SUPER CAVIAR microcomputers are responsible for the control and monitoring of all the equipment. The CERN standard link (CERNET) provides the communication with the CERN central computer facilities and with a remote Megatek interactive graphic system driven by a VAX11-760.

4.1.1 The NORD computers. The NORD 100/500-type machine is a new Norsk Data product. As its hardware and software development fell slightly behind the evolution of the experiment, temporary configurations were installed during the first phase of the UAL run. At present we are converging toward the final configuration, consisting of two identical NORD 100/500 systems with 2 Mbyte memory, STC 6250 bpi 125 ips magnetic tape units, and 75 Mbyte disks. They are referenced as NORD A and NORD B systems and are the main on-line computer support of the experiment.

The NORD 100 runs the multi-user, multi-task virtual memory operating system SINTRAN III, allowing standard real-time programming and the implementation of direct tasks associated with hardware interrupts. The NORD 500 is a powerful 32-bit processor equivalent to a 0.3 IBM/370 168. It runs in multi-user mode and has the NORD 100 as front-end.

A CERN-developed package (DAS) performs all the basic operations of data taking, namely the system initialization, the CAMAC readout, the magnetic tape recording and replay, the communication with the data sampling programs, the error handling, and the production of run summaries for the bookkeeping. The over-all system is fast and efficient, and its speed is essentially limited by the hardware.

A data base is installed on the two machines for the purpose of having a common mechanism for storing and retrieving the information concerning the apparatus parameters and the experiment running conditions.

Several multi-video terminals (MVIT) provide the machine/operator interface during the experiment. The MVIT is a 6800 microprocessor terminal developed in UAL; it consists of a keyboard, four alphanumeric video signal

outputs, and a touch panel. The status information is presented as histograms on four CRTs, scrolling text in selected frames of the screen or as horizontal circular messages, whilst inputs are chosen from a menu list by programmable touches.

4.1.2 NORD system general tasks. The identical configuration of the two NORD systems and the common access to CAMAC allow any task and program running in one machine to be, in principle, transportable to the other, thus providing a continuous functional back-up. However, the two systems play different roles according to the running condition of the experiment. The function of each machine is defined by its task configuration. The definition and the function assignment of each computer system are still in an evolutive state, and more experience with the data handling and the on-line use of the 168E processors is needed for a definitive consolidation of the over-all system. Listed below are the more general hardware and software configurations foreseen for the NORD computers.

Data-taking and experiment monitor

The NORD 100 of system A runs DAS as master; it reads CAMAC and writes tape. Only very efficient and consolidated tasks are activated; they provide a check of the readout system, a monitor of the trigger and collider performances, and a first data analysis based on the energy deposition in the calorimeters. Full event analysis with accumulation of physical result statistics is done at the same time on the NORD 500 A. The NORD 100 of system B runs DAS in spy mode, servicing a variety of user-developed data-sampling programs for display, monitoring, alarm, and supervision of the distributed intelligence controlling the detectors' equipment. The remote VAX11-780 graphic station is serviced as well. During this phase, the NORD B is the real host-computer system. If one of the computers hangs up because of an unrecoverable failure, then all its tasks or a subset are moved to a single machine that will carry on the data acquisition but with limited efficiency.

High-luminosity, dual trigger data taking

When running at high luminosity it seems convenient to separate the trigger into two classes: the 'few' trigger and the 'many' trigger, these being the two trigger selections made either at the first level of hardware logic decision or at the level of 168E filter processors. To increase data-taking efficiency to the maximum, the NORD B system is devoted to the prior collection of the 'few'-type events. A trigger supervisor processor controls the data routing between the two computers according to the incoming trigger type and monitors the 'many' trigger dead-time in order to keep its rate lower than the data-recording saturation of the NORD A, thus always allowing free space in the parallel readout FIFOs for the acquisition of 'few'-type event data.

Calibration and maintenance

By setting the Temus Router Units, the readout can be split into a large set of independent subsystems for hardware maintenance. Calibrationwise, the UAL detector can be divided into two parts: the calorimeter and the image chamber. At the level of computer data collection, the over-all system is partitioned off into two independent ones by setting the calorimeter branch router, NORD A being used to calibrate hadron and electromagnetic calorimeters and NORD B to calibrate the central detector via the SUPER-CAVIAR ROP controller.

Off-line preprocessing

It is foreseen that the off-line DST tape production will run on NORD A, using the NORD 500 machine and

the 16BE processors; the NORD B system is devoted to program development and apparatus maintenance.

4.2 Dedicated Tasks

These functions are taken away from the main computers in order to off-load their charge. They are still activated and controlled by the NORD B computer, but their execution is performed by separate processors.

4.2.1 Luminosity chamber data acquisition. The UAI luminosity monitor runs as an experiment apart. The data acquisition is performed by a CERN standard HP21MXE system using its own CAMAC readout and magnetic tape storage. A CAMAC-to-CAMAC link provides communication between the luminosity monitor and the host computer.

4.2.2 Histogramming machine (HM). The histogramming and the average and sigma calculations are the simplest tools for evaluating the performance of a data channel such as an ADC. Histogramming is a time- and memory-consuming task that can become very heavy for a multi-user computer system such as the NORD when the number of channels and events to be treated in a short time is high. The UAI calorimeter detectors consist of 7500 ADC channels, and their calibration procedures need the accumulation of several hundred events taken with different external conditions (simulation pulses, laser flashes, etc.).

At the beginning of the experiment it was thought necessary to provide additional histogramming facilities in the main computers. In the case of the central detector readout, these were included in the design of the system, and for the ADC channels a HP21MX minicomputer (HM) with 384 kbyte memory was completely dedicated to the task of mass histogramming.

The HM runs a software optimized for fast histogramming and statistics parameter evaluation, allowing the filling of one thousand histograms at the rate of 10 events per second, or the first and second moments calculation of 7500 channels taking one second per event⁸. The HM has only access to the calorimeter data via a RRU, and it can operate in spy mode during data acquisition or in master mode during the calibration. The NORD B system communicates with the HM via a serial link. The NORD initializes, books, and reads back accumulated histograms for display and updating of tables of constants. The HM is treated as a peripheral of the NORD computer with a limited and well-defined set of functions. During data taking, the HM role is complementary to that of the main computer, where histogramming tasks are devoted essentially to monitoring the physical information contained in the data.

4.2.3 Mass storage. The data collected by the NORD system are recorded by STC 6250 bpi 125 ips magnetic tape units (MTUs). Owing to the 60 kbyte event size, the MTUs are saturated by a trigger rate of 10 events per second, which fills a reel in four minutes.

When the collider luminosity attains the design value of $10^{30} \text{ cm}^{-2} \text{ s}^{-1}$, the problem of handling over 200 tapes per day will become serious unless a very selective trigger is used to reduce the event rate.

To provide greater capacity of high-rate data recording, a digital video-tape system⁹ has been installed which records data at 1 million bits per square inch by helical scanning. The system is a dual-transport development of a configuration which was successfully employed in ISR experiments R605 and R606¹⁰ and is controlled by an HP21MXE computer. Video-tape data are recorded at 11,000 bpi by Miller code in scanlines of 100 kbits. An interleaved data structure is implemented to avoid requiring a fast disk for intermediate data staging. Scanline addressing and the status information required to log the structure are recorded in separate longitudinal tracks, which can be read at search speeds up to 400 ips.

The video-tape system records 9 Gbyte per reel of tape, equivalent to 50 reels of 6250 bpi tape, and can take data at maximum rate on a single reel for over 3.5 hours of running. It will be brought on line when dual selective/open triggers have been implemented and stable behaviour of the experimental apparatus has been achieved.

4.3 Equipment Control and Monitoring

Microprocessor systems are used for the control of all the equipment associated with detector functions, such as power on/off, parameter setting, current and voltage monitoring, and calibration pulse generation.

The host computer (usually the NORD) is able to interact with these systems via CAMAC, to control their operation, and to communicate with the programs they are running.

4.3.1 General-purpose microprocessor controller (GPMC)⁸. This is a single-unit CAMAC module based on the 6800 microprocessor with 16K EPROM, 2K RAM, RS232 and ADLC ports, and a 6800 bus extension to which is connected an interface module (IM) specific to the device to be controlled. According to the application, each IM replaces a well-defined electronics logic and measuring system that would be expensive to implement with standard CAMAC and NIM modules. Different IMs were developed in order to handle the central detector calibration pulse generation, the very forward chamber (VFC) electronics control, and the central detector high-voltage and current monitor. The GPMC firmware runs an interactive monitor, processing commands coming from CAMAC or the RS232 port, the command firmware depending on the IM application.

4.3.2 CAVIAR and SUPER CAVIAR microcomputers. CAVIAR is a CERN-developed stand-alone microcomputer which is used extensively in the laboratory and associated institutes for CAMAC system development, monitoring, and control.

It is an integrated microcomputer system based on the 6800 microprocessor and 9511 floating-point arithmetic and function processor, and the standard unit incorporates 32K RAM, 29K EPROM, a EUR 4600 CAMAC branch driver, an IEEE 488 GPIB controller, an audio cassette interface, two RS232 communication ports, and a raster-scan video monitor with alphanumeric and graphic capability.

The SUPER CAVIAR¹¹ enhancement includes a memory mapping system, 256K RAM, up to 85K EPROM, an ADLC port, and a real-time clock. Multipage colour graphics are currently being developed.

SUPER CAVIAR firmware includes BAMB1, a high-level interactive programming system with a language similar to BASIC but which uses pre-run compilation to achieve execution speeds substantially faster than BASIC interpreters. The system incorporates a comprehensive range of over 200 assembly-written routines for CAMAC, GPIB and ADLC operations, graphics, histogramming, array handling and remote computer communications.

The main control room CAVIARs and SUPER CAVIARs are the primary interactive interface facilities between the operators and the UAI experiment complex. They allow direct control and monitoring of the experimental apparatus by keyboard commands or easily written programs, and operate autonomously on the equipment connected to their CAMAC systems. However, each CAVIAR system is seen by the host computer (Fig. 4) as a CAMAC device with which it can communicate programs, data, and control functions for the supervision of the status of all the apparatus.

CAVIARs or SUPER CAVIARs are employed for the following control, monitoring, and development tasks in UAI:

central detector high-voltage, gas, and temperature;

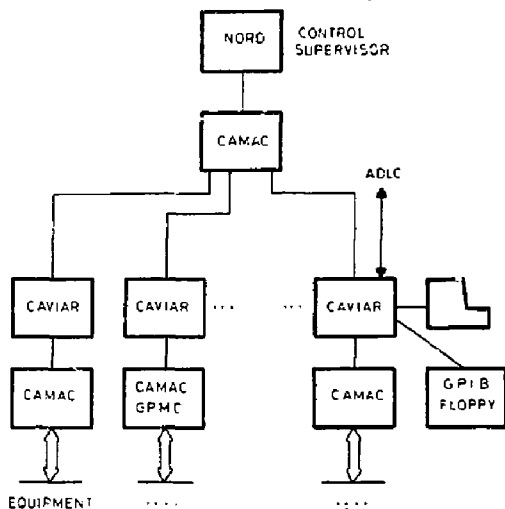


Fig. 4. Configuration of CAVIARs for equipment control.

central detector transient recorder monitor;
 central detector ROP control and calibration;
 central detector electronics testing (four units);
 photomultiplier power supply¹²;
 trigger processor control;
 experiment and collider status;
 magnet control;
 electronics test and development;
 readout setting and control;
 local data sampling and monitoring (seven units).

In addition, the spin-off from the CAVIAR program (MVI1, GPMC, ROP development system, electronics production test system) has resulted in a somewhat unified approach to this first large-scale application of microprocessor systems to a complex experimental facility.

4.3.3 Local area network. A simple and cheap serial data-link was developed in order to provide an independent control and data communications path to all the distributed intelligence associated with the front-end electronics, such as the central detector ROPs and the very forward detector GPMC electronics controllers. This local area network is based on the 6854 advanced data-link controller (ADLC)⁸ using a data communication protocol based on HDLC. The network is organized as a set of closed loops, each having a SUPER CAVIAR primary station and up to 254 secondary stations (ROPs). Via the ADLC link the SUPER CAVIAR can read or write variable length data blocks at specified addresses in each ROP control processor RAM or send specific commands for initialization, internal calibration, and selection of the ROP data-acquisition mode.

5. Conclusion

The UAL experiment started taking data at the CERN pp collider during the second half of 1981. The major part of the basic software and hardware elements of the data acquisition system was installed and running. During the latest data-taking period in December 1981, half a million events were read and written onto tape.

The experience accumulated so far has shown that microprocessor-based devices play a central role in large and complex experiments such as UAL. Remus CAMAC readout enhanced by the parallel processing, buffering, and partitioning facilities performs satisfactorily at the present scale of the experiment.

However, when introducing multiprocessor facilities for the third-level trigger implementation, the lack of a modular event data-staging architecture is felt. Intermediate solutions have been adopted for the near future, whilst FASTBUS would appear to be the most feasible long-term scheme for the event data-collection stage of the system.

Acknowledgements

The UAL data-acquisition system was developed by several members of the collaboration. We would like to thank DD/OC/ND Group for their support with the NORD on-line programming, and EP Electronics Group for the development of the readout and control electronics; in particular B. Lofstedt for the development of the ROP, and B.G. Taylor for the development of the dual videotape system and the CAVIAR and SUPER CAVIAR microcomputers.

References

1. A. Astbury et al., A 4π solid-angle detector for the SPS used as pp collider at c.m. energy of 540 GeV CERN/SPSC/78-06, SPSC/P 92, 30 January 1978.
2. M. Calvetti et al., Electronics and results of the central detector, preprint CERN-EP/80-42 (1980).
3. S. Cittolin and B. Lofstedt, A Remus crate controller for the autonomous processing of multichannels data streams, Proc. Topical Conf. on the Application of Microprocessors to High-Energy Physics Experiments, CERN 81-07 (CERN, Geneva, 1981), p. 91.
4. S. Cittolin, B. Lofstedt and E. Zurfluh, High-speed serial link for UAL microprocessor network, Proc. Topical Conf. on the Application of Microprocessors to High-Energy Physics Experiments, CERN 81-07 (CERN, Geneva, 1981), p. 573.
5. P.J. Ponting, A guide to Remus/Remus data-acquisition systems, preprint CERN-EP/80-01 (1980).
6. S. Cittolin and B.G. Taylor, CAVIAR: Interactive microcomputer control and monitoring of multi-crate CAMAC systems, Proc. Conf. on Microprocessors in Automation and Communications, Univ. of Kent, 1978 (IERE No. 41, London, 1978), p. 309.
7. J.T. Carroll, 168E on-line configuration, UAL Technical Note TN 81-46 (1981).
8. UAL On-line Manual, 1981.
9. S. Cittolin and B.G. Taylor, Digital video-tape data-handling in a CAMAC system, Proc. Conf. on Video and Data Recording, Univ. of Birmingham, 1976 (IERE No. 35, London, 1976), p. 99.
10. B.G. Taylor, Mass storage for on-line experiments, preprint CERN-EP/77-105 (1977), presented at the All Union Seminar on Physics Data Processing, Erevan (USSR), 1977, p. 27.
11. S. Cittolin and B.G. Taylor, SUPER CAVIAR: Memory mapping the general-purpose microcomputer, Proc. Topical Conf. on the Application of Microprocessors to High-Energy Physics Experiments, CERN 81-07 (CERN, Geneva, 1981), p. 533.
12. W.J. Haynes, Photomultiplier high-voltage control, UAL Technical Note TN 81-30 (1981).

I. Gaines
Fermi National Accelerator Laboratory
Batavia, IL 60510

Summary

The Collider Detector Facility (CDF) collaboration is designing and constructing a powerful, general purpose detector system for use at the Fermilab 2 TeV center of mass energy antiproton-proton collider. The detector will have approximately 75,000 channels of electronics and must be able to deal with a raw event rate of 50 kHz, corresponding to a luminosity of 10^{30} . The multi-level trigger processing system to be used in this detector is described, with emphasis on the general features of detectors at hadronic colliders which have imposed certain architectural choices on the CDF triggering and data acquisition system.

Introduction

A number of considerations lead one to consider different types of triggering schemes for experiments at hadron colliders than for those at electron-positron colliders. In particular, the high event rates and extreme complexity of the events requires powerful, yet flexible triggers that can make relatively high level physics decisions, are easily programmable so they can be modified and checked, and do not contribute significant amounts of dead time to the data acquisition process.

Unfortunately, these three requirements are somewhat contradictory. Speed must often be traded for flexibility and ease of programming. A well-known solution to this problem is to provide a series of increasingly complex triggers, each successive level of which makes more detailed decisions (in correspondingly larger amounts of time) on fewer events (due to the rejections by earlier levels of the trigger).

This is the solution which has been adopted for the Collider Detector Facility (CDF) at Fermilab. This detector will be used at the Fermilab 2 TeV center of mass energy antiproton-proton collider. The detector design attempts to provide full coverage over the 4π solid angle around the interaction region for particle

tracking, fine-grained electromagnetic and hadronic calorimetry, and muon identification using a variety of different detectors. Magnetic analysis is provided for tracks in the central region by a large superconducting solenoid, and for muons in the antiproton direction using iron toroidal magnets. An isometric view of the detector is shown in Fig. 1.

In total, there will be approximately 75,000 individual signal sources including drift chambers, photomultipliers, cathode strip chambers, and cathode pad chambers. Further information regarding the detector can be found in the CDF Design Report.¹

The data acquisition system is described in Ref. 2. It is a multi-function, distributed intelligence, measurement and control system which provides a variety of services in addition to data gathering. In general terms, the system consists of signal conditioning and digitizing front end electronics located on the detector which are controlled remotely by a FASTBUS based network of processors. The precise configuration is still under design and will continue to evolve as experience is gained at Fermilab and elsewhere.

Other features of the CDF triggering system besides its multi-level character are also dictated by general considerations. The first of these is the relatively long time (expected to be at least 3.5 microseconds) between beam crossings at a proton-antiproton collider. These mean that the lowest level of the trigger will contribute no dead time as long as it makes its trigger decision faster than this interval, and that there is nothing to be gained by making the first level decisions any faster than that. This allows a certain simplicity of design and means that there is no need for ultra high speed elements in the triggering system.

Finally, the overall cost of the system is another important consideration. With the large number of channels needed in a general purpose detector, the cost per channel must be kept as low as possible. This means that the majority of channels will have no provision for fast read-out, as this would add substantially to the cost per channel. A relatively small number of channels, possibly 10 percent of the total, will be equipped with special fast read-out electronics independent of the standard data acquisition read-out path. The first levels of the trigger will make use only of these fast read-outs. Only after the event has passed the first few levels of triggering will the slow process of reading out the entire event be initiated, and the full event data will then be available at the highest levels of the trigger.

Thus, general considerations of the triggering needs for a general purpose detector for a hadron collider set the basic structure of the trigger system for CDF. There will be a multi-level trigger, with the early stages examining a portion of the event data using a special read-out path, but with no requirement for any decisions faster than a few microseconds. Higher levels of the trigger will examine the entire event, and should allow complex physics related algorithms to be used for final event selection. The details of the CDF triggering system will be described in the remainder of this paper.

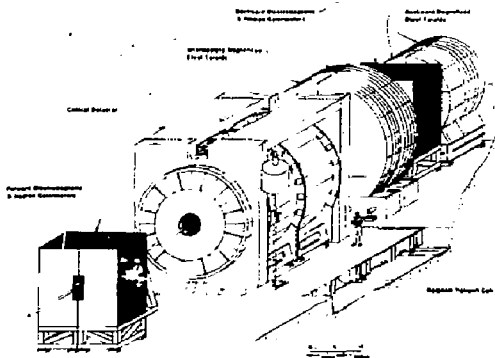


Fig. 1. An isometric view of the CDF detector.

*Operated by the Universities Research Association under contract with the United States Department of Energy.

Triggering Overview

At the design luminosity of $10^{30}/\text{cm}^2/\text{sec}$, the inelastic interaction rate is approximately 50 kHz which must be reduced to the tape writing rate by the trigger system. The rate for writing events to magnetic tape is constrained to about 5 Hz by two independent considerations. First, 5 events per second is close to the maximum rate at which a standard 6250 bpi tape drive can be operated. Second, data written at this rate for one month is estimated to require at least one year of available off-line analysis capability. A three level hierarchical trigger strategy has been chosen in which each level produces a rate low enough so that the dead time introduced by the next level is not significant. Within this constraint, the trigger requirements at each level are as loose as possible, leaving more restrictive decisions to higher levels where more information from the detector is available, and a longer decision time per event is allowed.

The first two levels of the trigger system will be used to reduce the rate from 50 kHz to about 500 Hz before digitization. Prompt signals from the detector for these two levels of the trigger structure are provided by the front end electronics in the form of drift chamber hit bits and analog sums of calorimeter towers. The level 1 trigger decision occurs in the time between beam crossings and so is deadtimeless. If a candidate event is flagged by level 1, prompt signals are passed on to level 2 for a more complex and time consuming selection process, incurring dead time. Level 2 is estimated to require of order 20 microseconds to make its decision. Limiting the level 1 rate to 5 kHz then gives an acceptable dead time due to level 2 of 10 percent. An event accepted by level 2 is digitized and stored in buffer memory. Since the digitization process takes approximately 1 msec, the level 2 trigger rate is limited by deadtime considerations to about 500 Hz.

Level 3 of the trigger structure is used to reduce the event rate from 500 Hz to the tape writing rate of 5 Hz. This level's decision criteria should be easily modifiable to accommodate changing physics requirements and increasing knowledge of both the trigger and detector operation. Accordingly, level 3 is configured as a set of independent processors which work on the entire event record using an event analysis and selection program written in a high level language. Those events which pass the filter criteria are sent to a data logger to be written on magnetic tape at an average rate of 5 events/second.

The bandwidth and processing power requirements for the level 3 system are formidable. Assuming 10 percent to 20 percent detector element occupancy and full data compaction, an event is expected to consist of approximately 10,000 32-bit words. This requires a bandwidth of up to 5×10^6 words per second at the input to level 3. Then, assuming that about 10^7 machine instructions are needed to process an event on the average, level 3 must achieve the equivalent of 5×10^7 instructions per second in performance.

The CDF data acquisition system is then composed of two cooperating and concurrent subprocesses. The first, or triggering and digitization subprocess, involves the lower system levels, including the front end electronics, scanners, local processors, and level 1 and level 2 triggers. The second, or event selection subprocess, employs the level 3 trigger processors to select a subset of the digitized events for logging to magnetic tape and/or transferral to the host computer. The data flow for an event in this system is shown on

Fig. 2, while a schematic diagram of the system components and interconnection is shown in Fig. 3. Further details on the CDF data acquisition system besides the triggering aspects discussed here can be found in Ref. 2, 4, and 5.

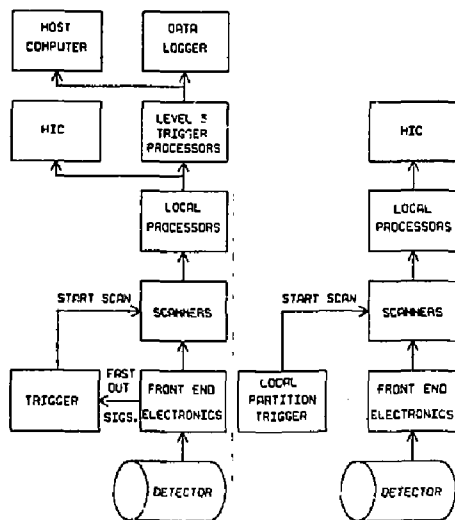


Fig. 2. a) Data flow in the global partition, illustrating the process of normal data acquisition. b) Data flow in a local partition, illustrating the use of an independent subsystem for running diagnostics and doing calibration. HIC stands for "Human Interface Computer." There are several of these minicomputers distributed throughout the system.

Level 1 and 2 Triggers

These triggers respond to analog signals and drift chamber hit bits delivered directly to the trigger logic from the front end electronics over 5,000-10,000 dedicated cables. These signals include pulse height information from sums of calorimeter modules, timing signals from muon drift chambers, hit bit latches from tracking chambers, and current division pulse heights from tracking chambers. The trigger logic will be located outside the shielding wall. The trigger cables represent the majority of the cables for the experiment that must penetrate the shielding wall, and these cables must either be disconnected or manipulated in some manner when the detector is moved in and out of the interaction region.

The level 1 trigger makes its decision in the time between beam crossings (roughly 3.5 microseconds) so as to generate no dead time. This is expected to provide enough time to allow the level 1 trigger to identify all inelastic events with a transverse energy greater than a predetermined minimum, with more than a given number of calorimeter cells having a transverse momentum deposit greater than a preset value, and to identify events with muon candidates in either the central muon drift chambers or the forward toroids.

Beyond that, the level 1 trigger should introduce as small a bias as possible into the event sample. Up to a luminosity of 10^{29} , the level 1 trigger could in

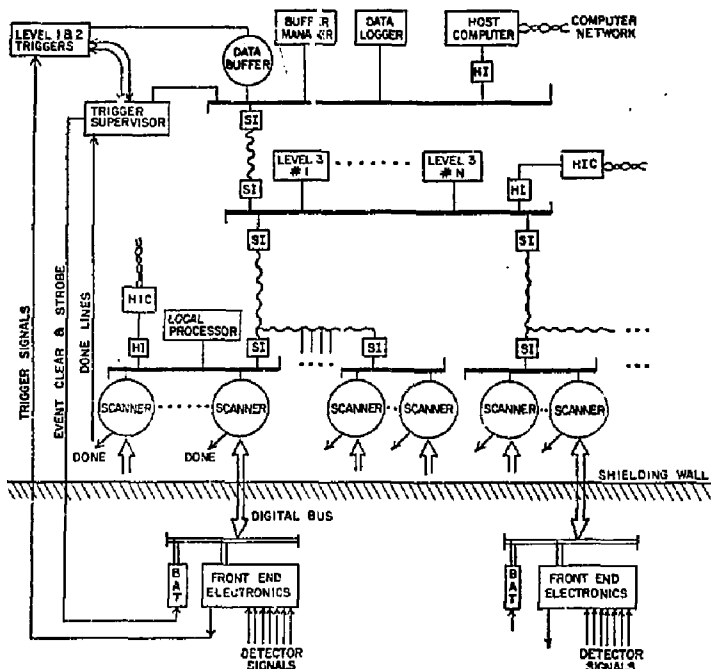


Fig. 3. Data acquisition system block diagram. SI's are FASTBUS Interconnects and HI's are FASTBUS Host Interfaces.

fact accept every inelastic interaction without introducing significant dead times at later levels of the trigger system. At higher luminosities, level 1 will be expected to select roughly 10 percent of the total inelastic interaction rate, or about 5,000 events/second.

A schematic outline of the level 1 logic is shown in Fig. 4. This fairly straightforward logic should not require the development of any special processors, but can be implemented using conventional electronics.

The level 2 trigger makes a more sophisticated decision based on the same data as that available to level 1. It selects events according to the general topology of the event, including energy clusters in the electromagnetic and hadronic calorimeters and muons in both the central and forward muon detectors.

The speed requirements on level 2 are that it not introduce large amounts of dead time when processing as many as 5,000 events per second, and thus the level 2 decision process can average no more than 20 microseconds per event. However, since the trigger decision can be asynchronous and analog information is preserved for a few milliseconds on sample and hold circuits, the level 2 processors can take up to several hundred microseconds for a subset of events provided that the majority of events are rejected in less than 10 microseconds. The level 2 processors must reduce the rate by at least another factor of 10, down to roughly 500 events per second. Events passing the level 2 selection criteria are then digitized by the normal readout process (a

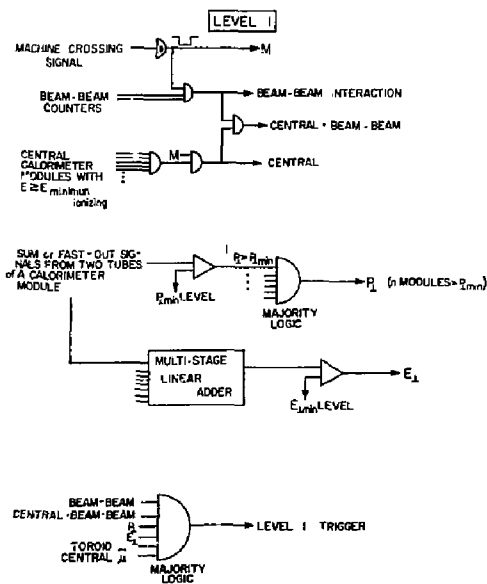


Fig. 4. Schematic of the level 1 trigger logic.

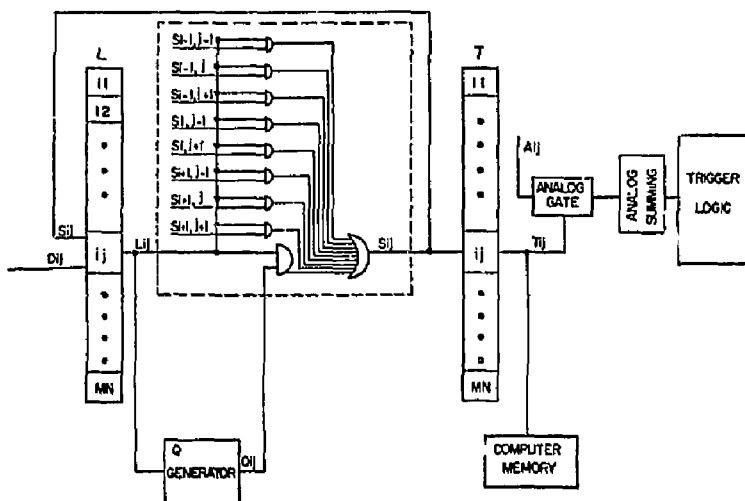


Fig. 5. The cluster finder.

slow process, requiring up to 1 millisecond per event), and the entire event will then be available for consideration by the level 3 triggering system.

The level 2 trigger processors will consist of two major portions: a collection of processing engines and a series of decision engines. The processing engines have the job of doing the actual processing of the input data and producing lists of muon tracks, energy clusters in the calorimeters, and central tracking candidates. These will be primarily hard wired modules, programmable only by reloading memory look-up tables or changing a programmed logic array. They need to work relatively rapidly to allow quick rejection (less than 10 microseconds) for most events, but do not need to be particularly flexible, as the types of calculations needed can be well predicted in advance. New types of triggers (for instance, selecting particle types with Cerenkov counters) will require additions of new detectors and new triggering cables as well as new level 2 processing engines. The initial complement of processing engines should be sufficient for almost all types of triggers which could be formed from the information initially available for level 2.

An example of a processing engine is the cluster finder shown in Fig. 5 and described more fully in Ref. 6. This device will use analog pulse heights and find a group of neighboring calorimeter modules all of which have transverse momentum deposits above a minimum threshold. It will prepare lists of the size, location, total transverse momentum, and electromagnetic or hadronic nature of each cluster.

The decision engines, on the other hand, can be somewhat slower and thus more flexible. They will be programmable devices, possibly using bit-sliced microprocessors, which will run simple programs using the lists of tracks, jets, muons, and electromagnetic showers prepared by the processing engines. A large number of triggering criteria based on the overall event topology are then possible, allowing the trigger requirements to be easily modified as the physics interests of the experiment evolve.

The overall timing of the level 1 and 2 trigger processors is shown in Fig. 6. This diagram shows how the gate and clear process is suspended by a level 1 accept decision, resuming after either a level 2 reject decision, or after the full event readout following a level 2 accept decision.

Level 3 Trigger Processors

The level 3 trigger processors have the task of performing the final event selection, reducing the event rate from 500/second down to about 5/second. The event has already been digitized through the standard read-out path, and so the level 3 processors will have the entire event at full precision to examine.

Despite the very large total processing required at level 3, as described above, there is no particular speed required for any individual event. This is due to the fact that the events are buffered, and thus level 3 processing produces no dead time regardless of how long a single event takes to process, provided that the total amount of level 3 processing can handle the total event rate.

The premium at level 3 is therefore not on processing capability of an individual CPU, but rather on total processing capability per dollar. The most cost-effective way of providing the large total amount of level 3 processing power is with a large number of small CPU's, each of which will process one event for a relatively long time. The overall processing demands are satisfied by many CPU's processing many events in parallel.

However, the individual level 3 CPU's cannot get too small. Aside from the requirement that a single processor be able to handle an entire event, the processors must be programmable in high-level languages. The level 3 trigger selection criteria will likely involve complex physics calculations including extensive pattern recognition and reconstruction of both tracking and calorimetric data, and such programs can be conveniently written only in high level languages.

TRIGGER SELECTION OF EVENTS

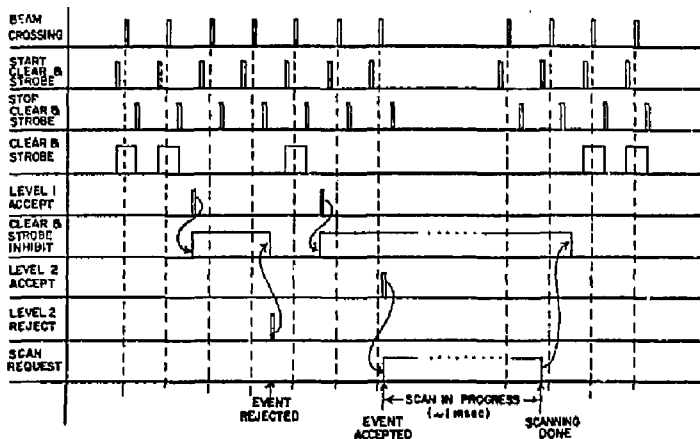


Fig. 6. Timing diagram showing the interaction between the level 1 and level 2 triggers and the trigger supervisor.

Moreover, it will aid program development and debugging if the level 3 processors can execute the instruction set of some larger CPU, which can then be used to develop and test the programs to be used for event selection.

Thus, the preferred implementation for the level 3 processors is a CPU that executes the instruction set of some popular main frame computer together with a large amount of memory, all built on a single FAST[™]'s card. It is hoped that such devices will be commercially available by the time they are needed in the CDF detector; if not, we will need to develop such processors ourselves.

References

1. Design Report for the Collider Detector Facility (CDF), D. Ayres et al., Fermilab internal document, CDF 111.
2. Design of the Collider Detector Facility Data Acquisition System, A. E. Brenner et al., Fermilab internal document, CDF 108 (1981).
3. FASTBUS Modular High Speed Data Acquisition System for High Energy Physics and Other Applications, U.S. NIM Committee.
4. The Fermilab Collider Detector Facility Data Acquisition System, A. E. Brenner et al., Submitted to IEEE Nuclear Science Symposium, 1981 (also Fermilab publication FN-350).
5. RABBIT System Specifications, T. F. Droege, K. J. Turner, T. K. Ohska, Fermilab internal document, PIN 52.
6. A Fast Cluster Finder, J. Freeman, Submitted to the IEEE Nuclear Science Symposium, 1981.

DATA DRIVEN PROCESSING

H. Cunitz, Y. Hsiung, B. Knapp, W. Sippach
Columbia University, New York, NY 10027

ABSTRACT

Herein is described a very high speed processing method. It is based on the data driven principle, and depends on constructing algorithms from hardware operators that are generally interconnectable. A set of modules and their application to Fermilab E 605 is discussed.

INTRODUCTION

In order to deal with the very high information rates provided by modern detectors, we are forced to introduce some sequential processing in the data stream. To achieve high bandwidth, we must consider the limitations of each part of the system. If we are willing to treat the system as a pipeline structure and fully buffer the data stream, then the time for encoding the data into numerical form can overlap the processing time. By the same token, we can distribute the processing in the pipeline so that only the average processing time of any section limits the rate in the data stream. In addition, raw data can be passed thru the structure for recovery to permanent storage. This view leads to the concept of a data driven structure, where the natural segmentation of the detector is imposed on the data formatting and buffering arrangement, and the processing algorithm appears in a hardware pipeline.

DATA DRIVEN CONCEPT^{1,2}

The traditional stored program computer treats computation as an ordered sequence of operations to be performed on a set of data. A data driven processor is based on the principle that any operation can proceed when its operands are available and the destinations of the results are able to receive them.

The step to a hardware processor is quite simple. We must build a set of useful operators that are generally interconnectable, and then put together computation structures that match the natural structure of the problem. This will result in genuine concurrency of computation, and an enormous increase in speed.

This structure requires no central control, except for maintenance. Data words and blocks are aligned by the operators, so that quite complex systems involving nested loops can be constructed that are completely determinate and free of conflicts.

DATA TRANSFER PRINCIPLE

The basis of this scheme is the data

transfer principle that allows generalized interconnectability.

We define a cable with a 16 bit data value field, and an 8 bit control field. The control field contains a bit called valid that defines a non-empty data word for that clock cycle, a bit called complete that defines a block boundary, and 4 bits called name that identify the data subset to which the valid belongs. A bit called hold is produced by any destination module on the cable that is unable to accept the data transfer, and a bit called block reset allows data within a block boundary to be destroyed by a downstream device. Data transfers between modules, and internal to modules, are register to register, synchronous to a central clock. The hold presents a special problem since it propagates backwards in the sequence. The hold is de-skewed with respect to the clock at the output of each module, where a normally transparent latch is provided to prevent loss of data because the output register sees the hold one cycle too late. A register that contains no valid data can be loaded regardless of a downstream hold, effectively blocking the hold for that cycle. The data flow is optimally controlled in complicated structures, where the process of data alignment generates both empty words forwards and holds backwards, that annihilate on contact.

More than one module is allowed to receive the same cable, and branches are constructed by pre-programming each module to accept a subset of the name space.

PROCESSING SYSTEM

A system includes the readout, the data buffering, the data transfer buses, the processor(s), the host, tape units, etc.

Figure 1 shows a fully pipelined system.

Here e
er so
at a
be pr
The bu
no com
their
readou
cept fo
merge a
Th
puts to
ternal
event
contai
old ev
The out
skip or
ring buf

read bus and are expected to accept this skip/read command in unison. Hold, on this read bus, allows any buffer, momentarily unable to execute this command, to prevent other modules from prematurely acting on the command.

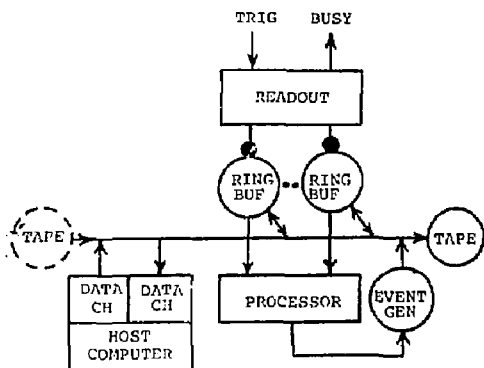


FIG. 1 PROCESSOR SYSTEM

A property of this system is that it can be data driven either from the readout, which is a parallel structure, or from the data bus, where data can be written into ring buffers from the host, or from tape. The same data tape that is written from the data bus can be rewound, written directly into the ring buffers, and processed to produce a reduced tape. The holds, and alignment of block boundaries between events guarantees determinancy.

The processor and readout have a control bus that attaches to every module, and is used to maintain the system and to load fixed data into the modules. All registers, counters, and memory locations are accessible via this bus. The internal registers are constructed from shift register IC's, so that these off line operations can be bit serial on this bus, which requires only one data and one response bit (in addition to address and control bits). For system testing, blocks of code are sent from the host data channel into the system, and output code from the system is independently received by an input data channel, which interrupts the host either when it is filled or when an interrupt word appears in the output code. This way the host requires no special knowledge of the system state for transfer of data in and out.

The readout bus is based on the data transfer principles described in the previous section, except that it has four more control bits in the name (address) space; a tag control bit that allows the name to be associated with the data source or to represent the address of a destination, and a tag control bit that defines use of the data field as a

value or as command information. These tags result from merging control and data transfers onto the same physical bus. Because the bus is synchronous, and all words are fully specified by the name and tag fields, it is possible to have interleaved, autonomous communication on the bus. A small number of additional module types allow asynchronous communication to external devices, for example the host, tape units, etc.

PROCESSOR MODULES

So far we have constructed a set of 14 modules found to be useful in track following and data organization problems. The modules are based on ECL 10K logic and operate at a 40 Mhz clock rate. The modules can be organized into four groups; lists, sequences, functions, relations.

The list modules are differentiated by the way the data is organized for access.

List/Index-Data is written in sequence at the write port, and assigned an index or word count. This index defines the data storage location, so that data can be retrieved from the read port by index value. The write complete word is held at the write port until the read port complete is received, at which point the words are merged to produce the output complete word, and reset the index.

List/Counter-Data at the write port passes thru the output port, and those data elements that match the pre-assigned name are written into memory and assigned an index (i.e. word count) that defines the storage location in memory. In order to retrieve data via the input port, a read index is generated by counting data elements at this port and reading from memory those elements that match a pre-assigned name. This subset of the data that entered the write port corresponds to a relation on the original set. It is assumed here that all the elements that pass thru the list counter via the write port are tested by a processing relation and passed back to the read port with a name assigned by the test that indicates which elements pass the test and therefore belong to the relation. Any number of list counters can be connected in series, where there are multiple nested loops in the relation. The output complete is produced when all elements sent from the module have been counted at the read port. The index counters are reset when the output complete is formed.

Buffer-This is a FIFO that allows data alignment between different parts of the processing structure without causing holds in the connecting path. Data can be written and read during the same 25 nanosecond cycle. Data is available at the output port whenever the buffer is not empty and there is no hold

on the output. Holds cannot propagate to the input port if the average output rate is equal to or greater than the input rate, and the dynamic space of 128 words is not filled.

Map-This is a storage device that allows associative data retrieval. A memory cell is assigned for each possible write data value, with all cells initially set to zero. Data is retrieved via the read port by value in the form of nine contiguous cells around the integer part of the input value. An optional form of the map allows 16 cell access around the integer read value, but requires two read cycles. The truncated part of the read value is passed to the output and concatenated with the cell data. If data is written as an ordered sequence, the read hold is used to prevent reads until the last write value exceeds the value at the read port. For unordered write data, a read hold must be present until the write complete is transferred. When both write and read completes have been received, the output complete is sent, and the map is erased from an internal list containing the last block of cell numbers loaded into the map.

These modules generate sequences from the data:

Binary Index Generator-This module generates the cartesian cross product of two data sets in index pair form by counting the data elements at each of two input ports, and generating all possible index pairs at the output port. Outputs are produced as soon as two or more inputs are counted, under control of two read counters and two pointer registers. No input holds are produced except by the input completes which are held until the full array has been generated, at which point the output complete is sent and the index counters are initialized.

Unary Index Generator-This module generates all the unique index pairs of the product of the set on itself. The diagonal elements of the set, that is the elements themselves, are generated with a different name to distinguish them. No holds are produced on the input port, except by the input complete which passes to the output when all index pairs have been produced.

Page Generator-This module is used to copy the data elements a pre-selected number of times. Only data with a pre-specified name will generate this copy sequence, all other data elements pass directly thru in one cycle.

The following modules are available for generating functions:

Arithmetic Operator-This operator performs any of the standard binary arithmetic and logical operations on the output data (add,

subtract, and, or, exclusive or, etc.) provided by the ECL 10181 ALU. A plug-in patch allows the 20 bit name and data space to be connected in a general way to the two 16 bit inputs and to the control space of the ALU. Alignment of data in the input registers causes data transfer to the output and new data to be entered at the input registers, under control of the holds. Alignment of completes at the input ports produces a complete at the output port.

Normalizer-The normalizer is used to give a linear function value $ax+b$ of its input value x . Two internal memories (8 address bits each) can be preloaded with 16 bit function values. A plug-in patch allows any 16 of the bits of input data and name to be connected to the two 8 bit address tables, and the outputs of the tables are added with 16 bit precision. In order to normalize 16 bit input words, the 8 high order bits are patched to the high order table, and the 8 low order bits to the low order table. For smaller size values, name bits can be connected in common to the two tables, resulting in sets or normalizations. Any function of $F_n(X_1) + G_n(X_2)$ can be produced, where X_1 and X_2 are separate data fields of the input words. The complete passes thru the normalizer without producing holds.

Binary Table-The table is used to give a general function value of $F(X_1, X_2)$ of its two input values. A plug-in patch for each of the inputs allows any part of the value, name space of the two input words to be patched into the 8 bit address space to produce a 16 bit function value at the output. Alignment of data in the input registers causes data transfer to the output under control of the holds. The table can also be a test if appropriate output function bits are patched into the output name space.

Unary Table-this is identical to the binary table, except that only one data input is provided.

The following modules are available for generating relations involving greater than, less than tests. A relation results in a name being assigned to the output data depending on the test result.

Ordered Merge-This binary input module merges two ordered data sets into a new ordered set. The data elements at each input port are compared over a selectable part of their data fields. The larger (or smaller) word is passed to the output, and the other input is held until it is larger (smaller) than the word at the other input port. When the inputs are equal, either the value is passed to the output with a special name, or optionally both values are passed in sequence with their

tinguished by name, they are allowed to co-exist in the sequence without causing conflicts. The computation proceeds at the highest possible speed since the operations take place concurrently at the 40 Mhz clock rate, moderated only by holds and data alignment in the modules. Any amount of parallelism can be added to the computation part of the structure by expanding the number of normalizers and other arithmetic devices, or alternatively the structure can be re-used by adding more nested loops where we use list counters to close the loops. The use of a buffer (B) at the table output allows data from the table to be automatically aligned with the downstream data without producing holds.

We can duplicate this structure for each of 3 or 4 wire plane views, and fold them onto each other to reduce hardware, or unfold them to gain speed. If we consider the more complete problem of finding tracks in three views, the nested loop structure decomposes into loops for lines in front of the magnet, those for tracking to the back, and those for matching tracks found in each view. This decomposition leads to a high degree of concurrency, where the delay thru the structure is irrelevant since the new events keep the pipeline optimally filled.

TRIGGER PROCESSOR FOR FERMILAB E605

We have built a small trigger processor for E605. The detector configuration is shown in Figure 3. The target is in the field of a focusing magnet which focuses high mass pairs around a beam dump into the detector. There are two UYV MWPC chambers in front of an analyzing magnet, and two drift chamber stations behind it, with staggered pair UYV planes. In addition to this tracking system, there is an imaging Cerenkov counter between the drift chambers, and there

are electron, hadron and muon detectors in the back.

Three planes of x,y hodoscope counters are used to define a fast trigger for gating the readout systems. The data subset required for the trigger processor transfers thru the ring buffers to the processor inputs.

The preliminary form of the processor selects tracks that are consistent with the target and constrains P_y . The system modularity will allow development of the trigger as running experience accumulates.

Wire hits from the staggered pair drift chambers are merged with ordered merge modules. Adjacent wire pairs and singles are encoded by associator modules which assign a low order bit to the wire number corresponding to one-half wire space.

Wire hits from the MWPC chambers are written into separate maps. A binary loop structure, similar to the one described in the previous section, forms lists of the associated signals from the two drift chambers and generates all possible line projections for the MWPC plane maps. Both projections are calculated simultaneously to gain speed.

A binary table transforms the output road data from the maps into a cut. If the test is met, a new name causes the list counter module to retrieve the index pair for the track, and the linear combinations of Y_3, Y_4 for calculating the P_z and P_y momentum components are simultaneously accessed in the normalizers (the test name is used to address the appropriate pages of the normalizer memory). Log tables are used to generate logs of these two quantities which are subtracted to give the log P_y . A table forms a cut on P_y .

The projections on the calorimeter, muon detector, and counter hodoscope are also

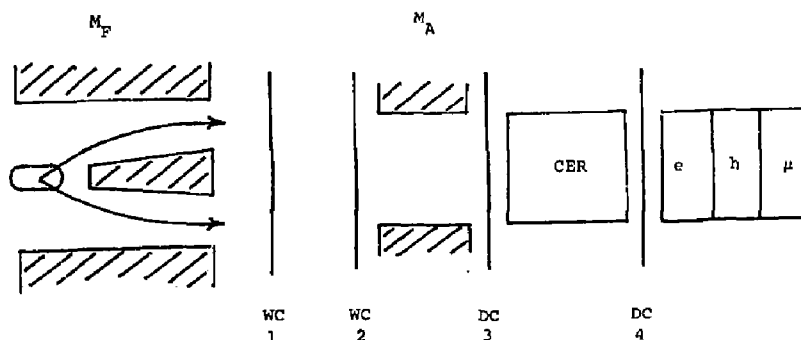


FIG. 3 E605 DETECTOR

copied out during this pass of the loop. The various cuts are buffered, to eliminate holds, and concatenated to form a parametrization for each track candidate. A unary index generator module forms all track pairs and singles, and a trigger cut is produced in a binary table. The trigger output word assigns trigger identification to 12 unique bits, and a frequency which is matched against an event counter in the event generator module. A match sets a flag that causes the ring buffers to transfer the last event in the ring to the readout. If the flag is not set when the event boundary passes out of the processor, the event generator causes the last event in the ring to be skipped. The identification bits are accumulated in flip-flops and sent with the event count whenever the ring buffers are read. Track parameters from the processor are also sent, and all data is transferred to a mega-byte

memory³, at a 10 Mhz word rate for PDP-11 processing during the beam-off time. The system deadtime due to the trigger processing is 1 to 2 μ s.

NEW MODULES

For economy, we wish to vary the amount of hardware for a particular computation to match the desired speed of computation. For the modules described so far, this can be accomplished in an obvious but limited manner by varying the degree to which modules are repeated. For less frequently performed calculations we use another family of modules in which data transfer is serial rather than parallel, i.e., rather than transmitting one word each clock period with a 24 bit cable, we transmit n bit words on one bit of cable in n clock periods. Communication and computation thus require less hardware to operate more slowly.

Another feature of previously outlined computations was the presence of frequent decisions based on simple computations, which then alter the sequence of subsequent operations. Large computations with fixed sets of operations permit additional optimization of the hardware, because more operations may be performed in parallel.

An interesting arithmetic structure with serial communication, but performing normally distinct computations in parallel, is the Σ module used to provide linear combinations of several variables:

$$Y_n = \sum_{i=1}^n A_{ni} X_i + A_n$$

The variables X_i are transmitted simultaneously but bit serially on a narrow bus cable which may have several Σ modules. Each transmission provides an 8 bit address for a 256 word table of sums of all constants A_{ni} for which the corresponding bit of the address is one. The table entry is added to a

shifting accumulator. If the 8 bit address is inadequate, the computation must be distributed over more than one Σ module and the results added. Bit serial addition is sufficiently simple that Σ modules can simply be cascaded with increased propagation delay, or another simple module can add up to eight pairs of numbers in parallel. For large computations, we can quite freely vary speed with module count. A single Σ module, for example, could provide 8 different linear combinations of five variables.

Examples of large computations without branches are plentiful in the processor which we are building to reconstruct charged particle trajectories measured in a magnetic spectrometer. A measurement consists of one-dimensional projections of particle trajectories in 24 drift chamber planes inside a moderately non-uniform magnetic field. Each of the 24 measurements of a single trajectory is a separate nonlinear function of a single set of 5 parameters. A moderately accurate initial estimate of these parameters is five linear combinations of 6 measurements found in the initial pattern recognition.

To accurately determine the five parameters with a least-square fit of 24 measurements, we generate an initial parameter estimate, using Σ modules to provide the linear combinations of 6 measurements, then carry out nine multiplications to form 6 higher order products of these parameters. An eleven term polynomial expansion of the predicted track coordinates is then carried out for each of the 24 planes. Generation of the initial estimate of the 5 parameters and the 24 measurements implied, can be performed for a new track every 300 nanoseconds with about 70 modules, or more slowly with corresponding reduction in the number of modules.

READOUT MODULES

High speed data driven processing may well require data to be supplied in numerical form at very high rates. Detector systems developed at Nevis consist of several small subsystems, each capable of supplying encoded measurements at tens of Mhz. By buffering these subsystems in parallel, a single measurement consisting of several hundred numbers can be completely transferred in less than a microsecond. These subsystems attach to a control bus, so that each readout module can be addressed from the host for testing time and charge. Signals can be automatically injected into modules for calibration and testing.

The following readout modules have been built:

MWPC System-This is a coincidence register system that has been in use for many years, consisting of chamber mounted discriminators, flat polyethylene signal delay cables to 32

channel coincidence register cards. These cards attach to a read bus segmented by wire plane. A newly designed wire number encoder allows sparse readout at a 20 Mhz word rate onto our standard processor cable, where the word format is the binary encoded 10 bit wire number and crate name. The encoder also generates a word count for limiting the block size to a pre-set number of words, and a truncated event number in the complete word.

Drift Chamber System-This is a single hit time recording system designed for relatively close wire spaced drift chambers. The time is directly encoded into 6 bit gray code for time bins greater or equal to 4 nanoseconds, or 5 bit code for 2.5 nanosecond time bins. 32 signal TDC cards attach to a read bus segmented by wire plane. The sparse data can be transferred to a standard processor cable with a valid word every 25 nanoseconds. The data word contains a 10 bit wire number, a 6 bit time, and the plane number. A word counter in the readout allows the block size to be limited to a pre-set number, and a truncated event count is sent with each complete word.

ADC Readout⁴-This 8 channel ADC was developed by a member of the E 605 group for readout into our system. The ADC has 8 bits of square root encoding, and a digital cut for each channel to sparsify the data. The sparsified data can be transferred at a 20 Mhz rate to the processor cable.

Unencoded Register Data-This system consists of 16 bit fast coincidence registers. The data is read out in an unencoded, fixed block size form, at a 20 Mhz rate to the processor cable.

SUMMARY

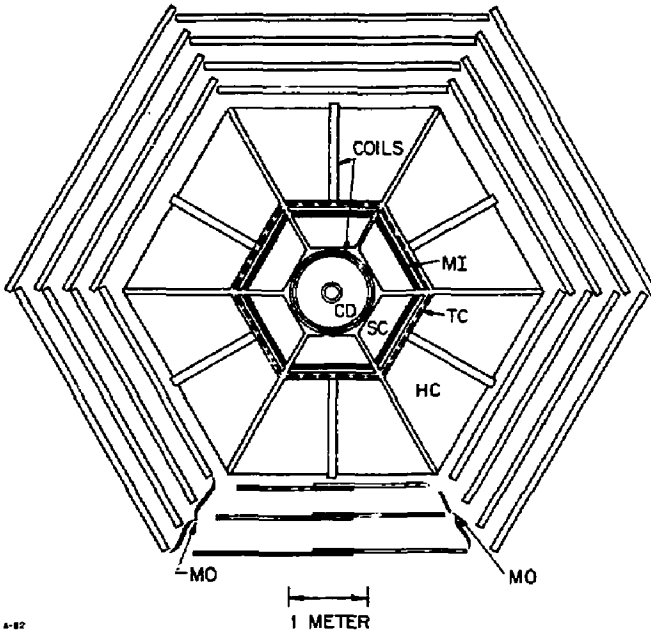
Data driven machines have no natural scale association. The computation time does not have to increase as more computation is added, and the physical size of the system is not constrained since there is no centralized communication.

The cost per operation per second seems to be much lower than any other method. This is a result of the property of concurrency, the close match of the operators to the calculation, and to the simplicity of the operators.

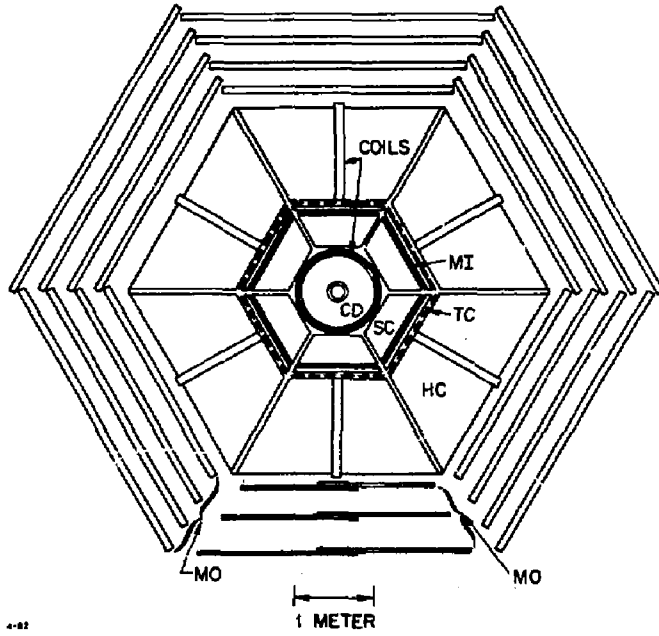
REFERENCES

1. "A Hardware Architecture For Processing Detector Data In Real Time", G. Benenson, B. Knapp, W. Sippach, in Proceedings of 1978 Summer Workshop, Brookhaven National Laboratory.
2. "Real Time Processing of Detector Data", W. Sippach, G. Benenson, B. Knapp, IEEE Transactions of Nuclear Science, Vol. NS-27, No. 1, Feb. 1981
3. J. Rutherford, University of Washington
4. D. Kaplan, Fermi National Laboratory

CALORIMETERS



CALORIMETERS



THE UA2 CENTRAL CALORIMETER

UA2 Collaboration (Bern-CERN-Copenhagen-Orsay-Pavia-Saclay)
Presented by A. Clark
CERN, Geneva, Switzerland

Summary

The UA2 experiment¹ was recently installed at the CERN Super Proton Synchrotron (SPS) proton-antiproton collider², to study collisions at an energy $\sqrt{s} = 540$ GeV.

A major objective of this experiment is to identify the weak intermediate bosons (Z^0, W^\pm) via their electronic decay modes:

$$\begin{aligned} \bar{p}p &\rightarrow Z^0 + X^0; & Z^0 &\rightarrow e^+e^- \\ \bar{p}p &\rightarrow W^\pm + X^\mp; & W^\pm &\rightarrow e^\pm\nu. \end{aligned}$$

Current theoretical models³ predict a production cross-section $\sim 3 \times 10^{-33}$ cm² and a leptonic fraction $\sim 3\%$ for Z^0 , $\sim 8\%$ for W^\pm .

The low expected Z^0, W^\pm production rate implies the need for good electron identification and energy measurement over a maximal solid angle. The UA2 detector is instrumented over $\sim 80\%$ of the solid angle by segmented lead/scintillator sandwich counters, providing a $Z^0 \rightarrow e^+e^-$ acceptance of $\sim 63\%$. At luminosities $L \sim 10^{30}$ cm⁻² s⁻¹, ~ 0.15 events/h should be detected with a mass resolution at the Z^0 peak $\sim 1.5\%$.

Another major objective of this experiment is to study high- p_T hadron jets. For this reason, and to enhance electron identification, segmented iron/scintillator sandwich counters are installed in the central region.

This talk describes the electromagnetic and hadronic calorimetry in the central region of the UA2 detector.

Experimental Apparatus

General

Figure 1 is a plan view of the apparatus. At the centre is the vertex detector. It consists of four multiwire proportional chambers (MWPC) with cathode strip readout, a cylindrical scintillator hodoscope, and two JADE-type drift chambers⁴ with charge division and multi-hit readout. The detector is surrounded by 1.5 radiation lengths tungsten and a fifth proportional chamber (PROP5) to provide an accurate position measurement of e.m. showers. This chamber allows improved hadron rejection, and rejection against overlap background (\approx low-momentum hadron near a π^0 , simulating an electron) in the following calorimeter.

Covering ± 1 rapidity units about 0, the vertex detector is surrounded by electromagnetic and hadron calorimeters.

The forward and backward directions (20° to 37.5° , 142.5° to 160°) are each instrumented by twelve toroidal-magnet sectors (0.38 T·m) and associated spectrometry. Following each sector, nine drift chamber planes allow a momentum measurement on charged tracks. After this, a 6 mm lead converter and two proportional-tube planes define the position of e.m. showers in a calorimeter.

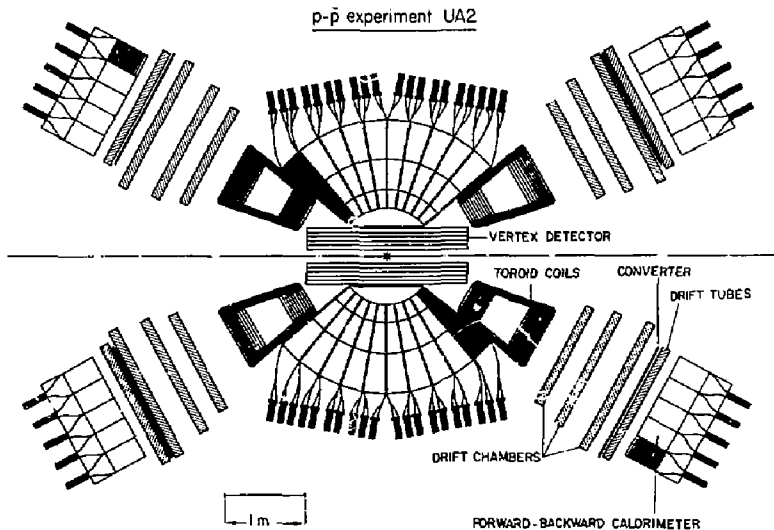


Fig. 1. Plan view of the UA2 detector.

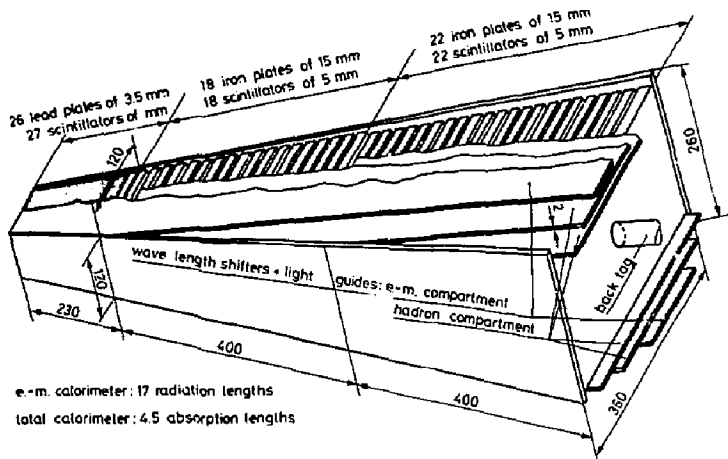


Fig. 2. Typical cell of the UA2 central calorimeter.

The 12 forward and 12 backward calorimeter sectors are each divided into ten cells (15° in ϕ , 3.5° in θ). Each cell is a lead/scintillator sandwich in two longitudinal sections (24 r.l. and 6 r.l.). The light of each section is collected in two phototubes via BRQ-doped wavelength-shifting light-photodes. The calorimeter performance is similar to that of the central region.

Central Calorimeter

The lead/scintillator electromagnetic and iron/scintillator hadronic counters cover from 40° to 140° in polar angle, and all azimuthal angles. A spherical structure, the calorimeter is segmented into 240 individual cells (towers) pointing to the pp interaction vertex. Each cell has three longitudinal sections (plus PROPS). In addition, the last 0.35 attenuation lengths are separately measured to provide a tag on late hadronic showers. Each cell has an e.m. length ~ 17.5 r.l. and a hadronic length ~ 4 a.l. (Fig. 2).

The light of each section is transferred via 2 mm thick BRQ-doped light-guides to a total of seven phototubes per cell (XP2008, XP2012). The scintillator is 4 mm NE104B (e.m.), and 5 mm PMMA doped with 1% PBD, 0.1% POPOP, and 10% naphthalene (hadron). Wavelength-shifting techniques⁵ minimize the dead-space between adjacent cells (Table 1). In practice the polar dead-space is negligible except for particles of normal incidence.

Table 1. Maximum separation between calorimeter cells

Compartment	Polar (mm)	Azimuth (mm)
EM	4.6 (light guide)	1 (Fe) + 1 mm (air)
HADRON 1	9 (light guide)	10 (Fe)
HADRON 2	13.6 (light guide)	10 (Fe)

To monitor phototube stability, a xenon light-flasher is associated with each azimuthal slice of ten cells. Light (diffused and filtered to approximate the light spectrum reaching the phototube) is passed via plastic fibres to the light-guide of each phototube. The net flasher stability and pulse-to-pulse variations in light output are monitored by a box containing three vacuum photodiodes. The relative stability of different azimuthal slices is monitored by sending light from each flash-tube to a box (J-BOX) containing a scintillator slab in front of three selected phototubes (XP2012). The stability of these phototubes is monitored by d.c. current measurements from ^{60}Co and ^{90}Sr sources.

An identical but independent flasher on each slice sends light to two scintillator plates of each e.m. compartment. The same photodiodes monitor flash stability.

Calibration Stability

An initial calibration of each cell was made using 10 GeV/c electrons (e.m. compartment) and 10 GeV/c muons (hadronic compartments). Since installation in November 1981, phototube gains have been monitored using the flash-tube of each slice, normalized with respect to the response of:

- i) vacuum photodiodes (discarded because of gain changes);
- ii) mean e.m. phototube response: the r.m.s. spread, for individual e.m. phototubes with respect to the mean, is $\pm 2.6\%$; the mean hadron response is unchanged with respect to the e.m. phototubes, with an r.m.s. spread for individual tubes of 3%;
- iii) J-BOX response: this indicates a mean change in e.m. light response of 0.5%, with an r.m.s. spread of 2%.

A mean change of $\leq 1\%$ (r.m.s. of $\sim 0.6\%$) has been measured in e.m. response, from periodic ^{60}Co d.c. current measurements on each cell. In the extreme forward (proton) direction, the mean change reaches 1.7%, suggesting minor radiation damage.

The stability of the phototubes, between their initial calibration and installation at the pp collider, is being analysed.

Electron Response Measurements

In addition to the calibration of each e.m. cell with 10 GeV/c electrons, data were collected between 1 and 70 GeV/c for all 5 e.m. cell types. Figure 3 illustrates the nomenclature of this section.

Response Linearity and Resolution

Figure 4 shows the normalized light response to electrons of between 1 GeV/c and 70 GeV/c passing through the centre of an e.m. cell. Following a non-linearity correction $0.977 [1.0 + 0.01 \ln (E+1)]$, the light response can be estimated to $\pm 1\%$. Figure 5 shows the variation of σ/\sqrt{E} (0.14) with electron momentum. The beam momentum spread ($\sim 1\%$) has not been subtracted. In each figure, error bars represent the r.m.s. spread of all measurements on all cell types.

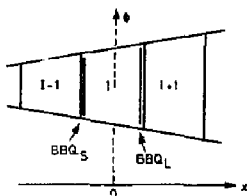


Fig. 3. Nomenclature used in following section. ϕ and x are measured with respect to the centre of the cell I.
 BBQ_S = light response of small BBQ
 BBQ_L = light response of large BBQ
 $BBQ_{SL} = \sqrt{BBQ_S \cdot BBQ_L}$

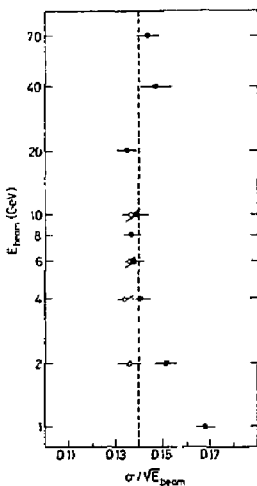


Fig. 4. Deviation from linearity of the light response BBQ_{SL} as a function of incident electron energy. The superimposed curve is $\propto [1 + 0.01 \ln (E+1)]$.

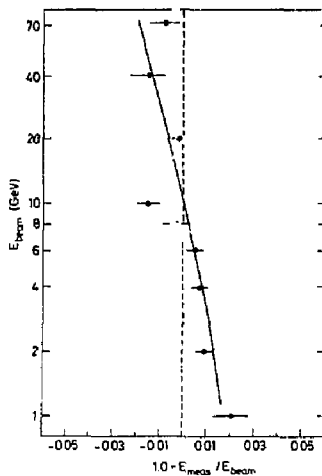


Fig. 5. Resolution of light response BBQ_{SL} , as a function of incident electron energy. (a) show data collected with tungsten converter 90 cm from the e.m. calorimeter, (c) show data collected with tungsten converter in final UA2 position.

Response Variation with Position (Normal Incidence)

Spatial scans were made for several examples of each cell type. The r.m.s. spread of measurements in different examples of the same cell type is $< \pm 1\%$. Figure 6 shows the uncorrected response for cell 2 (the second smallest) as a function of position. Similar variations exist in other cell types. Figure 7 shows the same data after correction according as:

$$BBQ(\text{corr}) = BBQ(\text{raw}) \cdot \exp(\text{corr})$$

$$\text{corr} = \left(\begin{array}{l} A_1 \cdot x + A_2 \cdot x^2 + A_3 \cdot x^3 \\ + (B_1 + B_2 \cdot x + B_3 \cdot x^2) \cdot |\phi| \\ + (C_1 + C_2 \cdot x + C_3 \cdot x^2) \cdot |\phi|^2 \end{array} \right) / |\phi|^2$$

Constants A_i , B_i , C_i have been determined for each BBQ of the five cell types. Data from muons provide a consistent parametrization. For beam impacts > 5 mm from a cell interface, the r.m.s. spread of corrected light response for individual measurements of a cell type is $< 1.1\%$. The resolution σ/\sqrt{E} is unaffected. The ratio $BBQ_R = BBQ_S/BBQ_L$ provides a measure of the beam impact position in the cell ($\sigma \leq 5$ mm). However, because of differing light collection efficiencies for BBQ_S and BBQ_L , a variation of light response exists along each BBQ_S contour. For that small class of e.m. showers having no associated track or PROPS signal, this variation defines the effective resolution of the e.m. calorimeter.

Response Near a Cell Interface (Normal Incidence)

The azimuthal separation between two cells is small, and a maximum response correction of 10% is required within ± 2 mm of the cell interface. Few normal-incidence electrons pass through the BBQ (smeared pp vertex). At the BBQ interface, $\sim 20\%$ of electrons are within 3 st. dev. of the peak, and $\sigma/E = 0.25/\sqrt{E}$. The light response of remaining events is distributed below the peak (longitudinal escape and Čerenkov light).

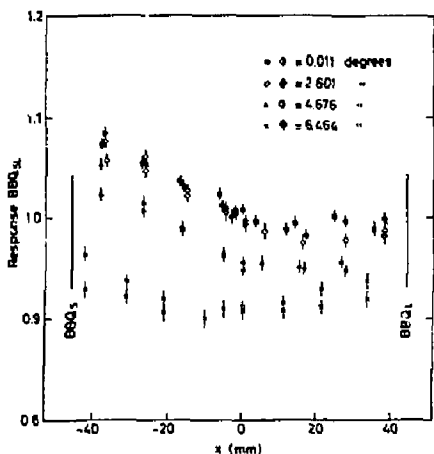


Fig. 6. Variation of light response BBQSL with position, in cell type 2 of the e.m. calorimeter.

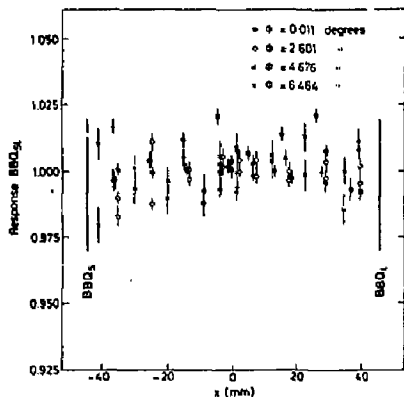


Fig. 7. Data of Fig. 6, after correction for the position of beam impact in calorimeter.

Non-Normal Beam Impact

At the $p\bar{p}$ collider, the interaction vertex is smeared along the beam direction with $\sigma \sim 1.1$ cm, and data were collected to simulate vertices in the range $-20 < x < 20$ cm. For $|z| > 2$ cm, no deterioration of the efficiency or resolution is measured near the BBQ interface, and no additional response corrections are required. Using the correction formulae above, the average response at each vertex position changes by $< 1.4\%$ with respect to normal incidence. The r.m.s. spread of individual measurements is $< 1\%$ for each cell type.

Hadron Response Measurements

Data have been collected at π^- momenta of 1 to 70 GeV/c and π^+ momenta of 1 and 2 GeV/c. Preliminary results are shown for π^- data of momenta above 6 GeV/c.

The UA2 calorimeter is short (4 s.l.), so significant longitudinal escape is expected. However, high-energy hadron jets should be better contained since their behaviour is similar to that of a single particle interacting at the calorimeter entrance. Data exist both for single particles and for simulated jets.

Event Selection

To ensure good energy containment, cuts were applied: $E(\text{hadron section 2})/E(\text{calorimeter}) \leq 0.8$, and $E(\text{e.m.}) \geq 1$ GeV or $E(\text{hadron section 1}) \geq 1.5$ GeV. The resultant event efficiency is shown in Fig. 8.

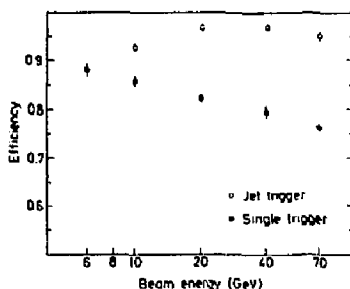


Fig. 8. Efficiency of detection in hadron calorimeter as a function of incident π^- energy. Applied cuts are described in text.

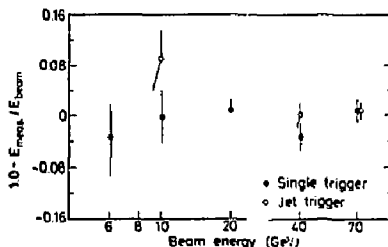


Fig. 9. Deviation from linearity of the light response BBQSL as a function of incident π^- energy.

Light Response

A fit was made to normal-incidence JET and SINGLE data to find parameters, relating the response of each compartment, that optimize the response linearity (Fig. 9). The resultant resolution is shown in Fig. 10.

Response Uniformity

The above light-response analysis used available data in the median plane of each cell ($\phi = 0$), with linear attenuation corrections. The resultant response was uniform to $< 1\%$ for each cell type. For normal-incidence data near a BBQ interface, the acceptance is reduced for SINGLE triggers, but not for JET triggers (Fig. 11). The resolution is not significantly affected, as shown in Fig. 12.

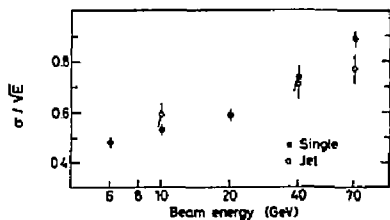


Fig. 10. Resolution of light response BBQSL as a function of incident π^- energy.

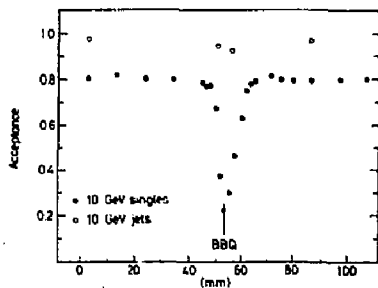


Fig. 11. Variation of π^- acceptance across cell interface of the central calorimeter.

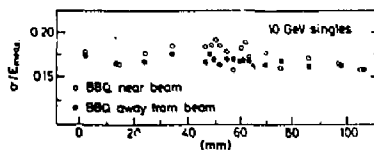


Fig. 12. Variation of π^- resolution across cell interface of central calorimeter.

Non-Normal Incidence

Data collected at an effective vertex position of ± 10.4 cm shows an average change in light response of $< \pm 1\%$. The resolution is unchanged. The variation in aperture across a BBQ interface is reduced to $< \pm 5\%$ for SINGLE triggers.

References

1. UA2 Collaboration (M. Banner et al.), CERN/SPS/78-08 (1978) and CERN/SPS/78-54 (1978).
2. C. Rubbia, F. McIntyre and D. Cline, in Proc. Int. Neutrino Conference, Aachen, 1976 (eds. H. Faisanor, H. Reithler and P. Zerwas) (Vieweg, Braunschweig, 1977), p. 683.
S. Van der Meer, CERN/SPS/423 (1978).
Design study of a p \bar{p} colliding beam facility, CERN/PS/AA 78-3 (1978).
3. See, for example: C. Quigg, Rev. Mod. Phys. 44, 297 (1977).
4. JADE Collaboration (W. Farr et al.), Nucl. Instrum. Methods 156, 283 (1977).
5. R.L. Garwin, Rev. Sci. Instrum. 31, 1010 (1960).
W.B. Atwood, C.Y. Prescott, L.S. Rochester and B.C. Barish, SLAC-TM-76-7 (1976).

Alupe

THE MAC CALORIMETERS AND APPLICATIONS*

MAC Collaboration:
Colorado-Frascati-Northeastern-SLAC-Utah-Wisconsin†
Presented by W. T. Ford, Colorado

Summary

The MAC detector at PEP features a large solid-angle electromagnetic/hadronic calorimeter system, augmented by magnetic charged-particle tracking, muon analysis and scintillator triggering. Its implementation in the context of electron-positron annihilation physics is described, with emphasis on the utilization of calorimetry.

Detector Description

The MAC detector is shown in Fig. 1. Charged particles produced with polar angles between 17° and 163° are analyzed in the central tracking chamber, which comprises 833 drift cells arranged as 10 layers in a common gas volume. Each cell contains a double sense-wire pair connected to differential electronics so that drift distance is determined without right-left ambigu-

ity. The wires in four of the layers are axial; these are interspersed with six stereo layers at plus and minus three degrees to determine axial positions. The setting accuracy is $200 \mu\text{m}$; with the solenoidal magnetic field of 5.7 kG, the momentum resolution is $\Delta p/p = .065 p \text{ min}$.

Surrounding the solenoid coil is the central shower chamber (referred to below as SC), a calorimeter optimized for electromagnetic shower analysis and composed of 32 lead plates interspersed with proportional wire chambers for a total thickness of 16 radiation lengths. Each anode wire is suspended parallel to the beam at the center of a rectangular aluminum cathode about 1 cm thick \times 2 cm wide. Groups of wires are combined for readout as 192 azimuthal sectors in each of three layers. Axial position is determined by current division, i.e., the ratio of pulse heights measured at both ends of the wire group through low impedance preamplifiers.

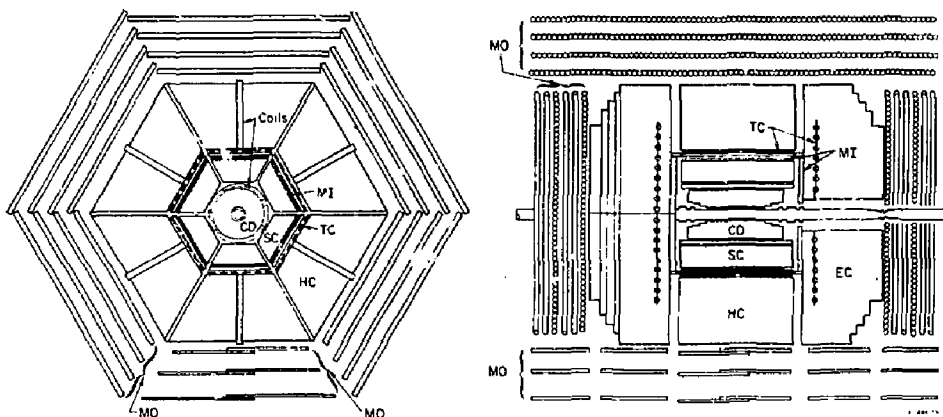


Fig. 1. MAC detector layout. The components labelled in the figure are: central drift chamber (CD), shower chamber (SC), trigger/timing scintillators (TC), central and endcap hadron calorimeters (HC, EC), and the inner and outer muon drift chambers (MI, MO). Also indicated are the solenoid and toroid coils.

*Work supported in part by the U. S. Department of Energy, under contract numbers DE-AC02-76ER02114, DE-AC03-76SF00515, and DE-AC02-76ER00881, by the National Science Foundation under contract numbers NSF-PHY77-21210, NSF-PHY77-21297, and NSF-PHY5-39485, and by I. N. F. K.

†MAC Collaborators are: W. T. Ford, J. S. Marsh, A. L. Read, J. G. Smith, Department of Physics, University of Colorado, Boulder, CO 80309; A. Marini, J. Peruzzi, M. Piccolo, F. Ronga, Laboratori Nazionali Frascati dell' I.N.F.N. (Italy); K. Appert, L. Baksey, H. R. Band, W. L. Faissler, M. W. Gettner, G. P. Goderre, B. Gottschalk, R. B. Hurst, D. A. Meyer, J. H. Moromisato, W. D. Shambram, E. von

Goeler, Roy Weinstein, Department of Physics, Northeastern University, Boston, MA 02115; J. V. Allaby, W. W. Ash, G. B. Chadwick, S. H. Clearwater, R. W. Coombes, Y. Goldschmidt-Clermont, H. S. Kaye, K. H. Lau, R. E. Leedy, S. P. Leung, R. L. Messner, S. J. Michalowski, K. Rich, D. M. Ritson, D. E. Wiser, R. W. Zdrako, Stanford Linear Accelerator Center, Stanford University, Stanford, CA 94305; D. E. Groom, Hoyun Lee, E. C. Loh, Department of Physics, University of Utah, Salt Lake City, UT 84112; M. G. Delfino, M. Frankowski, B. K. Heltsley, J. R. Johnson, T. Maruyama, R. M. Morse, R. Prepost, Department of Physics, University of Wisconsin, Madison, WI 53706.

The central hadron calorimeter (HC) which surrounds the shower chamber has a very similar structure except the absorbers are 24 1-inch-thick steel plates, followed by three 4-inch-thick plates. The three thick plates and their associated proportional chambers are for muon tagging.

The steel plate calorimeter is extended to small polar angles by the two endcap sections (EC), whose absorber plates stand perpendicular to the beam. Each endcap has 28 1-inch-thick calorimeter plates followed by 2 4-inch-thick muon tagging layers. The endcap sampling detectors are planar proportional chambers, each covering a 30-degree azimuthal sector. The anode wires run parallel to the edges of the hexagonal endcaps and are grouped, for readout, into four radial panels. Each cathode is divided into three 10-degree azimuthal wedges which are read out as well. The chambers occupying the first 9 gsp (15 radiation lengths) have finer segmentation to match them to the electromagnetic showers which are outside the acceptance of the central shower chamber. In these chambers each segment measures about 5° in azimuth by 5° in zenith. The endcap signals are grouped into four layers in depth.

One layer of scintillation counters for triggering and time-of-flight are inserted into one gap near the entrance face of the hadron calorimeter, in the central and both endcap regions. There are 144 separate scintillators.

The muon tracking system consists of one central and three endcap planes of drift chambers located before the entrance faces of the hadron calorimeter, four layers of drift chambers surrounding the calorimeter, and six layers covering the end faces. For momentum analysis the calorimeter/absorber steel is magnetized by toroid coils, one at the center of each sextant. The entrance chambers, and those underneath the calorimeter, are planar; the remaining exit planes are assembled from 10-cm-diameter tubes each containing a single wire. The wires are all oriented to determine axial position, since the toroidal field causes a change in the tracks' polar angle, except for the endcap planes of which two layers have horizontal wires, and two each have wires at 60° and 120° respectively.

Triggers for the experiment may be summarized, with some simplification, as the logical OR of: (1) scintillator opposite sextants or end quadrants; (2) scintillator hits on any 3 or more of the 8 faces of the hexagonal prism with ends; (3) showers of at least 2 GeV in any 2 of: 6 SC sextants, 2 endcaps, or any part of the HC; (4) one or more penetrating tracks, defined by a string of central drift hits within a 20° sector and the corresponding scintillator and central hadron calorimeter sextant registering at least 400 MeV.

Calibration and Resolutions

The electromagnetic calorimeters have been calibrated with electrons from Bhabha scattering. The energy response for the central shower counter is shown in Fig. 2. The observed width of 8% (standard deviation) is greater than the 5% we would expect on the basis of earlier tests with one of the sextants in an electron beam. Those tests gave $\Delta E/E = .20/\sqrt{E}$ from .5 to 16 GeV. The difference is largely attributable to scattered non-functioning channels which number about 3-7% of the total. (The curve accompanying the data of Fig. 2 includes the effect of 5% randomly-distributed non-responding channels.) Presumably the importance of this effect is smaller at lower energies relative to inherent ionization fluctuations. In any case, the resolution of this device is not the limiting one for hadron calorimetry. The directional resolution, measured by comparing the shower centroid with the extrapolated central drift chamber track, is 0.3° in $\phi \times 1.3^\circ$ in θ . The ϕ error corresponds to about 0.4 times the wire group segmentation. The θ error corresponds to about 12% of the wire length from current division.

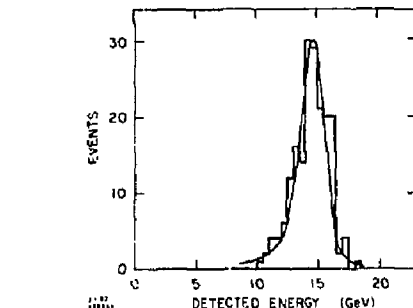


Fig. 2. Energy response of the central shower chamber to 14.5-GeV electrons. The curve is the predicted resolution function.

The corresponding information for the endcap shower chamber is presented in Fig. 3. The low-energy tail in Fig. 3A is caused by the insensitive regions occupied by the frames of the proportional chambers. These regions occur every 30 degrees and are about 10 cm wide, independent of radius, and hence have maximum impact near the poles which are preferentially illuminated by the Bhabha electrons. The directional resolution is 2° in ϕ (cathode strips) $\times 1.5^\circ$ in θ (anode wire groups).

The shower detectors alone accomplish both triggering and analysis of 77 events, for which we show, in Fig. 4, the noncollinearity angle distribution compared with the QED calculation.

For calibration of the response of the calorimeter system to hadrons, we have only the total energy of multihadron events as a known reference point. To produce the corresponding measured total pulse height, we

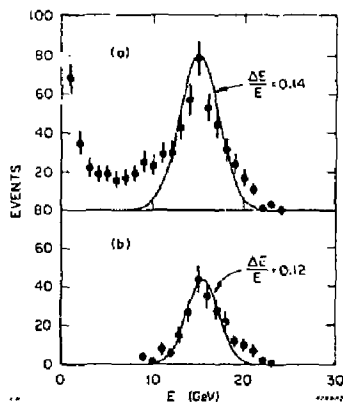


Fig. 3. Energy response of the endcap calorimeter to 14.5-GeV electrons for (a) all azimuthal angles, and (b) events within fiducial area.

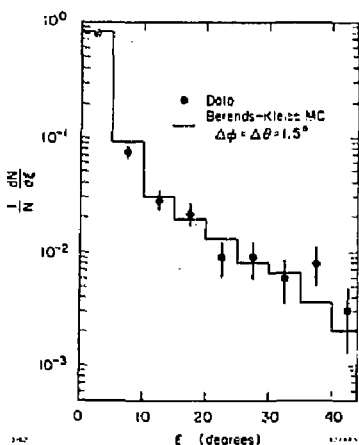


Fig. 4. Noncollinearity angle distribution for $ee \rightarrow \gamma\gamma$.

must bring into register the three separate calorimeters (SC, HC and EC), for samples containing a fluctuating mixture of hadrons and gammas from neutral pion decay incident over a wide range of entrance angles. The response to gammas per GeV will presumably be the same as that measured for electrons; for incident hadrons we expect an average of about 30-40% of the energy is lost to nuclear binding and heavily ionizing fragments. With these expectations in mind, we may write

$$a P(SC)_i + b P(HC)_i + c P(EC)_i = E_{cm}$$

where a , b , and c are the factors for converting each calorimeter's pulse height, P , into energy units, and i is the event index. (In general one may treat separately the several layers within SC, etc., as well.) The coefficients are determined by a fit to all the events in the multihadron sample.

The measured response to multihadron events with narrow jet structure and thrust axis pointed toward the central calorimeter is given in Fig. 5a. For comparison, Fig. 5b shows results of a calculation using the Monte Carlo programs EGS¹ and HETC² with our geometry. Both curves give $\Delta E/E \approx .16$. We may compare this with our earlier beam tests of a model of the HC alone with pions of several energies at normal incidence. These can be summarized as $\Delta E/E = .75/\sqrt{E}$, which gives .14 at 29 GeV. The corresponding results for $37^\circ \leq \theta_{\text{thrust}} \leq 143^\circ$ which covers all three calorimeters but avoids losses near the poles, are shown in Fig. 6. In this case, we get $\Delta E/E = .18$, and again our results agree quite well with the calculation.

The directional resolution for hadrons is set by the spread of the hadronic cascade in the calorimeters. One measure of this is the mass of a hadron jet. The hadronic decays of tau leptons provide a sample of known, limited mass: $M_{\text{jet}} \approx M_{\text{tau}} = 1.8$ GeV. The mass determined for such events by calorimetry is shown in the distribution of Fig. 7a. This resolution function is narrow compared with the distribution for multihadron events seen in Fig. 7b.

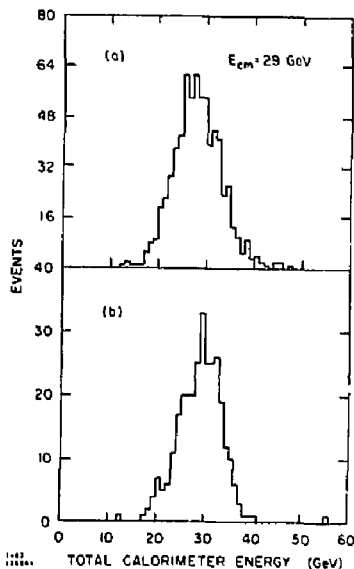


Fig. 5. Total energy of multihadron events, central region: (a) data; (b) Monte Carlo calculation.

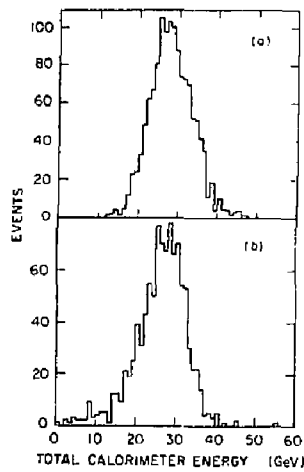


Fig. 6. Same as Fig. 5 for all non-polar events.

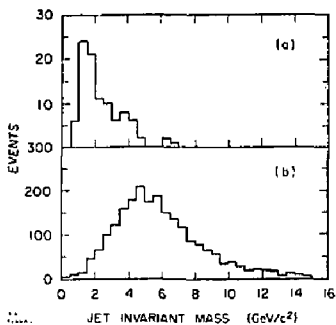


Fig. 7. Invariant mass of one jet for (a) hadronic τ decays, and (b) multihadron events.

Multihadron Event Selection

The large acceptance calorimeter system is well suited to the efficient extraction of multihadron events from single photon annihilation of electrons and positrons, even in the presence of copious multihadron production by two-photon annihilation. The solid histogram of Fig. 8 shows the tau distribution in total visible energy of all events triggering the experiment and having at least five charged prongs forming a vertex within the interaction volume of the colliding beams. For one-photon events the total visible energy 4-vector is, except for measurement error, very nearly that of the initial state, i.e., energy = $2 E_{beam}$ and net momentum = 0. The two-photon events have two final-state electrons carrying a substantial fraction of energy generally outside the acceptance of the detector (typically inside the vacuum pipe). The visible 4-vector therefore has energy less than $2 E_{beam}$ net momentum along the beam direction, and limited momentum perpendicular to the beam. We measure the net motion of the visible energy by the imbalance vector,

$$\vec{b} = \sum E_i \hat{n}_i / \sum E_i,$$

and the perpendicular energy by

$$E_{\perp} = \sum E_i \sin \theta_i,$$

where E_i is the energy, θ_i the polar angle, and \hat{n}_i the unit direction vector for energy parcel i . Fig. 9a and b show the distributions in $b = |\vec{b}|$ and E_{\perp} , respectively, for the event sample plotted in Fig. 8. The

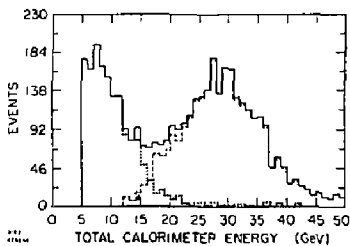


Fig. 8. Total energy for all 25-prong events. The dashed histogram represents events passing the selection criteria for multihadron events; events in the dotted histogram are the remainder.

indicated cut in b (Fig. 9a) is chosen to remove a substantial fraction of background without reducing the signal significantly. The cut in E_{\perp} (Fig. 9b) does take out that fraction of the signal which is essentially indistinguishable from background; it amounts to an acceptance loss, estimated to be about 5% of all one-photon events. After application of several selection criteria of which the foregoing are the most important, the distribution in total visible energy is decomposed into the signal and background parts indicated by the dashed and dotted histograms in Fig. 8.

An alternative analysis (method 2) has been performed which accomplishes this decomposition of the multihadron sample by fitting signal and background shapes to the total distribution with adjustable scale factors. The parent shapes were extracted by requiring more than 8 prongs and small b_{\perp} to get the signal function and by taking events with large b_{\perp} to model the background (see Fig. 10). The full distribution was cut near the minimum between the two peaks and the fitted components used to estimate the loss of signal and the residual background.

The event yields which result from these analyses for a particular data collection period (representing a subset of the data of Fig. 8) are:

$$N = 1839 \pm 45 \text{ (Method 1)}$$

$$N = 1801 \pm 49 \text{ (Method 2)}.$$

We expect that with improved statistical precision, yield measurements accurate within 2-3 percent should be possible. The model-dependent acceptance correction is very small; a precise measurement of τ multihadron events should be possible, assuming such factors as the luminosity, radiative corrections, etc. are also well understood.

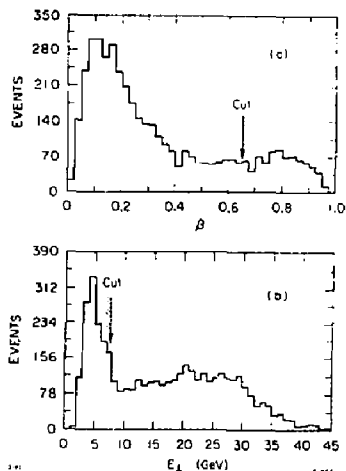


Fig. 9. (a) Imbalance and (b) E_{\perp} distributions for all 25-prong events.

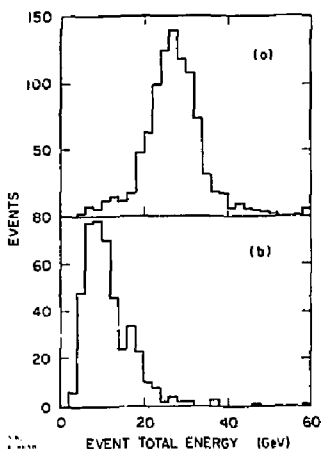


Fig. 10. (a) Events having 28 prongs and $B_z < 0.57$. (b) events having 25 prongs and $B_z > 0.57$.

Hadronic Energy Flow

A further objective of the study of multihadron final states is to map the distribution of energy as a function of production angle. For example, in Fig. 11 we show the distribution in polar angle of the thrust axis. The thrust T is defined by

$$T = \max \left\{ 2 \sum E_i \cos^2 \theta_i / E_{cm} \right\},$$

where i runs over all energy parcels, θ_i is the angle between the thrust axis and parcel i , and the maximization is with respect to the direction of the thrust axis. The curve in Fig. 11 represents $1 + \cos^2 \theta$, the distribution expected from the quark-parton model. From Fig. 11 it is clear that the region of diminished acceptance of the calorimeter system is restricted to $|\cos \theta| > .9$, and that, barring anomalous rapid change of the true cross section very near the poles, all but six or seven percent of the integral is included in the observed distribution.

A measure of the "jettiness" of the events is the distribution in thrust, T , shown in Fig. 12 as inferred both from the calorimeter and from the charged tracks

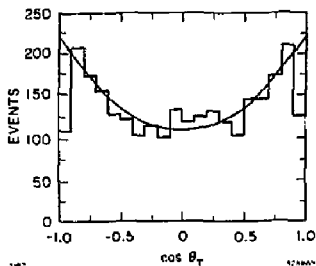


Fig. 11. Angular distribution of the thrust axis for multihadron events, determined from calorimeter energy.

seen in the central drift chamber. The calorimetric measurement appears to give a somewhat narrower peak, presumably because of the more complete sampling of the energy, but one that is displaced toward smaller average values. This may be caused by the lateral spread of the hadronic cascades which tends to produce a minimum observed jet width.

One approach to the study of energy flow in multihadron events which addresses the question of two-jet versus three-jet structure has been employed by the authors of ref. 3. A coordinate system is defined for each event such that when the angular distribution of all the energy parcels is plotted for a sample of events, the axes of two-jet events, and the production planes of three-jet events, etc., are aligned. The result is a set of three orthogonal projected energy-flow patterns as shown in Fig. 13a for our data (see ref. 3 for definitions of the major and minor axes; the thrust axis is as defined above). One can see clearly the dominant collinear two jet structure. In Fig. 13b we show the "production plane" view for events selected for maximal deviation from the two-jet character. The events appear to consist, on average, of three jets. More quantitative study is required to evaluate the significance of these features in the context of models.

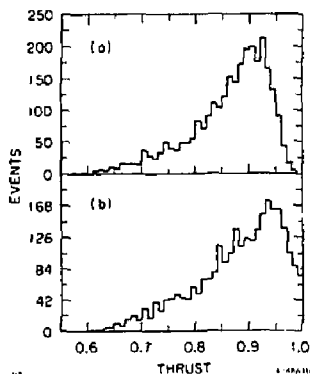


Fig. 12. Thrust distribution for multihadron events, determined from (a) calorimeter energy and (b) charged track moments.

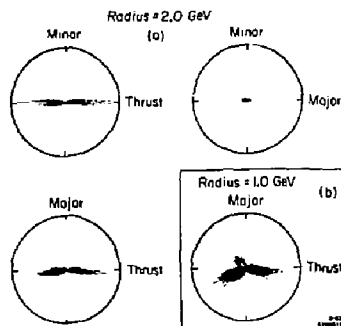


Fig. 13. (a) Energy-flow plots for the multihadron events aligned according to the directed thrust and major axes. (b) The view normal to the event plane for events having thrust 0.8 and oblateness 0.1 (See ref. 2).

Muon Identification

The calorimeter system serves also as an active filter which in combination with the muon tracking provides excellent muon identification. Preliminary data have been presented⁴ on collinear QED $\mu\mu\gamma$ and $\pi\pi\pi e$ events. Another example is equal final states in which only the muons are detected; we show in Fig. 14 the invariant mass distribution for the pairs within certain fiducial cuts.

The inclusive muon distribution from multihadron events as a function of the momentum perpendicular to the thrust axis is plotted in Fig. 15. The curves show contributions from decays of known particles, and that expected from a hypothetical t-quark of mass 10 GeV having a 10% muonic branching ratio. The contribution from hadronic punch-through, which before cuts is comparable to that from π/K decay, was reduced by a factor of 5 to 10 by excluding candidates accompanied by more than 4 hits in the outer layers of the hadron calorimeter.

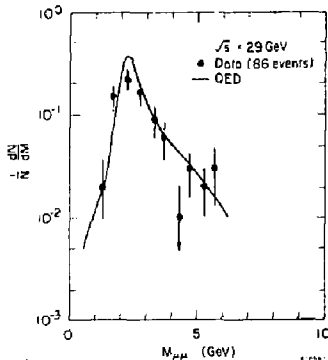


Fig. 14. Invariant mass distribution of μ pairs from $ee \rightarrow e\mu\mu$.

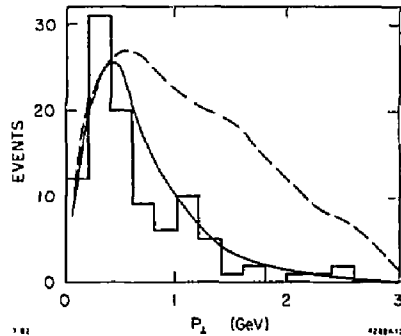


Fig. 15. Momentum perpendicular to the thrust axis for muons in multihadron events. Solid curve: calculated contribution from π , K , c , and b decay. Dashed curve: contribution of a 10-GeV t-quark with 10% muonic branching ratio.

Conclusion

The MAC detector is operating near design performance as measured in a variety of electron-positron annihilation processes at PEP. In particular, the hadron calorimeter resolution in energy and directionality agree well with calculations. The effectiveness of the large-acceptance calorimeter in detecting multihadron events has been demonstrated and precision total and differential cross section measurements can be anticipated.

References

1. R. L. Ford and W. R. Nelson, SLAC-210(1978).
2. T. A. Gabriel and B. L. Bishop, Nucl. Instr. and Methods **155**, 81(1978), and references therein.
3. The Mark J Collaboration, Physics Reports **63**, 337(1980).
4. R. Hollebeek, in Proceedings of the 1981 International Symposium on Lepton and Photon Interactions at High Energies, Bonn, Edited by W. Pfeil (Physikalisches Institut, University of Bonn, 1981), p. 1.

THE TASSO LIQUID ARGON CALORIMETERS

A. Ladage
Deutsches Elektronen-Synchrotron DESY, 2000 Harburg 52, Notkestraße 85

Summary

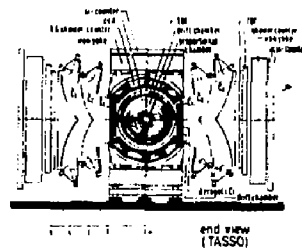
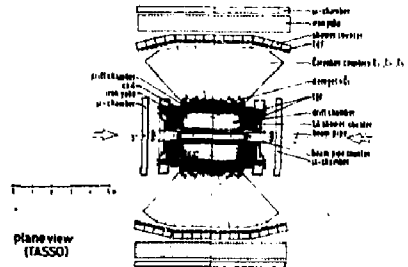
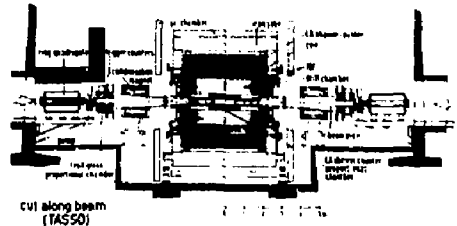
The shower counter system of the TASSO-collaboration consists of large lead/liquid Argon Calorimeters. The calorimeters are subdivided into 4 barrel- and 2 end cap counters. The highly granulated lead stacks are composed into towers looking onto the interaction point of the experiment. Altogether there are 16 000 electronic channels, which allow for a precise energy and position measurement of high energy photons and electrons even in jets. A description of the design of the calorimeters, operational experience and performance of 2 years running time, together with results on the data taken in the TASSO experiment are presented.

Description of the calorimeters

In Fig. 1 cross sectional views of the TASSO detector¹⁾ are shown. As can be seen there are 4 barrel liquid Argon shower counters and two endcap counters, while the so called hadron arms have shower counters in lead-scintillator-sandwich technique with wave length shifters. Since the principal design of the endcap counters is similar to the barrel counters I will concentrate here on the barrel counters only. The barrel counters are each 4 m long, 2 m wide and 0.5 m high. All counters are vacuum insulated, with superinsulation on the inner surface of the vacuum tank. Two barrel counters on top or bottom are mechanically coupled together in the middle, so that the vacuum forces on the middle wall are compensated. By this, the middle wall of the vacuum tanks can be kept rather thin, thereby reducing the loss of sensitive area in the center to a minimum. Each of the 4 modules have 12 feed through flanges on the back circular vacuum wall, to allow for the 3000 electronic channels to be connected to the preamplifiers sitting in crates close to the flanges. The preamplifiers are double shielded, the inner shielding is connected to the inner liquid Argon tank, while the outer shielding is in contact with the vacuum tank, sitting on rails with insulated rollers inside the large magnet yoke. These precautions have been taken to avoid ground loops and to keep the noise level low. The entrance face of the vacuum tank is made of thin stainless steel, 1.5 mm only, equivalent to 0.085 rad. length. The inner tanks for the liquid argon and lead stacks are made of aluminum. Here, the entrance face is made from two 5 mm Aluminum plates with 50 mm spacers inbetween, every 100 mm repeated. The average thickness of this structural beam entrance is 0.14 rad. length. Altogether with superinsulation, liquid Argon and tank walls, a particle entering the calorimeter sees approximately 0.25 r.l. before entering the first ionizing gap, while the total amount of material in front of the calorimeter, due to beam pipe, proportional chamber, drift chamber and magnetic coil is 1.3 r.l.

The two base plates of the inner tank serve as mounting tables for the lead stacks and carry each six feed through flanges made from stainless steel with glass-steel feed-throughs welded into the flanges. The flanges are sealed with indium, while the large mounting plates are sealed to the tank with Cefilac seals (Spring loaded C-shaped stainless tubing covered with soft Aluminum). This seal works fine, as long as the hardness of the Aluminum surfaces of tank and plates are guaranteed.

The connection of the inner feed through flanges to the outer feed throughs is done with multiwire flat cable as commonly used in computer techniques but



Two Arm Spectrometer Solenoid TASSO

Central Magnet R_0 135cm B_0 0.5T
L 1400cm
Weight 500 ton
Overall Dimensions Length ~16m
Width ~16m
Height ~8m

Fig. 1: Sectional views of TASSO detector.

instead of copper stainless steel leads have been used. This reduces the heat-conductivity by a factor of 50 compared to copper; so only 50 cm long cables are necessary. The cables are folded like an accordion bellow, thereby acting as superinsulation.

In Fig. 2 a drawing of the lead stack is shown. The stack is divided into front- and back towers. Four front towers cover the face of one back tower. In-between the front towers are immersed z, y strips, orthogonally to each other and dE/dx strips. The strips are made by etching copper plated fiber glass plates. A particle entering the calorimeter first traverses a front tower gap of 2×5 mm liquid argon, then two dE/dx gaps, which act also as z coordinates, then a

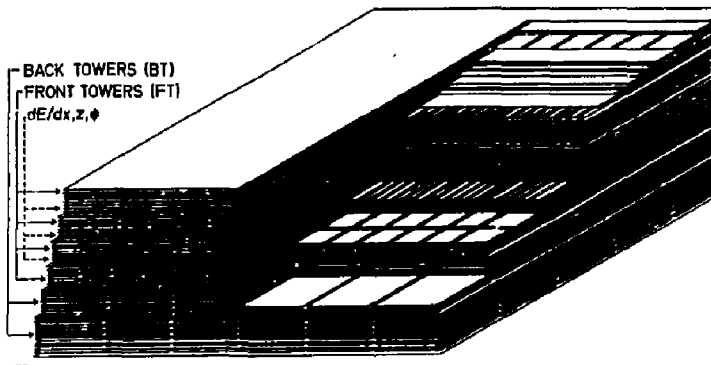


Fig. 2: Lead Stack

ϕ gap. After this approximately one rad. length of lead front tower gaps is traversed. Then again z and ϕ strips are hit. Thereafter again one rad. length of lead front towers and again z and ϕ strips. This set up has been chosen to have a high conversion efficiency for photons and a good positioning of the photons in the 20 mm wide strips. The small size of the front towers ($70 \times 70 \text{ mm}^2$) is valuable in separating showering particles in a jet and for n^0 measurements. The division between front and back towers helps distinguishing hadrons from electrons. The electrical and mechanical connection between the tower plates is done with bolts and insulators. These bolts are stacked up together with the lead plates. Since all towers are focused onto the interaction point, the stacking bolts are in certain planes offset.

Each lead stack is 4 m long by 1 m wide. Two stacks make up one module.

The electrical connections for the towers emerge from connecting fiberglass-plates on the front and back towers, while the z and ϕ strips have connectors at the sides of the stack. Flat multiwire copper cables take the signals to the feedthrough flanges on the base plate.

The lead plates are 2 mm thick. They contain 3% antimony and have been hardened by heating for 5 hours at 250°C . After that they were dumped into cold water and obtained their strength within a few days due to a recrystallization process. The surface of the plates was cleaned from oxide layers by glasspartl blasting. This was a necessity, since otherwise small oxide pieces would short-circuit the gaps under high voltage. Each completed stack was tested in dry air with 5 kV on the gaps. It was judged clean when the total leakage current was smaller than $1 \mu\text{A}$.

The cooling system

In Fig. 3 a drawing of the cryogenic system has been sketched. Each module is connected by two vacuum insulated lines to a recondensation vessel of about 100 l volume. The recondensation of argon is done with liquid nitrogen running through a heat exchanger. The amount of nitrogen is adjusted by the argon gas pressure acting on a proportional valve. If a cool down of a module is going to be started, argon gas is condensed by the nitrogen heat exchanger into the recondensation vessel. Since this vessel is seated $1/2 \text{ m}$ higher than the top point of the modul, liquid argon starts flowing into the module through the so called

spray line. The spraying action is achieved inside the module by Teflon tubes which have small holes (0.7 mm) in their walls. These tubes are mounted along the lead stack on the sides as well as on top and

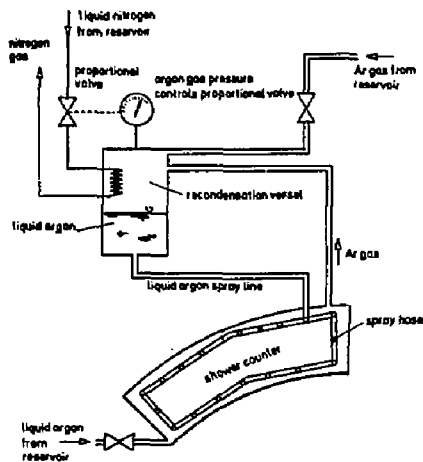


Fig. 3: Cooling System.

bottom. The number of holes per unit length increases from the entrance to the end exponentially, to assure a cool down with only small temperature gradients (40°C). What happens to the liquid argon in the Teflon tubes is that it evaporates due to heat taken in from the surrounding, so that cold argon gas sprays out of the fine holes, thereby cooling the lead and tank. The number of holes has to increase with tube length, because with length more gas is produced and it also warms up more. This procedure goes from room temperature down

to -160°C . From here on also liquid argon drops out of the holes, but this does not harm the temperature gradient smoothness, since only 23°C are left to reach liquid argon temperature. This cooling procedure lasts 3 days with about $2.5^{\circ}\text{C}/\text{hour}$ cooldown speed. The nitrogen heat exchanger needs about 3 kW cooling power, since $4 \cdot 10^6$ Wattssec have to be cooled away. When the module has reached liquid argon temperature, it can be filled with liquid argon from the reservoir, which takes one more day. The amount of liquid nitrogen used for cool down and filling is about 3 m^3 per module, while only 200 l/day are needed per module to take care of the heat losses of 250 Watts under normal running conditions. This system works very reliably since now about 2 years. Since the liquid argon, once in the module, is not in contact with the outside world, it stays clean: the oxygen content is only 0.3 ppm; in two years it has never been exchanged. To get the liquid argon delivered with only 0.3 ppmO₂, needed some education of the people handling the argon at the delivery company and at DESY. This education was already achieved during testruns with a small module and later on with the large modules on test beams at the DESY synchrotron.

Electronics and readout system

In Fig. 4 a block diagram of the electronics is shown. The signal pulse from the calorimeter is on virtual ground, so no high voltage capacitors in the liquid argon are used. There are also no transformers for capacity matching, since our tests showed that we could work without them, thereby avoiding shielding problems in the stray magnetic field of the detector and inductance matching problems due to different cable lengths. The preamplifier of standard design is however protected against high voltage breakdown by diodes and a small spark gap, which short-circuits pulses of 200 Volts or larger. This protection works so well that preamplifiers do not break. From the preamplifier the pulse is sent through a shaping network and a cable driver over 50 m long double shielded

coax cables into the readout electronics. A fast trigger pulse (after 1 μsec) is taken off before the second shaper stage and main amplifier. Here 32 front covers and 8 back towers are ganged together for a stand alone trigger from the liquid argon calorimeter into the general TASSO trigger logics. A trigger is produced if in one liquid argon submodul 2 GeV are deposited or 0.5 GeV in 2 submodules or 5 clusters of 250 MeV. A trigger is also produced if one charged track and a cluster of 250 MeV is found, or two charged tracks in the drift chamber. If an event was found in the shower calorimeter a clock is started and a 12 bit DAC produces a voltage ramp in 4000 steps, each 1 mV for 500 channels in common. When the ramp voltage and the sample and hold voltage show the same size in the comparator a latch is produced and the addresses of towers and the clock value are stored in a data buffer. Pedestals and gain factors are then taken into the data by control of a microprocessor and a constant memory. The data are then stored in an on-line computer. Pedestals and gain factors are controlled every two weeks off line with testpulses. Only towers with more than 20 MeV true shower energy are stored. The noise level is only 10 MeV. The amount of data stored is relatively small. On average a good event has 40 data words.

Results

One of the most remarkable features of the liquid Argon calorimeter is its stability and reliability. Besides the high granularity and therefore position resolution, good energy resolution was achieved. In Fig. 5 the energy resolution in a test beam up to 4 GeV is shown, while Fig. 6 shows the energy resolution at 18 GeV for Bhabha scattering. In Fig. 7 π^0 -production²⁾ is shown, while Fig. 8 shows a 3 jet event with several photons releasing energy in the liquid argon calorimeters. Fig. 9 is a Bhabho event.

Table 1 collects some basic data of the barrel liquid argon calorimeters. Besides the low noise of only 10 MeV equivalent shower energy, the small heat loss of 250 Watts per module only, may be worth mentioning.

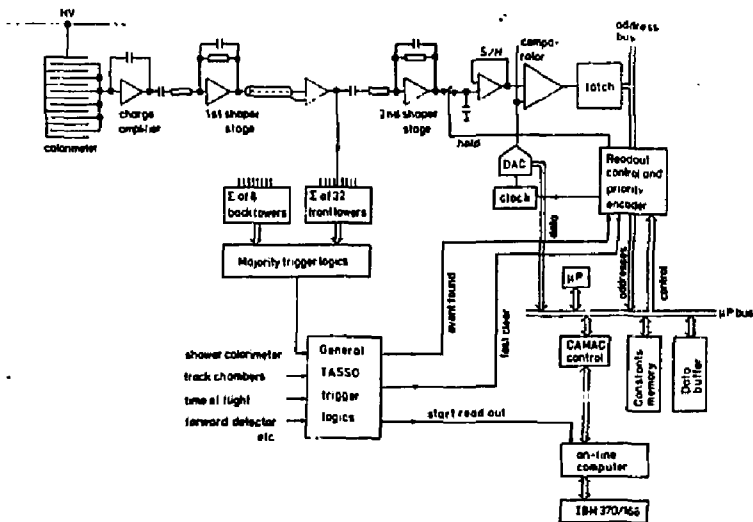


Fig. 4: Electronics and readout system.

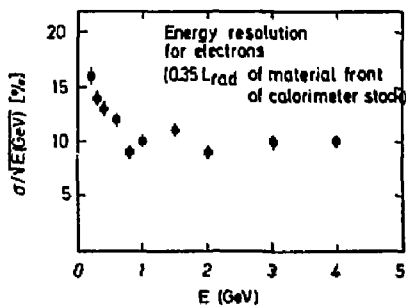


Fig. 5: Energy resolution up to 4 GeV.

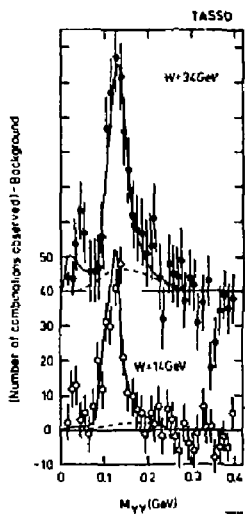
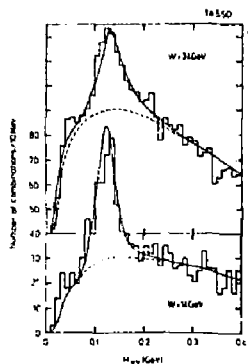


Fig. 7: π^0 production.

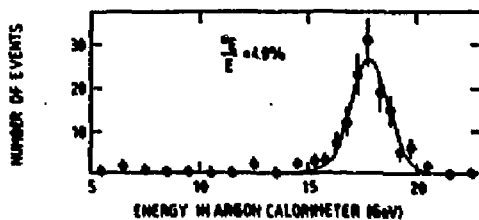


Fig. 6: Energy resolution at 18 GeV. Bhabha scattering.

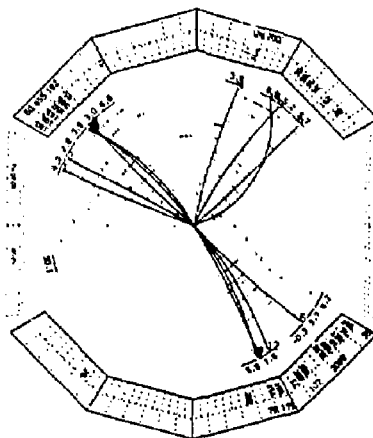


Fig. 8: 3 jet event, several photons have energy deposited in the liquid argon calorimeters.

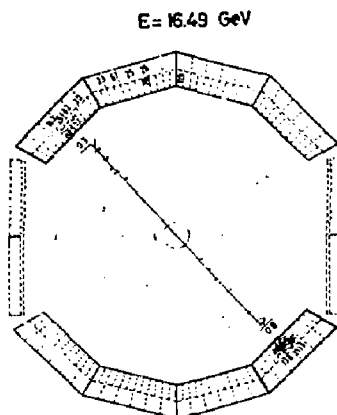


Fig. 9: Bhabha event.

Table 1: Data collection of barrel liquid Argon counters:

Active area	32 m ²
Covered solid angle	42 % of 4π
Granularity for energy measurement	1.5 meter for the first 6 X ₀ and 6 meter for 8 X ₀
Energy resolution with 1.6 rad. length before counter due to coil and walls	$\left\{ \begin{array}{l} \frac{15\%}{\sqrt{E}} \text{ for } E_{\gamma} \approx 300 \text{ MeV} \\ \frac{10\%}{\sqrt{E}}, \quad 1 < E_{\gamma} < 4 \text{ GeV} \\ 5\% \text{ for } E \geq 4 \text{ GeV} \end{array} \right.$
noise	10 MeV shower energy
Show er-position resolution for γ's	σ ≈ 5 mrad.
Number of electronic channels	12 000
Number of towers	6 000
of that small towers	4 800
large towers	1 200
z, φ and dE/dx strips	6 000
Total weight	80 to
of that lead	25 to
liquid Argon 10m ³	14 to
Insulation vacuum	10 ⁻⁴ ... 10 ⁻⁵ mbar
Cooling power per module	3 kW
Cool down speed	2.5°C/h → 3 days
Temperature gradients during cool down	40°C
Heat losses per module	250 Watts
Consumption if liquid Nitrogen for 6 counters + lines and so on	1 m ³ /day
Total manufacturing costs per channel	500 DM/channel

Acknowledgements

The design, construction and installation of the liquid argon calorimeters required the effort of many people. We thank the DESY directorate, in particular Prof. E. Lohrmann, H. Schopper, G.-A. Voss, G. Weber, and also Dr. C. Söhngen for their continuous support. We are deeply indebted to Mr. A. Papakonstantinou and Mr. M. Müller for design and supervision of the construction of the tanks. In the construction of the stacks, the electronics and the programs for read-in and testing Messrs. M. Boehnert, B. Hoppe, A. Jacob, M. Klinkmüller, G. Kraft, W. Neff, P. Ratzke, K. Rehlich, H.-H. Sabath, W. Schütte, K. Spatzber, K. Westphal, K.-H. Wroblewski and Mrs. H. Siegner have done a superb job. We are also indebted to Mr. F. Czempik and Dr. F. Schwickert for their invaluable help with the installation. We are grateful to Dr. R. Nelson for help with EGS.

List of References

- 1) A description of the detector components used for charged particle tracking can be found in TASSO Collaboration, *Z. Physik C4* (1980) 87; *Phys.Lett.* **83B** (1979) 621.
- 2) TASSO Collaboration, DESY-Report 81-069; *Phys. Lett.* **108D** (1982) 71.

HARP: HIGH PRESSURE ARGON READOUT FOR CALORIMETERS

M. Barranco-Luque, C. W. Fabjan, P. K. Frandsen, G. Lecoq, T. Ludlam,
J. Perez, P. Queru, E. Rosas, A. Rudge, D. Soria-Suñil, W. Willis
CERN, Geneva, Switzerland

Abstract

Steel tubes of approximately 8 mm O.D., filled with Argon gas to ~200 bar, are considered as the active element for a charge collecting sampling calorimeter readout system. The tubes are permanently sealed and operated in the ion chamber mode, with the charge collection on a one-millimeter concentric anode. We present the motivation for such a device, including Monte Carlo predictions of performance. The method of construction and signal collection are discussed, with initial results on leakage and ageing of the filling gas. A prototype electromagnetic calorimeter is described.

I. Introduction

Among the several readout techniques employed for sampling calorimeters at colliding beams, liquid argon systems stand out for two important reasons:

- 1) They provide excellent energy and space resolution.
- 2) They have demonstrated control of instrumental effects (calibration and uniformity of response) at the 1% level required to achieve the intrinsic precision of calorimetric measurements at very high energies.

The drawback of these devices is the high fabrication costs of the cryogenic construction, and inevitable dead spaces in detectors covering large solid angles.

We describe here a new read-out system for calorimeters, presently under development, in which the active sampling elements are sealed tubes of high pressure argon gas operating as individual ion chambers. The motivation for this approach is to achieve a relatively inexpensive, well-segmented calorimeter structure of design similar to proportional wire devices, with energy measurement capability and control of systematics comparable to liquid argon systems.

II. The HARP Concept

Our approach has evolved from recent studies of a "high density" proportional wire calorimeter:^{1,2} a structure in which individual sampling channels penetrate bulk absorber, in contrast to the conventional geometry of multivire planes sandwiched between sheets of absorber. A test device of this type is shown in Fig. 1. It was found that acceptable energy resolution can be achieved with very sparse sampling volumes, and that the high net density of the device (which limits the lateral shower development), coupled with a fine-grain array of sampling channels can be exploited to give excellent space resolution, separation of near-by showers and discrimination between electromagnetic and hadronic showers. In addition, this type of structure lends itself to a number of interesting options for construction methods. (We return to this point in Sec. IV.)

Figure 2 shows the calculated energy resolution of such a device for electromagnetic showers, as a

function of the sampling ratio, $R = \text{sampling volume} / \text{total volume}$. These results are obtained for argon sampling gas at 1 atmosphere.² The resolution width is dominated by Landau fluctuations, which in principle can be reduced by increasing the gas pressure. In Fig. 3 we show the same calculation, comparing the net resolution for a range of gas pressures and for liquid argon. The performance figures of liquid argon are approached at pressures which are not difficult to achieve in practice. Hence the concept of HARP (High Pressure Argon Pipes): we replace the proportional wire sampling channels in such a structure with sealed tubes of argon gas pressurized to ~200 atmospheres. For sampling channels of 25 mm² cross section in an iron structure with $R = .25$ (a practical packing fraction for such tubes) the calculated energy resolution for 1 GeV electrons is 15% at 250 atmospheres, as compared with 13% for liquid argon. The signal charge at this pressure ($\sim 10^6$ electrons per GeV of shower energy) is sufficient to allow operation in the ion chamber mode, with no avalanche gain: i.e., in nearly exact analogy with liquid argon readout.

III. Charge Collection in Ion Tubes

The tube construction which we have adopted is illustrated in Fig. 4. It consists of a standard steel pipe with 8 mm outside diameter and 5.6 mm inside diameter. The gas tightness is achieved by two plastic stoppers which are crimped at the two ends of the pipe in such a way that the gas pressure helps ensure the gas tightness. The stopper at one end of the pipe serves as an insulating feed-through for the central electrode.

These tubes are permanently sealed with the aim of being operational for ≥ 10 years. In tests carried out with the collaboration of the CERN HS Dept. the breaking pressure was found to be ~850 atm., which allows a safe working pressure up to 250 atm. The leakage rate, measured at 200 atm., corresponds to a maximum drop in pressure of 3% (i.e., 6 atm.) over a period of five years.

The thick central electrode (≈ 1 mm diameter) is held in the center of the pipe by thin plastic spacers; it carries both the operating voltage (3-4 kV) and the signal, the external wall of the pipe being grounded. The electrical capacitance of a 1 meter long tube is about 50 pF.

The time development of signal charge in cylindrical ion tubes is closely analogous to that of the familiar parallel plate geometry used in liquid argon calorimeters. This is illustrated in Fig. 5, for a gas mixture of 90% argon, 10% CH₄. (For the illustrated geometry, with an applied voltage of 4 kV and 250 atm. pressure, the reduced electric field ranges from $E/P = .25$ V/cm/mm Hg at the anode to $.05$ V/cm/mm Hg at the cathode. In this range the small admixture of methane increases the electron drift velocity by a factor of 5 over purge argon.)

The readout electronics requires little development as the needs are similar to those of several other charge collection devices now in operation (e.g., liquid argon calorimeters, low-gain wire chambers,

*Permanent address:
Brookhaven National Laboratory, Upton, NY 11973
Research supported by the U.S. Department of Energy
under Contract No. DE-AC02-76OR 016.

silicon strip detectors). The electronics chain illustrated in Fig. 6 has been implemented for initial tests, using existing components, and yields a measured equivalent noise charge of 350 electrons RMS.

A series of tests have been initiated with tubes constructed with α -emitting radioactive sources sealed inside. These are being kept continuously at operating voltage and the pulse-height spectrum monitored to investigate the stability of response and possible ageing effects due, e.g., to degradation of the gas mixtures. Results to date for the two earliest tubes are shown in Fig. 7. It will be seen that there is a "conditioning" period in each case lasting for a few days, after which the response remains very much constant.

IV. Possible Application and Plans for a Prototype Detector

With each tube being an independent, self-contained detector, which operates at room temperature and should perform well in a magnetic field, one has a great deal of flexibility for configuring them in some matrix of absorber. We mention two classes of applications:

- a) Pole Tip Calorimeters (see discussion in Ref. 1): Here we envisage the pipes to be inserted into channels drilled into the steel, as illustrated schematically in Fig. 8a. Drilling of such holes in iron (8 mm diameter, 1 m length) can be done without great difficulty, and at reasonable cost, by specialized companies. We have evaluated test drillings in magnet iron and found them to be satisfactory, with deviations from straightness $\leq .001$ m over 1 m lengths.

- b) Large Angle (EM or Hadronic) Calorimeters: Here a great variety of geometries can be realized with either magnetic or non-magnetic materials. Fig. 7b visualizes a close-packed array of hexagonal tubes, as an example. Arrays of tubes may also be imbedded in molded castings. An interesting possibility is to consider these tubes in a matrix of heavy metal oxides cast in plastic.³ This approach offers the possibility of uranium calorimeters using powdered oxides (which are plentiful and easily cast in plastic) rather than metallic uranium, which is difficult and expensive to machine.

We are presently constructing a prototype electromagnetic shower detector for test beam studies. This device will incorporate 150 tubes inserted in 8 mm diameter holes drilled in an iron block. The tubes will be 30 cm long, with readout electronics as illustrated in Fig. 6.

References

1. T. Ludlam *et al.*, IEEE Trans. Nucl. Sci. **NS-28**, 517 (1981).
2. T. Ludlam *et al.*, BNL Report 30607, 1981 (to be published, Nucl. Instr. and Methods).
3. H. Gordon *et al.*, Physica Scripta **23**, 564 (1981).

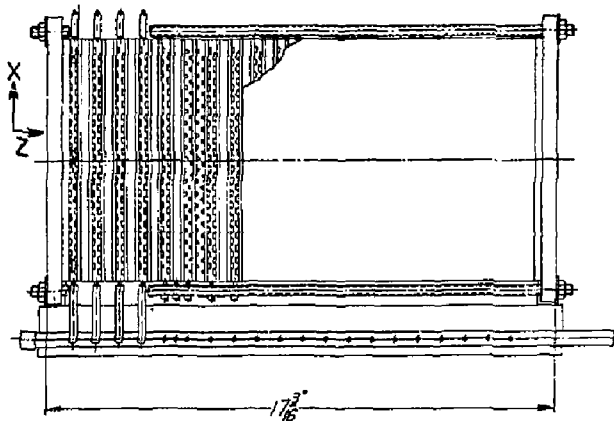


Figure 1. The test calorimeter of Refs. 1, 2. The module is assembled from steel plates. Machined slots in alternate plates form the sampling channels, which are 2 mm x 5mm and 2 mm x 2 mm in cross section. In this device, which was operated with proportional wires, the sampling gas occupies only 10% of the total volume.

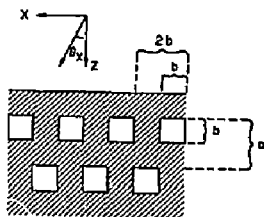


Figure 2a. Sampling geometry used for the Monte Carlo results shown below. The absorber material is iron; the sampling medium is argon gas at atmospheric pressure; the beam is parallel to the Z direction and randomly distributed in X. For this configuration the ratio of sampling volume to total volume is given by

$$R = \frac{b}{2a}$$

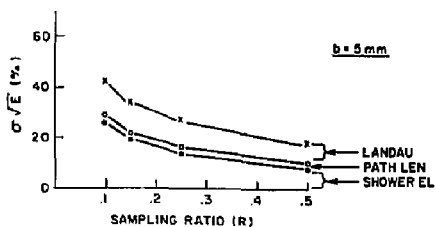


Figure 2b. Energy resolution for incident electrons, as a function sampling ratio, for $5 \times 5 \text{ mm}^2$ sampling channels. The lowest curve corresponds to fluctuations in the number of sampled shower electrons, the next incorporates path length fluctuations, and the top curve gives the net resolution (Ref. 2).

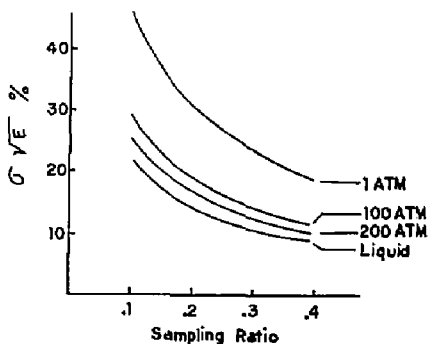


Figure 3. The net energy resolution, calculated as in Fig. 2, for various pressures of the sampling gas.

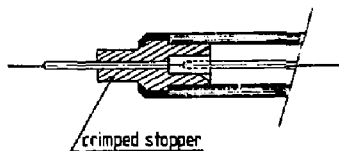
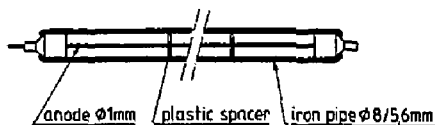


Figure 4. Construction details of the ion tube.

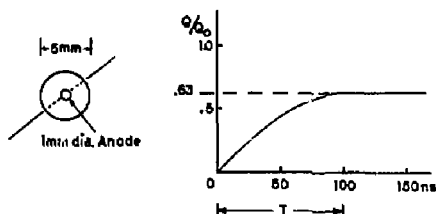


Figure 5. Time development of the signal charge for a track crossing an ion tube in the illustrated geometry, producing ionization charge Q_0 . The gas mixture is 90% argon/10% methane, with the central anode at +4 kV. The time (T) for full signal collection is 100 nsec.

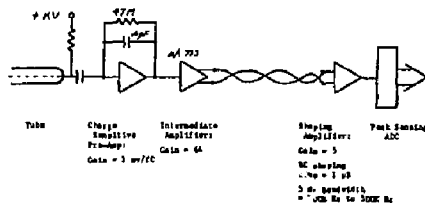


Figure 6. Electronics chain for ion tube readout.

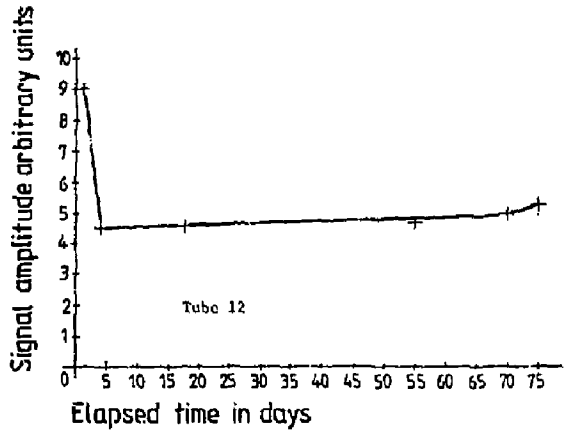
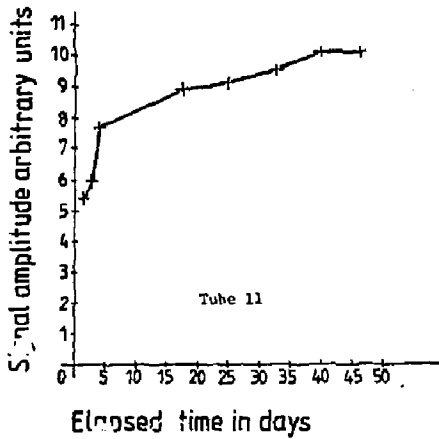


Figure 7. Time history of pulse-height measurements with two tubes in which α -emitting radioactive sources have been imbedded. Due to the high ionization density produced by the α particles they provide a more sensitive check on impurity effects than minimum ionizing tracks. Tube 11 was operated with an ^{241}Am source with an applied voltage of 1 kV; tube 12 had a ^{235}U source and was operated at 3 kV.

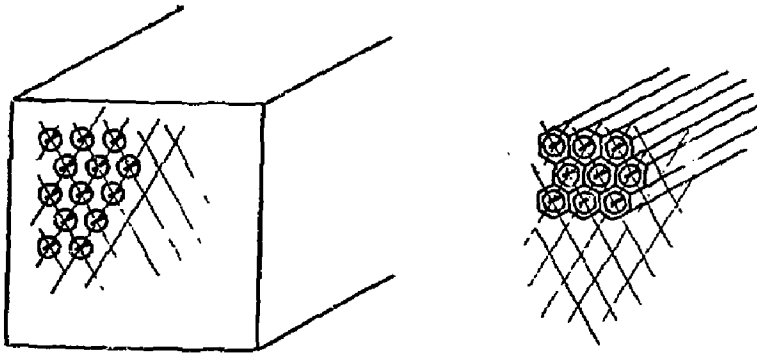


Figure 8. Possible detector configurations (see text).

SATURATED AVALANCHE CALORIMETER*

M. Atac
Fermi National Accelerator Laboratory
Batavia, IL 60510

S. Kim
Tsukuba University
Ibaraki-ken 300-31, Japan

M. Mishina
KEK
Ibaraki-ken 300-31, Japan

W. Chinowsky, R. Ely, M. Gold, J. Kadyk
P. Rowson, K. Shinsky, and Y. Wang†
Lawrence Berkeley Laboratory
Berkeley, CA 94720

R. Morse and M. Procaro
University of Wisconsin
Madison, WI 53706

T. Schaad
Harvard University
Cambridge, MA 02138

Summary

A gas sampling electromagnetic calorimeter running in a "Saturated Avalanche Mode" was tested at SLAC with positrons incident at energy up to 17.5 GeV. With this new method, good energy resolution, 16 percent/ \sqrt{E} , and good linearity were obtained with arrays of thirty-four 0.5 radiation length thick lead plates interleaved with 34 wire counters. There was no measurable systematic effect. Amplifiers are not needed; the signals are large enough to be connected directly to the ADC's.

Introduction

Gas sampling calorimeters operating in a proportional mode have been tested and used by several groups¹⁻¹⁰ but, with one reported exception⁸, their energy resolution has been much inferior to that achieved with calorimeters that use plastic scintillator counters. Improved resolution has been demonstrated in a calorimeter operated in the Geiger mode,¹¹ and may be expected also with the limited streamer^{12,13} mode. Those devices are intrinsically different from proportional counter energy sampling calorimeters. The former, in effect, use the number of tracks in the shower, while the latter use the magnitude of total collected charge as measures of the energy deposited in the gas. In this paper, we report results of tests of gas sampling calorimeters run in neither of these modes, but in an intermediate, partially saturated mode. Their resolution is comparable to that of plastic scintillator calorimeters.

These tests were made as part of the program to develop calorimeter modules for the Collider Detector Facility¹⁴, an apparatus to detect products of pp interactions at the 2 TeV colliding beams machine now under construction at Fermilab. The present design calls for gas sampling electromagnetic and hadronic calorimetry in the forward and backward angular regions. Respectably small granularity will be achieved with tower structures of cathode readout pads.

Experimental Arrangements

The detector studied was a MAC prototype⁶ which was tested previously in proportional mode at SLAC. Thus, only limited details of construction will be given here.

The MAC prototype was composed of 34 lead plates of 2.8 mm thickness and 34 planes of 50 μ m diameter anode wires enclosed in 9.5 mm x 9.5 mm cells which are separated by 1.5 mm thick aluminum ribs, a 17.8 radiation length shower detector. Fig. 1 shows the arrangement and the cell structure. The anode wires of each

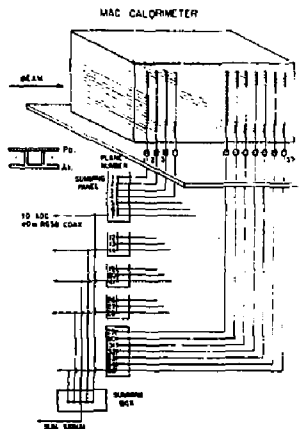


Fig. 1. The experimental configuration of the MAC electromagnetic calorimeter.

†Present address: Institute of HEP, Ac. Sinica, Beijing, P. R. China.

*Operated by Universities Research Association under Contract with the United States Department of Energy.

plane were connected to a common strip, and seven such planes were further grouped together, resulting in five groups to be read out. Most of the results that will be presented in this paper were obtained from the total sum of these five groups. Results on the longitudinal development in the shower will be reported later.

The counter gas was a mixture of 49.3 percent Argon, 49.3 percent ethane, and 1.4 percent ethyl alcohol. Negative high voltage was applied to the cathode tubes. Distributed high voltage capacitors totalling 0.25 μ f were the charge storage elements. As indicated in the figure, there was no need for amplifiers between the wires and the ADC's. Indeed, it was necessary to attenuate the large signals obtained between 2 db and 30 db depending on the high voltage and gas pressure. Forty meters of RG58 coaxial cables carried the signals to the LeCroy 2249W ADC's. The ADC pedestals were determined with a linear extrapolation of the measured variation of pulse height with incident energy.

A ISI-II computer system with a SLAC program "ATROPOS" was used for data taking and on-line display monitoring.

Beam Parameters

The detectors were tested in the 19° beam of the Stanford Linear Accelerator which provided positrons of 17.5 GeV maximum energy. SLAC ran in the SLED mode during the entire tests with a bunch length of about 20 nsec, FWHM 8 nsec, and 10 bunches per second. About 95 percent of the beam at the detector was within the 2 mm x 2 mm area of the beam defining counter. The intensity was, on the average, between 1/10 and 10 positrons per bunch. The momentum spread of the beam, $\Delta p/p$ was less than 10.25 percent rms.

Experimental Results

For 10 GeV incident positrons, the total pulse height distribution is shown in Fig. 2 together with a Gaussian fit to the data. Only that portion of the distribution within $\pm 2\sigma$ of the mean were used in the fitting procedure. The shape of the distribution, typical of all, is well represented by the Gaussian function.

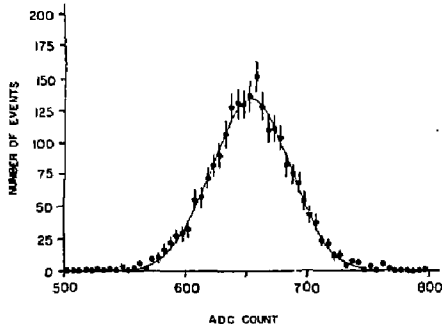


Fig. 2. A typical pulse height distribution and Gaussian fitted points for obtaining σ and mean values using 2 σ fit.

With fixed gas pressure, the resolution σ/E varies with high voltage as shown in Fig. 3. As the voltage increases from 2100 V, the resolution slowly decreases to a shallow minimum at ~ 2250 V and then slowly increases.

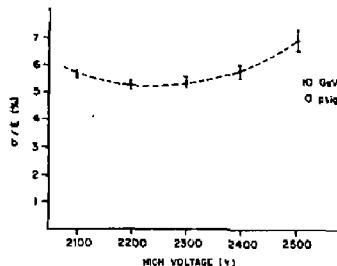


Fig. 3. σ/E versus high voltage for 10 GeV positrons at 0 psig.

Fig. 4 presents the calorimeter output as a function of incident positron energy showing no departure from linearity at energies up to 17.5 GeV. For this run, the counters were run at 2300 V.

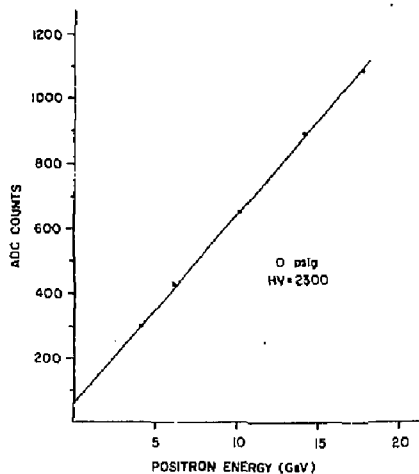


Fig. 4. The total pulse height response of the calorimeter as function of the e^+ energy for 0 psig. The linearity is excellent.

Higher energy response of the detector was simulated by using multiple positrons in a single rf bucket. This is a fair simulation since the positive ions do not move appreciably from where they were produced during the beam spill. Fig. 5 shows the detector response to multiple positrons of 17.5 GeV. It shows that

as many as 11 simultaneous positrons the energy resolution of the detector is sufficiently good to resolve them with clear minima between the peaks of the pulse height distributions for the corresponding number of positrons. In fact, this is a Poisson distribution for $n = 4.5$. That the pulse height for the multiple positrons deviate in a smooth way from linear behavior for more than 2 positron (35 GeV) shower is seen in Fig. 6. An expanded view of the pulse height distribution for 10 GeV positrons is shown in Fig. 7. It dramatically shows the symmetric, Gaussian-like shapes with clean valleys between the multiple-hit peaks. The energy resolution as a function of equivalent energy deposits of multiple 17.5 GeV positrons is shown in Fig. 8 after correction for the non-linear response.

The energy resolution as a function of energy for single incident positrons is shown in Fig. 9. σ/E shows the usual $E^{-1/2}$ dependence with a constant factor of 16.2 percent as indicated in Fig. 10. The shape of the dependence of resolution on energy indicates no systematic term since it extrapolates to the origin. This is, perhaps, because there is no active device (amplifier, pulse shaper, etc.) between the detector and the ADC, and small variations among individual wire gain average out over the detector.

The detector was rotated to make angles to the beam axis of as much as 23 with 17.5 GeV positrons incident, the results of Fig. 11 were obtained. It is seen that the pulse height increases by a small amount (maximum 2.3 percent), and the σ/E decreases slightly with increasing angle. This improvement may be due to a better containment of energy in the effective thickness of the angled calorimeter.

Saturated Avalanche Mode

We have investigated the ionization region¹² between the proportional region and the self quenching streamer region in detail using a 9.5 mm x 9.5 mm tube having a 50 μ m wire, a replica of one cell of the prototype MAC detector, in order to understand the improved energy resolution of the apparatus relative to calorimeters running in the proportional mode.

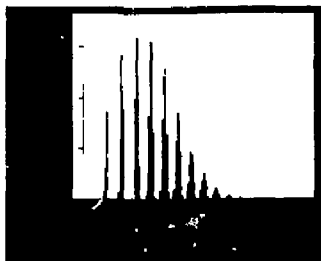


Fig. 5. The response of the detector to simultaneous multiple positrons of 17.5 GeV.

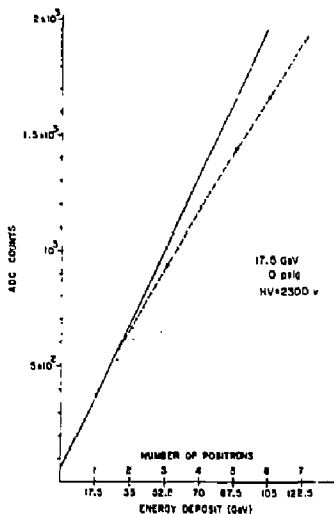


Fig. 6. The pulse heights as a function of simultaneous 17.5 GeV multiple positrons for 0 psig.



Fig. 7. Pulse height distributions for 10 GeV multiple positrons.

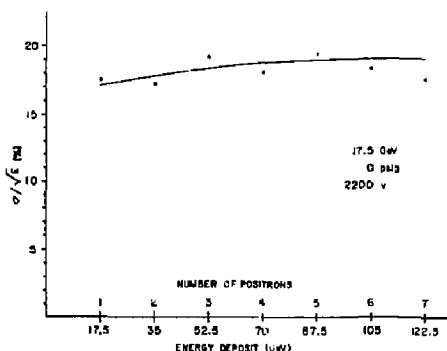


Fig. 8. σ/\sqrt{E} versus simultaneous multiple 17.5 GeV positrons after correction for non-linear response.

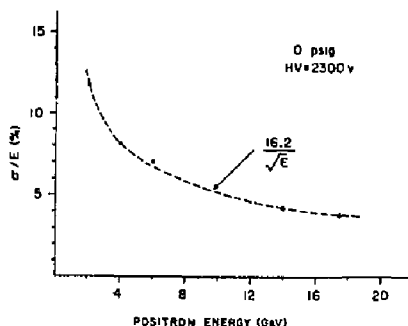


Fig. 9. σ/E versus positron energy.

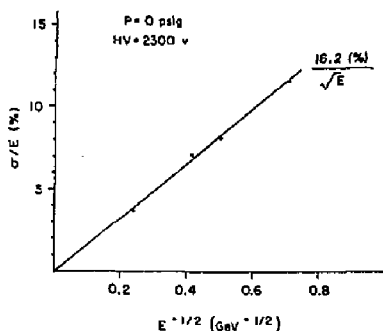


Fig. 10. σ/E versus $E^{-1/2}$ indicating no systematic effects.

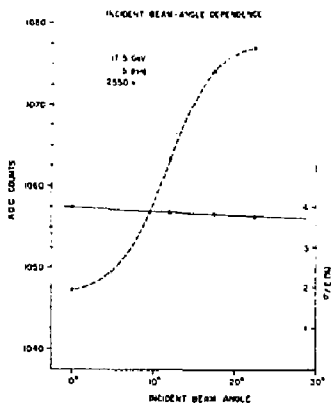


Fig. 11. Total pulse height and σ/E versus incident beam angle for 17.5 GeV positrons.

A small fraction of the wire pulse was amplified and used to form the ADC trigger, as shown in Fig. 12. A LeCroy 2285 ADC system was used for measuring the charge. The gain of the ADC was 20 counts per picocoulomb. An Fe^{55} x-ray source was used to measure the wire gain as a function of high voltage. As seen in Figs. 13a and b, the resolution is insufficient to separate the 5.9 keV x-ray line and 2.9 keV argon escape line when the gas gain, at 2300 V, is in the region of limited proportionality. The gain here was $\sim 5 \times 10^4$. The 2.9 keV line is hidden in the left side of the asymmetric pulse height distribution. Fig. 14 shows the gain as a function of the high voltage. The rate of growth of the avalanche is seen to decrease continuously as the high voltage increases above 2200 V until the streamer threshold is reached. Then the gain increases very little to the point of full streamer operation around 2650 V.

The distribution of pulse heights recorded by passage of minimum ionization tracks was also investigated in this voltage region using a Sr^{90} β -source. A telescope made from a pair of small thin scintillation counters provided a gate pulse for the ADC's. The discriminator thresholds were set to accept mainly the minimum ionizing β 's. Fig. 15 shows the pulse height distribution obtained at 2300 V. This histogram shows that the distribution is almost symmetric with a small tail. The distribution made by the β 's is not like a typical Landau distribution obtained in a gas gap of 9.5 mm thickness at atmospheric pressure. The tail is greatly suppressed. An expanded view of the histogram of Fig. 15a is shown in Fig. 15b. It has a ratio of σ to mean of 34 percent. Landau fluctuations clearly have been reduced, an indication that the greater the concentration of primary ionization, the more saturation (less gain) occurs as has been observed earlier¹⁵.

From the data of Fig. 13, we find a ratio of mean pulse heights produced by the two photons of ~ 1.4 , rather than the ~ 2.0 ratio of energies. Similar conclusions about the departure from strict linear, proportional response follows from comparison of the signals from the β and x-ray sources. Those observations and the suppression of the Landau tail indicate partial saturation of the avalanche charge at the collecting wire. Thus, the resolution is improved compared to that obtained when the counters operate in the proportional mode. We find a resolution somewhat smaller than, but not really inconsistent with that predicted by Fischer¹⁶, which is based on a calculation of the response without the effect of Landau fluctuations. Deterioration in resolution at voltages much higher than 2400 V may be caused by fluctuations in gain where streamer and saturated avalanche modes overlap (see Fig. 14). Depending on the amount of ionization deposited locally on the wire, the gain may be low (saturated avalanche) or more than an order of magnitude higher (streamer).

Acknowledgments

The authors express their appreciation to Drs. R. Coombes, R. Prepost, and D. M. Ritson for providing the MAC prototype; to Drs. R. Schwitters and A. Tollestrup for support; to Dr. R. Gearhart and the SLAC operating crew for assisting and supporting the runs; and to P. Clancy and S. Mackenzie for help with the data acquisition system.

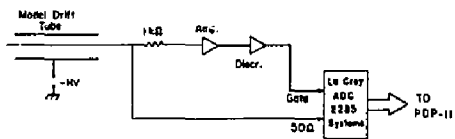


Fig. 12. The circuit diagram for investigating the saturated avalanche region.

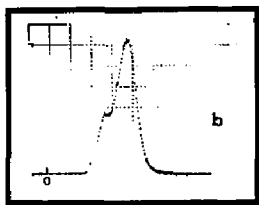
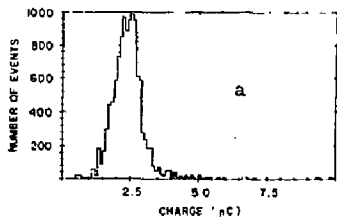


Fig. 13⁵⁵ Pulse height distributions for the 5.9 x-rays from Fe⁵⁵. Fig. 13a shows the ADC distribution without amplifier. Note the 3 keV argon escape line is not visible in the saturated avalanche region because of poor proportionality. Fig. 13b shows the amplified distribution where the escape line is just visible because of the better resolution at high pulse heights.

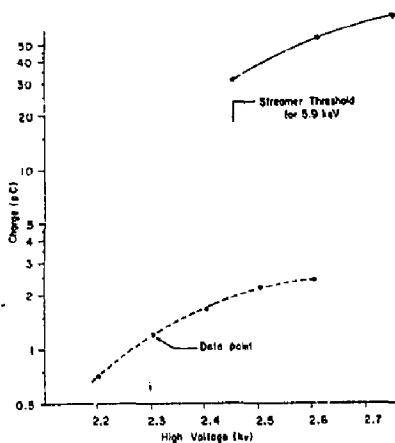


Fig. 14. The model tube gain as a function of the high voltage in the saturated avalanche region using the ADC without amplifier.

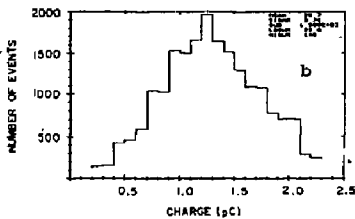
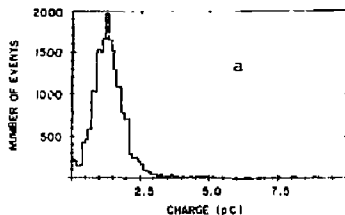


Fig. 15a and b. The pulse height distribution for minimum ionizing tracks in the saturated avalanche region showing almost symmetric distribution with very small Landau tail. Fig. 15b is the expanded detail of Fig. 15a.

References

- | | | | |
|--------|--|---------|---|
| Ref. 1 | W. Murzin, Progr. Element. Part. Cosmic Ray Phys. (1967) 245. | Ref. 9 | H. Tyco et al., UCLA Report. |
| Ref. 2 | M. E. Nordberg, Jr., Cornell Univ. Report, CLNS 138 (1971). | Ref. 10 | M. Mishina et al., IEEE Trans. on Nucl. Sci. (Feb. 1982). |
| Ref. 3 | T. Kotsura et al., Nucl. Instr. and Meth. 105 (1972) 245. | Ref. 11 | W. Carithers et al., private communication; will be published in Nucl. Instr. and Meth. |
| Ref. 4 | M. Atac, IEEE Trans. on Nucl. Sci., Vol. NS-28, No. 1, Feb. 1981. | Ref. 12 | M. Atac et al., Fermilab Report FN-337 (1981), and Proc. of INS International Symp. on Nucl. Radiation Detectors (March 1981), Tokyo. |
| Ref. 5 | M. Atac et al., IEEE Trans. on Nucl. Sci., Vol. NS-28, No. 1, Feb. 1981. | Ref. 13 | M. Jonker et al., Physica Scripta Vol. 23, 677-679, 1981. |
| Ref. 6 | R. L. Anderson et al., IEEE Trans. on Nucl. Sci., Vol. NS-25 (1978). | Ref. 14 | Fermilab $\bar{p}p$ Colliding Detector Proposal (1979). |
| Ref. 7 | C. Bosio et al., Nucl. Instr. and Meth. 157 (1978) 35. | Ref. 15 | H. Frehse et al., Nucl. Instr. and Meth. 156 (1978) 87. |
| Ref. 8 | P. Skubic et al., IEEE Trans. on Nucl. Sci., Vol. NS-28, No. 1, Feb. 1981. | Ref. 16 | G. Fisher, Nucl. Instr. and Meth. 156 (1978) 81. |

PLASTIC STREAMER TUBE CALORIMETERS

G. Battistoni, G. Bologna, P. Campagna, V. Chiarella, U. Denni, B. D'Etto-
Piazzoli, E. Iarocci, G. Mannocchi, G. P. Nurtas, G. Nicoletti and P. Picchi.
LNF-INFN, Frascati (Italy)

Abstract

We present the results of a preliminary test on an e.m. calorimeter test module using Plastic Streamer Tubes with external pad readout. We have measured energy response and resolution between 2 and 10 GeV, and π/ν discrimination at 10 GeV.

1. Introduction

Plastic Streamer Tube devices (PLA.S.Tubes in the following) are based on the use of resistive cathode¹ and are operated in the limited streamer mode². PLA.S.Tubes have a high resistivity cathode (f.i. graphite coated plastics) which is transparent to transients and external electrodes (strips, pads, delay lines) are used to pick-up induced pulses. This device has been or is being used in several experiments (see f.i. ref.^{3,4,5}) as the sensitive device of tracking calorimeters with simple digital (yes/no) readout of individual projective elements. The digital readout allows to record the detailed spatial pattern and is convenient in those experiments, such as proton

decay⁴ and neutrino detectors⁵, where tracking is of relevance. Good shower energy measurement is limited to relatively low energies⁶, due to track pile-up on the same readout element, the limit depending on the granularity and density of the calorimeter.

Here we present the results of a preliminary test performed with a PLA.S.Tube calorimeter with streamer charge readout by pick-up pads, which shows its possible use as e.m. shower calorimeter in the energy range of interest for high energy colliders. The idea of measuring shower energy by measuring the total charge collected in a saturated mode device has been already used in the Limited Geiger e.m. calorimeter of PEP-4⁷. Total charge measures the total number of elementary discharges, which is equivalent to count tracks and so to measure energy. The response is linear and resolution varies as $1/\sqrt{E}$, up to energies (several GeV) for which track pile-up occurs in the elementary Geiger cell. Limited streamer mode allows to operate in an analogous way. Now the elementary cell area is given by the

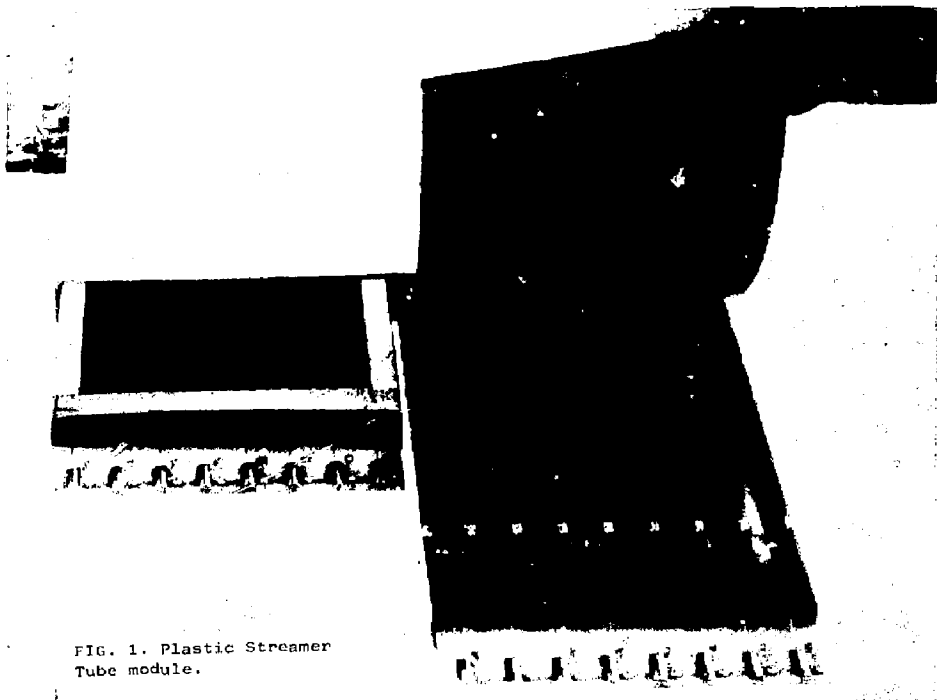


FIG. 1. Plastic Streamer Tube module.

tube width times the streamer obscuration length, i.e. the length of the dead wire region due to a single streamer. With respect to the limited Geiger device, the mechanics of streamer tubes looks simpler, since they do not need a mechanical device to localize the discharge, and smaller elementary cells appear feasible, by acting on the gas mixture. The use of PLA.S. Tubes makes possible simple construction of both oriented tower and strip structures.

We have built the test module using tube modules of the Mont Blanc proton decay experiment. We will briefly describe their technology in par.2, before discussing the e.m. calorimeter test module and the experimental results.

2. Plastic Streamer Tubes

The Mont Blanc proton decay experiment (Frascati, Milano, Torino, CERN) makes use of about 50.000 PLA.S. Tubes equipped with about 100.000 x and y strips, for a total pick-up area of 3400 m². Details of the device structure are shown in fig.1 and 2. The constructive unit⁸ is an 8-cell open profile, coated with graphite ($\approx 5 \times 10^{21}$ /square). The 100 μ m Be-Cu wires are kept in central position by PVC spacers every half a meter. A top cover, also coated with graphite ($\approx 10^{21}$ /square), completes the tube structure. The tube element is 0.9 x 0.9 x 350 cm³. Two 8-tube units are inserted into a PVC hitube container.

Detection planes are made by simple juxtaposition of PLA.S. Tube modules and two-dimensional readout is performed by 16-strip units^{8,9} facing the tube elements as shown in fig.2.

Modularity, thick sense wires, uncriticality of the streamer mode, splitting of pick-up and active element function, use of thermoplastics and their technology, make this detector cheap and simple to build and operate.

3. Test Module Description

The test module (34 x 50 cm² x 50 cm depth) consists of 16 lead sheets 5 mm thick (0.9 r.l.) interleaved with the PLA.S. Tube modules described before. The total depth is 14.5 r.l. and the average distributed r.l. is 3.3 cm. The single element of the sandwich is shown in fig.3. The 100 μ m thick wires are not read out being simply connected to the H.V. (fig.4).

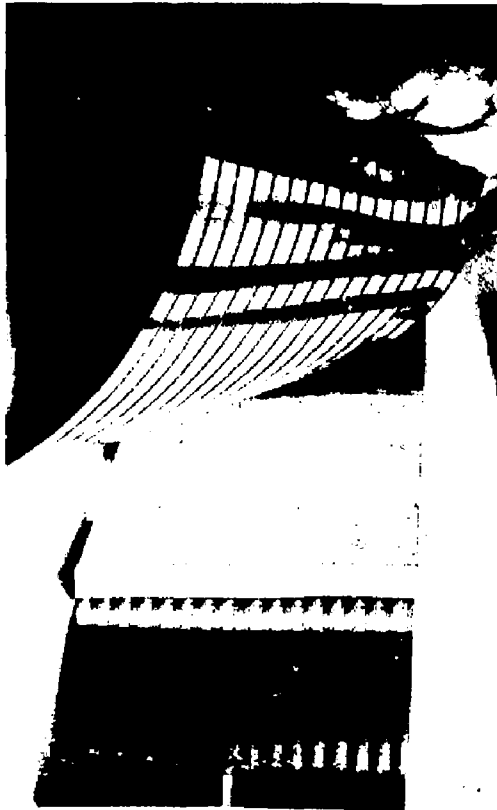


FIG. 2. Plastic Streamer Tube module with x and y pick-up strips.



FIG. 3. Geometry of one sampling layer of the test module.

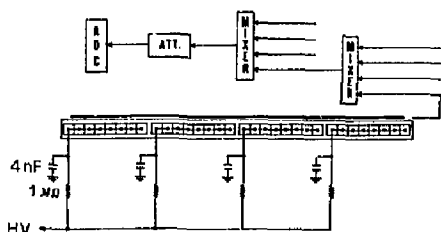


FIG. 4. H.V. and readout scheme.

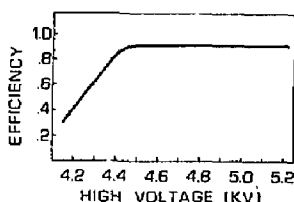


FIG. 5. Single tube layer efficiency as a function of H.V. for orthogonal tracks.

Streamer induced pulses are picked-up by external pads which are $34 \times 56 \text{ cm}^2$ printed circuit boards, with copper on both faces as signal and ground electrodes. On the tube side opposite to the readout pad, there is a grounded aluminium sheet. The 16 pads are connected through linear mixers and attenuators, to one or more ADC circuits (fig.4), to read out induced streamer charge.

The tubes are operated in the streamer mode with an Argon + Isobutane (1+3) mixture. The working voltage (4.6 KV) is about 100 V above the knee of the efficiency plateau for streamer production by minimum ionizing particles (fig.5). A typical single streamer pulse as detected on wires (50 Ohm termination) is shown in fig.6: the shape is triangular, with $\sim 1 \text{ mA}$ peak current and 40 ns duration. Typical single and double streamer pulses as detected on a pad are shown in fig.7: the pulses are integrated by the large pad capacitance ($\sim 4000 \text{ pF}$), which discharges through the 50 Ohm termination with a 200 ns time constant.

The induced charge distribution on the pad facing one tube layer for tracks at normal incidence, is shown in fig.8. The distribution is substantially due to single streamers. It peaks at 14 pC, with a 50% FWHM.

4. Experimental Results

The test module was exposed to electron and pion beams at CERN-PS, at four different energies: 2,4,7,10 GeV. In fig.9 the total charge distribution collected on the pads is shown for 10 GeV electrons: the narrow peak near the origin is due to residual pions in the electron beam trigger.

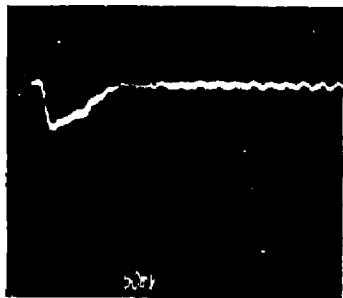


FIG. 6. A typical single streamer pulse as detected on the wire (50Ω load).

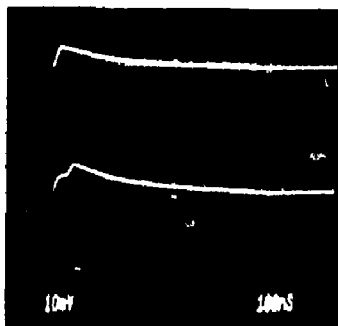


FIG. 7. Signals on a pad due to single and double streamers (50Ω load).

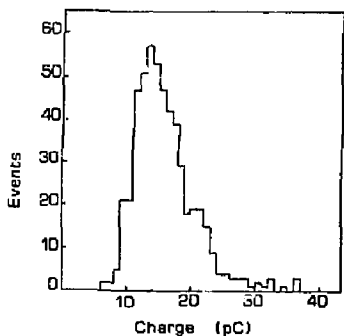


FIG. 8. Collected charge distribution on a single pad for single orthogonal tracks.

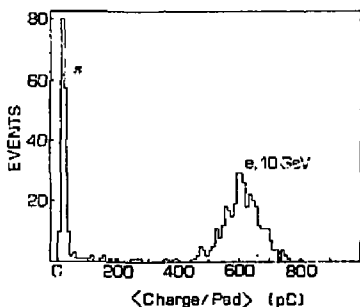


FIG. 9. 10 GeV electron spectrum together with residual pions, in units of the average charge induced on the 16 pads.

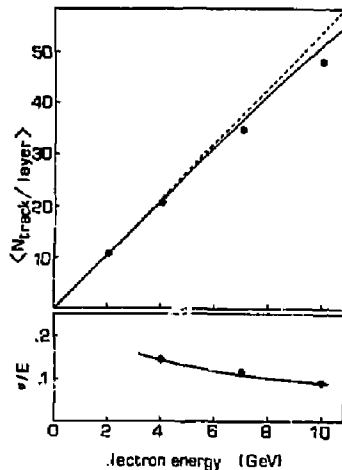


FIG. 10. Signal and energy resolution as a function of electron energy. The signal is in units of orthogonal track signal (non interacting pions).

The total collected charge at the electron peak corresponds to ~ 650 streamers: a 28 db attenuation was necessary to match the ADC operation range. Making use of transition curves for electron showers¹⁰, from the total number of streamers we have estimated an average number of ~ 100 streamers on the plane at the depth of the shower maximum.

Total charge readout as a function of electron shower energy is plotted in fig.10. The solid line comes from the experimental points, corrected for shower losses on the back of the calorimeter. The linear behaviour below 2 GeV has been somewhat arbitrarily assumed. However it appears a reasonable assumption from the $1/\sqrt{E}$ behaviour of energy resolution. This is reported also in fig.10. The experimental points have been corrected for shower loss fluctuations (the maximum correction was at 10 GeV, from 10% to 9%). The solid line corresponds to $28\%/\sqrt{E}$. Due to tight beam schedule we have not explored operation conditions (gas and H.V.) different from those quoted above, which are the standard ones for the digital readout of the Mont Blanc detector. However in one electron run at 10 GeV we have operated the tubes at 4.5 KV, measuring a spread corresponding to $25\%/\sqrt{E}$. The measured energy resolution is equivalent to that obtained with the Limited Geiger calorimeter quoted above, when scaled with \sqrt{t} .

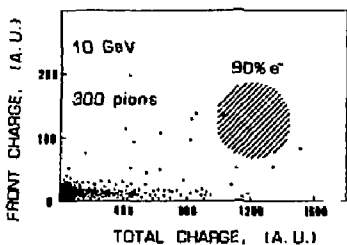


FIG. 11. Scatter plot of the charge collected on the first three pads vs. total charge, for 10 GeV pions.

By comparison of non linearity at 10 GeV, between our calorimeter and the limited Geiger one, and correcting for different densities ($\bar{X}_0 = 3.3$ and 5 cm respectively), we have estimated a streamer obscuration length of ~ 1.5 mm. We have assumed a negligible effect on linearity due to the high resistivity cathode.

The test module was exposed to a 10 GeV pion beam, to measure π/e discrimination. In both the electron and pion tests in addition to the total charge, the charge collected on the first three pads was measured. The scatter plot in fig.11 shows the front-radiator vs. total charge distribution for a sample of 300 pions. Only one event gives an amplitude in the 90% acceptance region (shown dashed in the figure) for 10 GeV electrons.

5. Future Development

The results obtained concerning the energy response do not appear as a limit. They can be improved by reducing the tube width (PLA.S.Tubes down to 4×4 mm² have been operated¹¹, and the streamer obscuration length (by increasing the quenching fraction in the gas mixture, to reduce streamer charge).

Due to reduced track density in hadron showers with respect to e.m. showers, from the results with the e.m. calorimeter one can infer¹² a comparatively larger linear range for PLA.S.Tube hadron calorimeters.

The PLA.S.Tube device allows simple arrangement of oriented towers and strip geometries for optimal spatial information (shower vertices and profiles, tracking through iron¹²).

The use of a saturated mode simplifies controls and stability problems.

Within the work to prepare proposals for LEP, tests will be performed with both e.m. and hadron calorimeter PLA.S.Tube test modules, with fine sampling, tower and strip arrangement.

REFERENCES

- 1) G.Battistoni et al. Nucl.Instr.Meth. 152 (1978) 423
- 2) G.Battistoni et al. Nucl.Instr.Meth. 614 (1979) 57
- 3) J.E.Augustin et al. Physica Scripta vol.23 (1981) 623
- 4) M.Jonker et al. Physica Scripta vol 23 (1981) 677
- 5) Proposal for a Nucleon Stability Experiment, Frascati-Milano-Torino (1979) unpublished.
- 6) G.Battistoni et al. Study of neutrino induced background for the proton decay experiment in the Mont Blanc tunnel, to be published on the proceedings of the 1981 EPS Conference on High Energy Physics, Lisbon.
- 7) Presented by A.Barbaro-Galtieri at the General Meeting on LEP, Villars-on-Ollon, 1981.
- 8) G.Battistoni et al. Nucl.Instr.Meth. 176 (1980) 297
- 9) G.Battistoni et al. LNF-82/6, submitted to Nucl.Instr.Meth.
- 10) U.Amaldi, Physica Scripta vol.23 (1981) 409; S.Iwata, Calorimeters for High Energy Experiments at accelerators, DPNU-3-79.
- 11) G.Battistoni et al. Limited Streamer Tubes with Resistive Cathodes, to be published on the proceedings of the 1981 EPS Conference on High Energy Physics, Lisbon.
- 12) ELECTRA collaboration, Letter of intent to study e^+e^- annihilation at LEP, January 1982, unpublished.

INTELLIGENT TOWERS FOR ELECTROMAGNETIC SHOWERS*

C. Blocher, G. W. Brandenburg, R. Carey, T. Edberg,
M. Levi, J. Oliver, N. Patz, E. Sadowski, T. Schaad, R. Schwitters
Harvard University
High Energy Physics Laboratory
Cambridge, MA 02138

Gas tube calorimetry is an attractive alternative to the methods entailing light collection. It is possible to design calorimeters with a flexible geometry and fine granularity for a lower cost than those having complicated light guides and many phototubes. Although the energy resolution is not as good for the gas tube counters, it is perfectly adequate for applications in the multi-GeV range.

We have designed and tested a gas-tube calorimeter that incorporates the modularity and tower structure of a lead glass block array. We combine the signals from the individual tubes using a resistive weighting technique to obtain the transverse moments of the energy distribution within a tower or block. These moments provide excellent position and angle information about the shower as well as π^0/γ separation. This design could prove valuable in applications where a large area electromagnetic calorimeter is needed downstream of a high energy interaction point. One application we have considered is to cover the small angle region in a high energy colliding beam experiment.

The basic element in our detector is a $5\frac{1}{2}'' \times 5\frac{1}{2}'' \times 12''$ (16 r.l.) shower tower containing twenty alternating layers of lead and proportional tubes. This size tower is somewhat larger than the transverse dimensions of an electromagnetic shower and contains 96% of the longitudinal energy at 20 GeV. Each layer consists of a row of fourteen proportional tubes with a 2 cm by 1 cm cross section. The tubes are formed from an aluminum extrusion with the cells open on one side. The other wall is a $3/16''$ thick (0.8 r.l.) piece of lead, which is specially grooved to fit over the extrusion. Before the lead is pressed on the extrusion, tungsten wires (2 mil.) are strung in each of the tubes and soldered to welded electrode strips at the ends. The resulting $5\frac{1}{2}''$ by $5\frac{1}{2}''$ proportional tube planes can be individually checked out before they are assembled into a tower. When the planes are stacked together, the tube directions are alternated to provide position information in both transverse projections.

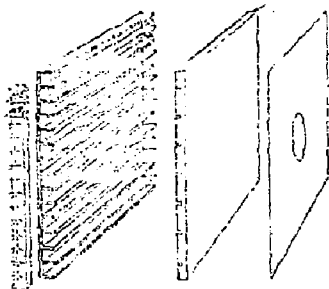


Fig. 1. Single proportional tube plane with Pb radiator for one wall.

* Work supported by US Department of Energy under Contract #DE-AC02-76ER03066.

The signals from the 280 tubes are brought to the top of the tower using C10 circuit boards in a manner similar to the use of BBQ sheets on the sides of Pb-scintillator towers. Strips on the circuit boards gang the tubes together longitudinally (along the shower direction). The longitudinal ganging is done for three separate regions in both transverse projections to improve the discrimination against charged hadrons. These regions are 6 layers, 6 layers, and 8 layers deep, starting from the upstream end of the tower. For each of these regions there are fourteen signals available corresponding to the fourteen transverse tube positions. The resulting $6 \times 14 = 84$ signals are further reduced to 18 or fewer per block by a resistive weighting technique described below. The tower body is run at negative high voltage so that the wires and the exposed strips will be at ground potential.

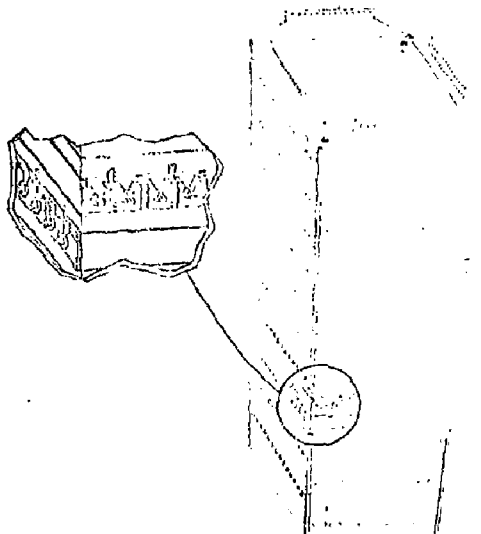


Fig. 2. Assembled shower tower. Electronics are attached on the top.

The electronics for readout and digitization of the signals are attached to the front (upstream) end of each tower. This was done so that the blocks could be cantilevered from a thick steel mounting plate, possibly the front layer of a hadron calorimeter. In addition to the preamplifier, sample and hold, and multiplexed ADC circuitry, each block has resistive weighting networks for each of the six regions. Here each of the fourteen signals is split by three parallel resistors R_A , R_B , and R_C . All fourteen R_A signals are bussed together into a preamp as are the R_B and R_C signals. The result is that three signals, S_A , S_B and S_C , instead of 14 are sampled for each region.

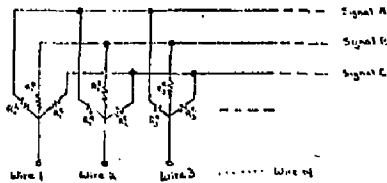


Fig. 3. Resistive weighting schematic. This is repeated for each of the six tower regions.

An "intelligent" choice of the 14 x 3 resistors R_A, R_B, R_C must be made so that the three remaining signals contain a maximum amount of information about the transverse shower distribution. An important constraint is that $1/R_A + 1/R_B + 1/R_C = 1/R_0 = \text{Constant}$ so that each tube sees the same input impedance. The resistive weighting function $f_i = R_0/R_i$ gives the fraction of the total charge in the *i*th preamp channel. We have chosen the following quadratic resistive weighting functions:

$$f_A = \frac{R_0}{R_A} = a(x-c)^2 + b$$

$$f_B = \frac{R_0}{R_B} = a(x+c)^2 + b$$

$$f_C = \frac{R_0}{R_C} = 1 - f_A - f_B$$

where $-7 < x < 7$ is the transverse coordinate in tubes and $a \approx .008, b \approx 0, c \approx 4.5$. The effective input impedance, R_0 , was 500 Ω . The choice of quadratic functions allows one to extract the zeroth, first, and second moments of the transverse energy distribution in each region; the particular choice of constants optimizes the resolution of these moments. The moments are given by

$$E = S_A + S_B + S_C$$

$$\bar{x} = \frac{S_B - S_A}{4acE}$$

$$\overline{x^2} = \frac{S_B + S_A}{2aE} - c^2 - b/a$$

$$\sigma_x^2 = \overline{x^2} - \bar{x}^2$$

where E is the total energy deposited in a region, \bar{x} is the centroid of the energy distribution, and σ_x is the half width of the distribution.

The latter quantity is particularly useful for distinguishing single gammas from π^0 's. If E_0 is the total energy deposited in a tower, then for two gamma cases:

$$m_{YY}^2 = E^2 \frac{\sigma_x^2 + c^2}{L^2} = E_1 E_2 \theta_{12}^2 \quad (3)$$

where L is the distance to the interaction point. However, this relationship is complicated by the intrinsic width of a single gamma. In the middle region of this detector $\sigma_x^2 + c^2 \approx 4 \text{ cm}^2$ for a single photon. This implies that π^0/γ separation is possible for $E_0/L \gtrsim 3 \text{ GeV/m}$. It should be noted that the moments can be continued across tower boundaries for showers or pairs of showers which are not contained in a single tower.

We have constructed an array of four such shower towers and have tested them in the SLAC e^+e^- test beam. Our primary objectives were to test the resistive weighting readout scheme and to investigate the effects of the tower boundaries on the calorimeter response. We also checked the linearity of the energy response and the energy resolution of the device, but did not attempt to optimize these. The detector was run in the proportional mode at 1600 volts with a 93-7 Ar-CO₂ gas mixture. Beams of 2, 4, 10 and 16 GeV e^+ were used, and the beam spot size was less than 2mm x 2mm. By running the beam at >1 particle per pulse we were also able to simulate higher energies by observing the multiparticle peaks. This was possible because of the narrow time structure and spatial width of the beam.

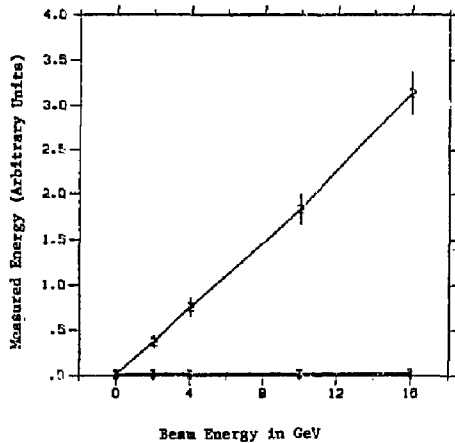


Fig. 4. Energy sweep with beam centered in block #2.

Figure 4 shows the total energy response of one tower (#2) where beams of 2, 4, 10 and 16 GeV were incident at 0° directly on the center of the tower. The absence of transverse leakage can be seen from Figure 4, where the energy deposited in the remaining three towers appears as a heavy line just above the X axis.

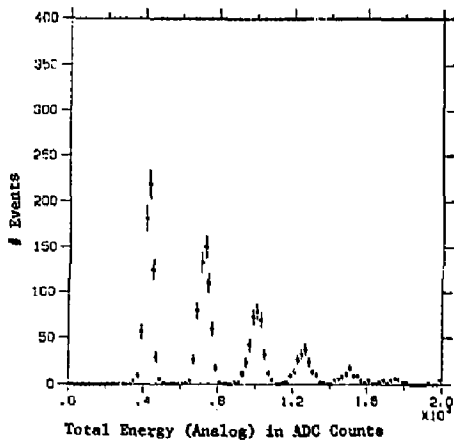


Fig. 5. Total block #2 pulse height spectrum with high intensity 16 GeV run.

The total energy spectrum from a single high intensity run at 16 GeV is shown in Figure 5. The peak positions from this run are plotted in Figure 6. The calorimeter begins to show saturation around an equivalent energy of 50 GeV.

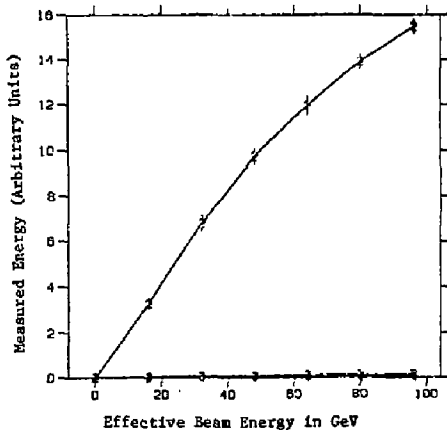


Fig. 6. Peak positions and widths from Figure 5.

The energy resolution, $\Delta E/E$, of the calorimeter is plotted against $1/\sqrt{E}$ in Figure 7 for both the energy sweep data of Figure 4 and the multiparticle peak data of Figure 5. Both data sets are reasonably well described by the relationship $\Delta E/E \approx \frac{20\%}{\sqrt{E}} + 1\%$. The

total energy signal for each tower was an analog sum of the 18 resistively weighted signals.

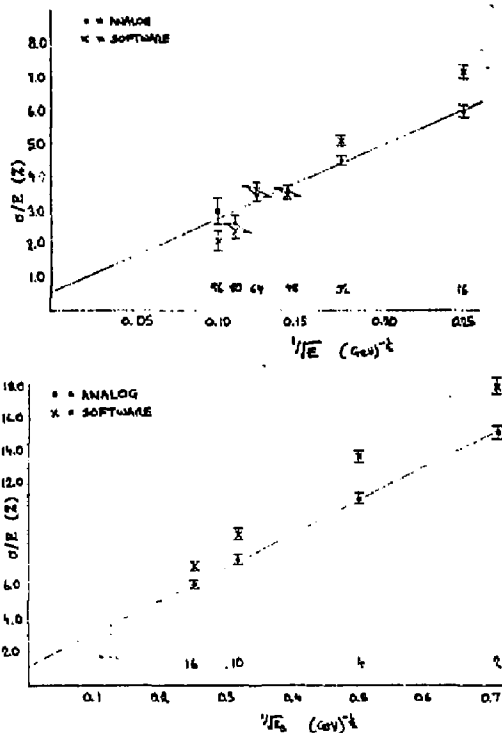


Fig. 7. Energy resolution from Figures 4 and 6 plotted vs. $1/\sqrt{E}$. Circles (crosses) are from analog (software) sum of all 18 tower signals.

We next present the data from two position sweeps made with a 10 GeV beam. In both cases the beam was swept in half inch or smaller steps in the y direction from the center of block #2 to the center of block #3. In one case the beam was at 0° with respect to the tower axis, and at 20° in the other. These two angles span the expected range for the applications being considered.

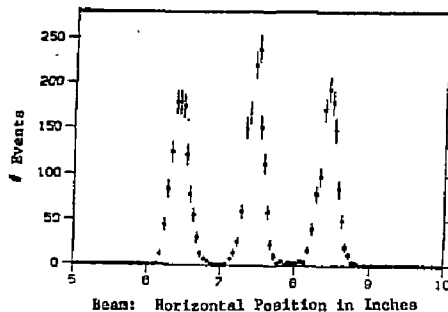


Fig. 8. Position (first moment) measurement distribution for three runs with beam position increment 1 inch.

The beam position distributions are shown in Figure 8 for three 0° data points which were separated from each other in block 3 by 1 inch. The histogrammed quantity is the first moment, \bar{y} , obtained in the second longitudinal region, which includes shower maximum. The standard deviation of the peaks is 0.1 inch, which is slightly larger than the expected beam width. Because we did not have an independent beam monitor we cannot unfold our position resolution. The position resolution in the front region of the tower is about the same as the middle, while it is about twice as bad in the third region at the tail of the shower.

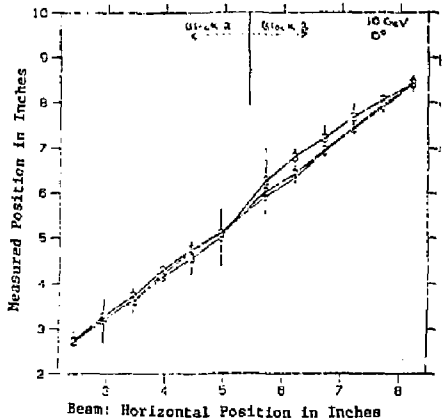


Fig. 9. First moment vs. beam position for all three tower regions with 10 GeV beam incident at 0° .

The averages of the first moments are plotted in Figure 9 versus the beam position in y . The moments from all three longitudinal regions are superposed in the figure. Near the boundary of blocks 2 and 3 at $y = 5.75$ " the moments are averages of the signals from both blocks. An excellent shower position measurement is obtained in all three depth regions at all positions. The data for \bar{y} in the second region is plotted by itself in Figure 10. The points are seen to be in excellent agreement with the 45° line.

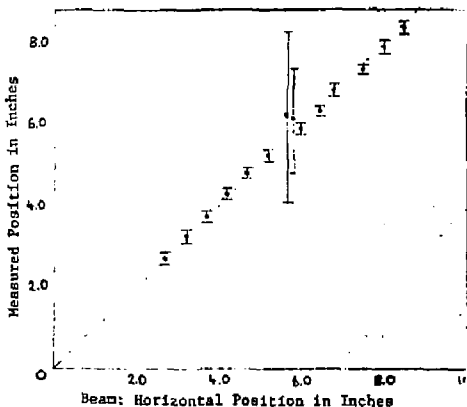


Fig. 10. First moment vs. position for region 2Y alone with 45° line superposed.

The position measurements from the 20° sweep are shown in Figure 11. Here the \bar{y} data is especially impressive, where the points from the three regions form offset parallel lines. The offsets are consistent with tangent 20° times the longitudinal separation of the regions. To calculate the offsets exactly it would be necessary to know the longitudinal centroid of the energy distribution for each region. The points for region 3y fall off at one end because the angled beam was no longer striking region 3.

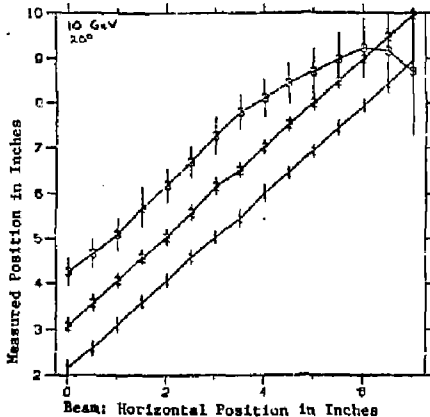


Fig. 11. Same as Fig. 9 with beam incident at 20° .

We now turn to the results on the second moments or transverse positional variances. Figure 12 is a histogram of σ_y^2 in the second longitudinal region with the beam centered in block #3 at 0° incident angle. The distribution of σ_y^2 in region 1 is very similar, while in region 3 it is much broader and is centered above zero. From previous shower data we would expect the shower to have $\sigma_y^2 \approx .4$ inches square for the central region of the tower, whereas in Figure 14 our result is slightly below zero. However, if the constant b in the resistive weighting functions of Equation (1) is slightly adjusted, the scale of σ^2 will be shifted by a constant. We have already adjusted the resistive weighting constants a and c to ensure linearity of the first moments and variances with position; we did not choose to adjust b because we have no independent measurement of the shower widths in our test data. In general the resistive weighting constants needed to decode the signals differ from the "ideal" ones given by the resistor values, but seem to be consistent from region to region and block to block. Hence they only need to be calibrated once using a single tower.

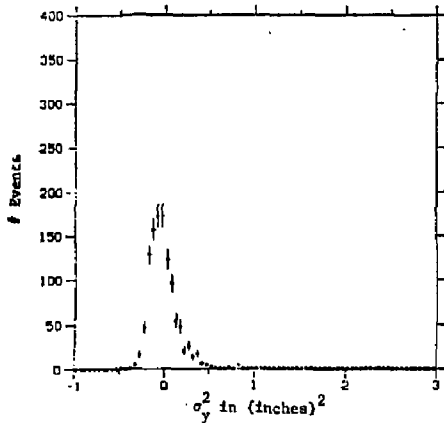


Fig. 12. Position variance distribution in region 2Y with 10 GeV, O^0 beam in center of tower.

The positional dependence of the variances from all regions with the beam at normal incidence is shown in Figure 13. The values of σ^2 for longitudinal regions 1 and 2 are constant within errors, while region 3 of block #3 has a larger value of σ^2 than block #2. The jump in the value of σ^2 for region 3 is probably the result of poorer gas gain in block #3. In general one would only make use of the variance measurements in the front two regions where the shower has a dependable profile. In these regions the uncertainty is typically ± 0.2 sq. in.

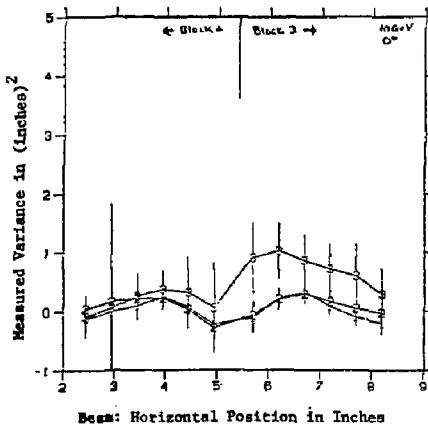


Fig. 13. Position variance (second moment) vs. position with 10 GeV beam at O^0 .

As seen in Equation (3), the invariant mass for two incident gammas is dependent on $\sigma_x^2 + \sigma_y^2$. A histogram of $\sigma_x^2 + \sigma_y^2$ in region 2 of block 3 is shown in Figure 14 for the beam incident at O^0 . Assuming the same resolution for a π^0 and a distance L to the interaction point of 10 meters, we have sketched the expected peak for a 30 GeV π^0 in the same figure. For energies below 30 GeV the π^0 peak moves to higher values of $\sigma_x^2 + \sigma_y^2$, there should be no problem separating single gammas and π^0 's.

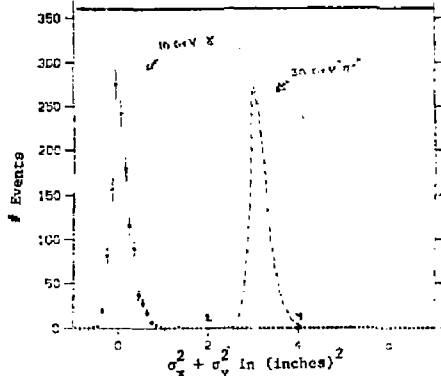


Fig. 14. Sum of sum of X and Y position variances in region 2 with 10 GeV, O^0 beam. Darkened line shows expected signal for 30 GeV π^0 decaying to two gammas (assuming single gamma resolution).

Finally we present the energy response of our detector as a function of position. For the O^0 data, the total energy broken down by individual blocks is shown in Figure 15. The energy in block #3 was renormalized by a factor of 1.16 to balance its gain with that of block #2. There is a large dip in the response of the calorimeter at the boundary between two blocks. In fact at an angle of O^0 it is possible to pass the narrow beam directly down the gap. The energy response drops practically to zero at the gap, but there is backscplash as the beam moves into the neighboring block.

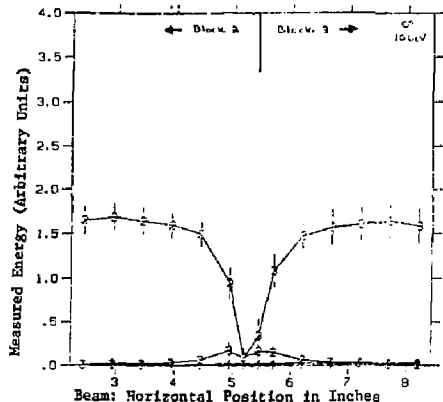


Fig. 15. Total energy response of each tower vs. position as 10 GeV, O^0 beam is swept from block #2 to #3.

In Figure 16 the total energies of the x direction and y direction tubes are plotted separately. The dip at the boundary is much narrower in the case where the tubes are parallel to the boundary, namely the y-direction. Inefficiency due to field inhomogeneities at the wire ends cause this. For uniform illumination of the calorimeter at normal incidence the tubes perpendicular to boundaries have an uncorrected 20% inefficiency, while the parallel tubes are 11% inefficient. However, using the accurate position information from the resistive weighting we can correct the energy response near the boundaries so that the losses are at most a few percent. The losses are considerably smaller when the angle of incidence is finite.

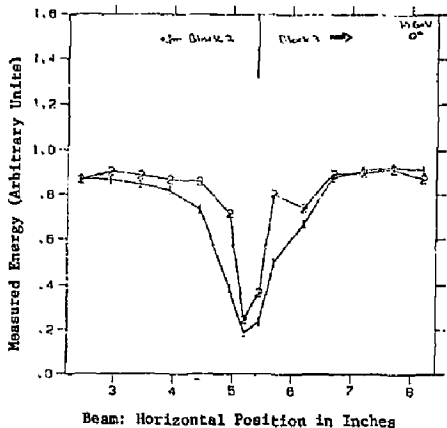


Fig. 16. Total energy response vs. position for tube perpendicular (1) and parallel (2) to the boundary with 10 GeV, 0° beam.

Figure 17 shows the same quantities as Figure 16 but for the 20° incident angle sweep. For this case the effect at the boundary is much smaller. In Figure 17, the raw inefficiencies for uniform illumination are now 14% for the boundary perpendicular tubes and 7% for the parallel ones. Here using the accurate position and angle information it is possible to completely correct for the boundary losses.

In conclusion the shower towers with resistive weighting provide excellent position angle information on electromagnetic showers coupled with a width measurement which allows one to discriminate between π^0 's and gammas. The energy response is uniform except at the tower boundaries, but here it can be corrected using the position information. Finally because of their modularity they can be used in many possible configurations.

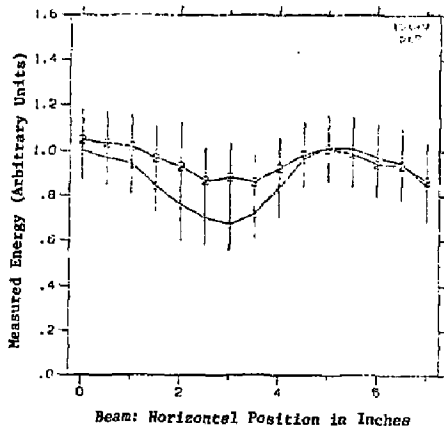


Fig. 17. Same as 16 for 20° beam.

Copy

LONG DRIFT TECHNIQUES FOR CALORIMETERS

L. E. PRICE
Argonne National Laboratory
Argonne, IL 60439

There are several advantages that can be expected from the use of long drift chambers as the sensitive element in gas-sampling calorimeters in place of closely-spaced proportional cells. These advantages include a sharply reduced number of wires to read out, a detailed image of each shower, and the possibility of processing the detailed signals to improve the energy resolution. We report here on the development of the thin-gap chambers, up to 50 cm long, that are needed for calorimetry, on the results of tests of a working drift-collection calorimeter, and on the design of a calorimeter for use in a solenoidal detector at the SLAC Linac Collider. Operation in a magnetic field is discussed.

Introduction

Long drift chambers have gained a prominent position among detectors for High Energy Physics (viz. ISIS, IPC, JADE) because of the large quantity of information they produce about an individual event. Typically a complete "image" of the event is formed with the spatial coordinates. Equally important advantages can be expected from the application of the long drifting technique to calorimeters, i.e., the use of long (but now thin) drift chambers as the sensitive element between radiator plates in a gas-sampling calorimeter¹.

1. A time history of each signal element--wire or cathode pad--can be read out to provide a complete image of the cascade.

2. Processing of the detailed map of ionization --either later in a computer or immediately in hardware--can be used to improve the energy resolution and regain some of the degradation of resolution that is normally associated with gas as a sampling medium.

3. Readout in time buckets produces a high degree of segmentation while keeping the number of fragile wires and the number of readout channels modest.

4. Along with the number of readout channels, the cost is modest.

On the negative side, the long readout time will preclude the use of drifting calorimeters in very high rate environments.

Development of Long Drift Chambers

The new problems that must be overcome for the use of long drift chambers in calorimeters can be discussed in connection with Figure 1, which shows a sketch of the 50 cm drift chambers we are developing for a nuclear decay search². The drift electric field is produced by a pattern of conducting strips on an insulating substrate which are connected to an external resistor chain. At the end of the drift region, the ionization electrons are amplified by an anode wire surrounded on three sides by cathode, which can be segmented and readout as pads to give the coordinate along the wire. The chambers must normally be kept thin so the density of the calorimeter remains high. Thus the drifting electrons are always near the walls and in danger of drifting into the walls and being lost.

Two effects in particular produce the loss of electrons on the walls. The effects and our solutions to them, are as follows:

1. With a discrete drift electrode, conductors outside of the drift chamber can affect the field inside. In particular, with the applied potentials as shown in Figure 1, the grounded radiator plates outside the chamber distort the field in such a way that most drifting electrons which start from the maximum drift distance drift to the walls instead of to the anode wire. Calculated equipotential lines are shown in Figs. 2a (no grounded plates) and 2b (with grounded plates). We have overcome this distortion of the drift field by covering the drift electrode--both conducting strips and dielectric--with resistive ink of surface resistivity approximately 10^{10} ohm/square. The resistive ink continues the resistive divider chain to every point inside the chamber, so that the potential is determined at every point on the boundary and hence the field inside the chamber is completely determined. The resulting calculated equipotentials are shown in Fig. 2c.

2. Even when the electric field inside the chamber does not direct the drift electrons into the walls, some electrons will be lost by transverse diffusion into the walls³. This loss is an inescapable consequence of drifting in extreme aspect ratio geometries. The system we have developed minimizes this effect, however by a) using a gas with a low electron temperature⁴ such as 90Ar, 10CO₂; and b) applying a focussing drift electric field, i.e. one with a component at the walls that will drift electrons toward the center of the chamber. A constant angle of the field at the walls is provided by an exponentially distributed potential⁵.

$$\phi = \phi_0 + a \exp(-bz) \cos(\theta y),$$

where the origin of coordinates is at the anode wire,

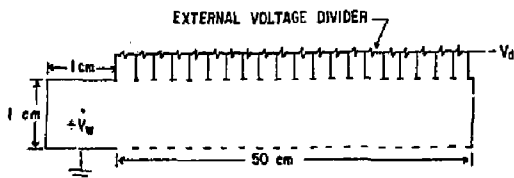


Fig. 1. Cross-section of prototype chamber with 50 cm drift length. The drift field is shaped by the conducting strips (printed circuit lines) connected to an external resistor chain as shown and also by a continuous film of resistive ink (not shown) that interpolates the potential between conducting strips. Top and bottom conductors are connected to the same resistor chain. Note that the vertical and horizontal scales are different.

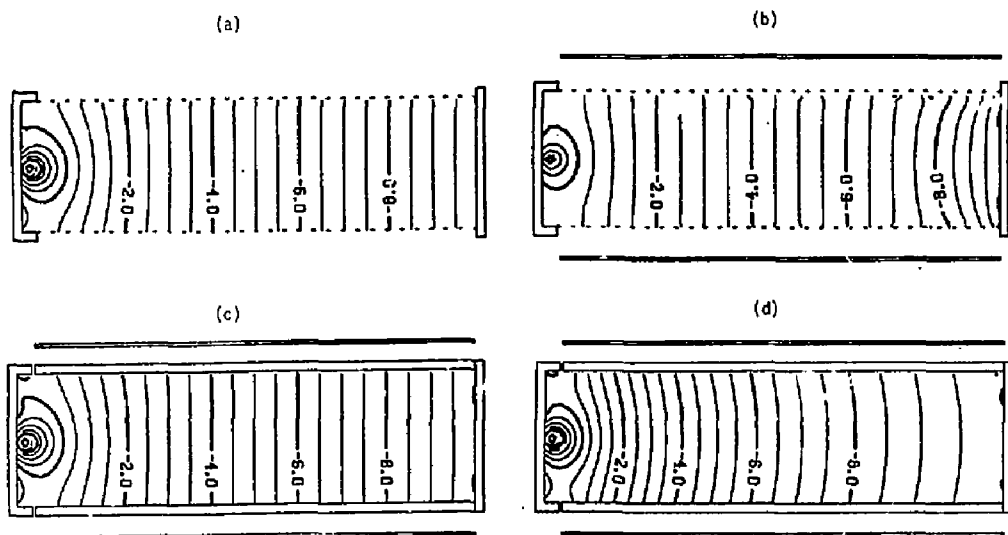


Fig. 2. Equipotential plots in the 50 cm chamber for a) linear resistor chain with discrete electrodes; b) same with nearby grounded plates; c) linear resistor chain with continuous electrode (resistive ink), showing no effect from grounded plate; and d) exponential resistor chain with continuous electrode. The equipotentials are labeled in kilovolts.

the z axis is parallel to the drift direction, and the y axis is perpendicular to the anode wire. Since diffusion is related to random thermal processes, the focussing field does not completely eliminate losses of electrons, but can substantially reduce them. Equipotentials produced by an exponential resistor chain in a chamber with resistive ink on the walls, are shown in Fig. 2d.

The drifting performance of a chamber built along the lines described above is shown in Fig. 3. The gas used was 90Ar, 10Co, with a total applied drift potential of 10kV. With a linear resistor chain, the attenuation after 50 cm drift is 30%—exactly what is predicted from diffusion alone. Only 12% attenuation is found with the exponential—or focussing—resistor chain, where the focussing parameter b was 0.03/cm. Again, this is consistent with what is expected from diffusion.

Electromagnetic Calorimeters

An electromagnetic calorimeter has been built and tested using long drift gaps. Although the aspect ratio for the drift gaps is similar to the chambers discussed above, the dimensions are smaller: drift gaps as small as 2.4 mm were used for drift distances up to 76 mm. As shown in Fig. 4, the calorimeter was built in a single gas volume, with the electrons drifting to a PNC plane at one end of the radiator plates. Drifting performance with non-showering particle is shown in Fig. 5: the attenuation is 12% in a 2.4 mm gap after 76 mm drift, with an applied field of 350 v/cm in 90Ar, 10CH₄ gas. With showering particles, the energy resolution of the calorimeter has been measured. As shown in Fig. 6, with 1% sampling, the resolution corrected for variations

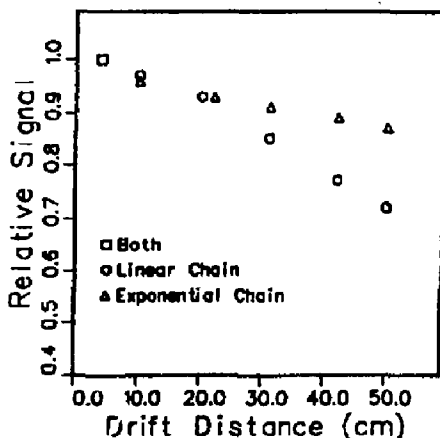


Fig. 3. Signal on sense wire as a function of drift distance for linear and exponential resistor chains. Measured signals have been corrected for attenuation from oxygen contamination and normalized to those outlined with 4 cm drift distance. All measurements are for $V_d = 10$ kV.

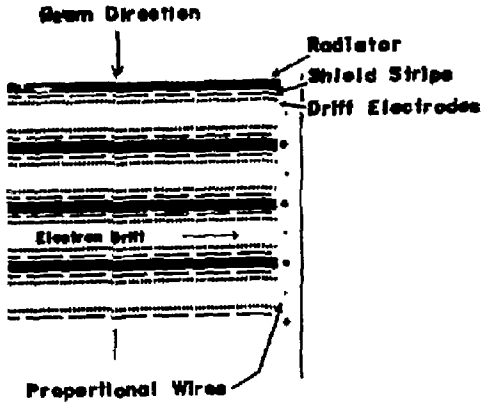


Fig. 4. Sketch of drift-collection electromagnetic calorimeter used in test beam. The drift region is 76 mm long and gaps as small as 2.4 mm were used. The lead radiator plates are 1 radiation length thick.

In the wire gain is $0.23/\sqrt{E}$. Fig. 7 shows the response of the calorimeter as a function of energy which is seen to be quite linear.

We have shown that the performance of the calorimeter is not degraded by the use of long drift gaps as sampling elements. Can the resolution be improved by processing the drifting signals? In Fig. 8, we show the results from the EGS Monte Carlo program of processing the signal in the following way:

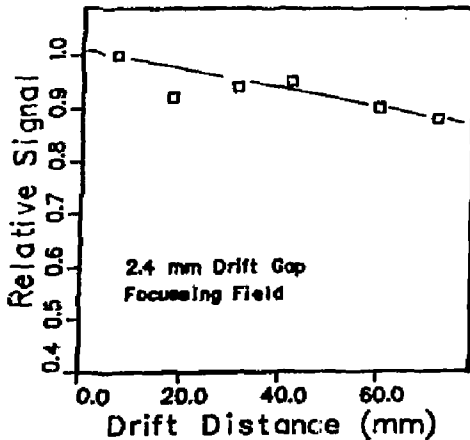


Fig. 5. Attenuation of drifting signals from non-showing signals in calorimeter with 2.4 mm drift gap width. See text for operating conditions.

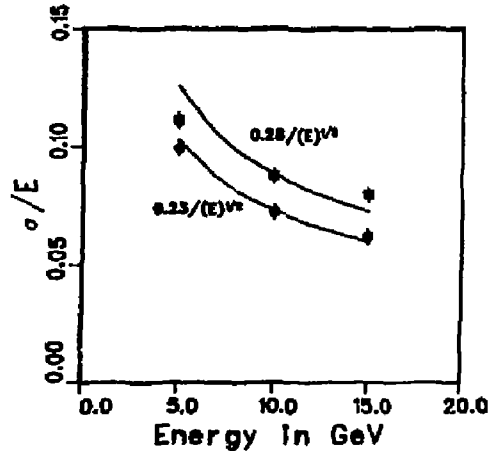


Fig. 6. Energy resolution for positrons in drift collection calorimeter at three energies with $1X_0$ sampling. After correcting for variations in the wire gain, the resolution is $0.23/\sqrt{E}$.

- The signal is digitized in 1 mm bins along the drift direction.
- Three longitudinal samples are used, with thicknesses $4X_0$, $6X_0$, and $10X_0$.
- Outside a central core whose width in the

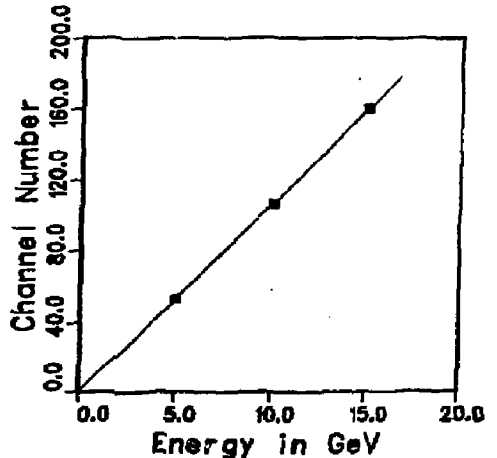


Fig. 7. Response of electromagnetic calorimeter as function of positron energy. No saturation is seen.

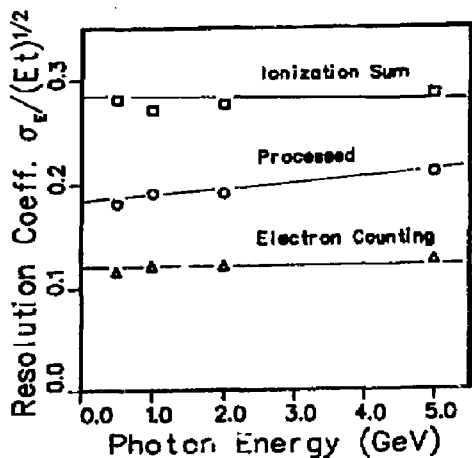


Fig. 8. Improvement of energy resolution by processing results of EGS Monte Carlo simulation as described in text. Up to 5 GeV, the result is a resolution about midway between ideal electron counting and simply summing the total ionization signal.

drift direction varies from ± 2 mm at 0.5 GeV to ± 6 mm at 5 GeV, any 1 mm bin whose signal is at least three times the single-electron average has that signal replaced by the single-electron average.

As seen in Fig. 8, the coefficient $\sigma_e/E\Delta$ is improved from 0.28 to an average of 0.20 in the energy range from 0.5 to 5 GeV. The slow growth of the coefficient with increasing energy is related to the increasing width of the core region excluded from the processing.

Calorimeters for the SLC

A system of hadronic and electromagnetic calorimeters has been designed for use in a solenoidal magnetic detector at the proposed SLAC Linac Collider (SLC)⁶. The very low repetition rate of the SLC allows maximum use of drifting and of hardware processing before readout to a computer. The proposed calorimeter is shown in Fig. 9. It is arranged in a projective geometry, with the electromagnetic calorimeter inside the coil and the hadronic calorimeter outside the coil. Readout is only from cathode pads in the readout gaps (which are conical). The longitudinal and azimuthal segmentation of the readout is determined by the shapes of the cathode pads. A list of parameters of the SLC calorimeter is given in Table I. The whole calorimeter including electromagnetic and hadronic sections in the barrel and endcap regions is read out with less than 25,000 electronic channels and gives segmentation of 1.5 mrad \times 25 mrad.

Effect of Magnetic Fields

The calorimeter shown here has an electromagnetic part inside a solenoid magnet coil and therefore in the full magnetic field of the detector. The hadronic

portion of the calorimeter is partly outside the coil, where it is subjected to smaller, but less predictably oriented magnetic fields. Can drift-collection calorimeters coexist with real magnetic fields?

Two directions of drift are used: axial drift between cylindrical plates in the barrel region; and radial drift between plates perpendicular to the magnet axis in the endcap region. The solenoidal field in which the drifting takes place is primarily axial, with a smaller radial component. In addition, there will be small azimuthal components arising from lack of cylindrical symmetry of the coil and flux return iron. The motion of drifting electrons is governed by the Lorentz force $F = e(E + v \times B)$, where v is the instantaneous velocity. Although the actual motion of the electrons is discontinuous, punctuated by frequent collisions with gas molecules, an adequate approximation is obtained by assuming a constant velocity $\langle v \rangle$ in the direction

$$(E + \langle v \rangle \times B). \quad (1)$$

With this approximation, we can now discuss drifting in the barrel and endcap portions of the calorimeter. In the barrel, the large axial component of the magnetic field is not troublesome, as the electrons drift along it. Further, radial fields produce an azimuthal component of drift, which is still acceptable in a cylindrical drift gap. It can be largely eliminated by pitching the drift electric field so that $(E + \langle v \rangle \times B)$ is still axial. If the compensation is not exact, the result will be an azimuthal distortion of position at the readout wires which can be corrected for. Thus only the azimuthal component of magnetic field—which produces radial components of drift velocity and hence tends to lose drifting electrons on the plates—are damaging, and they can be kept small by proper design of the magnet.

In the endcap portion of the calorimeter, the radial component of B is along the direction of drift, while the main axial component produces an azimuthal component of drift velocity, which as above is tolerable and largely correctable by the direction of the electric field. Here again, it is the azimuthal magnetic field which produced drift into the plates, now with an axial motion.

We can use the approximate direction of equation (1) to calculate a limit on the azimuthal magnetic field. The parameters shown are such that half of the drifting charge will be lost if the angle of drift toward the plates is 0.005 radians. We equate this angle to $\langle v \rangle B_\theta / E$, where B_θ is the azimuthal component of B . If we take typical values of $\langle v \rangle = 1 \times 10^6$ m/sec and $E = 2 \times 10^6$ v/m (e.g. in 90 Ar, 10 CO₂) we find $B = 0.01$ Tesla = 100 gauss. In an axial field of, say, 5 kg this should be attainable. This analysis of drift directions agrees within about 25% with measured drift angles in magnetic fields. The disagreement with measurements, and indeed with a fuller analysis—are such that our calculations from (1) overestimate the effect of azimuthal fields.

The situation is improved by the use of focussing electric fields. In this case, the electric field at the plates always has a component toward the center of the drift gap, which tends to lessen the effect of azimuthal magnetic fields and of diffusion in the gas. In this case, the tolerable B_θ can realistically be 300 gauss.

Electrodeless Drift Planes

A Manchester group has developed drift chambers that have no drift electrodes, but charge internal

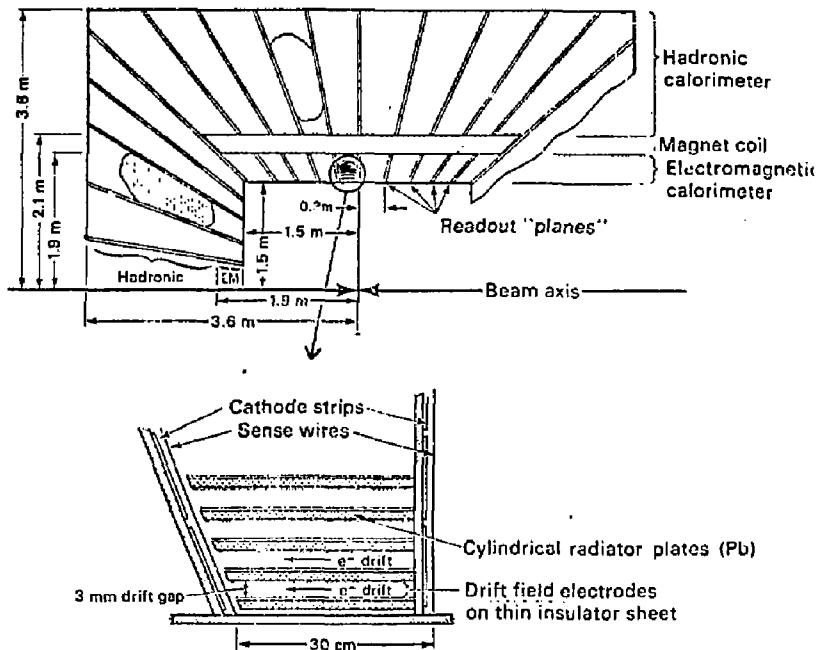


Fig. 9. Application of drift-collection calorimetry to a solenoidal detector for the SLC.

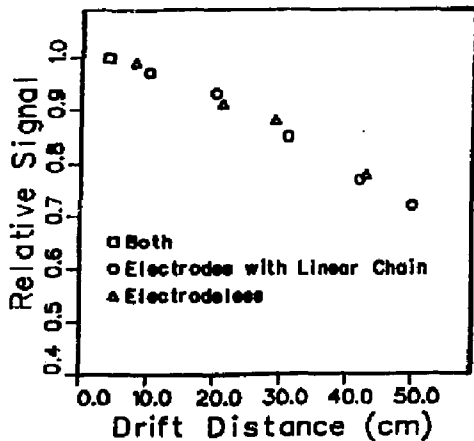


Fig. 10. Attenuation of drifting signals in electrodeless chamber with same dimensions as chamber in Fig. 1. See text for operating conditions.

dielectric surfaces to produce a drift field parallel to the walls⁷. Potentials are applied so that the outside surface of the chamber, which is conducting, is at the most negative potential. Positive ions, from avalanches at the wire, deposit themselves on the dielectric surfaces until field lines from the anode wire no longer intersect the wall but go all the way to the far end of the chamber, where there is a cathode inside the chamber. If such chambers are practical, the construction of a drift-collection calorimeter will be considerably simplified.

We have built an electrodeless drift chamber with the geometry of Fig. 1; we retained the local cathode on three sides of the anode wire as shown in Fig. 1 so that the wire gain could be controlled independently of the drift field. The chamber was operated similarly to the Nucleon Decay 50 cm chambers so that a good comparison could be made. The gas used was again 90Ar, 10 CO₂ with a drift field of 140 v/cm and the voltage between the anode and the local cathode was set to 1.7 kV. Drifting performance of this electrodeless chamber, after 24 hours charging with cosmic rays, is shown in Fig. 10. It is seen to be very similar to the attenuation obtained with electrodes and resistive ink using the linear resistor chain (Fig. 3). Further charging, however, over a period of 10 days, produced a deterioration of the drift performance. Our initial interpretation of this effect is that the charging of the dielectric surfaces continued beyond the optimum point by diffusion of the positive ions into the walls. If this is true, it may be difficult to achieve long-term stable behavior of these chambers. We are continuing to investigate these problems.

On the positive side, we note that the automatic charging of these chambers to the optimum field may make possible chambers that curve around a beam pipe or target. It may even be possible to make chambers that automatically compensate for magnetic fields that would bend drifting electrons into the walls. With magnetic fields, however, the charging will have to be done by electrons because the positive ions move with much lower velocities and therefore have less effect from the magnetic field.

Summary

We have shown that drift-collection calorimeters can deliver high quality calorimetry at low cost. The long drifting in thin gaps that is needed is shown to be practical using resistive ink and focussing drift fields. Electrodeless chambers offer the possibility of simplified construction and perhaps compensation for curved geometries and magnetic fields. A particular calorimeter design for use at SLC is presented.

Table I. Suggested Parameters for SLC Calorimeter

	ELECTROMAGNETIC	HADRONIC
Plate thickness	0.2 λ_0	0.2 λ_1
Drift gap	3 mm	6 mm
Drift distance	30 cm	40-70 cm
Total thickness	15 λ_0	5 λ_1
Polar segmentation (drift)	1.5 mrad	1.5 mrad
Azimuthal segmentation	25 mrad	25 mrad
Longitudinal segmentation	3 segments	3 segments
Channels	Barrel: Endcap:	7500 7500
Energy resolution $\times \%$	7500 4250 0.12	4250 Fe: 0.60 U: 0.35
Drift Electric Field		200 V/cm
Drift chamber gas		90% Ar, 10% CO
Drift velocity		1 cm/ μ sec

λ_0 = radiation lengths
 λ_1 = nuclear interaction lengths

References

1. L.E. Price, *Physica Scripta* **23**, 685 (1981)
 L.E. Price and I. Ambats, *IEEE Trans. Nuc. Sci.* **NS-28**, 506 (1981)
 H.G. Fischer and O. Villalad, *IEEE Trans. Nuc. Sci.* **NS-27**, 381 (1980)
2. J. Bartelt, et al., "Soudan 2, A 1000 Ton Tracking Calorimeter for Nuclear Decay," Univ. Minnesota Preprint COO-1764-410 (1981)
3. Manufactured by Microcircuits Co., New Buffalo, Michigan 49117
4. L.E. Price, et al., *IEEE Trans. Nuc. Sci.* **NS-29**, (1982)
5. P.W. Warren and J.H. Parker, Jr., *Phys. Rev.* **128**, 2661 (1962)
6. SLC Workshop Report, SLAC (1982)
7. J. Allison, et al., U. Manchester Preprint MC81/33 (1981)
8. Ch. Becker, et al., Siegen Univ. Report SI-82-1, (1982)

PROGRESS IN HIGH DENSITY PROJECTION CHAMBERS

E. Albrecht, G. Cerutti, H.G. Fischer, M. Flammier, P.G. Innocenti, J.C. Legrand,
E. Lillethun*, G. Mourgue and O. Ullaland

CERN, Geneva, Switzerland

The High density Projection Chamber (HPC) is a sampling calorimeter where shower conversion and detection is separated. It offers a simple and homogeneous large volume detector with an energy resolution of $(10-11)\%/E$, an inherent resolution transverse to the shower axis of 100 μm and an exceptionally fine granularity along the shower. The use of this detector in a colliding beam experiment will be discussed.

Introduction

The expected well collimated jet topology of the event structure at the new colliding beam facilities will put new demands on the capabilities of the detectors to separate electrons from hadrons and single gammas from π^0 decays. The HPC¹ aims at giving a uniform and fine grained coverage of the total solid angle maintaining a good energy resolution. In contrast to more classical devices the HPC adds fine granularity along the shower and not only transverse to the shower axis, a feature which is required for an excellent discrimination between electromagnetic and hadronic showers. The read-out of space points will in addition simplify the pattern recognition.

In this paper we are discussing the features of the HPC as an electromagnetic shower detector in a colliding beam experiment (fig. 1). The converter is a laminated stack of grid structured lead plates. Each plate is electrically insulated from its neighbour by an epoxy coating. This also serves as a plate-to-plate bonding of the stack. The grids will in this way be superimposed and make up long sampling slots perpendicular to the incident particle trajectories (fig. 1(b)).

The electrons are then drifted along the sampling slot/drift channel onto the active detector plane under the influence of an electric field built up by a simple voltage gradient between the plates.

The detector is a single plane proportional chamber with cathode pad read-out (fig. 1(c)). The gas amplification field and the drift field are decoupled via a cathode wire grid. The grid is made of 100 μm diameter copper wires which are spaced by 1 mm (fig. 2). The charge transparency of such a grid has been investigated. For $E_{\text{chamber}}/E_{\text{drift}} > 6$ there is full charge transmission, in agreement with previously published data².

The converter structure with its pick up chamber is placed inside the solenoidal field of the analyzing magnet. This solution minimizes the material in front of the calorimeter. Since the magnetic field is parallel to the electric field it has no adverse effect on the charge transport.

Read-out system

The main components of the read-out system are shown in fig. 3. The two projected coordinates are given by the cathode pad size (fig. 1(c)). With only one read-out plane for a drift length of more than a meter the system facilitates an optimization of the granularity along and transverse to the shower axis. The coordinate along the drift channel is given by the drift time of the charges. This is done with a duplex charge integrator system. The induced charges on each cathode pad are integrated in small time buckets. One integrator can then be read out and reset via a fast

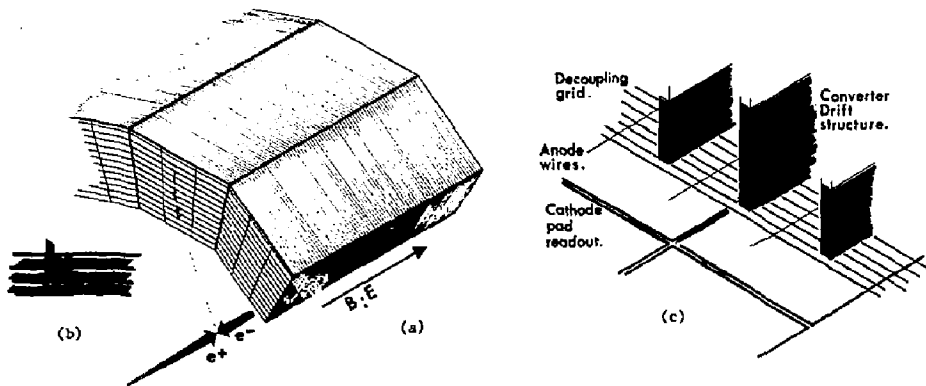


Fig. 1 - (a) Long drift High density Projection Chamber modules enclose a beam intersection region. (b) Detail of the sampling structure. (c) Layout of the pick up chamber.

(*) On leave of absence from University of Bergen, Norway.

analog to digital converter, during the time the other integrator on the same line accumulates the incoming charges. We are planning to work with time buckets 100-200 ns long. This corresponds to a few mm drift length depending on the gas mixture and the drift voltage.

The inherent space resolution of this detector is about 100 μm in the transverse plane if we use the centre of gravity method. Longitudinal to the shower axis the space resolution is one sampling gap wide. It should be pointed out that the resolution along the drift direction is only dependent on the length of the time bucket and the drift velocity and does not increase the number of electronics channels.

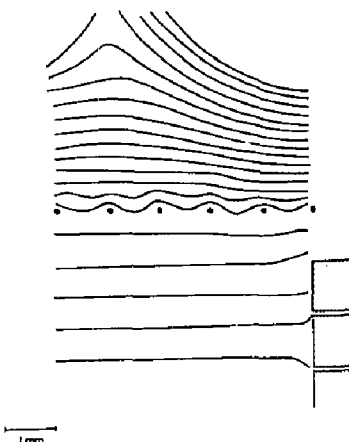


Fig. 2 - Equipotential lines at the junction between the converter stack and the pick-up chamber. The points represent the 100 μm diameter grid wires.

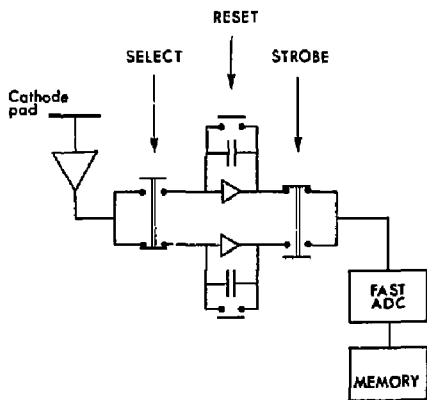


Fig. 3 - Schematic diagram of the HPC electronics.

Charge transport

We have previously published data on charge transport in a confined geometry¹. Only diffusion inflicted charge losses play a role when the ratio between the gas gap and the step size of the electric field is optimized. Attenuation lengths of 15 μm have been observed in a drift channel made up of 10 μm gas and 1 μm plate thickness. The gas mixture was 80% Ar/20% CO₂.

We have limited our choice of gas mixtures to the ones used by the ISIS³ and the TPC⁴ groups. The diffusion coefficients in 80% Ar/20% CO₂ and 80% Ar/20% CH₄ gas mixtures at NTP have been investigated. The characteristic energy spectrum from a Fe⁵⁵ gamma source is a valuable tool to determine the transverse diffusion behaviour of a single electron. The observed gamma spectrum has two energy lines, the escape line at ~ 3 keV and the Auger line at ~ 6 keV. The charge losses due to the diffusion of the electrons into the walls of the drift channel result in a characteristic filling up of the valley between the two lines. A Monte-Carlo program has been set up to simulate the physical processes from the gamma conversion to the gas amplification on the anode wire. It can thereby be shown that the ratio between the height of the Auger peak and the valley between the two energy lines is a measure of the transverse diffusion for a single electron (fig. 4).

The measurements for 20% CO₂ and 20% CH₄ admixture in argon is shown in figs 5 and 6 together with other data for transverse and longitudinal diffusion.

CO₂ is known to be an excellent electron cooling gas^{5,6} where the influence of the argon plays no major role in the diffusion process. Our measurements are here in excellent agreement with the data⁵ from pure CO₂, scaled to its partial pressure. Also the direct measurement⁵ of the longitudinal diffusion in 80% Ar/20% CO₂ coincides with our data points.

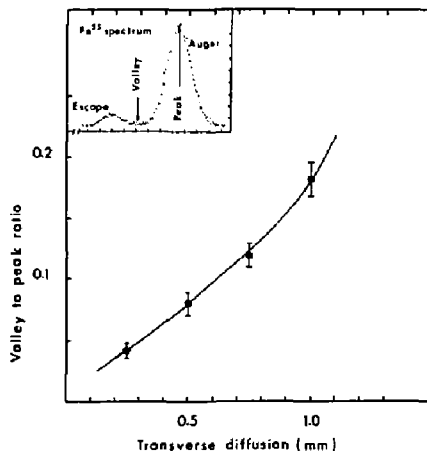


Fig. 4 - Simulation calculation of the transverse diffusion as a function of the ratio of the counting rate at the Auger line and the valley between the Auger and the escape line.

The transverse diffusion coefficient for 20% CH₄ exhibits a much stronger dependence on the electric field than in the case of the CO₂. We find here a minimum at about 90 V/cm where as it is about 450 V/cm at NTP in the gas mixture with CO₂. We do not however observe the strong deteriorations of the transverse diffusion by going from 20% CO₂ to 20% CH₄ admixture in argon as reported by the TPC group⁴.

We have also investigated the electron drift efficiency under the influence of a magnetic field. It can be shown⁹ that the deflection angle, θ , due to a magnetic field, B, perpendicular to the electric field can be written as

$$\theta \approx \omega t = a * B,$$

The best fit to our data gives $a = 0.27 \text{ Tesla}^{-1}$. This corresponds to an overall charge displacement of 1 mm for 40 Gaussmeter perpendicular to the drift direction.

Electron capture by positive ions¹⁰ is not expected to give any problems since the electronics chain enables us to work at a gas amplification of only a few thousand. The converter structure should also be effectively shielded against background events. Oxygen contamination will however deteriorate the attenuation length in a gas mixture with CO₂. Methane is less critical. For this gas, no influence on the drift properties have been observed for O₂ concentrations smaller than 80 ppm.

The calorimeter

We have demonstrated that the charge transport causes no problem in the converter structure. The projected charge includes all the necessary information for the detector to operate as a fine grained quantimeter.

Two calorimeter modules with a geometry similar to the one shown in fig. 1 have been built. The first one has a copper converter with 18 samples 2/3 X, apart. It was used for optimization of the drift properties and of the charge collection efficiency⁴. It has also been run in an electron beam to study its resolution. The EGS¹¹ program was used to simulate the detector. The measured and expected energy resolution coincide (fig. 7).

The second module is a lead converter stack. The converter plates are lead frames with 1.5 mm wide lead bars spaced 10 mm apart. A 50 μm epoxy insulator bonding layer is deposited on the grids with a silk screen printing technique. The stress exerted perpendicular to the lead bars is taken up by spokes running from the front of the module to the back of it (fig. 1). These thin stiffening spokes are placed ~ 20 cm apart. Further optimization of the internal stability is under study by minimizing the number of spokes without losing the self stable structure.

Energy resolution

As far as energy resolution is concerned, the HPC performance should be superior to the one expected for normal multiwire proportional quantimeters¹². This has two main reasons:

- (a) The good granularity allows the study of the three-dimensional shower development with high resolution. At energies below about 2 GeV, simple digital counting methods of set detector cells or rows of such cells should yield a resolution close to the lower limit given by the fluctuation of the number of shower electrons¹³. The additional

information due to the analog charge measurement in each drift cell, will avoid saturation effects close to the shower axis at higher energies.

- (b) The magnetic field orthogonal to the shower axis eliminates most of the track length fluctuations which are known to deteriorate the energy resolution: low energy, large angle shower electrons are quickly bent back into the lead converter.

On the other hand, long range ionization electrons produced in the gas, which will be trapped by the magnetic field, can be recognized and eliminated by their characteristic track pattern along the field lines.

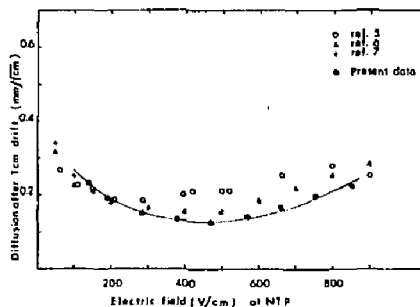


Fig. 5 - Electron diffusion as a function of the electric field in 80% Ar/20% CO₂. One measurement of the transverse component is compared to the longitudinal in the same gas⁵. The data from R.W. Warren et al.⁶ and E.B. Wagner et al.⁷ are in CO₂ and recalculated for 0.2 atm of CO₂.

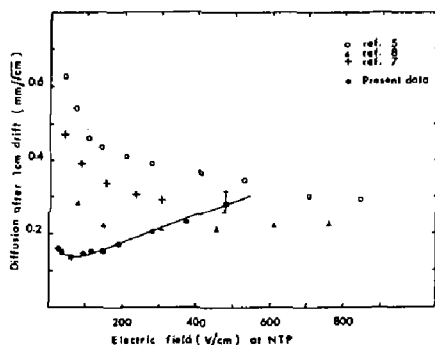


Fig. 6 - Electron diffusion as a function of the electric field in 80% Ar/20% CH₄. Our measurement of the transverse component is compared to T.L. Cottrell et al.⁶ in CH₄. Also plotted is the measurement from F. Piuze⁵ of the longitudinal diffusion in 80% Ar/20% CH₄, together with E.B. Wagner et al.⁷ in CH₄.

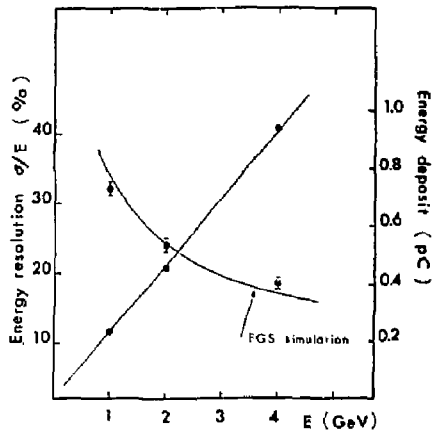


Fig. 7 - Energy resolution and energy response for electron showers in a test module with 18 samples over 13 radiation lengths of copper. The energy resolution is compared to a Monte-Carlo simulation.

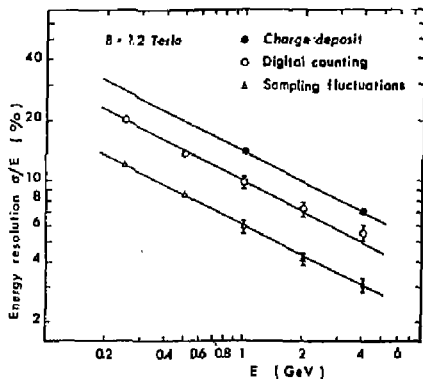


Fig. 8 - EGS calculation of the energy resolution in a lead converter structure with 60 samples $1/3 X_0$ apart.

We are at present studying some of the possibilities indicated above with the EGS Monte-Carlo routine¹¹ adapted to operation in a magnetic field¹⁴. Preliminary results suggest that resolutions of $(10-11)\%/E$ can be achieved with a sampling thickness of $1/3 X_0$ of lead (fig. 8).

It is however clear that the full potential of this new device will only reveal itself in conjunction with powerful pattern recognition techniques. This is especially true for an environment like LEP where problems like shower overlap and hadron rejection become a major concern.

Conclusion

The HPC is a promising calorimeter for future colliding beam experiments. It is a simple and stable large volume detector with few active elements which offers high spatial and energy resolution.

We are indebted to A. Pullia and S. Ragazzi, University of Milano, M. Jezabek, University of Cracow, and P.S. Iversen, University of Bergen, for their shower calculations. We wish to thank A. Minten for his active interest and support. Also acknowledged is the effort of the CERN technical services in the realization of the converter modules.

References

1. H.G. Fischer and O. Ullaland, IEEE Trans. Nucl. Sci. NS-27 (1980) 38.
2. S.C. Curran and H.W. Wilson, ed. K. Siegbahn, Alpha, Beta and Gamma Ray Spectroscopy (North Holland 1965);
A. Breskin et al., Nucl. Instr. Meth. 161 (1979) 19.
3. W.W.M. Allison et al., Nucl. Instr. Meth. 119 (1974) 499.
4. D. Fancher et al., Nucl. Instr. Meth. 161 (1979) 383.
5. F. Piuze, to be submitted to Nucl. Instr. Meth.
6. R.W. Warren and J.H. Parker, Phys. Rev. 188 (1962) 2668.
7. E.B. Wagner et al., J. Chem. Phys. 47C (1967) 3138.
8. T.L. Cottrell and I.C. Walker, Trans. Faraday Soc. 63 (1967) 549.
9. A. Breskin et al., Nucl. Instr. Meth. 124 (1975) 189.
10. D. Friedrich et al., Nucl. Instr. Meth. 158C (1979) 81.
11. R. Ford and W.R. Nelson, SLAC 210 UC - 32 June 1978.
12. H.G. Fischer, Nucl. Instr. Meth. 156 (1978) 81.
13. L. Federici et al., Nucl. Instr. Meth. 151 (1978) 103.
14. M. Jezabek, A. Pullia and S. Ragazzi, Private communication.

PROPERTIES OF BISMUTH GERMANATE AND ITS USE FOR ELECTROMAGNETIC CALORIMETRY*

M. Cavalli-Sforza, D.G. Coyne, S. Cordes, J. Hawley, C. Newman-Holmes, R. Sonnenfeld
 Physics Department, Princeton University, Princeton, NJ, 08540
 G.I. Kirkbride
 High Energy Physics Laboratory, Stanford University, Stanford, CA, 94305

Summary

The calorimetric and fluorescence properties of Bismuth Germanate are discussed and compared to those of NaI(Tl). Results on the energy resolution of BGO are presented for energies up to 50 MeV; the energy and position resolution are studied by Monte Carlo at higher energies. The performance of a 4" BGO e.m. calorimeter is compared to that of NaI and is specified for a compact fieldless calorimeter designed for the Z^0 energy region. Cost, optical uniformity and radiation sensitivity are areas needing further work before a large BGO detector can be built.

Introduction

Large solid angle, highly segmented sodium iodide detectors have emerged over the last few years as a novel and fruitful way to measure many of the parameters of the final states produced in e^+e^- annihilation. Two such detectors are at present active in e^+e^- physics: the Crystal Ball, that after more than three years of very productive existence at SPEAR is about to begin exploring b-quark physics at DORIS II, and the CUSB detector, working in the region of the ψ 's at CESR.

As plans for detectors at the next generation of e^+e^- machines are getting more detailed, considerable attention has been devoted to Bismuth Germanate (BGO) as a possible alternative to NaI(Tl) for large solid angle detectors that seek superior energy resolution coupled with good angular resolution.

General and calorimetric properties of BGO

Bismuth Germanate ($\text{Bi}_2\text{Ge}_2\text{O}_{12}$) is a transparent, crystalline material of high density and high atomic number with large scintillation light yield. BGO crystals are grown from a melt of a 2:3 stoichiometric mixture of Bismuth Oxide (Bi_2O_3) and Germanium Oxide (GeO_2). Crystal boules of up to 30 cm in length and ranging in diameter from 5 to 10 cm are pulled from the melt by the Czochralski method; the boules are then cut, machined and polished to the desired dimensions. Crystals are presently available from at least two manufacturers.¹ Table 1 lists the properties of BGO in comparison to NaI(Tl).

The calorimetric properties of BGO are of course the main reason for its emergence as a particle detector. The radiation length of BGO is 2.3 times shorter than that of NaI(Tl), and the Moliere radius (determining the scale of the lateral spread of e.m. showers) is a factor 1.75 less than NaI(Tl). The nuclear absorption length, $\Lambda = 23$ cm, prohibits its use as a hadron absorber, although the ratio Λ/X_0 is marginally higher than for NaI(Tl) and may thus improve slightly the hadron-electron separation.

The crystals are mechanically rugged, do not cleave, are reasonably hard to scratch and are impervious to most chemical solvents - water in particular. These latter properties are in marked contrast to NaI(Tl), that is very delicate and difficult to handle on all these counts. On the other hand, growing long (20 cm) crystals of uniform transparency appears to be a challenging task, requiring high-purity starting

TABLE I
 BGO - NaI(Tl) COMPARISON

	BGO	NaI(Tl)
<u>General Properties</u>		
Specific Gravity	7.13	3.67
Hardness	~5 (soft glass)	~2 (rock salt)
Stability	rugged	cleaves, shatters easily
Chemical Stability	good	poor
Solubility (H_2O)	none	very hygroscopic
<u>Calorimetric Properties</u>		
Radiation Length, X_0	1.12 cm	2.59 cm
Moliere Radius	2.24 cm	4.4 cm
dE/dx (min)	~9 MeV/cm	4.8 MeV/cm
Nuclear Absorption Length Λ	~23 cm	~41 cm
<u>Optical and Fluorescence Properties</u>		
Refractive Index	2.13	1.85
λ_{max} Emission	480-500 nm	420 nm
Fall Time	300 ns	250 ns
Photoelectrons/MeV	300-600 (tube depn'd't)	
Light Output	16	100

materials and carefully controlled growth conditions. The optical quality of BGO crystals is not yet on a par with that of NaI(Tl), although it must be pointed out that the technology for BGO is still developing.

Optical and fluorescence properties

The fluorescence of BGO has been assigned to the $3p_1 + 1s_0$ transition of the Bi^{+++} ion. The large Stokes shift between the absorption spectrum² (peaked in the near UV) and the emission spectrum makes the material highly transparent to its own light. The index of refraction is about 2.15 over the visible range (compared to n=1.85 for NaI(Tl)). Such a high index makes the light transfer through photomultiplier windows (typically n=1.46) rather inefficient; graded index couplings do not help significantly. On the other hand, the high index helps in keeping most of the light into a long parallelepipedal crystal; in fact, all of the light that is within the critical angle for transmission through the interface to a PMT is totally reflected off the sides for parallelepipedal crystal geometry. This circumstance suggests that in parallelepipedal crystals light collection uniformly along a crystal could be very good. Scattering centers in crystals would worsen the uniformity of light collection; we see examples both of macroscopic scattering centers and of the expected effect in 20 cm long crystals we have under test. These issues have been investigated in detail by Monte Carlo for smaller crystals in view of applications in positron emission tomography.³

*Work supported under NSF Grant PHY-8--02409 and PHY-79-16461.

The emission spectrum^{2,4,5} peaks at 480 to 500 nm, with a substantial tail in the green and red. It is thus not ideally matched to the response curve of alkali photocathodes, while matching very well the response of Silicon photodiodes.

The fluorescence decay time has long been known¹⁴ to be about 300 ns at room temperature. A recent, accurate measurement of the light pulse shape, done with the single photon method¹⁵, confirms that the decay time is 300 nsec at room temperature but shows in addition an additional component decaying with a 60 ns time constant and accounting for ~10% of the total light. The risetime is measured in the same study to be 2.8 ns and is probably dominated by light collection time in the crystal used.

The integrated light output of BGO is often measured relative to NaI(Tl); it depends of course on the PMT response curve. Furthermore, it is very sensitive to crystal purity and optical quality, as well as surface treatment. Using alkali PMT's, light yields of up to 16% of NaI(Tl) have been reported.⁶ We have measured the photoelectron yield using an RCA 8B50 Quantacon tube on a 1 inch diameter x 1 inch long, cylindrical crystal, with polished sides; we observe 192±5 photoelectrons using 0.662 photons (Cs¹³⁷), with a FWHM/peak resolution of 12±1%. Within the errors, the resolution is explained by photoelectron statistics. On the same crystal and similar ones, but using Hamamatsu alkali PMT's, we get typical FWHM/peak resolution of 12.5% with Cs¹³⁷ gamma rays. This resolution indicates a higher photoelectron yield, roughly 600 electrons/MeV.

It is known that the energy resolution of BGO scales roughly like $E^{-1/2}$ up to a few MeV.¹⁴ The resolution falls more slowly for NaI(Tl) crystals; these circumstances encouraged us to investigate the resolution of BGO at higher energies.

Before closing this review of material properties, we note that both fluorescence decay time and integrated pulse height of BGO decrease rapidly with temperature. Both quantities are approximately linear vs. temperature from 10°C to 55°C, with $\Delta P/P = -1\%/^{\circ}\text{C}$ at 20°C, where P is the pulse height.⁷ The light output saturates at ~200%K, where it is ~5 times more than at room temperature.² While all this may speak for cooling BGO crystals, it also demands that any future detector be carefully temperature controlled, and that the uniformity be better than 1°C across the detector.

Energy resolution measurements for $E \leq 50$ MeV

Two cylindrical crystals, 4 inches in diameter x 3 inches long, were grown for us by the Harshaw Chemical Co. The size was chosen to optimize containment of electron-induced showers up to 100 MeV using the two crystals juxtaposed. The crystals were mildly straw colored, of good transparency except for an axial region of impurities about 1.5 inch in diameter, starting from a flat face and tapering off towards the other face.

The measurements have been described in detail elsewhere⁸; only the essentials are summarized here. The results are in Fig. 1. Measurements were made at the following energies:

- Source region: 0.66 MeV photons from Cs¹³⁷; 0.51 and 1.27 MeV photons, from Na²².
- Nuclear reaction region: Using the Crystal Ball's Van de Graaff accelerator to induce (p,γ) reactions on nuclear targets, we took data at 4.44 MeV and at 11.67 MeV ($p+^{11}\text{B} \rightarrow \text{C}^{12} + \gamma_1 + \gamma_2$) and at 6.13 MeV ($p+^{19}\text{F} \rightarrow \text{Ne}^{20} + \text{Ne}^{20} + \gamma$).
- Higher energies: We took data with the Linac of the Naval Postgraduate School at Monterey.

The electron beam was run at 1 particle per pulse with energies of 30 and 50 MeV; it had an energy width of 0.4%.

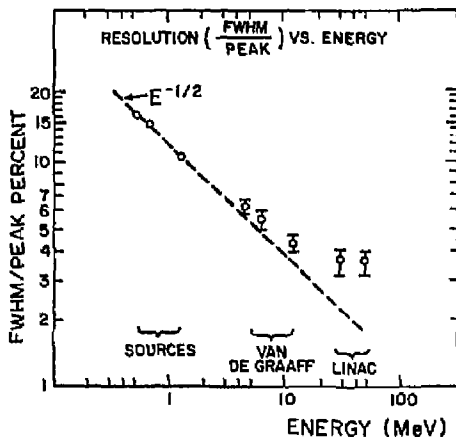


Fig. 1. Energy resolution measured with the 4 inch x 3 inch BGO crystal.

For all measurements, one of the two crystals was grease-coupled to a Hamamatsu R1069 5 inch PMT.

In the Van de Graaff data, the photons were collimated to impinge axially on an area of approximately 1 inch square, offset by 1 inch from the crystal axis. This was to assure that the scintillation light would neither be produced nor transmitted in the impurity "cloud" that faced the incoming photons. Different cloud-beam geometries gave worse resolutions than the arrangement described. At 30 and 50 MeV, the crystal was complemented with an array of 6 large NaI(Tl) detectors, arranged to maximize the solid angle viewed from the center of the BGO crystal. The array was used as a veto to eliminate events in which more than 0.3 MeV of the shower energy would escape the crystal and thus measure the intrinsic resolution of the crystal. We note that, at these energies, it is not possible to keep the shower or its light from the "cloud" in the crystal.

The results in Fig. 1 show a gradual departure from the $E^{-1/2}$ low-energy extrapolation; we feel this is due to the impurity "cloud" either in light generation or in light transmission, based on the tests done at Van de Graaff energies. The resolutions obtained at 30 and 50 MeV, however, compare not unfavorably with resolutions obtained with NaI(Tl) crystals of larger size at similar energies.⁹ We conclude that BGO shows some promise as a material for electromagnetic calorimetry and discuss it further in view of large solid angle detectors for future e^+e^- experiments.

Leakage and resolution at higher energies

As the energy of the incident particle increases, total shower containment becomes impossible and the fluctuations of energy leakage dominate the resolution. Cost considerations and overall apparatus design constraints set a limit on the thickness and thus set the scale of rear shower leakage. Back scattering and leakage out of the side are a limit even for a full solid angle detector, since backscattered energy or energy deposited outside a maximum allowed volume cannot be associated to the shower they originate from if there is more than one shower in the event.

We have studied the lateral spread of showers by Monte Carlo using the EGS3 code.¹⁰ Fig. 2 shows the fraction of the energy escaping out of a 20 R.L. thick cylinder of the radius r with 100 MeV photons incident along the cylinder axis, for both BGO and NaI(Tl). This radial energy distribution (integrated along the axis) is to very good approximation independent of the energy and charge (e^+ , γ) of the incident particle. Fig. 2 shows that $r=7.5$ cm is sufficient to contain >98% of the energy; the analogous radius for NaI(Tl) is about 16 cm.

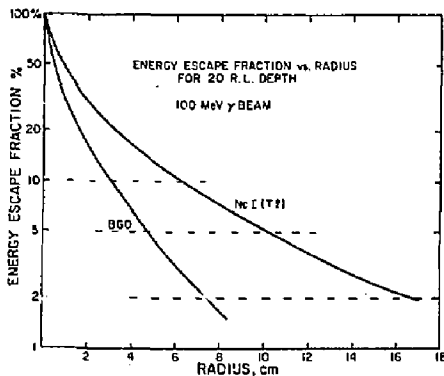


Fig. 2. Fraction of energy escaping from a BGO or NaI cylinder 20 X_0 long vs. radius of cylinder for 100 MeV photons incident on cylinder axis.

We intend to learn more about the use of BGO for future large, multi-segmented calorimeters by building and instrumenting a test array of long (20 cm) parallelepipedal crystals. The results of Fig. 2 indicate that a width of 15 cm would be sufficient to contain more than 98% of the energy of the shower. We studied, again by the EGS Monte Carlo, the expected energy resolution of a 15 cm x 15 cm x 20 cm BGO parallelepiped for electrons incident at the center along the major axis. The resolutions obtained for 10 MeV $< E_e < 10$ GeV are shown in Fig. 3; the calculation includes a photoelectron statistics term, falling like $E^{-1/2}$ and taken to give a FWHM/pvise = 16% at the Ca^{137} γ energy - a result that we get from 20 cm long crystals. It can be seen that photoelectron statistics dominates the

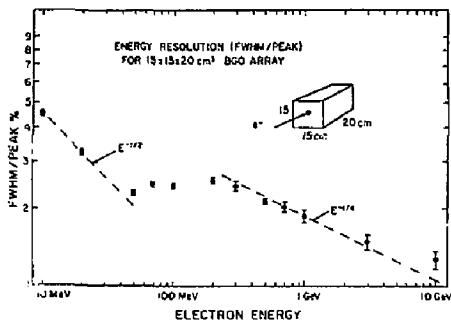


Fig. 3. Energy resolution for a 15 x 15 x 20 cm³ BGO parallelepiped vs. incident electron energy.

calculated resolution up to about 50 MeV incident energy. Between 50 and 200 MeV the onset of significant leakage causes an increase in resolution; at higher energies, the resolution falls again, with an energy dependence close to the $E^{-1/4}$ behaviour that is often quoted for large NaI(Tl) detectors.

This Monte Carlo does not include the effect of other inevitable contributions to the resolution that are harder to predict, such as uncertainties in the relative calibration of the readout elements, or the effect of possible nonuniformities of the material, or in light collection, etc. Such effects are almost certain to mask the curious rise of the resolution occurring above 50 MeV.

Position resolution

It is important to have a precise estimate of the resolution on the entry point of a photon in an array of crystals of given modularity in order to optimize the dimensions of modules. The quickest way to obtain an estimate of the entry point using as input the energy deposited in each module is to form the average of the modules hit weighted by their energy deposit:

$$\bar{x} = \frac{\sum E_i x_i}{E_t} \quad x_i = \text{coord. of the center of each module}$$

This "center of energy" method has a bias intrinsic to the choice of the center of each module as the average for energy deposition in that module. The lateral profile of showers is sharp, as Fig. 2 shows, particularly in the central region; if the entry point is off the center of the module hit by the incident particle, the bias will not be cancelled by the energy distribution in the adjacent modules unless the granularity is very fine. To set the scale, a 1 x 1 x 22.4 cm³ module hit along the axis will contain approximately 55% of the energy of the incident photon, for $E_\gamma = 100$ MeV.

This bias can be all but eliminated by using a different procedure that has been used extensively in the Crystal Ball software.¹¹ The entry point is varied until the best fit is found between a Monte Carlo-calculated average shower profile (which is a function of the entry-point coordinate) and the observed shower profile. The fundamental limit is set by the lateral fluctuations of the shower energy distributions that have a scale of 10 to 30 MeV.

Fig. 4 and 5 show the resolutions we obtain on the entry point of photons of three energies for three module sizes, using the center of energy method and the shower profile method respectively to determine the shower entry point. The latter algorithm is obviously superior, in particular at high energy. The results of the shower profile method show - as expected - that one does not gain resolution in direct proportion to the number of segments, due to the shower fluctuations. At the higher energies, of course, the latter are less important and the resolution gets to be 10% or less of the module size.

Comparing BGO and NaI(Te) for a 4 π electromagnetic calorimeter

On the basis of our experimental results on BGO, the Monte Carlo studies and the experience of some of us with the Crystal Ball at SPEAR, we can now attempt a more general comparison between the performance of two hypothetical large calorimeters, one built with BGO and the other with NaI(Te).

First we can ask which one will have the best energy resolution. This is a natural question to ask even if energy resolution will not be the most important parameter for the physics aims of such detectors,

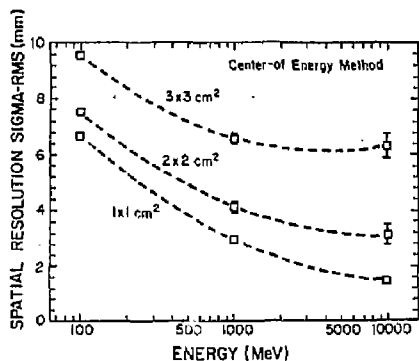


Fig. 4. Rms position resolution (projected) for 1x1 cm², 2x2 cm² and 3x3 cm² segmentation vs. incident photon energy. The entry point is calculated with the center of energy method.

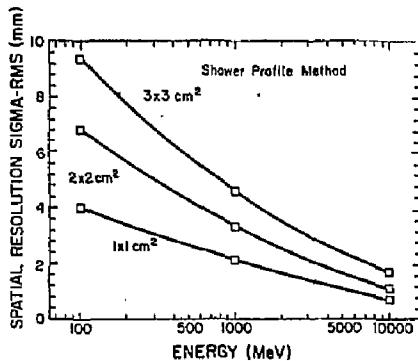


Fig. 5. Like Fig. 4 but with the entry point calculated using the shower profile method.

since this parameter is one of the attractive characteristics of both materials. We have seen that for BGO energy leakage dominates photoelectron statistics as the main cause of resolution above ~100 MeV incident energy. We note in this context that the resolution of the Crystal Ball's prototype¹² (a cluster of 56 crystals) above 1 GeV is only marginally better than what we obtain from our Monte Carlo: at 1 GeV, we calculate FWHM/peak = 1.9% ± 0.1% and the cluster-of-54 prototype measured 3.0 ± 0.2%. It is easy to explain the difference with any of a number of instrumental effects. The first conclusion is that there seems to be no intrinsic difference between the ultimate resolution of the two kinds of detectors in the leakage-dominated region. At lower energies we should compare our results with the 4 inch BGO crystal to results obtained with large NaI(Tl) crystals; here, BGO performs marginally below NaI(Tl), largely due to problems of crystal purity on which progress has recently occurred (see below). The tentative conclusion at the present time is that we do not expect a significant improvement in energy resolution over NaI(Tl) from a BGO detector: improvement over the Crystal Ball's performance, if achieved in the future, will rather depend on better intercalibration of the readout elements or other material-independent instrumental matters.

The more important advantage of BGO is the fact that the radial energy spread is a factor of two less than for NaI(Tl), as can be checked using Fig. 2. We only need to specify the inner radius of the e.m. calorimeter to compare the performance of the alternative approaches; we assume that this choice would not be determined by cost considerations only, but would have the most crucial inputs from the design aims of the whole detector. It is easy then to list the advantages that a BGO calorimeter would have over an NaI(Tl) calorimeter of the same inner radius.

- The solid angle "lit up" by e.m. showers or nuclear interactions in BGO would be 4 times less than for NaI(Tl), leading to a large reduction in overlaps of particles. The precise numbers are of course model-dependent.
- The angular resolution for photons would be x2 better for BGO.
- Overlap of photons from symmetric π^0 decays would occur above a π^0 momentum value 2x higher for BGO than the corresponding momentum for NaI(Tl).
- π^0 mass resolution would improve (due to (b)) and the combinatorial background would correspondingly be reduced.

- Improved π^0 reconstruction efficiency would dramatically reduce the background in inclusive photon spectra.
- Last, if the e.m. calorimeter is followed by a hadron calorimeter, the latter would be more compact if the e.m. part consists of BGO. Whether this would result or not in an overall cost saving depends on the large quantity cost of BGO (see below).

A design exercise for a compact calorimeter for $E_{CMS} = 100$ GeV

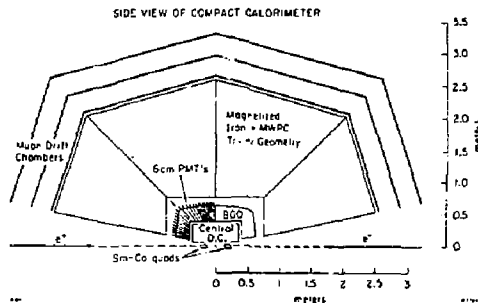


Fig. 6. Schematic diagram of the compact calorimeter (SLC note #34) discussed in text.

Some of the above considerations can be made more precise by referring to the design of a full detector. Fig. 6 schematically represents a compact detector system for physics in the region of the Z^0 at the Stanford Linear Collider.¹³ The design and performance parameters are described more in detail in the reference. The detector is based on a fieldless electromagnetic calorimeter using BGO, followed by a magnetized iron hadron calorimeter and by drift chambers for muon momentum measurements. We quote here some of the characteristics of the electromagnetic calorimeter. The inner radius was chosen to be 40 cm, due primarily to cost; it is not clear, though, that there is much to be gained from a larger inner radius in the absence of magnetic field and for any reasonable (not too high) calorimeter segmentation. The inner cavity was chosen

to be cylindrical, rather than spherical like the Crystal Ball, to use optimally the limited internal volume available. The BGO shell is 20 X₀ thick, and is segmented in ~10⁴ modules. Projective tower geometry was chosen to optimize solid angle segmentation in view of the very high multiplicities expected. Each module would have an inner side of 1.4 x 1.4 cm² and an outer side of 2.4 x 2.4 cm², and would be viewed axially by a PMT in this design.

We list rough estimates of some performance parameters referred to in the previous section:

- (a) The angular resolution for photons, based on Fig. 5, depends on energy and lies in the range of 15 to 3 mr for 100 MeV < Eγ < 10 GeV.
- (b) The angular resolution for noninteracting hadrons is ~10 mr.
- (c) Scaling with radiation length from the Crystal Ball experience, we estimate that we can separate overlapping photons from π⁰ decays for opening angles >17 mr, corresponding to p(π⁰) < 8 GeV/c.
- (d) The rms resolution on π⁰ mass is 6%, for p(π⁰) = 1 GeV/c; it deteriorates rapidly with momentum.
- (e) Separate energy measurements for each e.m. particle in a jet will not be possible due to overlaps; the situation will be helped somewhat if, as QCD MonteCarlos indicate, ~1/3 of all particle lie in a ±200 mr core. Outside this core, most of the showers should be separable. Within the jet core e.m. energy flow measurements can be done.

Are we ready to build a 4m BGO detector?

We conclude that BGO is not only an attractive material for electromagnetic calorimetry, but that a BGO calorimeter would be a very useful component in a 4m non magnetic calorimeter. The promising first results on photodiode readout of BGO (presented in the next talk) make the magnetic calorimeter option possible and very appealing. Therefore we should ask whether we can design and construct a large BGO calorimeter at the present time. We feel that three problems need more work.

(1) Cost. The current cost of BGO is about 14\$/cm³ in quantities of a few liters. This translates to 10.5x10⁶¢ for the crystals only in the design exercise we described - and would certainly rule out more ambitious designs. We have investigated in some detail both the material and growing costs of the crystals, and feel that the quoted cost would be largely unjustified for amounts of a few tons. We estimate that a reasonable cost on this scale should not exceed 5\$/cm³. One uncertainty in the projected cost is due to the relative scarcity of Germanium and the demand for it on the world market. GeO₂ dominates the price of materials in BGO production; the current cost is 600\$/kg in the required purity and represent 21% of the projected cost of finished crystals assuming that none of the purchased GeO₂ is wasted in the production process.

(b) Optical uniformity of crystals. All designs for future detectors are based on crystals at least 20 cm long. Obtaining such crystals with good transparency throughout has proved to be a challenge. There has been progress in the last few months at Harshaw in this regard, and we received in the last few weeks crystals of much improved quality. Thin transversal bands of scattering centers are still visible, though, irregularly distributed along the main axis of crystals. We do not know yet whether these bands produce a significant deterioration of the uniformity of the crystal response along its axis. We feel, though that given the recent trend the prognosis in this respect is good.

(c) Radiation hardness. The radiation background at some of the future e⁺e⁻ colliding facilities is

expected to be very large, and to put heavy constraints on any future detector. A paper contributed to this conference by M. Kobayashi et al working at KEK on BGO contains encouraging results; BGO is shown to be more resistant to radiation damage from low-energy photons and high energy hadrons than NaI(Tl) and Cerenkov or scintillating glasses. The damage is seen as a loss of light transmission through 1 cm of BGO, and, for e.m. radiation in particular, disappears in a few weeks. The typical exposure to see an effect several hours after irradiation is 10⁵R for e.m. radiation and 10⁴R for hadrons.

We have observed a loss of transmittance in 20 cm long crystals irradiated with UV. The effect totally disappears in about 2 weeks and may be the same as that observed by the KEK group; however, most of the transmittance loss we observe decays in a few minutes, and we also observe a component that decays in a few hours. These effects would not have been seen in the KEK experiments, while our experiments would not have seen damages that disappear in a few seconds or less. Our UV exposures correspond to particle fluxes much larger than what can be realistically expected.

We feel that more work is needed on at least the following points: (1) a 1% loss of transmittance/cm is intolerable over a 20 cm long crystal. Either very precise tests on short crystals or tests on long crystals are necessary. (2) It must be checked whether the optically impure parts of the presently available crystals are more or less sensitive to radiation damage. (3) The possibility of very short-duration radiation effects must be investigated, probably down to the 1 μs time scale.

References

1. Harshaw Chemical Co. and Hitachi Chemical Co.
2. M.J. Weber and R.R. Monchamp, J. Appl. Phys. 44, 5495, (1973).
3. S.E. Derenzo and J.K. Riles, IEEE Trans. Nucl. Sci. NS-29, (1982).
4. H.V. Piltingerud, J. Nucl. Med. 20, 1279, (1979).
5. R. Moncorgé et al, J. Luminescence 14, 337 (1976).
6. Takegi et al, J. Crystal Growth 52, 584, (1981).
7. G. Blamar et al, Contributed paper to the EPS Conf. of High Energy Physics, Lisbon, 1981 - unpublished.
8. F. Buekirk et al., IEEE Trans Nucl. Sci. NS-29 (1982), and HEPL 900, Oct. 1981.
9. B. Ziegler, J.M. Wyckoff and M.W. Koch, Nucl. Instr. and Meth. 24, 301 (1963).
10. R.L. Ford and W.R. Nelson, SLAC-210 report, 1978.
11. F. Bulos and A. Liberman, Crystal Ball group internal note, unpublished.
12. E.D. Bloom, Proc. Ninth Int. Symp. on Lepton and Photon Interactions at High Energies, Batavia, Illinois, 1979, p.92.
13. M. Cavalli-Sforza and D.G. Coyne, SIC Workshop note #34, Aug. 1981.
14. O.H. Nestor and C.Y. Huang, IEEE Trans. Nucl. Sci. NS-22, 68 (1975).
15. M. Moszinski et al., Nucl. Inst. and Meth. 188, 403 (1981).

PHOTODIODE READOUT OF BGO AND NaI(Tl)*

G. Blunar, H. Dietl, J. Dobbins, G. Eigen, E. Lorenz, F. Pauss,
W. Pimpl, H. Vogel, and P. Weissbach
Max-Planck-Institut fuer Physik, D-8000 Munich, West Germany

(Presented by Helmut Vogel)

SUMMARY

We present first results using a photodiode readout for BGO and NaI(Tl) crystals. The measurements indicate that photodiodes might replace photomultiplier tubes in electromagnetic calorimetry. Using commercial photodiodes, a noise equivalent r.m.s. error of 1-2 MeV has been observed using cosmic ray measurements at T = 20° C. Preliminary tests at T = -25° C yield significantly lower values. Limitations and possible future improvements are discussed.

INTRODUCTION

In high energy physics experiments at e⁺e⁻ colliders, compact high resolution electromagnetic (e.m.) calorimeters can be built with Bismuth Germanate (BGO), a novel scintillator of short radiation length X₀ = 1.12 cm (NaI(Tl): 2.6 cm). The energy resolution should be equal or superior to that of NaI(Tl). By now, crystals of BGO up to 18 X₀ long are grown routinely with good uniformity. Further details on BGO are discussed in Ref. 1. The high light output of BGO suggests to replace the standard photomultiplier (PM) readout by a photodiode (PD) readout. Recently large area photodiodes of acceptable quality became available commercially. Replacing PM readout of BGO and NaI by PD readout is very appealing because of

- (i) The high stability (short and long term) of PDs,
- (ii) Their large dynamic range and linearity,
- (iii) Simple routine monitoring and calibration, and
- (iv) The possibility of operating the calorimeter in magnetic fields.

A comparison of the features of PDs and PMs is given in Table 1. Additionally some optical characteristics versus wavelength are shown in Fig. 1. The

Table 1. Comparison of properties of PDs versus PMs

Item	PM	Photodiode
<quantum efficiency> ¹	12%	60%
int. amplification	yes	no
stabilized HT	yes	not necessary
typical dynamical range	10 ⁴	10 ⁸
short term stability	1 (.3) %	<.01 %
long term stability	1 (.3) %	<.1 %
temperature coeff.	<.2 % /°C	<.2 % /°C
rise time	5-50 nsec	>100 nsec (area dep.)
magn. shield	complicated, impossible for high fields	unnecessary
noise immunity	high	low
price ²	>USD 50	USD ~10
price of amplifier ²	USD 5	USD 15

¹integrated from 450-550 nm wavelength

²estimated for very large quantities

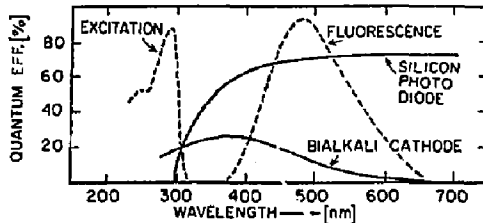


Fig. 1 Some spectral characteristics of BGO, PMs, and PDs^{2,3}

slow signal speed of PDs (<1 MHz) does not limit their use at large e⁺e⁻ colliders. The basic problem using PD readout is how to minimize the noise equivalent r.m.s. error (NES), defined by

$$NES \text{ (MeV)} = \frac{\text{r.m.s. noise (PE)}}{\text{signal (PE/MeV)}}$$

(where PE = no. of photoelectrons).

Under unoptimized conditions, PDs yield signal = 0 (500 PE/MeV) and noise = 0 (5000 PE), thus NES = 0 (10 MeV). Aiming for energy resolution of 0 (1%) at all energies >10 MeV, NES figures of 0 (.3 MeV) have to be achieved.

TESTS WITH BGO

The tests were performed with commercial PDs of the type Hamamatsu S 1337 BR 1010 (high resistivity silicon, area = 1 cm² per diode, plastic encapsulation). Figure 2 shows the basic circuit for the photodiode readout. For low noise performance the diode is reverse biased. The signal is amplified by a high quality charge sensitive preamplifier (Canberra 2003 BT) which in turn is connected to a second amplifier with a pulse shaping network for best signal/noise filtering (Ortec 472, shaping time constants 2 us or 6 us). The final unipolar output was fed into a voltage sensitive MCA.

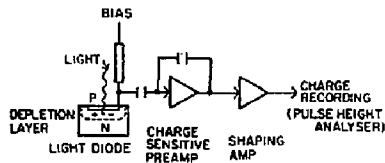


Fig. 2 Principal setup for PD readout

Three diodes were coupled to a BGO crystal with optical grease. The crystal was wrapped in white paper and made light tight. The crystal had a size of $150 \times 44 \times 20$ mm and was viewed through its smallest face, the area of which $(7\text{K}_0)^2$ is typical for calorimetry application. The external diode case dimensions were 15×15 mm², resulting in an area matching factor of 0.34. An increase of 20% of the signal was observed after painting the areas between diodes with white paint. The diodes were reverse biased up to 40 volts. Increasing the voltage decreases the diode capacitance $C_d(C \sim 1/\sqrt{U})$ until fully depleted) but increases the leakage current I_d . For optimization the PDs had to be preselected. About 50% of the PDs (normally rated for max. U_b of 5 V) had sufficiently high breakdown voltage and acceptably low I_d to balance the noise contribution of the diode capacitance C_d at $U_b = 40$ V. Cosmic ray muons were used as test particles. They deposit by ionization about 9 MeV per traversed cm of BGO. The passage of a cosmic muon was sensed by two scintillation counters mounted above and below the BGO crystal. The fast coincidence signal was used to generate a gate signal for the pulse height analyzer. Additionally a precision pulser was connected to the input of the charge sensitive preamp through a 1 pF capacitance. The pulser was used for charge calibration, linearity tests and noise evaluation. Figure 3 shows the block diagram of the test setup.

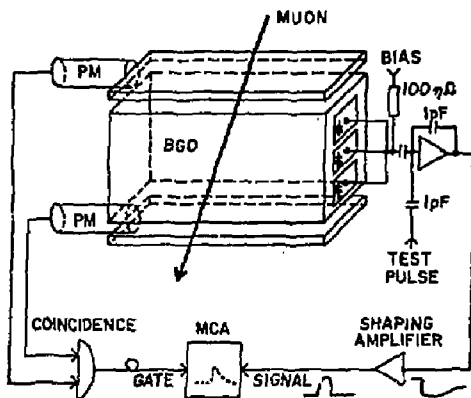


Fig. 3 Setup for PD readout used in the test

Figure 4 shows the observed pulse height distribution together with the distributions of both pedestal and calibration pulses. The width of the energy loss spectrum was measured to be 33%. Correcting for the angular acceptance of our triggering setup, the width extrapolated to perpendicular passage becomes $22 \pm 2\%$ which is consistent with results obtained in a test beam of 140 GeV pions using PM readout. The results together with that of a crystal of different dimensions are summarized in Table 2.

Remarks

- (i) Note the improvement of the noise figure with increasing shaping time constant.
- (ii) The numbers given for low temperatures are still preliminary since tests are currently under progress.

TESTS WITH NaI(Tl)

Due to the substantially higher light output of NaI(Tl) per MeV energy deposit w.r.t. BGO, the PD readout of NaI(Tl) yields satisfactory results even under non-optimized conditions. At $T = +25^\circ\text{C}$ we measured NaI(Tl) pulse height spectra for

- (i) A crystal of size $280 \times 40 \times 40$ mm³, viewed by three PDs through a plexiglass light guide with a very low area matching factor of 0.16 using cosmic rays.
- (ii) A cylindrical crystal of size $\varnothing 38 \times 38$ mm, viewed by four PDs, the space between the PDs being treated with diffuse reflector. In this case, we were able to take spectra of Co^{60} and Cs^{137} sources in a self triggering mode (see Fig. 5). The results are shown in Table 2 also.

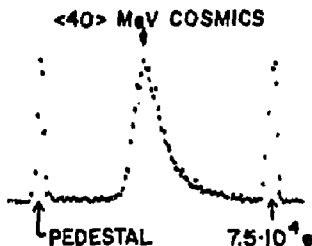


Fig. 4 Observed energy loss spectrum of cosmic muons in 44 mm of BGO, together with pedestal and calibration pulse distribution

Table 2. Summary of test results using PD readout⁵

Crystal, dimensions (mm)	Number of diodes	T (°C)	τ shaping (µsec)	AMF*	Number PE/MeV	NES (MeV)
BGO						
$150 \times 44 \times 20^1$	3	+20	2	0.34**	910	1.80
$150 \times 44 \times 20^1$	3	+20	6	0.34**	850	1.12
$200 \times 30 \times 30^1$	4	+20	6	0.44	860	1.15
$200 \times 30 \times 30^1$	4	-12	6	0.44	1430	0.60
$200 \times 30 \times 30^1$	4	-25	6	0.44	1680	0.54
NaI(Tl)						
$280 \times 40 \times 40^2$	3	+20	2	0.16	1200	1.10
NaI(Tl)						
$38 \times 38 \beta^3$	4	+20	6	0.35**	7000	0.16

¹ $U_b = 39$ V, ² $U_b = 30$ V, ³ $U_b = 25$ V

* area matching factor, ** white reflector paint between diodes

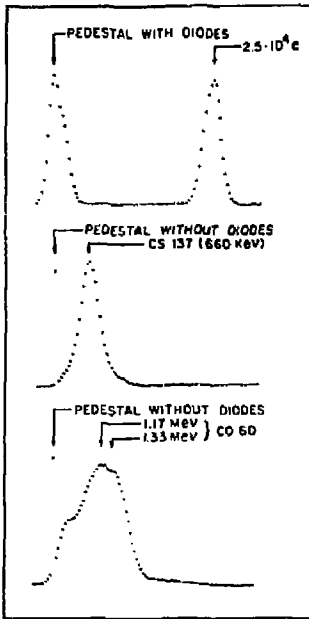


Fig. 5 Spectra obtained with a small volume crystal of NaI(Tl):
 (a) pedestal and calibration pulse distribution
 (b) spectrum of Cs(137) source
 (c) spectrum of Co(60) source

FURTHER IMPROVEMENTS AND TRADEOFFS

The aim of this study was to establish the feasibility of the photodiode readout with acceptable low noise. The main contribution to the noise comes from

- (i) shot noise of the preamplifier input FET multiplied by the diode and input parallel capacitance.
- (ii) shot noise of the diode leakage current for large bias voltages.
- (iii) noise due to leakage current of the electrical connections and diode p-n edge effects.

A typical example of the noise figure versus diode capacitance and dark current as a function of bias is shown in Fig. 6.

Modern charge sensitive preamplifiers have intrinsic typical noise values of equivalent of 300-1000 PE and slopes of 5-10 PE per pF of detector capacitance. For best NES values a low diode capacitance is always necessary. The contribution of shot

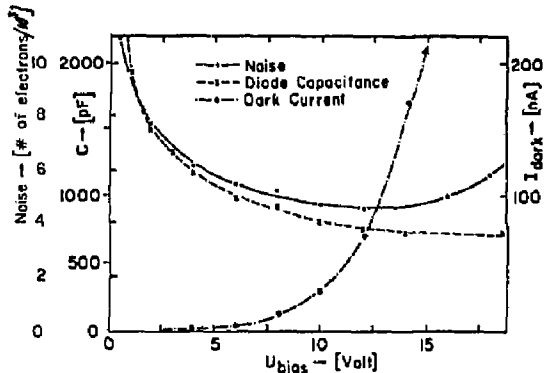


Fig. 6 NES, diode leakage current, and capacitance versus reverse bias voltage for a set of 3 parallel connected diodes of moderate quality

noise of the diode leakage current becomes only significant above ~200 nA. Diode p-n edge effects or connector leakage currents can sometimes be quite unpleasant and require the selection of adequate materials or diodes.

Compared with the described tests further improvements of the noise figure are possible:

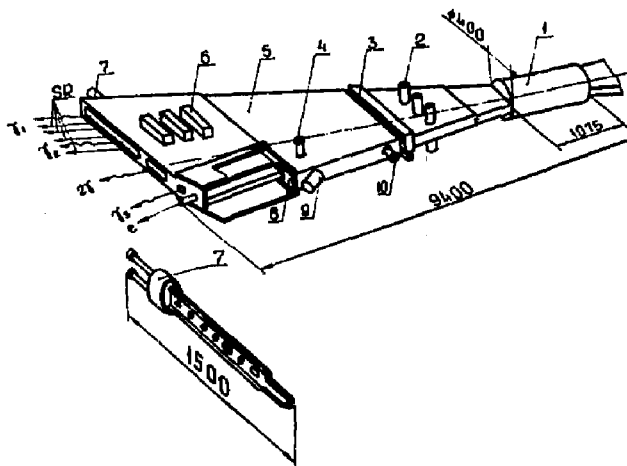
- (i) Better area matching together with preamplifiers with low noise for large diode capacitances.
- (ii) Improved optical coupling with high refractive index materials, antireflex coating or BGO surface treatment with diffuse reflectors.
- (iii) Use of photodiodes made of high resistivity Silicon and high bias voltage, i.e., low diode capacitance.
- (iv) Cooling of the BGO will result in a substantial signal increase (in first order the reduction of 40° will result in an increase of a factor 2).

The reduction of the diode capacitance can only be achieved by increasing their depletion layer. This might have an unpleasant side effect. The photodiodes act as nuclear counters and traversing charged particles will create a signal of about 100 charged pairs per micron depletion layer (minimum ionizing particles). This effect is well demonstrated in a test exposing the photodiodes to a β source. We observe a signal of ~10000 PE corresponding to an equivalent energy loss of ~12 MeV in the BGO. For critical applications the diodes have to be placed into areas of low charged particle flux.

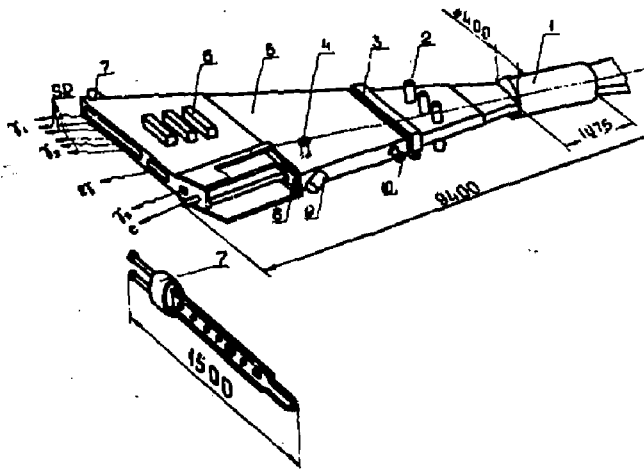
REFERENCES

1. G. Blunar et al., Bismuth germanate, a novel material for electromagnetic shower detectors. Max-Planck-Institut Munich, MPI-PAE/Exp. EL.94 (1981)
G. Blunar et al., Max-Planck-Institut Munich, A design study for a compact LEP detector, presented at the 1st LEP-HERA Seminar, Max-Planck-Institut Munich, September 2, 1980, and the 2nd Workshop for Detectors and Experiments for e^+e^- at 100 GeV, Cornell University, January 9-11, 1981; also institute report MPI-PAE/Exp. EL.99 (1981).
P. Franzini et al., A detector for CESR II, presented at the 1st Workshop for Detectors and Experiments for e^+e^- at 100 GeV, Cornell University, November 14-16, 1980, updated 3rd Workshop April 3-5, 1981; CLNS 81-515, p. 57-79.
M. Cavalli-Sforza, D. Coyne (Princeton University), A Compact Calorimeter for e^+e^- Annihilations in the 100 GeV Region, SLC Note CN-34, SLAC (Stanford), August 1981.
M. Cavalli-Sforza, these proceedings.
2. M. J. Weber, R. R. Monchamp, Journal Applied Physics 44 (1973) 5495.
3. Hamamatsu catalog: Photomultiplier Tubes 1980. Hamamatsu catalog: Silicon photocells 1981.
4. DOW CORNING optical coupling grease Q2-3067, $n = 1.4648$ ($\lambda = 589$ nm)
5. Errors on the number of photoelectrons are typically 10%. Error numbers are normally omitted as the quoted numbers are only meaningful for the above described test setup and will change significantly for different arrangements.

POLARIZATION, BACKGROUNDS, AND MAGNETS



POLARIZATION, BACKGROUNDS, AND MAGNETS



J. Buon
 Laboratoire de l'Accélérateur Linéaire
 91405 Orsay Cedex (France)

Abstract

Polarised electron and positron beams in storage rings appear still practicable in the tens of GeV energy range. Recent results at PETRA show the possibility of reducing depolarising effects of ring imperfections and the possibility of polarised beams in collision at high energy. The main limitation comes from the large beam energy spread at very high energy. 90° spin rotators for longitudinal polarisation are in progress.

Introduction

The physics interest of electron and positron beams in storage rings increases very much with energy, due to the increasing role of electroweak interactions. Polarised electron and positron beams are foreseen in both ep and e⁺e⁻ new facilities.

A natural polarisation build-up has been observed in storage rings at low energies. However it is expected that depolarisation effects become stronger and stronger as energy increases. This is due to the fact that spin rotates faster and faster than the particle velocity does.

The purpose of this report is to review the feasibility of polarised beams in electron storage rings at high energy. It is restricted to the use of "conventional" devices, which appear the simplest ones at the moment. The only polarisation mechanism studied is the Sokolov-Ternov¹ effect. One does not consider "Siberian snakes", for reducing depolarisation effects, not easy to use, although they may become necessary at very high energies.

The Sokolov-Ternov polarisation mechanism is studied in section 1 from a practical point of view. Generalities on depolarisation effects are reviewed in section 2. The possibilities of reducing these depolarising effects are studied in section 3 as well as the increase of depolarisation due to large energy spread. In section 4 information on beam-beam depolarisation is reported. Two current examples of 90° spin rotators are discussed in section 5 for obtaining longitudinal polarisation. Finally in section 6 the experimental use of longitudinal polarisation is studied for ep or e⁺e⁻ interactions.

1. Polarisation Mechanism

The Sokolov-Ternov¹ polarisation mechanism in electron storage rings has been widely observed and is still the only practicable one up to now. It is due to a small asymmetry of the synchrotron radiation: For an electron the radiation probability with spin-flip is slightly greater when the electron spin is parallel to the bending magnetic field. The population of the antiparallel spin state increases gradually with time and transverse polarisation reaches a 92.4 % maximum value in an homogeneous magnetic field. In the same way positrons are also transversally polarised parallel to the magnetic field.

The characteristic polarisation time τ_p is inversely proportional to the photon emission rate times the mean square relative photon energy ϵ/E

$$\tau_p^{-1} = \frac{9}{11} \langle N \frac{\epsilon^2}{E^2} \rangle$$

and varies rapidly with electron energy E :

$$\tau_p \text{ (sec)} = 98.66 \frac{\rho^3 \text{ (m)}}{E^5 \text{ (GeV)}} \times \frac{R}{\rho}$$

where ρ is the magnet bending radius and R the ring average radius.

Fig. 1 shows the polarisation time for high energy electron rings. Short times, less than one hour, are obtained in their upper energy range.

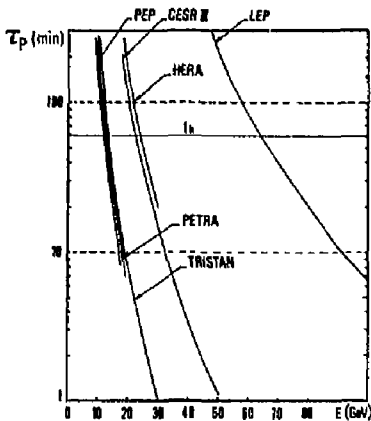


Fig. 1. Polarisation time τ_p versus beam energy E for several electron storage rings.

However for LEP phase I (50 GeV) the polarisation time (~ 3 h) is too long, and needs to be reduced. This can be achieved using an asymmetric wiggler (fig. 2) with a high field (1.25 T) central part. A polarisation time less than one hour would be obtained at the price of a ten percent increase of synchrotron energy loss, mainly concentrated downstream the wiggler, and a large increase ($\times 1.8$) of beam energy spread.

^M Work supported by the "Institut National de Physique Nucléaire et de Physique des Particules"

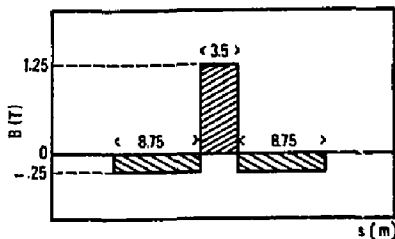


Fig. 2. The magnetic field versus the distance in an asymmetric wiggler proposed for LEP phase I.

The polarisation level will only be reduced by ten percents due to the compensating low field of the wiggler in the example given here.

One conceivable alternative² to the Sokolov-Ternov polarisation mechanism is to collide the stored electron beam with a circularly polarised photon beam. The polarisation mechanism results from the spin dependence of Compton scattering and from a spin-orbit coupling of the stored electron. The photon beam must have a very long wavelength ($> 100 \mu$) and high intensity. An adequate photon source, probably a free electron laser, may become available in future.

2. Depolarisation effects in general

Small field imperfections always reduce the effective polarisation level³ below the 92.4 % maximum value. These imperfections lead to a vertically distorted orbit, and consequently to small spin tilts from the vertical direction. These tilts depend on the particle energy and the amplitude of its betatron oscillation. Hence depolarisation results from the finite distribution in energy and betatron amplitude among the particles. Moreover jumps in energy and amplitude are steadily generated by synchrotron photon emission, and produces a spin diffusion. At the end an equilibrium between the Sokolov-Ternov effect and the spin diffusion is reached with a polarisation level given by the ratio τ_p/τ_d of their respective characteristic times.

$$P = \frac{92.4 \%}{1 + \tau_p/\tau_d}$$

A large depolarisation needs a constructive effect of successive small spin rotations. It occurs when the spin precession frequency coincides with some frequency of fields rotating the spin. The general resonant condition is given in terms of the spin tune ν by :

$$\nu = k + k_x \nu_x + k_y \nu_y + k_B \nu_B$$

²The spin tune is the spin precession number per turn :

$$\nu = \gamma \frac{g-2}{2} = \frac{E(\text{GeV})}{.44065}$$

where ν_x, ν_y, ν_B are respectively radial, vertical and synchrotron tunes, and k, k_x, k_y, k_B are any integers.

The most important depolarisation resonances due to machine imperfections are :

- i) integer resonances $\nu = k + k_B \nu_B$ including synchrotron satellites ($k_B = \pm 1, \pm 2, \dots$)
- ii) betatron resonances $\nu = kS \pm \nu_{x,y}$ where S is the ring superperiodicity. They are driven by betatron oscillations around closed orbit.

At high energies, the most important imperfections are the radial field errors due to magnet tilts and vertical misalignments of quadrupoles.

3. Depolarisation resonances of a single beam

The integer resonances $\nu = k$ are dangerous as they are ordinarily strong and separated only by 440 MeV in energy. Their depolarisation effect scales roughly like the square of the particle energy. For example corresponding to a 25 % polarisation at 15 GeV, observed at PETRA, one can only expect about 5 % polarisation at 50 GeV, for CESR II and LEP, assuming similar orbit distortions.

These resonances cannot be sufficiently reduced even with a very careful alignment of the magnetic elements. However the harmonic components of the orbit distortion which drive these resonances can be cancelled out. Such an harmonic correction procedure needs only a special programming of the correcting coils already used for reducing the average orbit distortion. A first recent attempt⁴ of harmonic correction at PETRA has been successful. The polarisation has been increased from 20 % up to 80 % at 15 GeV. Quite similarly a complete cancellation of some integer resonances has been recently achieved⁵ in the proton synchrotron SATURNE. These resonances can be crossed during the acceleration cycle without any appreciable loss of polarisation.

Betatron resonances are also very dangerous. However in rings with superperiodicity S larger than one, the strongest betatron resonances can be made more spaced than the integer ones. The maximum separation between these betatron resonances is equal to the superperiodicity S in units of the spin tune. It is obtained by choosing the betatron tunes ν_x, ν_y with an integral part being a multiple of $S/2$. Therefore the depolarisation effect of betatron oscillations is strongly reduced at energies midway between two successive betatron resonances.

At low energies ($< 25 \text{ GeV}$), considering again the integer resonances, their synchrotron satellites $\nu = k + k_B \nu_B$ are weak, except the first one ($k_B = \pm 1$), as the beam energy spread is small compared to the resonance spacing (440 MeV). The preceding conclusions on integer resonances are not affected, as ν_B is normally small ($< .1$).

However energy spread increases with energy (fig. 3). Consequently synchrotron satellites become stronger and stronger. Unavoidably spin tune is always in the vicinity of these satellites and the depolarisation due to closed orbit distortion increases.

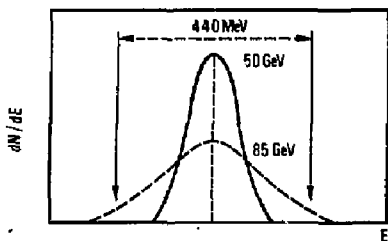


Fig. 3. Energy distribution of a stored beam in LEP at 50 GeV and at 85 GeV.

This phenomenon can be understood as follows. The synchrotron oscillation of energy leads to a frequency modulation of spin precession:

$$\nu = \nu_0 + a \cos \nu_0 \theta$$

where a is the modulation amplitude, proportional to the energy spread σ_E/E , and θ is the azimuth giving the particle location in time. The spin precession can be looked at as a gyroscope modulated in frequency. Its phase angle is given by:

$$\psi = \int \nu d\theta = \nu_0 \theta + \frac{a}{\nu_s} \sin \nu_0 \theta$$

The frequency spectrum of such a gyroscope is a set of satellite lines:

$$\nu + k \frac{\nu_s}{\nu_0}$$

The amplitude of these lines is governed by the modulation index $I = a/\nu_s$, which is in average proportional to the energy spread:

$$I = \frac{\sigma_E}{E} \cdot \frac{\nu}{\nu_s}$$

Above 30 GeV the modulation index becomes generally large ($\gg 1$) and several satellites are strongly excited.

At the moment a preliminary study⁶ indicates that appreciable polarisation could only be achieved up to about 50 GeV, depending of how much the strength of the integer resonances can be reduced by harmonic correction.

The only proposed alternative is to use double siberian snakes⁷ which make the spin tune equal to $1/2$, independently of energy variations. However they greatly complicate the ring design and could affect its performances.

4. Beam-beam depolarisation

The spin motion is perturbed by the space charge field of an opposite beam as well as the particle trajectory. Depolarisation resonances will be excited by this perturbation. A theoretical approach is difficult due to the non-linearity of the space charge field.

Experimentally 70% polarisation has been observed at SPEAR with e^+e^- colliding beams at 7.4 GeV centre of mass energy. This polarisation has been used in a well-known experiment⁸, which has played an important role in the progress of understanding high energy interactions. However polarisation in colliding mode could not be observed again at a later stage of SPEAR operation.

Very recently at PETRA again⁴ polarisation has been observed with two colliding beams. A polarisation level of 80% for the electron beam has been measured at a luminosity of $2.7 \times 10^{30} \text{ cm}^{-2}$ and at 16.5 GeV energy per beam.

Polarisation in collision mode has to be more investigated in order to find good operating conditions for experiments.

5. Longitudinal polarisation

Assuming that transversally polarised beams can be obtained in an electron ring, one has still to rotate the spin by 90° in order to obtain longitudinal polarisation at some interaction points.

Several types of 90° spin rotators have been proposed in the past. However they were never really optimized in what concerns beam optics and polarisation. Only recently, one has begun to study this optimisation in particular for the ep rings HERA and for the e^+e^- ring CESR II.

In the case of CESR II an "S-bend rotator" is studied⁹. It consists (fig.4) of vertical bends antisymmetric with respect to the interaction point. At this point the reference orbit is bent by an angle (14 mrad at 50 GeV) which corresponds to 90° rotation for the spin. At other energies it is necessary to maintain the same orbit geometry for beam optical properties and for synchrotron background. Therefore the fields in vertical bends are ramped in energy as the fields in the horizontal magnets. Consequently the spin rotation is not exactly 90° . However the longitudinal component is only reduced by less than 10% in a large energy range: $\pm 30\%$.

The antisymmetry of the S-bend rotator allows to restore the vertical spin direction in the rest of the ring. It avoids depolarisation that a tilted spin direction in the major part of the ring would produce, as discussed in section 2. This is true at any energy and allows the S-bend spin rotator to be operated in a large energy range, as desirable for e^+e^- physics.

In the case of HERA a pair of 90° spin rotators has been considered¹⁰ for each interaction region. These two rotators are symmetrically located with respect to the interaction point, between the arcs and the RF sections, at more than 100 m from the interaction point.

Each rotator is a "mixed rotator" including vertical bends and an horizontal bend (fig. 5). At the designed energy each vertical bend rotates the spin by 45° . The horizontal bend, which is part of the normal radial bending in the ring, rotates the spin by 180° . At the end of each rotator the orbit is again in the plane of the ring.

The corresponding vertical bends in the two rotators of an interaction region are opposite. Therefore each pair of rotators is antisymmetric in the vertical plane with respect to the interaction point. However the corresponding horizontal bends are identical as they both participate to the normal radial bending. Each pair of rotators is symmetric in the horizontal plane.

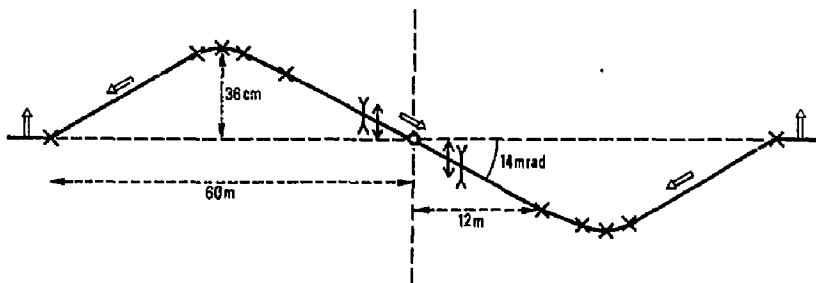


Fig. 4. schematic side view of an "S-bend rotator" proposed for the CESR II e^+e^- ring.

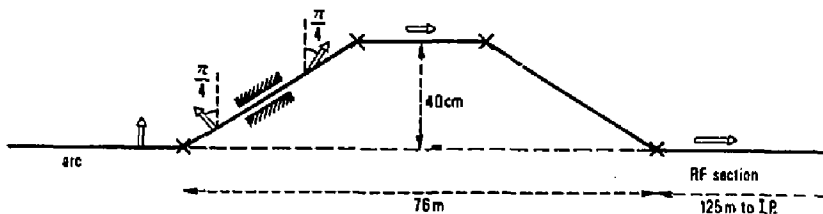


Fig. 5. Schematic side view of a "mixed rotator" proposed for the HERA electron ring.

The magnetic field in these horizontally bending magnets must be ramped in energy as normal magnets in the arcs. The 180° spin rotation is only obtained at the designed energy (27.5 GeV for HERA). What is more, the vertical spin direction in the arcs of the ring is only restored at this designed energy. This tilt of spin direction at off-energy set can be corrected¹¹, but only in a small energy range ($\pm 3\%$).

This small energy range is the main difference of the "mixed rotator" with the "S-bend rotator". The mixed rotator can be sufficient for an ep facility as the electron ring energy, much smaller than the proton ring energy, does not need to be varied.

One must also mention that both types of rotators slightly increase the synchrotron energy loss and the vertical beam emittance, but only by a few percent.

Finally one must also minimize new depolarising effects introduced by the rotators.

Firstly the Sokolov-Ternov polarising effect is slightly reduced in the rotator bends as the spin direction is no more parallel to the magnetic field. Normally this reduction of the maximum degree of polarisation is small (a few percent) for not too strong magnetic fields.

Secondly, and what is more, the rotator vertical bends, acting as field errors do, excite depolarisation resonances, in particular the betatron ones. For example the radial betatron resonances are excited due to the longitudinal spin direction in the interaction region. A particle undergoing a radial betatron oscilla-

tion experiences a vertical field in the quadrupoles of the interaction region. This field will rotate the spin which is longitudinal by an angle depending on the betatron amplitude. Consequently radial betatron resonances are strongly enhanced.

However, contrary to the usual field errors, the rotator vertical bends are "known errors", and can be corrected. For example one can manage that the spin rotations, due to radial oscillations in the interaction region, cancel out exactly. This can be obtained by a proper phase advance of these oscillations in the interaction region¹². One can find similar conditions¹³ for other depolarisation resonances excited by the rotator bends.

Any ring lattice, including spin rotators, must be designed in order to satisfy these conditions. This operation is called¹⁴ "spin matching". One must realize that introducing rotators in a ring after completion will need a modification of the lattice in order to satisfy "spin matching". This modification may be difficult and expensive.

6. Experimental use of longitudinal polarisation

In an electron ring of an ep facility one would like to accelerate electrons and positrons. They can be obtained longitudinally polarised in the same way. One would like also to have both helicities for each of them. Both helicities can only be easily obtained by reversing the fields of the vertically bending magnets.

For an electron-positron ring the cross-section of e^+e^- annihilation is¹⁵

$$d\sigma = (1 - P_e^+ P_e^-) d\sigma_{\text{unpol}} + (P_e^+ - P_e^-) d\sigma_p$$

according to the standard model of electroweak interactions. (P_e^+ , P_e^- are the longitudinal polarisation of positrons and electrons respectively).

Compared to the cross-section $d\sigma_{\text{unpol}}$ with unpolarised beams, a new information, contained in the cross-section $d\sigma_p$, is obtained with polarised beams.

Even striking spin effects are expected: the annihilation rate would vanish for 100% polarised beams of same helicity. However this effect is reduced for partially polarised beams.

On the contrary the rate would be increased for opposite electron and positron helicities, but this cannot be easily achieved.

In fact it is much more important and more interesting to build a longitudinal polarisation asymmetry.¹⁶ Assuming two bunches of electrons (and also of positrons), it can be easily obtained by depolarising selectively one of the two electron bunches (and also one of the two positron bunches). At every interaction point one will observe alternatively (fig. 6) collisions of polarised electrons with unpolarised positrons, and collisions of polarised positrons with unpolarised electrons.

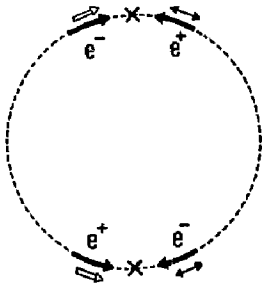


Fig. 6. Collisions of two electron bunches with two positron bunches. For each beam one bunch is longitudinally polarised, and the other bunch is unpolarised.

The obtained longitudinal polarisation asymmetry is linear in the beam polarisation P_p :

$$A = \frac{N(e^- \uparrow) - N(e^+ \uparrow)}{N(e^- \uparrow) + N(e^+ \uparrow)} = P_p \frac{d\sigma_p}{d\sigma_{\text{unpol}}}$$

and picks-up the parity violating contributions to the cross-section. This asymmetry measurement has the great advantage to cancel out most of systematic errors.

Conclusion

The Sokolov-Ternov polarisation mechanism allows to obtain short polarisation times in upper energy range of electron rings. However an asymmetric wiggler is needed for LEP at 50 GeV.

Large transverse polarisation has been easily observed in low energy rings. However depolarising effects increase with the energy. At high energies it becomes necessary to choose carefully the energy and the betatron tunes for avoiding the main depolarisation resonances. It becomes also necessary to correct imperfec-

tions in a similar way to the usual orbit correction. A recent experiment on PETRA at 15 GeV shows that efficient correction procedures exist.

The possibility of transverse polarisation in presence of beam-beam interaction at high luminosity has been investigated at SPEAR (2×3.7 GeV) and now at PETRA (2×16.5 GeV). The results are encouraging.

However at very high energies polarisation is questionable due to the increase of energy spread which becomes comparable to the depolarisation resonance spacing. The limit in energy for polarisation is not yet known. It will depend on the efficiency of correction procedures.

The design of 90° spin rotators is presently studied for new electron rings. The conditions for efficient spin rotation have been found. They must be included in the lattice design.

The conventional ways to obtain polarised electron beams, studied here, are still practicable in the tens of GeV energy range. However one must be more and more clever as the energy increases.

References

1. I.M. Ternov, Yu.M. Loskucev and L.I. Korovina, Sov. Phys. - JETP, **14**, 921 (1962)
2. A.A. Sokolov and I.M. Ternov, Sov. Phys. - Dokl **8**, 1203 (1964)
3. Ya. S. Derbenev, A.M. Kondratenko and E.L. Saldin, Novosibirsk preprint 78-64 (1978)
4. V.N. Baier and Yu.F. Orlov, Sov. Phys. - Dokl **10**, 1145 (1966)
5. R. Rossmannith, private communication
6. J. Arvieux, Internal Report LNS 059-81, Saclay (1981)
7. C. Biscari and J. Buon, Int. Rep. NI/40-81, LAL Orsay (1981)
8. Ya.S. Derbenev and A.M. Kondratenko, Novosibirsk preprint 76-84 (1976)
9. Ya.S. Derbenev and A.M. Kondratenko, Proc. AIP Conf. on HEP with polarized beams and polarized targets, Argonne (1978), (AIP conf. Proc. n°51) p292
10. C. Hanson et al., PRL **35**, 1609 (1975) and R.F. Schwitters, SLAC-PUB 2258 and IIIrd Int. Symp. on H.E.P. with Polarized Beams and Polarized Targets, Argonne (1976)
11. K. Steffen, Internal Report CBN 81-30, Cornell (1981)
12. K. Steffen, Int. Rep. HERA 80/08, DESY (1980) and HERA proposal, HERA 81/10, DESY (1981)
13. J. Buon, Int. Rep. NI/35-81, LAL Orsay (1981)
14. J. Buon, Int. Rep. NI/07-81, LAL Orsay (1981)
15. A.W. Chao and K. Yokoya, Int. Report. KEK 81-7 (1981)
16. K. Steffen, Int. Rep. HERA 82/02, DESY (1982)
17. D. Silvers, Proc. of the 1980 Int. Symp. on HEP with Polarized Beams and Polarized Targets, p82 (1980)
18. C.Y. Prescott, Proc. of the 1980 Int. Symp. on HEP with Polarized Beams and Polarized Targets, p 34 (1980).

LONGITUDINALLY POLARIZED COLLIDING BEAMS

A. N. Skriasky

Institute of Nuclear Physics, 630090, Novosibirsk, USSR

The feasibility of experiments with the polarized colliding beams expands significantly possibilities of getting information on fundamental interactions. Even the use of the transversely polarized beams enables getting the more reliable and clear definition of spins for the intermediate states and final particles,^{1,2} as well as to introduce the precise absolute energy scale.³⁻⁵ But only the use of the longitudinally polarized colliding beams with particles of certain helicities, enables one to get basically new information. This circumstance forced us, in Novosibirsk, commencing from 1969, to develop the principles and structures of the storage rings which provide at a given azimuth the stability of any spin direction needed, including longitudinal direction^{6,7} (see also Refs. 8 and 9).

1. In the storage ring of "conventional" type which magnetic field along the equilibrium closed orbit has a constant, for example, vertical z-direction (the field sign can vary) the spin orientation conserved from turn to turn is z-direction. In other words, when particles are moving along the equilibrium orbit their spins precess around this direction and the spin projection on this direction is constant. For example, if initially the particle spin has z-projection $+\frac{1}{2}$, this value does not change with time (of course, unless either dissipative or diffusional processes will affect). The projection $-\frac{1}{2}$ will be conserved just the same way. This statement is valid if the precession frequency (because of anomalous part of a particle magnetic moment) is not resonant to the frequency of orbital rotation along the equilibrium orbit.

The similar situation became valid also for the case of the storage ring with arbitrary oriented magnetic fields.^{6,7} Namely, along any closed orbit there always is such a unit vector $\vec{n}_0(\theta)$, the projection on which of the spins of particles moving along this orbit has a constant value. In particular, if the particle spin is oriented along $\vec{n}_0(\theta_0)$ at some

initial azimuth θ_0 , this spin will be oriented along (different in direction) $\vec{n}_0(\theta)$ at any other azimuth θ at any turn.

Selecting the shape of closed orbit which curve at any azimuth unambiguously determine the transverse magnetic field value for this azimuth and (or) introducing the azimuthal distribution of the longitudinal magnetic field one can achieve the required orientation \vec{n}_0 for the necessary azimuth; this orientation is the same at the sections with zeroth magnetic field on the closed orbit. In particular, one can achieve the longitudinal orientation \vec{n}_0 at the storage ring sections where colliding beam interactions are occurred. In this case, if the means are made polarized one can obtain interaction of particles with certain helicities. Varying the polarization sign for one or both beams one can consequently vary helicities of interacting particles.

Let us note that for studying, for example, the interactions which do not conserve the spacial parity, in principle, it is enough to have even one of interacting beams polarized (with the controllable level of polarization). Though, of course, experiments can be performed with better purity if there is a possibility to control the polarization in its sign and level for both beams.

2. Having in mind the possibility to achieve the desired behavior of the spin along the equilibrium orbit the first question is to find the spin motion while the particle motion deviates from the equilibrium one, i.e. in the presence of energy and betatron oscillations in the beam. This problem is "dynamic" part of the general question of conservation of the beam polarization level in a storage ring.

The particle motion with deviation of their orbital motion $\vec{R}(t)$, determined by initial conditions, from the equilibrium motion described by $\vec{R}_0[\theta(t)]$ can be presented by

$$\vec{r}[\theta(t), t] = \vec{R}(t) - \vec{R}_0[\theta(t)] ;$$

similarly, the particle momentum deviation $\vec{p}(t)$ from the equilibrium $\vec{p}_0[\theta(t)]$ can be written down as

$$\vec{p}[\theta(t), \tau] = \vec{p}(t) - \vec{p}_0[\theta(t)]$$

The total spin motion can be described as a precession around the unit vector $\vec{n}(\theta, \vec{\tau}, \vec{p})$ with the conserving in time of spin projection value onto this vector.¹⁰⁻¹²

The variation of \vec{n} at small deviations of $\vec{\tau}$ and \vec{p} is large in the vicinity of the precession frequency resonances with the combined frequencies of orbital motion (spin resonances) and decreases with the shifting from these resonances.

For the stationary energy deviations in the absence of betatron oscillations this follows directly from the general statement for closed orbits. In the case of betatron and energy oscillations the vector $\vec{n}(\theta, \vec{\tau}, \vec{p})$ can be determined with the steep transition from the equilibrium motion to the given one. This can be done, for example, by introducing the condition that the spin oriented along $\vec{n}(\theta, \vec{\tau}, \vec{p})$ at some moment of time will tend to some vector when in a certain number of turns the values $\vec{\tau}$ and \vec{p} at the same azimuth θ will be close to initial ones.

All mentioned above can be presented in terms of formulae. Let us consider a particle with the charge e , mass m , spin s and magnetic momentum μ . The vector $\vec{\mu}$ is related to \vec{S} by the equation

$$\vec{\mu} = g\vec{S}$$

where $g = g_0 + g_A$ is the particle gyromagnetic ratio, g_A is its anomalous part ($g_0 = e/mc$).

Then, at every given moment t the spin precession is described by the equation:¹³

$$\frac{d\vec{S}}{dt} = \vec{W} \times \vec{S}$$

where for the particle, moving in magnetic field with the component \vec{H}_1 transverse to the particle velocity \vec{v} and longitudinal component \vec{H}_v , the value \vec{W} at the particle location point will be equal to

$$\vec{W} = - \left(\frac{E_0}{Y} + g_A \right) \vec{H}_1 - \frac{g}{Y} \vec{H}_v$$

For motion along the closed orbit $\vec{W} = \vec{W}_0(\theta)$. In this case, $\vec{n}_0(\theta)$ is determined as a periodical solution (eigenvector) of the equation

$$\frac{d\vec{n}_0(\theta)}{d\theta} = \frac{\vec{W}_0(\theta) \times \vec{n}_0(\theta)}{\omega_0}$$

For this closed orbit the precession frequency will be the eigenvalue of the spin rotation matrix for one turn.

The slowly varying energy deviations ϵ will lead to "shaking" of \vec{n} which depend on ϵ (appearance of the "spin chromaticity"); $\vec{n}(\epsilon, \theta)$ can be found out similarly to the previous with an account of total dependence of \vec{W} on ϵ including the field variations on the deviated orbit corresponding to ϵ . This can be done according to the perturbation theory if one takes

$$\vec{W}(\epsilon, \theta) = \vec{W}_0(\theta) + \vec{w}(\epsilon, \theta), \quad \omega = \omega_0 + \Delta\omega(\epsilon)$$

Similarly, with the presence of betatron oscillations the deviations of field (on the particle orbit) from their values on the equilibrium orbit can be described by introducing the perturbation \vec{w} , which depends on the phase and amplitude of betatron oscillations with an account of the dependence on the same variables in $\Delta\omega$. The calculations of such a kind confirm that already said: deviations of the spin precession axis from the equilibrium (closed) spin trajectory $\vec{n}_0(\theta)$ rise with the particle precession frequency nearing the integral number combinations of the orbital motion frequencies. One should also take into account that even for the equilibrium orbit of the precession frequency is far from resonances, for particles deflected from the equilibrium motion such resonances can occur.

3. The behavior of the averaged polarization of the beam particles injected into a storage ring being initially polarized along $\vec{n}_0(\theta)$, will strongly depend on the certain situation. If the storage ring has neither orbital nor spin damping and diffusions, the established polarization level can be found out by the appropriate averaging over the phase volume of the coasting beam. If there are damping and diffusion, one should make the comparison between the resulting diffusion spin rate and the spin damping rate. In this case, the initially injected beam can be polarized. If the spin damping is low or there is no damping at all, one can find out the decrement of the beam polarization level with time affected by the spin diffusion.

The spin damping in a storage ring (with no loss in the beam intensity) can be done sufficiently effective but still only for

electrons and positrons by using the spin effects at e^{\pm} radiation in the external electromagnetic fields.^{12,14} The spin diffusion can occur either as a direct result of the spin overturns during interactions between particles and quanta and other particles, or as a consequence of orbital diffusion in a beam under influence of various factors. As a rule, the strongest (needed most care to overcome its influence) is the diffusion of a second type where the spin and orbital motions are closely interrelated. In this case, the orbital diffusion causes the corresponding trembling of precession axis^{15,16} leading with time to lowering the beam polarization level.

The orbital diffusion depending on its nature can variously affect the spin diffusion rate. The orbital diffusion can occur by jumps due to quantized losses on synchrotron radiation or scattering. The combined action of such jumps and the orbital friction form the equilibrium orbital beam characteristics and simultaneously determine the spin diffusion rate which is the higher the stronger are deviation of \vec{n} from \vec{n}_0 within the equilibrium beam emittance, and the deviations are the larger the closer and stronger are the spin resonances. In this case, as a rule, the spin resonances proceed rapidly and nonadiabatically.

With a weak orbital diffusion, caused by the stochastization of orbital motion with the combined action of many orbital resonances, the spin resonances can proceed slowly, with the total but reversible spin overturn while intersecting, and the spin diffusion resulting rate should be evaluated more specifically.

A special case for obtaining polarized beams in a storage ring is the "knock-out" of particles mainly with undesired polarization from the initial nonpolarized beam. The polarization resulting level is determined by the relation of the particle loss probability for particles with desired and undesired polarity and of the agreeable intensity loss, and also by the spin diffusion resulting rate.

As the examples should serve the proposals to obtain on storage rings the e^{\pm} beams by "knocking-out" due to the inverse Compton effect with longitudinally polarized photons in the section with longitudinal \vec{n}_0 and¹⁹ \vec{p}

beams polarization using the difference of the total cross sections of nuclear interaction for opposite orientations of spin \vec{p} at interaction with the superfine polarized target;^{20,21} in this case, it is more profitable to use the storage ring section with stable longitudinal \vec{p} polarization and similarly polarized p of the atomic hydrogen beam.

4. With an account of all mentioned above let us consider some versions of longitudinally polarized electron-positron colliding beams.

First, let us assume that in the storage ring under consideration (until it has no special insertion for getting the longitudinal polarization) the equilibrium level of radiative polarization is sufficiently high and the equilibrium polarization direction is vertical. Now let us install into one of straight sections the insertion (Fig. 1) incorporated such sections with radial magnetic field which enable the vertical polarization in the ring part to transform at the collision point into the longitudinal polarization. If the H_x distribution in the section is antisymmetric with respect to collision point, the equilibrium orbit outer of the insertion will be restored. If, in this case, there is no lenses through the whole section with the H_x fields introduced, \vec{n} in the main part of circumference will not also be disturbed.

As a rule, though at the collision section (a,b) the arrangement of a small β -function is needed. To this end it is required to install quadrupole lenses on this section. In this case, for preservation of \vec{n} perturbation on the main part of a storage ring, it is necessary to have zeroth vertical dispersion on the main part of storage ring even after introducing the special section and the particles vertically polarized at the section input should be similarly polarized at the output even in the presence of energy deviations and betatron oscillations. This corresponds to satisfying some conditions:

$$\psi_z(0) = \psi_z(L) = 0;$$

$$f_x'(a) = f_x'(b) - (2 \text{ conditions})$$

Satisfying these conditions will provide the spin diffusion conservation on the main part of circumference at the same level as before introducing the special section. An additional

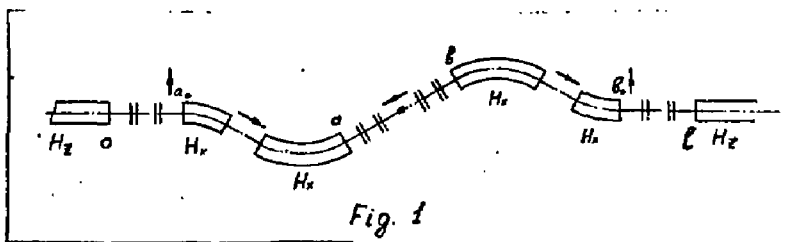


Fig. 1.

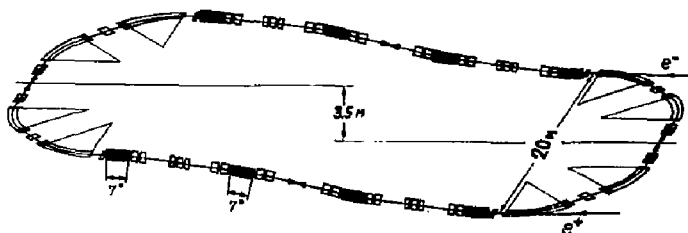
diffusion introduced by radiation in the section itself is small and it is only connected with radiation processes in the field H_x ; consequently, the H_x fields should not be excessively high compared to the storage ring fields. The contribution of the section into the spin friction is zero in the case.

The schemes of the type considered seem to be promising for producing longitudinally polarized beams in storage rings at an energy above 10 GeV. The H_x field required do not vary with an energy increase (for the electron spin rotation from the vertical to longitudinal direction it is needed $H_x \ell = 26 \text{ kGs} \cdot \text{m}$) and the orbit vertical distortions decrease inversely proportional to energy.

5. For producing longitudinally polarized beams at an energy range $\sqrt{s} = 1.5 \rightarrow 5 \text{ GeV}$ with

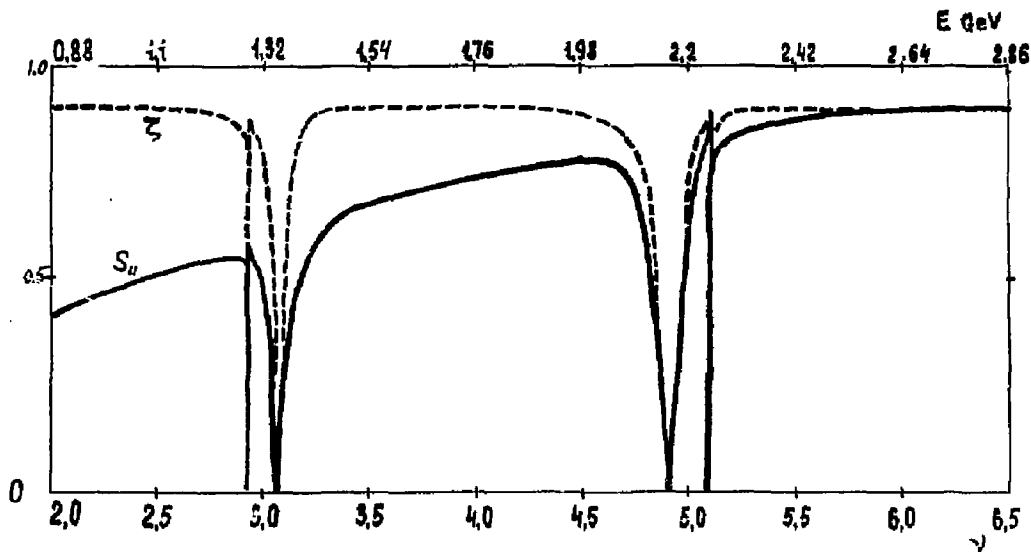
an acceptable way a special structure of the "two-level" storage ring (Fig. 2) has been developed. The structure of sections for transition between H_z -magnets located at different levels should satisfy the conditions similar to those given in point 4. The scheme given in Fig. 2 was adopted as an optimum for obtaining simultaneously the high level of equilibrium longitudinal polarization and high luminosity. The polarization level as a function of energy at a certain given geometry is given in Fig. 3.

6. At moderate energies the schemes look quite attractive where for equilibrium polarization control the sections with longitudinal magnetic field are used (the required $H_V = 100 E_{\text{GeV}} \text{ kGs} \cdot \text{m}$ are reasonable to be obtained with the superconductive solenoids). Two



Layout of the e^+e^- storage ring with two inclined straight sections for experiments using longitudinally polarized beams in the energy range from $2\alpha 0.7$ up to $2\alpha 0.5 \text{ GeV}$.

Fig. 2.



Polarization vs. energy.

Fig. 3.

schemes of such a kind are quantitatively considered for the VEPP-4 storage ring.²²

The first scheme designed for producing longitudinal polarization in the region of the resonances is given in Fig. 4. Radiative polarization in the field of the main storage ring is used. Its rate might be made higher using the H^3 -snakes. In the beginning of the experimental section the vertical polarization is transformed into the radial one with longitudinal magnetic field and subsequent vertical fields complete the spin rotation to the longitudinal direction. Upon passing the collision point all the actions with spin are performed in the opposite order resulting in that the spin (more precisely - magnetic moment) of the equilibrium particle turns out to be oriented along the storage ring magnetic field. As a final bending magnetic field in the collision point region one can use the magnetic spectrometer MD-1 (Fig. 4) field.

Let us note two moments.

The sections with longitudinal magnetic field couple the orbital x - and z -motions. In order to avoid this parasitic effect both at

the main part of storage ring and collision point the solenoids should be combined with the skew-quadrupoles.²²

The finally bending magnets should not be too large in order to prevent radiation fluctuations in them (at these sections the spin chromaticity is large) not too much enlarged the spin diffusion and hence not to decrease the equilibrium polarization level. Figure 5 represents the equilibrium polarization degree ζ as a function of energy for one of versions of the experimental section structure.

7. Completely different version turned out to be promising for producing longitudinal polarization on VEPP-4 at low energies down to 2 GeV. The spin diffusion due to synchrotron radiation in this case is rather weak and particle polarization can be achieved due to initial radiative polarization in a booster storage ring VEPP-3 which radius is smaller and therefore polarization time at an energy 2 GeV turns out to be of the order of half an hour.

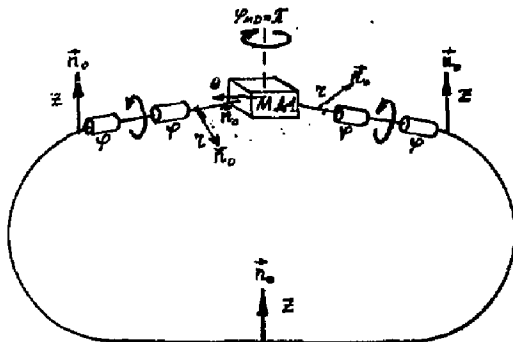


Fig. 4.

The longitudinality of the equilibrium polarization of beams at the collision point is achieved due to the section with the longitudinal magnetic field rotating the spin at an angle π around the velocity direction and occurred exactly in half a turn (along the phase of orbital and correspondingly spin motion).²³ The storage ring structure and behavior of the spin closed trajectory is shown in Fig. 6. The main contribution into depolarization rate is put by the storage ring bending section where \vec{n}_0 lies in the orbit plane and the energy jumps because of quantization of synchrotron radiation make the maximum contribution into the spin diffusion. The depolarization rate behavior as a function of energy is given in Fig. 7.²³

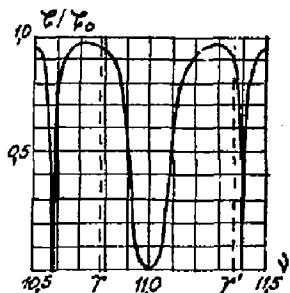


Fig. 5.

Let us note that in the case under consideration the spin precession frequency is equal to 1/2 for all energies and it is suf-

ficient to achieve the absence of resonance effects at any energy.

The spin of injecting particles should be directed along \vec{n}_0 at the injection point; orientation adjustment of the injecting particle spin is accomplished with placing the solenoids at the appropriate sections of injection channels of VEPP-3 - VEPP-4.

8. In the experiments with the proton and antiproton colliding beams at high energies it is impossible (yet) to use any kind of polarization method during the experimental run; particles should be injected already polarized. The optimal method for producing the intense proton (deuteron) beams is their charge exchange stacking with the use of H^- beams with polarized protons, and for producing polarized antiprotons one should apparently use the "knock-out" method (see point 3).

The maintenance of p^\pm beam polarization while their acceleration in the storage ring during the experimental run is the problem which is ever complicated with an energy growth. At energies above tens of GeV one should use the pairs of π -snakes²⁴ rotating the spins around various axes (longitudinal and radial). The π -snakes, however, are also needed for e^\pm storage rings at energies of a few tens of GeV and higher (π -snakes = "Siberian snakes").

The use of special sections performing longitudinal orientation of \vec{n}_0 at the collision sections with fulfillment of conditions similar to those given in point 4 does not make in practice additional spin diffusion.

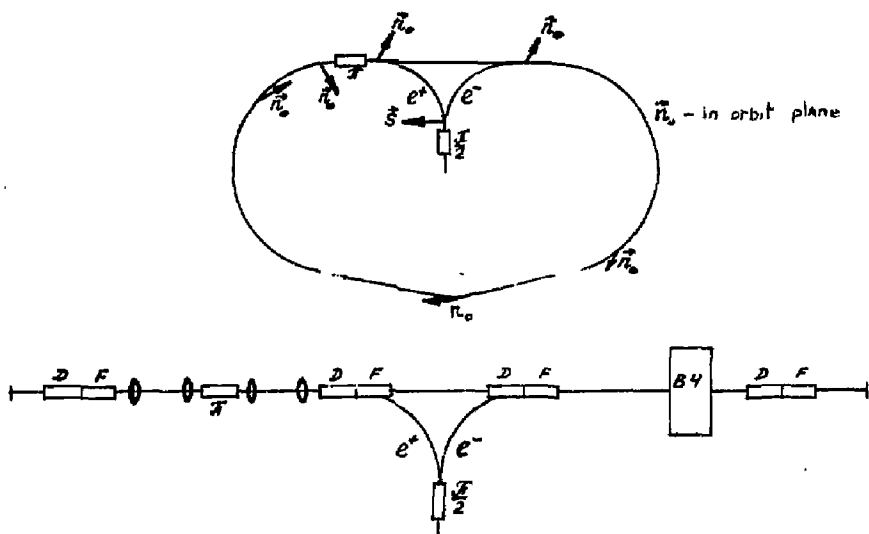


Fig. 6.

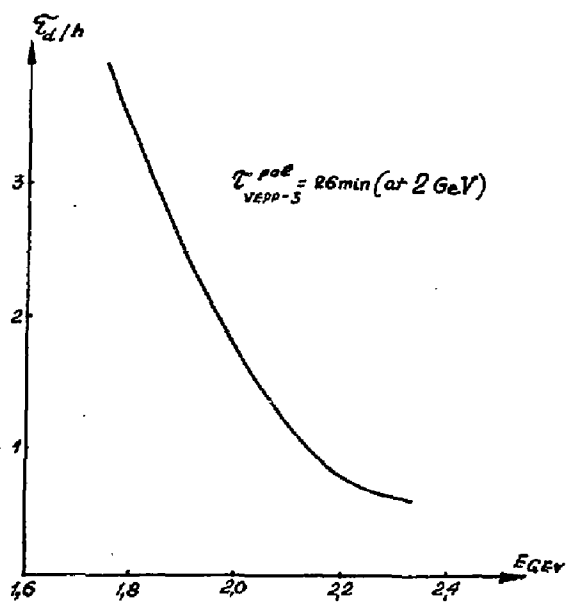


Fig. 7.

There are no questions new in principle with respect to those already considered while planning ep experiments with longitudinally polarized colliding beams.

9. In the experiments with longitudinally polarized colliding beams it is of great importance to provide the control of helicities for interacting particles. At high energies the initial particle helicities make a dramatic effect on the cross sections of fundamental processes.

So, the electromagnetic process cross sections (proceeding through the single photon channel) depend on the relative helicity of e^+ : with equal helicities (the total spin is equal to zero) this channel is completely closed and the processes of $e^+e^- + \mu^+\mu^-$ kind proceed only due to diagrams of higher orders which make the total cross section of the process sharply decreased. But namely this circumstance enables one to hope for studying the higher orders of QED and possibly definition of contributions from other interactions.

At weak interactions proceeding via Z^0 , W^\pm bosons the absolute helicities of colliding particles become also essential. So, the reaction $e^+e^- \rightarrow Z^0$ will only proceed with left helicity of e^- and right helicity of e^+ . In other variants this process should be profoundly suppressed and then some other interactions will become noticeable. The similar effects are also characteristic for other fundamental interactions q^+q^+ , e^+q^+ , which will dominate in the experiments with $p\bar{p}$, pp , e^+p colliding beams.

There could be some various ways for the control of helicities of interacting particles. If there is no polarizing mechanism just in the experiment, the beam polarization is established by injection of initially polarized particles. For the experiments of not too high accuracy, as was mentioned above, it is enough to have only one beam polarized. The effects connected with helicities can naturally be found out with variation of polarization sign of initially injected particles and the comparison of interactions of the polarized and unpolarized beams. The fine and weak effects can be detected while varying the particle polarities due to spin overturn with slow adiabatic pass through the spin resonance with

external RF electromagnetic field (with no perturbation of the orbital motion). This process has been realized at VEPP-2M without any substantial decrease in the polarization level.

The independent effect (on sign and level) on polarization of particles circulating in the same storage ring can be produced due to relevant time modulation of RF field and the use of fields propagating with the velocity of light towards the particles to be affected.

For e^+ storage ring under conditions when radiative polarization is dominant, the equilibrium polarization is always such that the sum of spins e^+ and e^- equal to zero; correspondingly the particle helicities are equal at the interaction section with longitudinal polarization. For studying interactions as functions of helicities one has to use the "comparison mode" with forced depolarization of one of the beams. Greater possibilities for independent control of helicities provide the use of a two-track storage ring (of the "old" DORIS type). An example of the interaction section scheme providing the production of e^+ and e^- with opposite helicities is given in Fig. 8.

With e^\pm storage rings at high energies it is especially promising to use radiative polarization in HF laser fields propagating toward the polarizing beam.^{26,27} In this case, at the point of interaction with the laser field one should have the longitudinal component of $\partial\vec{n}/\partial\epsilon$ high enough and the laser field should be longitudinally polarized. This technique enables one to establish the helicities of colliding beams independently.

10. Depolarizing effect of the counter beam coherent fields in the case of longitudinal polarization at the beam collision point is mainly similar to that of transversal polarization.^{17,18} Some specific feature is that the deflecting effect on the longitudinally polarized spin is produced by any component (transverse to the velocity) of the counter beam field. In the case of transversal spin orientation an influence is caused only by the orbital force component directed along the spin. This point, which is especially substantial for the usual case of the beams flat at the interaction point, should be taken into account while optimizing experimental conditions

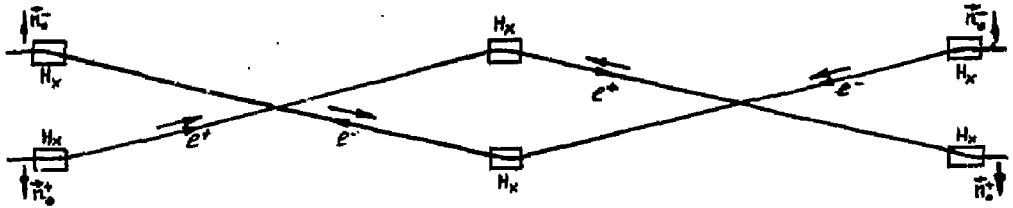


Fig. 8.

for getting high luminosity of longitudinally polarized colliding beams.

11. Above was considered the stable longitudinal polarization at a certain section of the storage ring from the view point of using this for implementation of colliding beams with pure helicities, only. Though, there are some other important applications of storage rings with similar structures. First of all, one should mention application of such storage rings in the mode of a thin and super-thin internal polarized target (when the orbital diffusion processes are suppressed with appropriate cooling) located at the section with longitudinal \vec{n}_0 .

Such kind of experiments can turn out to be most promising, in particular, for studying the deep inelastic scattering on nucleons with given helicities of initial particles (these experiments are of special interest at high energies as at storage rings PETRA, PEP and then HERA, LEP). The attainable luminosity of such experiments is $10^{30} + 10^{32} \text{ cm}^{-2} \text{ s}^{-1}$.

The use of the mode considered for proton storage rings enables one to carry out experiments with the given initial helicities under clean conditions with much higher luminosities (because of feasibility of higher proton currents including those polarized in comparison with currents at superhigh energies for e^\pm case).

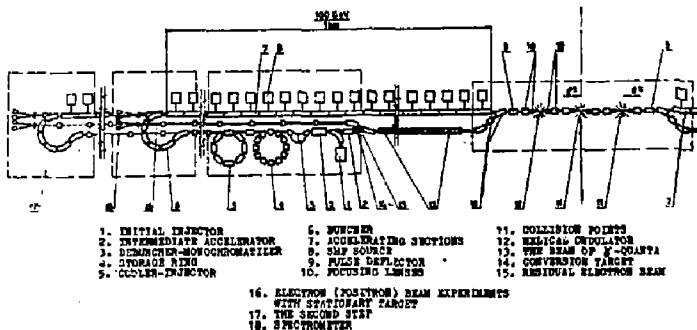
The mode considered is of special interest for operation with polarized antiprotons. As mentioned above, this mode is optimum for producing polarized \bar{p} with the use of cooling (optimal polarization energy is 1-2 GeV).²⁰ The resulting rate for producing polarized \bar{p} can be only one order lower than the total efficiency for \bar{p} (now visible ultimate possibilities are of 10^8 polarized \bar{p} per second).

Subsequent use of the considered mode at the desired experimental energy (generally speaking, at the other storage ring) can provide in future the luminosity up to $10^{33} \text{ cm}^{-2} \text{ s}^{-1}$.

The entire different application of cyclic storage rings with the structures, providing longitudinal \vec{n}_0 at the major part of the storage ring circumference, can be the producing of the high energy intense polarized muon beams.²⁰ If injecting into the track, for example, with two long straight sections where provided the longitudinal and with the same sign direction \vec{n}_0 in both straight sections the intense pion beam with an energy of tens or hundreds of GeV, the muons, generated by the pion decay in the long sections with momentum direction (in the system of pion) along the direction of its laboratory motion, will have nearly full energy of pions and well enough fixed laboratory helicity. The muons of the opposite helicity will be strongly deflected in energy and can easily be extracted from the beam.

12. New prospects for experiments with e^+e^- , $e\gamma$, $\gamma\gamma$ colliding beams with the given helicities will be opened up with development and creation of the electron-positron linear colliding beam facility with an energy of hundreds GeV - the VLEPP project²⁹ (experiments with electron polarized beam is envisaged in the SLC project³⁰).

Generation of polarized electrons and positrons at energies above 100 GeV will be carried out with the use of synchrotron radiation of "worked-out" electrons and positrons in the long helical undulators (see Fig. 9) with further conversion of the longitudinally polarized γ -quanta with an energy of 10 MeV into the longitudinally polarized e^+ and e^- and their further final acceleration and orbital radiative cooling down to the required very small emittances.



The Scheme of VLEPP

Fig. 9.

By controlling the direction of e^+ spins prior the injection into the main linear accelerator one can provide the experiments with any required combination of helicities with ultimate luminosity of the VLEPP-facility (it is designed on the level of $10^{32} \text{ cm}^{-2} \text{ s}^{-1}$ for the whole operating range of energies $\sqrt{s} = 300 + 1000 \text{ GeV}$).

The highly effective conversion of electrons on laser targets with desired helicity^{31,32} can allow to carry out the experiments with $e\gamma$ and $\gamma\gamma$ polarized colliding beams with luminosity nearing that of e^+e^- .

13. Carrying out the polarization experiments in high energy physics and especially the colliding beam experiments with particles with certain helicities becomes very important for development of elementary particle physics. The results of such experiments should entirely justify the considerable efforts necessary for their implementation.

In preparation of the report participated Drs. Ya. S. Derbenev, A. M. Kondratenko, I. A. Koop, and Yu. M. Shatunov.

References

1. L.M. Kurdadze et al., Proc. V Intern. Conf. on High Energy Physics (Warszawa, 1975), Dubna, 1975.
2. G. Hanson et al., Phys. Rev. Lett. **35**, 1609 (1975).
3. A.D. Bukin et al., Proc. V Intern. Conf. on High Energy Physics (Warszawa, 1975), Dubna, 1975, p. 138.
4. Ya.S. Derbenev et al., Part. Acc. **10**, 177 (1980).
5. N.A. Vinokurov et al., Proc. VII National Meeting on Charged Particle Accelerators, v. 1, p. 250, Dubna, 1981.
6. Ya. S. Derbenev, A.M. Kondratenko, A.N. Skrinsky, Preprint INF 2-70, Novosibirsk (1970).
7. Ya. S. Derbenev, A.M. Kondratenko, A.N. Skrinsky, Sov. Phys. Dokl. **15**, 583 (1970).
8. V.N. Baier, Usp. Fiz. Nauk **105**, 441 (1971).
9. Ya.S. Derbenev et al., Proc. X Intern. Conf. on Charged Particle Accelerators, v. 2, p. 55, Serpukhov, 1977.
10. Ya.S. Derbenev, A.M. Kondratenko, A.N. Skrinsky, Sov. Phys. JETP **60**, 1216 (1971).
11. Ya.S. Derbenev, A.M. Kondratenko, Sov. Phys. JETP **35**, 1230 (1972).
12. Ya.S. Derbenev, A.M. Kondratenko, Sov. Phys. JETP **37**, 968 (1973).

(References continued on following page)

13. Berestetsky, E.M. Lifshits, L.P. Pitayevsky, "Relativistic Quantum Theory," part 1, Moscow, 1968.
14. A.A. Sokolov, I.M. Ternov, Sov. Phys. Dokl. 8, 1203 (1964).
15. V.N. Baier, Yu.F. Orlov, Dokl. Akad. Nauk. SSSR 165, 783 (1965).
16. Ya.S. Derbenev, A.M. Kondratenko, Sov. Phys. Dokl. 19, 438 (1975).
17. A.M. Kondratenko, Sov. Phys. JETP 39, 592 (1974).
18. Ya.S. Derbenev, A.M. Kondratenko, A.N. Skrinsky, Part. Acc. 9, 247 (1979).
19. Ya.S. Derbenev, A.M. Kondratenko, E.L. Saldin, Nucl. Instrum. Methods 165, 15 (1979).
20. G.I. Budker, A.N. Skrinsky, Uspekhi P.N., 124, 4 (1978).
21. V.G. Zelevinsky, S.G. Popov, A.N. Skrinsky, Preprint INP 78-45, Novosibirsk (1978).
22. S.A. Nikitin, E.L. Saldin, M.V. Yurkov, Preprint INP 81-116, Novosibirsk (1981).
23. S.A. Nikitin, E.L. Saldin, Preprint INP 81-19, Novosibirsk (1981).
24. Ya.S. Derbenev, A.M. Kondratenko, Proc. V National Meeting on Charged Particle Accelerators, v. 1, p. 263, "Nauka," Moscow, 1977.
25. Ya.S. Derbenev, A.M. Kondratenko, A.N. Skrinsky, Yu.M. Shatunov, Proc. X Intern. Conf. on High Energy Charged Particle Accelerators, v. 2, p. 76, Serpukhov, 1977.
26. Ya.S. Derbenev, A.M. Kondratenko, E.L. Saldin, Nucl. Instrum. Methods 165, 201 (1979).
27. Ya.S. Derbenev, A.M. Kondratenko, E.L. Saldin, Nucl. Instrum. Methods (in print).
28. A.N. Skrinsky, Proc. XX Intern. Conf. on High Energy Physics, Madison, 1980.
29. V.E. Balakin, G.I. Budker, A.N. Skrinsky, Proc. V National Conf. on Accelerators, Dubna, 1978.
30. W. Panofsky, Proc. of Intern. Symposium on Lepton and Photon Interactions on High Energies, Bonn, August 1981.
31. I.F. Ginzburg, G.L. Kotkin, V.G. Serbo, V.I. Telnov, Pis'ma ZhETF 9, 514 (1981); Preprint INP 81-102, Novosibirsk (1981).
32. A.M. Kondratenko, E.V. Pakhtusova, E.L. Saldin, Preprint INP 81-85, Novosibirsk (1981).

BACKGROUND CONDITIONS IN THE DETECTOR MD-1
WITH PERPENDICULAR MAGNETIC FIELD

S.E.Baru, A.E.Blinov, A.E.Bondar,
V.R.Groshev, G.M.Kolachev, S.I.Mishnev,
A.P.Onuchin, V.S.Panin, I.Ya.Protopopov,
A.G.Shamov, V.A.Sidorov, A.N.Skrinsky,
V.I.Telnov, Yu.A.Tikhonov, G.N.Tumalkin,
A.I.Vorobiov, A.A.Zholentz

Institute of Nuclear Physics, Siberian Division
of the USSR Academy of Sciences, Novosibirsk

Summary

The magnetic field in the MD-1 is perpendicular to the orbit plane of a storage ring. This allows the analysis of the particles going out even at zero angles, that is especially important for the two-photon processes. The background problems caused both by the showers of the particles lost in the storage ring and by synchrotron radiation are considered in the paper presented here. With the trigger conditions sufficiently weak at an energy of 1.8 GeV the background due to showers does not exceed 1 Hz/mA. The background caused by synchrotron radiation in the Υ - meson region is not essential for the beam current up to 10 mA.

I. Introduction

The distinctive feature of the detector MD-1 is that its magnetic field is perpendicular to the orbit plane¹. Such a version has the following advantages compared to the detectors with the longitudinal field.

1. There is a possibility to detect particles and to analyze their momenta for the whole range of angles θ , including $\theta = 0$. It is essential especially for the two-photon processes with an angular distribution of the scattered electrons and produced particles peaked forward.

2. It is convenient to detect the γ - quanta going out at zero angles - the low background level and large aperture. This opportunity has been already used in the experiment on the study of the Bremsstrahlung process where the interesting effect of the cut-off of large impact parameters has been observed².

The main disadvantage of the detector with the perpendicular field is the more com-

plicated background problems because of the particle loss in the storage ring and synchrotron radiation. The study of the background caused by lost particles has been carried out at the VEPP-4 injection energy of 1.8 GeV. The measurement of the background due to synchrotron radiation has been performed in the Υ - meson region.

II. The detector MD-1.

The layout of MD-1 at VEPP-4 is shown in Figs. 1,2. The interaction region is insi-

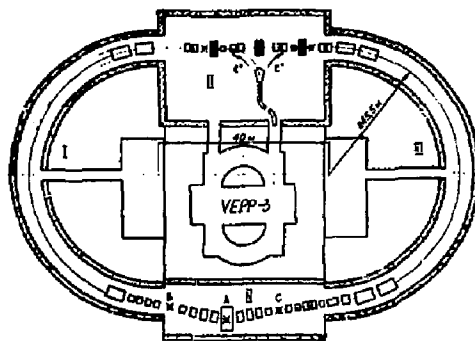


Fig. 1. The layout of VEPP-4:
A - interaction region for the detector MD-1; B,C - interaction regions.

de the large magnet. From both sides of the magnet two additional magnets have been placed with separate supplies. This allows variation of the detector field keeping the angle of the orbit bending constant and equal to 16° .

The electron tagging system for studying the two-photon processes is installed

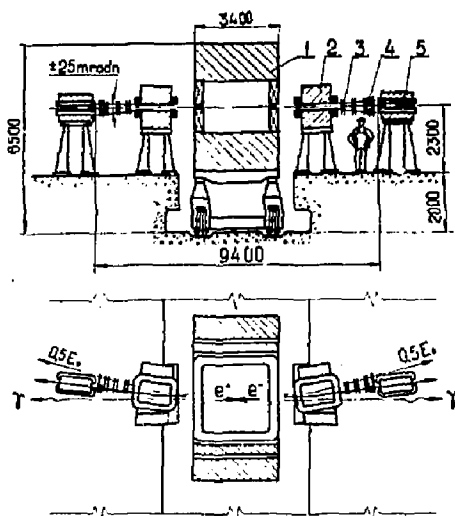


Fig. 2. The central interaction region: 1 - detector MD-1; 2 - additional bending magnets; 3, 4 - electron tagging and luminosity monitoring system; 5 - lenses.

between additional bending magnets and lenses. The system consists of induction proportional chambers, measuring the radial coordinate with an accuracy $\sigma = 100 \mu\text{m}$, usual proportional chambers and scintillation counters. The accuracy of measuring the energy of scattered electrons is 1%. The system is placed from the inner side of the orbit and also above and below the beam. The system ensures detection of the electrons scattered at $\theta = 0^\circ$, with the energy loss of 15-50%. The electrons with the beam energy are detected at the angles $\theta = 12 \pm 100 \text{ mrad}$.

The central part of the detector is shown in Fig. 3. The magnet is a closed-type solenoid. The internal size of the coil is $2.3 \times 2.3 \text{ m}^2$, the copper coil thickness is 30 cm, the gap is 1.8 m, the maximum field is 16 kG. Starting from the interaction region the detector contains a vacuum chamber, coordinate chambers, scintillation counters, gas Cerenkov counters and shower-range chambers. Besides that the muon chambers are placed beyond the magnet winding, inside and beyond the yoke.

A trigger is arranged by the hierarchy

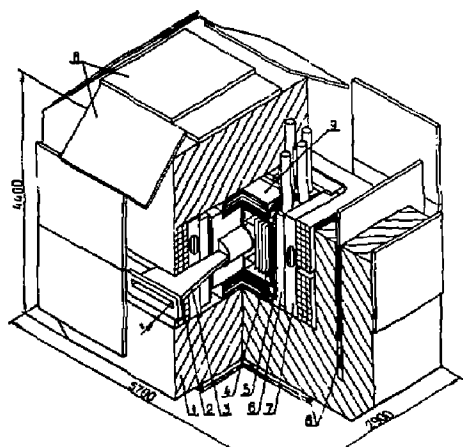


Fig. 3. Magnetic detector MD-1: 1 - yoke, 2 - copper winding, 3 - vacuum chamber, 4 - coordinate chambers, 5 - scintillation counters, 6 - gas Cerenkov counters, 7, 9 - shower-range chambers, 8 - muon chambers.

principle: primary trigger, secondary trigger computer³.

III. Background due to the loss of the particles in beams

The background counting rates from the particles lost from the beam have been studied at the injection energy of 1.8 GeV. Measurements were carried out at the current of $0.3 \pm 1 \text{ mA}$. The large currents are restricted by the collision effects. At these currents the beam lifetime was 10 ± 3 hours and determined mainly by the Bremsstrahlung radiation on the residual gas as well as by the Touschek effect.

Our measurements have shown the following nature of the background in the detector.

At first, there are particles leaving the equilibrium orbit and performing many turns before their ruin. The spacial density distribution of these particles (halo) is fairly broad and has sharp bounds. The cut-off of the halo occurs in the point where the storage ring aperture is the smallest.

lest. If this point is near the detector, it causes an increase in the background counting rate.

Secondly, the beam electrons lose their energy by the Bremsstrahlung radiation on the residual gas in the straight section in front of the detector and hit the detector after bending by the magnetic field.

In Fig. 4 the result of the halo size measurement is shown. The probe, placed be-

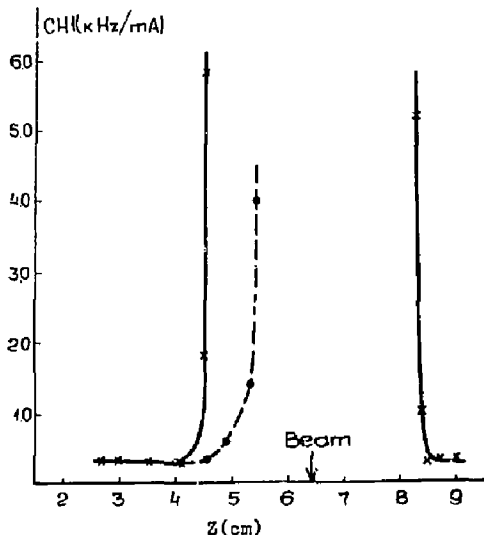


Fig. 4. The dependence of the primary trigger counting rate on the position of the probe; solid line - no cut-off of the storage ring aperture, dotted line - with the restriction of the aperture in the injection section.

yond the first lens from the detector is moving in the vertical direction. The dependence of the primary trigger counting rate on the probe position was measured. The solid line shows the result when the probe approaches the beam from below and above. It is seen that the halo size is about 4 cm. The dotted line shows the result of the similar measurement at an aperture restriction in the injection section. The decrease in the halo size can be seen.

In Fig. 5 the dependence of the background counting rate of the detector on the vertical position of the beam in the detec-

tor is presented. Curve 1 - without restriction of the aperture, curve 2 - with the restriction of the aperture in the injection section. It is seen that the background has been decreased and the dependence on the beam position has disappeared. The cut-off of the halo in the injection section was performed in vertical, radial and in both directions simultaneously. The background counting rate is practically the same in all these cases. This shows that particles in the halo live many turns.

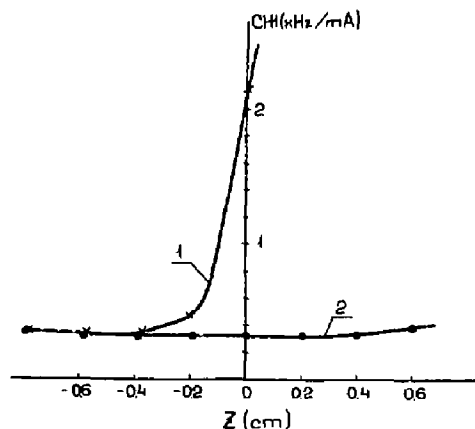


Fig. 5. The dependence of the primary trigger counting rate (CH) on the vertical beam displacement in the MD-1; 1 - no restriction of the aperture, 2 - with the restriction of the aperture in the injection section.

In Fig. 6 the dependence of the background counting rate on the radial displacement in the detector is shown. Such a large orbit displacement is possible due to large sizes of the vacuum chamber in the detector and is carried out by the variation of the field in the central and additional bending magnets.

For experiments at the energies close to the injection one we have chosen the radial displacement $Y = 9$ cm and have used the halo cut-off in the injection section.

Different chambers and counters have highly different background counting rates.

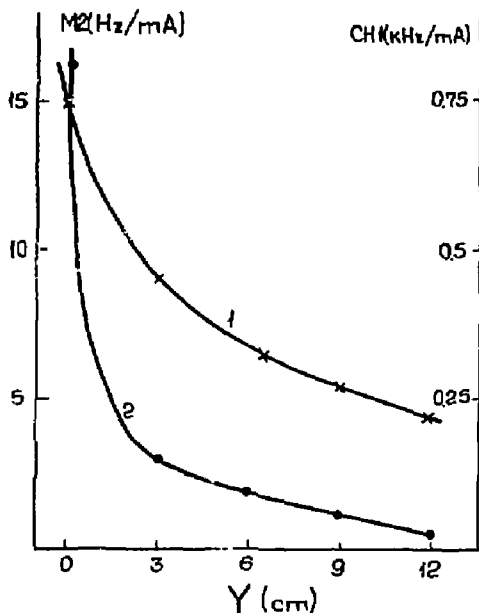


Fig. 6. The dependence of the background counting rate of the detector on the radial displacement of the beam in the MD-1. The restriction of the aperture is made. 1 - counting rate of the primary trigger (CH), 2 - counting rate of the secondary trigger (M2).

In the Table 1 the data for the chambers and counters with the maximum counting rate are presented.

Table I. The background for the chambers and counters with the maximum counting rate at $E = 1.8$ GeV.

System	Background counting rate, kHz/mA
1. Coordinate chamber	0.3
2. Scintillation counter	0.3
3. Shower-range chamber	1
4. Tagging system	1

To decrease the trigger counting rate from the background due to the Bremsstrahlung radiation of electrons on the straight

section in front of the detector we have used scintillation sandwiches detecting the Bremsstrahlung γ - quanta. The vacuum chamber has thin windows in these directions. The angular distribution of these photons is fairly sharp, therefore the sizes of the sandwiches are small (10×10 cm²). The counting rates of these counters are about 3 kHz/mA. These counters are included in the trigger on anticoincidence that leads to the reduction of the trigger counting rate by a factor of 2+3.

Upon these conditions the counting rate of the primary trigger via the channel of charged particles CH1 (at least one particle is needed in the unit of three coordinate chambers and firing of at least one scintillation counter) is about 0.2 kHz/mA, and via the neutral channel N1 (firing of two of ten chambers in the shower-range module is required) is about 0.5 kHz/mA.

The use of various combinations of the secondary trigger allows to reduce strongly the number of the tape recorded events. Below we present the data on the counting rates for some combinations of the secondary trigger in terms of our notations jargon.

1. $M1 = CCND = 10$ Hz/mA

Two units of the coordinate chambers and at least one scintillation counter were fired.

2. $M2 = CCND \cdot CCU \cdot CCI \cdot SCUL = 1$ Hz/mA

Two units of the coordinate chamber were fired, one of them is near upper (near lower), another one is a distant lower (distant upper) and there are scintillation counters below and above. The data on the counting rates for these trigger conditions are presented in Fig. 6.

3. $M3 = M2 \cdot SHND = 0.15$ Hz/mA

Besides the condition 2 firing of two shower-range units is required.

IV. Background due to synchrotron radiation

The special paper⁴ is devoted to the solution of the background problem caused by synchrotron radiation (SR) in the MD-1 de-

detector. The basic idea of the solution consists in creation of the special vacuum chamber allowing to synchrotron radiation to pass the detector without touching the vacuum chamber walls (Fig. 7). Radiation receivers are placed at a rather long distance from the detector center, so that only backward scattered photons hit the detector. This allows to reduce considerably the photon flux on the central part of the vacuum chamber, especially in the hard part of the spectrum because at the Compton backward scattering the photon energy decreases and the angular distribution for hard photons is peaked forward. The movable collimator allows to choose an optimal size of the vertical aperture. The radiation receivers made of copper, are water cooled.

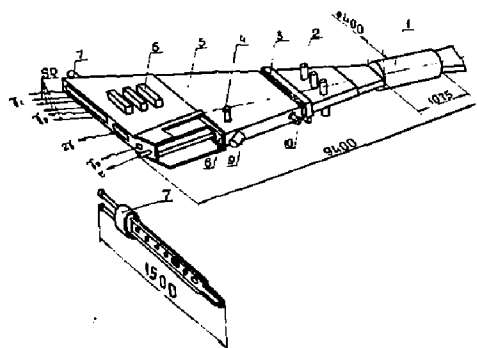


Fig. 7. The layout of the vacuum chamber in the central interaction region: 1 - cylindrical part, 2 - movable collimator, 3 - latch, 4 - vertical probe, 5 - chamber for SR escape, 6 - vacuum pumps, 7 - SR receivers, 8 - entrance window of the electron tagging system, 9 - electron escape for quanta monochromatization, 10 - radial probe.

Such a construction of the vacuum chamber has reduced the photon flux at the central part of the detector by a factor of 10^6 . An additional attenuation is achieved by placing a thin foil at the thin cylindrical part of the vacuum chamber and in front of

the scattered electron tagging system. Now the cylindrical part is of 3 mm thick Al ($1/30 X_0$) and 0.1 mm Ta ($1/20 X_0$) and the tagging system window is of 0.17 mm thick Fe ($1/100 X_0$) and 0.3 mm Sn ($1/40 X_0$).

The background due to synchrotron radiation is essential only for the coordinate chambers and for the tagging system; the remaining elements of the detector are protected by a thick layer of material. For simplicity of the event analysis it is desirable to have the number of wires fired for the one beam passage less than one.

We have performed the measurement at the beam energy of 4.7 GeV. The number of fired wires during one beam passage at the current of 1 mA was 0.1 for the coordinate chamber nearest to the beam and 0.03 for the most distant one. For the chamber of the tagging system the corresponding value is 0.01. The experimental data are in agreement with calculations with an accuracy of about 2%.

It is seen that at the present conditions the background due to synchrotron radiation allows to operate at the T -meson energy with the currents up to 10 mA.

The authors express their gratitude to the staff of VEPP-4 for a possibility to perform the experiment.

References

1. S.E.Baru et al., Preprint INP 77-75, Novosibirsk (1977).
2. A.E.Blinov et al., Preprint INP 82-15, Novosibirsk (1982); presented to the International Conference on Instrumentation for Colliding Beam Physics, Stanford, 1982.
3. S.E.Baru et al., Proceedings of III International Conference on Proportional and Drift Chambers, Dubna, 1978, p. 272.
4. A.P.Onuchin, Yu.A.Tikhonov, Preprint INP 77-77, Novosibirsk (1977).

SUPERCONDUCTING MAGNETS FOR DETECTORS

R.D. Kephart

Fermi National Accelerator Laboratory*
P.O. Box 500, Batavia, Illinois 60510

SUMMARY

A Fermilab/KEK/University of Tsukuba, Japan collaboration is designing a large superconducting solenoid for the Fermilab Collider Detector Facility (CDF). A review of the status of other superconducting solenoids built for colliding beam machines is presented and progress on the design of the CDF magnet is discussed. Two types of superconducting coils appear to be feasible; a bath-cooled cryostable design or an indirect cooled design using force flow helium. Advantages and disadvantages of each design are pointed out. Sealing up such coils to larger detectors is also discussed.

History

Many of the large general purpose detectors used at colliding beam machines rely on gas ionization devices located in a magnetic field to measure the angles and momenta of charged secondaries produced in the collisions. For most systems the position measurement error of the ionization device limits the momentum resolution, resulting in a resolution that tends to degrade as the momenta of the secondaries increase. The resolution of such a system can be improved by increasing the track length in the magnetic field over which the particle trajectories are measured and, within limits, by increasing the magnetic field strength. As the center of mass energy of colliding beam machines has increased, there has been a continuing desire to construct magnets producing high fields over ever larger volumes. Although such magnets can take many forms (depending upon the type physics one wishes to emphasize), axial field solenoids have often been chosen to provide the

magnetic field for large general purpose detectors. By aligning the solenoid axis with the beam axis, the magnetic field of the detector has only minimal impact on the circulating beams. In addition, the uniform fields provided by the solenoid simplify track reconstruction of complex events.

The characteristics of the SC solenoids built thus far for colliding beam machines are summarized in Table I.¹ The first such coil to be built was used in the PLUTO detector² built for the Doris electron-positron storage ring at DESY. The coil employed a multiple layer winding of copper stabilized NbTi superconductor immersed in a bath of liquid helium. Since no electromagnetic calorimetry is used outside the coil, no attempt was made to reduce the amount of material used in its construction. The coil was tested in 1972 and is still successfully being operated at PETRA. The solenoids built after PLUTO have had the additional constraint that their structures be as "transparent" as possible to secondaries produced in beam-beam collisions. This constraint is a result of both physics and economics. The physics often dictates that both electrons and photons be detected with good position and energy resolution. In addition the number of pions misidentified as electrons by the detector should be as small as possible. These goals are best achieved with a minimum of material located between the beam crossing point and the detector's EM calorimetry. Thus ideally the coil that provides the magnetic field for tracking chambers ought to be located outside the calorimetry. However, locating the coil outside the calorimetry requires that both it and the return yoke of the magnet be substantially larger and thus more expensive. In addition, access to the calorimetry is

TABLE I

SUPERCONDUCTING SOLENOIDS USED FOR COLLIDING BEAM PHYSICS

MAGNET	PLUTO PETRA/DESY	ISR-II CERN	CELLO PETRA/DESY	TPC-LBL PEP/SLAC	CLEO CESR/CORNELL
Type	Pool-boiling cryostable	Pool-boiling cryostable	Force flow indirect cooled	Force flow indirect cooled	Force flow indirect cooled
Useful bore (m)	1.4	1.38	1.5	2	2
Winding length (m)	1.2	1.8	3.4	3.4	3.15
Design central field (T)	2.2	2.5	1.5	1.5	1.5
Tested Central field (T)	2.2	1.5	1.3		1.0
Stored energy (MJ) at design field	4.3	3.0	7.0	10.9	9.4
Design Current (A)	1270.0	2200.0	3400.0	2230.0	2200.0
Tested Current Date	1270.0 (1972)	2200.0 (1976)	3200.0 (1979)	1200.0 [†] (1980)	1600.0 (1981)
Radiation Thickness (λ)	---	1.1	0.5	0.68	0.75

[†]TPC magnet was damaged during testing by an insulation breakdown. It is currently being rewound.

*Operated by Universities Research Association, Inc., under contract with U.S. Department of Energy.

severely limited by the coil. A reasonable compromise has been to locate the coil inside the calorimetry but construct it in such a way that it is as thin as possible both in terms of radiation and absorption lengths.

In practice this has meant using structural aluminum vacuum shells and radiation shields as well as using high purity aluminum instead of copper to stabilize the superconductor. The reasons for this last choice are apparent from Fig. 1. As can be seen, the electrical resistance of high purity aluminum at a temperature of 4K is substantially smaller than that of copper. There are, however, several complications encountered when using high purity aluminum in large coils. The two most important difficulties are its very low yield strength (≈ 1200 psi as compared to 7000-13000 psi for OFHC copper) and the fact that its resistivity can increase substantially if it is subjected to cyclic strains in excess of $\approx 0.3\%$ (Fig. 2). In spite of these problems, aluminum's 8.9 cm radiation length vs. 1.4 cm for copper makes it very attractive as a stabilizer for "thin" solenoids.

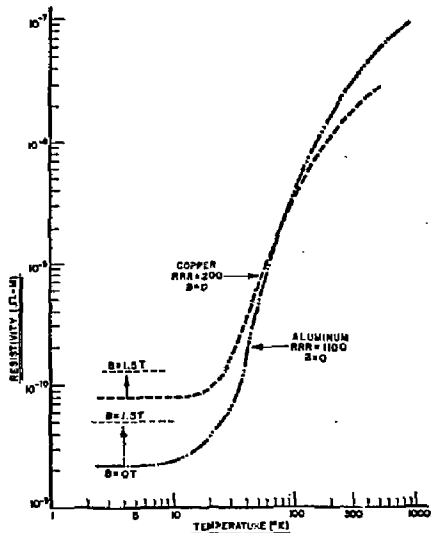


Fig. 1 Resistivity of Aluminum and copper. S = list lines include magneto-resistivity effects

The first such magnet built with this design criterion was one completed by Morpurgo in 1976 for the CCR experiment at the CERN Intersection Storage Rings.³ This coil like PLUTO's was cryostable and bath cooled. It was, however, unusual in that the bulk of the stabilizer for the conductor was provided by soldering a relatively small Cu-NbTi superconductor between two larger high purity aluminum strips⁴ (see Fig. 3). The coil has a useful bore of 1.4 meters, is 1.8 meters long and produces a central field of 1.5 T. The six layer coil and cryostat correspond to 1.1 radiation lengths (λ_p). Except for minor problems with refrigeration and a failed epoxy fiberglass coil support member, the coil has operated very successfully for more than five years at the ISR. The magnet is operating at present at the ISR.

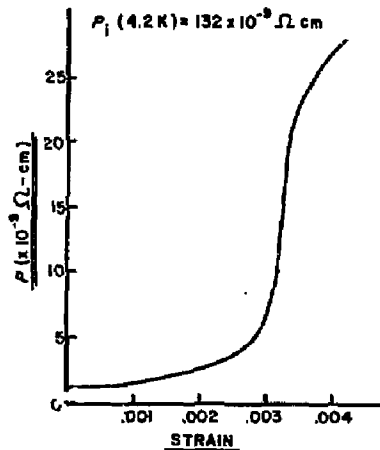


Fig. 2 Cyclic strain behavior of the resistivity of high purity aluminum. Ref.5

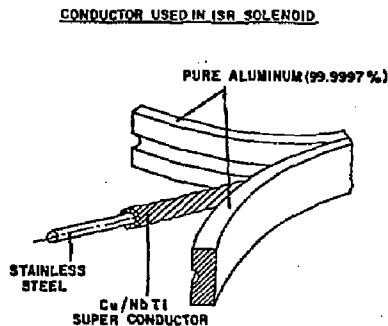


Fig. 3 Aluminum stabilized conductor

The next "thin" solenoid was built by CEN(Saclay)/ITP(Karlsruhe) collaboration for the CELLO detector at PETRA⁶. The coil has a design central field of 1.5 T, a 1.5 m useful bore, and is 3.4 m long. This coil employs a single layer coil cooled by helium force flowed in an external electrically insulated cooling pipe. Although its conductor also uses a Cu-NbTi superconductor soldered to a high purity aluminum strip, the design philosophy was quite different. Both the ISR and PLUTO solenoids were bath cooled cryostable magnets. In these magnets full cryostability implies that there is sufficient liquid helium in direct contact with the conductor such that if a "normal zone" is formed (e.g., by conductor motion, cracking epoxy, etc), then the ohmic heating generated in the conductor's stabilizer is less than the available cooling power to the helium bath. As a result, any conductor normal zone is rapidly cooled below the critical temperature T_c of the superconductor and the conductor returns to the superconducting state. Thus so long as a fully cryostable coil is covered by liquid helium it cannot

quench. The CELLO magnet on the other hand does not have helium directly in contact with the conductor. For stability, the design relies on the high thermal diffusivity and specific heat of the aluminum stabilizer to prevent small local heat pulses from quenching the coil. The coil is however designed to quench safely. During such a quench the high natural quench velocity in the aluminum shunt causes the energy deposited in the coil to be spread over a large region thus avoiding excessive conductor temperatures. The CELLO magnet was tested in 1979. A defect in the superconductor required the coil to be repaired by bypassing 6 turns. The magnet was subsequently tested successfully, however, the operating current of the coil was limited to a value corresponding to 1.3 T by spontaneous quenches presumably because of additional conductor defects. After initial refrigeration problems were solved, the magnet has run very successfully for two years, the last continuous run being 4500 hours without interruption.⁷ This magnet is particularly impressive in that its total radiation thickness is $0.5 \lambda_R$.

Two other indirectly cooled solenoids have been built. One is for the TPC detector built by LBL for PEP⁸ and the second for the Cornell CLEO detector at CESR⁹. A cross section of the CLEO coil is shown in Fig. 4. Both magnets have a useful bores of 2 m and design central fields of 1.5 T. These coils differ from CELLO primarily in their method of quench protection. The SC winding is not shunted by aluminum stabilizer. Instead, both coils use a mandrel made of a low resistivity aluminum alloy to form a "shorted secondary". (The TPC magnet uses a second low resistivity "shorted secondary" wound on the mandrel underneath the superconductor.) These secondaries are designed to be well coupled inductively to the primary winding and have time constants that are comparable with the primary winding/dump resistor time constant. During a quench a portion of the primary current is rapidly transferred from the primary winding to the "shorted secondaries". Ohmic heating in the secondaries cause the SC primary to become normal faster than it would through normal zone propagation alone. In addition the secondary circuit absorbs a substantial fraction of the stored energy avoiding high conductor temperatures in the primary winding. Both the TPC and CLEO coils have been tested. The Cornell coil was tested in 1981 up to 73% of its rated current, but the test was terminated by a power lead failure. Fortunately only external damage resulted, and the magnet was subsequently tested successfully to a field of 1.0 T and installed in the iron. Figure 5 shows the primary current vs. time for a quench in the CLEO magnet. The current in the primary is seen to drop quickly from its initial value of 1600 A to 1040 A as current is transferred to the magnet's bore tube. There are currently no plans to test the magnet up to its design field of 1.5 T. The magnet is in use at 1 T at CESR and the magnet's operation has stabilized such that during two months of recent operation the magnet quenched only once.¹⁰ Unfortunately, the TPC solenoid was severely damaged during its initial testing in 1980 by an insulation breakdown.¹¹ However, the magnet's cryogenic and electrical performance were verified up to half the rated current before the failure. The coil is currently being rebuilt at LBL.

CDF Solenoid

Next I would like to describe progress on the design of a superconducting solenoid for the Fermilab Collider Detector Facility. This will be the major detector used at the Fermilab collider to study pp

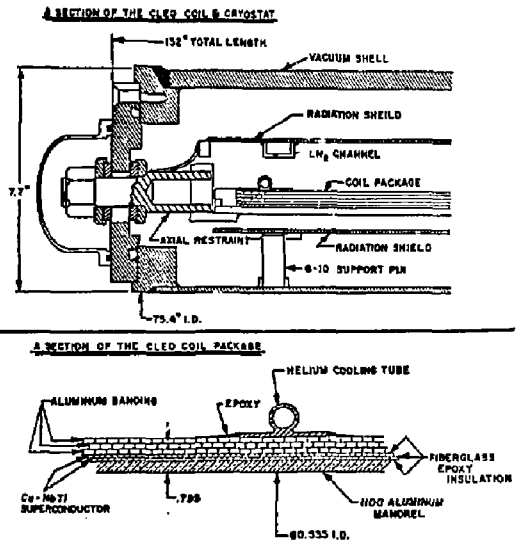


Fig. 4. Coil & cryostat of the CLEO indirect cooled cable.

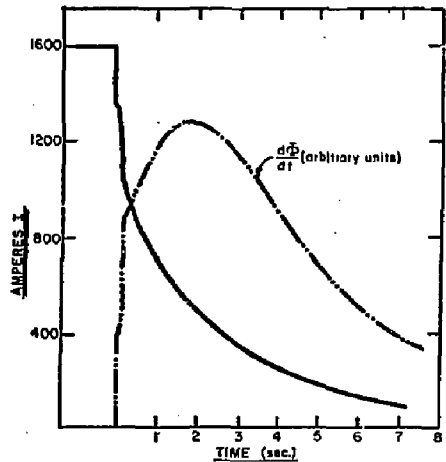


Fig. 5. Current vs. time during quench of CLEO magnet.

collisions at center of mass energies up to $\sqrt{s} = 2000$ GeV. When the collider is operating, the detector will be located in an experimental hall at the BQ collision area. When the accelerator operates for fixed target physics, the detector will operate in a nearby (30 m) assembly building for testing and field mapping. The detector and its physics goals have been described elsewhere¹².

The central detector for CDF (shown in Figs. 6 and 7) employs a large axial magnetic field volume instrumented with a cylindrical drift chamber and a pair of intermediate tracking chambers. This system will determine the trajectories, signs and momenta of charged particles produced with polar angles between 10 and 170 degrees. The magnetic field volume required for tracking is approximately 4 m long and 3 m in diameter. To provide the desired $\Delta p_T/p_T \leq 1\%$ at 50 GeV/c using chambers with $\sim 200 \mu$ resolution the field inside this volume should be 1.5 T and as uniform as is practical to simplify track finding and reconstruction.

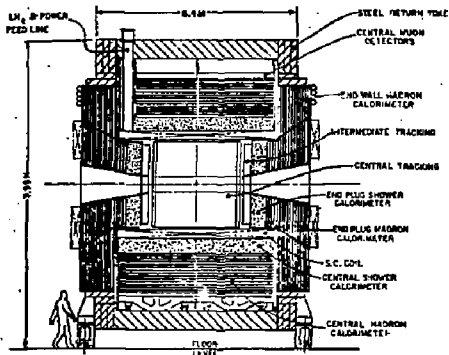


Fig. 6 CDF Central Detector (Side View)

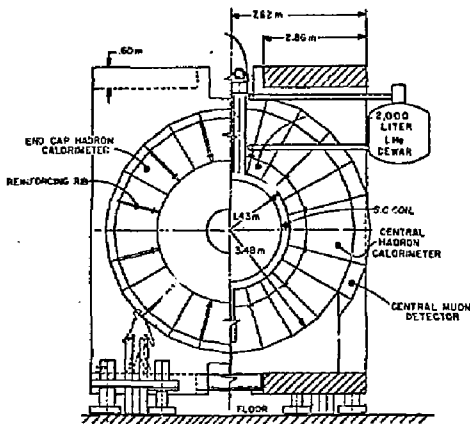


Fig. 7. CDF detector end view.

This field will be produced by a solenoid with a uniform linear current density of 1.2×10^6 A/m surrounded by a partially calorimeterized iron return yoke. The coil itself will be approximately 3 m in diameter and 5 m long. Since both central electromagnetic and hadronic calorimetry are located outside the coil, the coil must be "thin" both in physical thickness and radiation and absorption lengths. In addition, because the magnet must be off during p accumulation, and the stored p beam lifetimes may be short initially, the magnet must be capable of being charged to full field quickly (~ 10 minutes).

We have investigated the feasibility of building a conventional water-cooled aluminum coil (see Figs. 8 and 9). While such coils could be built, the electrical power costs would be enormous, exceeding the capital cost of a comparable SC coil in ~ 1 year. Therefore we have decided the coil will be superconducting. The short magnet charge time makes TPC or CLEO type coils with low resistance bore tubes unattractive since a 10 minute linear charge would produce over 1200 watts of eddy current heating in a low resistivity (1100-0 aluminum alloy) bore tube of our size. Thus we are currently considering two possible designs, a bath cooled coil¹³ similar to Morpurgo's ISR magnet as well as an indirectly cooled CELLO type coil. A summary of the characteristics of a bath cooled solenoid for the CDF detector appears in Table II. The proposed conductor for this design is shown in Fig. 10. It consists of a Cu/NbTi superconductor coextruded with a high purity (RRR ≥ 1200) aluminum stabilizer. The coil would be a single layer of conductor wound on an insulated structural aluminum bobbin. Turn to turn insulation would be provided by epoxy fiberglass spacers, while the coil "bursting forces" would be contained by high strength aluminum banding wound over the conductor (see Fig. 11). This geometry permits 50% of the surface area of the conductor to be exposed to the He bath.

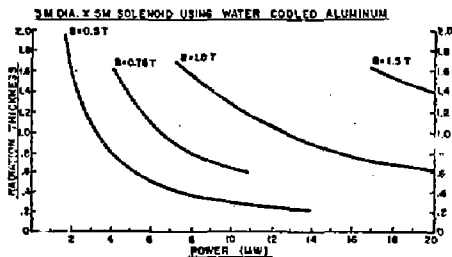


Fig. 8. DC power vs. radiation thickness for a conventional coil.

OPERATING COST vs. ΔR
CONVENTIONAL WATER COOLED ALUMINUM SOLENOID
3M DIA. x 5M LONG $B_0 = 1.0$ TESLA

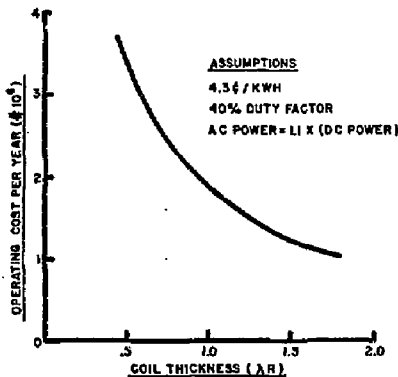


Fig. 9. Operating costs for conventional coil.

TABLE II

CDF POOL BOILING MAGNET PARAMETERS

Useful Bore:	2.86 m
Outer Diameter:	3.35 m
Length:	5.07 m
Central Field:	1.5 T
Coil Diameter:	2.99 m
Coil Length:	4.79 m
Winding Scheme:	Single layer helix (870 turns)
Operating Current:	6600 A
Stored Energy:	31 MJ
E_J^2	2×10^{23} A-J/m ²
Inductance:	1.38 H
Max. Discharge Voltage:	30 V ($\tau = 300$ sec) 202 V ($\tau = 45$ sec)
Compressive Axial Force at Midplane:	86 metric tons
Axial Decentering Force:	15.2 metric tons/cm
Max. Radial Decentering Force:	12.3 metric tons/cm
Est. LHe Consumption:	56 L/h (40 W)
He Capacity of Cryostat:	~ 800 L
He Reservoir Capacity:	1750 L
He Cryostat Pressure Rating:	4.76 Atm
Est. LN ₂ Consumption:	11 L/h (500 W)
Cold Mass (Magnet)	7200 kg
Est. Cooldown Time:	300K to 80K $\leq \sim 6$ days 80K to 4.2K ≤ 2 days
Weight of Steel Yoke:	~ 1000 metric tons
Weight of Central Detector:	~ 2000 metric tons

The coil would be fully cryostable according to the Stekly criterion¹⁴ and thus should not be able to quench. Nevertheless, the cross sectional area of the stabilizer is sized very conservatively such that even if the coil should quench (e.g., low liquid helium level), then it could be discharged into an external dump resistor such that the maximum conductor temperatures would not exceed 250K.

The entire coil would be preloaded axially and radially to prevent conductor motion during excitation and enclosed in an outer aluminum shell. This shell would serve both as the He containment vessel and provide attachment points for supports. A cross section of this proposed coil is shown in Fig. 12. The coil would be supported to its vacuum shell by 30 metallic (Inconel 718) support members: 6 axial supports at one end and 12 tangentially attached radial supports at each end of the coil. Each support is LN₂ intercepted and equipped with spherical bearings to allow for differential thermal contraction of the coil during cooldown. The coil will be surrounded with superinsulation, LN₂ cooled radiation shields and an aluminum vacuum shell. The entire package is 25 cm thick and corresponds to 1.04 radiation lengths and 0.24 nuclear absorption lengths. The contributions of various components to the thickness of the coil are shown in Table III.

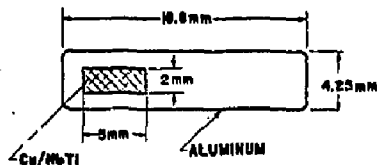


Fig. 10. Proposed Cu/NbTi/Al conductor for CDF bath cooled coil.

Conductor

General	Cu/NbTi coextruded with high purity aluminum stabilizer
Overall dimensions:	4.25 mm x 18.8 mm
Al:Cu:Nb-Ti area ratios:	14:1:1
Short sample current:	13.2 kA at 2.0 T, 4.2 K
Bare conductor current density:	8260 A/cm ²
<u>Aluminum Stabilizer</u>	
Residual resistivity ratio:	≥ 1200

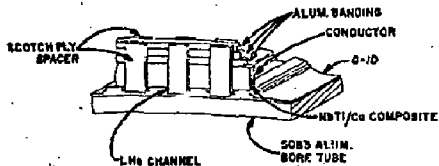


Fig. 11. Proposed CDF bath cooled coil geometry

Electrical Insulation:

On coil bobbin:	epoxy-fiberglass with channels
Turn to turn:	0.050" (1.25 mm) epoxy fiberglass

Liquid helium will be supplied to the coil from a dewar mounted on the magnet yoke through a vertical "power chimney" containing the gas cooled power leads. The estimated helium consumption for the magnet and its transfer lines is approximately 56 liters/hr (40 W).

An indirect cooled CELLU type design for the CDF coil is also being investigated. It is similar in many respects to the bath cooled design. The vacuum shell, supports, radiation shields, conductor and bore tube are nearly identical. The outer helium shell however is replaced by a serpentine LHe cooling tube attached to the coil banding. The banding would be electrically insulated from the conductor. In addition the turn to turn insulation would be thin polyamide-imide tape or similar material to enhance longitudinal quench propagation (see Fig. 13). The overall radiation length of this coil would be almost the same as the bath cooled coil since material removed by eliminating the outer He vessel and thinning the bore tube is partially compensated for by increasing the conductor's Al stabilizer (to keep

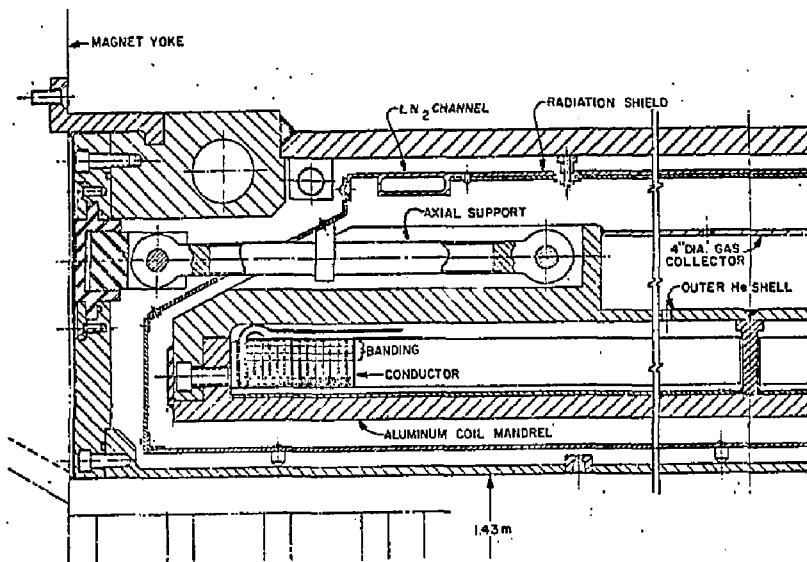


Fig. 12 Cross section of a bath cooled CDF coil

conductor temperature $\leq 100^{\circ}\text{K}$ during a quench) and by the addition of the He cooling circuit. The physical thickness required is also about 25 cm.

To investigate the problems associated with such a magnet a 1 m diameter x 1 m long R&D solenoid was constructed and tested¹⁵ in Japan by Hitachi Ltd. using conductor and banding techniques similar to that proposed for the full sized coil. The coil was successfully excited to 1.6 T (70% of short sample)

without spontaneous quenches. Normal zone velocities for quenches induced by a heater were measured and are shown in Fig. 14. The estimated velocity of the normal zone along the conductor length (if we assume that the quench only spreads that way) is shown on the left ordinate axis. The effective velocity along the axis is shown on the right axis. These velocities have in turn been input to a computer quench simulation program and used to estimate the quench behavior of the 3 m diameter x 5 m by full sized coil.

TABLE III
3m DIAMETER x 5m LONG PATH COOLED SOLENOID

Item	Material	cm	Radiation Length	Absorption Length
Inner vacuum shell	Aluminum	0.64	0.071	0.0170
Inner helium shell (coil bobbin)	Aluminum	1.59	0.178	0.0426
Conductor	Aluminum Copper NbTi	1.7	0.232	0.04000
Insulation	Epoxy/fiberglass	0.6 + spacers	0.046	0.019
Banding	Aluminum	1.5	0.169	0.0404
Outer helium shell	Aluminum	0.79	0.089	0.0213
Radiation shields	Aluminum	2 x 0.20	0.044	0.0106
Outer vacuum shell	Aluminum	1.90	0.214	0.0512
TOTAL THICKNESS			1.04	0.242

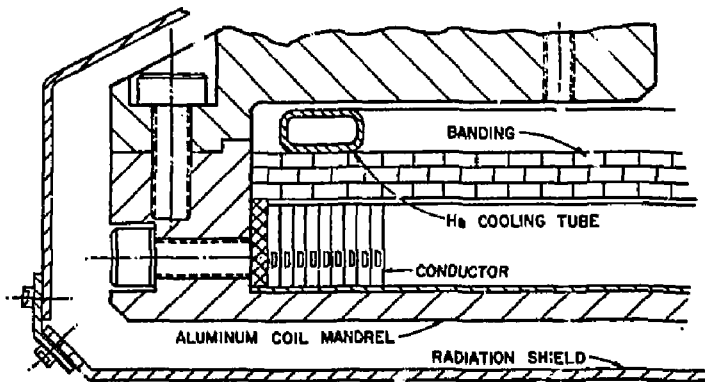


Fig. 13 Indirect cooled coil & cryostat

The results indicate that such a coil will quench safely with conductor temperature not exceeding 100K.

Both coil alternatives are still under examination. Some of the author's perceived advantages and disadvantages of each are summarized in Table IV. We plan to decide which coil to build and begin final engineering design and construction in May of 1982 with a goal of completing the coil for testing in 1984.

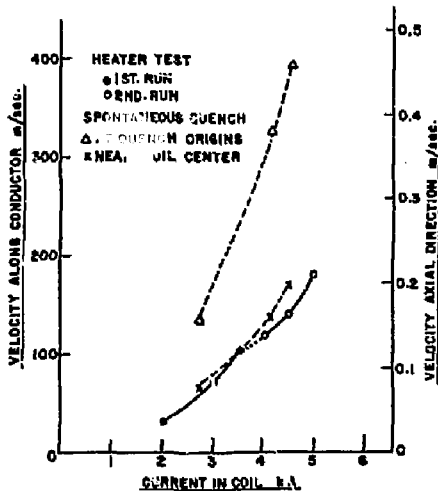


Fig. 14 Quench velocities in CDF R&D coil

TABLE IV
COMPARISON
BATH COOLED VS. INDIRECT COOLED COILS

	BATH COOLED	INDIRECT COOLED
A	Coil can't quench	Small amounts of helium in coil → no cryogenic safety problems
D	Coil insensitive to small conductor motions, cracking epoxy, etc.	Coil cryogenics & leak checking simpler
V	Low voltage during coil discharge	Coil may be cheaper
A	He bath can absorb large amounts of eddy current heating during charge cycle	Faster cooldown rate
T	Insensitive to short refrigerator interruptions	Coil can be better electrically insulated
A	Large He reservoir in coil requires large vent pipes and safety reliefs	Coil can quench
G	Helium cryostat more complicated and expensive	Must avoid conductor motion, cracking epoxy, etc.
E	Leak checking harder	Small defects in superconductor can limit maximum current
S	Cooldown takes longer	Leak checking harder
		Must avoid "hot spots" in coil (e.g., at support attachments)
		Recovery from quench takes many hours
		Higher voltages during quench → insulation more critical
		More sensitive to eddy current heating during charge cycle
		Short refrigerator interruption can quench coil

Larger Coils

Finally I would like to discuss briefly what the prospects are for scaling up magnets of the types I have described for future colliders. Table V contains a list of the world's currently approved accelerator projects as well as those that have been proposed recently. With the exception of the UNK and TEVATRON fixed target accelerators, all other approved or proposed machines are colliders. The increased center of mass energies at these machines will probably result in a several new large detectors being built that employ superconducting solenoids substantially larger than those built thus far. There are no fundamental reasons why the SC technology presently applied to solenoids at colliders cannot be extended to these larger coils. In addition, other new techniques such as cryostable force flow coils (perhaps using "cable in conduit" conductors similar to those developed for large fusion magnets) may be attractive for these large coils. It is interesting to consider what scaling laws apply that will allow us to extrapolate from existing coils to larger ones.

Scaling Laws

Momentum Resolution

For a solenoid whose volume is instrumented with a track detector with fixed position measurement error the resolution of the solenoid/tracking chamber system varies as

$$\frac{\Delta P_T}{P_T} = K \frac{P_T}{B_0 R^2}$$

where P = transverse momentum
 B_0 = solenoid field
 R = radius of solenoid
 K = constant (= 0.01 for 200 μ drift chambers)

Thus the most effective means of improving the detector resolution for high momentum particles is to increase the radius of the coil since the resolution depends inversely on the square of this quantity.

Stored Energy of the Magnet

The stored energy of the solenoid is a useful parameter since the construction costs, quench protection, and thickness of SC solenoids all increase rapidly as the magnet's stored energy is increased. The stored energy is given by

$$E = \int \frac{B^2}{2\mu} dV$$

which for a solenoid with a non-saturated iron return yoke is approximately

$$E = \frac{B^2}{2\mu_0} (\pi R^2 \ell)$$

where ℓ is the length of the coil. A useful number is that 1 m^3 of magnetic field volume at 1.5 T corresponds to about 0.9 MJ of stored magnetic energy in the coil.

TABLE V

WORLD ACCELERATOR PROJECTS

APPROVED

Europe	$p\bar{p}$	CERN	270 x 270 GeV $p\bar{p}$
USA	ISABELLE	Brookhaven	400 x 400 GeV $p\bar{p}$
	TEVATRON	Fermilab	1 TeV Fixed Target
	$p\bar{p}$	Fermilab	1 x 1 TeV $p\bar{p}$
USSR	UNK.	Scerpkhov	400 GeV Fixed Target (3 TeV Fixed Target)
Japan	TRISTAN	KEK	27 GeV e^+e^-
Europe	LEP	CERN	50 x 50 GeV e^+e^-

PROPOSALS

Europe	HERA	DESY	30 GeV/820 GeV p
USA	SLC	SLAC	50 x 50 GeV e^+e^-
	CESR II	Cornell	50 x 50 GeV e^+e^-
	CHEER/ Columbia	Fermilab	10 GeV e/1000 GeV p
Japan	TRISTAN	KEK	27 GeV e/300 GeV p

Thickness of the Coil

For detectors with their EM calorimetry outside the coil, the coil thickness in radiation lengths is particularly important. Although the actual thickness depends on the details of a specific design, several useful scaling laws can nevertheless be applied. The main contributors to the coil thickness are the outer vacuum tank wall, the conductor banding and conductor stabilizer.

Outer Vacuum Shells

The outer vacuum shell of an SC coil must withstand external atmospheric pressure and thus is subject to elastic buckling failure. If this shell is formed out of solid sheets of aluminum alloy, then it contributes a substantial fraction of the total coil thickness (see, e.g., Table III for the CDF coil). The collapse pressure of this shell is given by the Southwell equation

$$P_c = 0.807 \left(\frac{1}{1-\nu^2} \right)^{3/4} \frac{E t^{2.5}}{\ell r^{1.5}}$$

where E is Young's modulus, ν is Poisson's ratio, and P_c is the collapse pressure. The thickness required is given by

$$t = \frac{P_c^{2/5} R^{3/5} \ell^{2/5}}{0.918 E^{2/5}} \left(\frac{1}{1-\nu^2} \right)^{3/10}$$

Note however that this thickness can be reduced in several ways. Reinforcing rings can be added periodically to reduce ℓ (the unsupported length); materials can be selected that have both high Young's modulus and long radiation lengths (e.g., Graphite epoxy) or honeycomb type structures can be used to

increase the shell thickness while adding minimal material. Figure 15 shows the effects of support rings or honeycomb construction on the radiation thickness of the vacuum shell for the 3 m diameter CDF coil. It should be pointed out however that while such solutions are attractive in terms of radiation thickness, they require more physical space, and may be substantially more expensive than solid sheer vacuum shells.

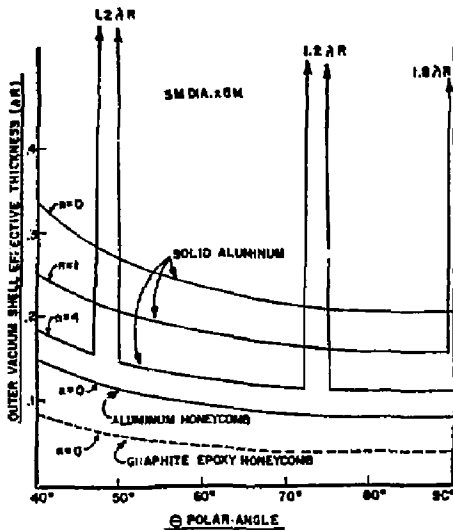


Fig. 15 Thickness vs. angle for various vacuum shell types n = no. of support rings used.

Conductor Banding

The conductor banding must contain the coil bursting forces. Its thickness is determined by the stress limit σ_M in the banding material.

$$t \propto \frac{B^2 R}{\sigma_M}$$

thus the banding thickness will increase linearly with radius for large coils and as the square of the field.

Conductor Stabilizer

Similarly we can determine the thickness of the conductor's stabilizer if we make the pessimistic assumption that the conductor heats up adiabatically while the current is discharged into an external dump resistor r with time constant $\tau = L/r$ where the inductance $L = 2E/1^2$. If we further assume that maximum allowable voltage across the coil is limited to a value U_M then one can demonstrate that the required thickness of the stabilizer is given by

$$t = \frac{B^2 R}{\mu_0} \left(\frac{\pi \lambda}{2 \mu_0 U_M \eta F(\theta) I} \right)^{1/2}$$

where

$$F(\theta) = \int_0^\theta \frac{C(T)}{\rho(T)} dT$$

and

- η = the fraction of the conductor with respect to the whole package
- θ = maximum hot spot temperature
- C = specific heat
- ρ = resistivity

Thus both the stabilizer and banding in the coil will increase in thickness $\propto B^2 R$ while the vacuum shell scales as $R^{3/2}$. As a result, the overall coil thickness for the large "thin" coil will increase nearly linearly with its radius. Indeed, as a result, several of the largest detectors proposed for LEP would have had coils that were too thick to permit the desired electromagnetic calorimeter resolution and π/e separation. As a result, these detectors have been designed to put the EM calorimetry inside the coils.

Figure 16 shows one representative detector of those proposed for LEP¹⁶. It would use a 1.5 T SC solenoid instrumented with a time projection chamber. Its indirect cooled CELLO type coil would have a 5 m bore and be 6.4 m in length. Since the detectors EM calorimetry will be located inside the coil, the coil is relatively thick ~ 0.5 nuclear absorption lengths. In addition to this coil several other high field SC solenoids with diameters 4-5.5 m and lengths of 6-7 m are being considered for LEP. Similarly, detectors using large SC solenoids have been proposed for Tristan, Isabelle, etc.

Conclusion

A number of SC solenoids have been built for colliders, and it seems likely that many more large SC solenoids will be built in the future. The solenoids built thus far have not, however, been free of construction and operational difficulties. Nevertheless, several large SC solenoids are now operating reliably at Colliders, and there is reason

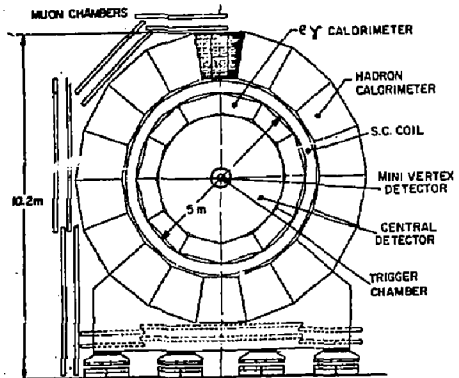


Fig. 16 Proposed LEP detector

to believe that new larger solenoids can be constructed using straight forward extrapolation of existing techniques. It seems likely that improvements in conductors, coil technology and refrigeration techniques will permit their reliable construction and operation.

Acknowledgments

The author wishes to express his thanks to R. Fast, J. Grimson, E. Leung, M. Mruzek, R. Wands, and R. Yamada at Fermilab, as well as our collaborators from KEK and University of Tsukuba, Japan for their efforts on the CDF coil design. Information on large coils for LEP obtained from H. Desportes is appreciated. Thanks also to S. Jones for typing this manuscript.

References

1. H. Desportes, IEEE Transactions on Magnetics, Vol. MAG-17, No. 5, pg. 1560, September 1981.
2. G. Horlitz, et al., Fourth International Conference on Magnet Technology, pg. 275, Brookhaven (1972).
3. Morpurgo, Cryogenics, Vol. 17, pg. 89, (Feb. 1977).
4. Morpurgo, Cryogenics, Vol. 17, pg. 87 (Feb. 1977).
5. H.R. Segal, IEEE Transactions on Magnetics, Vol. Mag-13, No. 1, January 1977.
6. H. Desportes, et al., Advances in Cryogenic Engineering, Vol. 23, D-2 (1980).
7. J. Benichou et al., IEEE Transactions on Magnetics, Vol. MAG-17, No. 5, pg. 1567, Karlsruhe (1981) and private communication H. Desportes, Feb. 1981.
8. M.A. Green, Proceedings of the 6th International Conference on Magnet Technology, Bratislava (1977).
9. D. Andrews, Advances in Cryogenic Engineering, Vol. 27, Plenum Press, NY (1982).
10. Private communication from D. Andrews.
11. M.A. Green, IEEE Transactions on Magnetics, Vol. Mag-17, No. 5, pg. 1855, Karlsruhe (1981).
12. Design Report for the Fermilab Collider Detector Facility, Fermilab (August 1981).
13. Design Report for a Cryostable 3M Diameter SC Solenoid for the Fermilab CDF, TM-1075, Fermilab (Oct. 1981).
14. B. Turck, Cryogenics, 20(3):146(1980). Also see: Stekly, Z.J.J., and Zar, J.G., IEEE Transaction in Nucl. So., NS12:367 (1965).
15. S. Hori, et al., Advances in Cryogenic Engineering, Vol. 27, Plenum Press (1982).
16. Letter of Intent to Study e^+e^- Annihilation Phenomena at LEP, Bari-CERN-Demokritos Athens-Dortmund-Ecole Polytechnique Palaiseau-Edinburgh-Glasgow-Heidelberg-Lancaster-MPI Munchen-Orsay-Pisa-Rutherford-Saclay-Sheffield-Torino-Trieste-Westfield College London-Wisconsin Collaboration, CERN, Geneva (January 1982).



LIST OF PARTICIPANTS

Wade M. Allison Oxford University	William W. Ash SLAC	Muzaffer Atac Fermilab
Maged Atiya Columbia University	William Atwood SLAC	Jean-Eudes Augustin O. Jay
Paul Avery Cornell University	Vladimir E. Balakin Novosibirsk	Joseph Ballam SLAC
Angela Barbaro-Galtieri LBL	Alan Barns LBL	Etienne Barrelet Ecole Polytechnique
Elliott Bloom SLAC	Carlo Bosio Rome	George Brandenburg Harvard University
James Brau SLAC	Wolfgang Braunschweig Aachen	Martin Breidenbach SLAC
Albert E. Brenner Fermilab	Alan Bross LBL	Jean Buon Orsay
David L. Burke SLAC	Mario Calvetti CERN	William Garithers LBL
Matteo Cavalli-Sforza Princeton University	Chung Y. Chang Maryland	Robert L. Chase Orsay
Alexander Chilingarov Novosibirsk	Sergio Cittolin CERN	Allan G. Clark CERN
David Cline Wisconsin	Ernest Coleman DOE, Washington	Donald G. Coyne Princeton University
Huachuan Cui Beijing	Gordon T. Danby Brookhaven	Hobey C. DeStaebler SLAC
Jonathan Dorfan SLAC	Robert Downing Illinois	Richard Ehrlich Cornell University
Tord Johan Carl Ekelof CERN	G. V. Fedotovitch Novosibirsk	Gary J. Feldman SLAC
Michele Ferro-Luzzi CERN	William T. Ford Colorado	Erwin Gabathuler CERN
Irwin Gaines Fermilab	Howard Gordon Brookhaven	Donald Groom Utah
H. Richard Gustafson Michigan	Clifford Hargrove NRC Canada	Neville Harnes Michigan

Don Hartill Cornell University	Henning Hasemann DESY	Clem Heusch UC Santa Cruz
David G. Hitlin Cal Tech	Robert Hollebeek SLAC	Bernard Hyams CERN
Enzo Isrocci Frascati	Seigi Iwata Nagoya	John A. Jaros SLAC
Bernard Jean-Marie Orsay	Hans Jensen Fermilab	Robert Kephart Fermilab
Jasper Kirkby Stanford University	Masaaki Kobayashi KEK	Rainer Kotthaus Max Planck Institute
Hanns Krehbiel DESY	L. M. Kurdadze Novosibirsk	Alfred Ladage DESY
Giuliano Laurenti Bologna	Patrick LeDu Saclay	Wonyong Lee Columbia University
Ivan Lehraus CERN	David W. Leith SLAC	Clark Lindsey UC Riverside
Erich Lohrmann DESY	Adolph Lu UC Santa Barbara	Thomas Ludlam Brookhaven
Gerry Lynch LBL	L. Massonnet Annecy	T. McMahon Rutherford
Karl Hubert Mess DESY	Masanori Mishina KEK	Robert Morse Wisconsin
Robert F. Mozley SLAC	Francesco-Luigi Navarria Bologna	David R. Nygren LBL
Allen C. Odian SLAC	Harold Ogren Indiana	Takayoshi Ohshima Tokyo
A. P. Onuchin Novosibirsk	W. K. H. Panofsky SLAC	V. V. Paselsky Novosibirsk
David Pellett UC Davis	Yuri N. Pestov Novosibirsk	Edward D. Platner Brookhaven
Guenter Poelz Hamburg	Bernard Pope Princeton University	Charles Prescott SLAC
Lawrence Price Argonne	Veljko Radeka Brookhaven	Burton Richter SLAC
David M. Ritson Stanford University	James Roehrig SLAC	Bernard Sadoulet CERN

Noboru Sasao
Kyoto

S. I. Serednjakov
Novosibirsk

Melvyn J. Shochet
Chicago

Eric Siskind
Brookhaven

Karl Strauch
Harvard University

Klaus Tittel
Heidelberg University

Olav Ullaland
CERN

Henri Videau
Ecole Polytechnique

Albert Walenta
Siegen

Fred Wickens
Rutherford

Stanley Wojcicki
Stanford University

Charles Young
SLAC

Dieter Schinzel
CERN

Ronald Settles
Max Planck Institute

V. A. Sidorov
Novosibirsk

A. N. Skrinsky
Novosibirsk

Wolfgang Struczinski
Aachen

Nobukazu Toge
Tokyo

Jean Jacques Veillet
Orsay

Helmut Vogel
Max Planck Institute

Yoshiyuki Watase
KEK

Stephen Williams
SLAC

Wu-guang Yan
Beijing

Thomas Ypsilantis
Ecole Polytechnique

Abraham Seiden
UC Santa Cruz

Stephen L. Shapfro
SLAC

William Sippach
Columbia

E. P. Solodov
Novosibirsk

Richard E. Taylor
SLAC

Walter H. Toki
SLAC

Catherinus Verkerk
CERN

Albrecht Wagner
Heidelberg

Sebastian N. White
Rockefeller

Michael Witherell
UC Santa Barbara

Mingham Ye
Beijing

Yves Goldschmidt-Clermont
CERN